Mathematics and Biosciences in Interaction

SINGLE-CELL-BASED MODELS in BIOLOGY and MEDICINE

Alexander R.A. Anderson
Mark A.J. Chaplain
Katarzyna A. Rejniak

Editors

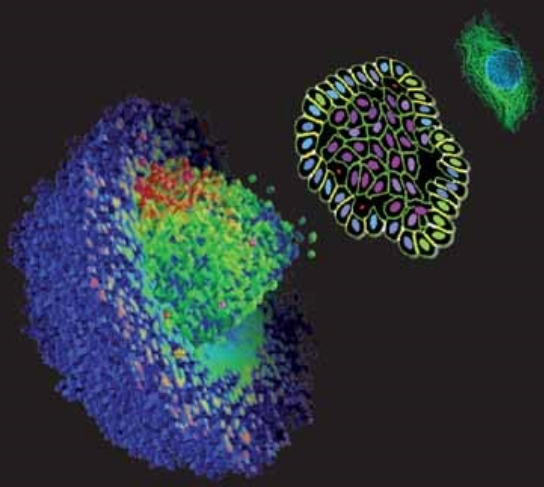

Birkhäuser

Mathematics and Biosciences in Interaction

Managing Editor

Wolfgang Alt
Division of Theoretical Biology
Botanical Institute
University of Bonn
Kirschallee 1
D-53115 Bonn
e-mail: wolf.alt@uni-bonn.de

Editorial Board

Mathematics and Biosciences in Interaction is devoted to the publication of advanced textbooks, monographs, and multi-authored volumes on mathematical concepts in the biological sciences. It concentrates on truly interdisciplinary research presenting currently important biological fields and relevant methods being developed and refined in close relation to problems and results relevant for experimental bioscientists.

The series aims at publishing not only monographs by individual authors presenting their own results, but welcomes, in particular, volumes arising from collaborations, joint research programs or workshops. These can feature concepts and open problems as a result of such collaborative work, possibly illustrated with computer software providing statistical analyses, simulations or visualizations.

The envisaged readership includes researchers and advanced students in applied mathematics – numerical analysis as well as statistics, genetics, cell biology, neurobiology, bioinformatics, biophysics, bio(medical) engineering, biotechnology, evolution and behavioral sciences, theoretical biology, system theory.

SINGLE-CELL-BASED MODELS IN BIOLOGY AND MEDICINE

Alexander R. A. Anderson
Mark A. J. Chaplain
Katarzyna A. Rejniak

Editors

Birkhäuser
Basel • Boston • Berlin

Editors:

Dr. Alexander R.A. Anderson
Division of Mathematics
University of Dundee
23 Perth Road
Dundee DD1 4HN
UK

Dr. Katarzyna A. Rejniak
Division of Mathematics
University of Dundee
23 Perth Road
Dundee DD1 4HN
UK

Prof. Mark A.J. Chaplain
Division of Mathematics
University of Dundee
23 Perth Road
Dundee DD1 4HN
UK

Library of Congress Control Number: 2007923086

Bibliographic information published by Die Deutsche Bibliothek
Die Deutsche Bibliothek lists this publication in the Deutsche Nationalbibliografie;
detailed bibliographic data is available in the Internet at <http://dnb.ddb.de>.

ISBN 978-3-7643-8101-1 Birkhäuser Verlag AG, Basel - Boston - Berlin

Part of Springer Science+Business Media
Printed on acid-free paper produced from chlorine-free pulp. TFC ∞
Cover design: Armando Losa, graphic designer
Cover illustration: The cover image is constructed from the 3-D simulation of a growing tumour by Alexander R.A. Anderson, the 2-D simulation of an epithelial acinus by Katarzyna A. Rejniak and from a real picture of an epithelial cell by David Russell, Division of Cell and Developmental Biology, School of Life Sciences, University of Dundee.

Printed in Germany
ISBN 978-3-7643-8101-1 e-ISBN 978-3-7643-8123-3

9 8 7 6 5 4 3 2 1 www.birkhauser.ch

Contents

General Introduction

> *"Cell and tissue, shell and bone, leaf and flower, are so many portions of matter, and it is in obedience to the laws of physics that their particles have been moved, moulded and conformed. They are no exceptions to the rule that God always geometrizes. Their problems of form are in the first instance mathematical problems, their problems of growth are essentially physical problems, and the morphologist is, ipso facto, a student of physical science".*
> **D'Arcy W. Thompson, "On Growth and Form", 1917.**

As the great D'Arcy Thompson implicitly notes, ever since Newton and his laws of motion, continuum mathematical models have been used to describe the behaviour of "portions of matter" and "particles" in what are essentially discrete physical systems. As a result, much time and effort has been spent in justifying these continuum formulations using methods from, for example, statistical mechanics to "average out" the discreteness of the system to derive the models.

More recently, in the fields of Life and Biomedical Sciences, the past 10–15 years have witnessed enormous advances in our understanding of the molecular basis of cell structure and function. The spectacular success of the human genome project and the consequent burgeoning interest in the related field of proteomics have brought these achievements to the attention not only of the scientific community but also the general public. Biochemists and cell biologists have made similarly impressive strides in elucidating the mechanisms mediating cell signalling and its consequences for the control of cell proliferation, motility and gene expression. It is, however, abundantly clear that reductionist logic using this impressive "sub-cell-level" information base is not sufficient to deduce an understanding of phenomena operating at higher levels of biological organisation. Employing a literary analogy, the vast "omic" databases of catalogued genes and proteins, taken together with our growing understanding of the inner workings of individual cells, provide a "dictionary" and a "grammatical syntax" required for the next great challenge i.e. understanding the "sentences" and "paragraphs" characteristic of emergent higher-level cellular phenomena.

With recent advances in applied mathematics, numerical analysis and computational techniques, multiscale mathematical modelling is now being brought to bear on many challenging problems in the Life and Biomedical Sciences, particularly where cellular systems are concerned. Indeed, in a somewhat ironic twist due to the enhancement of computational processing power, continuum models of discrete systems are frequently approximated by discrete models which can be solved computationally. As computers have become more powerful, there has been renewed interest in mathematical models of biological systems maintaining a discrete formulation from the outset.

In the words of D'Arcy Thompson yet again:
"I know that in the study of material things, number, order and position are the threefold clues to exact knowledge; that these three, in the mathematician's hands, furnish the 'first outlines for a sketch of the Universe'."

The development of new mathematical techniques and their application to biological systems will no doubt be beneficial for "both sides". In the words of David Hilbert, applying mathematics to specific problems is the best way to further develop and deepen one's understanding of the mathematics:
"He who seeks for methods without having a definite problem in mind seeks in the most part in vain. The further a mathematical theory is developed, the more harmoniously and uniformly does its construction proceed, and unsuspected relations are disclosed between hitherto separated branches of the science."

With regard to the specific content of this book, applied mathematics and modelling is sure to benefit from continued interaction with experimentalists working on cellular systems. In recent years many different single-cell-based models have been developed and applied successfully to various biological and medical problems. These models employ very different computational approaches: Monte-Carlo simulations, energy minimisation techniques, volume conservation laws, solutions of the equations of motion for each individual cell or for each point on a cell membrane. They also differ in the level of detail that defines the cell structure and subsequently differ in the number of individual cells that the model can incorporate. The principal aim of this book is to gather together a collection of different mathematical and computational single-cell-based models and present their applications in biology and medicine. This book is addressed equally to students starting their research in the field of mathematical biology and to scientists already modelling multi-cellular processes. Therefore, each chapter contains a detailed description of a particular model and an extensive review of suitable biological and medical applications. This book is also accompanied by a DVD containing simulation movies of all presented models and applications.

What is certain at the present time, and for the foreseeable future, is that interdisciplinary activity between biology and mathematics, with a genuine dialogue between the participating partners, may be viewed as the most fruitful way to advance scientific understanding in both subjects. These are genuinely exciting times to be involved in the subject. Over a century later, the words of David Hilbert are particularly apposite and have a powerful resonance for the application of discrete modelling techniques in the area of cell biology:

"Who of us would not be glad to lift the veil behind which the future lies hidden; to cast a glance at the next advances of our science and at the secrets of its development during future centuries? What particular goals will there be toward which the leading mathematical spirits of coming generations will strive? What new methods and new facts in the wide and rich field of mathematical thought will the new centuries disclose?"

D. Hilbert, opening of his speech to the 1900 Mathematics Congress in Paris.

Finally, the editors of this book would like to express their sincere thanks to all the contributors.

Dundee, February 2007

Single-Cell-Based Models in Biology and Medicine
ed. by A.R.A. Anderson, M.A.J. Chaplain, K.A. Rejniak
Mathematics and Biosciences in Interaction, 1

I. Hybrid Multiscale Models

General Introduction

Many mathematical models of biological process that consider space explicitly, fall into one of two categories: (i) continuum population models or (ii) discrete individual based models. Discrete, stochastic interactions between individual organisms cannot be captured by the continuum approach and likewise global population interactions cannot be captured by the discrete approach. In recent years a third category of models has emerged: hybrid models which allow modellers to exploit the advantages of both continuum and discrete models. The advantages of using such hybrid approaches are clear when dealing with organisms that involve processes at different scales e.g. a cell migrating up a chemical gradient. Such hybrid models are by definition multiscale as they already model interactions between variables that occur on different scales (e.g. micro and macro scale). In this initial section of the book we examine a range of grid based hybrid approaches.

The first chapter from A. Anderson, A Hybrid Multiscale Model of Tumour Invasion: Evolution and Microenvironment, discusses the Hybrid Discrete-Continuum (HDC) technique that uses an initial continuum model as the basis for the derivation of the HDC model. This allows the tumour cells to be represented as discrete individuals with an internal life cycle that describes how they interact with continuum microenvironmental variables and one another. In addition, all cells are assigned phenotypic traits that define their behaviour which, via mitosis, are allowed to mutate using two different mutation algorithms.

In the following chapter from A. Deutsch, Lattice-gas Cellular Automaton Modelling of Developing Cell Systems, in which he defines this cellular automaton approach and examines both via simulation and analysis its dynamical properties. By applying the Boltzmann equations derived from the lattice-gas cellular automata (LGCA) the role of cell-based instabilities is examined. Application of LGCA to both chemotaxis and adhesion is considered.

In third chapter M. Alber presents a Two-dimensional Multiscale Model of Cell Motion in a Chemotactic Field. Focusing on the discrete cellular potts model (CPM) and, by means of a limiting procedure, the equivalent continuous model. In particular, the connection between a CPM of a cell reacting to a chemical field, and a Fokker-Planck equation for the cell probability density function is discussed. The Fokker-Planck equation is then reduced to the classical Keller-Segel equation which is then compared numerically to CPM simulations and shows good agreement.

Single-Cell-Based Models in Biology and Medicine
ed. by A.R.A. Anderson, M.A.J. Chaplain, K.A. Rejniak
Mathematics and Biosciences in Interaction, 3–28

I.1 A Hybrid Multiscale Model of Solid Tumour Growth and Invasion: Evolution and the Microenvironment

Alexander R. A. Anderson

Abstract. Cancer is a complex, multiscale process, in which genetic mutations occurring at a subcellular level manifest themselves as functional changes at the cellular and tissue scale. The importance of tumour cell/microenvironment interactions is currently of great interest to both the biological and the modelling communities. In this chapter we present a hybrid discrete-continuum (HDC) mathematical model of tumour invasion that considers the tumour as a collection of many individual cancer cells that interact with and modify the environment through which they grow and migrate. The HDC model we develop focuses on four key variables implicated in the invasion process: tumour cells, host tissue (extracellular matrix), matrix-degradative enzymes and oxygen. The model is considered to be hybrid since the latter 3 variables are continuous (i.e. concentrations) and the tumour cells are discrete (i.e. individuals). We shall examine how individual-based cell interactions (with one another and the microenvironment) can affect the tumour morphology. We will also discuss the evolutionary influence that the microenvironment has upon the tumours genetic makeup. The HDC model focuses on the microscale (individual cell) level to produce computational simulations of tumour at the tissue scale. As we shall discuss, this technique, developed in previous models of nematode migration and angiogenesis, is intrinsically multiscale and can easily incorporate a range of scales i.e. genetic, sub-cellular, cellular and tissue.

1. Tumour Invasion

The development of a primary solid tumour (e.g. a carcinoma) begins with a single normal cell becoming transformed as a result of mutations in certain key genes. This transformed cell differs from a normal one in several ways, one of the most notable being its escape from the body's homeostatic mechanisms, leading to inappropriate proliferation. An individual tumour cell has the potential, over successive divisions, to develop into a cluster (or nodule) of tumour cells. Further growth and

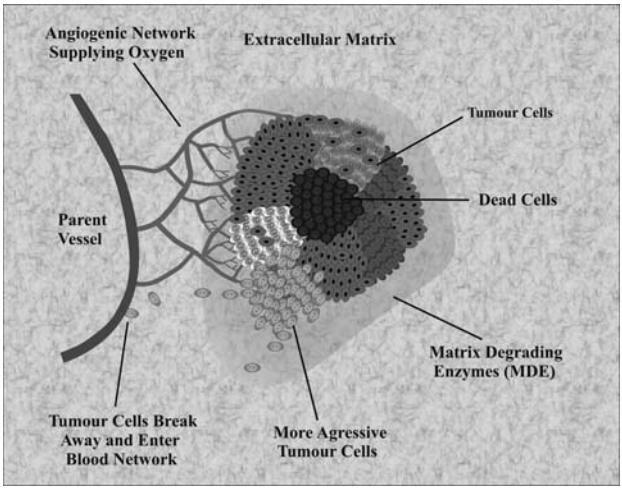

FIGURE 1. Schematic diagram showing the key variables involved in solid tumour growth: Tumour cells, extracellular matrix, matrix degrading enzyme and oxygen. The tumour contains a heterogeneous population of cells with varying degrees of aggressiveness.

proliferation leads to the development of an avascular tumour consisting of approximately 10^6 cells. Since the tumour is dependent on diffusion as the only means of receiving nutrients and removing waste products its growth is limited. For any further development to occur the tumour must initiate angiogenesis–the recruitment of blood vessels from a pre-existing vascular network. Once angiogenesis is complete, the perfused vascular network can supply the tumour with the nutrients it needs to grow further. There is also now the possibility of tumour cells finding their way into the circulatory system (via the vascular network) and being deposited at distant sites in the body, resulting in metastases (secondary tumours). Clearly angiogenesis, the process which results in the tumour having a vascular network, is a key process for metastatic invasion (see Fig.1).

Central to the invasive process are the molecules that facilitate interactions between cells and between cells and the *extracellular matrix* (ECM), known as cell adhesion molecules. A common feature of cell adhesion molecules is their ability to function as a molecular bridge between an external ligand and the cytoskeleton within the cell [13]. Over the past few years, it has become clear that receptors that mediate cell adhesion do not just affect cell migration, since occupancy of cell-surface receptors results in the initiation of signal-transduction pathways that regulate many aspects of cell function [13, 29] including transcription, proliferation, differentiation, cytoskeletal organisation and receptor activation [16].

A crucial part of the invasive/metastatic process is the ability of the cancer cells to degrade the surrounding tissue or *extracellular matrix* (ECM) [46]. This is a complex mixture of macromolecules (MM), some of which, like the collagens, play

a structural role and others (such as laminin, fibronectin and vitronectin) are important for cell adhesion, spreading and motility. We note that all of these macromolecules are *bound* within the tissue, i.e. they are non-diffusible. The ECM can also sequester growth factors and itself be degraded to release fragments which can have growth-promoting activity. Thus, while the ECM may have to be physically removed in order to allow a tumour to spread, its degradation may, in addition, have biological effects on tumour cells.

A number of *matrix degradative enzymes* (MDEs) such as the *plasminogen activator* (PA) system and the large family of *matrix metalloproteinases* (MMPs) have been described [50] and both of these have been repeatedly implicated in tumour invasion and metastasis. In addition to opening migratory pathways, MDEs can alter cell adhesion properties regulated through several classes of cell surface receptors. These receptors, including cadherins, CD-44, integrins, and receptors for fibronectin, laminin, and vitronectin, negatively regulate cell motility and growth through cell-cell and cell-matrix interactions [46]. Therefore, proteolytic degradation of receptor and/or ECM components could release tumour cells from these constraints. Recent studies have shown that CD-44 mediates the attachment of cells to various MM, in fact invasion of human glioma cells has been inhibited by antibodies against CD-44 [33]. Molecules which facilitate interactions between cells and between cells and the ECM, known as cell adhesion molecules, are now thought to be central to the invasive process [29]. Therefore it is important for any model that considers tumour invasion to include both cell-cell and cell-matrix interactions.

Tumour heterogeneity at the genetic level is well known and the so called "Guardian of the Genome", the p53 gene is widely considered as a precursor to much wider genetic variation [34]. The p53 protein links three cellular functions: proliferation, death and DNA repair. In normal cells, p53 blocks proliferation and enables damaged DNA to be repaired. If DNA repair is incomplete, apoptosis is initiated and the cell dies. Loss of p53 function (e.g. through mutation) allows for the propagation of damaged DNA to daughter cells [34]. Once the p53 mutation occurs many more mutations can easily accrue, these changes in the tumour cell genotype ultimately express themselves as behavioural changes in cell phenotype. As a step towards the inclusion of true tumour heterogeneity we shall consider a tumour that has phenotypic heterogeneity. The tumour cell phenotype will be defined here in terms of the level of a cell's aggressiveness, i.e. a combination of its cell-cell adhesiveness, proliferation, degradation and migration rates (further details will be discussed below).

The importance of the tumour microenvironment is currently of great interest to both the biological and the modelling communities. In particular, both the immediate microenvironment (cell-cell or cell-matrix interactions) and the extended microenvironment (e.g. vascular bed) are thought to play crucial roles in both tumour progression and suppression (see the recent series of papers in Nature Reviews Cancer for further detail, [2, 11, 39]). Aggressive tumours are often described as having an invasive phenotype, characterised by fingering margins as opposed

to more benign tumours which are characterised by smooth non-invasive margins. Recently it has been shown that not only can the microevironment promote tumour progression but it can also drive the invasive tumour phenotype. The work of Weaver [40] focuses on the impact of tissue tension in driving the invasive phenotype and clearly correlates higher tension in the tissue (a harsher environment) with an invasive phenotype. Similarly Pennacchietti [41] has shown a relationship between a hypoxic tumour microenvironment (again a harsher environment) and the invasive phenotype.

2. Hybrid Discrete-Continuum Technique

When deciding which model should be used, the number and scale of the organisms being modelled is important and the manner in which the organisms interact with their environment and each other is also important. Discrete, stochastic interactions between organisms cannot be captured by the continuum approach and likewise global population interactions cannot be captured by the discrete approach. Therefore the most appropriate modelling technique depends on both the number of organisms and scale at which they are being studied.

Over the last ten years or so many mathematical models of tumour growth, both temporal and spatio-temporal, have appeared in the research literature (see [20] for a review of many of these and for a more recent review see [10]). Deterministic reaction-diffusion equations have been used to model the spatial spread of tumours both at an early stage in its growth [44, 51] and at the later invasive stage [37, 26, 42, 5, 47, 48]. Typical solutions observed in all these models [37, 26, 42, 14] appear as invading travelling waves of cancer cells. Whilst these models are able to capture the tumour structure at the tissue level, they fail to describe the tumour at the cellular level and subsequently the subcellular level. On the other hand, cellular automata models provide such a description and allow a more realistic stochastic approach at both the cellular ([32, 45, 43, 7, 31, 21]) and subcellular levels [22, 23].

The model presented here is of a different type: we classify this as "Hybrid", since a continuum deterministic model (based on a system of reaction-diffusion-chemotaxis equations) controls the chemical/ECM dynamics and a discrete cellular automata like model (based on a biased random-walk model) controls the cell migration and interaction. Initially we define a system of coupled nonlinear partial differential equations to model tumour invasion of surrounding tissue. We then use a discretised form of the partial differential equation governing cell migration as the basis for the hybrid discrete-continuum model. This then enables specific cell properties to be modelled at the level of the individual cell, we shall consider proliferation, death, cell-cell adhesion, mutation, and production/degradation at the individual cell level. The crucial point of this technique is that it allows cells to be treated as discrete individuals and the cell processes to be modelled at the level of the cell whilst allowing the the chemicals/ECM to be treated as continuous. A

detailed discussion on the types of system that this technique is applicable to is given in [6]. Applications of the technique can be found in [3]–[9].

In the last few years there has been a rapid development in such hybrid models in application to tumour growth. The work of Deutsch [36], Deisboeck [52] and Alarcon [1] have all coupled individual tumour cells with continuous chemical dynamics. However, non of these has explicitly modelled the direct impact of the microenvironment upon both the tumour cell population at the phenotype scale and the resulting changes in tumour geometry at the organ scale.

The aim of this chapter is to show how the tumour microenvironment impacts directly upon both tumour morphology and tumour heterogeneity. By using a combination of different microenvironments (e.g. homogeneous, heterogeneous tissue, low/high nutrient concentration) with different mutation algorithms (i.e. linear or random) we will show that how aggressiveness of a tumour is directly correlated with the microenvironment in which it grows.

3. The Continuum Model

We will base our mathematical model on the growth of a generic three dimensional solid tumour. We will model both the full three dimensional tumour volume and a two dimensional slice through this, one cell diameter thick. We choose to focus on four key variables involved in tumour invasion, thereby producing a minimal model, namely; tumour cell density (denoted by n), MDE concentration (denoted by m), MM concentration (denoted by f) and oxygen concentration (denoted by c), see Fig.1. Initially we define a system of coupled nonlinear partial differential equations to model tumour invasion of surrounding tissue and use these as the basis for the *Hybrid Discrete-Continuum* (HDC) technique.

The complete system of equations describing the interactions of the tumour cells, MM, MDEs and oxygen is

$$\begin{aligned}
\frac{\partial n}{\partial t} &= \overbrace{D_n \nabla^2 n}^{random\ motility} - \overbrace{\chi \nabla \cdot (n \nabla f)}^{haptotaxis}, \\
\frac{\partial f}{\partial t} &= - \overbrace{\delta m f}^{degradation}, \\
\frac{\partial m}{\partial t} &= \overbrace{D_m \nabla^2 m}^{diffusion} + \overbrace{\mu n}^{production} - \overbrace{\lambda m}^{decay}, \\
\frac{\partial c}{\partial t} &= \overbrace{D_c \nabla^2 c}^{diffusion} + \overbrace{\beta f}^{production} - \overbrace{\gamma n}^{uptake} - \overbrace{\alpha c}^{decay},
\end{aligned} \tag{1}$$

were D_n, D_m and D_c are the tumour cell, MDE and oxygen diffusion coefficients respectively, χ the haptotaxis coefficient and δ, μ, λ, β, γ and α are positive constants. We should also note that cell-matrix adhesion is modelled here by the use of haptotaxis in the cell equation i.e. directed movement up gradients of MM. Therefore χ maybe considered as relating to the strength of the cell-matrix adhesion.

Since this model has already been published [8, 9] we will not discuss its derivation here. However, some explanation should be given to the manner in which oxygen is modelled. Oxygen is assumed to diffuse into the MM, decay naturally and be consumed by the tumour. For simplicity oxygen production is proportional to the MM density, this might be considered as modelling the pre-existing blood supply. This is a crude way of modelling an angiogenic oxygen supply, see Anderson & Chaplain [4] for a more appropriate way of modelling the angiogenic network. Since oxygen production is directly proportional to MM density, as the MM is degraded the oxygen production will drop.

The above system of equations can be used to model both two- and three-dimensional tumour invasion. In 2D the system is considered to hold on a square of tissue Ω of length L, while in 3D it holds on a cube of tissue Ω of side L both with appropriate initial conditions for each variable. We assume that the MM, oxygen, tumour cells and consequently the MDEs, remain within the domain of tissue under consideration and therefore no-flux boundary conditions are imposed on $\partial\Omega$, the boundary of Ω.

3.1. Non-dimensionalisation and Parameterisation

In order to use realistic parameter values we first of all non-dimensionalise the equations in the standard way. We rescale distance with an appropriate length scale L (e.g. the maximum invasion distance of the cancer cells at this early stage of invasion, approximately 1cm), time with τ (e.g. the average time take for mitosis to occur, approximately $8-24$hrs [15], tumour cell density with n_0, ECM density with f_0, MDE concentration m_0 and oxygen concentration with c_0 (where n_0, f_0, m_0, c_0 are appropriate reference variables). Therefore setting

$$\tilde{n} = \frac{n}{n_0},\ \tilde{f} = \frac{f}{f_0},\ \tilde{m} = \frac{m}{m_0},\ \tilde{c} = \frac{c}{c_0},\ \tilde{\mathbf{x}} = \frac{\mathbf{x}}{L},\ \tilde{t} = \frac{t}{\tau}$$

in Eq.(1) and dropping the tildes for notational convenience, we obtain the scaled system of equations:

$$\begin{aligned}
\frac{\partial n}{\partial t} &= \overbrace{d_n\nabla^2 n}^{random\ motility} - \overbrace{\rho\nabla\cdot(n\nabla f)}^{haptotaxis},\\
\frac{\partial f}{\partial t} &= -\overbrace{\eta m f}^{degradation},\\
\frac{\partial m}{\partial t} &= \overbrace{d_m\nabla^2 m}^{diffusion} + \overbrace{\kappa n}^{production} - \overbrace{\sigma m}^{decay},\\
\frac{\partial c}{\partial t} &= \overbrace{d_c\nabla^2 c}^{diffusion} + \overbrace{\nu f}^{production} - \overbrace{\omega n}^{uptake} - \overbrace{\phi c}^{decay},
\end{aligned} \tag{2}$$

where $d_n = \tau D_n/L^2,\ \rho = \tau\chi f_0/L^2,\ \eta = \tau m_0\delta,\ d_m = \tau D_m/L^2,\ \kappa = \tau\mu n_0/m_0,\ \sigma = \tau\lambda,\ d_c = \tau D_c/L^2,\ \nu = \tau f_0\beta/c_0,\ \omega = \tau n_0\gamma/c_0,\ \phi = \tau\alpha.$

The cell cycle time depends on the specific tumour under consideration, as a rough guide we take $\tau = 16$hrs, halfway between $8 - 24$hrs [15]. The cell motility parameter $D_n \sim 10^{-9}\text{cm}^2\text{s}^{-1}$ was estimated from available experimental evidence [12]. Tumour cell diameters again will vary depending on the type of tumour being considered but are in the range $10 - 100\mu m$ [35] with an approximate volume of $10^{-9}cm^3 - 3 \times 10^{-8}cm^3$, [25, 17]. We will assume that a tumour cell has the volume $1.5 \times 10^{-8}cm^3$ and therefore take $n_0 = 6.7 \times 10^7$ cells$/cm^3$. The haptotactic parameter $\chi \sim 2600\text{cm}^2\text{s}^{-1}\text{M}^{-1}$ was estimated to be in line with that calculated in Anderson *et al.* [4] and the parameter $f_0 \sim 10^{-8} - 10^{-11}$M was taken from the experiments of Terranova *et al.* [49]. We took D_m to be $10^{-9}\text{cm}^2\text{s}^{-1}$, which is perhaps small for a diffusing chemical, but recent experimental evidence implies that it is in fact a combination of the MDE and MM which results in degradation of the MM and that this bound chemical diffuses very little [28]. An *in vivo* estimate for the MDE concentration m_0 is somewhat difficult to obtain since there is currently no published value (that we are aware of). Plasma levels of specific MDEs have been measured (e.g. MMP-2, [53]) and are approximately $130ng/ml$ with further increases observed in patients with cancer [30]. How this relates to the MDE concentration within the ECM is not clear, we have therefore left this parameter undefined. Estimates for the kinetic parameters μ, λ, δ were not available since these are very difficult to obtain experimentally, we therefore use the values of [4]. Oxygen is known to diffuse through water at a rate of $D_c = 10^{-5}\text{cm}^2\text{s}^{-1}$ and cells consume oxygen at a rate of $6.25 \times 10^{-17}\text{Mcell}^{-1}\text{s}^{-1}$[17]. The background oxygen concentration within the tissue was somewhat difficult to estimate, we shall use $c_0 = 6.7 \times 10^{-6}\text{MO}_2\text{cm}^{-3}$ as discussed in [8].

4. The Discrete Model

Now that we have defined the continuum model of tumour invasion we can implement the hybrid discrete-continuum technique (see [3]–[9]) which will allow us to follow the paths of individual tumour cells. This first involves discretising (using standard finite-difference methods) the system of partial differential equations (2). We then use the resulting coefficients of the finite-difference stencil to generate the probabilities of movement of an individual cell in response to its local milieu (see Appendix of [5] for the full discrete system). Once the movement probabilities have been defined, both two and three dimensions will be discussed, we then consider the specific individual based processes that we will incorporate into the model.

4.1. Two Dimensions

As an illustration of the technique we only consider the tumour cell equation and discretise Eq.(2) in two spatial dimensions using central finite difference approximations to obtain the following,

$$n_{i,j}^{q+1} = n_{i,j}^q P_0 + n_{i+1,j}^q P_1 + n_{i-1,j}^q P_2 + n_{i,j+1}^q P_3 + n_{i,j-1}^q P_4. \tag{3}$$

where the subscripts specify the location on the grid and the superscripts the time steps. That is $x = ih$, $y = jh$ and $t = qk$ where i, j, k, q and h are positive parameters. In a numerical simulation of the continuous model Eq.(2), the purpose of the discrete equation Eq.(3) is to determine the tumour cell density at grid position (i, j), and time $q + 1$, by averaging the density of the four surrounding neighbours at the previous time step q. However, for the HDC technique, we will use the five coefficients P_0 to P_4 from Eq.(3) to generate the motion of an individual tumour cell. The central assumption of the HDC technique is that these five coefficients can be thought of as being proportional to the probabilities of a cell being stationary (P_0) or moving west (P_1), east (P_2), south (P_3) or north (P_4) one grid point (h) at each time step (k).

The coefficient P_0, which is proportional to the probability of no movement, has the form,

$$P_0 = 1 - \frac{4kD_n}{h^2} - \frac{k\rho}{h^2}\left(f^q_{i+1,j} + f^q_{i-1,j} - 4f^q_{i,j} + f^q_{i,j+1} + f^q_{i,j-1}\right), \tag{4}$$

and the coefficients P_1 ,P_2 ,P_3 and P_4, which are proportional to the probabilities of moving west, east, south and north respectively, have the forms,

$$\begin{aligned} P_1 &= \frac{kD}{h^2} - \frac{k\rho}{4h^2}\left[f^q_{i+1,j} - f^q_{i-1,j}\right], \\ P_2 &= \frac{kD}{h^2} + \frac{k\rho}{4h^2}\left[f^q_{i+1,j} - f^q_{i-1,j}\right], \\ P_3 &= \frac{kD}{h^2} - \frac{k\rho}{4h^2}\left[f^q_{i,j+1} - f^q_{i,j-1}\right], \\ P_4 &= \frac{kD}{h^2} + \frac{k\rho}{4h^2}\left[f^q_{i,j+1} - f^q_{i,j-1}\right], \end{aligned} \tag{5}$$

where the subscripts specify the location on the grid and the superscripts the time steps, all parameters are positive and are as discussed above. From these we see that if there were no MM the values of P_1 to P_4 would be equal, with P_0 smaller (or larger, depending on the precise values chosen for the space and time steps) i.e. there is no bias in any one direction and the tumour cell is less (more) likely to be stationary - approximating an unbiased random walk. However, if there are gradients in the MM, haptotaxis contributes to the migration process and the coefficients P_1 to P_4 will become biased towards the direction of increased MM concentration. The equation P_0 represents the probability of a cell being stationary and takes into account the situation when a single cell does not experience a gradient between neighboring points because they contain equal concentrations of MM; if neighbouring points contain higher (lower) MM concentrations, the probability of being stationary is diminished (increased) by the sign and magnitude of the term $\left(f^q_{i+1,j} + f^q_{i-1,j} - 4f^q_{i,j} + f^q_{i,j+1} + f^q_{i,j-1}\right)$ see Anderson [8] for a full derivation. The motion of an individual cell is therefore governed by its interactions with the matrix macromolecules in its local environment. Of course the motion will also be modified by interactions with other tumour cells.

4.2. Three Dimensions

This technique can easily be extended to three dimensions by employing the same standard finite-difference methods but this time we use the resulting coefficients of the seven-point finite-difference stencil to generate the probabilities of movement of an individual cell in response to its environment. Again, we only consider the discrete tumour cell equation:

$$\begin{aligned} n^{q+1}_{i,j,w} = n^q_{i,j,w}P_0 &+ n^q_{i+1,j,w}P_1 + n^q_{i-1,j,w}P_2 + n^q_{i,j+1,w}P_3 \\ &+ n^q_{i,j-1,w}P_4 + n^q_{i,j,w+1}P_5 + n^q_{i,j,w-1}P_6, \end{aligned} \tag{6}$$

The coefficient P_0, which is proportional to the probability of no movement, has the form,

$$\begin{aligned} P_0 = 1 - \frac{6kD_n}{h^2} - \frac{k\rho}{h^2}(f^q_{i+1,j,w} &+ f^q_{i-1,j,w} + f^q_{i,j,w+1} - 6f^q_{i,j,w} \\ &+ f_{i,j,w-1} + f^q_{i,j+1,w} + f^q_{i,j-1,w}), \end{aligned} \tag{7}$$

and the coefficients P_1, P_2, P_3, P_4, P_5, P_6 which are proportional to the probabilities of an individual tumour cell moving west, east, south, north, down, or up respectively, have the forms,

$$\begin{aligned} P_1 &= \frac{kD}{h^2} - \frac{k\rho}{4h^2}\left[f^q_{i+1,j,w} - f^q_{i-1,j,w}\right], \\ P_2 &= \frac{kD}{h^2} + \frac{k\rho}{4h^2}\left[f^q_{i+1,j,w} - f^q_{i-1,j,w}\right], \\ P_3 &= \frac{kD}{h^2} - \frac{k\rho}{4h^2}\left[f^q_{i,j+1,w} - f^q_{i,j-1,w}\right], \\ P_4 &= \frac{kD}{h^2} + \frac{k\rho}{4h^2}\left[f^q_{i,j+1,w} - f^q_{i,j-1,w}\right], \\ P_5 &= \frac{kD}{h^2} - \frac{k\rho}{4h^2}\left[f^q_{i,j,w+1} - f^q_{i,j,w-1}\right], \\ P_6 &= \frac{kD}{h^2} + \frac{k\rho}{4h^2}\left[f^q_{i,j,w+1} - f^q_{i,j,w-1}\right], \end{aligned} \tag{8}$$

where the subscripts specify the location on the grid and the superscripts the time steps. That is $x = ih$, $y = jh$, $z = wh$ and $t = qk$ where i, j, w, k, q and h are positive parameters.

These seven probabilities P_0 to P_6 from Eq.(7) and Eq.(8) are used to generate the motion of each tumour cell in three spatial dimensions. As with the two dimensional probabilities, they are functions of the local MM concentration and therefore the motion of an individual cell is governed by its interactions with the the local MM environment and with one another.

4.3. Individual-Based Processes

Since we model individual tumour cells we have the ability to incorporate individual based processes. We now discuss in detail the processes each tumour cell will experience as it migrates through the MM field, driven by either the two-dimensional or three-dimensional movement probabilities defined in the above sections. As a step towards the inclusion of true tumour heterogeneity we shall consider a tumour that has phenotypic heterogeneity. The tumour cell phenotype

will be defined here by the level of the cell's aggressiveness, i.e. a combination of its cell-cell adhesiveness, proliferation, degradation and migration rates (see cell phenotype paragraph below).

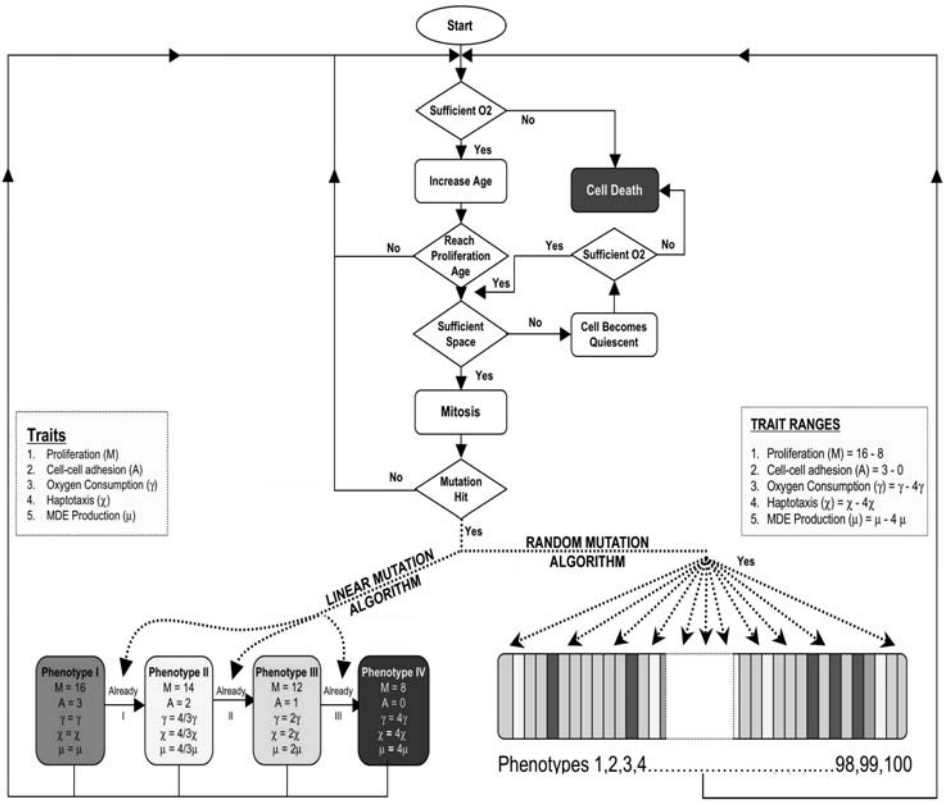

FIGURE 2. Flowchart of the tumour cell life-cycle within the hybrid discrete-continuum simulation. At the point where a mutation can occur, either follow the linear mutation algorithm only, or the random mutation algorithm only. See text for further details.

Life Cycle

Fig.2 shows a flowchart of a tumour cell's "life-cycle" within the hybrid discrete-continuum simulation. At each time step a tumour cell will initially check if it can move with regards to cell-cell adhesion restrictions (see the next paragraph for criteria), if it can, then the movement probabilities (above) are calculated and the cell is moved. A check is then made to see if there is sufficient oxygen for the cell to survive (see the paragraph on necrosis) if not, the cell dies. If there is sufficient oxygen, the cells age is increased and a check is performed to see if it has reached proliferation age. If it has not reached this age then it starts the whole loop again.

If proliferation age has been reached then a check is made to see if the criteria for proliferation are satisfied (see proliferation paragraph for details). If proliferation criteria are not met then the cell becomes quiescent. If they are satisfied then we check to see if this mitosis results in a mutation hit. All mutations in a particular simulation will be assumed to occur in either a Linear (Fig.2, left) or Random (Fig.2, right) manner (see mutation paragraph for details). This whole process is repeated at each time step of the simulation.

Cell-Cell Adhesion
To model cell-cell adhesion explicitly we assume each cell has its own internal adhesion value (A_i, see Table 1) i.e. the number of neighbours that it will preferentially adhere to. We therefore examine the number of external neighbours each cell has (A_e) and if $A_e \geq A_i$ then the cell is allowed to migrate, otherwise it remains stationary. Whilst this is a somewhat crude way of modelling cell adhesion, it does capture some features of cell-cell adhesion e.g. certain cells are more likely to bind to others and in so doing restrict their own ability to migrate.

Necrosis
For a tumour cell to survive it requires sufficient oxygen, since some tumour cells have been found to survive in very poorly oxygenated environments, we make the assumption that the concentration has to drop to 0.05 non-dimensional units (where 1 would be the initial concentration) for cell death to occur. This assumption is also applied to quiescent tumour cells. The space that dead cells occupy becomes available to new cells as soon as they die.

Proliferation
In our model we assume that each individual cell has the capacity for proliferation and will produce two daughter cells, provided: (i) the parent cell has reached maturity (Mhrs, see Table 1) and (ii) there is sufficient space surrounding the parent cell for the two new daughter cells to occupy. In order to satisfy condition (ii), we assumed that one daughter cell replaces the parent cell and the other daughter cell will move to any one of the parent cell's four orthogonal neighbours that is

Phenotype	Proliferation Age M	O_2 Uptake	MDE Production	A_i	Haptotaxis
Linear I (orange)	16hrs	ω	κ	3	ρ
Linear II (green)	14hrs	$4/3\omega$	$4/3\kappa$	2	$4/3\rho$
Linear III (cyan)	12hrs	2ω	2κ	1	2ρ
Linear IV (blue)	8hrs	4ω	4κ	0	4ρ
Random	$8-16$hrs	$\omega-4\omega$	$\kappa-4\kappa$	$0-3$	$\rho-4\rho$

TABLE 1. Parameter values for each of the four different Phenotypes in the linear mutation algorithm as well as the ranges for each trait in the random mutation algorithm. Colours are used to identify the different phenotypes in the simulation results.

empty. If more than one of the neighbouring grid points is empty then the new cell position is chosen randomly from these points. If no empty neighbours exist then the cell becomes quiescent and proliferation is delayed until space becomes available. We therefore do not consider the possibility that cells may push neighbouring cells to create free space in which to proliferate. Quiescent tumour cells are assumed to consume half the oxygen of tumour cells [24].

Production/Degradation/Diffusion
Since we are modelling individual tumour cells we must consider MDE production at the level of a single cell. In the continuum model Eq.(2) we have MDE production as being proportional to the tumour cell density. Now MDE is only produced at a grid point if a tumour cell is occupying that grid point. Since we have no precise parameter estimates for this production rate, we take $n = 1$ in the discrete form of the MDE equation when a tumour cell is occupying the current location and take $n = 0$ otherwise. Similarly for O_2 uptake, we take $n = 1$ (since ω is scaled as per cell) in the discrete form of the oxygen equation when a cell is consuming oxygen at the current location and $n = 0$ otherwise. Since the tumour cells occupy physical space within the ECM we should consider how this might impact upon oxygen diffusion. It seems logical that oxygen diffusion will be reduced as the space occupied by the tumour increases, this is consistent with tumour spheroid results i.e. as the spheroid diameter increases the necrotic region also increases. To model this at the individual level, we assume that oxygen diffusion decreases at the grid point a tumour cell occupies i.e. the oxygen diffusion rate at that grid point will be $d_{c_{cell}} < d_c$.

Cell Phenotype
Each cell has predefined phenotypic traits that describe its behaviour. We have chosen these phenotypes based on the current views of the invasive phenotype [27]. Table 1 shows the different values each phenotype takes and clearly type IV is the most aggressive, having the shortest proliferation age, consuming the most O_2, producing the most MDE, having the largest haptotaxis coefficient and requiring no neighbours for migration. We have chosen to correlate tumour cell aggressiveness with proliferation age, O_2 uptake, MDE production, cell-cell adhesion coefficient and haptotaxis coefficient. We assume that O_2 uptake, MDE production and haptotaxis coefficients all increase and the proliferation age and adhesion coefficients decrease as the tumour cell phenotype becomes increasingly aggressive.

Mutation Algorithm
Since the manner in which tumour cell mutation is modelled will directly impact on the cell life-cycle flowchart and consequently the resulting tumour population heterogeneity, we will consider two different mutation algorithms: (a) Linear (Fig.2, left) and (b) Random (Fig.2, right). (a) In the linear algorithm, all cells are initially assigned the values of phenotype I (as defined in Table 1, the least aggressive). For each subsequent proliferation there is a small probability (P_{mutat}) of further mutations occurring which will lead to phenotype II and so on in a linear fashion.

All mutations in the linear algorithm are assumed to be irreversible. (b) The random mutation algorithm on the other hand does allow mutations to be reversible, albeit within the constraints of the 100 randomly pre-defined phenotypes, as each of these phenotypes has an equal probability of being selected (see Fig.2, right). Each of the 100 phenotypes will have a randomly selected proliferation age, O_2 consumption, MDE production, haptotaxis coefficient and adhesion value all within the ranges of values defined in Table 1. Each initial cell is assigned the values of one of the 100 randomly selected phenotypes and for each subsequent proliferation there is a small probability (P_{mutat}) of further mutations occurring which will lead to another randomly selected phenotype and so on.

4.4. Simulation Process for the Hybrid Discrete-Continuum Model

Each time step of the simulation process involves solving the discrete form of the system Eq.(2) numerically to generate the five coefficients P_0 to P_4, Eqs.(4)–(5), in two dimensions (in three dimensions we generate the seven coefficients P_0 to P_6 using Eqs.(7)–(8)). We then normalise these coefficients to obtain the corresponding final probabilities of motion, where normalisation simply means division by the total of the five coefficients. Probability ranges are then computed by summing the coefficients to produce 5 ranges (in two dimensions), $R_0 = 0$ to P_0 and $R_i = \sum_{j=0}^{i-1} P_j$ to $\sum_{j=0}^{i} P_j$, where $i = 1$ to 4. In three dimensions we similarly compute 7 probability ranges, $R_0 = 0$ to P_0 and $R_i = \sum_{j=0}^{i-1} P_j$ to $\sum_{j=0}^{i} P_j$, where $i = 1$ to 7. We then generate a random number between 0 and 1, and depending on the range which this number falls in, the current individual tumour cell under consideration will remain stationary (R_0) or move west (R_1), east (R_2), south (R_3) or north (R_4) in two dimensions, and additionally can move down (R_5) or up (R_6) in three dimensions. The larger a particular range, the greater the probability that the corresponding coefficient will be selected. Each tumour cell is therefore restricted to move to one of its four orthogonal neighbouring grid points (and additionally can move either up or down in three dimensions) or remain stationary at each time step.

All cells are given a unique identification number which is assigned as each new cell is produced (or is assigned initially for the first 50 cells). Each time step of the simulation involves firstly updating all of the cells positions (via the identification number i.e. the larger the identification number the later the update) then secondly updating the individual based processes for all the cells e.g. proliferation, death, mutation. Therefore cells are not updated simultaneously or in a left-to-right, top-to-bottom manner but as per the identification number. For the migration part of the update the identification method gives preference to cells which have smaller identification values (since they get to move before the others do) but since the cells are distributed all over the tumour this should not introduce any visible bias. Once the cells have moved the individual based processes are updated and this is done again per cell identification number but this time the

cells update as soon as a process occurs e.g. proliferation, this should avoid any conflicts for space.

5. HDC Simulation Results

Now that we have discussed the HDC model of tumour invasion in detail we shall use it to examine the impact of different microenvironments (e.g. homogeneous, heterogeneous tissue, low/high nutrient concentration) in combination with different mutation algorithms (i.e. linear or random). Most of the results will be presented in two dimensions, but in the final results section we consider tumour invasion in a random three dimensional tissue.

5.1. Invasion In Two Dimensions

The following simulations were carried out on a 400×400 grid, which is a discretisation of the unit square, $[0,1] \times [0,1]$, with a space step of $h = 0.0025$ and a time step of $k = 0.0005$. Note that with this choice of space step each square of grid is approximately the same area as a tumour cell i.e. $6.25 \times 10^{-6} cm^2$ (or $1.56 \times 10^{-8} cm^2$ as a volume, with cells of side $0.0025cm$). No flux boundary conditions were imposed on the square grid, restricting the tumour cells, MDE, MM and oxygen to within the grid. Initially, 50 tumour cells are centred around $(0.5, 0.5)$ with an assigned phenotype I, a random age between $0hrs - 16hrs$, the MDE concentration is zero throughout the domain ($m(x,y) = 0$) and the oxygen concentration is taken to be one ($c(x,y) = 1$). We consider the effects, upon tumour invasion, of three different MM initial distributions: (i) homogeneous ($f(x,y) = 1$), (ii) heterogeneous ($0 \leq f(x,y) \leq 1$), with f(x,y) being generated from a combination of sin and cos functions of the x and y directions and (iii) random ($0 \leq f(x,y) \leq 1$) in combination with two different mutation algorithms: (A) Linear and (B) Random. For clarity we shall label the resulting tumour cell distributions as A(i) homogeneous tumour, A(ii) heterogeneous tumour and A(iii) random tumour for the Linear mutation algorithm and similarly for the Random mutation algorithm but use the labels B(i), B(ii) and B(iii) for homogeneous, heterogeneous and random respectively. The non-dimensional parameter values used in all the following simulations are $d_n = 0.0005$, $d_m = 0.0005$, $d_c = 0.5$,$d_{c_{cell}} = 0.25$, $\rho = 0.01$, $\eta = 50$, $\kappa = 1$, $\sigma = 0$, $\nu = 0.5$, $\omega = 0.57$ and $\phi = 0.025$. We also take the phenotype mutation probability to be $P_{mutat} = 0.1$. Other values were considered and produced similar results but for shorter or longer times depending on whether the probability was larger or smaller.

Fig.3 shows the resulting tumour cell populations from simulations using either the linear or random mutation algorithms along with each of the three different initial MM distributions at $t = 200$ time units. What is immediately apparent is that all of the tumour cell distributions show a mainly dead central region with a thin dispersed proliferating boundary. What is also clear is that the tumours that grew in the homogeneous MM distribution, A(i) and B(i), have a more circular and symmetric morphology in contrast to those grown in the heterogeneous or random MM distributions, A(ii), A(iii), B(ii), and B(iii), which

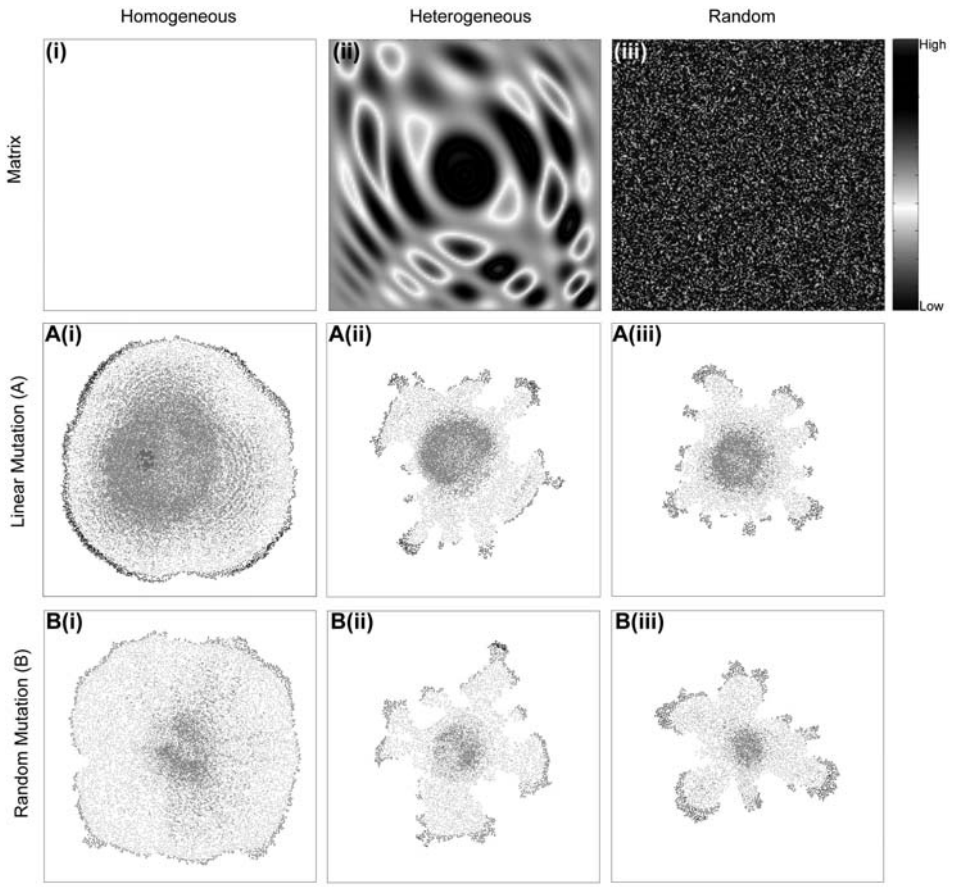

FIGURE 3. HDC tumour simulation results, at time $t = 200$ units, using three different initial MM distributions: (i) homogeneous, (ii) heterogeneous and (iii) random (upper row), using either the linear (middle row, A) or random (lower row, B) mutation algorithms. Density of MM is represented by colouration, as depicted in the color bar on the right. Cell colouration reflects dead cells (brown) or cell-cell adhesion (zero cell-cell adhesion = blue). For the linear mutation algorithm, blue also represents the most agressive phenotype (type IV, see Table 1). Simulation movies showing the growth of the tumour as well as the other three variables (i.e. MDE, MM and oxygen) for all six sets of results can be found on the accompanying DVD.

have a radically different geometry showing a more fingered morphology, with clusters of cells protruding from a central core.

For the linear mutation results, A(i)–A(iii), the fact that the resulting tumour cell populations consists of only one living cell type IV might not be surprising due to the linear nature of the mutations. However, it seems logical to assume that

it will be the most aggressive tumour cells that dominate the tumour population and they do so only at the boundary of the tumour. This is due to the fact that all the oxygen has been consumed within the main mass of the tumour, although, as can be seen in Fig.3 A(i), a small cluster of cells has survived in the centre of the tumour. This is partly because quiescent cells consume less oxygen and therefore allow for the diffusion of a little oxygen back into the centre of the tumour. Given more time, these cells will also die due to lack of oxygen. However, this does imply that even necrotic regions may still offer some potential for tumour cell survival (in the short term).

It is also perhaps understandable why tumour cells that were invading through an initially homogeneous distribution of MM, Fig.3 A(i) and B(i) produce more symmetric tumours. These homogeneous tumours also produced the largest number of individual cells, due to the combined effects of a faster invasion rate and subsequently access to empty space for proliferation leading to further invasion. The faster invasion is mainly driven by the cell-matrix interactions via haptotaxis, giving directed motion towards higher concentrations of MM. Since all of the cells on the boundary have no cell-cell adhesion dependence (denoted by the blue colour) they can exploit this gradient the most.

For the random mutation results, B(i)–B(iii), the resulting tumour morphologies are remarkably similair to those of the linear mutation, as is the distribution of cell adhesion (denoted by the cell colour). With the resulting tumour cell populations consisting of living cells with zero cell-cell adhesion all these occurring at the tumour perimeter. Due the random nature of the mutations this is somewhat surprising, as any of the 100 possible phenotypes can be randomly chosen. Given that all three linear mutation simulations, Fig.3 A(i)–A(iii), and all three random mutation simulations, Fig.3 B(i)–B(iii), use the same parameters, with the exception of the MM initial distributions, these results illustrate the importance of tumour cell microenvironmental interactions in aiding or hindering the migration of individual cells that define the tumour geometry.

These results are consistent with the experimental findings of Weaver [40], although they consider differences in MM tension as opposed to MM heterogeneity. But the effect is the same: by making the microenvironment more difficult (harsher) for the tumour to invade into, a fingered tumour displaying an invasive morphology results, Fig.3 A(ii), A(iii), B(ii) and B(iii). One of the major advantages of working with a computational model is the ability to keep track of all variables/paramters at all times. This allows us to examine the precise distribution of phenotypes for the random mutation results, Fig.3 B(i)–B(iii), as the tumour invaded each of the different MM distributions.

From Fig.4 we can see the evolution of the tumour phenotype distribution for each of the different MM distributions using the random mutation algorithm. We note that there are approximately 6 phenotypes in the homogenous tumour, 3 phenotypes in the heterogeneous tumour and 2 phenotypes in the random tumour that dominate the tumour population and survive for most of the simulation. Of these phenotypes all have a zero cell-cell adhesion value, most have a short proliferation

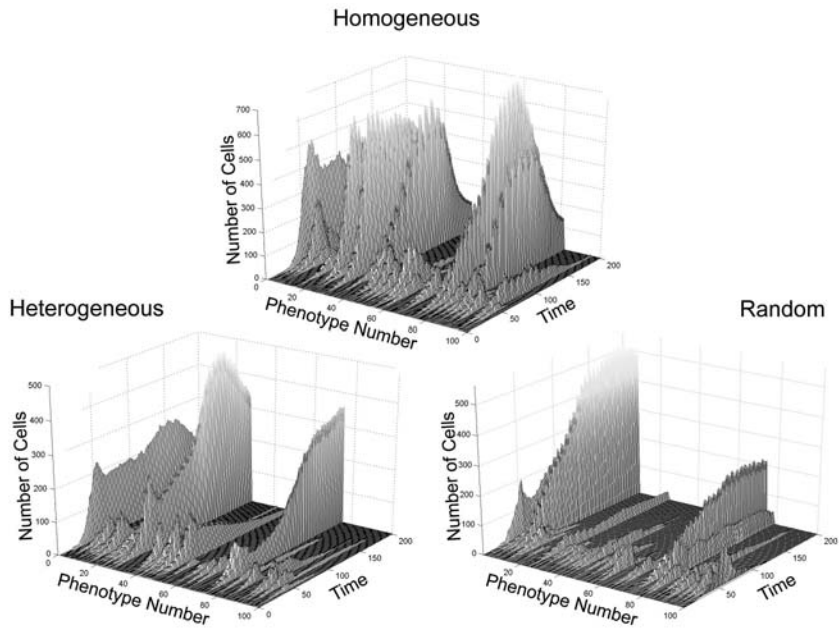

FIGURE 4. Phenotype distributions for each of the tumour populations in Fig.3 B(i)–B(iii), lower row, from simulations using the random mutation algorithm.

age, as well as high haptotaxis coefficients. Surprisingly, for each of the phenotypes that are selected, one in each population is the most aggressive phenotype, always being expressed by the largest fraction of cells in the tumour population, and always has the shortest proliferation age, highest haptotaxis coefficient, no cell-cell adhesion restrictions and, in contrast to the most aggressive type IV cells of the linear mutation algorithm, they mainly have low oxygen consumption rates. If we consider the random MM distribution, Fig.3(iii), as the harshest tissue microenvironment since cells will be receiving many conflicting migration signals from the rapidly varying MM density. Then not only do the more aggressive phenotypes get naturally selected but it would appear that the harsher the MM microenvironment the stronger the evolutionary pressure to select for the most aggressive clones i.e. MM heterogeneity enhances natural selection.

If the predictions made by these simulations are valid, they should be reproducible using different types of microenvironmental stress. Pennacchietti et al. [41] found very similar morphological and phenotypic changes when they grew tumour spheroids in either normoxic or hypoxic conditions. Fig.5 shows some of their results and the switch from the circular non-invasive morphology to the fingered invasive morphology can easily be seen. These results imply that starving

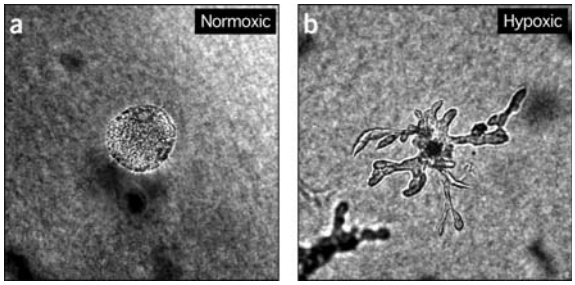

FIGURE 5. Experimental results adapted from Fig.6, Pennacchietti et al. [41], showing a tumour spheroid grown under normoxic and hypoxic conditions. Note the invasive morphology of the hypoxic tumour.

the tumour of oxygen will produce similar changes to that seen when changes in the MM distribution are made. Experimentally, the results shown in Fig.5 are obtained by placing pre-grown spheroids into two different oxygenated environments and allowing them to grow [41].

In order to try and replicate these results with the HDC model of invasion we will initially grow the tumour in an oxygen rich microenvironment (normoxic) then switch to a poorly oxygenated microenvironment (hypoxic), to ensure we only consider the influence of the oxygen concentration we will use the homogenous MM distribution, Fig.3(i), and since we are interested in how the oxygen will effect

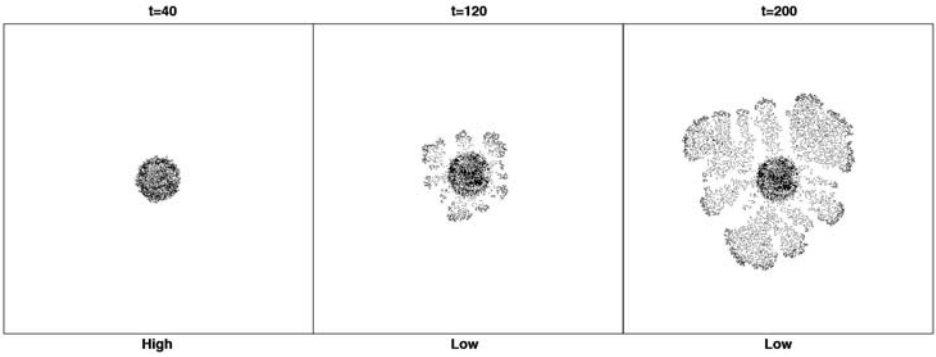

FIGURE 6. HDC tumour simulation results in a homogeneous MM (see Fig.3, top row) using the random mutation algorithm in combination with varying oxygen concentrations: From t=0-40, oxygen is kept at a high concentration and then t=41-200 oxygen is switched to a very low concentration. Note the switch in morphology between high and low oxygen concentrations. A simulation movie showing the growth of the tumour as well as the other three variables (i.e. MDE, MM and oxygen) for this result can be found on the accompanying DVD.

the genetic make up of the tumour we will use the random mutation algorithm. Fig.6 shows the resulting tumour cell distribution for three different snapshots in time. The oxygen rich tumour at $t = 40$ has a well defined circular non-invasive morphology with a mixture of many different phenotypes (seen by the different cell colours which represent the adhesion value of each cell, see Table 1). It is interesting to note that even though the mutations are random, and there is no real evolutionary pressure due to the high levels of oxygen, the tumour naturally sorts the cells with the lowest cell-cell adhesion to the boundary and those with higher adhesion are in the centre. As soon as the oxygen level is switched the morphology changes with a dead inner core of cells surrounded by invasive fingers ($t = 120$) that grow as time evolves ($t = 200$) i.e. an invasive morphology.

These results qualitatively match what is seen in the experimental situation (Fig.5). But they also give an extra level of detail that can only be seen by examining the phenotype distribution. Fig.7 shows how the numbers of the different phenotypes in the tumour population evolve in time. In the normoxic microenvironment ($t = 0 - 40$) most of the 100 phenotypes are present at similar numbers. However, almost as soon as the switch to hypoxic conditions occurs ($t = 41 - 200$) we see the number of phenotypes present drops, leaving only three to dominate for the rest of the simulation. By examining each of these dominant phenotypes we find that, just as under the harsh MM conditions (cf. Fig. 4), each of them have a zero cell-cell adhesion value, a short proliferation age, as well as high haptotaxis coefficients and of course low oxygen consumption rates. Therefore, we again see that under harsh microenvironmental conditions, an increase in the evolutionary pressure occurs causing selection in the resulting tumour population for the most aggressive clones that result in a tumour with an invasive morphology.

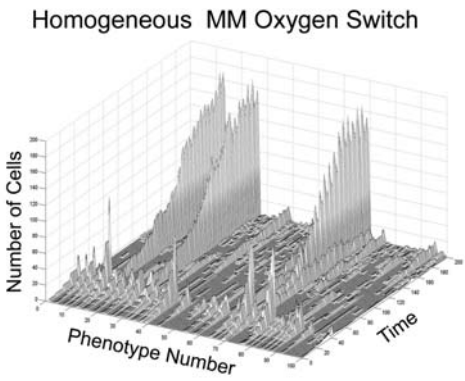

FIGURE 7. Phenotype distribution for the tumour population in Fig.6

5.2. Invasion In Three Dimensions

Whilst a model of a two dimensional section through a three dimensional tumour can give a great deal of insight, as we have seen above, we are aware of its limitations. In particular, cell migration is greatly restricted in two dimensions, as is cell-cell adhesion both of which are central to the invasive process. We therefore extended the model to three dimensions, which is fairly straightforward to do as the parameters and variables in the model do not change, the only real change that occurs is that we switch to using the movement probabilities given in Eqs.(7)–(8) as well as a three dimensional representation of the continuous variables in system Eq.(2).

The following simulation was carried out on a $160 \times 160 \times 160$ grid, which is a discretisation of the unit cube, $[0,1] \times [0,1] \times [0,1]$, with a space step of $h = 0.00625$ and a time step of $k = 0.0005$. Note that with this choice of space step this cube of tissue could possibly contain well over four million tumour cells. In comparison to the two dimensional case of at most 40000 cells, the computational magnitude of working in three dimensions is brought sharply into focus. No flux boundary conditions were imposed on the cubed grid, restricting the tumour cells, MDE, MM and oxygen to within the grid. Initially, 50 tumour cells are centred around $(0.5, 0.5, 0.5)$ with an assigned phenotype I, a random age between $0hrs - 16hrs$, the MDE concentration is zero throughout the domain ($m(x,y,z) = 0$) and the oxygen concentration is taken to be one ($c(x,y,z) = 1$). We will specifically focus on the effect that a random ($0 \leq f(x,y,z) \leq 1$) initial MM distribution has on the growing tumour in three spatial dimensions using the linear mutation algorithm. for both speed and simplicity.

Fig.8A shows the tumour almost filling the entire volume after 200 time units. Another issue when dealing with three dimensional results is being able to visualise them suitably [18]. In order to see what is actually happening within this tumour volume I only visualise two orthogonal slices (Fig.8B-D). Perhaps unsurprisingly we see a very similair fingered morphology to that obtained in the equivalent two dimensional results (Fig.3A(iii)). This fingered morphology is seen no matter how the tumour volume is sliced and therefore further strengthens the two dimensional results that show the emergence of an invasive phenotype under harsh microenvironmental conditions. The phenotypes that make up this cube of tumour tissue have a similar distribution to that seen in the two dimensional case, where the bulk of the outer boundary is dominated by the most aggressive type IV cells and the bulk of the inner core is dead cells.

6. Conclusions

In this chapter we examined the effects of the tumour microenvironment upon both the morphology and genetic makeup of a growing invading tumour. By using a combination of different microenvironments (e.g. homogeneous, heterogeneous tissue, low/high oxygen concentration) with different mutation algorithms (i.e.

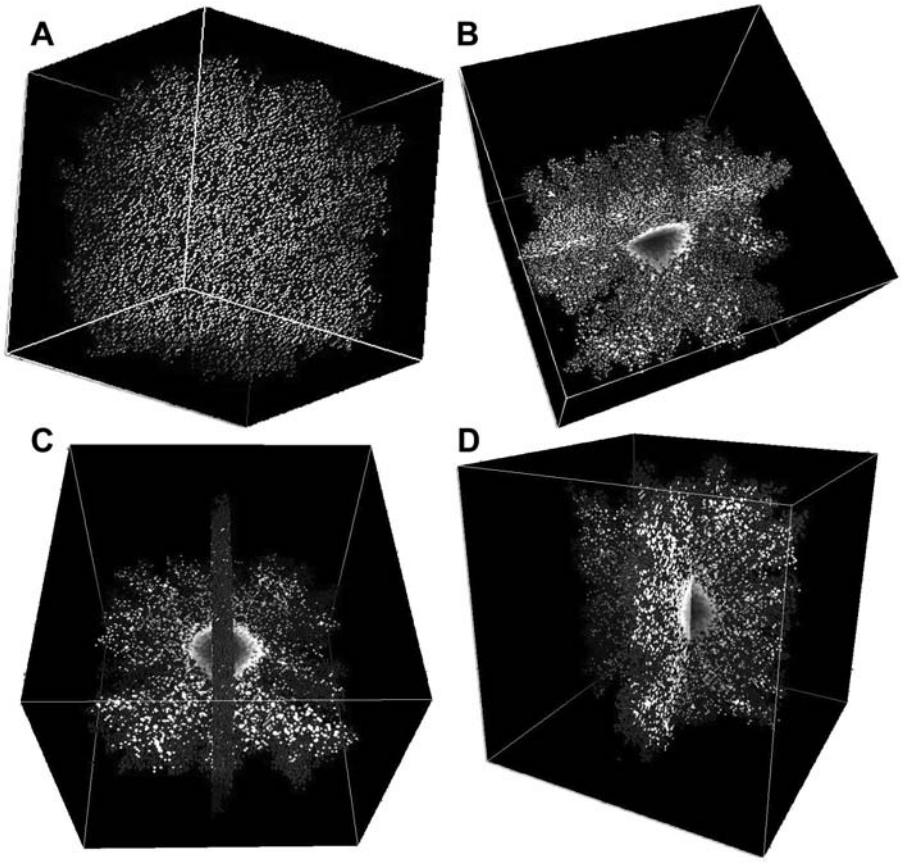

FIGURE 8. Three dimensional HDC tumour simulation results at time $t = 200$ units in a random MM (see Fig.3, top row) using the linear mutation algorithm: Visualisation of a cube of tumour tissue (A); two orthogonal slices, 10 cells thick, of the same cube of tumour tissue (B); two other views of the same orthogonal slices (C, D). Colouration is used only to show different tumour cells and does not represent a particular phenotype. Simulation movies showing a rotational view of both the full tumour and the orthogonal slices can be found on the accompanying DVD.

linear or random) we were able to show that both the aggressiveness and invasiveness of a tumour are directly correlated with the microenvironment in which it grows. In particular, we found that the harsher the tumour microenvironment (e.g. heterogeneous/random MM distributions, low oxygen concentration) the more finger like the tumour morphology (invasive phenotype) and the more aggressive the tumour population.

In the linear mutation algorithm the phenotypes are predetermined (see Table 1) and due to the linear unidirectional manner of the mutations, this algorithm will always lead to the most aggressive phenotype dominating. The evolutionary selective pressure that the microenvironment exerts was only found when the random mutation algorithm was employed. Since each of the 100 randomly defined phenotypes has an equal chance of being selected any phenotype that dominates must do so as result of some kind of selective pressure. We found that this pressure could be exerted by a harsh microenvironment.

These results clearly have important clinical implications, since almost all current tumour treatments involve making the tumour microenvironment harsher (e.g. radiotherapy, chemotherapy, antiangiogenesis therapy). The tumour microenviroment should play an active role in treatment and not be considered as an innocent bystander which is currently the case. One possibility would be to combine treatments that simultaneously suppress the selective influence of the microenvironment and at the same time attack/starve the tumour population. Whilst this is probably very difficult to achieve using current treatment protocols, it seems likely that as the crucial role of the microenvironment is unravelled such stratagies will become a reality.

7. Discussion

We have presented a simple technique for deriving a hybrid discrete-continuum model from a purely continuum one. In general this technique is useful for mathematical models that involve variables on different scales and in particular consider organism migration. Since it is the migration terms in the continuum model (e.g. diffusion, chemotaxis, convection) that drive the movement probabilities of the HDC technique. In effect, we derive a biased random walk governing the motion of an organism based on a system of partial differential equations. This may seem somewhat back-to-front, as random walk models are often used to derive continuum approximations. Othmer and Stevens [38] do precisely this, in particular the transition probabilities of their gradient model are very similar to the probabilities of movement that were derived in this chapter. They show that in the continuum limit such transition probabilities result in a diffusion chemotaxis equation, the same sort of analysis can be carried out on the cell movement probabilities defined here (see [6]) for further details). However, it should be noted that such continuum approximations are only valid for individual organisms that do not interact with one another. Deriving continuum limit approximations for populations of interacting organisms is much more difficult and ultimately reflects the fact that these models should be developed at the scale of the individual organism.

One question which might arise from using the HDC technique is: why derive a discrete model from the continuum PDE model instead of starting with a discrete model in the first place? There are two main reasons for this: (i) when modelling the migration of cells that are influenced by stimuli at different scales it is easier to

model these initially at the continuum level; (ii) since the movement probabilities, in the HDC technique, have been derived from a numerical discretisation of the PDE (governing cell migration), the space and time steps for the individuals already match those for the numerical solution of the "continuous" variables (the external stimuli) and therefore make interactions between these discrete and continuous variables much more straightforward.

Another advantage of the HDC technique is that individual based process are modelled at the individual level. This is of course true of virtually all of the techniques discussed in this book. But what gives the HDC technique the edge is its speed, computationally it is very efficient and can model the interactions of millions of cells (see Fig.8).

Due to the derivation of the discrete model being based on a finite difference approximation of a PDE there is some restriction in the choice of the space (h) and time (k) steps in order to insure stability. A basic rule for stability of a diffusion driven model requires that the constants h and k should satisfy the condition $\frac{4kD}{h^2} < 1$ where D is the diffusion coefficient. Since in general the spatial grid size (h) will be fixed by the scale of the organism (this need not always be the case), the time step (k) requires to be chosen sufficiently small in order to satisfy the above condition. This could result in slower computations.

In conclusion, whilst the HDC technique will not be applicable to every migration system, the idea of using standard numerical techniques for solving partial differential equations to derive individual based models is clearly a very simple way of obtaining a hybrid model of individual organism migration. Indeed, the HDC technique provides a powerful means of linking micro-scale events to macro-scale events, individual behaviour to population behaviour and is therefore intrinsically multiscale and can easily incorporate a range of scales i.e. genetic, sub-cellular, cellular and tissue. The HDC technique has potential application to a wide range of problems in mathematical biology and has already been applied to several, initially developed and applied to nematode migration in heterogeneous microenvironments [3] and subsequently applied to endothelial cell migration in both two and three dimensional tumour induced angiogenesis [4] and has also been used to model amoebae migration in Dictyostelium discoideum aggregation [7].

References

[1] Alarcon, T., Byrne, H. M., Maini, P. K. (2005). A multiple scale model for tumor growth. *Multiscale Model Simul.* **3**, 440-475.

[2] Albini, A. & Sporn, M. B. (2007). The tumour microenvironment as a target for chemoprevention. *Natrure Rev. Cancer*, **7**, doi:10.1038.

[3] Anderson, A. R. A., Sleeman, B.D., Young, I.M. & Griffiths, B.S. (1997) Nematode movement along a chemical gradient in a structurally heterogeneous environment: II. Theory. *Fundam. appl. Nematol.*, **20**, 165-172.

[4] Anderson, A. R. A. & Chaplain, M. A. J. (1998). Continuous and Discrete Mathematical Models of Tumour-Induced Angiogenesis Angiogenesis. *Bull. Math. Biol.*, **60**, 857-899.

[5] Anderson, A. R. A., Chaplain, M. A. J., Newman, E. L., Steele, R. J. C. & Thompson, A. M. (2000) Mathematical Modelling of Tumour Invasion and Metastasis. *J. Theoret. Med.*, **2**, 129-154. 2

[6] Anderson, A. R. A. A Hybrid Discrete-Continuum Technique for Individual Based Migration Models in *Polymer and Cell Dynamics*, eds. W. Alt, M. Chaplain, M. Griebel, J. Lenz, 2003, Birkhauser.

[7] Anderson, A. R. A. & Pitcairn, A. Application of the Hybrid Discrete-Continuum Technique in *Polymer and Cell Dynamics*, eds. W. Alt, M. Chaplain, M. Griebel, J. Lenz, 2003, Birkhauser.

[8] Anderson, A. R. A. (2005) A hybrid mathematical model of solid tumour invasion: The importance of cell adhesion. *IMA J. Math. Med. and Biol.*, **22**, 163-186.

[9] Anderson, A. R. A, Weaver A.M., Cummings P.T. & Quaranta V. (2006) Tumor Morphology and Phenotypic Evolution Driven by Selective Pressure from the Microenvironment. *Cell*, **127**, 111.

[10] Araujo, R. P., and McElwain, D. L. S. (2004). A history of the study of solid tumour growth: the contribution of mathematical modeling. *Bull. Math. Biol.* **66**, 10391091.

[11] Bierie, B. & Moses, H. L . (2006). Tumour microenvironment: TGF: the molecular Jekyll and Hyde of cancer. *Nature Rev. Cancer*, **6**, 506-520.

[12] Bray, D. *Cell Movements*, **1992** Garland Publishing, New York.

[13] Burridge, K. & Chrzanowska-Wodnicka, M. (1996) Focal adhesions, contractability, and signalling. *Annu. Rev. Cell Dev. Biol.*, **12**, 463-518.

[14] Byrne, H.M., Chaplain, M.A.J., Pettet, G.J. & McElwain, D.L.S. (1999) A mathematical model of trophoblast invasion. *J. theor. Med.*, **1**, 275-286.

[15] Calabresi, P. & Schein, P.S. editors: *Medical Oncology*, 2nd ed. **1993**, McGraw-Hill, New York.

[16] Clark, E. A. & Brugge, J. S. (1995) Integrins and signal transduction pathways: the road taken. *Science*, **268**, 233-239.

[17] Casciari, J. J., Sotirchos, S. V. & Sutherland, R. M. (1992) Variation in tumour cell growth rates and metabolism with oxygen-concentration, glucose-concentration and extracellular pH. *J. Cell Physiol.*, **151**, 386-394.

[18] Enderling, H., Anderson, A. R. A., Chaplain, M. A. J., Rowe, G. W. (2006). Visualisation of the Numerical Solution of Partial Differential Equation Systems in Three Space Dimensions and its Importance for Mathematical Models in Biology. *Math. Biosci. Eng.* **3**, 571-582.

[19] Chaplain, M.A.J. & Sleeman, B.D. (1993) Modelling the growth of solid tumours and incorporating a method for their classification using nonlinear elasticity theory. *J. Math. Biol.*, **31**, 431-479.

[20] Chaplain, M.A.J. (1996). Avascular growth, angiogenesis and vascular growth in solid tumours: the mathematical modelling of the stages of tumour development. *Mathl. Comput. Modelling* **23**, 47-87.

[21] Dormann, S. & Deutsch, A. (2002). Modeling of self-organzied avascular tumor growth with a hybrid cellular automaton. *In Silico Biology* **2**, 0035.

[22] Düchting, W. (1990a). Tumor growth simulation. *Comput. & Graphics* **14**, 505-508.

[23] Düchting, W., W. Ulmer & T. Ginsberg. (1996). Cancer: A challenge for control theory and computer modelling. *Euro. J. Cancer* **32A**, 1283-1292.

[24] Freyer, J.P., Tustanoff, E., Franko, A.J. & Sutherland, R.M. (1984) In situ consumption rates of cells in v-79 multicellular spheroids during growth. *J. Cell. Phys.* **118**, 53-61.

[25] Folkman, J. & Hochberg, M. (1973). Self-Regulation of growth in three dimensions. *J. Exp. Med.* **138**, 745-753.

[26] Gatenby, R.A. & E.T. Gawlinski. (1996). A reaction-diffusion model of cancer invasion. *Cancer Research* **56**, 5745-5753.

[27] Hanahan, D., and Weinberg, R.A. (2000). *The hallmarks of cancer. Cell* **100**, 5770.

[28] Hotary, K., Allen, E.D., Punturieri, A., Yana, I. & Weiss, S. J. (2000) Regulation of cell invasion and morphogenesis in a 3-dimensional type I collagen matrix by membrane-type metalloproteinases 1, 2 and 3. *J. Cell Biol.*, **149**, 1309-1323.

[29] Hynes, R. O. (1992) Integrins: versatility, modulation, and signalling in cell adhesion. *Cell*, **69**, 11-25.

[30] Johansson, N., Ahonen, M. & Kahari, V-M. (2000) Matrix metalloproteinases in tumour invasion. *Cell. Mol. Life Sci.* **57**, 5-15.

[31] Kansal, A. R., Torquato, S., Harsh, G. R., Chiocca, E. A. & Deisboeck, T. S. (2000). Simulated Brain Tumor Growth using a Three-Dimensional Cellular Automaton, *J. Theor. Biol.* **203**, 367-382.

[32] Kimmel, M. & D.E. Axelrod. (1991). Unequal cell division, growth regulation and colony size of mammalian cells: a mathematical model and analysis of experimental data. *J. Theor. Biol.* **153**, 157-180.

[33] Koochekpour, S., Pilkington, G. J. & Merzak, A. (1995) Hyaluronic acid/CD44H interaction induces cell detachment and stimulates migration and invasion of human glioma cells in vitro. *Intl. J. Cancer*, **63**, 450-454.

[34] Lane, D. P. (1994) The regulation of p53 function. Steiner Award Lecture. *Int. J. Cancer* **57**, 623-627.

[35] Melicow, M.M. (1982) The three-steps to cancer: A new concept of carcinogenesis. *J. Theor. Biol.* **94**, 471-511.

[36] Moreira, J. & Deutsch, A. (2002). Cellular automaton models of tumour development - a critical review. *Adv. in Complex Systems*, **5**, 1-21.

[37] Orme, M.E. & Chaplain, M.A.J. (1996). A mathematical model of vascular tumour growth and invasion. *Mathl. Comp. Modelling*, **23**, 43-60.

[38] Othmer, H. and A. Stevens. (1997). Aggregation, blowup and collapse: The ABCs of taxis and reinforced random walks. *SIAM J. Appl. Math.* **57**, 1044-1081.

[39] Overall, C. M. & Kleifeld, O. (2006). Tumour microenvironment Opinion: Validating matrix metalloproteinases as drug targets and anti-targets for cancer therapy. *Nature Rev. Cancer*, **6**, 227-239.

[40] Paszek, M. J., Zahir, N., Johnson, K. R., Lakins, J. N., Rozenberg, G. I., Gefen, A., Reinhart-King, C. A., Margulies, S. S., Dembo, M., Boettiger, D., Hammer, D. A.,

Weaver, V. M. (2005). Tensional homeostasis and the malignant phenotype. *Cancer Cell*, **8**, 241-254.

[41] Pennacchietti, S., Michieli, P., Galluzzo, M., Mazzone, M., Giordano, S., & Comoglio, P.M. (2003) Hypoxia promotes invasive growth by transcriptional activation of the met protooncogene. *Cancer Cell*, **3**, 347361.

[42] Perumpanani, A.J., Sherratt, J.A., Norbury, J. & Byrne, H.M. (1996) Biological inferences from a mathematical model of malignant invasion. *Invasion and Metastases*, **16**, 209-221.

[43] Qi, A., Zheng, X., Du, C. & An, B. (1993) A Cellular Automaton Model of Cancerous Growth. *J. theor. Biol.*, **161**, 1-12.

[44] Sherratt, J.A. & Nowak, M.A. (1992) Oncogenes, anti-oncogenes and the immune response to cancer: a mathematical model. *Proc. R. Soc. Lond. B*, **248**, 261-271.

[45] Smolle, J. & Stettner, H. (1993) Computer simulation of tumour cell invasion by a stochastic growth model. *J. theor. Biol.*, **160**, 63-72.

[46] Stetler-Stevenson, W.G., Aznavoorian, S. & Liotta, L.A. (1993) Tumor cell interactions with the extracellular matrix during invasion and metastasis. *Ann. Rev. Cell Biol.*, **9**, 541-573.

[47] Swanson, K. R., Bridge, C., Murray, J. D., Alvord Jr., E. C. (2003). Virtual and Real Brain Tumors: Using Mathematical Modeling to Quantify Glioma Growth and Invasion. *J. Neuro. Sci.*, **216**, 1-10,

[48] Swanson, K. R., Alvord Jr., E. C., Murray, J. D. (2004). Dynamics of a Model for Brain Tumors Reveals a Small Window for Therapeutic Intervention. *Disc. Cont. Dyn. Sys. B*, **4**, 289-295

[49] Terranova, V.P., Diflorio, R., Lyall, R.M., Hic, S., Friesel, R. & Maciag, T. (1985) Human endothelial cells are chemotactic to endothelial cell growth factor and heparin. *J. Cell Biol.*, **101**, 2330-2334.

[50] Thorgeirsson, U.P., Lindsay, C.K., Cottam, D.W. & Gomez, D.E. (1994). Tumor invasion, proteolysis, and angiogenesis. *J. Neuro-Oncology*, **18**, 89-103.

[51] Ward, J.P., King, J.R. (1999) Mathematical modelling of avascular-tumour growth II: modelling growth saturation. *IMA J. Math. Appl. Med. Biol.*, **16**, 171-211.

[52] Zhang, L., Athale, C. A. & Deisboeck, T. S. (2007). Development of a three-dimensional multiscale agent-based tumor model: Simulating gene-protein interaction profiles, cell phenotypes and multicellular patterns in brain cancer. *J. Theo. Biol.* **244**, 96-107.

[53] Zervoudaki, A., Economou, E., Pitsavos, C., Vasiliadou, K *et al.* (2004) The effect of Ca^{2+} channel antagonists on plasma concentrations of matrix metalloproteinase-2 and -9 in essential hypertension. *A.J.H.* **17**, 273-276.

Alexander R. A. Anderson
Division of Mathematics, University of Dundee
Dundee DD1 4HN, Scotland, UK
e-mail: anderson@maths.dundee.ac.uk

Single-Cell-Based Models in Biology and Medicine
ed. by A.R.A. Anderson, M.A.J. Chaplain, K.A. Rejniak
Mathematics and Biosciences in Interaction, 29–51

I.2 Lattice-gas Cellular Automaton Modeling of Developing Cell Systems

Andreas Deutsch

Abstract. Cellular automata can be viewed as spatially extended decentralized systems made up of a number of individual components and may serve as simple models of complex systems. Here, we show that a particular cellular automaton class, lattice-gas cellular automata (LGCA), is well suited for the modeling of developing cell systems characterized by motion and interaction of biological cells. As examples, we present LGCA models of adhesion and chemotaxis. We conclude with a detailed discussion on the relevance of LGCA models.

1. Introduction

Complex systems and biological development. The notion of a cellular automaton originated in the works of John von Neumann (1903-1957) and Stanislaw Ulam (1909-1984). Cellular automata as discrete, dynamical systems can be equally well interpreted as a mathematical idealization of natural systems, a discrete caricature of microscopic dynamics, a parallel algorithm or a discretization of partial differential equations. According to these interpretations distinct roots of cellular automata may be traced back in biological modeling, computer science and numerical mathematics which are well documented in numerous and excellent sources [5, 8, 42, 48]. Cellular automata may be viewed as simple models of self-organizing complex systems in which collective behavior can emerge out of an ensemble of many interacting "simple" components. In complex systems, even if the basic and local interactions are perfectly known, it is possible that the global behavior obeys new laws that are not obviously extrapolated from the individual properties, as if the whole is more than the sum of all the parts. This property makes cellular automata a very interesting approach to model physical systems and especially to simulate complex and nonequilibrium phenomena (examples are introduced in [14]). Accompanying the availability of more and more computing power, numerous automaton applications in physics, chemistry, and biology have been studied extensively [9, 13, 17, 34, 49].

Biological development is a particularly important complex system. What are the rules underlying the emergence of an adult organism out of a single fertilized egg cell? It is clear that biological development is the result of complex interactions of biological cells. It has been shown that insight into the principles of developing biological systems can be expected from mathematical models, analysis and simulations (e.g. [36, 37]). Interest in "cell-based" mathematical models has lately grown due to the availability of "individual cell data" (metabolic, genetic and proteomic) and has triggered the development of new cell-based mathematical models (for a review see [19]). Cell-based models are required if one is interested in understanding the organization principles of interacting cell systems down to length scales of the order of a cell diameter in order to link the individual cell (microscopic) dynamics with a particular collective (macroscopic) phenomenon. Cell-based models, particularly cellular automata, allow to follow and analyze the spatio-temporal dynamics at the individual cell level [17].

Are there microscopic cellular automaton rules, which can model the mechanisms of cell interaction? An important insight of complex system research is that macroscopic behavior is rather independent of the precise choice of the microscopic rule. For example, it was shown that simple collision rules can give rise to the intricate structures of hydrodynamic flow as long as the rules conserve mass and momentum (lattice-gas cellular automaton, [21, 27]). Could it be similar for biological systems, with basic rules of cellular interaction underlying the complex developmental pattern formation? In this chapter, we introduce lattice-gas cellular automaton models in order to analyze the dynamics and principles of interacting cell systems. In particular, we demonstrate how appropriately constructed lattice-gas cellular automata allow for straightforward analysis of spatio-temporal pattern formation beyond mere simulation.

Lattice-gas cellular automata. The basic ingredient of lattice-gas models are point particles moving on a lattice according to appropriate rules so as to mimic a fully discrete "molecular" dynamics. The dynamics obeys an exclusion principle and can be described as a sequence of particle collision and propagation steps. Lattice-gas cellular automata (LGCA) have been introduced as a fully discrete fluid model operating on a square lattice in 1973 [26]. An interesting extension on a hexagonal lattice is the FHP model [21] which behaves as predicted by the Navier-Stokes equation when the observation time and length scales are much larger than the lattice spacing and the automaton time step. The LGCA idea has turned out to provide valuable models of morphogenetic motion describing translocation of individual cells during development [17]. Thereby, cell motion is influenced by the interaction of cells with elements of their immediate surrounding (haptotaxis and differential adhesion, interaction with the basal lamina and the interstitial matrix, contact guidance, contact inhibition, mechanical guidance within preestablished channels) and processes that involve cellular response to signals that are propagated over larger distances (chemotaxis, galvanotaxis) [4]. LGCA can be viewed as cellular automata supplied with a particular set of "morphogenetic local rules"

defining *interaction* and *convection* of polarized biological cells. The essential modeling idea is the appropriate formulation of a local field characterizing a given cell interaction. We will assume that the specificity of a particular cell interaction can be transformed into a corresponding local field, which is a functional determined from the neighborhood configuration in the automaton. In this chapter, for simplicity, we focus on linear interaction functionals. The interaction rules are not defined by a rigorous minimization of the interaction energy, instead the post-interaction state is chosen probabilistically according to "Boltzmann weights". The biological interpretation is that a cell attempts to minimize the work against the surrounding field by a biased random change of polarization and not by a deterministic approach to a local energy minimum.

The applications in this chapter provide examples how elementary cell interactions (particularly differential adhesion and chemotaxis) can be translated into corresponding local fields. This chapter is organized as follows: We give a precise definition of the lattice-gas cellular automaton in the next section (2). In the remainder we present examples of selected cell interactions. In section 3 we introduce a lattice-gas cellular automaton of adhesively interacting cells and in section 4 a model of chemotaxis. We conclude with a discussion (section 5).

2. Definition of lattice-gas cellular automata

A lattice-gas cellular automaton is a cellular automaton with a particular state space and dynamics. Therefore, we start with the introduction of cellular automata which are defined as a class of spatially and temporally discrete dynamical systems based on local interactions. Accordingly, a cellular automaton is a 4-tuple (L, S, N, F), where

- L is an infinite regular lattice of cells/nodes (discrete space),
- S is a finite set of **states** (discrete states); each cell $i \in L$ is assigned a state $s \in S$,
- N is a finite set of neighbors, indicating the position of one cell relative to another cell on the lattice L; Moore and von Neumann neighborhoods are typical neighborhoods on the square lattice,
- F is a deterministic or probabilistic map

$$F : S^{|N|} \quad \rightarrow \quad S \tag{1}$$

$$\{s_i\}_{i \in N} \quad \mapsto \quad s, \tag{2}$$

which assigns a new state to a cell depending on the state of all its neighbors indicated by N (local rule).

The evolution of a cellular automaton is defined by applying the function F synchronously to all cells of the lattice L (homogeneity in space and time).

States in lattice-gas cellular automata. In lattice-gas cellular automata, velocity channels $(r, c_i),\ c_i \in \mathcal{N}_b,\ i = 1, \ldots, b$, are associated with each node r of the lattice. In addition, a variable number $\beta \in \mathbb{N}_0$ of rest channels (zero-velocity channels),

$(r, c_i),\ b < i \leq b+\beta$, with $c_i = \{0\}^\beta$ may be introduced. Furthermore, an exclusion principle is imposed. This requires, that not more than one particle can be at the same node within the same channel. As a consequence, each node r can host up to $\tilde{b} = b + \beta$ particles, which are distributed in different channels (r, c_i) with at most one particle per channel. Therefore, state $s(r)$ is given by

$$s(r) = \big(\eta_1(r), \ldots, \eta_{\tilde{b}}(r)\big) =: \boldsymbol{\eta}(r) \ ,$$

where $\boldsymbol{\eta}(r)$ is called node configuration and $\eta_i(r), i = 1, \ldots, \tilde{b}$, *occupation number*. Occupation numbers are Boolean variables that indicate the presence $(\eta_i(r) = 1)$ or absence $(\eta_i(r) = 0)$ of a particle in the respective channel (r, c_i). Therefore, the set of elementary states $\mathcal{E}$ of a single node is given by

$$\mathcal{E} = \{0, 1\}^{\tilde{b}} \ni s(r) \ .$$

The *local configuration* $\boldsymbol{s}_{\mathcal{N}(r)}$ is given by

$$\boldsymbol{s}_{\mathcal{N}(r)} = \big(\eta(r_i)\big)_{r_i \in \mathcal{N}_b(r)} =: \boldsymbol{\eta}_{\mathcal{N}(r)} \ .$$

For any spatial coordinate $r \in \mathcal{L}$, the nearest lattice neighborhood $\mathcal{N}_b(r)$ is a finite list of neighboring nodes and is defined as

$$\mathcal{N}_b(r) := \{r + c_i \ : \ c_i \in \mathcal{N}_b \, , \ i = 1, \ldots, b\} \ ,$$

where b is the *coordination number*, i.e. the number of nearest neighbors on the lattice. Fig.1 gives an example of the representation of a node in a two-dimensional lattice with $b = 4$ and $\beta = 1$, i.e. $\tilde{b} = 5$.

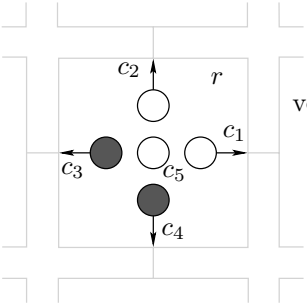

$$\begin{aligned}
\tilde{b} &= 5 \\
\text{velocity channels:} &\quad (r, c_1),\ (r, c_2),\ (r, c_3),\ (r, c_4) \\
\text{rest channel:} &\quad (r, c_5) \\
\boldsymbol{\eta}(r) &= \big(\eta_1(r), \eta_2(r), \eta_3(r), \eta_4(r), \eta_5(r)\big) \\
&= \big(0, 0, 1, 1, 0\big) \\
\mathrm{n}(r) &= 2
\end{aligned}$$

FIGURE 1. Node configuration: channels of node r in a two-dimensional square lattice ($b = 4$) with one rest channel ($\beta = 1$). Gray dots denote the presence of a particle in the respective channel.

In multi-component LGCA, ς different types (σ) of particles reside on separate lattices $(\mathcal{L}_\sigma)$ and the exclusion principle is applied independently to each lattice. The state variable is given by

$$s(r) = \boldsymbol{\eta}(r) = \big(\boldsymbol{\eta}_\sigma(r)\big)_{\sigma=1}^{\varsigma} = \big(\eta_{\sigma,1}(r), \ldots, \eta_{\sigma,\tilde{b}}(r)\big)_{\sigma=1}^{\varsigma} \in \mathcal{E} = \{0, 1\}^{\tilde{b}\,\varsigma} \ .$$

Dynamics in lattice-gas cellular automata. The dynamics of a LGCA arises from repetitive application of superpositions of local (probabilistic) *interaction* and *propagation* (migration) steps applied simultaneously at all lattice nodes at each discrete time step. The definitions of these steps have to satisfy the exclusion principle, i.e. two or more particles of a given species are not allowed to occupy the same channel.

According to a model-specific *interaction* rule ($\mathcal{R}^{\mathtt{I}}$), particles can change channels (e.g., due to interactions, see Fig.2) and/or are created or destroyed. This rule can be *deterministic* or *stochastic*. The dynamics of a state $s(r,k) = \boldsymbol{\eta}(r,k) \in \{0,1\}^{\tilde{b}}$ in a LGCA are determined by the dynamics of the occupation numbers $\eta_i(r,k)$ for each $i \in \{1,\ldots,\tilde{b}\}$ at node r and time k. Therefore, the pre-interaction state $\eta_i(r,k)$ is replaced by the post-interaction state $\eta_i^{\mathtt{I}}(r,k)$ determined by

$$\eta_i^{\mathtt{I}}(r,k) = \mathcal{R}_i^{\mathtt{I}}\big(\boldsymbol{\eta}_{\mathcal{N}(r)}(k)\big), \tag{3}$$

$$\mathcal{R}^{\mathtt{I}}\big(\boldsymbol{\eta}_{\mathcal{N}(r)}(k)\big) = \big(\mathcal{R}_i^{\mathtt{I}}\big(\boldsymbol{\eta}_{\mathcal{N}(r)}(k)\big)\big)_{i=1}^{\tilde{b}} = \boldsymbol{z} \quad \text{with probability} \quad W\left(\boldsymbol{\eta}_{\mathcal{N}(r)}(k) \to \boldsymbol{z}\right) ,$$

with $\boldsymbol{z} \in \{0,1\}^{\tilde{b}}$ and the time-independent transition probability W.

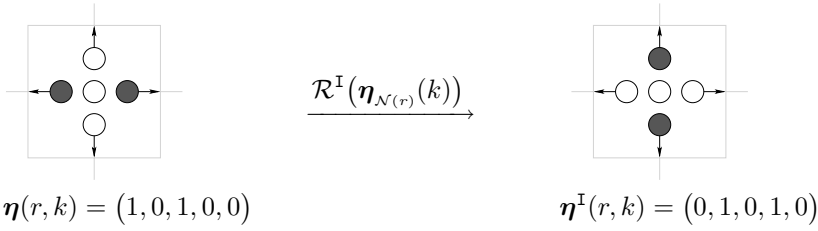

FIGURE 2. Example for reorientation of particles at two-dimensional square lattice node r; gray dots denote the presence of a particle in the respective channel. No confusion should arise by the arrows indicating channel directions.

In the deterministic *propagation* or streaming step ($\mathtt{P}$), all particles are moved simultaneously to nodes in the direction of their velocity, i.e. a particle residing in channel (r,c_i) at time k is moved to another channel $(r + m\,c_i, c_i)$ during one time step (Fig.3). Here, $m \in \mathbb{N}$ determines the *speed* and $m\,c_i$ the *translocation* of the particle. Because all particles residing at velocity channels move the same number m of lattice units the exclusion principle is maintained. Particles occupying rest channels do not move since they have "zero velocity". In terms of occupation numbers, the state of channel $(r + m\,c_i, c_i)$ after propagation is given by

$$\eta_i^{\mathtt{P}}(r + m\,c_i, k+1) = \eta_i(r,k), \quad c_i \in \mathcal{N}_b\ . \tag{4}$$

Hence, if only the propagation step would be applied then particles would simply move along straight lines in directions corresponding to particle velocities.
Combining interactive dynamics with propagation, Eq.(3) and Eq.(4) imply that

$$\eta_i^{\mathtt{IP}}(r + mc_i, k) = \eta_i(r + mc_i, k+1) = \eta_i^{\mathtt{I}}(r,k)\ . \tag{5}$$

This can be rewritten as the *microdynamical difference equations*

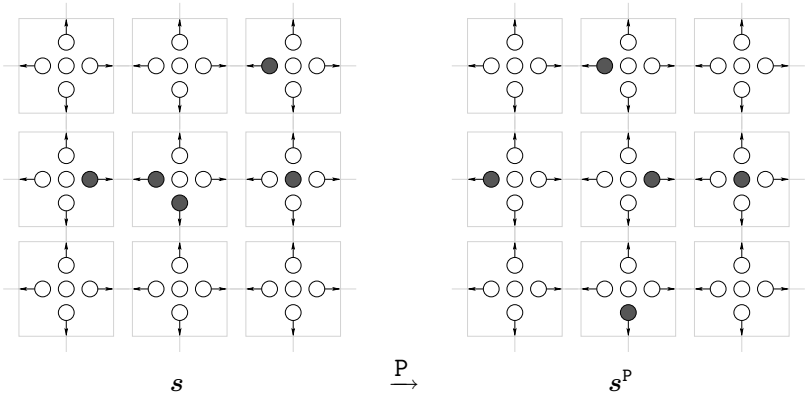

FIGURE 3. Propagation in a two-dimensional square lattice with speed $m = 1$; lattice configurations before ($\boldsymbol{s}$) and after ($\boldsymbol{s}^{\mathrm{P}}$) the propagation step; gray dots denote the presence of a particle in the respective channel.

$$\begin{aligned} \mathcal{R}_i^{\mathrm{I}}\left(\boldsymbol{\eta}_{\mathcal{N}(r)}(k)\right) - \eta_i(r,k) &= \eta_i^{\mathrm{I}}(r,k) - \eta_i(r,k) \\ = \eta_i(r+mc_i, k+1) - \eta_i(r,k) &=: \mathcal{C}_i\left(\boldsymbol{\eta}_{\mathcal{N}(r)}(k)\right) \qquad i = 1,\ldots,\tilde{b}, \end{aligned} \tag{6}$$

where the *change in the occupation numbers* due to interaction is given by

$$\mathcal{C}_i\left(\boldsymbol{\eta}_{\mathcal{N}(r)}(k)\right) = \begin{cases} 1 & \text{creation of a particle in channel } (r,c_i) \\ 0 & \text{no change in channel } (r,c_i) \\ -1 & \text{annihilation of a particle in channel } (r,c_i) \end{cases}$$

In a multi-component system with $\sigma = 1,\ldots,\varsigma$ components, eqn. (6) becomes

$$\eta_{\sigma,i}^{\mathrm{I}}(r,k) - \eta_{\sigma,i}(r,k) = \eta_{\sigma,i}(r+m_\sigma\, c_i, k+1) - \eta_{\sigma,i}(r,k) = \mathcal{C}_{\sigma,i}\left(\boldsymbol{\eta}_{\mathcal{N}(r)}(k)\right) \tag{7}$$

for $i = 1,\ldots,\tilde{b}$, with speeds $m_\sigma \in \mathbb{N}$ for each component $\sigma = 1,\ldots,\varsigma$. Here, the change in the occupation numbers due to interaction is given by

$$\mathcal{C}_{\sigma,i}\left(\boldsymbol{\eta}_{\mathcal{N}(r)}(k)\right) = \begin{cases} 1 & \text{creation of a particle } X_\sigma \text{ in channel } (r,c_i)_\sigma \\ 0 & \text{no change in channel } (r,c_i)_\sigma \\ -1 & \text{annihilation of a particle } X_\sigma \text{ in channel } (r,c_i)_\sigma, \end{cases}$$

where $(r,c_i)_\sigma$ specifies the ith channel associated with node r of the lattice $\mathcal{L}_\sigma$.

3. A lattice-gas cellular automaton model for adhesively interacting cells

Stable cell interactions are required to maintain the structural integrity of tissues, and dynamic changes in cell adhesion are essential in the morphogenesis of developing tissues. Adhesion mechanisms are highly regulated during tissue

morphogenesis and are intimately coupled to cell migration processes. In particular, molecules of the cadherin and integrin families are involved in the control of cell movement. Cadherin-mediated cell compaction and cellular rearrangements may be analogous to integrin-mediated cell spreading and motility on the extracellular matrix. Recently, the first in vivo example of cell sorting depending on differential adhesion mediated by cadherin has been demonstrated in *Drosophila* [24, 38]. Regulation of cell adhesion can occur at several levels, including affinity modulation, clustering, and coordinated interactions with the actin cytoskeleton. Structural studies have begun to provide a picture of how the binding properties of adhesion receptors themselves might be regulated. However, regulation of tissue morphogenesis requires complex interactions between the adhesion receptors, the cytoskeleton, and networks of signaling pathways. Signals generated locally by the adhesion receptors themselves are involved in the regulation of cell adhesion. These regulatory pathways are also influenced by extrinsic signals arising from the classic growth factor receptors. Furthermore, signals generated locally by adhesive junctions can interact with classic signal transduction pathways to help control cell growth and differentiation. This coupling between physical adhesion and developmental signaling provides a mechanism to tightly integrate physical aspects of tissue morphogenesis with cell growth and differentiation, a coordination that is essential to achieve the intricate patterns of cells in tissues. In the following we neglect the precise physico-chemical nature of cell adhesion and analyze (macroscopic) spatio-temporal pattern formation in an adhesively interacting (microscopic) cell system.

Consider a lattice-gas cellular automaton defined on a two-dimensional lattice with periodic boundary conditions ($b = 4$ or $b = 6$). Let the number of particles at node r at time k be denoted by

$$\rho(r,k) = \sum_{i=1}^{b} \eta_i(r,k)$$

and the flux be denoted by

$$\mathrm{J}(\eta(r,k)) = \sum_{i=1}^{b} \mathrm{c}_i \eta_i(r,\, k).$$

During interaction the number of cells at each node r remains constant (i.e. mass conservation),

$$\sum_{i=1}^{b} \eta_i(r,k) = \sum_{i=1}^{b} \eta_i^I(r,k)$$

We define the *gradient field* in the local density,

$$\mathrm{G}(r,k) = \sum_{p=1}^{b} c_p \rho(r + c_{\mathrm{p}}, k). \tag{8}$$

"Adhesive" interaction rules are formulated in such a way that cells preferably move in the direction of increasing density, i.e. parallel to G, which mimics adhesive attraction between cells. The sensitivity is tuned by a parameter α. The probability

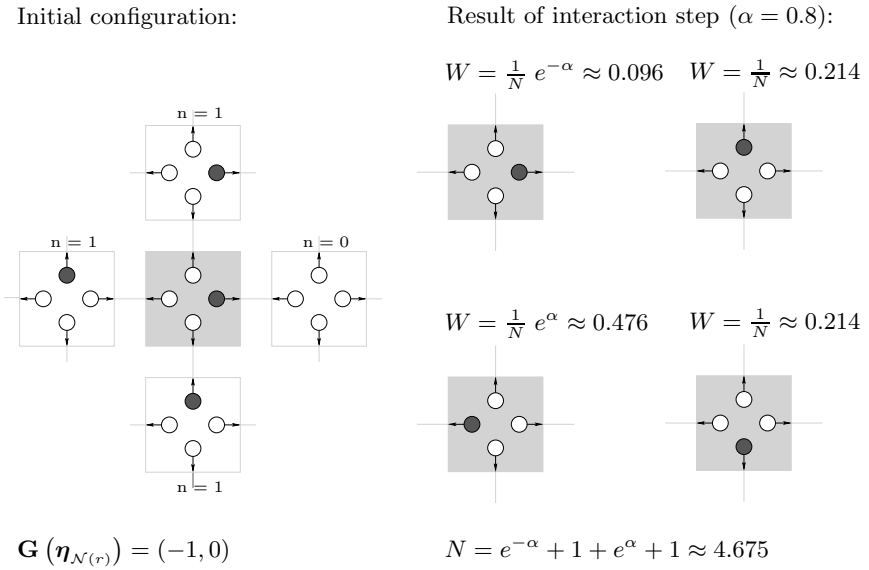

FIGURE 4. Example of adhesive interaction in the square lattice. Gray dots denote channels occupied by cells, while white dots denote empty channels. With probability W each node configuration on the right side ($\boldsymbol{\eta}^{\mathrm{I}}$) is a possible result of the interaction step applied to the middle gray node ($\boldsymbol{\eta}$) of the initial configuration.

that η^I is the outcome of an interaction at node r, when η is the pre-interaction state at r and $\mathrm{G} = \mathrm{G}(r)$ is the local density gradient, is defined by

$$W(\eta \to \eta^I | G) = \frac{1}{Z} \exp(\alpha \mathrm{G} \cdot \mathrm{J}(\eta^{\mathrm{I}}))\delta(\rho(\eta), \rho(\eta^{\mathrm{I}})),$$

where the normalization constant is given by

$$Z = Z(\eta, \mathrm{G}) = \sum_{\eta^{\mathrm{I}} \in \mathcal{E}} \exp(\alpha \mathrm{G} \cdot \mathrm{J}(\eta^{\mathrm{I}}))\delta(\rho(\eta), \rho(\eta^{\mathrm{I}})).$$

Accordingly, the dynamics is fully specified by the following microdynamical equation

$$\eta_i(r + c_i, k + 1) = \eta^I(r, k).$$

Note that for small sensitivities ($\alpha \approx 0$) the gradient G does not have any effect on the interaction outcome: the outcome η^I is chosen with equal probabilty among all states that have the appropriate number of cells ($\rho(\eta) = \rho(\eta^I)$). In this limit a random walker model is obtained with positive diffusion coefficient. For sufficiently large α-values the actual gradient field matters and the outcome is chosen with larger probability among states that make the scalar product $\mathrm{G} \cdot \mathrm{J}(\eta^{\mathrm{I}})$ maximal (Fig.4 and Fig.5). The question arises if the critical α_c-value can be calculated for which pattern formation is observed.

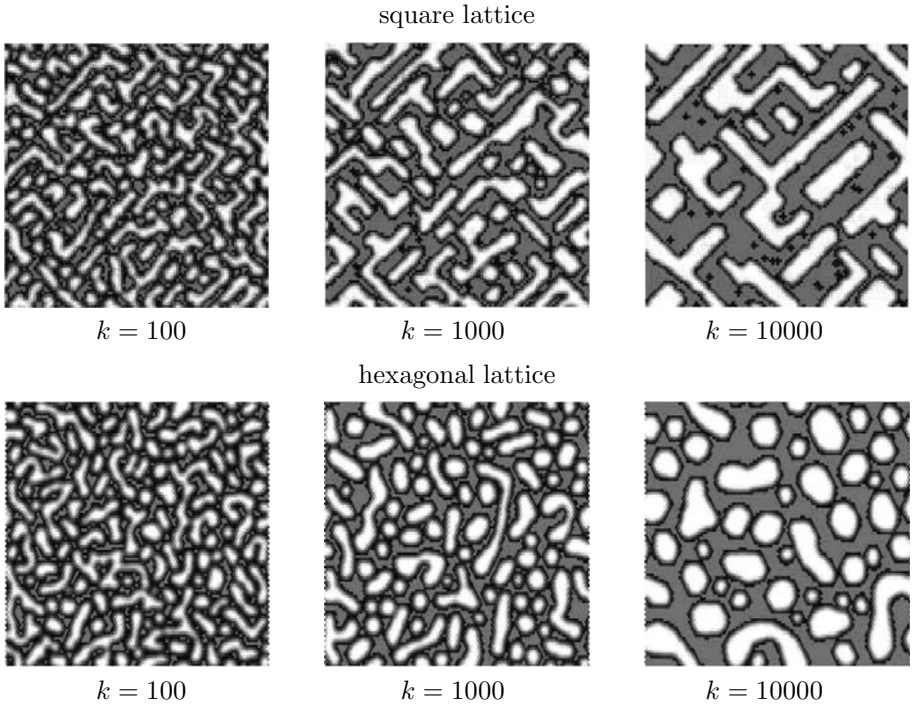

FIGURE 5. Adhesive pattern formation in the LGCA model on different lattices. Different gray levels represent cell densities (dark: low cell density), black marks empty nodes. On the square lattice, strong anisotropies are visible in diagonal directions which are absent on the hexagonal lattice. An explanation for the anisotropy is provided by the eigenvalue spectra which yield corresponding anisotropies for the square, but not the hexagonal lattice; parameters: $\alpha = 0.8\ (> \alpha_c),\ \bar{\rho} = 0.4,\ L = 100.$

3.1. The non-linear Boltzmann equation

The LGCA stochastic process is a stationary Markov chain, i.e. there is no memory effect and transitions are time-independent. Define the single particle distribution function as

$$f_i(r,k) = E(\eta_i(r,k)).$$

Then the Chapman-Kolmogorov (or master) equation for the LGCA is as follows:

$$\begin{aligned} f_i(r+c_i,k+1) - f_i(r,k) &= E(\eta_i^I(r,k) - \eta_i(r,k)) \\ &= \sum_{\eta^I(r)} \sum_{\eta_{N(r)}(r)} [\eta_i^I(r) - \eta_i(r)] \\ &\quad \times\ W(\eta(r) \to \eta^I(r), \mathrm{G}(r)) \\ &\quad \times\ p(\{\eta|_{N(r)}\}, k), \end{aligned} \tag{9}$$

where $p(\{\eta(r)\}, k)$ is a probability distribution on the LGCA phase space ($2^{b \cdot L \cdot L}$ elements).
Under mean-field assumption we get

$$p(\{\eta(r)\}, k) = \prod_{r,i} [f_i(r,k)^{\eta_i} [1 - f_i(r,k)]^{1-\eta_i}$$

Let $\Omega_i(r,k) = E(\eta_i^I(r,k) - \eta_i(r,k))|_{MF}$.
Then

$$f_i(r + c_i, k+1) - f_i(r,k) \approx \Omega_i.$$

3.2. Stability analysis

For a given average number of cells per node ρ the non-linear Boltzmann equation has a spatially homogeneous stationary solution

$$f_i(r) = \bar{f} = \rho / b$$

satisfying

$$\Omega(\bar{f}) = 0.$$

Question: Can this solution be destabilized (i.e. is there pattern formation)? In order to answer, we introduce fluctuations

$$\delta f_i(r,k) = f_i(r,k) - \bar{f}.$$

Taylor expansion yields the **linearized Boltzmann equation**:

$$\delta f_i(r + c_i, k+1) - \delta f_i(r,k) \tag{10}$$

$$= \sum_{r'} \sum_j \frac{\partial \Omega_i(r)}{\partial f_j(r')}|_{eq} \delta f_j(r', k) \tag{11}$$

$$= \sum_{p=0}^{b} \sum_j \Omega_{ij}^{11,p} \delta f_j(r + c_p, k), \tag{12}$$

$$\tag{13}$$

where $c_0 = 0$ and the linearized Boltzmann operator $\Omega_{ij}^{11,p}$ is defined as

$$\Omega_{ij}^{11,p} = \frac{\partial \Omega_i(r)}{\partial f_j(r + c_p)}|_{eq}.$$

Define the Fourier transform as

$$f_i(q,k) = \sum_r \exp(-\imath < q, r >) \delta f_i(q,k)$$

Then each Fourier component evolves independently according to

$$f_i(q, k+1) = \sum_j \Gamma_{ij}(q) \delta f_j(q,k).$$

The one-step **Boltzmann propagator** $\Gamma_{ij}(q)$ is defined as

$$\Gamma_{ij}(q) = \exp(-\imath < q, c_i >)[\delta_{ij} + \sum_{p=0}^{b} \exp(\imath < q, c_p >) \Omega_{ij}^{11,p}].$$

One can show that the eigenvalues of Γ are given as

$$\lambda_1(q) = \sum_{i=1}^{b} e^{-\mathbf{i}\,\frac{2\pi}{L}\,q\cdot c_i} \left(\frac{1}{b} + \sum_{n=1}^{b} e^{\mathbf{i}\,\frac{2\pi}{L}\,q\cdot c_n}\ \omega_i^n \right), \tag{14}$$
$$\lambda_2(q) = \ldots = \lambda_b(q) = 0\ .$$

For the square lattice and $\bar{f}=\frac{1}{2}$, the symmetries[1] of ω_i^n can be used to obtain

$$\lambda_1(q) = \quad \big(\cos(q_1)+\cos(q_2)\big) + 4\left(\omega_1^1+\omega_2^1\right)\left(\sin^2(q_1)+\sin^2(q_2)\right)$$
$$-\,4\,\omega_2^1\ \big(\cos(q_1)-\cos(q_2)\big)^2$$

In two-dimensional systems, groups of unstable modes with identical absolute value of the wave number $|q| = \mathfrak{q}$ simultaneously start to grow, i.e.

$$\delta f_i(r,k) \sim \sum_{\substack{q\in Q^c \\ |q|=\mathfrak{q}}} e^{-\mathbf{i}\,\frac{2\pi}{L}\,q\cdot r}\ F_i(q,k)\ .$$

Therefore, according to linear theory, any superposition of these modes determines the dynamics of the system.

It follows that the adhesive LGCA on the square lattice may become unstable, i.e. $\lambda_1(q) > 1$, if $\left(\frac{1}{4} - 4\left(\omega_1^1+\omega_2^1\right)\right) < 0$. The coefficients of the Boltzmann propagator ω_i^n depend on the sensitivity α and the averaged node density $\bar{\rho}$. Therefore, for a fixed averaged node density $\bar{\rho}$ a *critical sensitivity* α_c is defined by the condition

$$\lambda_1(q) \approx 1 \Leftrightarrow \left(\frac{1}{4} - 4\ \left(\omega_1^1(\bar{f},\alpha_c)+\omega_2^1(\bar{f},\alpha_c)\right)\right) = 0\ .$$

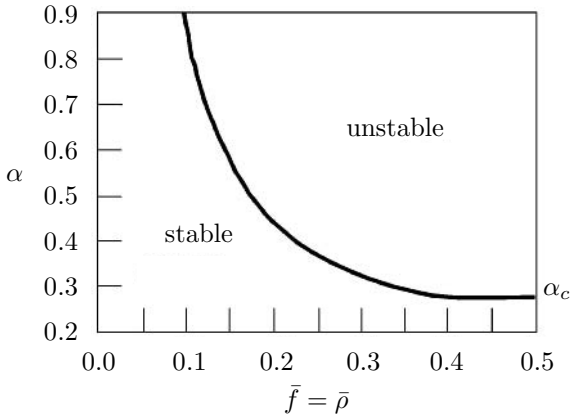

FIGURE 6. Phase diagram of the adhesive one-species LGCA model for the square lattice (b=4). The regions of stable ($0<\lambda_1(q)<1$) and unstable ($\lambda_1(q)>1$) behavior are shown as a function of sensitivity α and averaged single-channel density $\bar{f}=\bar{\rho}$. For any $\bar{\rho}$ the critical sensitivity α_c value can be determined.

[1] i.e. , $\omega_3^1 = -\omega_1^1$ and $\omega_4^1 = \omega_2^1$, [17]

Fig.6 shows the numerically determined phase diagram for the adhesive LGCA. For example, in the case of the half-filled square lattice ($\bar{\rho} = 0.5$) the critical sensitivity is $\alpha_c \approx 0.263$. In conclusion, Fourier analysis can deduce important features of the patterns observed in LGCA simulations.

4. A cellular automaton model for chemotaxis

Chemotaxis describes the dependence of individual cell movement on a chemical signal gradient field (see the glossary by Alt/Tranquillo in [3]). Accordingly, spatial patterns at the level of cells and chemical signals can be distinguished. Chemotactic patterns result from the coupling of two different spatio-temporal scales at the cell and the molecular level, respectively. Morphogenesis of the cellular slime mold *Dictyostelium discoideum* has developed as an experimental model system for chemotactic dynamics, particularly governing the formation of aggregation centers and the formation of slugs and fruiting bodies [25, 33]. In the case of the slime mold, the major signaling molecule has been identified as cyclic adenosine monophosphate (cAMP, see [10, 12]).

The first mathematical model of chemotactic pattern formation was proposed in the early seventies and is formulated as partial differential equation system [28, 29, 30]. Later on, hybrid models distinguishing discrete cells and continuous signal concentrations have been suggested (e.g. [1, 16, 39]). So far, hybrid models have been solely studied by means of simulations [46]. Here, we present a hybrid lattice-gas cellular automaton which allows to explicitly analyze spatial pattern formation depending particularly on the chemotactic sensitivity of cells to the gradient field[2]. The analysis is similar to the adhesive interaction model (cp. section 3) since in both cases gradients – in cellular density and chemical concentration, respectively – are governing the interaction.

Our model is based on motile cells moving on a two-dimensional lattice ($b = 4$) with one rest channel ($\tilde{b} = 5$). We assume that $|\mathcal{L}| = L_1 \cdot L_2 = L^2$. The cells are able to produce and secrete a substance. In the absence of this substance, the cells perform a random walk on the lattice, otherwise they are sensitive to the substance such that they move towards regions of higher concentrations of the signal (c_{sig}) in the outer von Neumann interaction neighborhood. The signal decays continuously and diffuses on the lattice.

Chemotactic interaction rule. The interaction rule of the LGCA for chemotaxis comprises the following processes in sequential order

1. the decay of chemical substance,
2. each cell secrets with a given probability a fixed amount of chemical substance,
3. the diffusion of chemical substance and

[2]No confusion should arise with hybrid cellular automata defined by non-uniform rules, i.e. different rules are applied to the cells of the lattice [11].

4. the redistribution of cells on node channels depending on the local signal concentration.

The interaction step is followed by a propagation step.

Diffusion of the signal In order to model diffusion of the signal, a method of "moving averages" is applied as a discrete approximation of the continuous diffusion equation. This method allows an efficient implementation of the diffusion process even for large lattices [47].

Redistribution of cells In order to determine the probability for transition from the pre-interaction state $\boldsymbol{\eta}(r) = (\eta_1, \ldots, \eta_5)$ to the post-interaction state $\boldsymbol{\eta}^{\mathrm{I}}(r) = (\eta_1^{\mathrm{I}}, \ldots, \eta_5^{\mathrm{I}})$ we define rules for the occupation of the rest channel (c_5) and the velocity channels ($c_1, \ldots, c_4$) separately. The rest channel of node r gains a cell with probability $\mathrm{n}(r)/5$, where $\mathrm{n}(r) = \sum_{i=1}^{5} \eta_i(r)$ is the number of cells at node r. Let $\hat{\mathrm{n}}(r) \leq \mathrm{n}(r)$ be the number of the remaining cells at r.

For the chemotactic response to the local signal concentration of the remaining cells, we define the *normalized signal gradient field*

$$\bar{\boldsymbol{G}}_{sig}\left(\boldsymbol{\eta}_{\mathcal{N}(r)}\right) := \sum_{p=1}^{4} c_p \,\mathrm{on}\,(r + c_p)\ , \tag{15}$$

where $\mathrm{on}(r + c_p)$ is the *order number* of the signal concentration $c_{sig}(r + c_p)$. It is determined by ordering the four neighboring nodes of r according to their signal concentration[3], such that node r' with maximal signal concentration receives $\mathrm{on}(r') = 4$, and node r'' with the lowest concentration $\mathrm{on}(r'') = 1$. Note that we consider order numbers rather than signal concentrations in the computation of the gradient field, in order to normalize absolute differences of neighboring signal concentrations (which are usually very small) to relative differences (which are at least 1 after normalization). With this trick cells are made more sensitive to the substance gradient field.

The probability for transition from $\hat{\boldsymbol{\eta}}(r) := (\eta_1, \ldots, \eta_4)$ to $\hat{\boldsymbol{\eta}}^{\mathrm{I}}(r) := (\eta_1^{\mathrm{I}}, \ldots, \eta_4^{\mathrm{I}})$ in the presence of $\bar{\boldsymbol{G}}_{sig}\left(\boldsymbol{\eta}_{\mathcal{N}(r)}\right)$ is given by

$$\boxed{W\left(\hat{\boldsymbol{\eta}}_{\mathcal{N}(r)} \to \hat{\boldsymbol{\eta}}^{\mathrm{I}} | \alpha\right) = \frac{1}{Z}\, \exp\left(\alpha\, \bar{\boldsymbol{G}}_{sig}\left(\hat{\boldsymbol{\eta}}_{\mathcal{N}(r)}\right) \cdot \boldsymbol{J}\left(\hat{\boldsymbol{\eta}}^{\mathrm{I}}\right)\right)\, \delta_{\hat{\mathrm{n}},\hat{\mathrm{n}}^{\mathrm{I}}},} \tag{16}$$

where the normalization factor $Z = Z(\hat{\mathrm{n}}, \bar{\boldsymbol{G}}_{sig})$ is chosen such that

$$\sum_{\hat{\boldsymbol{\eta}}^{\mathrm{I}} \in \{0,1\}^4} W\left(\hat{\boldsymbol{\eta}}_{\mathcal{N}(r)} \to \hat{\boldsymbol{\eta}}^{\mathrm{I}} | \alpha\right) = 1, \quad \forall\, \hat{\boldsymbol{\eta}} \in \{0,1\}^4\ ,$$

and the cell flux is defined as

$$\boldsymbol{J}\left(\hat{\boldsymbol{\eta}}(r)\right) = \sum_{i=1}^{4} c_i\, \eta_i(r)\,;$$

α is the *chemotactic sensitivity* of the cells. Fig.7 gives an example of the transition probability.

[3] If, e.g., $c_{sig}(r+c_3) > c_{sig}(r+c_4) > c_{sig}(r+c_2) > c_{sig}(r+c_1)$ then $\mathrm{on}(r+c_3) = 4$, $\mathrm{on}(r+c_4) = 3$, $\mathrm{on}(r + c_2) = 2$, $\mathrm{on}(r + c_1) = 1$.

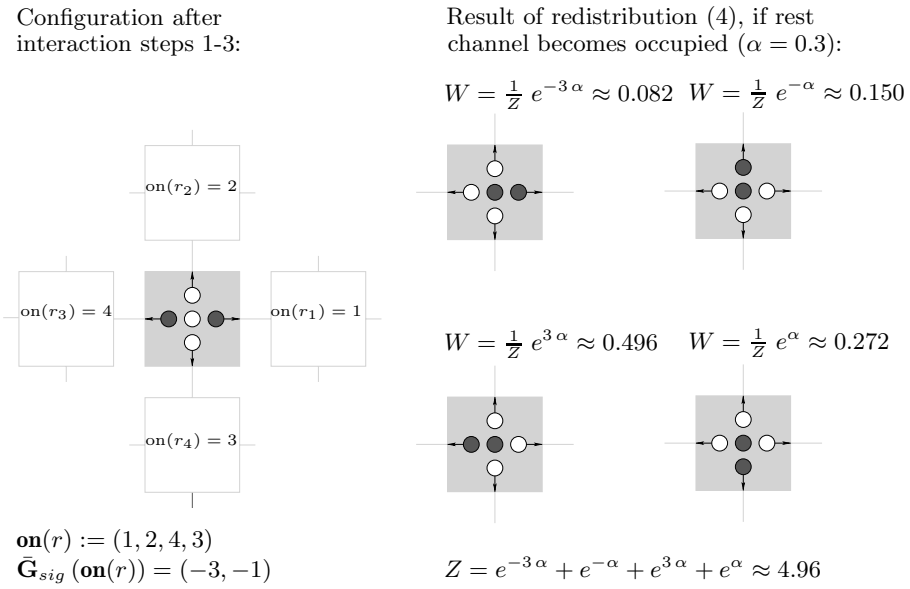

FIGURE 7. Example of cell redistribution on a lattice node due to chemotactic response. The rest channel becomes occupied with probability 2/5. The signal concentration in the interaction neighborhood can be ordered such that $c_{sig}(r_3) > c_{sig}(r_4) > c_{sig}(r_2) > c_{sig}(r_1)$.

Simulations. We performed simulations on a 100×100 square lattice with a random spatial distribution of cells of density 0.05. Fig.8 shows resulting spatial cell distributions for chemotactic sensitivities $\alpha = 0.1$ and $\alpha = 0.3$ and different signal diffusion constants.

Spatial patterns are observed for both sensitivities, but on different time scales. Clearly, a high sensitivity enhances the formation of aggregation clusters (cp. Fig.8, $k = 100$). If simultaneously the diffusion constant of the chemical signal is increased, fewer but larger clusters appear.

Note that the presented chemotaxis LGCA is a generalization of the adhesive LGCA (introduced in the previous section). With a particular choice of parameters, the chemotactic interaction rule reduces to the adhesive interaction rule: namely in the case, that each cell secrets equal amounts of chemical substance, and that the substance *decays instantaneously* (no diffusion!), the order number is proportional to the number of cells in the outer interaction neighborhood (i.e. $\bar{\boldsymbol{G}}_{sig}\left(\boldsymbol{\eta}_{\mathcal{N}(r)}\right) \propto \boldsymbol{G}\left(\boldsymbol{\eta}_{\mathcal{N}(r)}\right)$, cp. eqn. (8), and eqn. (15)), and hence both models are determined by identical transition probabilities.

An *incomplete decay* of the diffusing signal introduces on one hand a memory effect (the information about local cell densities is "stored" in the signal concentration for longer times) and on the other hand an indirect interaction between

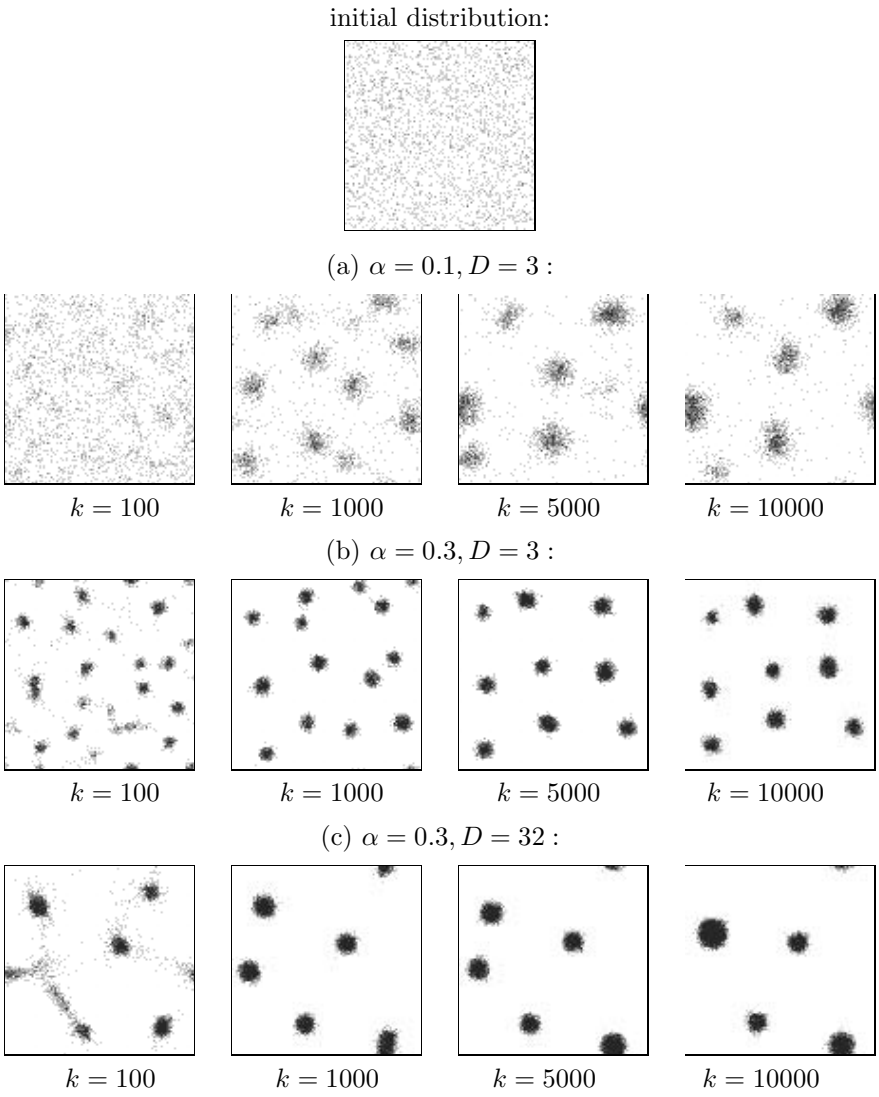

FIGURE 8. Chemotaxis pattern formation in the LGCA model. Gray levels represent cell densities (dark: high cell density); parameters: cell density: 0.05, a cell produces a signal of amount 1 with probability 0.01, continuous signal decay of 70%, diffusion coefficient of signal: $D\ [\triangle l^2/\triangle k]$ ($\triangle l$: unscaled unit for length of lattice node, $\triangle k$ unscaled unit for time step), chemotactic sensitivity: α, lattice size: $L = 100$.

cells of a larger spatial range than the interaction neighborhood (transmission of the information about local cell densities by the diffusion of the signal).

5. Discussion

There is still no standard model for describing interacting discrete biological cells. In this chapter, lattice-gas cellular automata are proposed as models for spatially extended systems of interacting cells. While in physico-chemical processes typically the macroscopic equation is known *a priori*, the master equations in biological pattern formation are often far from clear. It is a challenge for the future to systematically link pattern formation models as presented in this article to intracellular genetic and signaling networks. This implies covering a whole range of cellular and molecular scales. First steps are *hybrid cellular automata* which have been suggested as models for avascular tumor growth and angiogenesis [1, 18]. These models incorporate discrete cells and continuous nutrient and signal molecule concentrations.

In the following discussion we focus on a critical evaluation of the modeling potential of lattice-gas cellular automata which simultaneously allow for the modeling of morphogenetic motion and the analysis of spatio-temporal pattern formation. *Lattice-gas models* have been originally introduced as discrete microscopic caricatures of hydrodynamical systems where it was shown that simple collision rules for discrete particles can give rise to the intricate structures of hydrodynamic flow as long as the rules conserve mass and momentum [21, 27]. Lattice-gas automata as models of local biological cell-cell interaction maintain the discrete particle nature of lattice-gases, but incorporate additional degrees of modeling freedom – in particular, less conservative constraints are imposed (e.g. momentum or energy conservation are abandoned). This is justified since biological cells typically perform an active creeping motion with negligible small inertia and with dissipative friction.

Viewing lattice-gas cellular automata as interacting cell systems allows to apply analytic tools from statistical mechanics. In particular, corresponding Boltzmann equations may be derived for lattice-gas cellular automata. One can trace back pattern initiation to *cell-based instabilities* in lattice-gas cellular automata – these automata are prototypes of cellular self-organization. At the *microscopic level* lattice-gas cellular automata represent only a caricature of the forces between the cells in the real biological system. A molecular dynamics approach taking into account the detailed form of molecular and intra-cellular interactions is much more appropriate to obtain information at the smallest scales and to model exact cellular shapes[4]. However, in the intermediate *mesoscopic regime* focusing on the dynamics of cell-cell interactions, lattice-gas cellular automata are a promising model tool. As in the hydrodynamic lattice-gas automata, it turns out that for many important cell-cell interactions the coarse-grained perspective of cellular automata suffices to capture the qualitative behavior at the macroscopic level.

The discreteness of the state space in lattice-gas cellular automata reflects the discrete nature of biological cells and is a desired property. In addition, interactions

[4] A modeling strategy for a dynamic phenomenological description of cell shapes is provided by the extended Potts model (see for example [23, 33, 43]).

are defined with respect to a discrete local neighborhood in the cellular automaton. Since a neighborhood in the automaton (e.g. the von Neumann interaction neighborhood) can host only a discrete number of cells, the cellular automaton is a natural tool to model cell interactions of a limited number of spatially adjacent cells, which characterizes the biological situation of local cell interaction. This property of *discrete and local interaction* is more difficult to achieve in other microscopic approaches and impossible to describe in the framework of continuous models.

A synchronous update is inherent in the dynamics of LGCA and an exclusion principle is imposed on the state space. The exclusion principle with respect to the individual velocity channels implies that at any time at most one cell is allowed in each channel at every lattice node. An asymmetric update would break the exclusion principle because a cell could migrate to a node that already hosts a cell with the same orientation leading to a state space conflict. It is, however, possible to allow for asynchronous update in modified lattice-gas automaton models (see for example [6]). Anisotropies induced by synchronous and asynchronous updates in cellular automaton models have been systematically investigated in [40, 41]. There is a close relation between asynchronous probabilistic cellular automata and interacting particle systems ([20], see also [45]).

The discrete structure of the underlying lattice is also a wanted property of the automaton model since this allows a straightforward modeling of hard-core cell repulsion. In the automaton, cells are distributed at the nodes of a regular discrete lattice, which introduces a natural physical distance defined by the lattice spacing. However, the discrete lattice may induce artefacts, and care has to be taken to choose an appropriate lattice. In particular, the lattice may induce *spurious modes* and *spatial anisotropies*. It is an important advantage of the cellular automaton concept that many artefacts can be deduced already from a linear approximation, i.e. the Fourier spectrum of the underlying Boltzmann equation. These artefacts may be avoided, in particular by the introduction of resting cells and the use of hexagonal lattices. Spatial artefacts can be expected, if Fourier analysis indicates dominance of particular lattice directions. This is, for example, the case in the adhesive LGCA. Here, diagonal directions are prevailing in square lattice simulations, while bias of any directions is much less pronounced in hexagonal simulations (cp. Fig.5. The artefact here comes from the fact that the 4th order tensor (i.e, momentum flux) is anisotropic on a square lattice). The Fourier spectrum, however, also allows to explain such "spatial artefacts" (data not shown). For example in the adhesive LGCA, the "anisotropic" distribution of maxima in the spectrum corresponding to the square lattice is responsible for "diagonal anisotropies" in the square simulations, that are nearly absent on the hexagonal lattice (cp. Fig.5 and [17]).

All the examples introduced here operate on finite lattices. A biological embryo or a tissue culture are definitely finite systems and special care has to be taken to choose appropriate boundary conditions in a corresponding model. We have, typically, applied periodic boundary conditions in the models introduced in

this paper. This is justified, whenever a model focuses on a local developmental aspect, for example the transition from an unordered cell distribution to the formation of relatively small (oriented) clusters.

Modelling cell interaction. The adhesive LGCA mimics a single cell type model corresponding to an experiment in which cells are randomly distributed on a two-dimensional substratum and their adhesive dynamics of local monolayer formation and movement is observed. A similar model has been introduced as a model for phase segregation in a quenched binary alloy [2]. The microdynamical equation of the automaton is non-linear. Stability analysis of the linearized Boltzmann equation shows that in the stable regime the dominant mode is diffusive. Conditions for a *cell-based, adhesion-driven instability* can be derived – this instability occurs if cell adhesion or cell density are sufficiently large (Fig.6). Then, the dominant mode destabilizes implying initial periodic spatial pattern formation with a characteristic wave length that can be deduced from the mean-field analysis.

The model suggests a mechanism for periodic pattern formation based on local interactions of a single cell type without chemical communication mediated by reaction-diffusion dynamics. However, the periodicity of the patterns is only maintained within the short time scale of the linear regime which may comprise days or hours in corresponding tissue experiments (Fig.5, $k = 100$). The initial local aggregation is due to the anti-diffusive dynamics of the automaton. Accordingly, aggregation neighborhoods become void of cells implying spatially heterogeneous patch formation. On a larger time scale, coalescence of neighboring aggregation patches with corresponding growth of single-phase domains and increasing wave length of the patch distribution are observed (cp. Fig.5, $k \geq 1000$) – a scaling law for the growth of average domain sizes ($R(k) \sim k^{1/3}$) has been derived in ([2]).

In contrast to the adhesive automaton model, the Turing mechanism (of diffusion-driven instability) in reaction-diffusion systems – yielding a similar dispersion relation as the adhesive automaton (cp. [17]) – is able to stabilize an initially formed periodic pattern which may, eventually, lead to a bounded, stationary, spatially non-uniform, steady state (cp. ([36])). The stabilization is due to an appropriately chosen nonlinear reaction dynamics. Note that in Turing's original model [44], the reaction dynamics was assumed linear. This means that if a uniform steady state becomes unstable, then the chemical concentrations could grow exponentially which is, of course, biologically (and chemically) unrealistic. Since then a number of nonlinear reactions have been proposed that can stabilize initial spatial heterogeneities (see [31] for an overview).

Nevertheless, the adhesive automaton model (cp. Fig.5) has relevance for the explanation of animal patterns, for example stripe patterns of some fish, which have previously been attributed to long-range communication in reaction-diffusion systems [32]. The necessary assumption is that the pattern formation process is "frozen" in a particular state which is justified by biological observations. In particular, it is known that non-junctional cell-surface adhesion proteins (e.g. cadherins)

that dominate the migratory phase may also induce tissue-specific cell-cell adhesion, which is furthermore stabilized by the assembly of cell junctions. Since many transmembrane cadherins (in particular glycoproteins) are used for junctional as well as non-junctional adhesive contacts – they are able to accumulate at sites of cell-cell contact, these molecules are candidates to induce a transition from the migratory to the stationary state. Further processes characterizing a turnover from dynamic to static interactions and contributing to the stabilization of tissue organization are contact inhibition of pseudopodal activity and reversible loss of the cell's contractile machinery [4]. However, for a more realistic modeling of animal pigment pattern formation it is important to consider the effects of interactions with other cell types and with the extracellular matrix.

Modelling tumour growth. It has become clear that mathematical modeling can contribute to a better understanding of the still largely unknown cancer dynamics [22]. In particular, a number of cellular automaton models for different phases of tumor growth have been suggested (see review in [35]). We have previously introduced a hybrid LGCA model for the avascular growth phase in multicellular spheroids [18]. A better understanding of *in vitro* avascular tumor dynamics might allow for the design of treatments which transfer a growing tumor into a saturated (non-growing and therefore non-dangerous) regime by means of experimentally tractable parameter shifts. The hybrid cellular automaton approach implements a lattice-gas automaton picture on the level of the cells and explicitly takes into account mitosis, apoptosis and necrosis as well as nutrient consumption and a diffusible signal that is emitted by cells becoming necrotic. All cells follow identical interaction rules. The necrotic signal induces a chemotactic migration of tumor cells towards maximal signal concentrations. Starting from a small number of tumor cells automaton simulations exhibit the self-organized formation of a layered structure consisting of a necrotic core, a ring of quiescent tumor cells and a thin outer ring of proliferating tumor cells.

The research strategy presented in this chapter is "modular", i.e. starting from "basic interaction modules" (module examples are adhesion and chemotaxis-based interactions) coupling of the modules is required to design models for specific morphogenetic problems. The focus of future activities is the analysis of extended and combined interactions, which are not necessarily restricted to cells but could also comprise interactions at the organismic or the subcellular level. The resulting models contain a multitude of spatio- and temporal scales and impose enormous difficulties for analytic treatment.

Further analysis. The master equation that fully specifies a probabilistic cellular automaton is a Chapman-Kolmogorov equation. A Boltzmann equation can be derived if all correlations are neglected and the system dynamics is expressed solely by means of single particle distribution functions. The Boltzmann equation is typically non-linear due to the interactions imposed. In this chapter we have restricted attention to the linear analysis of the Boltzmann equation, i.e. we have analyzed

the Fourier spectrum of the linearized and Fourier-transformed Boltzmann equation (cp. adhesive LGCA). However, it is possible to refine the approximation by including higher order *correlations*.

The Boltzmann equation arises under the assumption that the probability of finding two cells at specific positions is given by the product of corresponding single particle distribution functions, i.e. any correlations are neglected and distributions fully factorize. By including two-, three-, etc. particle distribution functions the effect of correlations can be systematically studied. In particular, if pair correlations are taken into account, but third and higher order correlations are neglected, a *generalized Boltzmann equation* for the single particle distribution function is obtained, coupled to the so-called *ring equation* describing the evolution of the pair correlation function. For the adhesive (density-dependent) cellular automaton (Alexander model) the ring equation has been successfully evaluated [7]. It is a challenge to determine corresponding equations for other cellular automata. This analysis could particularly improve the understanding of long time behavior.

Furthermore, it is straightforward to directly simulate the Boltzmann equation arising from the mean-field assumption as described in [15]. There is, however, an essential difference between Navier-Stokes lattice Boltzmann methods and lattice Boltzmann versions of cellular automaton models described in this chapter, since in the latter we are not primarily interested in a numerical scheme for solving a given macroscopic equation but in a better understanding of collective behavior arising in microscopic interaction models. The most simple Navier-Stokes lattice Boltzmann models use a single relaxation time or lattice-BGK approximation (BGK named after Boghosian, Coveney and Emerton). This approach is equivalent to the exclusive consideration of the dominant mode in the Fourier spectrum of the linearized Boltzmann equation. Accordingly, a systematic *bifurcation theory* for cellular automaton models of cellular interaction might be developed. Based on the variability in the local dynamics, we demonstrated that cellular automaton modeling provides an intuitive and powerful approach to capture essential aspects of complex phenomena on various scales. In conclusion, there are both challenging future perspectives with regards to interesting applications of the lattice-gas cellular automaton idea and possible refinements of analytical tools for the investigation of lattice-gas cellular automata. Hopefully, the potential of cellular automata for modeling essential aspects of biological systems will be further exploited in the future.

Website

A simulation platform containing various LGCA models with biological applications can be found at www.biomodeling.info

Acknowledgments

The author greatfully acknowledges Andreas Dress (Bielefeld, Leipzig, Shanghai) for his introduction to the world of cellular automata and Sabine Dormann (Cologne) who contributed to the design, simulation and analysis of the lattice-gas cellular automata introduced in this chapter. Furthermore, financial support of Deutsche Forschungsgemeinschaft (through DFG grant DE 842/2) and of the European Commission (through grant EU-RTD-IST-2001-38923) are acknowledged.

References

[1] T. Alarcon, H. Byrne, and P. K. Maini. A cellular automaton for tumour growth in inhomogeneous environment. *J. Theor. Biol.*, 225:257–274, 2003.

[2] F. J. Alexander, I. Edrei, P. L. Garrido, and J. L. Lebowitz. Phase transitions in a probabilistic cellular automaton: growth kinetics and critical properties. *J. Statist. Phys.*, 68(3/4):497–514, 1992.

[3] W. Alt and G. Hoffmann, editors. *Biological motion*. Springer-Verlag, Berlin, Heidelberg, New York, 1990.

[4] P. B. Armstrong. The control of cell motility during embryogenesis. *Cancer Metast. Rev.*, 4:59–80, 1985.

[5] F. Bagnoli. Cellular automata. In F. Bagnoli, P. Lio, and S. Ruffo, editors, *Dynamical modelling in biotechnologies*. World Scientific, Singapore, 1998.

[6] U. Börner, A. Deutsch, H. Reichenbach, and M. Bär. Rippling patterns in aggregates of myxobacteria arise from cell-cell collisions. *Phys. Rev. Lett.*, 89:078101, 2002.

[7] H. Bussemaker. Analysis of a pattern forming lattice gas automaton: mean field theory and beyond. *Phys. Rev. E*, 53 (2):1644–1661, 1996.

[8] J. L. Casti. *Alternate realities*. John Wiley, New York, 1989.

[9] J. L. Casti. Science is a computer program. *Nature*, 417:381–382, 2002. book review.

[10] Y. Y. Chang. Cyclic 3',5'-adenosine monophosphate phosphodiesterase produced by the slime mold D*ictyostelium discoideum*. *Science*, 161:57–59, 1968.

[11] P. P. Chaudhuri, D. R. Chowdhury, S. Nandi, and S. Chatterjee. *Additive cellular automata – Theory and Applications, vol. 1*. IEEE Computer Society Press, CA, USA, 1997.

[12] M. Y. Chen, R. H. Insall, and P. N. Devreotes. Signaling through chemoattractant receptors in D*ictyostelium*. *Trends Genet.*, 12:52–57, 1996.

[13] B. Chopard and M. Droz. *Cellular automata modeling of physical systems*. Cambridge University Press, Cambridge, 1998.

[14] B. Chopard, A. Dupuis, A. Masselot, and P. Luthi. Cellular automata and lattice Boltzmann techniques: an approach to model and simulate complex systems. *Adv. Compl. Syst.*, 5(2), 2002.

[15] A. Czirók, A. Deutsch, and M. Wurzel. Individual-based models of cohort migration in cell cultures. In W. Alt, M. Chaplain, M. Griebel, and J. Lenz, editors, *Models of polymer and cell dynamics*, Basel, 2003. Birkhäuser.

[16] J. C. Dallon, H. G. Othmer, C. v. Oss, A. Panfilov, P. Hogeweg, T. Höfer, and P. K. Maini. Models of D*ictyostelium discoideum* aggregation. In W. Alt, A. Deutsch, and G. Dunn, editors, *Dynamics of cell and tissue motion*, pages 193–202. Birkhäuser, Basel, 1997.

[17] A. Deutsch and S. Dormann. *Cellular automaton modeling of biological pattern formation*. Birkhauser, Boston, 2005.

[18] S. Dormann and A. Deutsch. Modeling of self-organized avascular tumor growth with a hybrid cellular automaton. *In Silico Biol.*, 2:0035, 2002.

[19] D. Drasdo. On selected individual-based approaches to the dynamics in multicellular systems. In W. Alt, M. Chaplain, M. Griebel, and J. Lenz, editors, *Models of polymer and cell dynamics*. Birkhäuser, Basel, 2003.

[20] R. Durrett and S. Levin. The importance of being discrete (and spatial). *Theor. Popul. Biol.*, 46:363–394, 1994.

[21] U. Frisch, B. Hasslacher, and Y. Pomeau. Lattice-gas automata for the Navier-Stokes equation. *Phys. Rev. Lett.*, 56(14):1505–1508, 1986.

[22] R. Gatenby and P. K. Maini. Cancer summed up. *Nature*, 421:321, 2003.

[23] J. A. Glazier and F. Graner. Simulation of the differential adhesion driven rearrangement of biological cells. *Phys. Rev. E*, 47(3):2128–2154, 1993.

[24] D. Godt and U. Tepass. D*rosophila* oocyte localization is mediated by differential cadherin-based adhesion. *Nature*, 395:387–391, 1998.

[25] A. Goldbeter. Oscillations and waves of cyclic AMP in D*ictyostelium discoideum*: a prototype for spatio-temporal organizaation and pulsatile intercellular communication. *Bull. Math. Biol.*, 68:1095–1109, 2006.

[26] J. Hardy, Y. Pomeau, and O. de Pazzis. Time evolution of a two-dimensional model system. i. invariant states and time correlation functions. *J. Math. Phys.*, 14:1746, 1973.

[27] L. P. Kadanoff. On two levels. *Phys. Today*, Sept.:7–9, 1986.

[28] E. F. Keller and L. A. Segel. Initiation of slime mold aggregation viewed as an instability. *J. Theor. Biol.*, 26:399–415, 1970.

[29] E. F. Keller and L. A. Segel. A model for chemotaxis. *J. Theor. Biol.*, 30:225–234, 1971.

[30] E. F. Keller and L. A. Segel. Travelling bands of chemotactic bacteria: A theoretical analysis. *J. Theor. Biol.*, 30:235–248, 1971.

[31] P. K. Maini. Mathematical models in morphogenesis. In V. Capasso and O. Dieckmann, editors, *Mathematics Inspired by Biology*, pages 151–189. Springer, Berlin, 1999.

[32] P. K. Maini, K. J. Painter, and H. N. P. Chau. Spatial pattern formation in chemical and biological systems. *J. Chem. Soc., Faraday Trans.*, 93(20):3601–3610, 1997.

[33] A. F. M. Marée and P. Hogeweg. How amoeboids self-organize into a fruiting body: Multicellular coordination in D*ictyostelium discoideum*. *Proc. Natl. Acad. Sci. USA*, 98:3879–3883, 2001.

[34] M. Mitchell. Is the universe a universal computer? *Science*, 298:65–68, 2002. book review.

[35] J. Moreira and A. Deutsch. Cellular automaton models of tumour development – a critical review. *Adv. Compl Syst. (ACS)*, 5(2):1–21, 2002.

[36] J. D. Murray. *Mathematical Biology*. Springer, New York, 3 edition, 2002.

[37] H. G. Othmer, P. K. Maini, and J. D. Murray, editors. *Experimental and theoretical advances in biological pattern formation*, New York, 1993. Plenum Press.

[38] M. Pfeifer. Developmental biology: birds of a feather flock together. *Nature*, 395:324–325, 1998.

[39] N. J. Savill and P. Hogeweg. Modeling morphogenesis: from single cells to crawling slugs. *J. Theor. Biol.*, 184:229–235, 1997.

[40] B. Schönfisch. Anisotropy in cellular automata. *BioSystems*, 41:29–41, 1997.

[41] B. Schönfisch and A. de Roos. Synchronous and asynchronous updating in cellular automata. *BioSystems*, 51:123–143, 1999.

[42] K. Sigmund. *Games of life – explorations in ecology, evolution, and behaviour*. Oxford University Press, Oxford, 1993.

[43] J. Starruss, T. Bley, L. Soegaard-Andersen, and A. Deutsch. A new mechanism for collective migration of M*yxococcus xanthus*. *J. Statist. Phys.*, 2007.

[44] A. M. Turing. The chemical basis of morphogenesis. *Phil. Trans. R. Soc. London*, 237:37–72, 1952.

[45] A. Voss-Böhme and A. Deutsch. An interacting particle approach to models of differential adhesion, 2007. in preparation.

[46] J. R. Weimar. Coupling microscopic and macroscopic cellular automata. *Parall. Comput.*, 27:601–611, 2001.

[47] J. R. Weimar, D. Dab, J.-P. Boon, and S. Succi. Fluctuation correlations in reaction-diffusion systems: Reactive lattice gas automata approach. *Europhys. Lett.*, 20 (7):627–632, 1992.

[48] S. Wolfram, editor. *Theory and applications of cellular automata*, Singapore, 1986. World Publishing Co.

[49] S. Wolfram. *A new kind of science*. Wolfram Media, Inc, 2002.

Andreas Deutsch
Center for Information Services and High Performance Computing
Dresden University of Technology
Zellescher Weg 12, D-01062 Dresden Germany
e-mail: `andreas.deutsch@tu-dresden.de`

Single-Cell-Based Models in Biology and Medicine
ed. by A.R.A. Anderson, M.A.J. Chaplain, K.A. Rejniak
Mathematics and Biosciences in Interaction, 53–76

I.3 Two-dimensional Multiscale Model of Cell Motion in a Chemotactic Field

Mark Alber, Nan Chen, Tilmann Glimm and Pavel Lushnikov

Abstract. The Cellular Potts Model (CPM) has been used at a cellular scale for simulating various biological phenomena such as differential adhesion, fruiting body formation of the slime mold *Dictyostelium discoideum*, angiogenesis, cancer invasion, chondrogenesis in embryonic vertebrate limbs, and many others. Continuous models in the form of partial differential, integral or integro-differential equations are used for studying biological problems at large scale. It is crucial for developing multiscale biological models to establish a connection between discrete microscopic stochastic models, including CPM, and macroscopic continuous models. To demonstrate multiscale approach we derive in this paper continuous limit of a two-dimensional CPM with the chemotactic interactions in the form of a Fokker-Planck equation describing evolution of the cell probability density function. This equation is then reduced to the classical macroscopic Keller-Segel model. We demonstrate that CPM Monte Carlo simulations are in excellent agreement with the numerics for the continuous macroscopic model with different forms of the chemical field term.

1. Introduction

Models of biological problems fall into two categories: continuous models that use families of differential or integro-differential equations to describe"fields" of interaction, and discrete models in which space, time or state may be discrete. Models may be deterministic or stochastic. Equations in the continuous models often describe fields of cell concentration or force and long-range interactions including chemotaxis. Discrete models describe individual (microscopic) behaviors. They are often applied to microscale events where a small number of elements can have a large (and stochastic) impact on a system. For example, while many periodic growth patterns can be modeled using continuous methods, such patterns

This work was partially supported by NIH Grant No. 1R0-GM076692-01: Interagency Opportunities in Multiscale Modeling in Biomedical, Biological and Behavioral Systems NSF 04.6071. Simulations were performed on the Notre Dame Biocomplexity Cluster supported in part by NSF MRI Grant No. DBI-0420980.

which depend sensitively on substrate concentration are best modeled with discrete methods including Cellular Potts Model (CPM) first introduced in [1, 2, 3, 4].

The hybrid models typical of systems biology tend to mix continuous, discrete, deterministic, and probabilistic approaches to address complex biological problems such as morphogenesis, regeneration, tumor growth and others. (For a review of the different multiscale and hybrid approaches to modeling in biology see [5]).

CPM is a cell-level, energy-minimization-based lattice model which uses an effective energy E coupled to external fields, e.g., the local concentrations of diffusing chemicals, to describe chemotaxis, cell-cell interactions, cell adhesion, motion, differentiation, division and apoptosis. The effective energy mixes true energies, like cell-cell adhesion, and terms that mimic energies, e.g., the response of a cell to a chemotactic gradient

$$E = E_{Adhesion} + E_{Volume} + E_{Chemical}. \tag{1}$$

Given an effective energy one can calculate the resulting cell motion, with individual lattice sites evolving according to the classical Metropolis algorithm with Boltzmann statistics, as the gradient of the effective energy. Since the cells' environment is extremely viscous, cells move to minimize their total effective energy, given the form of the energy, constraints and boundary conditions.

A hybrid model which involves CPM coupled to a continuous model for external fields, consists of a list of biological cells, a list of generalized cells, a set of chemical diffusants and a description of their biological and physical behaviors and interactions embodied in the effective energy, with auxiliary equations to describe absorption and secretion of diffusants and extracellular materials, state changes within the cell, mitosis and cell death, and the behavior of extracellular diffusants.

Multiscale, experimentally motivated hybrid models have successfully used the CPM to reproduce, amongst others, morphological phenomena in the cellular slime mould Dictyostelium discoideum [6, 7], vascular development [8] and behavior of eukariotic cells [9]. In [10, 11] a three-dimensional multiscale approach based on combining discrete and continuum models of biological mechanisms has been used for simulating the proximo-distal increase in the number of skeletal elements in the developing avian limb. Parallel implementation of the 3D CPM for simulating morphogenesis has been studied in [12, 13].

There is a vast literature on studying continuous limits of point-wise discrete microscopic models. In particular, classical Keller-Segel model [14] has been derived from a model with point-wise representation for cells undergoing random walk [15, 16, 17, 18]. However, much less work has been done on deriving macroscopic limits of microscopic models which treat cells as extended objects. One of the first attempts at combining microscopic and macroscopic levels of description of cellular dynamics has been described in [21] where the diffusion coefficient for a collection of noninteracting randomly moving cells has been derived from a one dimensional CPM. Recently a microscopic limit of subcellular elements model [22]

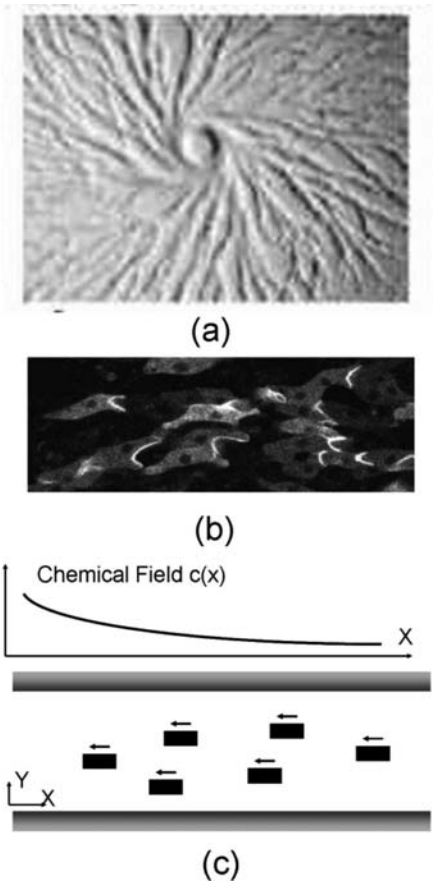

FIGURE 1. (a) Streaming of *Dictyostelium discoideum* towards the aggregation center. Cells move chemotactically towards the aggregation center leading to formation of cell streams and finally mounds. (Reproduced from [19] with permission). (b) Example of a quasi-one-dimensional motion of *Dictyostelium discoideum* inside a stream (this picture is on much smaller scale in comparison with (a)). Cells are moving parallel to each other in the direction of chemical gradient (from left to right). Chemical gradient also causes polarization of cells so that they become elongated in the direction of a gradient. (Reproduced from [20] with permission.) (c) Schematic picture of cell motion in a gradient of chemical field (e.g. chemo-attractant cAMP). The concentration of the chemical field is shown schematically above the main figure.

was derived in the form of an advection-diffusion partial differential equation for cellular density.

In the present paper we establish a connection between a two-dimensional CPM of a cell moving on a substrate and reacting to a chemical field, and a

Fokker-Planck equation for the cell probability density function. This equation is then reduced to the classical macroscopic Keller-Segel equation. In particular, we derive all coefficients of the Keller-Segel model from parameters of the CPM. We also compare Monte Carlo simulations for the CPM with numerics for the Keller-Segel model to support our theoretical results.

Unified multiscale approach, described in this paper and based on combining microscopic and macroscopic models, can be applied, amongst others, to studying biological phenomena of streaming in *Dictyostelium discoideum*. In starved populations of *Dictyostelium* amoebae cells produce and detect a communication chemical (cAMP). The movement of *Dictyostelium* cells changes from a random walk to a directed walk up the cAMP gradient resulting in formation of streams of cells towards the aggregation center (see Fig.1a) and subsequent formation of multicellular fruiting body. Fig.1b shows cells' movement from left to right in response to waves of cAMP travelling through the aggregation stream from right to left. The cAMP gradient on the up-down direction is very small and could be ignored. Fig.1c schematically demonstrates the main features of the cell movement. Unlike differential adhesion, chemotactic cell motion is highly organized over a length scale significantly larger than the size of a single cell. (For details about modeling *Dictyostelium discoideum* fruiting body formation see e.g. [10, 11, 23, 24]).

This paper is organized as follows. First, we describe in Section 2 a CPM for chemotactic cell movement in one spatial dimension. Models of this type arise e.g. in streaming of cells as mentioned above. We investigate the continuum limit of this model and recover the well-known Keller-Segel equations in the limit of the lattice grid size approaching zero. We have extensively tested our results numerically.

In Section 3 we extend our approach to a two-dimensional CPM for studying cell motion in a plane. We derive the continuum limit of this model and test our results numerically.

2. Continuous limit of a one-dimensional CPM

In this section we review results of [25]. Let us consider a quasi-one-dimensional CPM, which means that cells are assumed to move along x direction only and have fixed thickness l_y in y direction (see Fig.2). Let $\varepsilon\Delta x$ denote the size of a lattice site, where $0 < \varepsilon \ll 1$, ε is a small dimensionless constant and $\triangle x$ is a dimensional constant of order one. Each lattice site is described by its index $\mathbf{i} = 0, 1, \ldots$, so that the center of each lattice site is located at $x = \mathbf{i}\varepsilon\Delta x$ with the left and right borders at $x_l = (\mathbf{i} - \frac{1}{2})\varepsilon\Delta x$ and $x_r = (\mathbf{i} + \frac{1}{2})\varepsilon\Delta x$ respectively (see Fig.1.)

In what follows, we will consider dynamics of a single cell. However, our results remain valid for an ensemble of n cells which are well separated from each other, so that probability that two cells would try to occupy the same volume is negligible. This allows us to neglect cell-cell contact interaction. Therefore, we assume that the cell can interact only with the substrate and the chemical field $c(x)$. The chemical field is assumed to depend only on x but not on y. Cells can

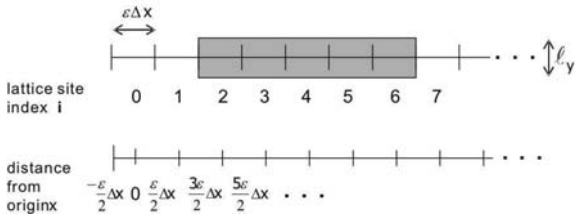

FIGURE 2. Example of a cell in a one-dimensional CPM. The cell (shaded domain) occupies lattice sites $2, \ldots, 6$. It has a length of $5\varepsilon\Delta x$. Its center of mass is located at $x = 4\varepsilon\Delta x$ and its end points are $x_l = 1.5\varepsilon\Delta x$ and $x_r = 6.5\varepsilon\Delta x$.

also produce a chemical which then diffuses. In Section 2.4 we discuss the specifics of production of chemicals by cells.

For a given configuration σ of spins let $N = N(\sigma)$ denote the number of lattice sites that the cell occupies. The length of a cell is equal to $L = N\varepsilon\Delta x$. We denote the position of center of mass of the cell by x and position of the left and right ends of the cell as x_l and x_r respectively. Then $L = x_r - x_l$. Spins of occupied and unoccupied nodes are equal to 1 and 0 and indicated by shaded and unshaded squares respectively (see Fig.2).

We assume that the chemical field $c(x)$ is a slow function of time so its typical time scale is much bigger than time step of a Monte Carlo algorithm. Then the Hamiltonian is given by the formula

$$E = J_{cm} \cdot (2L + 2\ell_y) + \lambda \left(L - L_T\right)^2 + \mu\, c(x)\, L. \tag{2}$$

The first term is a surface energy term which corresponds to the cell-medium interaction energy, where J_{cm} is an interaction energy between cell and medium per unit length. The second term is a length-constraint term which penalizes deviations of a cell length L from the target cell length L_T. Here λ is a positive constant. Choice of λ is determined by the typical scale of fluctuations of cellular membrane. The third term in Eq.(2) describes coupling chemical energy term favoring cell motion *down* or *up* the chemical gradient for $\mu > 0$ and $\mu < 0$ respectively. We assume that the concentration $c(x)$ is a slow function of x on a scale of the typical cell's length L :

$$x_c/L \gg 1, \tag{3}$$

where x_c is a typical scale for variation of $c(x)$ with respect to x. This is consistent with the generally accepted view that cells are typically too small to detect chemical gradients without moving. Notice that chemical energy can be defined as $\mu \int_{x_l}^{x_r} c(x)dx$ but in the limit (3) it is equivalent to the form used in the Hamiltonian (2).

2.1. Discrete evolution equation for probability density of a cell in CPM

In this section we develop analytical model for the stochastic dynamics of a cell in CPM.

Let $P(x, L, t)$ be a probability density for a cell with center of mass at x of length L at time t. Spins $\sigma(\mathbf{i})$ are defined on the lattice $\mathcal{L}$ so that the length of the cell L, which is the difference between the positions of right and left ends of the cell: $L = x_r - x_l$, can take values $n\varepsilon\triangle x$, $n = 1, 2, \ldots$. The position of the center of mass $x = (x_r + x_l)/2$ can take values $n\varepsilon\triangle x/2$, $n = 1, 2, \ldots$. That is, the CPM grid is twice the size of the grid of center of mass. In particular, if $\frac{2x}{\varepsilon\triangle x}$is an even number (i.e. x coincides with one of the lattice sites) then ratio $\frac{L}{\varepsilon\triangle x}$ is also an even number. Alternatively, if $2\frac{x}{\varepsilon\triangle x}$ is an odd number (i.e. x coincides with a boundary between two neighboring lattice sites) then the ratio $\frac{L}{\varepsilon\triangle x}$ is an odd number.

$P(x, L, T)$ is normalized in such a way as to make it a probability density function for a continuous limiting equation. This means that the probability for a cell to have its center of mass at x and a length L at time t is given by $(\varepsilon\triangle x)^2 P(x, L, T)$, where $\varepsilon\triangle x/2$ is the spacing between nodes, $2\varepsilon\triangle x$ is the spacing in L for a fixed x.

The time interval between two Monte Carlo steps is $\varepsilon^2\Delta t$, where Δt is a fixed time unit. This implies the following diffusive time-space scaling $\frac{\varepsilon^2\Delta t}{(\varepsilon\Delta x)^2} = \frac{\Delta t}{(\Delta x)^2}$ which is independent of the scaling parameter ε. We now switch from measuring time in Monte Carlo steps $n = 0, 1, \ldots$ to using a continuous time variable $t = n\,\varepsilon^2\,\Delta t$.

Suppose at time t the cell is at a state (x, L) meaning that it has length L and its center of mass is at x. The stochastic discrete system at time $t + \varepsilon^2\triangle t$ can switch to one of the following four possible states:

(a) $(x + \varepsilon\Delta x/2, L + \varepsilon\triangle x)$ by adding the lattice site $x_r + \varepsilon\Delta x$ to the right end of cell;
(b) $(x + \varepsilon\Delta x/2, L - \varepsilon\triangle x)$ by removing the site x_l from the left end of the cell;
(c) $(x - \varepsilon\Delta x/2, L + \varepsilon\triangle x)$ by adding the lattice site $x_l + \varepsilon\Delta x$ to the left end of cell;
(d) $(x - \varepsilon\Delta x/2, L - \varepsilon\triangle x)$ by removing the site x_r from the right end of the cell.

Therefore, the most general form of a master equation is as follows

$$
\begin{aligned}
P(x, L, t + \varepsilon^2\triangle t) = \big[1 - T_l(x - \frac{\varepsilon}{2}\triangle x,\ L + \varepsilon\triangle x;\ x, L, t) \\
- T_r(x + \frac{\varepsilon}{2}\triangle x,\ L + \varepsilon\triangle x;\ x, L, t) - T_l(x + \frac{\varepsilon}{2}\triangle x,\ L - \varepsilon\triangle x;\ x, L, t) \\
- T_r(x - \frac{\varepsilon}{2}\triangle x,\ L - \varepsilon\triangle x;\ x, L, t)\big] P(x, L, t) \\
+ T_l(x, L;\ x + \frac{\varepsilon}{2}\triangle x,\ L - \varepsilon\triangle x, t) P(x + \frac{\varepsilon}{2}\triangle x,\ L - \varepsilon\triangle x, t) \\
+ T_r(x, L;\ x - \frac{\varepsilon}{2}\triangle x,\ L - \varepsilon\triangle x, t) P(x - \frac{\varepsilon}{2}\triangle x,\ L - \varepsilon\triangle x, t) \\
+ T_l(x, L;\ x - \frac{\varepsilon}{2}\triangle x,\ L + \varepsilon\triangle x, t) P(x - \frac{\varepsilon}{2}\triangle x,\ L + \varepsilon\triangle x, t) \\
+ T_r(x, L;\ x + \frac{\varepsilon}{2}\triangle x,\ L + \varepsilon\triangle x, t) P(x + \frac{\varepsilon}{2}\triangle x,\ L + \varepsilon\triangle x, t),
\end{aligned}
\tag{4}
$$

where $T_l(x, L; x', L')$ and $T_r(x, L; x', L')$ denote transitional probabilities for a cell of length L' and center of mass at x' to change into a cell of length L and center

of mass at x'. Subscripts "l" and "r" indicate transitions due to addition/removal of a pixel from the left/right hand side of a cell respectively. These transition probabilities are given by

$$T_l(x, L; x', L') = T_r(x, L; x', L') = \frac{1}{4}\Phi\Big(E(x, L) - E(x', L')\Big), \tag{5}$$

where $E(x, L)$ is the Hamiltonian (2) and Monte Carlo probability $\Phi(\triangle E)$ is given by

$$\Phi(\triangle E) = \begin{cases} 1, & \Delta E \le 0 \\ \exp\big[-\beta\triangle E\big] & \Delta E > 0, \end{cases} \tag{6}$$

where β is an effective cytoskeletal fluctuation amplitude of cells in energy units. Factor $1/4$ in Eq.(5) accounts for transitions to 4 possible states (a)-(d). For computational purposes it is convenient to rewrite Eq.(6) in an equivalent form

$$\Phi(\triangle E) = 1 - \Big\{1 - \exp\big[-\beta\triangle E\big]\Big\}\Theta(\triangle E). \tag{7}$$

Here $\Theta(x)$ is a Heaviside step function: $\Theta(x) = 1,\ x \ge 0$, and $\Theta(x) = 0,\ x < 0$.

2.2. Continuous evolution equation for probability density of CPM

In what follows we assume ε to be small such that a change in cell size and position is small at each Monte-Carlo step.

Now we substitute Taylor's series expansion in ε in Eq.(33). One has to take special care of $\Theta(\triangle E)$ terms in the expansion because the Heaviside step function is not analytic. To avoid this difficulty we do not expand the function itself but its argument instead. There is an important simplification which comes from the fact that $\Theta(\triangle E) + \Theta(-\triangle E) = 1$ and yields the following equality,

$$T_{l,r}(x, L;\ x', L', t) + T_{l,r}(x', L';\ x, L, t) = (1/4)\exp\big(-\beta|E(x, L) - E(x', L')|\big)$$

which holds in (4) resulting in mutual cancelation of nonanalytical terms up to order $O(\varepsilon^2)$. Then, equating coefficients in Taylor's expansion in (4) up to $O(\varepsilon^2)$ yields the Fokker-Planck equation

$$\begin{aligned} \partial_t P(x, L, t) &= D(\partial_x^2 + 4\partial_L^2)P + 8D\beta\lambda\partial_L(\tilde{L}P) + D\beta L\mu\partial_x\big[c'(x)P\big], \\ \tilde{L} &= \frac{1}{\lambda}\big[J_{cm} + \lambda(L - L_T) + \frac{1}{2}\mu c(x)\big], \quad D = \frac{(\triangle x)^2}{8\triangle t}. \end{aligned} \tag{8}$$

We assume that terms $D4\partial_L^2 P + 8D\beta\lambda\partial_L(\tilde{L}P)$ dominate other terms in the right hand side of Eq.(8) under certain conditions to be described at the end of this section. This means that to leading order one can neglect terms with "x" derivatives which results in the probability density $P(x, L, t)$ approaching, exponentially in time at the rate of $8D\beta\lambda$, the Boltzmann distribution of cell's length:

$$P(x, L, t) = P_{Boltz}(x, L)p(x, t) \tag{9}$$

where $p(x, t)$ is a probability density function of finding the cell's center of mass at x. $P_{Boltz}(x, L)$ is a Boltzmann distribution of the cell's length given by

$$P_{Boltz}(x, L) = \frac{1}{Z}\exp(-\beta\triangle E_{length}), \tag{10}$$

$$\triangle E_{length} = E(L) - E_{min} = \lambda\tilde{L}^2, \tag{11}$$

where E_{min} is the minimum of energy $E(L)$ as a function of L for a given x

$$E_{min} = E(L_{min}), \quad L_{min} = L_T - \frac{J_{cm}}{\lambda} - \frac{\mu c(x)}{2\lambda}, \tag{12}$$

and Z is a partition function

$$Z(x) = 2\varepsilon\triangle x \times \sum_{L=(1+\alpha)\varepsilon\triangle x,\,(3+\alpha)\varepsilon\triangle x,\,(5+\alpha)\varepsilon\triangle x,\ldots} \exp(-\beta\triangle E_{length}),$$
$$\alpha = 1 \text{ for } \frac{x}{\varepsilon\triangle x} = n, \quad \alpha = 0 \text{ for } \frac{x}{\varepsilon\triangle x} = n + 1/2, \quad n \in \mathbb{N}. \tag{13}$$

Here we use the fact that due to discrete nature of our model, the position of the center of mass x is located at one of the lattice sites $x = m\varepsilon\triangle x$ (m being an integer number) if the length of a cell L is an even number of units $\varepsilon\triangle x$ or if x is located at a boundary between two neighboring lattice sites then L is equal to an odd number of units of $\varepsilon\triangle x$. The factor $(\varepsilon\triangle x)^2$ in the definition of the partition function (13) is chosen in such a way as to yield $\int P(x, L, t)dLdx = 1$ in the continuous limit. We can also normalize $\int P(x, L, t)dLdx$ to a total number of cells in the system.

In the continuous limit, as $\varepsilon \to 0$, the summation in (13) is transformed into the integral

$$Z \simeq \int_{-\infty}^{+\infty} \exp(-\beta\triangle E_{length})dL = \frac{\sqrt{\pi}}{\sqrt{\beta\lambda}}, \quad x \to 0. \tag{14}$$

Here we extend the limits of integration from $(0, +\infty)$ to $(-\infty, +\infty)$. Of course the length of a cell L is always positive. A typical fluctuation of a cell size $\delta L = L - L_{min}$ about L_{min} is determined by the Boltzmann distribution (9) as $\beta\lambda\delta L^2 \sim 1$. In what follows we make a biologically motivated assumption about fluctuations of a cell size being much smaller than L $|\delta L| \ll L_{min}$, which yields the following condition

$$\beta L_{min}^2 \lambda \gg 1. \tag{15}$$

This justifies the use of integration limits $(-\infty, +\infty)$ in (14) instead of $(0, +\infty)$ because under this condition $\exp(-\beta\triangle E_{length})$ peaks around L_{min} and replacement of integration limits results in an exponentially small correction.

Now we specify conditions for applicability of the Boltzmann distribution approximation (9). Because of $\beta\lambda\delta L^2 \sim 1$, one can neglect first term with the x derivative in right hand side of (8), $|\partial_x^2 P| \ll |4\partial_L^2 P|$, provided that

$$\beta x_0^2 \lambda \gg 1. \tag{16}$$

Here x_0 is a typical scale of P with respect of x. We assume that $L_{min} \ll x_0$, i.e. that the typical length of a cell is much smaller than x_0. Then condition (16) follows from (15). The second condition for applicability of Boltzman distribution approximations is an assumption of the last term with x derivative in (8) being small, $\left|\beta L\mu\partial_x\left[c'(x)P\right]\right| \ll |4\partial_L^2 P|$. This results in

$$|L_{min}\mu c_0|\big(1 + \frac{x_c}{x_0}\big) \ll \lambda x_0^2, \tag{17}$$

where c_0 is a typical amplitude of $c(x)$ and x_c is a typical scale of variation of $c(x)$ with respect to x. Lastly, recall that we derived the continuous equation Eq.(8) from master equation Eq.(33) under the condition of the step in x being small

$$\varepsilon \ll 1. \tag{18}$$

Notice that β in the expression for a diffusion coefficient D in Eq.(8) does not have the meaning of inverse temperature. It determines instead a rate of convergence $8D\beta\lambda$ of $P(x, L, t)$ to the Boltzmann distribution (9).

We have solved both master Eq.(4) and its continuous limit Eq.(8) numerically with initial conditions $P(x, L, 0)$ different from the Boltzmann distribution (4). Simulations described in Section 2.5 demonstrate that for each x solution, $P(x, L, t)$ indeed converges with respect to time to the Boltzmann distribution at an exponential rate of $\sim 8D\beta\lambda$.

2.3. Fokker-Planck equation for probability density function $p(x, t)$

We now turn to calculating the probability density $p(x, t)$ of a center of cell's mass being at x. It is given by summing over all possible lengths of a cell,

$$p(x,t) = 2\varepsilon\triangle x \sum_{L=(1+\alpha)\varepsilon\triangle x,\,(3+\alpha)\varepsilon\triangle x,\,(5+\alpha)\varepsilon\triangle x,\ldots} P(x,L,t) \simeq \int_{-\infty}^{+\infty} P(x,L,t)dL,$$
$$\varepsilon \to 0, \quad \alpha = 1 \text{ for } \frac{x}{\varepsilon\triangle x} = n, \quad \alpha = 0 \text{ for } \frac{x}{\varepsilon\triangle x} = n + 1/2, \quad n \in \mathbb{N}, \tag{19}$$

which reduces to (9) in the Boltzmann distribution approximation limit.

To derive a closed equation for $p(x, t)$ we substitute (9) into Eq.(8) and integrate both right hand and left hand sides with respect to L to obtain

$$\partial_t p = D\partial_x^2 p - \partial_x\big[\xi(x) p\, \partial_x c(x)\big],$$
$$\xi(x) = \frac{D}{\lambda}\beta\mu\Big[J_{cm} - \lambda L_T + \frac{1}{2}\mu c(x)\Big], \quad D = \frac{(\triangle x)^2}{8\triangle t}. \tag{20}$$

The conditions for applicability of Eq.(20) are given by (15), (16), (17) and (18).

2.4. Reduction to Keller-Segel model

In this section we extend the model to include a time dependent chemical field $c(x, t)$ (concentration of chemoattractant) by adding a diffusion equation with a source term determining cells' chemical secretion

$$\partial_t c = D_c\partial_x^2 c - \gamma c + a\, p \tag{21}$$

where D_c is a diffusion coefficient of a chemical, γ is a decay rate of the chemical field and a is a cell production rate of a chemical.

The system of equations (20) and (21) can be used under the assumption that the typical time scale of diffusion of $c(x, t)$, $\tau_c = \frac{\triangle x_c^2}{D_c}$ (where x_c is a typical spatial width of the distribution of $c(x, t)$) is large in comparison to the relaxation time $\tau_r = 1/(8D\beta\lambda)$ of $P(x, L, t)$ for the Boltzmann distribution (9). Namely, this condition has the form

$$\tau_c/\tau_r = 8D\beta\lambda\tau_c \gg 1. \tag{22}$$

Eq.(20) and Eq.(21) form a closed set of equations which is equivalent to the classical Keller-Segel model of chemotaxis [14]. Under the condition

$$|J_{cm} - \lambda L_T| \gg \frac{1}{2}|\mu| c(x) \tag{23}$$

Eq. (20) is reduced to the following commonly used the Keller-Segel form:

$$\partial_t p = D\partial_x^2 p - \xi_0 \partial_x \big[p\, \partial_x c\big],$$
$$\xi_0 = \frac{D}{\lambda}\beta\mu\Big[J_{cm} - \lambda L_T\Big], \quad D = \frac{(\triangle x)^2}{8\triangle t}. \tag{24}$$

where $p(x,t)$ is a microscopic density in the Keller-Segel model. Notice that both in the Keller-Segel model and the CPM considered in this section, there is no direct interaction between cells except through production and reaction to a chemical attractant. In other words, cells are treated in a way similar to a dilute gas with long range nonlocal interactions due to reaction to a chemical field.

2.5. Comparison between discrete and continuous models

In this section we compare Monte Carlo simulations and numerical solutions of discrete and continuous models for the probability densities $P(x,L,t)$ and $p(x,t)$.

2.5.1. Monte Carlo simulations. Computations of the CPM for the frequency distribution of a cells' center of mass and length were carried out as follows:

1. We run a large number N of CPM simulations with one cell and the same initial conditions
2. We fix the time interval at $\delta t = \varepsilon^2 \triangle t$ resulting in a fixed number of Monte Carlo steps. For each simulation we record the locations of the center of mass and cells' lengths at times $t = \delta t, 2\delta t, 3\delta t, \ldots$

The frequency distribution $P_{\rm cpm}(x,L,t) = M(x,L,t)/(N(\varepsilon\triangle x)^2)$ provides an approximation for the probability density function $P(x,L,t)$. In what follows we compare $P_{\rm cpm}(x,L,t)$ with the $P(x,L,t)$ which is a solution of either the master equation (4) or the Fokker-Planck equation (8). To approximate the probability density of a center of mass $p(x,t)$ we sum up over all values of L on the grid in the way used in Eq.(19)

$$p_{cpm}(x,t) = 2\varepsilon\triangle x \sum_{L=(1+\alpha)\varepsilon\triangle x,\,(3+\alpha)\varepsilon\triangle x,\,(5+\alpha)\varepsilon\triangle x,\ldots} P_{cpm}(x,L,t),$$
$$\alpha = 1 \text{ for } \frac{x}{\varepsilon\triangle x} = n, \quad \alpha = 0 \text{ for } \frac{x}{\varepsilon\triangle x} = n + 1/2, \quad n \in \mathbb{N}. \tag{25}$$

In what follows we compare $p_{\rm cpm}(x,t)$ for $\varepsilon \ll 1$ with the $p(x,t)$, a solution of the continuous equation (20), corresponding to the following choice of parameters

$$\lambda = 4, L_T = 5, J_{cm} = 2, \beta = 15, \mu = 0.1, \Delta x = 1, \Delta t = 1. \tag{26}$$

The size of the CPM lattice is chosen to be $L_{cpm} = 100$; and the model simulation is typically run from $t_0 = 0$ to $t_{end} = 200$. The number of the CPM lattice sites and the number of Monte Carlo steps are chosen to be $\frac{L_{cpm}}{\varepsilon\Delta x}$ and $\frac{t_{end}}{\varepsilon^2\Delta t}$ respectively. We use a range of values of ε between 0.001 and 0.2.

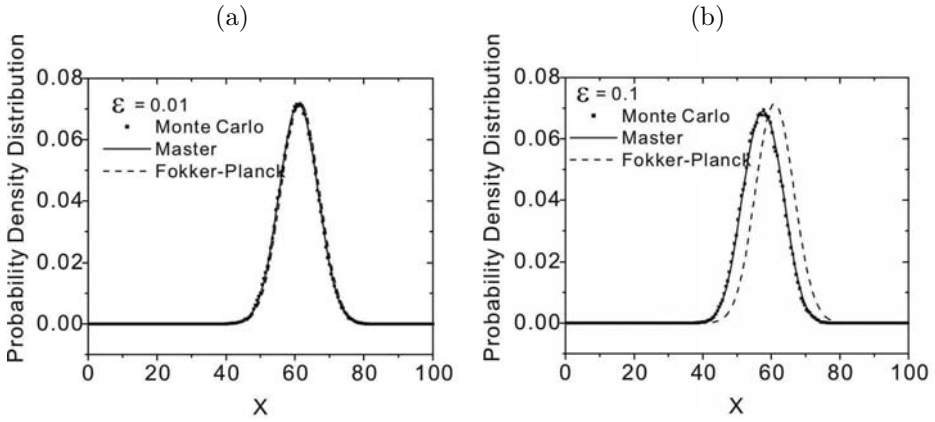

FIGURE 3. Probability densities of Monte Carlo simulations $p_{\rm cpm}(x,t)$ (dotted line), $p(x,t)$ of the Master Eq.(4) (solid line) and the Fokker-Planck Eq.(8) (dashed line) versus x for $t = t_{end}$. (a) $\varepsilon = 0.01$; (b) $\varepsilon = 0.1$. The difference between solid and dashed curves is negligibly small in (a). Number of Monte Carlo simulations is $N = 2 \times 10^5$. We used $c(x)$ as given by Eq.(27).

The initial conditions for each CPM run are chosen as follows. A random pixel in the interval $[40, 60]$ is selected as a center of mass of a cell, and then the length L for the cell is chosen with probability $Z_l^{-1} \exp(-\beta E(L))$. Here the normalization constant Z_l is chosen such that the total probability is equal to 1. In our simulations we use the following distribution for the chemical field $c(x)$

$$c(x) = \frac{(x-70)^2}{400}. \tag{27}$$

2.5.2. Monte Carlo simulations versus numerical solutions. We first compare Monte Carlo simulations with the numerical solutions of the master Eq.(4) and the Fokker-Planck Eq.(8). Numerical solutions of the Fokker-Planck Eq.(8) have been obtained by using a finite-difference scheme. Fig.3 shows the probability densities for all three types of simulation. Difference between the master Eq.(4) and the Fokker-Planck Eq.(8) simulations are negligibly small for $\varepsilon = 0.01$ (Fig.3a) but can be clearly seen for $\varepsilon = 0.1$ (Fig.3b). We conclude that for $N \to \infty$ Monte Carlo simulations converge to the solution of the master Eq.(4) for any ε. The rate of convergence is about $N^{-1/2}$. For small $\varepsilon \to 0$ the solution of the Fokker-Planck Eq.(8) also converges to the solution of the master equation.

2.5.3. Convergence of the probability density $P(x, L, t)$. To demonstrate quick convergence of $P(x, L, t)$ to the Boltzmann distribution (9) (indicated in Section 2.2) we solved numerically both the master Eq.(4) and its continuous limit Eq.(8) with initial conditions $P(x, L, 0)$ being different from the Boltzmann distribution (4). The linear-log plot in the Fig.4 indicates that convergence is indeed exponen-

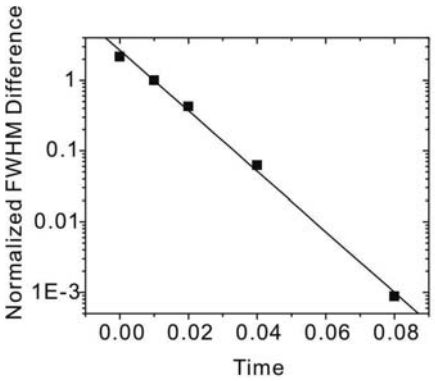

FIGURE 4. Exponential convergence of the Full Width Half Maximum (FWHM) of $P(x, L, t)$ as a function of time for $x = 50$. Vertical axes corresponds to normalized difference $\big[W(t) - W_\beta\big]/W_\beta$ where $W(t)$ is the FWHM at time t and W_β is FWHM for the Boltzmann distribution (9). Solid line is the best linear fit with exponential convergence $e^{-98.55t}$.

tial in time with high convergence rate τ_r^{-1} ($\tau_r^{-1} = 98.55$ for indicated parameters). Notice that the convergence rate of the x-dependent chemical field is also x-dependent and that the analytical expression for the convergence rate is closed. Therefore, it is difficult to obtain τ_r from Eq.(8) for a general form of $c(x)$. However, even a simple estimate $\tau_r^{-1} = 8D\beta\lambda$ of the convergence rate results in the value of 60 for parameters indicated in Fig.4 which is qualitatively close to 98.55 obtained from the linear fit.

Also, we observed that an increase in β in the Monte Carlo simulations resulted in violation of the condition (15), with in a significant departure from the Boltzmann distribution (9), which confirmed the theoretical prediction of Section 2.2.

2.5.4. $P(x, L, t)$ **vs.** $p(x, t)$ **.** Summing up over all values of L in the master Eq.(4) and taking into account Eq.(9) results in a discrete equation for the probability density $p(x, t)$

$$p(x, t + \varepsilon^2\triangle t) = \big[1 - T(x + \frac{\varepsilon}{2}\triangle x;\, x, t) - T(x - \frac{\varepsilon}{2}\triangle x;\, x, t)\big]p(x, t)$$
$$+T(x;\, x - \frac{\varepsilon}{2}\triangle x, t)p(x - \frac{\varepsilon}{2}\triangle x, t) + T(x;\, x + \frac{\varepsilon}{2}\triangle x, t)p(x + \frac{\varepsilon}{2}\triangle x, t), \qquad (28)$$

where $T(x;\, x', t)$ is a transition probability with a center of mass changing position from x' to x at time t. Expressions for $T(x;\, x', t)$ were described in [25]. They are calculated only once at the beginning of a simulation which makes the numerics for discrete Eq.(28) very efficient.

We have run simulations for the discrete Eq.(28) and the continuous Eq.(20) and compared them with the solutions of the discrete Eq.(4) and continuous Eq.(8), respectively. We found that, taking into account Eq.(9), the differences between

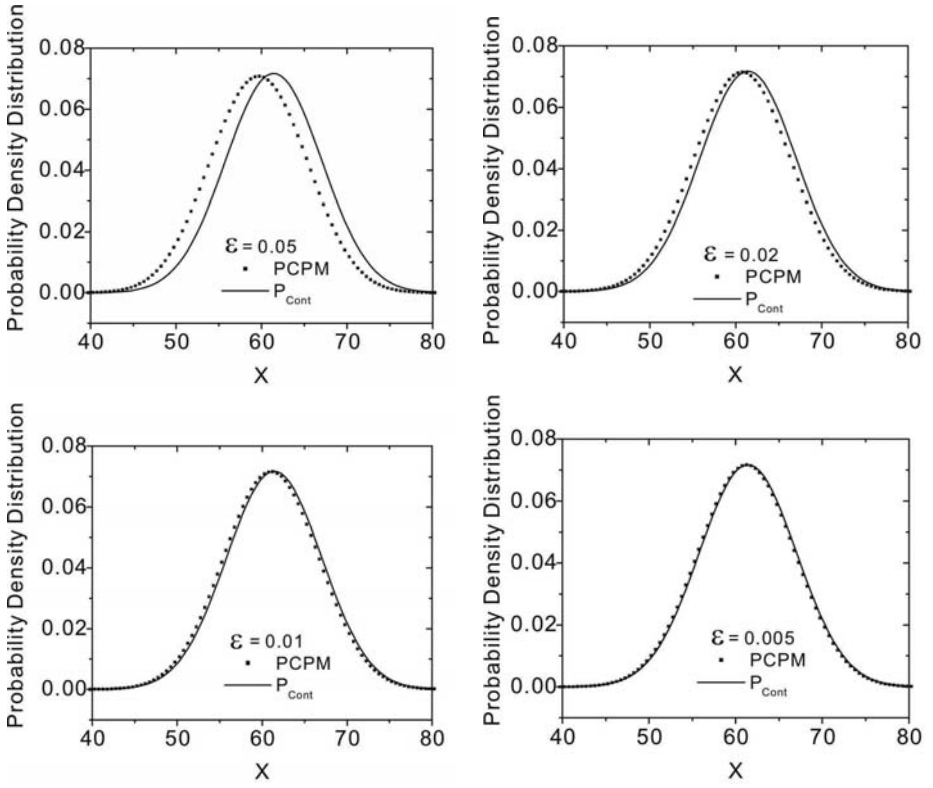

FIGURE 5. Plots of p_{cpm} (dotted line) and $p_{cont}(x,t)$ (solid line) as functions of x for a series of decreasing values of ε for $t = 200$. All other parameters are the same as in Fig.3.

these solutions are very small for typical values of the parameters. We conclude that CPM Monte Carlo simulations converge in the limit of large N to the the simulations of the discrete Eq.(28) for any ε.

2.5.5. Comparison of CPM with a continuous model. We denote as p_{cpm} both Monte Carlo simulation results and numerical solutions of Eq.(28) and as $p_{cont}(x,t)$ solutions of Eq.(20). Fig.5 demonstrates that CPM simulations (solid line) converge as ε decreases, to numerical solutions of the continuous Eq.(20) (dotted line).

We have also run series of tests for different forms of the chemical field $c(x)$ and demonstrated that solutions of the CPM and continuous Eq.(20) were close for small values of ε. Fig.6 shows a typical result of numerical simulations for a "double well" chemical concentration $c(x) = \cos(4\pi x/100)$. We conclude that numerical simulations show excellent agreement between CPM and the solution of continuous Eq.(20) provided that parameters satisfy conditions (15), (16), (17),(18) and $\varepsilon \to 0$.

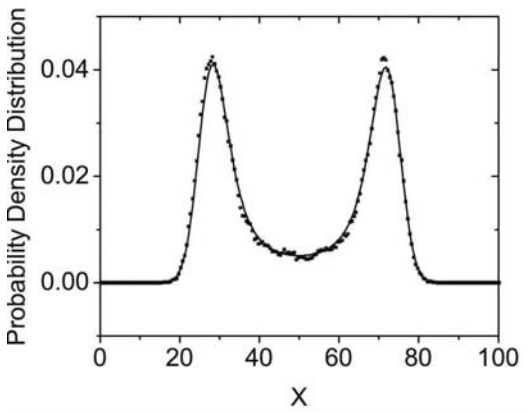

FIGURE 6. Typical results of CPM simulations. Time period is $t = 400$. Number of Monte Carlo simulations is $N = 2 \times 10^5$, $c(x) = \cos(4\pi x/100)$ and $\varepsilon = 0.01$. Notations for solid, dashed and dotted curves are as in Fig.3. The difference between solid and dashed curves is negligibly small.

3. Continuous limit of a two-dimensional CPM

In this section we extend our results to a two dimensional case. We assume that each cell now has a rectangular shape and it moves or changes its shape by adding or removing a row or column of pixels (Fig. 7).

In Eq.(1), $E_{Adhesion}$ phenomenologically describes the net adhesion or repulsion between cell membrane and ECM. It is a product of the binding energy per unit length, J_{cm}, and the length of an interface between cell boundary and ECM:

$$E_{Adhesion} = 2J_{cm}(L_x + L_y) \tag{29}$$

In the 2-D version of the CPM model considered in this paper, a cell has prescribed target lengths (L_x, L_y) in x and y directions which determine the dimensions of the rectangular cell. The energy term $E_{Perimiter}$ determines an energy penalty function for dimensions of a cell deviating from the target values:

$$E_{Perimiter} = \lambda_x(L_x - L_{T_x})^2 + \lambda_y(L_y - L_{T_y})^2 \tag{30}$$

where λ_x and λ_y are constants and L_{T_x} and L_{T_y} are target cell dimensions. An alternative constraint term would be $E_{Area} = \lambda(L_x L_y - A_T)$ where A_T is a target area. However, in what follows we will use Eq.(30).

Cells can move up or down gradients of both diffusible chemical signals (*i.e. chemotaxis*) and insoluble ECM molecules (*i.e. haptotaxis*). In this paper we use the following local energy terms for modelling both chemotaxis and haptotaxis:

$$E_{Chemical} = \mu\, c(\mathbf{r}) L_x L_y, \quad \mathbf{r} = (x, y), \tag{31}$$

where $c(\mathbf{r})$ is a local concentration of the particular species of signaling molecules in extracellular space and μ is an effective chemical potential constant.

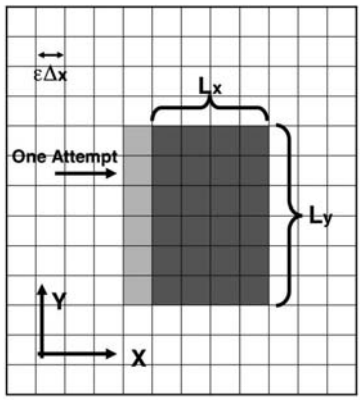

FIGURE 7. Cell representation in the two dimensional CPM. In this picture grey and white colors are used to indicate the cell body and ECM respectively. Cell can move, grow or shrink in X and Y direction by adding or removing one row (or column) of pixels. Change in the systems' potential energy determines whether to accept a flip attempt or not.

For a cell of a rectangular shape describe above a 2D Hamiltonian has the form

$$\begin{aligned} E(\mathbf{r},\mathbf{L}) = 2J_{cm}(L_x + L_y) + \lambda_x(L_x - L_{T_x})^2 \\ +\lambda_y(L_y - L_{T_y})^2 + \mu\, c(\mathbf{r}) L_x L_y, \\ \mathbf{r} = (x,y), \quad \mathbf{L} = (L_x, L_y). \end{aligned} \tag{32}$$

3.1. Function $P(\mathbf{r},\mathbf{L},t)$ in a two-dimensional case

Let $P(\mathbf{r},\mathbf{L},t)$ be a probability density function for a rectangular cell of dimensions (L_x, L_y) with center of mass located at $\mathbf{r} = (x,y)$ at time t. In what follows we will use vectors $\mathbf{e}_1 = \triangle r(1,0)$ and $\mathbf{e}_2 = \triangle r(0,1)$ to indicate changes in the x and y dimensions of a cell.

Notice that lengths of the vectors r and L can be made different by the factor L_x/L_y to reflect the fact that changes in cell size at each step can depend on the length of the cell in x or y directions, respectively. So that average change of cell size could be made proportional to either $1/L_x$ (in x direction) or $1/L_y$ (in y direction). From a computational point of view, however, it would be easier to not change lengths of the vectors $\mathbf{e}_{1,2}$ (to keep the computational grid fixed) but instead multiply the transition probabilities by an additional L_x and L_y dependent factors. However, we do not consider either of these two possible modifications for now.

The most general form of a master equation for the CPM considered in this section is as follows:

$$
\begin{aligned}
P(\mathbf{r},\mathbf{L},t+\varepsilon^2\triangle t) = \sum_{j=1}^{2}\Big\{\big[1/2 - T_1(\mathbf{r}-\frac{\varepsilon}{2}\mathbf{e}_j,\,\mathbf{L}+\varepsilon\mathbf{e}_j;\,\mathbf{r},\mathbf{L},t)\\
-T_2(\mathbf{r}+\frac{\varepsilon}{2}\mathbf{e}_j,\,\mathbf{L}+\varepsilon\mathbf{e}_j;\,\mathbf{r},\mathbf{L},t)\\
-T_1(\mathbf{r}+\frac{\varepsilon}{2}\mathbf{e_j},\,\mathbf{L}-\varepsilon\triangle x;\,\mathbf{r},\mathbf{L},t)\\
-T_2(\mathbf{r}-\frac{\varepsilon}{2}\mathbf{e}_j,\,\mathbf{L}-\varepsilon\mathbf{e}_j;\,\mathbf{r},\mathbf{L},t)\big]P(\mathbf{r},\mathbf{L},t)\\
+T_1(\mathbf{r},\mathbf{L};\,\mathbf{r}+\frac{\varepsilon}{2}\mathbf{e}_j,\,\mathbf{L}-\varepsilon\mathbf{e}_j,t)P(\mathbf{r}+\frac{\varepsilon}{2}\mathbf{e}_j,\,\mathbf{L}-\varepsilon\mathbf{e}_j,t)\\
+T_2(\mathbf{r},\mathbf{L};\,\mathbf{r}-\frac{\varepsilon}{2}\mathbf{e}_j,\,\mathbf{L}-\varepsilon\mathbf{e}_j,t)P(\mathbf{r}-\frac{\varepsilon}{2}\mathbf{e_j},\,\mathbf{L}-\varepsilon\mathbf{e_j},t)\\
+T_1(\mathbf{r},\mathbf{L};\,\mathbf{r}-\frac{\varepsilon}{2}\mathbf{e_j},\,\mathbf{L}+\varepsilon\mathbf{e_j},t)P(\mathbf{r}-\frac{\varepsilon}{2}\mathbf{e_j},\,\mathbf{L}+\varepsilon\mathbf{e_j},t)\\
+T_2(\mathbf{r},\mathbf{L};\,\mathbf{r}+\frac{\varepsilon}{2}\mathbf{e_j},\,\mathbf{L}+\varepsilon\mathbf{e_j},t)P(\mathbf{r}+\frac{\varepsilon}{2}\triangle\mathbf{r},\,\mathbf{L}+\varepsilon\mathbf{e_j},t)\Big\},
\end{aligned}
\tag{33}
$$

where the terms $T_1(\mathbf{r},\mathbf{L};\mathbf{r}',\mathbf{L}')$ and $T_2(\mathbf{r},\mathbf{L};\mathbf{r}',\mathbf{L}')$ are transition probabilities for transformations of a cells' length L' and position with center of mass x' to a cell of length L and position with center of mass x'. Subscript "1" corresponds to transformation due to addition ($|\mathbf{L}| > |\mathbf{L}'|$) or removal ($|\mathbf{L}| < |\mathbf{L}'|$) of an element from the left/upper side of a cell while subscript "2" corresponds to addition/removal of an element from the right/lower side of a cell. They can be calculated as follows

$$
T_1(\mathbf{r},\mathbf{L};\mathbf{r}',\mathbf{L}') = \mathbf{T_2}(\mathbf{r},\mathbf{L};\mathbf{r}',\mathbf{L}') = \frac{\mathbf{1}}{\mathbf{8}}\mathbf{\Phi}\Big(\mathbf{E}(\mathbf{r},\mathbf{L}) - \mathbf{E}(\mathbf{r}',\mathbf{L}')\Big). \tag{34}
$$

The factor 1/8 is due to the fact that there are 4 possibilities of increasing or decreasing L_x and L_y, $\Phi(\triangle E)$ is defined by Eq.(7). Substitution of the Taylor's series expansion for small ε in Eq.(33) results in an equation (the continuous limit model) for a probability density function $P(\mathbf{r},\mathbf{L},t)$

$$
\begin{aligned}
\partial_t P(\mathbf{r},\mathbf{L},t) = D_2(\partial^2_{\mathbf{r}} + 4\partial^2_{\mathbf{L}})P\\
+8D_2\beta\lambda_x\partial_{L_x}(\tilde{L}_x P) + 8D_2\beta\lambda_y\partial_{L_y}(\tilde{L}_y P) + D_2\beta L_x L_y\mu\partial_{\mathbf{r}}\big[P\partial_{\mathbf{r}}c\big],\\
\tilde{L}_x = \frac{1}{\lambda_x}\big[J_{cm} + \lambda_x(L_x - L_{T_x}) + \frac{1}{2}L_y\mu c(\mathbf{r})\big],\\
\tilde{L}_y = \frac{1}{\lambda_y}\big[J_{cm} + \lambda_y(L_y - L_{T_y}) + \frac{1}{2}L_x\mu c(\mathbf{r})\big], \quad D_2 = \frac{(\triangle r)^2}{16\triangle t},\\
\partial^2_{\mathbf{r}} = \partial^2_x + \partial^2_y, \quad \partial^2_{\mathbf{L}} = \partial^2_{L_x} + \partial^2_{L_y}.
\end{aligned}
\tag{35}
$$

Note the difference in the definition of the diffusion coefficient D_2 here in comparison with the definition of the diffusion coefficient D in the 1D case (see Eq.(20)).

3.2. Reduced model in the two-dimensional case

Now assume that

$$
P(\mathbf{r},\mathbf{L},t) = P_{Boltz}(\mathbf{r},\mathbf{L})p(\mathbf{r},t) \tag{36}
$$

where $P_{Boltz}(\mathbf{r},\mathbf{L})$ is a Boltzmann distribution given by

$$P_{Boltz}(\mathbf{r},\mathbf{L}) = \frac{1}{Z(\mathbf{r})}\exp(-\beta\triangle E_{length}) \tag{37}$$

and

$$\begin{aligned}\triangle E_{length} = E(\mathbf{r},\mathbf{L}) - E_{min} = \lambda_x\tilde{L}_x^2 + \lambda_y\tilde{L}_y^2 + \tilde{L}_x\tilde{L}_y\mu c(\mathbf{r}),\\ \tilde{\mathbf{L}} = \mathbf{L} - \mathbf{L}^{(min)}.\end{aligned} \tag{38}$$

E_{min} is the minimal value of the Hamiltonian as a function of $\mathbf{L}$ for a given $\mathbf{r}$, which is achieved at $\mathbf{L} = \mathbf{L}^{(min)}$:

$$\begin{aligned}E_{min} &= E(\mathbf{r},\mathbf{L}^{(min)}),\\ L_x^{(min)} &= 2\frac{-2\lambda_y(J_{cm}-\lambda_x L_{T_x}) + (J_{cm}-\lambda_y L_{T_y})\mu c(\mathbf{r})}{4\lambda_x\lambda_y - \mu^2 c(\mathbf{r})^2},\\ L_y^{(min)} &= 2\frac{-2\lambda_x(J_{cm}-\lambda_y L_{T_y}) + (J_{cm}-\lambda_x L_{T_x})\mu c(\mathbf{r})}{4\lambda_x\lambda_y - \mu^2 c(\mathbf{r})^2}\end{aligned} \tag{39}$$

where $Z(\mathbf{r})$ is a partition function

$$\begin{aligned}Z(\mathbf{r}) = (2\varepsilon\triangle r)^2\sum_{\mathbf{L}}\exp(-\beta\triangle E_{length}) \simeq \int_{-\infty}^{+\infty}\int_{-\infty}^{+\infty}\exp(-\beta\triangle E_{length})dL_x dL_y\\ = \frac{2\pi}{\beta\sqrt{4\lambda_x\lambda_y - \mu^2 c(\mathbf{r})^2}},\\ \triangle r \to 0.\end{aligned} \tag{40}$$

After substituting (36) into Eq.(35) and integrating both left-hand-side and right-hand-side over L_x and L_y we arrive at a reduced continuous model for the probability density function $p(\mathbf{r},t)$

$$\begin{aligned}\partial_t p &= D_2\partial_{\mathbf{r}}^2 p + \partial_{\mathbf{r}}\cdot\big[\xi p\big],\\ \xi(\mathbf{r}) &= D_2\mu\Big\{4\beta\frac{\eta_1\eta_2}{\big[4\lambda_x\lambda_y - \mu^2 c(\mathbf{r})^2\big]^2} - \frac{\mu c(\mathbf{r})}{4\lambda_x\lambda_y - \mu^2 c(\mathbf{r})^2}\Big\}\partial_{\mathbf{r}}c(\mathbf{r}),\\ \eta_1 &= \big[-2(J_{cm}-\lambda_y L_{T_y})\lambda_x + (J_{cm}-\lambda_x L_{T_x})\mu c(\mathbf{r})\big],\\ \eta_2 &= \big[-2(J_{cm}-\lambda_x L_{T_x})\lambda_y + (J_{cm}-\lambda_y L_{T_y})\mu c(\mathbf{r})\big]\\ D_2 &= \frac{(\triangle r)^2}{16\triangle t}.\end{aligned} \tag{41}$$

The conditions of applicability of Eq.(41) are similar to conditions (15), (16), (17) and (18) for applicability of Eq.(41) with straightforward generalization to a two-dimensinal case.

3.3. Reduction to a two-dimensional Keller-Segel

In this Section we demonstrate that 2D Potts model with chemotactic interaction is equivalent in macroscopic limit to the 2D Keller-Segel model for cellular density. We add to the model a time dependent chemical field c by adding a 2D equation similar to the one described in Section 2.4

$$\partial_t c = D_c\partial^2 c - \gamma c + a\,p \tag{42}$$

where D_c is a diffusion coefficient of the chemical field, γ is a decay rate of the chemical field and a is a production rate of the chemical field. The applicability conditions are the same as in Section 2.4.

Eq.(41) and Eq.(42) form a closed set of equations which is equivalent to the classical 2D Keller-Segel system of chemotaxis [14]. We also make the additional biologically motivated assumption that

$$4\lambda_x\lambda_y \gg \mu^2 c(\mathbf{r})^2 \tag{43}$$

meaning that the change of a typical cell size due to chemotaxis $(\delta L_x^{(chemo)}, \delta L_y^{(chemo)})$ is relatively small: $|\delta L_{x(y)}^{(chemo)}| \ll L_{x(y)}^{(min)}$. In such a case $L_{x(y)}^{(min)}$ does not depend on (x, y) and Eq.(41) further reduces to the most common Keller-Segel form

$$\begin{aligned} \partial_t p &= D_2 \partial_{\mathbf{r}}^2 p - \chi_0 \partial_{\mathbf{r}} \cdot \left[p\, \partial_{\mathbf{r}} c(\mathbf{r}) \right], \\ \chi_0 &= -D_2 \mu \beta L_x^{(min)} L_y^{(min)}, \\ D_2 &= \frac{(\triangle r)^2}{16 \triangle t}, \\ L_x^{(min)} &= L_{T_x} - \frac{J_{cm}}{\lambda_x}, \\ L_y^{(min)} &= L_{T_y} - \frac{J_{cm}}{\lambda_y}. \end{aligned} \tag{44}$$

3.4. Comparison of CPM with numerical simulations

In this section we describe numerical tests on comparing CPM Monte Carlo simulations and numerics for Eq.(33) and Eq.(41).

3.4.1. Monte Carlo simulations . The CPM Monte Carlo simulations have been carried out as follows:

1. We run a large number N of one cell CPM simulations with the same initial conditions.
2. We fix the time interval at $\delta t = \varepsilon^2 \triangle t$ between successive Monte Carlo steps. At each Monte Carlo step we randomly choose one of the four edges comprising the cell boundary, to make a flip attempt. Then we calculate the corresponding acceptance probability using the corresponding energy change. If the flip attempt is accepted, this results in changing the location of the center of mass and length of the cell.
3. For each simulation we record the position of the center of mass and the lengths (L_x and L_y) of the cell at each time step.
4. After N runs we calculate the frequency distribution $M(\mathbf{r}, \mathbf{L}, t)$ for the location of the center of mass and length of the cell.

The frequency distribution $M(\mathbf{r}, \mathbf{L}, t)$ approximates the probability density function $P_{cpm}(\mathbf{r}, \mathbf{L}, t)$ for the center of mass of a cell of length $\mathbf{L}$ being at $\mathbf{r}$ at time t

$$P_{cpm}(\mathbf{r}, \mathbf{L}, t) = M(\mathbf{r}, \mathbf{L}, t)/(N(\varepsilon \triangle r)^4).$$

We compare $P_{cpm}(\mathbf{r}, \mathbf{L}, t)$ with $P(\mathbf{r}, \mathbf{L}, t)$, a solution of either the master Eq.(33) or Eq.(41). To approximate the probability density function of the center of mass $p(\mathbf{r}, t)$, we sum up $P_{cpm}(\mathbf{r}, \mathbf{L}, t)$ over all values of $\mathbf{L}$ on the grid:

$$\begin{aligned} p_{cpm}(\mathbf{r}, t) &= (2\varepsilon\triangle r)^2 \sum_{Q1} \sum_{Q2} P_{cpm}(\mathbf{r}, \mathbf{L}, t), \\ Q1 : L_x &= (1+\alpha)\varepsilon\triangle r,\ (3+\alpha)\varepsilon\triangle r,\ (5+\alpha)\varepsilon\triangle r, \ldots \\ Q2 : L_y &= (1+\beta)\varepsilon\triangle r,\ (3+\beta)\varepsilon\triangle r,\ (5+\beta)\varepsilon\triangle r, \ldots \\ \alpha = 1 \text{ for } \frac{x}{\varepsilon\triangle r} &= n, \quad \alpha = 0 \text{ for } \frac{x}{\varepsilon\triangle r} = n + 1/2, \quad n \in \mathbb{N} \\ \beta = 1 \text{ for } \frac{y}{\varepsilon\triangle r} &= n, \quad \beta = 0 \text{ for } \frac{y}{\varepsilon\triangle r} = n + 1/2, \quad n \in \mathbb{N}. \end{aligned} \tag{45}$$

In what follows, we compare $p_{cpm}(\mathbf{r}, t)$ for $\varepsilon \ll 1$ with $p(\mathbf{r}, t)$, a solution of the continuous equation (41) corresponding to the following choice of parameters: $\lambda_x = \lambda_y = 4, L_T^x = 7, L_T^y = 1, J_{cm} = 2, \beta = 15, \mu = 0.1, \Delta r = 1, \Delta t = 1$.

The size of the CPM lattice is chosen to be $L_{cpm}^x = L_{cpm}^y = 100$ and the simulation is typically run from $t_0 = 0$ to $t_{end} = 200$. The number of the CPM lattice sites and the number of Monte Carlo steps are chosen to be $\frac{L_{cpm}^x L_{cpm}^y}{(\varepsilon\Delta r)^2}$ and $\frac{t_{end}}{\varepsilon^2 \Delta t}$respectively. We use a range of values of ε between 0.2 and 0.01.

The initial conditions for each CPM run are chosen as follows. A pixel is selected at random in the rectangle ([40, 60]x[40, 60]) as the center of mass of a cell and then the length $\mathbf{L}$ for the cell is chosen with probability $Z_l^{-1} \exp(-\beta E(\mathbf{L}))$. The constant Z_l normalizes total probability to 1. We shall use (unless specifically indicated otherwise) the following distribution for the chemical field $c(x, y)$

$$c(x, y) = \frac{(x-70)^2 + (y-60)^2}{400}. \tag{46}$$

3.4.2. $P(\mathbf{r}, \mathbf{L}, t)$ vs. $p(\mathbf{r}, t)$ simulations. Summing up over all values of $\mathbf{L}$ in the master Eq.(33) and taking into account Eq.(36), results in a discrete equation for the probability density function $p(\mathbf{r}, t)$

$$\begin{aligned} p(\mathbf{r}, t + \varepsilon^2\triangle t) = p(\mathbf{r}, t) + \sum_{all\,\boldsymbol{\Delta}\mathbf{r}} \big[& T(\mathbf{r}, \mathbf{r} + \boldsymbol{\Delta}\mathbf{r}, t) p(\mathbf{r} + \boldsymbol{\Delta}\mathbf{r}, t) \\ & - T(\mathbf{r} + \boldsymbol{\Delta}\mathbf{r}, \mathbf{r}, t) p(\mathbf{r}, t) \big] \end{aligned} \tag{47}$$

where $T(\mathbf{r}, \mathbf{r}', t)$ is a transition probability of a center of mass changing from $\mathbf{r}'$ to $\mathbf{r}$ at time t. Expressions for $T(\mathbf{r}, \mathbf{r}', t)$ are too bulky to be given here, and can be obtained as generalization of the 1D expressions given in the Appendix [25]. They are calculated only once at the beginning of a simulation which makes computation of the numerical solutions for the discrete Eq.(47) very efficient.

3.4.3. CPM Monte Carlo simulations vs. numerical solutions of the discrete master equation. Numerical solution of the equation Eq.(33) requires huge amount of computer memory to accommodate the four dimensional array $P(x, y, L_x, L_y)$ for values of small ε ranging from 0.2-0.01 and is nearly impossible. Instead of

(a)

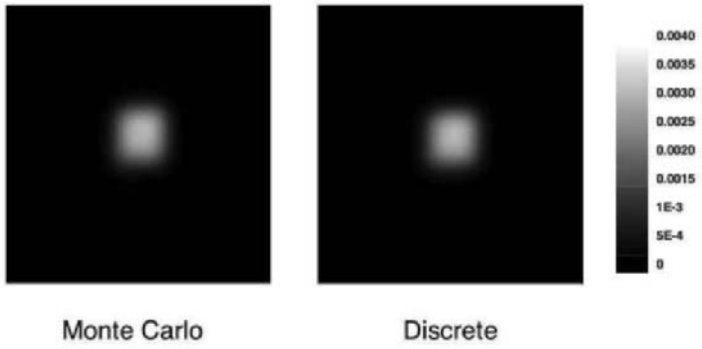

(b)

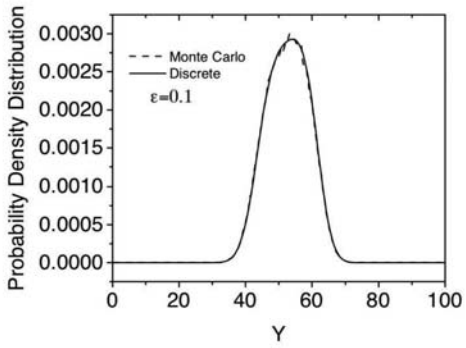

FIGURE 8. Comparison of $p_{cpm}(x, y, t)$ with $p(x, y, t)$. (a) Simulations of $p_{cpm}(x, y, t)$ and $p(x, y, t)$ for ε=0.1 and t_{end}=200. (b) Cross sections of $p_{cpm}(x_0, y, t)$ and $p(x_0, y, t)$ with x_0=55.25. Monte Carlo simulation and solution of the master equation are represented by the dashed and solid curves respectively. We used $c(x, y)$ in the form of (46).

direct comparison, we demonstrated convergence of the CPM Monte Carlo simulations to the solutions of the Eq.(33) in the following two steps. First, we used Monte Carlo simulations to verify that $P_{cpm}(\mathbf{r}, \mathbf{L}, t)$ converges with respect to $\mathbf{L}$ to the Boltzmann distribution (37) justifying use of Eq.(36) for deriving the equation (47) from Eq.(33). Second, we compared Monte Carlo simulations with the numerical solutions of the equation (47) for large values $\varepsilon \sim 0.1$ for which the continuous limit of the Eq.(41) is not valid. Fig.8 shows that CPM Monte Carlo simulations converge for large N (large statistical ensemble) to the numerical solutions of Eq.(47). Notice that for smaller ε the equation (47) can be reduced to the continuous equation (41) so that the second step is equivalent to comparison of the Monte Carlo simulations with the simulations of Eq.(41) which are described in Section 3.4.4.

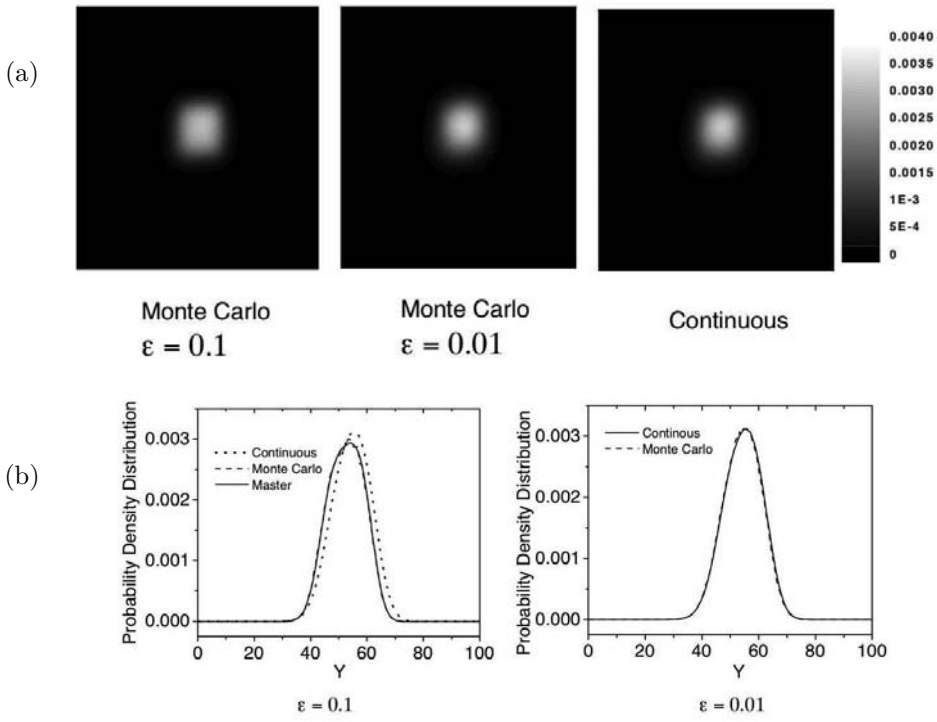

FIGURE 9. Comparison of $p_{cpm}(x, y, t)$ with $p(x, y, t)$. (a) Monte Carlo simulation of $p_{cpm}(x, y, t)$ for $\varepsilon = 0.1$, 0.01 and numerics for $p(x, y, t)$ with $t_{end} = 200$. (b) Cross sections of $p_{cpm}(x_0, y, t)$ for $\varepsilon = 0.1$ and 0.01 and numerics for $p_{con}(x_0, y, t)$ and $p(x_0, y, t)$ for $\varepsilon = 0.1$ and $x_0 = 55.25$.

3.4.4. Comparison of CPM with continuous model. We calculate $p_{cont}(x, y, t)$, solutions of Eq.(41), using a finite-difference scheme with mesh size 200×200 and time step 0.00002. (Notice that we also tried smaller time steps to ensure the convergence of the result.) The difference between the Monte Carlo simulation and the numerical solution of the continuous model Eq.(41) is negligible small for $\varepsilon = 0.01$ but can be clearly seen for $\varepsilon = 0.1$ (see Fig.9). For $\varepsilon = 0.1$ solution of the master equation (47) still converges to the Monte Carlo simulation (Fig.8). For small $\varepsilon \to 0$ the solution of the continuous equation (41) also converges to the solution of the master equation since the solution of the master equation converges in turn to the Monte Carlo simulation for small ε.

4. Conclusions

In this paper we derived a macroscopic level model from a microscopic two dimensional CPM with chemotaxis and without cell-cell adhesion. We studied a continuous macroscopic limit of the CPM as the size of Monte-Carlo step was made small under the assumption that changes in the cell's position and length were also small. In this limit we derived the Fokker-Planck equation for the cell probability density function $p(\mathbf{r}, t)$ and then reduced it to the well-known macroscopic continuous Keller-Segel model for cell motion in a chemotactic field.

We used numerical simulations for testing the established connection between the discrete and continuous models as well as for testing assumptions made for deriving continuous equations. In particular, we compared CPM Monte Carlo simulations with numerical solutions of the discrete master equation and the Fokker-Planck equation. We found that, as predicted by our theoretical analysis, all models agreed for small values of ε. Also, Monte Carlo simulations agreed with the numerical solutions of the discrete master equation for arbitrary ε. Lastly, we demonstrate that CPM Monte Carlo simulations were in excellent agreement with the numerics for the continuous macroscopic model with different forms of the chemical field $c(x)$. Combination of the CPM, discrete master equation and a system of continuous equations results in a multiscale model of cell motion in a chemotactic field.

We are currently working on deriving continuous 2D models analogous to the one described in this paper, for the cell culture experiments [26, 27] and streaming phase in Myxobacteria aggregation [28, 29, 30].

Acknowledgment

This work was partially supported by NIH Grant No. 1R0-GM076692-01: Interagency Opportunities in Multiscale Modeling in Biomedical, Biological and Behavioral Systems NSF 04.6071. Simulations were performed on the Notre Dame Biocomplexity Cluster supported in part by NSF MRI Grant No. DBI-0420980.

References

[1] F. Graner, J.A. Glazier, *Simulation of biological cell sorting using a two dimensional extended Potts model*, Phys. Rev. Lett. **69** (1992), 2013–2016.

[2] J.A. Glazier, F. Graner, *Simulation of the Differential Adhesion Driven Rearrangement of Biological Cells*, Phys. Rev. **47** (1993), 2128–2154.

[3] D. Weaire, J.A. Glazier, *Relation between Volume, Number of Faces and Three-Dimensional Growth Laws in Coarsening Cellular Patterns* Phil. Mag. Lett. **68** (1993), 363–365.

[4] J. Mombach, J.A. Glazier, *Single cell motion in aggregates of embryonic cells*, Phys. Rev. Lett. **76** (1996), 3032–3035.

[5] M. Alber, T. Hou, J.A. Glazier, Y. Jiang (Eds.), *Special Issue on Multiscale Modeling in Biology, Multiscale Modeling and Simulation: A SIAM Interdisciplinary Journal* **3** (2) 2005.

[6] A.F.M. Marée and P. Hogeweg, *How amoeboids self-organize into a fruiting body: multicellular coordination in Dictyostelium discoideum* Proc. Natl. Acad. Sci. U.S.A. **98**(7) (2001), 3879–3883.

[7] A.F.M. Marée, *From Pattern Formation to Morphogenesis*. Ph.D. thesis, Utrecht University, Netherlands (2000).

[8] R.M.H. Merks, S.V. Brodsky, M.S. Goligorsky, S.A. Newman, J.A. Glazier, *Cell elongation is key to in silico replication of in vitro vasculogenesis and subsequent remodeling* Dev. Biol. **289** (2006), 44–54.

[9] A.F.M. Marée, A. Jilkine, A. Dawes, V. A. Grieneisen, and L. Edelstein-Keshet, P*olarization and movement of keratocytes: a multiscale modelling approach* Bull. Math. Biol. **68**(5) (2006), 1169–1211.

[10] R. Chaturvedi, C. Huang, J.A. Izaguirre, S.A. Newman, J.A. Glazier, M.S. Alber, *On Multiscale Approaches to Three-Dimensional Modeling of Morphogenesis* J. R. Soc. Interface **2** (2005), 237–253.

[11] T. Cickovski, C. Huang, R. Chaturvedi, T. Glimm, H.G.E. Hentschel, M.S. Alber, J.A. Glazier, S.A. Newman, J.A. Izaguirre, *A Framework for Three Dimensional Simulation of Morphogenesis* IEEE/ACM Transactions on Computational Biology and Bioinformatics **3** (2005), 1545–1566.

[12] N. Chen, J.A. Glazier and M.S. Alber, *A Parallel Implementation of the Cellular Potts Model for Simulation of Cell-Based Morphogenesis* S. El Yacoubi, B. Chopard, and S. Bandini (Eds.): ACRI 2006, LNCS 4173, Springer-Verlag Berlin Heidelberg, (2006) 58–67.

[13] N. Chen, J.A. Glazier, J.A. Izaguirre and M.S. Alber, *A Parallel Implementation of the Cellular Potts Model for Simulation of Morphogenesis* (in press).

[14] E.F. Keller and L.A. Segel, *Model for Chemotaxis* J. Theor. Biol. **30** (1971), 225–234.

[15] W. Alt, *Biased random walk models for chemotaxis and related diffusion approximations* J.Math Biol. **9** (1980), 147–177.

[16] H.G. Othmer and A. Stevens, *Aggregation, Blowup, and Collapse: The ABCs of Taxis in Reinforced Random Walks* SIAM J. Appl. Math. **57** No.4 (1997), 1044–1081.

[17] A. Stevens, *A stochastic cellular automaton, modeling gliding and aggregation of myxobacteria* SIAM J.Appl.Math. **61** (2000), 172–182.

[18] T. J. Newman and R. Grima, *Many-body theory of chemotactic cell-cell interactions* Phys. Rev. E, **70** (2004), 051916.

[19] `http://www.personal.dundee.ac.uk/~cjweijer/dictyweb/projects.htm`

[20] C.J. Weijer, *Visualizing Signals Moving in Cells* Science **300** (2003), 96–100.

[21] S. Turner, J.A. Sherratt, K.J. Painter, N.J. Savill, *From a discrete to a continuous model of biological cell movement* Phys. Rev. E, **69** (2004), 021910.

[22] T. J. Newman, *Modeling multi-cellular systems using sub-cellular elements* Math. Biosciences and Engeneering **2** (2005), 611–622.

[23] D. Dormann, B. Vasiev, and C.J. Weijer, *Becoming Multicellular by Aggregation; The Morphogenesis of the Social Amoebae Dicyostelium discoideum* J. of Biol. Phys. **28** (2005), 765.

[24] B.N. Vasiev, P. Hogeweg, and A. V. Panfilov, *Simulation of Dictyostelium Discoideum Aggregation via Reaction-Diffusion Model* Phys. Rev. Lett. **73** (1994), 3173.

[25] M. Alber, N. Chen, T. Glimm and P. Lushnikov, *Multiscale dynamics of biological cells with chemotactic interactions: From a discrete stochastic model to a continuous description*; Phys. Rev. E. **73** (2006), 051901.

[26] M.A. Kiskowski, M.S. Alber, G.L. Thomas, J.A. Glazier, N. Bronstein, J. Pu, and S.A. Newman, *Interplay between activatorCinhibitor coupling and cell-matrix adhesion in a cellular automaton model for chondrogenic patterning* Dev. Biol. **271** (2004), 372.

[27] C.S. Christley, S.A. Newman, and M. Alber, *Agent-Based Model for Developmental Pattern Formation with Multiscale Dynamics and Varying Cell Geometry* In: Mathematical Modeling of Biological Systems, Volume I. A. Deutsch, L. Brusch, H. Byrne, G. de Vries and H.-P. Herzel (eds). Birkhuser, Boston, (2007), 155–167.

[28] M.S. Alber, M.A. Kiskowski, and Y. Jiang, *Two-stage aggregate formation via streams in myxobacteria* Phys. Rev. Lett. **93** (2004) 068301.

[29] O. Sozinova, Y. Jiang, D. Kaiser, and M. Alber, *A Three-Dimensional Model of Myxobacterial Aggregation by Contact-mediated Interactions* Proc. Natl. Acad. Sci. USA, **102** No.32, (2003), 11308-11312.

[30] O. Sozinova, Y. Jiang, D. Kaiser, and M. Alber, *A Three-Dimensional Model of Fruiting Body Formation* Proc. Natl. Acad. Sci., **103** No.46, (2006), 17255-17259.

Mark Alber
Department of Mathematics, Center of Study of Biocomplexity, University of Notre Dame
Notre Dame, IN 46637, The United States of America
e-mail: malber@nd.edu

Nan Chen
Department of Mathematics, Center of Study of Biocomplexity, University of Notre Dame
Notre Dame, IN 46637, The United States of America
e-mail: nchen1@nd.edu

Tilmann Glimm
Department of Mathematics, Western Washington University
Bellingham, Washington 98225 USA
e-mail: glimmt@wwu.edu

Pavel Lushnikov
Department of Mathematics and Statistics, University of New Mexico
Albuquerque, NM 87131, The United States of America
e-mail: plushnik@math.unm.edu

Single-Cell-Based Models in Biology and Medicine
ed. by A.R.A. Anderson, M.A.J. Chaplain, K.A. Rejniak
Mathematics and Biosciences in Interaction, 77

II. The Cellular Potts Model and Its Variants

General Introduction

In this chapter entitled The Cellular Potts Model and Its Variants mathematical lattice-based models are discussed that use stochastic changes at individual lattice sites to define configuration of all cells through the energy minimization process.

The chapter by J. Glazier, A. Balter and N. Popławski, Magnetization to Morphogenesis: a Brief History of the Glazier-Graner-Hogeweg Model, discusses development of the of the Glazier-Graner-Hogeweg (GGH) model starting with its ancestors: the Ising model of ferromagnetism, the Potts model and its extension to the Cellular Potts Model (CPM), and a current version that incorporates many biological mechanisms. The authors discuss also some peculiarities of this class of models and propose how to solve them.

The chapter by A. Marée, V. Grieneisen and P. Hogeweg, The Cellular Potts Model and Biophysical Properties of Cells, Tissues and Morphogenesis, discusses some properties of CMP formalisms and mapping of the CMP parameters to physical and biological properties of cells that makes the model suitable to investigate a large range of biological questions. The authors present several applications of their model, including cell deformation and adhesion, interplay between chemotaxis and adhesion, tumour growth and full morphogenesis of *Dictyostelium discoideum*.

The chapter by N. Savill and R. Merks, The Cellular Potts Model in Biomedicine, presents several applications of the CMP formalism to biological and medical problems. The authors discuss mechanisms for the dynamical control of size and shape of the cluster of cells; the growth of avascular tumours and the transition from benign to malignant tumours, and tumour invasion; blood vessel formation during embryonic development and the sprouting and splitting of existing blood vessels during agiogenesis; chemotactic cell aggregation and contact-inhibition of cell motility.

The final chapter by A. Balter, R. Merks, N. Popławski, M. Swat and J. Glazier, The Glazier-Graner-Hogeweg Model: Extensions, Future Directions, and Opportunities for Further Study, presents some off-lattice extensions to the GGH model and also discusses improvement on computational efficiency, parallel implementation of the GGH model and the GGH simulation packages.

Single-Cell-Based Models in Biology and Medicine
ed. by A.R.A. Anderson, M.A.J. Chaplain, K.A. Rejniak
Mathematics and Biosciences in Interaction, 79–106

II.1 Magnetization to Morphogenesis: A Brief History of the Glazier–Graner–Hogeweg Model

James A. Glazier, Ariel Balter and Nikodem J. Popławski

Abstract. This chapter discusses the history and development of what we propose to rename the Glazier–Graner–Hogeweg model (*GGH model*), starting with its ancestors, simple models of magnetism, and concluding with its current state as a powerful, cell-oriented method for simulating biological development and tissue physiology. We will discuss some of the choices and accidents of this development and some of the positive and negative consequences of the model's pedigree.

1. Introduction

Living cells, despite their great internal molecular complexity, do a few basic things. They stick to each other, move actively up and down gradients in their external environment, change shape and surface properties, exert forces on each other and their environment, secrete and absorb materials, differentiate, grow, divide, and die. A few may send electrical signals or perform other specialized functions. Many approaches to building physical models of tissues are possible. The GGH model uses a framework derived from statistical mechanics to describe cell behaviors, a choice which is not at all obvious at first glance.

The GGH model is a *cell-oriented*, as opposed to a *continuum* or *pointillistic* model. Continuum models ignore cells and treat tissues as continuous materials with specific mechanical properties, completely ignoring the division of tissues into cells. Pointillistic models treat biological tissues as collections of point-like cells, ignoring many cell characteristics that are important to biological behaviors, such as cell geometry and the adhesive interactions between cells at their membranes. While both approaches are convenient and have had many successes in explaining tissue development and physiology [33, and references therein], many biological structures have length scales of a few cell diameters, *e.g.*, capillaries or pancreatic islets, and thus require explicit spatial descriptions of cells.

The GGH model is actually a framework for defining biological models rather than a single model. GGH models define a biological structure consisting of the configuration of a set of *generalized cells*, each represented on a *cell lattice* as a

domain of lattice sites sharing the same *cell index* (generalized cells may represent all or part of a real cell or any non-cellular material in the simulation), a set of *internal cell states* for each cell (which may be quite complex), and a set of *auxiliary fields* (which may include diffusing chemicals, extracellular matrix (*ECM*), gravity, *etc.*). The heart of the GGH model is an *effective energy* or *Hamiltonian*, which encapsulates almost all interactions between model elements, and optionally, a set of partial differential equations (*PDE*s) and boundary conditions to describe the evolution of the fields, and a description of the evolution of the internal cell states. Terms in the effective energy often take the form of potential energies and elastic constraints. We call the energy *effective* because its terms primarily describe cell responses, which may not result from external forces (*e.g.*, when a cell uses its internal motile apparatus to move up or down a gradient of a chemical diffusing in extracellular space (*chemotaxis*), or attached to a substrate (*haptotaxis*)).[1] The GGH model also uses a few extra mechanisms, the most important of which is cell division. The generalized-cell configuration evolves through stochastic changes at individual lattice sites to minimize the effective energy. The classical GGH model uses a *modified Metropolis algorithm* for this evolution. Since the GGH model uses the cell as its natural level of abstraction and treats subcellular behaviors phenomenologically, it reduces the interactions among the 10^5–10^6 gene products within each cell to a set of governing equations for the variation of the roughly ten phenomenological behaviors we mentioned above. A key benefit of the GGH formalism is that we can include almost any biological mechanism or cell behavior we like, simply by adding appropriate terms to the effective energy. The GGH model then automatically handles the interactions between mechanisms (though we must be aware that its choices may not be the ones that we expect or want). Thus, the GGH model provides a compact and efficient way to describe complex biological phenomena. [2]

The global parameters of the effective energy and those describing the properties of cells may be static, or evolve according to simple or complex descriptions of biological or non-biological processes. *E.g.*, the adhesion of cells might depend on a model of cell signalling written in the form of reaction-kinetics (*RK*) coupled ordinary differential equation (*ODE*s), or the growth of cells might depend on a neural-network model of genetic regulatory pathways. The GGH model itself is agnostic about the models run inside each cell or outside the cell lattice, using its Hamiltonian to translate the information those models provide into physical structure and physiological behaviors [18, 19].

Glazier and François Graner derived their model as an extension of the *large-q Potts model* of statistical mechanics [17, 16], calling it the *Extended Potts model* and later the *Cellular Potts model* (*CPM*). The name Potts associates the CPM

[1] Cells can also haptotax in response to gradients in substrate texture or rigidity.

[2] The elements of the GGH model are separable. *E.g.*, we could use a GGH Hamiltonian and evolve it in a *lattice-free* way using a Finite-Element (*FE*) method (see chapter II.4, section 1.5), or we could use a force-based formalism instead of a Hamiltonian formalism and evolve it on-lattice using the modified Metropolis algorithm.

with statistical models of equilibrium domain formation, which was appropriate to Glazier and Graner's simple version. Later extensions to the model to describe cell behaviors mean that it now has little in common with its Potts ancestor. Key differences between the Potts and GGH models include:

1. A shift from calculating static equilibrium statistics to kinetics. While the modified Metropolis dynamics (which the GGH model uses to evolve a single configuration quasi-deterministically) derives from the Metropolis algorithm traditionally used with the Potts model, it does not obey the detailed-balance conditions required to generate equilibrium ensembles.
2. Initial conditions emulating a particular biological configuration rather than random initial conditions.
3. A shift from physically-motivated to biologically-motivated domain properties. *E.g.*, biological cells remain connected, while Potts cells do not, so GGH models often include mechanisms to enforce domain connectivity.

Because the GGH model's behaviors and goals are almost totally different from those of the Potts model, the analogy which the Potts name suggests is misleading. Therefore, we propose to name it after its originators, Glazier and Graner and the person who has done the most to extend it and bring it to its current prominence in biological modeling, Paulien Hogeweg. From its ancestors, the GGH model has inherited a number of peculiarities; we will discuss several of these and possible solutions to some in sections 6 and 7. Because of its flexibility, extensibility and ease of use, the GGH model has become the single most widely used cell-level model of tissue development [18, 19, 20, 21, 31, 32, 50].

2. Historical Origins of the Glazier–Graner–Hogeweg Model

The GGH model began as an extension of the large-q Potts Model, itself an extension of the *Ising Model*, a simple early model of ferromagnetism based on the magnetic moments, or *spins* (σ), of individual atoms and their interaction energies (J). The interaction between a single pair of neighboring spins is often called a *link*, or a *bond*. Spins interact via an energy function called a *Hamiltonian*, $\mathcal{H}$. Historical usage explains many of the otherwise obscure choices of terms and symbols in the mathematical formalism of the GGH model. We begin our historical survey with the progenitor of the GGH model, the Ising model of magnetism.

2.1. Ferromagnetism and the Ising Model

2.1.1. Ferromagnetism. Ferromagnetic materials develop a permanent magnetic field from a net orientation of the quantum-mechanical spins (σ) of their component atoms. The main goal of early statistical-mechanical models of magnetism was to explain the *2nd-order* (continuous) phase transition which occurs in iron at the *Curie temperature* (T_c). Below this temperature, materials such as iron are *ferromagnetic*. In ferromagnetic materials, stable *domains* (connected, spatially-extended areas with coaligned spins) form without an external field, giving a net

magnetic polarization. For temperatures above T_c, thermal energy disrupts domain formation, the material becomes paramagnetic and its spontaneous magnetization drops suddenly to zero.

2.1.2. The Ising model. Ernst Ising constructed a simple model of magnetization by making four radical simplifications [24]:

1. His atoms reside at regularly spaced points $\vec{i}$ on a lattice (throughout this chapter, the symbols $\vec{i}$, $\vec{j}$, $\vec{k}$ will denote two- or three-dimensional (*2D* or *3D*) vectors of positive integers indexing lattice sites, *e.g.*, $\vec{i}$=(k,l,m): $k,l,m \in \mathbb{N}$).
2. Spins have only two allowed orientations, *up* ($\sigma = 1$) and *down* ($\sigma = -1$).
3. Each atom only interacts with its nearest neighbors on the lattice.
4. The interactions are classical, rather than quantum-mechanical, so the spins obey Boltzmann statistics.

According to item 4 the relative probability of any configuration of spins $\{\sigma(\vec{i})\}$ is its *Boltzmann probability*, which depends on the configuration energy, or (Hamiltonian), $\mathcal{H}(\{\sigma(\vec{i})\})$:

$$P(\{\sigma(\vec{i})\}) = e^{-\frac{\mathcal{H}(\{\sigma(\vec{i})\})}{kT}}, \tag{1}$$

where k is Boltzmann's constant and T is the *temperature* in degrees Kelvin.[3] Thus, the higher the energy of a configuration, the less probable it is. In the absence of any external field, the Ising Hamiltonian is the sum of interactions $J(\sigma(\vec{i}),\sigma(\vec{j}))$ between all pairs of spins $(\vec{i},\vec{j})$ that are nearest-neighbors ($|\vec{i}-\vec{j}|$=1):

$$\mathcal{H}_{\text{Ising}} = \frac{1}{2} \sum_{(\vec{i},\vec{j})\ \text{neighbors}} J(\sigma(\vec{i})\sigma(\vec{j})). \tag{2}$$

The factor of $\frac{1}{2}$ comes because the summation double counts the interactions. In the Ising model $J(\sigma(\vec{i}),\sigma(\vec{j}))$ favors co-aligned neighbor spins (energy $-J$) and penalizes anti-aligned neighbors (energy $+J$), so we can write Eq.(2) as:

$$\mathcal{H}_{\text{Ising}} = -\frac{J}{2} \sum_{(\vec{i},\vec{j})\ \text{neighbors}} \sigma(\vec{i})\sigma(\vec{j}). \tag{3}$$

Lars Onsager analytically solved the Ising model in 2D and showed that the expected ferromagnetic phase transition did occur [38]. No analytical solution is known in 3D; however, a ferromagnetic phase transition still occurs for $T_c > 0$.

In the Ising model, the transition between ferromagnetic and paramagnetic states occurs because each unit of boundary between domains of opposite spin costs an energy $2J$, so configurations with contorted domain boundaries and many domains have higher energies than those with fewer, smoother domains. On the other hand, the number of configurations composed of many contorted domains is much larger than the number composed of a few smooth domains. If we pick a configuration at random from such an ensemble of configurations distributed

[3]From now on, we will set $k = 1$, which is equivalent to measuring temperature in units of energy, and omit k from our equations.

according to the Boltzmann probability in Eq.(1), the domain structure we expect to find depends on the product of the multiplicity of the structure with the Boltzmann probability. If $T \gg 2J$, the greater number of random configurations wins out over their smaller Boltzmann factors, so random configurations are much more probable. At low temperatures, the cost of domain boundaries is so high that the lower Boltzmann probabilities of random configurations overcomes their large number, and large-domain configurations dominate. In the limit that $T \to 0$, the most probable state has all the spins in the same direction (one infinite domain).

2.1.3. Summary. The Ising model contains two key ideas that carry forward to the GGH model:

1. The energy of mismatched links between neighboring spins on a lattice represents the energy per unit length of the boundaries between domains.
2. A temperature or *fluctuation amplitude* determines the probability of a configuration.

However, the Ising model is far from being a model of biological cells because:

1. It lacks dynamics.
2. Many domains may share the same spin, while for biological modeling we need a unique label for each cell.

2.2. The Potts Model

Renfrey B. Potts, in his PhD thesis, described a simple extension of the Ising model which allowed multiple *degenerate* values of the spin, (*i.e.* the energy of a link depends only on whether the neighboring spins are the same or different and not on their particular values) [40, 41]. We can write the Potts version of Eq.(2) as:

$$\mathcal{H}_{\text{Potts}} = J \sum_{(\vec{i},\vec{j})\ \text{neighbors}} (1 - \delta(\sigma(\vec{i}), \sigma(\vec{j}))), \tag{4}$$

where $\delta(x, y) = 0 \,\text{if}\, x \neq y \,\text{and}\, 1 \,\text{if}\, x = y$. We denote the number of possible spin values by q. The Potts model has ferromagnetic and other phase transitions [6, 71]. In the limit of large q, the Potts model can have many coexisting domains at low temperatures, but multiple domains can still share the same spin and it still lacks the concept of dynamics.

2.2.1. Summary. The Potts model contains two key idea for biological simulations:

1. Individual domains can have individual spins (which in CPM and GGH simulations we refer to as *cell indices*.)
2. Domains have a boundary energy that can be used to model adhesivity.

However, the Potts model still has several shortcomings as a basic biological simulation:

1. It still lacks dynamics.
2. Many domains can share a single spin. In biological simulations we require that each separate domain represent a unique object, such as a biological cell or part of one.

3. The Potts model specifies only a single contact energy between all spin values.
4. The Potts model does not have a way to control domain size and shape.

2.3. From Statistics to Kinetics

According to statistical mechanics, the distribution of equilibrium configurations of a set of classical spins depends only on the Hamiltonian and the temperature. Mathematically, we encapsulate the statistics for all configurations in the *partition function*, which sums the Boltzmann probabilities of every configuration:

$$\mathcal{Z} = \sum_{\{\sigma(\vec{i})\}} e^{-\frac{\mathcal{H}(\{\sigma(\vec{i})\})}{T}}. \tag{5}$$

Then the *expectation value* for any function $f(\{\sigma(\vec{i})\})$ is:

$$\langle f \rangle = \frac{\sum_{\{\sigma(\vec{i})\}} f(\{\sigma(\vec{i})\}) e^{-\frac{\mathcal{H}(\{\sigma(\vec{i})\})}{T}}}{\mathcal{Z}}. \tag{6}$$

2.3.1. Monte-Carlo methods. Unless the partition function and the relevant expectation values are soluble analytically, which is rare, we must evaluate them numerically, which is effectively impossible because of the enormous number of configurations to enumerate (in the Potts model, q^N, where N is the number of spins in the lattice). Computationally, Ashkin and Teller showed that we can neglect the vast majority of configurations which have high energies and thus very low probabilities, making the calculation tractable [5]. In their *Monte-Carlo* method, we start with any lattice configuration and 'jump' randomly from configuration to configuration with probabilities chosen so that the number of times we visit a configuration is proportional to its Boltzmann probability. If we then average the values of f that we calculate for such a sequence of configurations, the average converges to $\langle f \rangle$. In effect, we have replaced an integral over configurations with a time average. However, because the Ashkin–Teller method allows jumps between any two configurations, it still lacks the intrinsic time order that kinetic models require. The required probability for a transition between configurations $\{\sigma(\vec{i})\}$ and $\{\sigma'(\vec{i})\}$ is:

$$\frac{p(\{\sigma(\vec{i})\} \to \{\sigma'(\vec{i})\})}{p(\{\sigma'(\vec{i})\} \to \{\sigma(\vec{i})\})} = \frac{e^{\mathcal{H}(\{\sigma(\vec{i})\})/T}}{e^{\mathcal{H}(\{\sigma'(\vec{i})\})/T}}. \tag{7}$$

This condition is called *detailed balance*. Monte-Carlo methods do not obey detailed balance at $T = 0$.

2.3.2. The Metropolis algorithm. The *Metropolis algorithm* [35] radically modifies the Ashkin–Teller method because it is *local*; *i.e.*, instead of allowing transitions between any two configurations, it allows transitions only between configurations differing in their spin value at a single lattice site. We can think of the Metropolis algorithm as diffusion in configuration space. This local behavior allows a natural time ordering of configurations, because any configuration retains a memory of past configurations, and limits allowed future configurations. The Metropolis algorithm for a Hamiltonian, $\mathcal{H}$ is:

1. Choose a lattice site at random. We call this the *target site*, which we wil denote $\vec{i}_{\text{target}}$ and its spin, the *target spin*, which we will denote σ_{target}.
2. Pick any value of spin at random. We call this spin the *trial spin* and denote it σ_{trial}.
3. Calculate the current configuration energy, $\mathcal{H}_{\text{initial}}$, and the energy of the configuration if the target spin were changed to the trial spin value, $\mathcal{H}_{\text{final}}$.
4. Calculate the change this substitution would cause in the total energy, *i.e.*
$$\Delta\mathcal{H} = \mathcal{H}_{\text{final}} - \mathcal{H}_{\text{initial}}, \tag{8}$$
5. Accept this change (*i.e.* really change the spin value at the lattice site) with probability:
$$p(\sigma(\vec{i}_{\text{target}}) = \sigma_{\text{target}} \rightarrow \sigma(\vec{i}_{\text{target}}) = \sigma_{\text{trial}}) = \begin{cases} 1 & \text{if } \Delta\mathcal{H} < 0, \\ e^{-\Delta\mathcal{H}/T} & \text{if } \Delta\mathcal{H} > 0. \end{cases} \tag{9}$$
Steps 1 through 5 together are called a *spin-copy attempt.*
6. Go to 1.

On a lattice with N sites, we define one *Monte-Carlo step* (*MCS*) as N spin-copy attempts. We also define the *acceptance rate* to be the average ratio of the number of spin copies accepted to the number of spin-copy attempts. If the acceptance rate is small (as a rule of thumb, the acceptance rate should be greater than 0.01), the Monte-Carlo method is inefficient and we say that the computation is *stiff* for that Hamiltonian. Clearly, the acceptance rate increases as T increases. For $T > 0$ (because the transition probability, Eq.(9) obeys Eq.(7), the long-term distribution of configurations obeys Boltzmann statistics, Eq.(1).

2.3.3. The use of the Metropolis algorithm for quasi-deterministic kinetics. Two behaviors suggest the possibility of using the Metropolis algorithm for kinetic simulations:

1. While the long-time behavior of the Metropolis algorithm is purely statistical, at low temperatures, over short times, the transition probability tends to lower the configuration energy.
2. For $T = 0$, the Metropolis algorithm does not produce a statistical equilibrium. Instead it drives the configurations down energy gradients to a local energy minimum, where evolution stops.

Consider a sequence of configurations, each differing by one spin value, $\{\vec{S}_1, \vec{S}_2, ...\}$, with associated energies, $\{\mathcal{H}_1 > \mathcal{H}_2 > ...\}$. Then the net *rate of transition* (the difference between the forward and backward transition probablilities):
$$r(\vec{S}_i \rightarrow \vec{S}_{i+1}) = p(\vec{S}_i \rightarrow \vec{S}_{i+1}) - p(\vec{S}_{i+1} \rightarrow \vec{S}_i) = 1 - e^{\frac{-\mathcal{H}_i + \mathcal{H}_{i+1}}{T}}. \tag{10}$$
If we choose T such that $\frac{\mathcal{H}_i - \mathcal{H}_{i+1}}{T}$ is small, but not too small, for all i, [4] then,
$$1 - e^{\frac{-\mathcal{H}_i + \mathcal{H}_{i+1}}{T}} \sim \frac{\mathcal{H}_i - \mathcal{H}_{i+1}}{T} + \mathcal{O}((\frac{-\mathcal{H}_i + \mathcal{H}_{i+1}}{T})^2), \tag{11}$$

[4]The existence of such a T depends on energies being similar for nearby configurations, which is true for Ising, Potts, CPM and GGH Hamiltonians.

so the net rate:

$$r(\vec{S}_i \rightarrow \vec{S}_{i+1}) \sim \mathcal{H}_i - \mathcal{H}_{i+1}. \tag{12}$$

In this case, if we take one spin-copy attempt as our time unit, the average *speed* from $\vec{S}_i \rightarrow \vec{S}_{i+1}$ is:

$$vel(\vec{S}_i \rightarrow \vec{S}_{i+1}) = \frac{1}{T}\vec{\nabla}\mathcal{H} \cdot (\vec{S}_{i+1} - \vec{S}_i). \tag{13}$$

Thus, the average time evolution of the configuration obeys the *Aristotelian* or *overdamped* force–velocity relation:

$$\vec{\nabla}\mathcal{H} = \vec{F} = \mu\vec{vel}, \tag{14}$$

where μ is an *effective mobility*. The movements of individual boundary elements of a domain may be quite random, but the average velocities of large domains will be deterministic when the argument of the exponential in Eq.(10) is not too large.[5] When the argument is small enough, which is the case in most biological simulations, the deterministic velocity relationship is indeed linear and obeys Eq.(14), [70] (see also chapter II.2 by Marée et al.). This result is the fundamental justification for using Metropolis-like dynamics in kinetic simulations. Changing the dynamics, *e.g.*, from Metropolis to Glauber, may change the results in complex and sometimes unpredictable ways [70].

Using Metropolis dynamics for kinetic simulations causes a number of problems. That Eq.(13) requires that the argument of the exponential in Eq.(10) be small, makes our original use of the Boltzmann factor in Eq.(9) questionable. However, no one has studied the effects on GGH modeling of switching to a different weighting factor in Eq.(9).

The exact relation between Monte-Carlo spin-copy attempts and continuous time are still the subject of debate and are a persistent source of criticism of kinetic applications of Metropolis-like algorithms in GGH simulations. In addition, because only the time-averaged movement obeys the deterministic kinetics, the time order of events occurring at different lattice sites is ambiguous over short times. Several more sophisticated approaches to dynamics are possible (see chapter II.4, section 3.1).

3. Kinetic Potts Simulations – From Metal Grains to Foams

3.1. From the Potts Model to Coarsening

The use of Metropolis methods to reveal the quasi-deterministic kinetics of configurations evolving under a Hamiltonian, led to a great expansion of the range of questions that Monte-Carlo methods could address. One new area of interest in the early 1980s was the kinetics of metallic grain growth. Most simple metals are composed of microcrystals, or *grains*, each of which has a particular crystalline lattice orientation. The atoms at the surfaces of these grains have a higher energy than those in the bulk because of their missing neighbors. We can characterize this

[5] Like a ferromagnet, the CPM has a critical temperature analogous to the Curie temperature (see section 6.1). Quasi-deterministic motion occurs only for temperatures well below this critical temperature.

excess energy as a *boundary energy*. Atoms in convex regions of a grain's surface have a higher energy than those in concave regions, in particular than those in the concave face of an adjoining grain, because they have more missing neighbors. Thus, an atom at a convex curved boundary can reduce its energy by "hopping" across the grain boundary to the concave side. The movement of atoms, which we can equivalently view as the movement of grain boundaries, lowers the net configuration energy, but requires thermal activation because an atom has a higher energy when it is in the space between grains than when it is part of one. Thus, while grains are stable at low temperatures, at high temperatures metallic microstructure changes through *annealing* or *coarsening*, with the net size of grains growing because of grain disappearance.

3.1.1. The Exxon model of grain growth. In the early 1980s, a group of researchers at Exxon Research, Michael P. Anderson, Gary S. Grest, Paradeep S. Sahni, and David J. Srolovitz, noticed that the Potts Hamiltonian is simply J times the total boundary length of the configuration [45, 44, 46]. They drew an analogy between grain growth and the Potts model, where they took the lattice sites to correspond to atoms, the specific spin values to different crystalline orientations, and links between different spin domains to grain boundaries. They usually assumed that domains were initially connected and compact, with a different spin assigned to each grain to avoid grain coalescence.[6]

In grain growth *heterogeneous nucleation* does not occur, *i.e.* a spin of type σ will not suddenly appear in the middle of a domain of spin σ'. Since the Metropolis algorithm allows heterogeneous nucleation, the Exxon group *modified* the *Metropolis algorithm* to prevent it by selecting the trial spin from the neighborhood of the target spin. We will call the lattice site of the trial spin $\vec{i}_{\text{source}}$ and its value σ_{source} Though they did not recognize it at the time, the concept of a copy of lattice value with a source and target implied a copy *direction*, which proved crucial for later development of the GGH model. Forbidding heterogeneous nucleation means that evolution occurs only at domain boundaries. It also violates detailed balance, a further move away from statistical mechanics and towards purely kinetic modeling.

For low T, using the Potts Hamiltonian and the modified Metropolis dynamics, individual domains evolve in a manner that resembles the growth of metallic grains during annealing at high temperatures. The simulated evolution of the distributions of domain shapes, sizes and correlations agreed very well with experiments in metals [66].

3.1.2. Coarsening in foams. Glazier, working with the Exxon group, later showed that the simulated evolution also closely matched the experimental evolution of bubbles in 2D liquid soap froths, where gas diffuses across soap films depending on their curvatures [13, 15]. In this case, a link between two different spins represents

[6] Allowing multiple grains to have the same spin allows coalescence, which occurs in some metals. Since grain boundaries are simply links between lattice sites with different spins, when two grains with the same spin come into contact, they immediately fuse into one large grain.

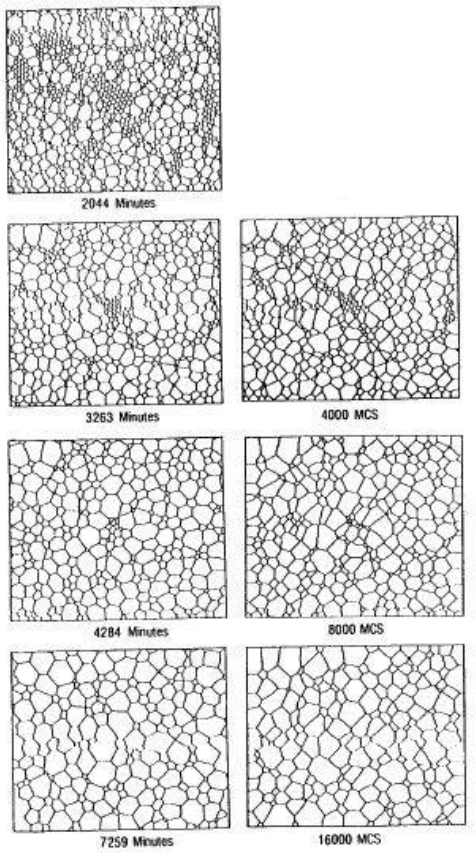

FIGURE 1. An evolving soap froth (left) and a large-q Potts model simulation of grain growth (right) using the state of the soap froth at 2044 min as the initial condition. Adapted from [15].

a physical object, a unit of soap film, and the spins represent the gas inside the individual bubbles. The use of a mismatched link to represent a physical object – a soap film – was an important conceptual advance towards the GGH model. Glazier later extended these results to 3D [14]. Fig.1 shows the evolution of a soap froth and a Potts simulation using the configuration of the soap froth at 2044 min as its initial condition [15]. The use of Potts-derived models to study coarsening remains an active field of research [22, 30, 61, 60, 58]. For a review of the earlier history of this work, see [66].

3.1.3. Lattice anisotropy. The Exxon group's grain-growth simulations revealed a problem with the Potts approach. The energy of a unit of grain boundary is *anisotropic*; *i.e.*, it depends on the boundary's orientation with respect to the

lattice. Such lattice anisotropy can lead to alignment of grain boundaries along preferred axes, and even to boundary pinning at low temperatures. Holm *et al.*'s studies of these effects [23] led to the general adoption of longer interaction ranges for Potts simulations, *i.e.* when calculating the boundary energy, we consider n^{th}-nearest neighbors, where n is an integer. Larger values of n reduce lattice anisotropy effects, but increase computation time, compared to simulations with smaller values of n. Hexagonal lattices greatly reduce anisotropy compared to square lattices with the same neighbor range and are not difficult to implement computationally, but have not been much used in simulations. The optimum choice of lattice and the use of a distance-dependent J factor to further reduce lattice anisotropy remain to be examined in a systematic fashion.

3.1.4. Summary. The Exxon simulations introduced many key ideas – the use of uniquely-labeled compact domains to identify different grains, the study of domain kinetics under the influence of boundary energy and fluctuations, the use of mismatched links to represent membranes, and the modification of the Metropolis algorithm to prevent heterogeneous nucleation. They also revealed the problem of lattice anisotropy, which still afflicts GGH simulations.

3.2. From Grains to Relaxed Foams – Constraints in an Extended Potts Model

One significant difference between foams and metallic grains is that the growth rate and relaxation rate of boundary shape of a metallic grain are the same, while in foams boundary relaxation is much faster than growth. The result is that grains can have irregular shapes, while foam boundary walls (soap films) are near-perfect minimal surfaces (circular arcs in 2D). In a brilliantly-presented and careful study, Weaire and Kermode extended the Potts model using constraints to simulate coarsening in 2D liquid foams [67, 68].

3.2.1. Constraints. The use of constraints to describe interactions comes from classical mechanics. *E.g.*, we can describe circular motion by imposing the constraint that a particle remains a constant distance from a specified point. We use the calculus of variations to derive equations of motion under a constraint, by minimizing an integral of a Hamiltonian (or Lagrangian) with an added physical *constraint condition*, which is the product of a *Lagrange multiplier*, λ (the generalized force needed to maintain the constraint), with a function which is minimal when the constraint is satisfied.

In the context of Monte-Carlo dynamics, we can write a *constraint energy* in a general *elastic* form: $\lambda(value - target\ value)^2$. This constraint is zero if $value = target\ value$ and grows as *value* diverges from *target value*. We call the constraint *elastic*, because the exponent of 2 occurs in ideal springs and elastic solids (we could, in principle, use any positive even integer). Because the constraint energy decreases smoothly to a minimum when the constraint is satisfied, the modified Metropolis algorithm automatically drives any configuration towards one that satisfies the constraint. In the presence of multiple terms in a Hamiltonian, no constraint is usually satisfied exactly, because no configuration will satisfy

all constraints and minimize all energies simultaneously (see chapter II.2, section 5). While increasing the appropriate λ can force the configuration to satisfy any constraint to any desired accuracy, increasing λ/T reduces the acceptance rate, which slows the simulation timescale and makes it computationally inefficient. If λ/T becomes too large, the simulation will *freeze* and only limited configuration evolution will occur. In the context of numerically solving differential equations, such constraints are appropriately called *stiff*. Since we can make *value* depend on the configuration in any way we want, and also make *target value* vary in any way we like in space or time, we can impose almost any behavior using constraints (although its expression may be cumbersome).

3.2.2. The Weaire–Kermode model for soap froths. Because Weaire and Kermode wanted domain growth to be slow compared to boundary relaxation and because they did not know that the domains in the large-q Potts model already obeyed von Neumann's law [65], they added an elastic constraint on the volume of each domain and evolved the target volumes very slowly according to this law. They then used a Potts boundary-energy term in their Hamiltonian to impose an effective surface tension on their domains, causing boundaries to relax towards foam-like minimal-surface shapes [69]:

$$\mathcal{H} = J \sum_{(\vec{i},\vec{j})\ \text{neighbors}} (1 - \delta(\sigma(\vec{i}), \sigma(\vec{j}))) + \lambda \sum_{\sigma} (v(\sigma) - V_{\mathrm{t}}(\sigma))^2, \tag{15}$$

where λ is an inverse gas compressibility, $v(\sigma)$ is the number of lattice sites in the domain with spin σ, and $V_t(\sigma)$ is the target number of sites for that domain. One useful result from the constraint formalism is that $P \equiv -2\lambda(v(\sigma) - V_{\mathrm{t}}(\sigma))$ is the *pressure* inside the domain. A domain with $v < V_{\mathrm{t}}$ has a positive internal pressure, while a domain with $v > V_{\mathrm{t}}$ has a negative pressure.

The shapes of the simulated domains in the Weaire–Kermode model were much more foam-like than those in Glazier's simulations. Unfortunately, this pioneering work was not followed up.

3.2.3. Summary. With Weaire and Kermode's extension of the Potts model to include a volume constraint [69], all that a model of biological cells still needed was a boundary energy that depended on domain type, an idea that goes back to the Heisenberg model of magnetism [72].

4. The Origin of the Cellular Potts Model

In this section we discuss the origin of the type-dependent boundary energies between cells used in the CPM and GGH model and write the full Hamiltonian for the CPM. The inspiration for the CPM came from experimental and theoretical work by the biologist Malcolm S. Steinberg at Princeton University on biological cell-sorting experiments and from later experiments on regeneration in aggregates of hydra cells (*Hydra vulgaris*) by the biophysicist Yasuji Sawada at Tohoku University, Sendai, Japan [48, 25, 42].

4.1. Cell Adhesion and Cell Sorting

Cell adhesion is fundamental to multicellular organisms, and to many unicellular organisms as well [10]. If cells could not stick to each other and to extracellular materials, building complex life would be impossible. Adhesion also provides a mechanism for controlling structures, as well as holding them together once they have formed.

In the late 1950s, Steinberg, while trying to understand how differences in gene expression between cells could translate into complex structures in embryos, noticed that during embryonic development, the behavior of aggregates of cells resembled the behavior of viscous fluids. For example, a random mixture of embryonic cells of two types, when formed into a 3D aggregate, reorganized into a compact ball with the more cohesive cell type surrounded by the less cohesive cell type in a phenomenon known as *cell sorting* [4, 3]. Differences in cohesion resulting from differences in the numbers and types of cell adhesion molecules on cell surfaces [11, 12, 9] could also explain the layered structure of the embryonic retina and the engulfment of a more cohesive tissue by a less cohesive tissue. Steinberg's *Differential Adhesion Hypothesis* (*DAH*) proposed that the final configuration of an initially arbitrary configuration of embryonic cells minimized their total free energy, so tissues really did behave like viscous fluids [54, 55, 56, 57].[7]

The many families of adhesion molecules (CAMs, cadherins, *etc.*) provided a mechanism for embryos to control the relative adhesivities of their various cell types to each other and to the noncellular ECM surrounding them, and thus to build complex structures. However, like the Ising model, the DAH was concerned only with equilibrium configurations, not kinetics.

4.2. The Cellular Potts Model

In 1991, Glazier joined the Sawada laboratory at Tohoku University in Sendai, Japan, which was famous for its studies on the regeneration of adult hydra from randomly mixed aggregates of their dissociated cells [48, 47, 49, 2, 53, 25, 42]. There, Glazier met Graner, who was studying the first phase of hydra regeneration, when endodermal cells sorted to the center of the aggregate and ectodermal cells to the surface [59]. Graner wanted to see if the DAH explained his results. Glazier realized that he could extend his foam simulations with the Exxon group to explore the kinetics and thermodynamics of biological cell sorting, *e.g.*, to determine whether the cell sorting that Steinberg and Armstrong had observed experimentally required active cell motility, which would imply that the energy landscape of the configuration space was *rough*, with many local minima, or could occur in the absence of fluctuations, which would imply that the energy landscape was *smooth*, with a single global minimum for the sorted state.

Glazier also realized that the domains could represent more than biological cells – in particular he introduced the concept of a domain as a *generalized cell*,

[7] In adult animal tissues and in plants, cells usually bind to each other tightly via specialized junctional structures and do not move relative to each other. Exceptions include wound healing, immune response and cancer.

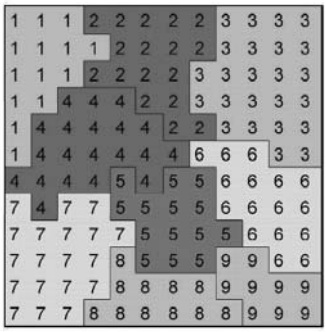

FIGURE 2. A typical configuration of the CPM or GGH model in 2D. The numerals indicate cell index values. The levels of gray indicate cell types. A cell is a collection of lattice sites with the same index value.

which could be a biological cell, a sub-element of a cell, allowing compartmental cell models, or part of the extracellular medium, a fluid or a solid, depending on the domains' characteristics. This redefinition of *everything* in the simulation to be composed of generalized cells allows the same model to treat many different types of object, greatly simplifying model building.

Glazier and Graner's model discretized the continuous cell configuration onto a square lattice. A collection of lattice sites with the same index represented a generalized cell, as shown in Fig.2, with a unique index for each cell $\sigma(\vec{i}) \in [1, \ldots, N]$ defined at each lattice site $\vec{i}$, and a *cell type* $\tau(\sigma)$ for each cell. Links between different indices represented regions of contact between two cell membranes. From now on, we will drop the confusing term *spin* and refer to cell *indices*, since spin has no meaning in our biological context.

Since the cell volumes were constant and uniform in cell-sorting experiments, Glazier and Graner used an elastic volume constraint based on Weaire and Kermode's work on foams [69] to maintain the size of the biological cells. To represent variations in adhesion between cells of different types, they defined a Potts-like boundary energy which depended on the cell types at a link, $J(\tau(\sigma), \tau(\sigma'))$ (see Fig.2), so the boundary energy term in the Potts model (equation 4) became:

$$\mathcal{H}_{\text{boundary}} = \sum_{(\vec{i},\vec{j})\ \text{neighbors}} J(\tau(\sigma(\vec{i})), \tau(\sigma(\vec{j})))(1 - \delta(\sigma(\vec{i}), \sigma(\vec{j}))), \tag{16}$$

where the boundary energy coefficients are symmetric,

$$J(\tau, \tau') = J(\tau', \tau). \tag{17}$$

Glazier and Graner assumed that the boundary energies were positive ($J > 0$), which proved to have unfortunate consequences (see section 6.2 below). The full

Hamiltonian for Glazier and Graner's CPM is:

$$\mathcal{H}_{\mathrm{CPM}} = \sum_{(\vec{i},\vec{j})\ \text{neighbors}} J(\tau(\sigma(\vec{i})),\tau(\sigma(\vec{j})))(1-\delta(\sigma(\vec{i}),\sigma(\vec{j}))) + \sum_{\sigma} \lambda_{\mathrm{Vol}}(\tau)(v(\sigma)-V_{\mathrm{t}}(\tau(\sigma)))^2, \tag{18}$$

where, $v(\sigma)$ is the volume in lattice sites of cell σ, V_{t} its target volume, and $\lambda_{\mathrm{Vol}}(\tau)$ the strength of the volume constraint. In Glazier and Graner's original papers, the value of V_{t} was constant for all biological cells and the volume of the generalized cell representing the surrounding medium was unconstrained ($\lambda_{\mathrm{Vol}}(\mathrm{medium}) = 0$) [17, 16].

If we add a constant to all Js, and also add the same constant to the interaction energy between like indices (which is 0 in $\mathcal{H}_{\mathrm{contact}}$ in Eq.(18) and requires us to change the form of the equation), the evolution is unchanged. Since the kinetics in the modified Metropolis algorithm depends only on two things, the sign of $\Delta\mathcal{H}$ and the value of $\Delta\mathcal{H}/T$ (see Eq.(9)), if we multiply all the terms in the Hamiltonian by a positive constant and multiply the temperature as well, the evolution of configurations remains unchanged. Therefore, we have two degrees of freedom, one additive and one multiplicative, in setting the scale for the CPM parameters (see chapter II.2, section 4.1).

Since biological cells move actively (in the case of vertebrate cells usually by extending and retracting their membrane using their cytoskeletons), since these membrane fluctuations are very roughly analogous to thermal fluctuations (though they have a non-thermal origin) and since cells do not suddenly appear inside other cells, Glazier and Graner used the modified Metropolis algorithm of the Exxon Group for the dynamics of their model.

4.2.1. Smoothing ("annealing"). The CPM runs with $T > 0$ and the usual values of of $\Delta\mathcal{H}/T$ are fairly small. Thus fluctuations are large, especially for more cohesive cells (those with lower J values) and cell boundaries can become highly contorted. In this case, cells can become disconnected by spinning off small (usually single lattice-site) *blebs* (we take the name from the small membrane-encased blobs of cytoplasm which migrating cells sometimes leave behind). Neither blebs nor contorted boundaries are biologically realistic. Both can affect calculations of surface areas, neighbors and volumes. In Glazier and Graner's original papers, before they calculated statistics for a configuration, they eliminated disconnected blebs and smoothed cell boundaries by running their simulation with $T = 0$ for five, or more, MCS, using the normal Hamiltonian and modified Metropolis dynamics. Rather confusingly, they called this smoothing *annealing*, even though it is not the same as normal annealing in metals. Later studies have generally not needed smoothing to reproduce biologically-observed behaviors.

5. Classical CPM Results

Because of Glazier and Graner's backgrounds in physics, their initial studies of cell sorting simulations resembled in many ways the Exxon group's statistical-mechanics studies of grain growth. They first validated the use of the CPM in a biological context by studying its phase transitions and the behaviors of simulated cells of a single type as a function of individual model parameters (*e.g.*, to establish the optimum range for J/T and to check for excessive lattice-anisotropy effects). They then tried to simulate Steinberg and Armstrong's experiments on cell sorting, studying the behavior of mixtures of two types of cells, high-boundary-energy, low-adhesivity cells, and low-boundary-energy, high-adhesivity cells, surrounded by a single generalized cell representing fluid medium.

Their single most important result was to show that cell sorting is an activated process requir-ing membrane fluctuations [16]. In their CPM simulations at low temperatures, cells clustered but clusters could not coalesce. This observation was a good example of the way that simulations can clarify a complex experimental situation. Experiments had previously shown (and later verified) that introducing drugs which blocked membrane fluctuations into the fluid medium containing the cell aggregates inhibited cell sorting [4, 36]. However, the drugs used interfered with the cells' cytoskeletons. Since the adhesion molecules, which determine cell-cell adhesivities, bind to the cytoskeleton and change their adhesivity when the cytoskeleton is disrupted, the experiments could not determine definitively whether the failure to observe sorting was due to lack of cell motility or to changes in cell-cell adhesivity. As in this case, biological experiments often lack clean control parameters. In their simulations, Glazier and Graner were able first to change cell motility while keeping adhesion constant and then to change cell adhesion while keeping cell motility constant. By comparing the results in these two cases, they were able to show that loss of cell motility indeed prevented sorting.

They then examined the various possible hierarchies of boundary energies (Js) to characterize the classes of typical patterns which they could obtain. The variety of outcomes, even in this very simple situation, showed the power of variations in the expression of cell adhesion molecules to control embryonic morphology (see a simulation MovII.1.1 form the accompanying DVD).

6. Peculiarities of the CPM

Glazier and Graner were trying to build a model so simple that they could understand the physics of all of its components. Thus the CPM has certain peculiarities, which, while not generally critical to biological simulations, may cause confusion and artifacts. If we are aware of these potential problems, we can usually take steps to make sure that they do not invalidate our results.

6.1. Temperature

We mentioned in section 5 that cell sorting (and indeed any interesting biological phenomenon we might want to investigate) requires cell motility both experimentally and in simulations. Thus we must pick a dynamics to go with our Hamiltonian. From a physical point of view, the modified Metropolis algorithm is the simplest choice.

Temperature can cause problems in a number of contexts in the CPM (see chapter II.2, section 6). The CPM has several phase transitions in temperature, three of which, in particular, are wholly non-biological and limit the range of temperatures which simulations can use. As a rough guide for picking appropriate values of J to avoid ill effects, we want to accept a significant fraction of index-copy attempts but not so many that the lattice pattern melts. Thus we need $0.2 \leq \Delta\mathcal{H}/T \leq 2$. If the number of neighbors per lattice site is n, the typical fluctuation energy per index-copy is $Jn/2$, so we need to pick all of our J values such that $0.2 < Jn/2T < 2$, which may not always be possible. If J is too large relative to T the boundaries of the cell will become rough and the cell will shed blebs. If J is too small relative to T the cell boundaries will become stiff and align with the lattice's preferred directions.

Only for small bacteria are actual thermal fluctuations important to motility. In all other cases, motility depends on molecular motors of varying kinds. The motivation for the use of the modified Metropolis dynamics was amoeboid motion of the mesenchymal cells in Steinberg and Armstrong's experiments, where fluctuations in a cell's cytoskeleton cause its membrane to *ruffle*, moving gently back and forth in a random manner. However, in most cases, cell motility results from different mechanisms [1], the geometries of which differ greatly from that of the typical membrane fluctuations in CPM cells.

Because active molecular motors drive all of these movements, the typical energy spectrum of membrane or cell movements need not follow the Boltzmann distribution of modified Metropolis dynamics. If the fluctuation spectrum of the movements matches the depth of local minima in a configuration-energy landscape, rearrangements may happen much faster than they would for thermal fluctuations, speeding the rate of configuration evolution. Worse, in almost every biological case, movements in a given direction tend to persist for fairly long times (up to a minute), because assembling and disassembling the molecular machinery responsible for cell movement takes time. Thus the assumption that motion is temporally uncorrelated, fails. We will discuss in chapter II.4, section 1.1 some ways to put these correlations back into GGH models. Sometimes these correlations have no significant effect. Unfortunately, when an energy landscape is rough, as it is for most biologically interesting problems, correlations and non-thermal fluctuation spectra can change not only time scales but time ordering [64]. Thus, in some cases, our assessment of the feasibility of a biological mechanism based on simulations may be incorrect.

Ironically, given these issues, the use of T in GGH simulations has almost never been a significant limitation. Where it has, simple fixes like including an inertial constraint (see chapter II.4, section 1.1) seem to have solved the problem. Nevertheless, improving the realism of GGH kinetics is worthy of attention, experimentally (to characterize actual kinetics), computationally and theoretically (to understand the significance of different kinetic behaviors to configuration evolution and scaling).

6.2. Diffusion, Energy and Parameter Choices

Glazier and Graner's original model, following the physical reality in foams and metallic grains, assumed that boundary energies were positive, so the boundary energy term served both to minimize boundary areas and to determine the optimal arrangement of cells. A negative J results in the cell boundaries breaking up to maximize their boundaries. When Glazier and collaborators began studying cell diffusion rates, they found that more cohesive cells (smaller $J > 0$) had more crumpled surfaces, larger membrane fluctuations, and diffused further than less cohesive cells, exactly the opposite of the expected result [42].[8] Since biological cells usually have adhesive interactions with each other and the ECM, the correct way to solve this problem is to use negative J and constrain the surface area separately (see section 7.1.1). Equivalently, Hogeweg further modified the modified Metropolis dynamics by shifting the Boltzmann probability in Eq.(9) to negative ΔE_0, which gives the same effect:

$$p(\sigma(\vec{i}_{\text{target}}) = \sigma_{\text{target}} \rightarrow \sigma(\vec{i}_{\text{target}}) = \begin{cases} 1 & \text{if } \Delta\mathcal{H} < \Delta E_0, \\ e^{-(\Delta\mathcal{H} - \Delta E_0)/T} & \text{if } \Delta\mathcal{H} \geq \Delta E_0. \end{cases} \tag{19}$$

We can equivalently view this modified dynamics as introducing an extra dissipation energy per index copy [31, 32]. Negative Js give correct diffusion hierarchies [42]. Since the configurations observed are independent of the sign of J (only the diffusion constants are wrong), many researchers continue to use simpler $J > 0$ models, when they do not care about relative rates.

While relating GGH parameters to experimentally-meaningful material properties has proved difficult, the recent derivation of the continuous limit of the CPM may help to connect simulation and physical parameters [63].

6.3. Intrinsic Dissipation and Viscosity

To make CPM simulations mechanically realistic, we would like to be able to specify the resistance to motion that cells experience when moving through a fluid due to dissipation and viscosity. *Dissipation* is the loss of energy due to motion, *i.e.* resistance to all motion. *Viscosity* is dissipation which results from velocity gradients. The CPM is intrinsically dissipative, but not viscous. Consider a channel filled with CPM cells, which strongly adhere to the walls of the channel (small J). If we push the cells through the channel by applying a gradient, the cells will experience *plug flow*, *i.e.* all cells move with the same average velocity. The cells touching the walls do not move slower than those in the center of the channel, as

[8] In certain situations, strong binding between cells can lead to cytoskeletal changes which increase cell motility, in which case using positive energies may be more appropriate biologically.

we would expect in a viscous fluid. We can implement viscosity in the CPM (see chapter II.4, section 1.2.1) to produce the correct velocity profile. However, an object moving through a fluid with CPM viscosity experiences both viscous and intrinsic dissipation, while a real fluid has no intrinsic dissipation.

7. From the CPM to the GGH Model

The basic CPM models only the effects of differential adhesion, cell volume and fluctuations. The GGH model adds many of the other biological mechanisms we discussed in section 1 and also addresses some of the issues in section 6.

7.1. Simple Extensions to the Hamiltonian

7.1.1. Surface area constraints and negative boundary energies. Biological cells have a defined amount of cell membrane, which we can represent with a surface area constraint:

$$\mathcal{H}_{\text{surface}} = \sum_{\sigma} \lambda_{\text{S}}(\tau)(s(\sigma) - S_{\text{t}}(\tau(\sigma)))^2, \tag{20}$$

where $s(\sigma)$ is the surface area of cell σ and S_{t} is its target surface area in lattice sites. Changing the ratio:

$$R = \frac{3\sqrt{4\pi}S_{\text{t}}^{3/2}}{V_{\text{t}}}, \tag{21}$$

changes the rigidity of the cell. Like a slowly inflated balloon (which corresponds to decreasing R), for $R > 1$ the cell is floppy, while for $R = 1$ the cell is spherical and for $R < 1$ increasingly rigid. While Eq.(20) is the simplest form of surface area constraint, other forms are possible and may be preferable, *e.g.*:

$$\mathcal{H}'_{\text{surface}} = \sum_{\sigma} \lambda_{\text{S}}(\tau)\big(s(\sigma)v(\sigma)^{-2/3} - S_{\text{t}}V_{\text{t}}^{-2/3}\big)^2, \tag{22}$$

keeps the R of a cell constant as it grows.

Constraining the cell surface area leaves us free to define cells' boundary energies J to be either positive or negative, depending on their real biological values, eliminating the diffusion-hierarchy problem we noted in section 6.2.

7.2. Non-Hamiltonian Extensions

7.2.1. Cell growth and proliferation. The simplest way to simulate the growth of cells is to allow V_{t} and S_{t} to increase gradually with time from a given initial value, V_{t0}, to double that value, $2V_{\text{t0}}$ [7], at a rate proportional to the concentration of a nutrient or growth factor C ([39], see also a simulation MovII.1.2 from the accompanying DVD):

$$\frac{dV_{\text{t}}}{dt} \propto C_{\text{growth factor}}. \tag{23}$$

For large C, a real cell's growth rate saturates, which we can include by replacing C by a *Michaelis–Menten* or *Hill* form $\frac{C^{\alpha}}{\beta + C^{\alpha}}$, where α and β are constants depending on cell type. Cells can also grow when they are stretched [43, 18].

7.2.2. Cell division. To model cell division (*mitosis*) when a cell σ reaches a given doubling volume, we assign a new index σ' to half of the existing cell's lattice sites, dividing the cell either along the cell's shortest axis [18, 19], or randomly [37, 39]. In both cases, the new cells have target volumes $V_t/2$ [7]. The new target volumes ensure that the pressure inside the cells (chapter II.2, section 5) does not change during mitosis.

7.3. Fields, Forces and Diffusion

A key early GGH extension of the CPM was the inclusion of multiple, additional lattices to track the concentrations of molecules (or external driving potentials) that affect the cell behaviors. We refer to the lattice of cell indices as the *cell field* and the additional lattices as *external* or *auxiliary fields*. The CPM automatically handles contact forces between cells. However, we would like to describe other influences on cell movement as well, for instance, external physical forces, or indirect effects like chemotaxis. In the context of the GGH model, we implement any influence on cell movement either through a generalized potential energy added to the Hamiltonian or by directional biasing of index-copy acceptance probabilities. The latter has the form of a *generalized force* (chapter II.2, section 3).

The primary use of fields is to record the concentration of signaling chemicals or other biomolecules, which we will usually denote $C(\vec{i})$, that may diffuse and react (section 7.3.2) and influence cell behavior via chemotaxis (section 7.3.1) or in other ways. Usually simple fields are thought of as occupying the same space as the cell lattice (*i.e.* cells do not exclude fields), although we can use repulsive haptotaxis to keep cells and fields spatially distinct. Fields may also be attached to cells or subcells rather than to the lattice (see chapter II.4, section 1.2.2) in which case we denote the field $C(\sigma)$ and its value at a lattice site is:

$$C(\vec{i}) = C(\sigma(\vec{i}))v^{-1}(\sigma(\vec{i})), \tag{24}$$

i.e. the amount of chemical at a particular lattice site equals the amount in the cell divided by the cell volume.

In some simple cases, we can represent the field as an analytic function of position. *E.g.*, a graviational field in direction $\hat{n}$ produces a gravitational potential energy:

$$\mathcal{H}_{\text{gravity}} = -\sum_{\vec{i}} \mu_{\text{gravity}}(\tau(\sigma(\vec{i})))(\vec{i}\cdot\hat{n}), \tag{25}$$

where $\mu_{\text{gravity}}(\tau(\sigma(\vec{i})))$ is the density of cell σ [28].

Yi Jiang in her PhD thesis [27] applied shear forces directly to cells by including a term in the Hamiltonian of form:

$$H = \sum_{\vec{i}} f(\vec{i}, \sigma, t). \tag{26}$$

The force can depend on position, cell type and time.

7.3.1. Chemotaxis and haptotaxis. If cell adhesion is the most important biological mechanism permitting multicellularity (allowing cells to stick together to form larger groups), chemotaxis is the second most important (see chapter II.2, section 7.3). Adhesion by itself can only produce layers and blobs, while adhesion in conjunction with chemotaxis can produce a plausible facsimile of a multicellular organism like a slime mold [32]. Cells can respond to diffusible chemicals which may be present in the ECM (*chemotaxis*) as well as to chemicals bound to substrates (*haptotaxis*, which also includes cell movement in response to changes in substrate rigidity, texture or strain). Chemotaxis is crucial for long-range signaling during morphogenesis, allowing cells at one end of a tissue to control the motion of cells at the other end. Haptotaxis is crucial for shape stabilization. For example, pre-cartilage mesenchymal cells will travel to regions where the substrate has more non-diffusing fibronectin, where they will differentiate into cartilage and then bone.

The ability to simulate chemotaxis in the GGH model depends on cells responding in a simple fashion to external chemical gradients. The simplest prototype for such a response is if,

$$\vec{v} \propto \mu_{\text{cell}} \vec{\nabla} C, \tag{27}$$

where $C(\vec{x})$ is a chemical field and μ_{cell} is the cell's *chemotactic response* parameter. Then C has the form of a *chemical potential* and $\mu_{\text{cell}} C$ has the form of a potential energy, so adding the term,

$$\mathcal{H}_{\text{chemotaxis}} = \mu_{\text{cell}} C(\vec{x}), \tag{28}$$

to the main Hamiltonian causes the cell to move up ($\mu < 0$) or down ($\mu > 0$) the chemical gradient.[9] Clearly this functional form is an oversimplification. Cells cannot respond to infinitely small gradients and cells do not go infinitely fast in large gradients. A sigmoidal response is more appropriate. Additionally, the value of μ is not static for a single cell. Cells *adapt* to external concentrations of chemicals, becoming less sensitive when chemical concentrations are high and more sensitive when they are low [52]. The timescale for adaptation varies greatly. In extreme cases cells respond only to abrupt temporal changes in chemical concentration rather than to spatial gradients.

Exactly how we translate the simple idea in Eq.(28) into an effective energy is somewhat complicated and depends on the idea of an index copy direction (see section 3.1.1), which corresponds physically to the direction of motion of a unit of cell membrane. The different implementations of chemotaxis/haptotaxis in the GGH model depend on whether we we consider the chemical field at the target lattice site only, at both the target and source lattice sites, or at the source lattice site only, and whether we use the chemotactic response of the source cell, target

[9]Most bacteria respond to chemical gradients in a totally different way, through *chemokinesis*. In this case, the bacterium moves (*runs*) in a roughly straight line for a period of time, then turns and randomizes its direction and moves off again in a straight line. If the external chemical concentration at the bacterium is increasing, the duration of the runs increases. If the concentration is decreasing, the duration of the runs decreases. The net result favors movement up the gradient and the net movement of the bacterium follows Eq.(28).

cell, or a combination. Depending on the particular biological situation, different choices may be appropriate. *E.g.*, when a cell forms a leading edge, it typically responds to chemical concentration changes at the leading edge only and not at the trailing edge, in which case we will want to consider the chemotactic response of the source cell only.

The most direct way to implement the phenomenological idea expressed in Eq. (28) is to use a Hamiltonian term of the form [27],

$$\mathcal{H}_{\text{chemotaxis}} = \mu(\sigma_{\text{source}})C(\vec{i}_{\text{target}}), \tag{29}$$

This reflects the potential energy form of Eq. (28), which makes it an equation of state. However, this form of chemotaxis also acts only at boundaries between differently chemotacting cells. Thus, a big block of identically chemotacting cells will respond very weakly because they only sense the chemical field at their edges. In practice, Eq. (29) leads to

$$\Delta\mathcal{H}_{\text{chemotaxis}} = (\mu(\sigma_{\text{target}}) - \mu(\sigma_{\text{source}}))C(\vec{i}_{\text{target}}). \tag{30}$$

Savill and Hogeweg [50], in their models of *Dictyostelium discoideum* chemotaxis, used an energy change proportional to the difference between the local chemical concentrations at the destination and source sites:

$$\Delta\mathcal{H}_{\text{chemotaxis}} = \mu(\sigma_{\text{source}})(C(\vec{i}_{\text{source}}) - C(\vec{i}_{\text{target}})). \tag{31}$$

An advantage of this form is that a cell responds to a chemical field in the same way, regardless of what types of neighbors it has. Merks also used this form in his model of endothelial vasculogenesis. However, he enforced contact inhibition, *i.e.* chemotaxis only at cell–medium interfaces, not at cell–cell interfaces [34] by only applying this energy at cell–medium interfaces when cells of type medium are not the source. To express this mathematically, one can multiply Eq. (31) by

$$\delta(\sigma_{source}, \sigma_{endothelial})\delta(\sigma_{target}, \sigma_{medium}). \tag{32}$$

All of the above methods are currently implemented in CompuCell3D[10] (see chapter II.4, section 5.1.1 and also a simulation MovII.1.3 from the accompanying DVD).

We know that for large C or ∇C, the cell's response saturates. We can include this effect using a Michaelis–Menten or Hill form:

$$\mathcal{H}_{\text{chemotaxis}} = \mu\frac{C^\alpha}{\beta + C^\alpha}. \tag{33}$$

Since all of these options may be appropriate in different biological circumstances, we propose to encapsulate all of them in a general term:

$$\Delta\mathcal{H}_{\text{chemotaxis}} = (a\mu(\sigma_{\text{source}}) + b\mu(\sigma_{\text{target}}))\frac{(cC(\vec{i}_{\text{source}}) - dC(\vec{i}_{\text{target}}))^\alpha}{\beta + (cC(\vec{i}_{\text{source}}) - dC(\vec{i}_{\text{target}}))^\alpha}, \tag{34}$$

where a, b, c, d, α and β are constants. In particular, α is the Hill coefficient, which determines how steeply the chemotactic response rises at its threshold value $C = \beta$. To model haptotaxis [62, 73], we can use a chemotaxis form with a non-diffusing C or make the surface energies $J'(\tau(\sigma(\vec{i})), \tau(\sigma(\vec{j})))$ depend on the con-

centration C. The simplest form is

$$J'(\tau(\sigma(\vec{i})),\tau(\sigma(\vec{j}))) = J(\tau(\sigma(\vec{i})),\tau(\sigma(\vec{j}))) - \beta\frac{C(\vec{i})+C(\vec{j})}{2}, \tag{35}$$

where β is a positive constant. The linear decrease of the values of J', as the concentration of the chemical corresponding to cell adhesion molecules grows, leads to observed density-dependent patterns in mesenchymal condensation *in vitro* where the average size of clusters is smaller at higher concentrations of these molecules, [73].

7.3.2. Diffusion on external-field lattices. Cells respond to diffusible signals from other cells or external sources. Typically, we implement diffusion using a separate solver which acts on the external fields, which we call a certain number of times per MCS. The simplest method, the *forward-Euler method*, evolves the diffusion equation by redistributing concentration between neighbor lattice sites from those with higher concentrations to those with lower concentrations. The proportion of concentration redistributed at each step relates to the diffusion constant for that substance. The Euler method is unstable when the ratio $D\Delta t/\Delta x^2$ is bigger than about $1/2^d$, where d is the dimension of the space, but we can maintain stability by calling the diffusion solver multiple times per MCS and using a smaller Δt each time.

An advantage of forward-Euler and other finite-difference schemes (for example, Crank–Nicholson) is that regions of the external field lattice corresponding to different cell types can have different secretion rates, decay rates and diffusion constants, including no diffusion and anisotropic diffusion. Since these properties correspond to individual cells (see section 7.4), which can move, we gain some of the benefits of advection–diffusion, at very little computational expense. For example, one iteration of a 2D diffusion equation with local decay rate $d(i,j)$ would be:

$$\begin{aligned} &C(i,j,t+\Delta t) = C(i,j,t) \\ &+D(i+1,j)C(i+1,j,t) + D(i,j+1)C(i,j+1,t) \\ &+D(i-1,j)C(i-1,j,t) + D(i,j-1)C(i,j-1,t) \\ &-4D(i,j)C(i,j,t) - d(i,j)C(i,j) + f(i,j)\Delta t, \end{aligned} \tag{36}$$

where $f(i,j)$ describes secretion, absorption and reaction of the chemical. This formula multiplies the concentration by the diffusion, secretion and decay rates site-by-site over the whole lattice prior to the iteration, which we sometimes call applying a *mask*. As the cell lattice evolves, the diffusion, secretion and decay rates update automatically.

7.4. Internal Cell States

As researchers have attempted more realistic biological simulations, they have devised methods to impart specific biological behaviors to individual cells. As a result, GGH simulations have focused more on the properties and interactions of generalized cells and less on the properties of individual lattice sites, though, of course, the actual movement of cells still occurs at the lattice-site level. This

change in focus has inspired methods to describe and generate increasingly complex *internal cell states* and to describe generalized-cell interactions. We call this general class of approaches, *off-lattice extensions* of the GGH.

In Hogeweg's model of genetic evolution [18, 19, 21, 29], cells have simple models of a genome and intergenomic pathways that determine cell–cell adhesion, cell division and death. Between cell generations, the genetic code of each cell evolves via gene mutations. The evolving regulatory pathways create cell colonies with unique morphogenetic tendencies, including many experimentally observed morphogenetic mechanisms and morphologies. Alternative methods for cell differentiation use preprogrammed type changes of the cells [51].

8. Outlook

The great advantages of the GGH model are its simplicity and extensibility, which have made it the most widely-used approach to cell-level modeling biology. GGH cells move according to effective-energy gradients $\vec{v} \propto \vec{\nabla}\mathcal{H}$, which means that $\vec{F} \propto \vec{v}$, as in biological experiments. As in experiments, the position and movement of membranes determine cell dynamics. Adding new biological mechanisms is as simple as adding new potential energies or constraints to the Hamiltonian. While the lattice discretization and modified Metropolis dynamics of the GGH model can cause certain artifacts, these rarely cause serious difficulties. Recent extensions of the GGH using subcells to model the behavior of fluids [8] and elastic media have addressed many of these issues (see chapter II.4, section 1). We discuss additional extensions to the GGH, which use generalized cells to provide many off-lattice enhancements to the GGH without abandoning the convenience of the GGH's underlying fixed lattice, in chapter II.4. As our understanding of the GGH model improves, we expect to be able to further improve both its accuracy and the range of biological problems it can address (see chapters II.2 and II.3) and to see it even more widely adopted.

This chapter has focused on the origin and development of the GGH model without discussing the computer-engineering aspects of its implementation. One of the most important developments in GGH modeling in the past few years has been the creation and release of open-source modeling packages like the *Tissue Simulation Toolkit* (*TST*) [33],[10] or *CompuCell3D* [26],[11] which provide standard platforms for model development (see the accompanying DVD for simulations: MovII.1.1, MovII,1,2 and MovII,1,3). The use of one of these standard packages allows users to reproduce published results and share new algorithms relatively painlessly, and opens the field of GGH modeling to a much broader audience.

[10] http://sourceforge.net/projects/tst.
[11] http://dustbunny.physics.indiana.edu/∼mswat/wwwCompuCell/index.html,
https://simtk.org/home/compucell3d,
http://www.nd.edu/ lcls/compucell/linux.htm.

Acknowledgments

We gratefully acknowledge support from the National Institutes of Health, National Institute of General Medical Sciences, grant 1R01 GM076692-01, an IBM Innovation Institute award, NASA Glenn Research Center, grant NAG 2-1619, the National Science Foundation, Division of Integrative Biology, grant IBN-0083653, and the Office of the Vice President for Research, the College of Arts and Sciences, the Pervasive Technologies Laboratories, the AVIDD and ODIN computer clusters and the Biocomplexity Institute at Indiana University.

References

[1] B. Alberts, A. Johnson, J. Lewis, M. Raff, K. Roberts, and P. Walter. *Molecular biology of the cell*. Garland, New York, 2002.

[2] H. Ando, Y. Sawada, H. Shimizu, and T. Sugiyama. Pattern formation in hydra tissue without developmental gradients. *Dev. Biol.*, 133:405, 1989.

[3] P. B. Armstrong and M. T. Armstrong. A role for fibronectin in cell sorting out. *J. Cell. Sci.*, 69:179, 1984.

[4] P. B. Armstrong and D. Parenti. Cell sorting in the presence of cytochalasin B. *J. Cell Biol.*, 55:542, 1972.

[5] J. Ashkin and E. Teller. Statistics of two-dimensional lattices with four components. *Phys. Rev.*, 64:178, 1943.

[6] S. G. Brush. History of the Lenz–Ising model. *Rev. Mod. Phys.*, 39:883, 1967.

[7] R. Chaturvedi, J. A. Izaguirre, C. Huang, T. Cickovski, P. Virtue, G. L. Thomas, G. Forgacs, M. S. Alber, S. A. Newman, and J. A. Glazier. Multi-model simulations of chicken limb morphogenesis. *Lect. Notes Comput. Sci.*, 2659:39, 2003.

[8] D. Dan, C. Mueller, K. Chen, and J. A. Glazier. Solving the advection–diffusion equations in biological contexts using the Cellular Potts model. *Phys. Rev. E*, 72:041909, 2005.

[9] G. Forgacs, R. A. Foty, Y. Shafrir, and M. S. Steinberg. Viscoelastic properties of living embryonic tissues: a quantitative study. *Biophys. J.*, 74:2227, 1998.

[10] G. Forgacs and S. A. Newman. *Biological physics of the developing embryo*. Cambridge Univ. Press, Cambridge, 2005.

[11] R. A. Foty, G. Forgacs, C. M. Pfleger, and M. S. Steinberg. Liquid properties of embryonic tissues: measurement of interfacial tensions. *Phys. Rev. Lett.*, 72:2298, 1994.

[12] R. A. Foty, C. M. Pfleger, G. Forgacs, and M. S. Steinberg. Surface tensions of embryonic tissues predict their mutual envelopment behavior. *Development*, 122:1611, 1996.

[13] J. A. Glazier. *Dynamics of cellular patterns*. PhD thesis, University of Chicago, 1989.

[14] J. A. Glazier. Grain growth in three dimensions depends on grain topology. *Phys. Rev. Lett.*, 70:2170, 1993.

[15] J. A. Glazier, M. P. Anderson, and G. S. Grest. Coarsening in the two-dimensional soap froth and the large-q Potts model: a detailed comparison. *Philos. Mag. B*, 62:615, 1990.

[16] J. A. Glazier and F. Graner. Simulation of the differential adhesion driven rearrangement of biological cells. *Phys. Rev. E*, 47:2128, 1993.

[17] F. Graner and J. A. Glazier. Simulation of biological cell sorting using a two-dimensional extended Potts model. *Phys. Rev. Lett.*, 69:2013, 1992.

[18] P. Hogeweg. Evolving mechanisms of morphogenesis: on the interplay between differential adhesion and cell differentiation. *J. Theor. Biol.*, 203:317, 2000.

[19] P. Hogeweg. Computing an organism: on the interface between informatic and dynamic processes. *Biosystems*, 64:97, 2002.

[20] P. Hogeweg. Computing an organism: on the interface between informatic and dynamic processes. In S. Kumar and P. J. Bentley, editors, *On growth, form and computers*, page 444. Elsevier, London, 2003.

[21] P. Hogeweg and N. Takeuchi. Multilevel selection in models of prebiotic evolution: compartments and spatial self-organization. *Orig. Life Evol. Biosph.*, 33:375, 2003.

[22] E. A. Holm and C. C. Battaile. The computer simulation of microstructural evolution. *JOM*, 53:20, 2001.

[23] E. A. Holm, J. A. Glazier, D. J. Srolovitz, and G. S. Grest. Effects of lattice anisotropy and temperature on domain growth in the two-dimensional Potts model. *Phys. Rev. A*, 43:2662, 1991.

[24] E. Ising. Beitrag zur Theorie des Ferromagnetismus. *Z. Physik.*, 31:253, 1925.

[25] T. Itayama and Y. Sawada. Development of electrical activity in regenerating aggregates of hydra cells. *J. Exp. Zool.*, 273:519, 1995.

[26] J. A. Izaguirre, R. Chaturvedi, C. Huang, T. Cickovski, J. Coffland, G. L. Thomas, G. Forgacs, M. S. Alber, H. G. E. Hentschel, S. A. Newman, and J. A. Glazier. Compucell, a multi-model framework for simulation of morphogenesis. *Bioinformatics*, 20:1129, 2004.

[27] Y. Jiang. *Cellular pattern formation.* PhD thesis, University of Notre Dame, 1998.

[28] Y. Jiang and J. A. Glazier. Extended large-q Potts model simulation of foam drainage. *Phil. Mag. Lett.*, 74:119, 1996.

[29] S. A. Kauffman. Metabolic stability and epigenesis in randomly constructed genetic nets. *J. Theor. Biol.*, 22:437, 1969.

[30] C. E. Krill and L. Q. Chen. Computer simulation of 3-D grain growth using a phase-field model. *Acta Mater.*, 50:3057, 2002.

[31] A. F. M. Marée and P. Hogeweg. How amoeboids self-organize into a fruiting body: multicellular coordination in *Dictyostelium discoideum. Proc. Natl. Acad. Sci. USA*, 98:3879, 2001.

[32] A. F. M. Marée and P. Hogeweg. Modelling *Dictyostelium discoideum* morphogenesis: the culmination. *Bull. Math. Biol.*, 64:327, 2002.

[33] R. M. H. Merks and J. A. Glazier. A cell-centered approach to developmental biology. *Physica A*, 352:113, 2005.

[34] R. M. H. Merks and J. A. Glazier. Dynamic mechanisms of blood vessel growth. *Nonlinearity*, 19:C1, 2006.

[35] N. Metropolis, A. W. Rosenbluth, M. N. Rosenbluth, A. H. Teller, and E. Teller. Equation of state calculations by fast computing machines. *J. Chem. Phys.*, 21:1087, 1953.

[36] J. C. Mombach, J. A. Glazier, R. C. Raphael, and M. Zajac. Quantitative comparison between differential adhesion models and cell sorting in the presence and absence of fluctuations. *Phys. Rev. Lett.*, 75:2244, 1995.

[37] J. C. M. Mombach, R. M. C. de Almeida, and J. R. Iglesias. Mitosis and growth in biological tissues. *Phys. Rev. E*, 48:598, 1993.

[38] L. Onsager. Crystal statistics. I. A two-dimensional model with an order–disorder transition. *Phys. Rev.*, 65:117, 1944.

[39] N. J. Popławski, M. Swat, J. S. Gens, and J. A. Glazier. Adhesion between cells, diffusion of growth factors, and elasticity of the AER produce the paddle shape of the chick limb. *Physica A*, 373:521, 2007.

[40] R. B. Potts. PhD thesis, University of Oxford, 1951.

[41] R. B. Potts. Some generalized order–disorder transformations. *Proc. Camb. Phil. Soc.*, 48:106, 1952.

[42] J. P. Rieu, A. Upadhyaya, J. A. Glazier, N. B. Ouchi, and Y. Sawada. Diffusion and deformations of single hydra cells in cellular aggregates. *Biophys. J.*, 79:1903, 2000.

[43] E. Ruoslahti. Stretching is good for a cell. *Science*, 276:1345, 1997.

[44] S. A. Safran, P. S. Sahni, and G. S. Grest. Kinetics of ordering in two dimensions. I. Model systems. *Phys. Rev. B*, 28:2693, 1983.

[45] P. S. Sahni, G. S. Grest, M. P. Anderson, and D. J. Srolovitz. Kinetics of the q-state Potts model in two dimensions. *Phys. Rev. Lett.*, 50:263, 1983.

[46] P. S. Sahni, D. J. Srolovitz, G. S. Grest, M. P. Anderson, and S. A. Safran. Kinetics of ordering in two dimensions. II. Quenched systems. *Phys. Rev. B*, 28:2705, 1983.

[47] M. Sato, H. R. Bode, and Y. Sawada. Patterning processes in aggregates of hydra cells visualized with the monoclonal antibody, Ts19. *Dev. Biol.*, 141:412, 1990.

[48] M. Sato and Y. Sawada. Regulation in the numbers of tentacles of aggregated hydra cells. *Dev. Biol.*, 133:119, 1989.

[49] M. Sato, H. Tashiro, A. Oikawa, and Y. Sawada. Patterning in hydra cell aggregates without the sorting of cells from different axial origins. *Dev. Biol.*, 151:111, 1992.

[50] N. J. Savill and P. Hogeweg. Modelling morphogenesis: from single cells to crawling slugs. *J. Theor. Biol.*, 184:229, 1997.

[51] N. J. Savill and J. A. Sherratt. Control of epidermal stem cell clusters by Notch-mediated lateral induction. *Dev. Biol.*, 258:141, 2003.

[52] G. Serini, D. Ambrosi, E. Giraudo, A. Gamba, L. Preziosi, and F. Bussolino. Modeling the early stages of vascular network assembly. *EMBO J.*, 22:1771, 2003.

[53] H. Shimizu, Y. Sawada, and T. Sugiyama. Minimum tissue size required for hydra regeneration. *Dev. Biol.*, 155:287, 1993.

[54] M. S. Steinberg. Reconstruction of tissues by dissociated cells. some morphogenetic movements and the sorting out of embryonic cells may have a common explanation. *Science*, 141:401, 1963.

[55] M. S. Steinberg. The problem of adhesive selectivity in cellular interactions. In M. Locke, editor, *Cellular membranes in development*, page 321. Academic, New York, 1964.

[56] M. S. Steinberg. Does differential adhesion govern self-assembly processes in histo-

genesis? equilibrium configurations and the emergence of a hierarchy among populations of embryonic cells. *J. Exp. Zool.*, 173:395, 1970.
[57] M. S. Steinberg and M. Takeichi. Experimental specification of cell sorting, tissue spreading and specific spatial patterning by quantitative differences in cadherin expression. *Proc. Natl. Acad. Sci. USA*, 91:206, 1994.
[58] A. Szolnoki and G. Szabo. Vertex dynamics during domain growth in three-state models. *Phys. Rev. E*, 70:027101, 2004.
[59] U. Technau and T. W. Holstein. Cell sorting during the regeneration of hydra from reaggregated cells. *Dev. Biol.*, 151:117, 1992.
[60] G. L. Thomas, R. M. C. de Almeida, and F. Graner. Coarsening of three-dimensional grains in crystals, or bubbles in dry foams, tends towards a universal, statistically scale-invariant regime. *Phys. Rev. E*, 74:021407, 2006.
[61] V. Tikare, E. A. Holm, D. Fan, and L. Q. Chen. Comparison of phase-field and Potts models for coarsening processes. *Acta Mater.*, 47:363, 1998.
[62] S. Turner and J. A. Sherratt. Intercellular adhesion and cancer invasion: a discrete simulation using the extended Potts model. *J. Theor. Biol.*, 216:85, 2002.
[63] S. Turner, J. A. Sherratt, K. J. Painter, and N. J. Savill. From a discrete to a continuous model of biological cell movement. *Phys. Rev. E*, 69:021910, 2004.
[64] A. Upadhyaya. *Thermodynamic and fluid properties of cells, tissues and membranes*. PhD thesis, University of Notre Dame, 2000.
[65] J. von Neumann. *Metal interfaces*. American Society for Metals, Cleveland, 1952.
[66] D. Weaire and J. A. Glazier. Modelling grain growth and soap froth coarsening: past, present and future. *Mater. Sci. Forum*, 94-96:27, 1992.
[67] D. Weaire and J. P. Kermode. Computer simulation of a two-dimensional soap froth. I. method and motivation. *Phil. Mag. B*, 48:245, 1983.
[68] D. Weaire and J. P. Kermode. Computer simulation of a two-dimensional soap froth. II. analysis of results. *Phil. Mag. B*, 50:379, 1984.
[69] J. Wejchert, D. Weaire, and J. P. Kermode. Monte Carlo simulation of the evolution of a two-dimensional soap froth. *Phil. Mag. B*, 53:15, 1986.
[70] S.-K. Wong. *A cursory study of thermodynamic and mechanical properties of Monte-Carlo simulations of the Ising model*. PhD thesis, University of Notre Dame, 2005.
[71] F. Y. Wu. The Potts model. *Rev. Mod. Phys.*, 54:235, 1982.
[72] K. Yosida. *Theory of magnetism*. Springer–Verlag, Heidelberg, 2006.
[73] W. Zeng, G. L. Thomas, and J. A. Glazier. A novel mechanism for biological cell clustering. *Physica A*, 341:482, 2004.

James A. Glazier
Biocomplexity Institute and Department of Physics, Indiana University
Swain Hall West 159, 727 East Third Street, Bloomington, Indiana 47405-7105, USA
e-mail: `glazier@indiana.edu`

Ariel Balter
Biocomplexity Institute and Department of Physics, Indiana University
Swain Hall West 117, 727 East Third Street, Bloomington, Indiana 47405-7105, USA
e-mail: `abalter@indiana.edu`

Nikodem J. Popławski
Biocomplexity Institute and Department of Physics, Indiana University
Swain Hall West 117, 727 East Third Street, Bloomington, Indiana 47405-7105, USA
e-mail: `nipoplaw@indiana.edu`

Single-Cell-Based Models in Biology and Medicine
ed. by A.R.A. Anderson, M.A.J. Chaplain, K.A. Rejniak
Mathematics and Biosciences in Interaction, 107–136

II.2 The Cellular Potts Model and Biophysical Properties of Cells, Tissues and Morphogenesis

Athanasius F. M. Marée, Verônica A. Grieneisen and Paulien Hogeweg

Abstract. In this chapter we examine the properties of the Cellular Potts Model (CPM) formalism which make it preeminently suitable for modelling biological cells. The most outstanding feature in which CPM differs from other modelling formalisms, is that a cell is modelled as a deformable object, and takes its shape from a combination of internal and external forces which act upon it. The energy minimisation based CPM formalism enables us to integrate these forces acting at different scales. We map the parameters of the basic CPM formalism to physical and biological properties of cells. We show through those mappings that the modelling formalism is a powerful tool for investigating a large range of biological questions, from those concerning biophysical properties of single cells, cell motion, tissue level properties, all the way up to understanding the full morphogenesis and life-cycle of an organism.

1. Introduction

The CPM is a spatial grid-based formalism that allows for mesoscopic cell description [12]: a cell is defined over a region composed of multiple lattice sites, with constraints acting on its area, while experiencing interactions at its boundary. The dynamics are based on the free energy minimisation principle, and generated by means of Monte Carlo simulations utilising a Metropolis algorithm [33][1]. Effectively, this means that cell motion comes about from the overall minimisation of the energy of deformation and stretching of the membrane through stochastic fluctuations, in which the global and local forces upon a cell edge are resolved [13]. It allows us to study dynamics of biological cells which cannot be (easily) described with other methods that treat cells as unit-pixels or centre-of-mass based (deformable rigid body) entities. This is both due to the intrinsic mesoscopic nature of the CPM, and due to its ability to describe potentially complex (local)

[1] We highly recommend to read Chapter II.1 for a more thorough introductory explanation and considerations about energy minimisation and metropolis algorithm. Nevertheless, for the sake of self-consistency, the general implementation procedure is repeated briefly.

deformations of the cell (such as epithelial cells stretching around a blood vessel or the dendritic shape of DCs in lymph nodes). Cell dynamics, both in the CPM and in reality, are due to this entanglement of subcellular cell deformations with cell properties like cell size. Moreover, cells do not displace as fixed units, but by successive subcellular movements, in which at any time a large part of the cell is stationary, connected to other cells or substrate. Essentially, protrusions are being created in the front and dismantling is occurring at the rear, while the centre contacts remain stable, as is the case in the CPM.

The CPM does not explicitly describe effective forces acting upon a cell, in contrast to other model-formalisms (see e.g. [40]). Generally, the force-based approach relies on the main assumption that the movement of the centre of mass of the cell, or of its subdivisions, can be adequately described by a limited number of forces acting upon or between them. This strategy is well suited for describing objects that undergo limited deformation. However, the CPM is a good formalism to adopt for any study in which it becomes relevant to take into account that cells are highly deformable, that the movement of each position depends on the movement of the rest of the cell (e.g. via turgor pressure), that cell membrane dynamics are locally highly correlated, but not fixed to the movement of the centre of mass, and that fluctuations play an important role in the nature of cell protrusion and motility. To represent the above aspects with explicit forces acting on each position of the membrane leads to a huge proliferation of variables, forces, and effects that have to be considered, and is very cumbersome. By computing changes in the Hamiltonian, local forces at the periphery of the cell are described implicitly (via energy gradients with respect to the position of each membrane element). The cell, by energetically exploring its configurational space, is effectively being subjected to forces on a microscopic level, but without them having to be defined explicitly.

In the following sections, we will show how one can relate the "material" properties of individual cells, such as deformability and adhesion, and tissue properties, such as surface tension, to morphogenetic processes. This is a pivotal issue in biology, because it will clarify to what extent developmental processes are emerging from "simple" cell properties, which will lead to a better understanding of the developmental program of organisms.

2. Basic formalism

The implementation of the model is extensively presented in Chapter II.1. Summing up: at each Monte Carlo time step, a random sampling through the lattice is done to determine whether pixels change their state into the state of one of their randomly chosen neighbours. This change (denoted here as "copying") corresponds to small deformations of the membrane (or any other boundary of a defined structure). To determine whether copying will occur, one calculates the Hamiltonian ($\mathcal{H}$), which basic structure is of the form

$$\mathcal{H} = \sum_{ij} \sum_{i'j'} J_{\tau(\sigma_{ij}),\tau(\sigma_{i'j'})} \left(1 - \delta_{\sigma_{ij},\sigma_{i'j'}}\right) + \sum_{\sigma} \lambda \left(a_\sigma - A_{\tau(\sigma)}\right)^2 . \qquad (1)$$

The Kronecker delta term $\left(1-\delta_{\sigma_{ij},\sigma_{i'j'}}\right)$ simply assures that neighbouring lattice sites of the same state (i.e. belonging to the same cell) do not contribute to the total energy of the system. Additional terms can be added to the Hamiltonian that either refer to mesoscopic properties of the cell (such as total perimeter), or to an external field to which the cell responds (such as a chemoattractant field, possibly produced by the cells themselves). As a result of the general form of Eq.(1) with positive J values, large bending fluctuations of the cell membrane, as well as large expansion or compression in the cell size, are avoided (due to first and second term, respectively). In a 2D model, $\mathcal{H}$ is a function of the cell area and the boundary length, corresponding in 3D to volume and surface area. $J_{\tau(\sigma_{ij}),\tau(\sigma_{i'j'})}$ is the coupling energy per boundary site between a cell site (of state σ_{ij} and cell type $\tau(\sigma_{ij})$) and an adjoining site (of state $\sigma_{i'j'}$ and cell type $\tau(\sigma_{i'j'})$); a_σ is the actual cell area, $A_{\tau(\sigma)}$ the target area, and λ an 'inelasticity' constant (a Lagrange multiplier, see Chapter II.1) that affects the constraint on cell area deformation.

Given a Hamiltonian, the energy of a certain configuration is determined, and the copying of the random neighbour to the chosen site is tested: the energies of the two configurations, before and after copying trial, are compared by computing the net change of energy,

$$\Delta\mathcal{H} = \mathcal{H}_{after} - \mathcal{H}_{before}\,. \tag{2}$$

Note that the calculation of $\Delta\mathcal{H}$ only requires information about the chosen site and its neighbours. The copying trial is then accepted with probability

$$p(\sigma_{ij} \to \sigma_{i'j'}) = \begin{cases} 1 & \text{if} \quad \Delta\mathcal{H} < -Y\,, \\ e^{\left(-\frac{\Delta\mathcal{H}+Y}{T}\right)} & \text{if} \quad \Delta\mathcal{H} \geq -Y\,, \end{cases} \tag{3}$$

where Y represents a yield – the ability of the membrane to resist a force –, and T (simulation temperature) determines the fluctuations. Eq.(3) states that configurational changes that lower the energy by at least Y are always accepted, whereas all other changes are made using the Boltzmann probability. That is to say, if the energy were to increase much due to such a change, that change becomes extremely improbable. Often Y is set to zero, which is how it was first implemented. The typical unit of time in the CPM is the Monte Carlo step (MCS), which is defined as a series of random copy trials, equal in length to the total number of lattice sites. Eq.(1) and Eq.(3) describe the whole model formalism. This quite limited set of components, however, produces a wide range of cell behaviours, which we will analyse through the individual roles of each component. As will become evident, the spectacular spectrum of cell behaviours is in fact mediated through the cell's capacity to deform. One could say that in the CPM, cell shape is the leitmotif of morphogenesis.

3. Forces on a cell ($\Delta\mathcal{H}$ and Y)

The energy-based description of the CPM can be linked to more direct measurable concepts such as forces acting upon a cell, by observing that $\Delta\mathcal{H}$ can be interpreted as the force applied to a local membrane element of the cell (because the negative

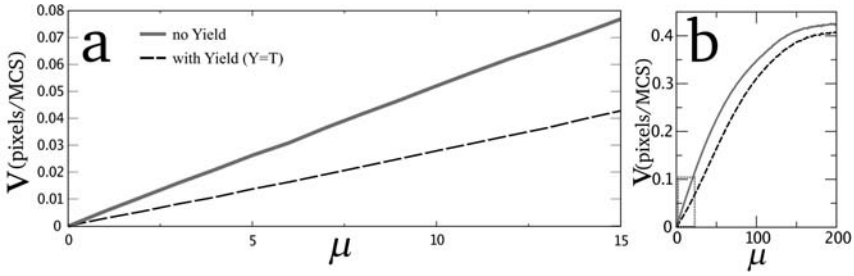

FIGURE 1. Cell speed and chemotaxis. (a) Speed of motion in 3D simulation of cells moving up a chemoattractant gradient as a function of chemotaxis strength μ, for cells without yield (solid line) and with yield (dashed line). Cell speed v, in pixels per MCS, is effectively linear. (b) This linear regime does not apply for large μ values.

gradient of a potential in a conservative system is the force). How do forces act on cells? Biological cells are actually highly dissipative objects (given the internal structure within a microscopic scale), for which viscosity dominates inertia [13]. Consequently, the effect of forces acting upon cells can be best described as being within the Aristotelean regime, i.e. $F \sim v$. Likewise, the CPM does not describe any inertia. Once $\Delta\mathcal{H}$ is perceived as a force, it becomes clear from Eq.(3) that Y is in fact an opposing force, a resistance intrinsic to the cell. It is a property of the membrane itself and not of the field or interactions of the cell. This resistance of the membrane to deform could be, e.g., due to the cortex of the cell.

Generalising this concept, the addition of any term to Eq.(2) in the form of an offset to $\Delta\mathcal{H}$ means introducing a force. Similarly, additional terms in the Hamiltonian, Eq.(1), are energy terms that give rise to forces. They are equivalent concepts. To illustrate, chemotaxis can be described by changing Eq.(2) into

$$\Delta\mathcal{H} = \mathcal{H}_{after} - \mathcal{H}_{before} - \mu(c_{site} - c_{neighbour})\,, \tag{4}$$

where c represents the chemoattractant concentration values at both sites, the one copying ('neighbour') and the one being copied into ('site'). The term was first introduced by Savill & Hogeweg [42] to describe the chemotactic response of *Dictyostelium* cells to cAMP. Here, the membrane is experiencing forces into the directions of the chemoattractant, with a strength set by μ. What type of behaviour does this generate within a simulation? Fig.1 shows that within a linear chemoattractant gradient, a cell is indeed not accelerated, but instead moves with constant velocity. Within a realistic range of parameters (i.e. the cell should not fall apart due to the applied forces), the relationship between the velocity and chemotactic strength is approximately linear, i.e. in the Aristotelean regime. Fig.1 also shows the effect of Y on motion: with higher yield cells move with reduced speed. Note, however, that in this description of chemotaxis, we leave out the internal cell dynamics, such as receptor kinetics and cytoskeleton turnover, which are the processes that are actually underlying the generation of the forces that are

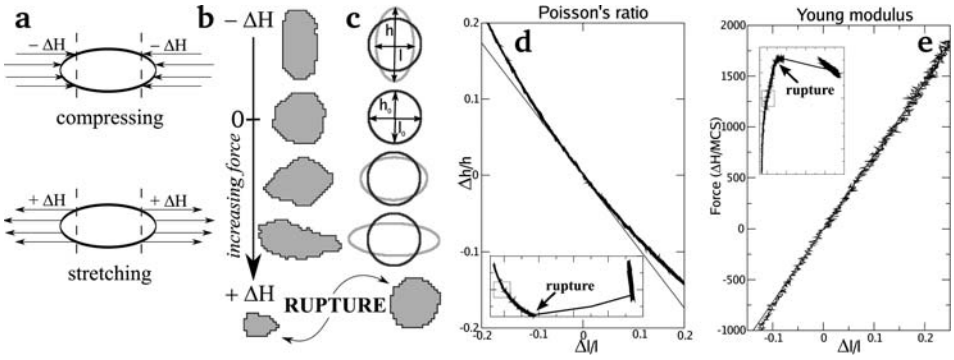

FIGURE 2. Cell deformation and forces. (a) To apply stretching and compressing forces on a CPM cell, $\Delta\mathcal{H}$ is exerted on all pixels along the horizontally opposing extremities of the cell. Within the simulation, we slowly increase $\Delta\mathcal{H}$ over time, permitting the cell's shape to relax at each value. The change in sign of $\Delta\mathcal{H}$ determines the directionality of the force. (b) Cell shape as a consequence of forces applied to the extremities of the cell. Here, five deformations are shown, from top to bottom increasing in applied force: compression, a null force, small positive force, large positive force, and a critical force, causing the cell to rupture. (c) The light ellipses show the inertia tensor representing the cell shape given by (b); the dark circles show the mean shape of a cell that undergoes no external applied force (both integrated over a time window of 1000 MCS); height, h_0, is given by the vertical, and length, l_0, by the horizontal axis. Deviations from the equilibrium shape are calculated, $\Delta h{=}h - h_0$ and $\Delta l{=}l - l_0$, with l, h given by the main axes of the inertia tensor. (d) The change in height as function of the change in length. The slope gives the Poisson's ratio with value $\nu{=}0.86$. (e) The applied force (in total $\Delta\mathcal{H}$ applied to the cell per MCS) as function of the length deformation. The slope gives the Young modulus $E{=}7225$. In both graphs, the insets reveal the function outside the linear regime with rupture point indicated. The boxes within the insets represent the zoomed magnifications (d) and (e). See also a simulation MovII.2.2bc.

applied, from the inside, on the membrane. In Section 6.2 we discuss in detail how this gap can be bridged, and why such a "shortcut" is appropriate.

Forces acting upon the cell do not only cause the cells to displace, but also to deform (see Fig.2a–c). This can be exploited by, inversively, analysing the cell deformations to determine stresses within a tissue (both experimental as in CPM simulations). As a basic example, we show how the Young modulus (the rate of change of stress with strain) and Poisson's ratio (the ratio of transverse contraction strain to longitudinal extension strain in the direction of stretching force) of a cell can be determined for a CPM simulation by means of applying a x-directional-force (through $\Delta\mathcal{H}$) on the extremities of a 2D cell and measuring the resultant change in length and height of the equilibrated cell (which we do by calculating the inertia tensor). In this case, the Poisson's ratio is simply the ratio of change in height over that of length, while the Young modulus is the slope of the applied $\Delta\mathcal{H}$ as a

function of the relative variation of the cell's length (see Fig.2d,e). The continuation of studies analysing material properties within the CPM is a most called for and promising field of research, as it can help to further link simulation parameters to measurable biophysical properties of cells, which should make it possible to obtain both realistic parameters for the CPM, as well as realistic estimates of forces within a tissue. Also, it is of pivotal importance to the understanding of development, because it is becoming increasingly clear that mechanotransduction (the ability of a cell to react towards mechanical stimuli of its environment, through stresses and strains) plays an important role [10, 43].

4. Cell deformation and adhesion (J)

Multicellular aggregates have the property of rounding up when in suspension (or when in contact to surfaces they do not adhere to) in a manner resembling oil droplets in water. Moreover, cells within an aggregate tend to sort themselves in distinct segregation patterns also resembling immiscible fluids that separate [2, 46, 48]. To properly link these observables, the cellular system should satisfy some conditions. It should be formed out of coherent subunits endowed with motility. Whereas liquids have molecules as subunits, tissues have cells. Molecules move thermodynamically whereas in tissues cells move through extensions and contractions. Taking this into account, Steinberg [45, 46] formulated the differential adhesion hypothesis (DAH), where cells are analogous with liquids with distinct superficial tensions. This later inspired Glazier & Graner [12] to introduce the DAH into a model formalism which we now know as the CPM.

Within the CPM, the DAH is implemented by attributing different interaction values between different cell types. Moreover, because these interaction energies act only on interfaces, they give rise to an energy which is proportional to the length of the boundary, due to which we can define surface tensions γ. Please refer to Chapter 1 for a discussion about tensions.

The interaction values ($J_{\tau,\tau'}$) can be termed either as cohesion or adhesion. Although the word adhesion is often used for both, as a more strict definition, cohesion is between cells of the same type, adhesion between cells of different types. The first results from cadherin molecule interactions, while the second can be of two forms. When the adhesion refers to the interaction between cells and substrates, $J_{c,s}$, it is describing the biological interaction mediated by integrins that form focal adhesion points with the substrate's extracellular medium components, such as for example fibronectin. Adhesion between different cell types, however, continues to be a result of cadherin interactions (although different cadherins might be involved).

4.1. Pure cell sorting

Although the surface tensions determine the final equilibrium configuration of biological systems (for example in a cell-sorting experiment) the *evolution* towards this equilibrium is affected by the simulation temperature T and the values J,

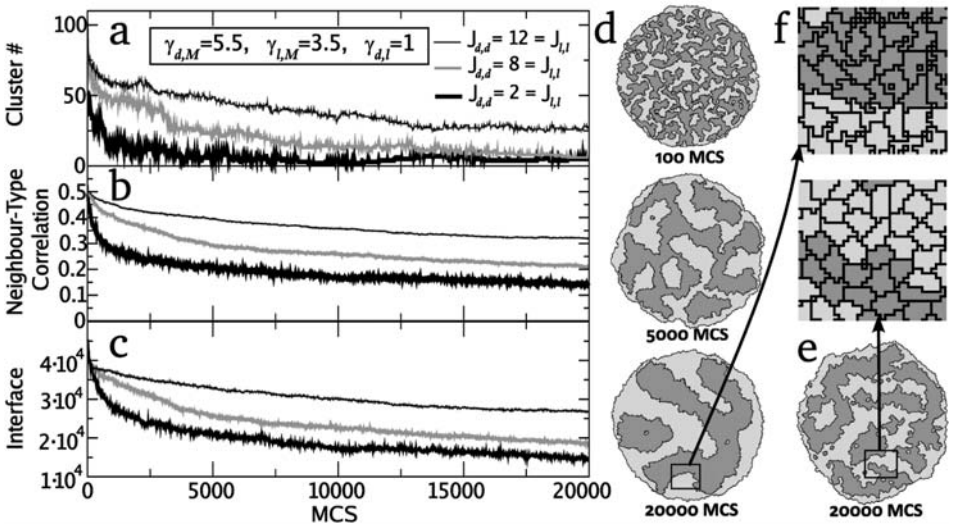

FIGURE 3. Cell sorting dynamics. In all these 2D simulations the superficial tensions are kept the same. The cohesions are varied together, such that $J_{d,d}$ is always equal to $J_{l,l}$. (a) Total number of clusters within the cell mass; (b) neighbour-type correlation, i.e. average ratio of neighbouring cells that are of a different type over the total number of neighbours; (c) total interface between the two cell types, in terms of the number of second neighbour sites belonging to different cell types; (d) time evolution for the case in which $J_{d,d}$=$J_{l,l}$=2; (e) established configuration for the case in which $J_{d,d}$=$J_{l,l}$=12; (f) Enlargement of tissue fragments, indicated by frames, of (d) (top) and (e) (bottom). Note that cells in (d) are more distorted than those in (e), and sort out more rapidly. In all simulations, λ=1 and T=6. See also a simulation MovII.2.3de.

which both act on the amount of deformation a cell undergoes. If both parameters are multiplied by a constant, αT, αJ, we simply scale the system in such a way that the evolution towards the equilibrium is unaltered. In contrast, keeping the surface tensions constant while varying the values of J, implies the addition of an offset to the J values, which cannot be correctly scaled through the temperature. A different energy landscape is thus formed, although the global minimum remains the same. To illustrate this effect, we simulate cell sorting of two cell types – dark, d, and light, l, cells –, with surface tensions that fulfil the total engulfment requirement $\gamma_{d,M} > \gamma_{l,M} + \gamma_{d,l}$ (light tissue surrounding dark tissue), where M represents medium. We run three simulations from random initial 2D conditions, for different values of J while keeping the surface tensions fixed. The evolution of three different cell-sorting observables of the system are shown in Fig.3, from which it becomes clear that cell sorting is slower for higher J values. This is due to the system getting trapped for longer periods in local minimums, as a consequence of a reduction of the amount of deformation that the cells undergo. Thus, one way to

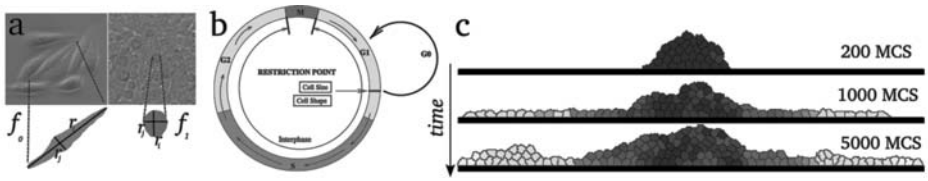

FIGURE 4. Cell deformation as cell regulation. (a) Cell shape measurements of the polarity of sparse cultured cells (f_0) and cells in confluent culture ($f1$). (b) Scheme of the mitosis-regulated cell-cycle, used in Eq.(5), in which interphase, cell size, and cell shape are taken into account. (c) Evolution of a tumour, modelled as a 2D cross section (with substrate at the bottom). Mitosis distribution within the cell mass is given through a shade gradient from dark to light, with white corresponding to the highest mitosis numbers. Note that mitotic activity is greater at the edges of the cell mass. We use T=6, λ=1, $J_{c,M}$=7, B=1.2, and h=4. (Adapted from [14].) See also a simulation MovII.2.4c.

understand the cell-sorting results of Fig.3, is that higher interaction energies more strongly penalise deformations, making it cumbersome for cells to explore their neighbourhood. Indeed, by comparing Fig.3d with Fig.3e, a significant reduction in cell deformation is seen (Fig.3f): the simulation with lower J values sorts out more efficiently, while giving rise to cells with more "ruffled" membranes.

As a general feature of surface-tension driven cell sorting, we see that sorting logarithmically slows down with time, i.e. the decrease in the number of clusters over time gives an approximately straight line on a log-log scale, which means that the sorting slows down as a power-law. Note that variations in cluster number are much larger than variations in either neighbour-type correlation or total interface, which decrease much more smoothly (Fig.3b,c).

The characteristic slowing down of the sorting implies, from a biological perspective, that morphogenetic processes would take very long to finalise. One can therefore ponder if another effect could not "help" the system to overcome the local minimums and sort out with a more constant, steady speed. One solution for this problem was presented by [24] (see Section 7.3).

4.2. Cell deformation and tumour growth

In section 3 we have shown how cell deformation can confer information about forces acting upon the cell. From a more biological perspective, we will now focus on how deformation, which can be influenced by the J values as mentioned above, can serve as regulational information for the cell itself. To illustrate this point, we use an example on tumour growth.

Due to alterations in cell regulation, cancerous cells proliferate differently, causing tissues to become "disorganised". The anomalous cell proliferation sheds light on the key regulational elements that orchestrate the (healthy) maintenance and establishment of multicellular organisms in general. Thus, approaching tumour growth through models gives us the possibility to test cellular hypothesis about

cell regulation (mitosis, cell differentiation, apoptosis etc). Please refer to Chapter II.3 for more detailed examples on modelling tumour growth.

Already in 1978, cell distortion has been correlated to mitosis [11]. It was observed that cells grown on a less adherent substrate tend to have a more rounded shape, whereas those in contact with adherent substrates become more distorted. Interestingly, rounded *isolated* cells undergo similar low mitotic rates as cells in "packed" configurations. It was therefore suggested that instead of the existence of a causal relation between contact-inhibition and diminishment of mitosis, cell shape itself could be the underlying 'signal'. This was indeed a novel idea in times in which mechanical-signal transduction pathways were not yet known (see [7, 41, 10, 43]).

To test this hypothesis in the context of tumour dynamics, we have measured the population growth of 6 lineages of human epithelial tumours. We observed that the growth curve of all lineages fitted to the well-known Gompertz growth model, $\frac{dN}{dt} = \beta \times N \times \ln(\frac{A}{N})$, where $N(t)$ is the number of cells at time t, A the carrying capacity and β the growth parameter. The phenotypic properties of these lineages, i.e. the polarity, f, of the cells, were also measured (being defined as the ratio between the longest, r_i, over smallest, r_j, diameter of a cell, $f = \frac{r_i}{r_j}$). The amplitude of variation in polarity can be expressed by the coefficient $D = \frac{f_0}{f_1} - 1$, where f_0 corresponds to cells in sparse cultures (low densities), and f_1 to cells in confluency (higher densities, a monolayer without breaches) (Fig.4a). D can be interpreted as the morphological deformation coefficient of adhered cells. After many measurements, an average coefficient, typical for each specific lineage, was obtained. Most interestingly, the coefficient D was found to be highly correlated to the the growth coefficient β of the Gompertz growth curve in a linear manner [6, 14]. In this way, a very strong experimental link was established between phenotypic properties of the shape-variation within a lineage and its growth rate, which means that the observed cell deformations have a very high predictive power for the rate of tumour growth. Although pathologists indeed extensively use cell shape to assess the malignancy of a lineage, such quantitative measurements are fundamental to start understanding how cell shape actually regulates cell behaviour.

Inspired by the above observations, we introduced distortion as a mitosis regulator in the CPM model [14]. To do so, we define distortion of a cell in the simulation as $\varepsilon_\sigma = \frac{\text{major axis}}{\text{minor axis}} - 1$, integrated over 100 MCS to reduce fluctuations. At every MCS, for each cell the probability to undergo mitosis, P_m, is calculated. Before division, cells have to pass through interphase, given by a time parameter in the simulation. Additionally a size-check is introduced, A_{min}, to guarantee that a cell is sufficiently large for division. Only when both requirements are met, there is a probability of mitosis, which then depends on the level of cell deformation, as was suggested by the experiments. The probability is thus given by

$$P_m = \begin{cases} 0 & \text{if} \quad \Delta t_\sigma < T_{interphase} \quad \text{or} \quad a_\sigma < A_{min} \\ \frac{\varepsilon_\sigma^h \cdot H}{\varepsilon_\sigma^h + B^h} & \text{if} \quad \Delta t_\sigma \geq T_{interphase} \quad \text{and} \quad a_\sigma \geq A_{min} \end{cases}, \tag{5}$$

where h is the hill-coefficient, B the critical distortion and H the maximum probability per MCS. These rules are depicted graphically in Fig.4b.

In Fig.4c we show a 2D simulation of distortion regulated mitosis, giving rise to tumour outgrowth. The shades indicate the number of mitoses undergone per cell. It shows that within the tissue a distribution in mitosis activity has emerged, with cells at the edge dividing more often. Although there is no explicit "contact-inhibition" in the model, nor diffusible substances entering from outside the tumour, we still observe a boundary-dependent growth. In fact, cell-shape by itself turns out to be able to give rise to Gompertzian-like growth curves, the form of which depending on the distortion regulated mitosis parameters B and h. Cells at the border are able to elongate more, and therefore present a higher growth rate. As the tumour grows, the ratio between border-cells and those in the middle of the aggregate diminishes, and as a result the growth rate of the tumour goes down.

4.3. Cohesion and adhesion in tumour growth

The above example can be extend by analysing, within the CPM, the separate roles of adhesion and cohesion in tumour growth. To do so, we assume that the tumour consists of only one cell type, so all cells have the same cohesion $J_{c,c}$, while adhesion to the substrate is given by $J_{c,s}$. Fig.5a shows that in such a scenario tumour growth can be enhanced by increasing the adhesion of cells to the substrate. This is because cells experiencing higher adhesions elongate more easily on the substrate, which stimulates mitosis (following Eq.(5)). In contrast, Fig.5b shows that increasing cohesion between cells yields an opposite type of response, because it tends to keep the cells together in a rounded aggregate. Diminishing cohesion

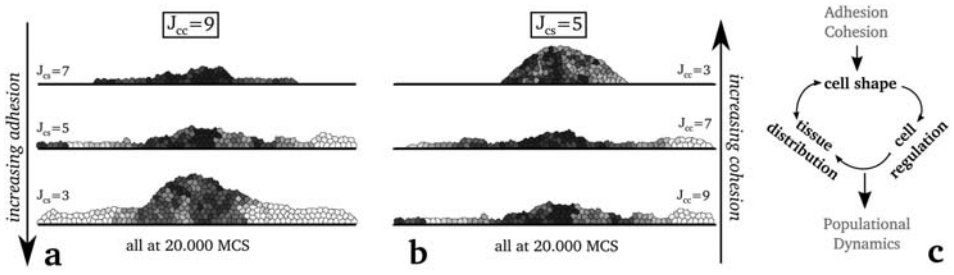

FIGURE 5. Influence of cohesion and adhesion on tumour growth. (a) Influence of adhesion, here shown by keeping the cohesion between the cells constant, while increasing the adhesion. (b) Influence of cohesion, here shown by keeping adhesion between cells and surface constant, while altering the cohesion. Note that increased adhesion brings forth faster growing tumours, while diminishing cohesion leads to more metastatic tumours. (c) Scheme of the feedbacks which link adhesion to growth. Each frame depicts growth after 20.000 MCS, starting from the same random initial condition. (Adapted from [14].)

favours that the cell mass spreads out onto the substrate in a non-agglomerate manner, resembling "metastatic" behaviour. Both observations are in agreement with what is known from tumour growth: mutations leading to malignant forms of cancer typically promote integrin molecules while diminishing the cadherins [20].

5. Compressibility (λ and A_τ)

Shrinkage due to the positive interaction energies J is counterbalanced by the volume conservation term in the Hamiltonian. Deviations from the target volume cause pressure changes in the cell, since pressure p is the conjugate variable to the area variable a_σ:

$$p = -\frac{\partial H}{\partial a_\sigma} = 2\lambda \left(A_{\tau(\sigma)} - a_\sigma \right) . \tag{6}$$

Because volume conservation is taking place on the level of the whole cell, pressure is constant throughout one cell. The main assumption for a volume conservation term at the cell level is that an infinitely fast redistribution of intracellular pressures occurs, i.e. pressure differences only occur between cells. This is a reasonable description, because the volume changes in biological cells are not due to compression of the cytoplasm (the fluid inside cells is effectively incompressible), but due to the flow of water through the semipermeable cell membrane. The external pressure on the cell is counterbalanced by osmotic pressure inside the cell, as has been shown experimentally for *Paramecium* [21]. In addition, active responses by the cytoskeleton counteract volume changes. Pressure changes outside the cell therefore require corresponding changes in the osmotic pressure in the cell, since large pressure differences would disrupt the membrane. Osmotic pressure can change by a water flow into or out of the cell, the process described by the volume conservation term. Cells can also respond to pressure differences by actively changing their osmolarity in order to maintain their original volume [21]. Within the CPM framework, this would correspond to changing the target volume in response to large changes in pressure.

The parameter λ describes the volume conservation caused by the viscoelastic properties of the cell. For larger λ, cells more stringently keep their target volume by being less flexible to volume changes, and therefore deformations become more difficult. Such viscoelastic properties have been studied for articular chondrocytes [15, 49], showing that cells are indeed compressible under mechanical force (chondrocytes have a Poisson's ratio of 0.36, i.e. significantly below 0.5, meaning that under pressure the cells are not able to keep their volume). Using alterations in the osmotic environment to determine the limits of the volume changes, it was found that cells can undergo more than three-fold volume changes until lysis. Typically, variations up to 20% are observed [15, 21].

Within the CPM, there is a rather complex entanglement between the interaction energies J and the compressibility given by λ. Because of the balance between compression and surface tension, cells are (slightly) smaller than the target volume, more deviated from it when J is larger. As an alternative it has been

proposed to use negative instead of positive J values [37]. In the case of negative J values, the cell's surface tension is negative, which means that the cell will loose its coherence, dissolving in its environment. Negative interaction energies therefore always have to be combined with a perimeter conservation term, typically in the form of $\lambda_p \left(p_\sigma - P_{\tau(\sigma)}\right)$, where $P_{\tau(\sigma)}$ is the target perimeter, p_σ the current perimeter of the cell, and λ_p the membrane inelasticity. This extra term has (at least) three advantages: (i) it allows to decouple and untangle the membrane tension (which makes a cell round up in suspension and is described by the perimeter conservation term) from the effects of adhesion and cohesion (which is then only described by the J values); (ii) it adds extra possibility to vary the typical cell shape, because by increasing the target perimeter, one can increasingly deviate the typical shape of the cell from a circular shape, allowing it to prefer more complex shapes; and (iii) when positive J values are used, independent of parameter choice, there always exists a critical cell diameter below which a cell shrinks to zero size. With respect to the last point, however, we would like to point out that this is actually what is typically observed for biological cells [7]. Nevertheless, having a perimeter constraint makes it possible to prevent such critical behaviour, simply because negative J values can be used, for which such an instability does not exist. (The last point is especially important for simulations in which large deformations occur, due to which cells might 'get lost').

An illustrative example of the usage of a perimeter conservation term can be found in [3], in which the dynamics within a lymph node are described, using a 3D CPM. Here, dendritic cells are endowed with a very large target perimeter, which causes them to form dendritic 'arms' to which many T cells can bind. We conclude that, with either positive or negative J values, the compressibility of biological cells is nicely represented in the CPM.

6. Energy exploration and membrane fluctuations (T)

Biological studies have revealed the importance of stochastic events for the behaviour of cells. Because dynamics of a cell depend highly on fluctuations, a noteworthy feature of the CPM is indeed its control of fluctuations through the 'simulation temperature' (i.e. statistical effects) within the Monte Carlo simulations. Tuning the 'temperature' allows us to turn up or down the effect of stochastic fluctuations (of possibly different origins) in the model. For example, the parameter T has been interpreted as the membrane fluctuation amplitude of cells, by comparing it with effects of the drug cytochalasin-B (a suppressor of membrane ruffling) [36]. Importantly, when T is set to zero, the dynamics very rapidly freeze into a pattern that is a local minimum, not being able to further explore the energy landscape. Such a parameter setting is unrealistic for biological cells, but for research on foams often a value of T of zero, or very close to it, is desired for obtaining appropriate foam characteristics. In such temperature regimes, often a method of annealing is applied to obtain the correct lower energy configurations while still overcoming energy barriers.

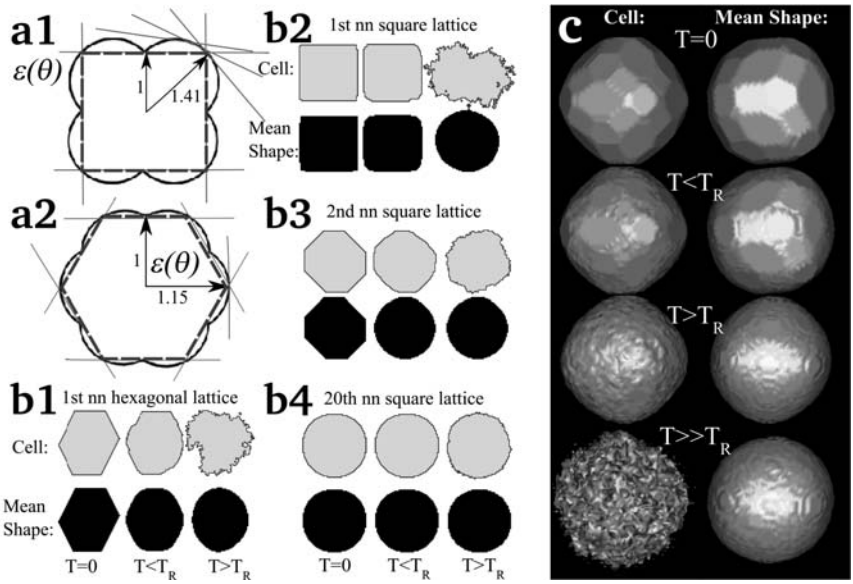

FIGURE 6. Cell shape and simulation temperature. (a) Wulff construction diagram. The blossoms show the energy per surface length, ϵ, as function of surface angle, θ. Lines shown how the final equilibrium shape (in dashed lines) is found geometrically. Diagrams shown are for nearest neighbour (nn) square lattice (a1) and for nn hexagonal lattice (a2). (b) Actual and mean shape of a 2D cell, for different neighbourhoods and temperatures. (c) Actual and mean cell shapes for simulations on a square 3D lattice, up to third nn. See also a simulation MovII.2.6c.

6.1. T and the lattice

There exists in the CPM an angular dependency of the surface tension, due the underlying lattice structure. For T=0, this dependency can easily be calculated, by determining the free surface energy per unit length, ϵ, along a straight surface laid out along different angles, Θ. Plotting the energy as a function of surface angle in polar coordinates results in a blossom-like structure, as can be seen in Fig.6a. The construction at each point of this polar plot of a plane perpendicular to the radius vector at that point, generates an enveloped volume, i.e. an enclosed geometric shape that can be reached from the origin without crossing any planes. Wulff [51] has shown that this volume is geometrically equivalent to the ultimate equilibrium shape for any surface-tension driven system (such as a crystal, [16]).When the free energy plot forms cusps, flat surfaces (facets) are formed. Accordingly, an isotropic free energy generates as minimal energy configuration a perfect circle. For the CPM at T=0, one thus sees, that for different possible neighbourhoods, multifaceted shapes (see Wulff construction in Fig.6a) arise. The free surface energy also has a temperature dependency that can cause the polar-plot to loose its cusps above a "roughening" temperature T_R. However, it is difficult to determine

the function $\epsilon(T, \Theta)$ [39], so it becomes easier to approach the equilibrium shapes through simulations. We do so by sampling the cell shape over time for a given T, and drawing the mean shape by plotting the distribution of occupancy relative to the centre of mass of the cell and then setting a threshold, e.g. of 50%. In this way, time averaged shapes are obtained, which are shown in Fig.6b,c. The angular dependency observed at temperatures below the roughening temperature is obviously, for biological cells, an unwanted grid-effect (unlike, for example, crystals, in which such angular dependencies can be observed even up to macro-scales over a wide range of temperatures). This effectively sets a lower limit to the values of T that can produce realistic, non-grid affected simulations. In many studies, however, a low temperature is required to correctly describe the limited flexibility of a certain cell type (think, for example, about plant cells). In such a case, the typical solution is to use larger neighbourhoods. Neighbours are ranked by their distance to a site, and the angular dependency at low temperatures drops dramatically when higher order neighbourhoods are being used, therewith effectively removing the grid-effect. For example, while the angular variation in surface tension in a square 2D grid is 41% for nearest neighbours (nn), and 12% for second nn, it drops to 4% for fourth nn. When a twentieth nn is used, an almost perfectly circular shape is obtained at zero temperature.

In most cases it is difficult to empirically and quantitatively connect T to physical aspects of biological cells. In the next section we will discuss how by taking the underlying biochemistry into account, a quantitative approach becomes feasible.

6.2. Fluctuations driven by cytoskeleton dynamics

A general criticism against the CPM is that cells are not driven by energy minimisation. The claim is, that this central assumption of the formalism implies that cells are passive objects, whereas in reality they do actively explore their surroundings. As discussed above, the simulation temperature takes to a certain extent the active exploration due to membrane fluctuations into account. But zooming in further into the generation of cell activity, reveals that these fluctuations are in fact due to local, subcellular forces exerted on the membrane. So, if we want to understand how a cell that is actively exploring its surrounding can be coupled to the 'passive' description of the CPM, and to understand how temperature and yield can be viewed in the light of this, we have to look at the detailed dynamics underlying cell motility. It also means we have to look at the feedbacks that exist between the cytoskeleton, the chemical signals controlling it, and the cell shape. We have shown that actually sufficient qualitative and quantitative detail of the biochemistry underlying cell motility is known to build such a quantitative model that can correctly describe the processes of cell polarisation and cytoskeleton turnover [29]. The main elements are as follows.

The dominant force in front-edge protrusion of a motile cell is the actin cytoskeleton [8, 1]. Actin filaments have two distinct ends, barbed ends, which extend through monomer addition and provide the polymerisation force that pushes the

membrane outwards, and pointed ends, which retract through actin disassembly. Actin filament growth at the front and loss at the back is called treadmilling: the filaments are predominantly stationary, networked and cross-linked to form a mesh that gives the cell its characteristic shape and structure.

Cells can respond to a wide range of inputs, e.g. chemotactic signals, physical stress, and cell-cell contacts. These signals are transduced by different families of receptors to 'central nodes', the small G-proteins Cdc42, Rac, and Rho [32, 9]. The small G-proteins regulate and fine-tune the polymerisation, disassembly, and nucleation of filaments, as well as the capping and uncapping of actin filament barbed ends, therewith 'steering' the cell motility. By modelling the cross-talk between the small G-proteins (see Fig.7a), it was shown that the known interactions are well-suited to stably polarise a cell, by correctly forming a front region within the cell with high levels of active Rac and Cdc42, and a back region with high levels of active Rho [29, 23]. (Note, that it is this polarisation in terms of the small G-proteins through which the front and back of the cell emerges; the model has not pre-defined which side should be considered front or back.) The power to generate robust polarisation is essentially due to the mutual inhibition between Cdc42 and Rho, combined with a rapid diffusion of their inactive forms through the cytosol, the latter effectively being the source of cell-wide information about the relative sizes of the active regions. After polarisation, the cell efficiently responds to small imbalances between the different small G-proteins. Even very small imbalances (below 1%) in activation of Cdc42 are sufficient to cause the polarisation to become correctly oriented [29, 23]. The small G-protein dynamics can then be coupled to the cytoskeleton dynamics [29]. Because of the detailedness of the description, it is feasible to use, and we have used [29], experimentally determined parameter values for all these processes.

The final step then is to couple these internal dynamics to the CPM. Because we are ultimately interested in the forces acting upon the membrane due to filament extension and contraction, we change Eq.(2) into

$$\begin{array}{l} \Delta\mathcal{H} = \mathcal{H}_{after} - \mathcal{H}_{before} - \sum_m P_{\theta_m} + \xi\,(\rho - \rho_{th}) \;\text{ when a cell extends,} \\ \Delta\mathcal{H} = \mathcal{H}_{after} - \mathcal{H}_{before} + \sum_m P_{\theta_m} - \xi\,(\rho - \rho_{th}) \;\text{ when a cell retracts,} \end{array} \tag{7}$$

where $\sum P_{\theta\ m}$ describes the forces exerted by all barbed ends pushing against the membrane towards the empty site. The term $\xi\,(\rho - \rho_{th})$ describes the effective Rho-dependent contraction forces. The value $1/\xi$ represents the elevation in Rho concentration whose resulting contraction counterbalances the force of one barbed end per nm pushing against the membrane. By writing Eq.(7) in this form, $\mathcal{H}$ (and therewith T and Y) carry the same units as P, i.e. the number of extending filaments pushing against the membrane per unit length (here $[\mathrm{nm}]^{-1}$).

How can Eq.(7) be linked to known physics about cell protrusion? Earlier, an effective force-velocity relationship for protrusion speed as a function of the number of barbed ends pushing at the cell edge had been derived [35, 34]: in a thermal ratchet driven by actin polymerisation, the relationship between the number of barbed ends at the membrane and the speed, v, of the lamellipodial

protrusion is approximately

$$v = v_0 \exp(-w/b)\,, \tag{8}$$

where v_0 is the free polymerisation speed, b the density of barbed ends per unit length at the membrane, and w the renormalised membrane resistance force per unit length ($w = F_m\delta/k_BT$, where F_m is the membrane resistance, δ the size of one monomer, and $k_BT \approx 4.1$pN nm is thermal energy). However, no direct one-to-one correspondence between the CPM parameters and those of this force-based equation exists, due to the contrasting natures of the different formalisms. Instead we can link these values by deriving a *comparable* relationship between the effective speed of protrusion and the density of barbed ends for the CPM model.

In [29], a simple one-dimensional situation similar to that considered in [34] is analysed. By, in line with [34], neglecting capping and side-branching, and assuming that all barbed ends are directed towards the cell edge, it was shown that the the implicit description of the mean speed of protrusion that stems from Eq.(7) is

$$v = \frac{\Delta x}{\Delta t} \exp\left(-Y/T\right) \left(\exp\left(\frac{(1 - v/v_0)b}{T} \right) - \exp\left(\frac{-(1 - v/v_0)b}{T} \right) \right)\,, \tag{9}$$

where Δx and Δt are the grid size and time corresponding to one MCS, respectively. The derivation closely resembles and extends the derivation of the typical protrusion velocity at a given force as presented in Eq.(13) in Chapter II.1. While not identical to Eq.(8), this equation also describes a relationship between protrusion velocity and the number of barbed ends, but here the relationship is expressed in terms of the CPM parameters T and Y. By fitting this relationship to Eq.(8) (for which the parameter values are well-established), the optimal values for T and Y are obtained. Fig.7b shows that for T=0.008 nm^{-1}; Y=0.046 nm^{-1}, the thermal ratchet force-velocity relationship of Eq.(8) and the effective force-velocity relationship, Eq.(9), are highly comparable, being very close to each other over the whole range of biologically relevant barbed end density values, typically observed to be in the range of 0.05-0.25 nm^{-1} at the lamellipod edge [1, 34]. Accordingly, the CPM gracefully leads to a reasonable depiction of actin-based protrusion forces, through energy minimisation: for the above values of T and Y the model quantitatively describes the response of the cell membrane to any possible load of pushing barbed ends. The strength of having matched this relationship, is that we now can apply it in a simulation of a complex shaped 2D motile cell, with large variations in pushing barbed ends along the edge, implicitly locally solving for the broad range of applied forces. This also allows us to determine the feedback between the cell shape and deformation on the underlying cytoskeleton dynamics.

7. "Moving on with the CPM"

In this section we explore the motile behaviour that is generated by including intracellular dynamics in the CPM. The two most important properties that arise, are the persistency of motion and the ability of tactic responses. We therefore analyse straightforward extensions of the CPM to describe these processes, and

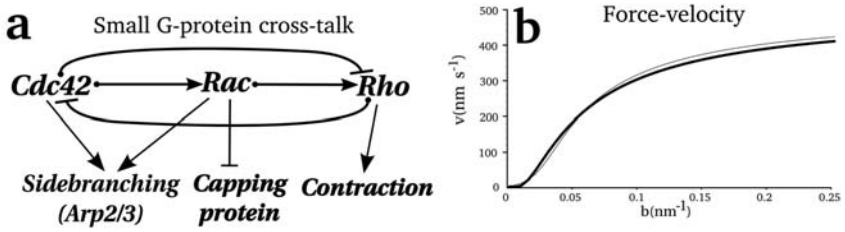

FIGURE 7. Establishment of protrusion forces. (a) Small G-protein crosstalk underlying polarity. Interactions and feedbacks between the 3 main players in our cell polarity model are shown, together with their effects on the actin cytoskeleton that are included in the model. (For details see [29]). (b) Comparison of the protrusion force-velocity relationship curve of the extended CPM (thin line) with the thermal ratchet model (thick line), where the velocity of the membrane (cell edge) v is shown as a function of the number of barbed ends b per nm at the membrane.

finish by illustrating the strength of the formalism by studying the full life cycle of an organism by means of this kind of extensions.

7.1. Keratocyte motion

A paradigm system for actin based cell motility is the fish epidermal keratocyte [47, 38], a cell that moves smoothly while retaining a typical crescent shape [25]. Remarkably, even well-prepared fragments of a keratocyte, lacking nuclei and organelles, can, given a transient mechanical stimulus, initiate and sustain such 'gliding' motility [50]. When the full model (Fig.8a,b) is run for biologically based parameter values and with all variables initiated at their typical levels (see [29]), then after any initial signal a moving cell is obtained, with a crescent shape closely resembling a moving keratocyte, and displacing at a more or less constant speed, independent of external signals (Fig.8c–e). Fig.8f shows a simulation of the model keratocyte within a linear chemoattractant field directed from above. We observe that the cell rapidly re-polarises and chemotactically moves upwards, in the direction of the region with the highest chemoattractant concentration, but also that the cell has a persistency in its motion, due to which it takes time to respond to the external signal.

Both the persistency and the reorientation behaviour emerge from the feedbacks and feedforwards between the multiple levels of organisation within the cell. Even in a rapidly protruding cell, the interface between high Cdc42 levels and high Rho levels within a cell is able to move with the same speed as the cell, keeping a straight (and, relative to the cell, fixed) boundary between front and back (Fig.8g). This is due to the rapid diffusion of the inactive forms of the small G-proteins which transfers the information about the relative sizes of the front and back region, and due to the fact that in a metastable bi-stable system the change of domain boundaries is strongly determined by the local curvature [4]. It effectively boils down to the well-known curvature effect, which plays a role

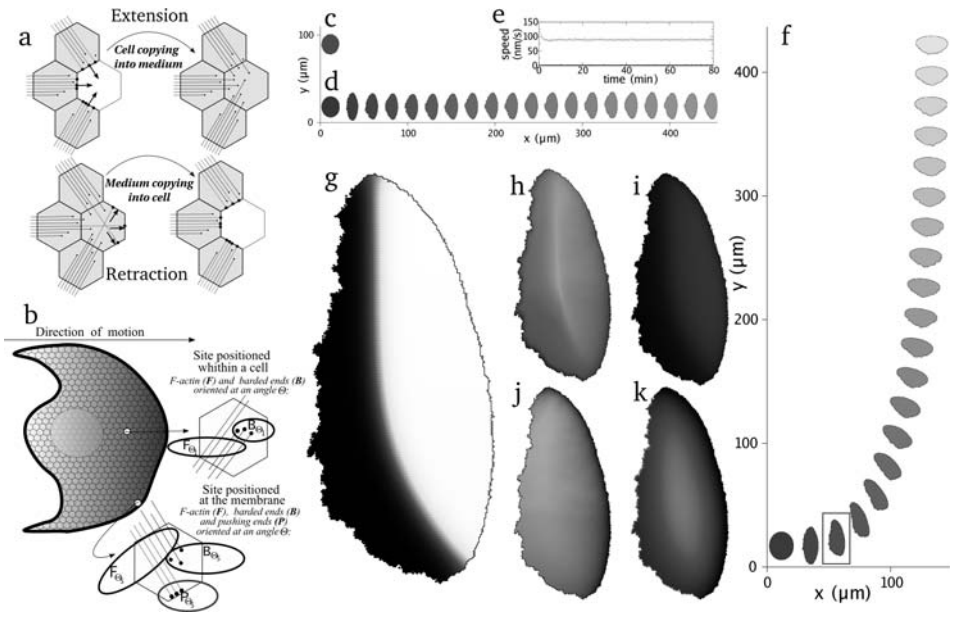

FIGURE 8. Cytoskeleton and the keratocyte. (a) Site copying, influenced by barded ends. Lines show F-actin (F), while dotted ends correspond to Barbed ends (B). Barbed ends can get "promoted" to pushing barbed ends, either due to their growth or due to retraction of the membrane. (b) 2D cytoskeleton-extended CPM. (c,d) Contour plots of modelled cell showing shape and relative position at 250 sec intervals. Without initial signal or instability the cell remains rounded and stationary (c); after any disturbance, however, it starts revealing a crescent-shape, and undergoes persistent movement (d) of around 90nm/s (e). (f) Chemotactic cell movement, gradient along the cell membrane is 3% over its cell length. (g–k) Internal distributions within the framed cell in (f). (g) Polarised distribution of Cdc42, with high concentrations (in white) in the front and low concentrations (black) in the back. Note the curvature in the internal gradient that causes the cell to turn. (h) Barbed end orientation, revealing that barbed ends are pointing towards membrane and (i) their density (red high, black low) is much higher in the front. (j) F-Actin orientation distribution; and (k) density distribution, showing that F-actin is distributed more homogeneously throughout the cell, predominantly oriented towards the direction of motion. Colouring of (h) and (j) represent local mean orientation, magnitude, and isotropy, with colour wheel coding depicting directions, e.g. red=East, green=NorthWest, and blue=SouthWest. See also simulations MovII.2.8c, MovII.2.8d, MovII.2.8f, MovII.2.8g.

in many systems, and which causes boundaries in bistable systems and excitable media to straighten out. Consequently, a small increase in Cdc42 activation at one flank of the cell not only inhibits the propagation of the Rho interface here, but also enhances the propagation at the opposite flank due to the global increase in inactive Rho. Together this causes an increase in curvature along the interface,

which, while being straightened out due the curvature effect, causes the polarity of the cell to rotate. If the cell were not moving, this would still be a relatively slow process, but within a moving cell the actin dynamics respond to the new situation (Fig.8h–k), leading to motion in the new direction, therewith actually increasing the curvature along the Cdc42-Rho interface again, and thus enhancing the turning process. Thus, the specific manner in which the cell is polarised and is moving sets up the cell's ability to efficiently integrate and 'communicate' external information along the whole membrane, generating rapid and directed responses with high sensitivity [29].

In the model, persistent cell motion and cell turning is completely self-generating: no other artificial "rules" beyond the molecular scheme have to be introduced. However, when studying persistency or chemotaxis we do not always want to describe the full biochemistry. Instead 'shortcuts' can be defined that are able to correctly grasp the essential features. These shortcuts will discussed in the next sections.

7.2. Persistency

Now that we can understand how polarity and persistent motion emerge from the lower levels of organisation within the cell, it is also interesting and useful to derive a shortcut to model persistency. Above we saw that cells typically form a front and a back, defining a direction of motion. This direction (polarity) can be described through a target direction of motion of a cell. We also saw that at the front cells more likely extend than retract, while the opposite is observed at the back. This can be implemented by changing Eq.(2) into

$$\Delta\mathcal{H} = \mathcal{H}_{after} - \mathcal{H}_{before} - \mu\cos(\alpha)\,, \tag{10}$$

where μ is the "directional propensity" of cells, and α is the angle between target direction and the considered displacement vector (the vector given by the coordinate of the position whose modification is considered and the mean position of the cell) (see Fig.9a and [3]).

We typically start by giving cells an initially random target direction. After a fixed number of MCS (here we use 10 MCS), the target direction is made equal to the displacement vector during the previous period. This gives rise to a self-adjusting and self-enhancing type of motility. To describe cell turning in a realistic way, i.e. to avoid abrupt directional changes, it is actually better to adjust the μ value according to its recent displacement: $\mu = \mu_{max}e^{-\rho(1-\cos\beta)}$, where μ_{max} is the maximum directional propensity cells can obtain, and β is the angle between the displacement and target vector of the previous period, while ρ determines how rapidly the directional propensity declines when a turn is occurring [3]. Fig.9b shows an individual cell moving within a 3D space. We observe a persistency in its motion on a timescale much longer than the target vector update. In a certain way, the sequential target vectors behave like a polymer, in which each next vector in most cases only shows a limited deviation from the previous vector, the deviations becoming smaller as μ becomes larger. At a sufficiently long timescale, however,

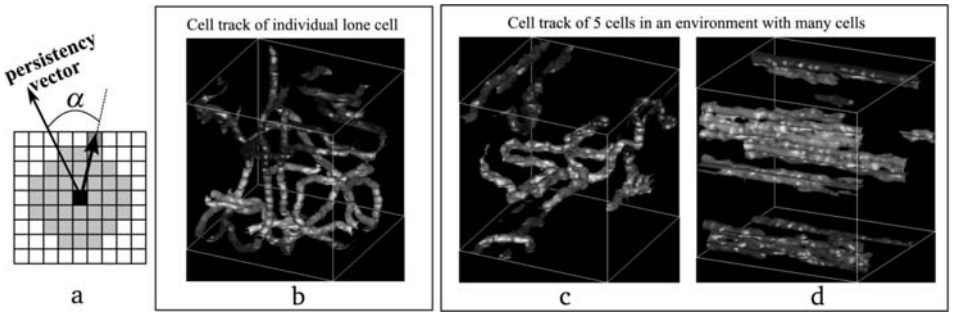

FIGURE 9. From persistency to coherence. (a) Implementation of persistent motion: persistency vector and dislocation vector form an angle α. A small angle makes it more likely to extend, but when the angle is larger than 90°, retraction is preferred. (b) Cell tracking of a single cell persistently moving within a 3D space. On a short timescale directed motion is observed, on a longer timescale random motion. Depicted is the motion during 15000 MCS. (c,d) Cell tracks of 5 cells within a densely packed population of 10000 cells. The cells rapidly organise into local streams, which slowly increase in scale until a globally coherent cell motion is reached. (c) Cell tracks during the initial 3000 MCS; (d) cell tracks after 10000 MCS. Note that the two simulations only differ in the number of simulated cells. See also simulations MovII.2.9b and MovII.2.9cd.

the cell motion becomes random: the build-up of small deviations causes the target direction to become uncorrelated with a target direction sufficiently long ago.

The dynamics change dramatically when a sufficiently high cell density is used (Fig.9c). Now the cells rapidly organise themselves into small streams. This is due to the fact that each cell takes up space, therewith excluding other cells from being too close. Cells 'on crash course' automatically correct their direction of motion due to the high energy penalty involved with the large deformations when trying to move trough one another. At the same time, cells which move in the same direction create space behind them for other cells to move into without being disturbed. Once local streams have been formed, the same process starts to take place at a larger scale, i.e. between streams. In the long run a global flow is formed, without there being any explicit coupling between cells of their direction of motion (c.f. Chapter II.1).

7.3. Chemotaxis

It is very uncommon that cells are moving without being guided by at least some kind of external cue. As stated earlier, chemotaxis is typically described using a term like Eq.(4). In this section we will show the strength of this shortcut by proving that the entanglement of chemotaxis and differential adhesion strongly determines the outcome of cell sorting, through the variations it creates in cell deformation [24]. Most importantly, due to chemotaxis sorting can become directional. Directional cell sorting is the process in which cells not only sort out, but

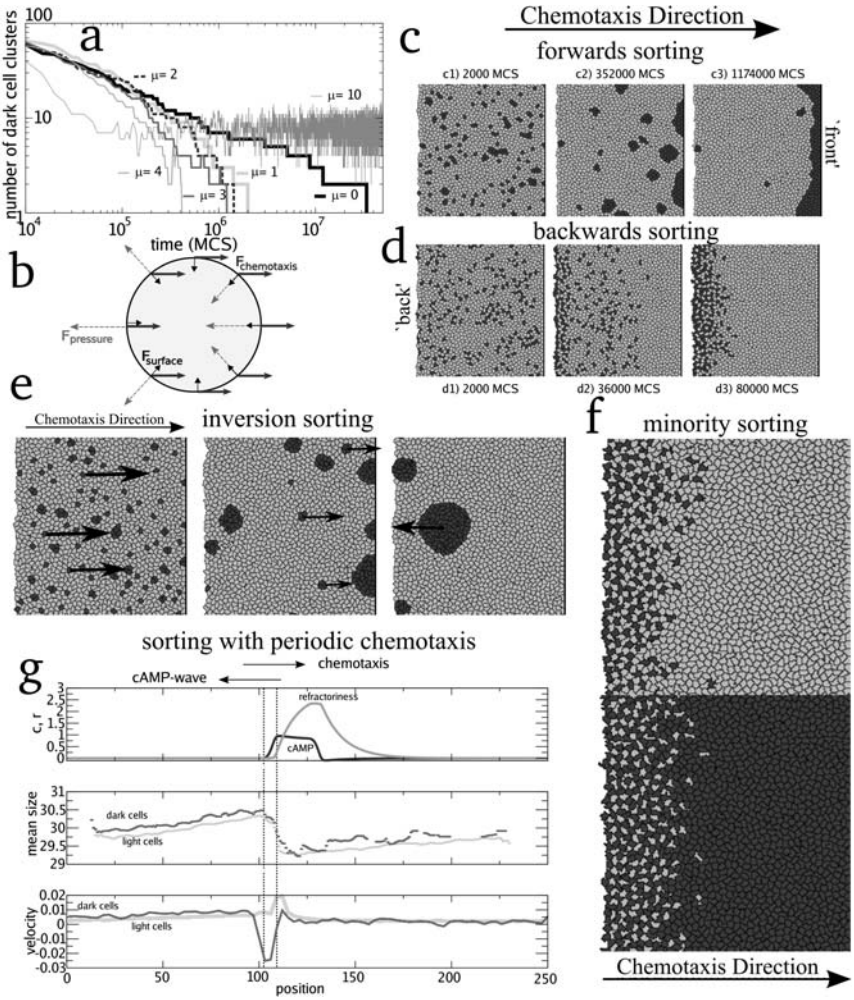

FIGURE 10. Interplay between chemotaxis and adhesion. (a) Rates of cell sorting for different chemotactic strengths; (b) illustration of forces acting upon different regions of a cell; sorting towards (c) and against (d) the direction of chemotaxis; (e) reversal of the direction of cell sorting due to the cell sorting itself; (f) minority sorting; (g) cell sorting due to a periodic chemoattractant wave. (Adapted from [24].) See also simulations MovII.2.10c, MovII.2.10d, MovII.2.10e, MovII.2.10f.

each cell type also ends up at a specific location or relative position. While this cannot be due to differential adhesion alone, it is readily observed once cells move chemotactically, even without variations in chemotactic strength.

Fig.10a shows the reduction in the number of cell clusters due to the fusion of small ones into larger ones, for a chemotactically moving cell mass. Without chemotaxis ($\mu = 0$), the decrease in the number of clusters over time slows down logarithmically (as is also shown in Fig.3b). Cell sorting, however, can be two orders of magnitude faster when the cells move chemotactically. One has to realise that chemotaxis is not equivalent to increasing the effective temperature of the simulation, i.e. increasing the level of fluctuations through other parameters, because the chemotactic term favours extensions in one direction while inhibiting them in the other, therewith not changing the ratio between attempted and accepted cell extensions. Thus, an effective change of T is not the explanation for the difference in timescale. Instead, the rapid sorting is caused by the fact that (clusters of) cells with different surface energies move at different speeds (even though the chemotactic response is equal for both cell types), therewith continuously causing medium-scale tissue rearrangements, which strongly reduce the collision time between clusters. This causes a dramatic speed up in cell sorting, and makes it scale linearly with tissue size, bringing sorting due to differential adhesion back into the realm of relevant biological timescales. The question now is what is causing this difference in speed, and how it depends on adhesion properties.

Surprisingly, the direction of cell sorting is fundamentally determined by whether a cell mass is confined or can move freely. Within a confined cell mass, the chemotactic motion of the cells gives rise to a volume gradient, effectively corresponding to a pressure gradient. Shortly after initiation of a simulation, the spatial derivative of the pressure (i.e. the slope in the volume times 2λ) counterbalances the chemotaxis, and motion stops. The claim that motion stops, however, is only partly true, because cells have a mesoscale structure, with a constant pressure within the whole cell. At the front of the cell (defined by the direction of chemotaxis), neighbouring cells are suffering larger pressure, while at the rear, the pressure is lower. Consequently, cells tend to extend at the rear and retract at the front, i.e. within the pressure gradient all cells tend to move backward. Moreover, the orientation of the forces differs as well: the chemotactic force is the same along the whole cell, and is always directed forward, while the force generated by the pressure differences varies strongly along the boundary of the cell, and is always directed perpendicular to the cell boundary (see Fig.10b). Consequently, all cells are squeezed by the high pressure of their neighbours at the front, and widened by the low pressure of their neighbours at the back, which gives cells an overall drop-like shape. If all cells are equal, the backwards squeezing leads to a small drop in the pressure gradient, until the backward motion is counterbalanced by the chemotaxis. That is, like Lewis Carroll's Red Queen [5], the cells have to move continuously to stay at the same space.

If cells differ in adhesion properties, however, the cells with a lower surface energy become more anisotropic. They are more flexible, due to the lower 'cost' of having non-optimal shapes (since non-optimal shapes have a higher perimeter/area ratio and thus higher surface energies), and are thus more efficiently squeezed

backward by the rounder, more rigid high-interface-energy cells. In short, the less deformable, the more strongly a cell moves forward (see Fig.10c).

One consequence is that even cell types with negative surface tension (thus forming a checkerboard pattern) can sort out, as long as one cell type is more deformable than the other (Fig.10d). This would be inconceivable by differential adhesion alone. Moreover, because the interaction energy is cell-type specific, and the neighbours of a cell change during sorting (see Fig.3a), the effective interaction energy (i.e. the total sum of interaction energies per cell) also changes. These alterations due to the sorting itself can even be so large as to invert the sorting direction (see Fig.10e), or can lead to minority sorting, when $J_{l,l} = J_{d,d} > J_{l,d}$, in which case each cell type will be squeezed backwards by the other as long as it is in the minority (see Fig.10f), so that one always ends up with a region in which both cell types are equally represented.

In contrast, when the cell mass is not confined, no pressure gradient forms. Consequently, no pushing backward takes place. The cell mass steadily moves forward, leaving as only variation to movement the degree of ease in which the forward dislocation occurs, letting more flexible cells move faster. Thus, the lack of a pressure gradient completely inverts the direction of cell sorting.

The story becomes more complicated when there is a periodic chemotactic signal (which, for example, is typical for chemoattractants produced through an excitable media, like the well-known cAMP waves in the cellular slime mould *Dictyostelium discoideum*). In *Dictyostelium*, the wave-like nature of the cAMP signal and refractoriness of the cells insures that there is only chemotactic activity during a short period of each cycle. This causes the creation of a more complicated pressure pattern (shown in Fig.10g). When the cells are active, their sudden strong chemotactic motion creates a steep pressure gradient opposite to the direction of motion, but also a pressure gradient outside the chemotactically active part, oriented in the same direction as the chemotaxis. Consequently, even before the arrival of the cAMP wave, cells are already pulled forward by the chemotactically moving cells in front of them, while after the wave has passed the cells keep on being pushed forward [42, 27]. This means that due to the generated pressure wave, the speed of the cells that don't move chemotactically, is still positive. The most flexible cells have the lowest speeds (or even move backward) during the cAMP wave, but otherwise have the fastest forward motion in between two cAMP waves, when the pressure gradient is inverted, because the most flexible cells respond most strongly to the pressure gradient. Because the pulse of the cAMP wave is very short compared to the period between the pulses, the non-chemotactic motion turns out to determine the end-result, and the most flexible cells sort to the front. (For a detailed analysis, see [24].)

It is clear that in this whole discussion, once again, the mesoscale structure of cells is of utmost importance. The CPM not only explicitly takes cell structure into account, but also resolves forces that are exerted on the cell on a subcellular scale, due to which it becomes apparent that forces act differently according to their location on the cell, causing cell deformation and eventually cell sorting.

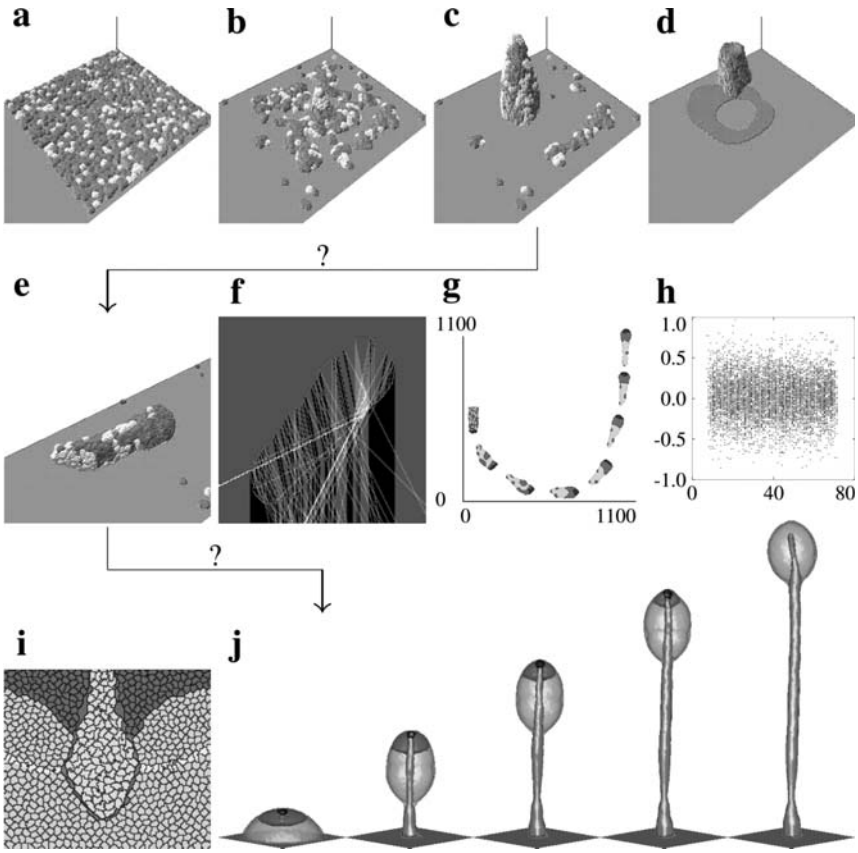

FIGURE 11. Modelling an organism. Overview of the different stages of *Dictyostelium discoideum* morphogenesis, as modelled using the CPM. (a) Aggregation; (b) stream formation; (c) mound formation; (d) cAMP waves; (e) crawling slug; (f) the lens-effect, leading to (g) phototaxis; (h) the slug can detect very noisy temperature gradients; (i) downward elongation of the stalk, akin to peristalsis, and essential for the (i) culmination. See also simulations MovII.2.11ae, MovII.2.11h, MovII.2.11j.

These insights can be used to develop an understanding of the life cycle of the cellular slime mould *Dictyostelium discoideum*, a morphogenetic process in which chemotaxis and differential adhesion form central ingredients.

7.4. Slime mould morphogenesis

Upon starvation, individual amoebae of *Dictyostelium discoideum* start to aggregate and form migrating multicellular slugs consisting of 10^4-10^6 cells. Early during development, the cells differentiate into two major cell types, prestalk and prespore cells, which sort out to the anterior, respectively posterior part of the slug.

The slug is able to sense cues from the external world, such as light, pH, and temperature gradients, and to adjust its behaviour in a coordinated way, such that it reaches the most suitable site for culmination. During culmination a fruiting body is formed consisting of a globule of spore cells on a slender stalk. In all phases of the morphogenesis, the motion of the cells is orchestrated by waves of cAMP, formed by a pulsatile cAMP excretion and a cAMP-mediated cAMP response, combined with chemotaxis towards cAMP. The cAMP waves are followed by a refractory period, in which cells are non-responsive to cAMP (neither cAMP production nor chemotaxis).

The emergence of multicellular organisms is regarded as one of the major transitions in evolution. *Dictyostelium* has shown itself to be a paradigm for the study of various aspects of multicellular development. It is a unique 'model' organism, because it presents us within 48 hours with a complete transition to multicellularity, which is inevitably attended by multicellular coordination and morphogenesis. At the same time, the organism does not have neurons or a global transport system, which means that all communication is essentially local, taking place on a (sub)cellular level. Because of these properties, *Dictyostelium* has excellently lent itself to be studied using the CPM, in order to unravel its morphogenesis. In fact, it has become the first organism of which the whole life cycle has been modelled [44].

Fig.11 shows the complete life cycle of *Dictyostelium*, as it has been modelled using the CPM. Savill & Hogeweg [42] analysed how individual amoebae can aggregate and organise themselves to ultimately form a crawling slug. cAMP waves, originating from autocycling prestalk (PstA) cells, and relayed by all other cell types, are driving periodic aggregating motions of the amoebae (Fig.11a). Due to their adhesiveness the cells rapidly organise into streams, a self-enhancing process, because cAMP waves move faster when cell density is higher, which then direct other amoebae into the streams (Fig.11b). Already in this early stage, an important entanglement between chemotaxis and adhesion can be observed within the streams, because due to the pressure waves that accompany the cAMP waves, the cells within a stream move faster. Said differently, they speed up because of 'pulling' and 'pushing'. And speeding up seems to be highly functional for a developmental process that only takes place during starvation. Due to the aggregation, a mound is formed, in which the PstA cells are pushed upwards, extending the structure until it topples over and forms a migrating slug (Fig.11c,e). The slug moves forward, driven by cAMP waves that originate from the autocycling PstA cells in the tip region, and propagate towards the rear to the slug (Fig.11d). The chemotactic motion of the cells behind the tip push the tip forward, and with it the source of the cAMP waves. That is, the slug crawls away [42]. Due to the entanglement between chemotaxis and differential adhesion, the prestalk cells sort out to the anterior part of the slug, while the prespore cells end up posteriorly ([42, 22, 30, 24], Fig.11g).

The whole slug presents an adequate tactic response to a thermal gradient, while individual amoebae can neither sense the gradient, nor show temperature-dependent differentiation in motion velocity. The behaviour is achieved by a modification of the cAMP waves: differences in temperature alter the excitability of the cell, and therewith the shape of the cAMP waves. Chemotaxis towards cAMP then causes the slug to turn. Furthermore, due to the fact that the wavefronts always keep a smooth shape (again, due to the well-known curvature-effect), the waves of excitation function as spatiotemporal noise-filters [30]. This spatiotemporal integration generates a very high sensitivity (even very small temperature gradients can be detected), as well as the ability to receive a signal in the presence of extreme noise (the signal-to-noise ratio can be 1/1500 ([26], Fig.11h). Interestingly, this integration of the information is possible without the information itself being locally available. The information is contained solely within the mesoscale patterns (i.e. the patterns formed by the cAMP waves), which span many cell lengths. The 'readout' by the cells takes place implicitly, due to the fact that the cells respond chemotactically to the cAMP waves, which, due to the steepness of the upstroke of the cAMP wave, is easily sensed by individual cells [30].

By extending the model with ammonia (NH_3) dynamics and light refraction, it could be shown that the phototactic response, which leads the slug to the soil surface, can also unfold from the interactions between the different modules [31]. Again the individual amoebae are unable to detect the signal (where does the light come from?), or to show an adequate response (move towards the light source). But because the slug refracts the light and has a rounded shape, the light is focused on the side opposite the light source (the 'lens-effect', Fig.11f). Production of NH_3 increases with light intensity, and the NH_3 decreases the excitability. Hence waves move more slowly on the side opposite to the light source, they become slanted, and chemotaxis towards the waves causes the slug to turn (Fig.11g).

When the slug enters culmination, a stalk primordium is formed at the border of the PstA region, which rapidly extends towards the base (in approximately 20 min). So called 'pathfinder' cells seem to guide the downward elongating stalk. The modelling work shows that the periodic upward movements, due to chemotactic motion towards cAMP, induce pressure waves, which are able to squeeze the stalk downwards through the cell mass [27, 28], akin to peristalsis (Fig.11i). These pressure waves again result from the combination of cAMP dynamics and (differential) adhesion, i.e. they are themselves observables generated by the model. Finally, a stable configuration is formed, a slender tapering stalk with the spore head on top (Fig.11j). The spores can be dispersed to initiate the next *Dictyostelium* life cycle. It completes the circle, although we should point out that there are still two main open questions, related to the initiation and termination of the slug phase.

Concluding remarks

Taken together, the CPM has proven to be a strong formalism to help unravel the multilevel entanglement, from the biophysics of deforming cells, through, for

example, the intricate pressure fields within tissues, to the complexity of morphogenesis itself. Most importantly, the insights continue to generate relevant questions which can be addressed experimentally, strengthening the feedback between the modelling and experimental approach.

By using the CPM to model an organism [44], we were able to show that morphogenesis in the full sense of the word can emerge from the interactions and feedbacks between a few simple modules, whose properties are in accordance with experimental findings, and which interact with each other only locally. It has given us an informative description of the *Dictyostelium* morphogenesis, from single cells all the way to the fruiting body. We have shown that in order to progress from (sub)cellular interactions towards a coordinated multicellular behaviour that is able to sense and respond to the environment in an appropriate way, the slime mould uses spatiotemporal patterns which are 'larger than life'. Such patterns are formed by interacting processes, and are used for feedback between different levels of organisation.

Thus, we "can compute an organism" [44]. But, quoting Segel, this is merely the "end of the beginning" [44]. An important next step in modelling developmental processes is to focus on the interplay between gene regulation and the dynamic properties of cells. Mechanisms of morphogenesis resulting from such an interplay were explored using an evolutionary approach [18, 17, 19]. Gene regulation networks were evolved which led to cell differentiation. Known morphogenetic mechanisms as meristematic growth and convergent extension appeared as side-effect of the interplay of the evolved networks and the dynamical properties of deformable cells as described by the CPM formalism. This study also uncovered intriguing evolutionary dynamics of morphogenesis, such as morphological 'reinventions', mosaic evolution and conservation of a 'zootype'. Interplay between processes at multiple space and timescales is one of the defining properties of biotic systems. The CPM formalism, by combining simplicity and extensibility, with a basically sound representation of a biological cell, provides a powerful basis for multilevel modelling of biological systems (see the accompanying DVD for simulations).

Acknowledgements

We would like to thank Rita de Almeida, Joost Beltman, Mauro Castro, Leah Edelstein-Keshet, François Graner, Jos Käfer, and Ramiro Magno for helpful discussions and collaboration.

References

[1] V. C. Abraham, V. Krishnamurthi, D. L. Taylor, and F. Lanni. The actin-based nanomachine at the leading edge of migrating cells. *Biophys. J.*, 77(3):1721–1732, 1999.

[2] P. B. Armstrong and R. Niederman. Reversal of tissue position after cell sorting. *Dev. Biol.*, 28(3):518–527, 1972.

[3] J. B. Beltman, A. F. M. Marée, J. N. Lynch, M. J. Miller, and R. J. De Boer. Lymph node topology dictates T cell migration behavior. *J. Exp. Biol.*, in press, 2007.

[4] J. Carr and R. L. Pego. Metastable patterns in solutions of $u_t = \varepsilon^2 u_{xx} - f(u)$. *Comm. Pure Appl. Math.*, 42(5):523–576, 1989.

[5] L. Carroll. *Through the Looking Glass*. Macmillan, London, 1872.

[6] M. A. Castro, F. Klamt, V. A. Grieneisen, I. Grivicich, and J. C. Moreira. Gompertzian growth pattern correlated with phenotypic organization of colon carcinoma, malignant glioma and non-small cell lung carcinoma cell lines. *Cell Prolif.*, 36(2):65–73, 2003.

[7] C. S. Chen, M. Mrksich, S. Huang, G. M. Whitesides, and D. E. Ingber. Geometric control of cell life and death. *Science*, 276(5317):1425–1428, 1997.

[8] L. P. Cramer, T. J. Mitchison, and J. A. Theriot. Actin-dependent motile forces and cell motility. *Curr. Opin. Cell Biol.*, 6(1):82–86, 1994.

[9] S. Etienne-Manneville. Cdc42 – the centre of polarity. *J. Cell Sci.*, 117(Pt 8):1291–1300, 2004.

[10] E. Farge. Mechanical induction of Twist in the *D*rosophila foregut/stomodeal primordium. *Curr. Biol.*, 13(16):1365–1377, 2003.

[11] J. Folkman and A. Moscona. Role of cell shape in growth control. *Nature*, 273(5661):345–349, 1978.

[12] J. A. Glazier and F. Graner. Simulation of the differential adhesion driven rearrangement of biological cells. *Phys. Rev. E*, 47(3):2128–2154, 1993.

[13] F. Graner. Can surface adhesion drive cell-rearrangement? Part I: biological cell-sorting. *J. theor. Biol.*, 164:455–476, 1993.

[14] V. A. Grieneisen. Estudo do estabelecimento de configurações em estruturas celulares. Master's thesis, Universidade Federal do Rio Grande do Sul, Porto Alegre, 2004.

[15] F. Guilak, G. R. Erickson, and H. P. Ting-Beall. The effects of osmotic stress on the viscoelastic and physical properties of articular chondrocytes. *Biophys. J.*, 82(2):720–727, 2002.

[16] C. Herring. Some theorems on the free energies of crystal surfaces. *Phys. Rev.*, 82:87–93, 1951.

[17] P. Hogeweg. Evolving mechanisms of morphogenesis: on the interplay between differential adhesion and cell differentiation. *J. theor. Biol.*, 203(4):317–333, 2000.

[18] P. Hogeweg. Shapes in the shadow: evolutionary dynamics of morphogenesis. *Artif. Life*, 6(1):85–101, 2000.

[19] P. Hogeweg. Computing an organism: on the interface between informatic and dynamic processes. *BioSystems*, 64(1-3):97–109, 2002.

[20] S. Huang and D. E. Ingber. The structural and mechanical complexity of cell-growth control. *Nat. Cell Biol.*, 1(5):E131–E138, 1999.

[21] M. Iwamoto, K. Sugino, R. D. Allen, and Y. Naitoh. Cell volume control in *Paramecium*: factors that activate the control mechanisms. *J. Exp. Biol.*, 208(Pt 3):523–537, 2005.

[22] Y. Jiang, H. Levine, and J. Glazier. Possible cooperation of differential adhesion and chemotaxis in mound formation of *Dictyostelium*. *Biophys. J.*, 75(6):2615–2625, 1998.

[23] A. Jilkine, A. F. M. Marée, and L. Edelstein-Keshet. Mathematical model for spatial segregation of the Rho-family GTPases based on inhibitory crosstalk. *Bull. Math. Biol.*, in press, 2007.

[24] J. Käfer, P. Hogeweg, and A. F. M. Marée. Moving forward moving backward: directional sorting of chemotactic cells due to size and adhesion differences. *PLoS Comput. Biol.*, 2(6):e56, 2006.

[25] V. M. Laurent, S. Kasas, A. Yersin, T. E. Schäffer, S. Catsicas, G. Dietler, A. B. Verkhovsky, and J.-J. Meister. Gradient of rigidity in the lamellipodia of migrating cells revealed by atomic force microscopy. *Biophys. J.*, 89(1):667–675, 2005.

[26] A. F. M. Marée. *From Pattern Formation to Morphogenesis: Multicellular Coordination in* Dictyostelium discoideum. PhD thesis, Utrecht University, 2000.

[27] A. F. M. Marée and P. Hogeweg. How amoeboids self-organize into a fruiting body: multicellular coordination in *Dictyostelium discoideum*. *Proc. Natl. Acad. Sci. U.S.A.*, 98(7):3879–3883, 2001.

[28] A. F. M. Marée and P. Hogeweg. Modelling *Dictyostelium discoideum* morphogenesis: the culmination. *Bull. Math. Biol.*, 64(2):327–353, 2002.

[29] A. F. M. Marée, A. Jilkine, A. Dawes, V. A. Grieneisen, and L. Edelstein-Keshet. Polarization and movement of keratocytes: a multiscale modelling approach. *Bull. Math. Biol.*, 68(5):1169–1211, 2006.

[30] A. F. M. Marée, A. V. Panfilov, and P. Hogeweg. Migration and thermotaxis of *Dictyostelium discoideum* slugs, a model study. *J. theor. Biol.*, 199:297–309, 1999.

[31] A. F. M. Marée, A. V. Panfilov, and P. Hogeweg. Phototaxis during the slug stage of *Dictyostelium discoideum*: a model study. *Proc. R. Soc. Lond. Ser. B*, 266:1351–1360, 1999.

[32] R. Meili and R. A. Firtel. Two poles and a compass. *Cell*, 114(2):153–156, 2003.

[33] N. Metropolis, A. E. Rosenbluth, M. N. Rosenbluth, A. H. Teller, and E. Teller. Equation of state calculations by fast computing machines. *J. Chem. Phys.*, 21:1087–1092, 1953.

[34] A. Mogilner and L. Edelstein-Keshet. Regulation of actin dynamics in rapidly moving cells: a quantitative analysis. *Biophys. J.*, 83(3):1237–1258, 2002.

[35] A. Mogilner and G. Oster. Cell motility driven by actin polymerization. *Biophys. J.*, 71(6):3030–3045, 1996.

[36] J. C. M. Mombach, J. A. Glazier, R. C. Raphael, and M. Zajac. Quantitative comparison between differential adhesion models and cell sorting in the presence and absence of fluctuations. *Phys. Rev. Lett.*, 75(11):2244–2247, 1995.

[37] N. B. Ouchi, J. A. Glazier, J.-P. Rieu, A. Upadhyaya, and Y. Sawada. Improving the realism of the cellular Potts model in simulations of biological cells. *Physica A*, 329(3-4):451–458, 2003.

[38] R. A. Ream, J. A. Theriot, and G. N. Somero. Influences of thermal acclimation and acute temperature change on the motility of epithelial wound-healing cells (keratocytes) of tropical, temperate and Antarctic fish. *J. Exp. Biol.*, 206(Pt 24):4539–4551, 2003.

[39] C. Rottman and M. Wortis. Exact equilibrium crystal shapes at nonzero temperature in two dimensions. *Phys. Rev. B*, 24:6274–6277, 1981.

[40] B. Rubinstein, K. Jacobson, and A. Mogilner. Multiscale two-dimensional modeling of a motile simple-shaped cell. *SIAM Multiscale Model. Simul.*, 3(2):413–439, 2005.

[41] E. Ruoslahti. Stretching is good for a cell. *Science*, 276(5317):1345–1346, 1997.

[42] N. J. Savill and P. Hogeweg. Modelling morphogenesis: From single cells to crawling slugs. *J. theor. Biol.*, 184(3):229–235, 1997.

[43] I. C. Scott and D. Y. R. Stainier. Developmental biology: twisting the body into shape. *Nature*, 425(6957):461–463, 2003.

[44] L. A. Segel. Computing an organism. *Proc. Natl. Acad. Sci. U.S.A.*, 98(7):3639–3640, 2001.

[45] M. S. Steinberg. Reconstruction of tissues by dissociated cells: some morphogenetic tissue movements and the sorting out of embryonic cells may have a common explanation. *Science*, 141:401–408, 1963.

[46] M. S. Steinberg. Adhesion-guided multicellular assembly: a commentary upon the postulates, real and imagined, of the differential adhesion hypothesis, with special attention to computer simulations of cell sorting. *J. theor. Biol.*, 55(2):431–443, 1975.

[47] T. M. Svitkina and G. G. Borisy. Arp2/3 complex and actin depolymerizing factor/cofilin in dendritic organization and treadmilling of actin filament array in lamellipodia. *J. Cell Biol.*, 145(5):1009–1026, 1999.

[48] W. A. Thomas, J. Thomson, J. L. Magnani, and M. S. Steinberg. Two distinct adhesion mechanisms in embryonic neural retina cells. III. Functional specificity. *Dev. Biol.*, 81(2):379–385, 1981.

[49] W. R. Trickey, F. P. T. Baaijens, T. A. Laursen, L. G. Alexopoulos, and F. Guilak. Determination of the Poisson's ratio of the cell: recovery properties of chondrocytes after release from complete micropipette aspiration. *J. Biomech.*, 39(1):78–87, 2006.

[50] A. B. Verkhovsky, T. M. Svitkina, and G. G. Borisy. Self-polarization and directional motility of cytoplasm. *Curr. Biol.*, 9(1):11–20, 1999.

[51] G. Wulff. Zur Frage des Geschwindigkeit des Wachstums und der Auflösung der Krystallflächen. *Z. Kristallogr. Mineral.*, 34:449–531, 1901.

Athanasius F. M. Marée
Theoretical Biology and Bioinformatics, Utrecht University
Padualaan 8, 3584 CH Utrecht, the Netherlands
e-mail: A.F.M.Maree@uu.nl

Verônica A. Grieneisen
Theoretical Biology and Bioinformatics, Utrecht University
Padualaan 8, 3584 CH Utrecht, the Netherlands
e-mail: V.Grieneisen@uu.nl

Paulien Hogeweg
Theoretical Biology and Bioinformatics, Utrecht University
Padualaan 8, 3584 CH Utrecht, the Netherlands
e-mail: P.Hogeweg@uu.nl

Single-Cell-Based Models in Biology and Medicine
ed. by A.R.A. Anderson, M.A.J. Chaplain, K.A. Rejniak
Mathematics and Biosciences in Interaction, 137–150

II.3 The Cellular Potts Model in Biomedicine

Nicholas J. Savill and Roeland M. H. Merks

Abstract. In this chapter we describe how the the Cellular Potts Model (CPM) has been applied to problems in the biomedical field. Examples are given in epidermal biology, cancer and vasculogenesis. They demonstrate the strength of the CPM and its rich set of extensions, in elucidating biomedically important phenomena.

1. Epidermal stem cells

Keratinocytes are the principal cell type of interfollicular epidermis. They are shed at the skin surface and replaced by division in the basal layer. There are three main types of keratinocytes in the basal layer: stem cells, transit–amplifying cells and postmitotic cells [5, 6, 8]. Stem cells reside in discrete clusters of about 20–40 cells [15, 17]. Given an appropriate signal, stem cells on the periphery of clusters differentiate into transit–amplifying cells [21] which divide for another 3–5 generations before becoming postmitotic and committed to terminal differentiation [1, 2, 14] and migration from the basal layer [15]. A possible differentiation signal comes from the Delta–Notch cell–cell signalling pathway [21, 22, 32]. By overexpressing Delta in keratinocytes three important effects were discovered [21]. First, a cell expressing high levels of Delta induces differentiation in its neighbouring cells. Second, a cell expressing high levels of Delta is deaf to the differentiation signal. Finally, stem cell clones overexpressing Delta form more compact clusters than wildtype clones, control clones and transit–amplifying cell clones overexpressing Delta. It was also found that mouse keratinocyte differentiation is induced by high Notch activation [32].

Savill and Sherratt [37] took this structural and biochemical description and posed two questions about the dynamical stability of clusters: what general rules cause stable cluster size and shape, and what is the mechanism that allows clusters to autonomously regulate their size? The CPM is the ideal formalism to address these questions.

The model incorporated the three keratinocyte cell types with differentiation from stem to transit–amplifying cells triggered by an appropriate signal (see below). Transit–amplifying cells divided for three generations before becoming postmitotic. The authors showed that regulation of differentiation is the most likely

mechanism for dynamically controlled cluster size and shape. Moreover, only stem cells on the periphery of the clusters must differentiate, and stem cells must adhere more strongly to each than they do to other cell types. A stable cluster is shown in Fig.1a, and simulation MovII.3.1a; differentiation of all stem cells on the periphery of the cluster occurs when the cluster reaches a predetermined size. If interior stem cells differentiate, or if stem cells adhere equally to all cell types, or if size is controlled by regulating division rate, then clusters fragment and growth is uncontrolled (Fig.1b and simulations MovII.3.1bi–MovII.3.1biii from the accompanying DVD).

The work then went on to examine how a cluster could autonomously control its size. They postulated that the Delta–Notch pathway in its lateral induction, positive feedback mode could be such a mechanism. An ODE system of equations was used to model the localised interaction of Delta on the surface of one cell

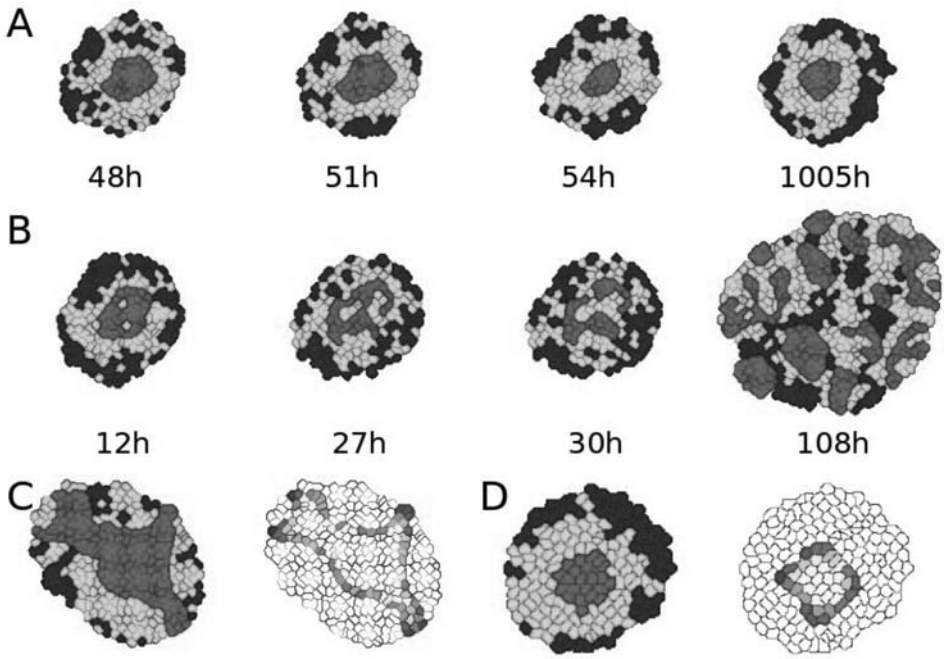

FIGURE 1. (A) A stable stem cell cluster. Red: stem cells, green: transit-amplifying cells, blue: postmitotic cells, time in hours. (B) An unstable cluster due to interior stem cells differentiating. (C) Differentiation of peripheral stem cells when the Notch expression passes a given threshold causes fingering. Right–hand plot: Red to white corresponds to low to high Notch expression. Differentiated cells do not express Delta so are coloured white. (D) An additional global signal, which causes stem cells with low Delta expression to differentiate, causes stability. Reprinted from [37], with permission from Elsevier.

with Notch on the surface of other cells. The fate of a cell was based on the total Delta and Notch expression summed over its surface. This model causes Delta and Notch expression to increase as the stem cell cluster increase in size. Peripheral stem cells have lower expression levels because part of their surface contacts differentiated cells that do not express Delta. The model showed that if only local positional information is used to determine differentiation, then clusters form fingers and grow without bound (Fig.1c and simulation MovII.3.1c). A global signalling mechanism was therefore suggested; when the Notch concentration of any cell in the cluster passes some threshold it signals to all stem cells in the cluster to differentiate. Only those with a low enough Delta expression (i.e., those on the periphery) were allowed to differentiate consistent with experimental evidence. This mechanism allows for stable clusters (Fig.1d and simulation MovII.3.1d).

2. Tumour growth and invasion

Many solid cancers begin with the abnormal but benign growth of cells. Many changes at the cellular level must occur before a benign tumour becomes life–threatening, or malignant. These changes include the detachment of abnormal cells from the primary tumour and their migration to distant sites within the body, called metastasis. Because detachment and invasion occurs at the cellular level it is beneficial to study the processes that govern individual cellular behaviour in order to understand how tumours evolve. The CPM is an obvious candidate formalism.

Stott *et al.* [39] were the first to use the CPM to model benign avascular tumour growth. Their model included equations describing the concentration gradient of diffusable nutrients. Tumour cell growth rate depended on nutrient concentration. The 3D model described remarkably well the dynamical spherical structure of benign avascular tumours.

A more detailed multiscale model of avascular tumour growth was developed by Jiang and coworkers [16]. At the subcellular level a Boolean network was used to model a protein expression regulatory network for control of cell–cycle arrest. At the cellular level the CPM was used to model proliferation, adhesion and viability. At the extracellular level reaction diffusion equations were used to model production, diffusion and consumption of nutrients, metabolites and growth promoters and inhibitors. The model was qualitatively and quantitatively compared to multicellular tumour spheroids cultured in suspension. It described extremely well avascular tumour growth rates, cell–cycle fraction and size of the viable rim for different oxygen and glucose medium concentrations. Fitting of the model gave estimates for diffusion coefficients of $10^{-6}\mathrm{cm}^2\mathrm{h}^{-1}$ for growth promoters and $10^{-7}\mathrm{cm}^2\mathrm{h}^{-1}$ for growth inhibitors. The model also suggested that cell–cycle arrest is caused by the induction of G1–phase regulatory proteins rather than restrictions on volumetric expansion.

The transition from benign to malignant tumours was first looked at by Turner and Sherratt [40]. Their model included secretion of proteolytic enzymes by malignant cells that caused dissolution of an extracellular matrix (ECM). Haptotaxis of malignant cells up ECM gradients could then occur. The authors examined the role of cell–cell and cell–ECM adhesion, proteolytic secretion, haptotaxis and cell proliferation on the ability of malignant cells to invade healthy tissue.

Fig.2 shows an example of the invasion of malignant cells. ECM dissolution by malignant cells on the boundary of the tumour causes a gradient in the ECM.

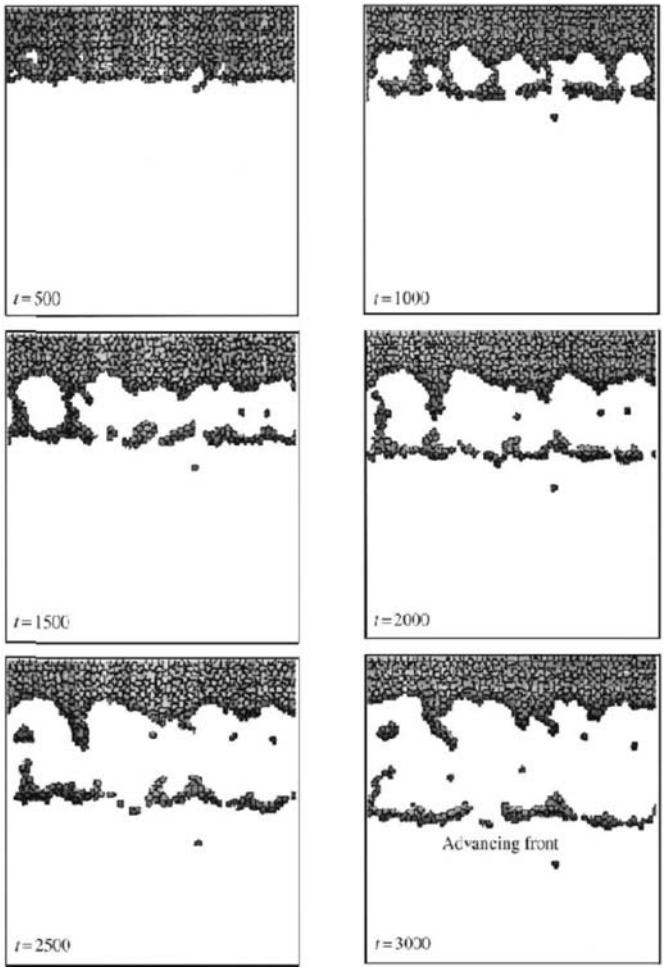

FIGURE 2. Development of an advancing front of cells. Cells at the front secrete proteolytic enzymes that degrade the ECM (not shown) and haptotaxis up the ECM gradient ensues. Reprinted from [40], with permission from Elsevier.

These cells then migrate up the gradient away from the main mass of the tumour. Fingering occurs ($t = 1,000$) leading to the formation of an invading front of cells anchored to the main cell mass. If the motive force caused by hapotaxis is stronger than the adhesive force caused by cell–cell adhesion the front breaks off from the main cell mass ($t = 2,500$). The authors showed that cell–ECM rather than cell–cell adhesion was a more important determinant of invasiveness, and that proteolytic enzyme secretion, in synergy with haptotaxis, promotes invasion. They also showed that cell proliferation inhibited invasion because it creates thicker and hence stronger anchors between the main cell mass and the invasion front.

In an extension to this model, Turner *et al.* [41] studied the effect of tamoxifen–stimulated upregulation of TGFβ secretion. This is known to inhibit mitosis and promote apoptosis, haptotactic sensitivity of malignant cells to ECM gradients and fibroblast secretion of ECM. Their main conclusion was that TGFβ can have a dual effect depending on the haptotactic sensitivity. Weak sensitivity and the tumour will remain benign. High sensitivity and the tumour, though smaller in size, will be more invasive.

Invasion of malignant cells into healthy tissue was also examined by Knewitz and Mombach [19]. This model was able to show that a sufficient condition for invasion is that malignant cells are more adhesive to healthy cells than they are to themselves. In other words, that the surface tension of the malignant cell mass is negative.

3. Blood vessel growth: angiogenesis and vasculogenesis

Another recent application of the Cellular Potts model aims to explain aspects of blood vessel formation from self–organization principles. Blood vessels form *de novo* during embryonic development when dispersed *endothelial cells* (*ECs*: the cells lining the inner walls of fully–formed blood vessels) organize into a vascular network (*vasculogenesis*), or form later during development and in adult life by sprouting or splitting of existing blood vessels (*angiogenesis*). Previous models of blood vessel formation focused on tissue–level phenomena, describing densities of endothelial cells rather than the behaviours of individual cells [3, 10, 23, 30, 31, 38] or describing growing blood vessels as branching networks of pipes whose elements were tubular lengths of vessel [4, 24]. Merks, Glazier, and others explicitly modelled the behaviour of individual endothelial cells using a cell–based modeling philosophy [25, 27, 28]. Their model reproduced aspects of both *de novo* and sprouting blood vessel growth, but did not reproduce all details of experiments. They used their model to identify the essential cell behaviours, by identifying which phenomenology their model reproduced and where it failed.

Initially, Merks *et al.* [25] captured the mechanisms of *in vitro* blood vessel growth as in human umbilical–vein endothelial–cell (*HUVEC*) cultures. This widely used experimental assay cultures endothelial cells obtained from umbilical cords in Matrigel, a commercial product which mimics the environment in which

blood vessels normally grow. The growth factors in the Matrigel stimulate initially randomly distributed cells to elongate and interconnect to form an fine network, which progressively coarsens. The cells do not penetrate into the Matrigel, forming instead a quasi–two–dimensional vascular–like pattern. HUVEC culture closely resembles quasi–two–dimensional blood vessel growth in the yolk sacs of avian and mammalian embryos.

Variants of their model also reproduced aspects of angiogenesis. Sprouting angiogenesis roughly involves the following steps. First the *basement membrane* (a tough wall of connective tissue surrounding most blood vessels) degrades enzymatically. Then endothelial cells migrate through it, proliferate and assemble, forming an initial sprout. Finally, a new basement membrane forms as the vessels mature. Merks *et al.* [28] asked if endothelial cell behaviour is sufficient for forming sprouts, or whether a remote chemoattractant source is prerequisite.

Following the general outline for modeling of developmental phenomena (see Chapter II.1), they started by identifying a small set of experimentally confirmed endothelial–cell behaviours, and tried one by one to see if these could explain formation of vascular networks. Endothelial cells:

a. secrete a morphogen [13] which slowly degrades,
b. preferentially extend protrusions (*filopodia*) up morphogen gradients, causing cell movement up those gradients [11],
c. rapidly elongate after contact with the extracellular matrix (*ECM*) [9] through internal remodeling of the actin cytoskeleton [29], and
d. modify their response to the chemoattractant vascular–endothelial growth–factor A (VEGF–A) if they are in contact with each other through the adhesion receptor vascular–endothelial–cadherin (*VE–cadherin*) [12].

The models by Merks, Glazier and others are based on a series of continuum model by Gamba, Serini and coworkers [3, 10, 38]. These models derive from the astrophysical *Burger's* equations of gravitational aggregation, and assume that endothelial cells secrete a chemoattractant, which diffuses and decays in the extracellular matrix (cell behaviours a. and b. in the list above). The equations are given by

$$\begin{aligned} \frac{\partial n}{\partial t} + \nabla \cdot (n\vec{v}) &= 0, \\ \frac{\partial \vec{v}}{\partial t} + \vec{v} \cdot \nabla \vec{v} &= \mu \nabla c, \\ \frac{\partial c}{\partial t} &= D\nabla^2 c + \alpha n - \tau^{-1} c, \end{aligned} \tag{1}$$

where n is the density of endothelial cells, $\vec{v}$ the velocity field, and c the chemoattractant concentration. According to this model, endothelial cells would accelerate in chemoattractant gradients. In the highly viscous environment which cells experience, however, endothelial cells have no inertia. Instead, they move as long as they exert or experience a force and stop when it is removed. Thus, cell inertia seems biologically implausible, although Ambrosi *et al.* [3] argue that it can represent endothelial cells' persistence of motility. Studies in other organisms and cell types

show that cells, while they do exhibit persistence, do not accelerate in response to chemoattractant gradients, primarily because their maximum velocity is limited [33, 42]. We therefore modify the Gamba and Serini equations to set the cell velocity rather than the cell acceleration to be proportional to the chemoattractant gradient. Further, the model assumes that (as Gerhardt *et al.* [11] observed) the response of the cell to the chemoattractant is local along the membrane rather than occurring at the cell center.

The Cellular Potts models aimed to reproduce experiments on quasi–two–dimensional vascular patterns, which form in yolk sacs and in *in vitro* experiments. Therefore the authors could employ a two–dimensional model of the endothelial cells. Working in two dimensions greatly simplified the modeling because the cells move on top of the ECM rather than through it and extracellular signals diffuse through the underlying ECM rather than through the complex and moving volume around cells in three dimensions. Releasing hundreds of such Cellular Potts endothelial cells into an "*in silico* Petri dish," they studied how cell–level phenomenology drove morphology and dynamics at the tissue scale.

3.1. Chemotactic Cell Aggregation

The initial Cellular Potts model of vasculogenesis implemented the basic assumption of the Gamba and Serini model [10, 38]: ECs migrate towards a chemoattract they themselves secrete (behaviours a. and b.). In a hybrid CPM–PDE model, the PDE layer described the diffusion and secretion of the chemoattractant in a uniform substrate underlying the cells, i.e.,

$$\frac{\partial c}{\partial t} = \alpha \ \delta_{\sigma_{\vec{x}},0} - (1 - \delta_{\sigma_{\vec{x}},0})\epsilon \ c + D\nabla^2 c, \tag{2}$$

where $\delta_{\sigma_{\vec{x}},0} = 1$ inside the cells. $\alpha = 10^{-3}$ s^{-1} is the rate at which cells release chemoattractant, $\epsilon = \alpha$ is the decay rate of the chemoattractant, and $D = 10^{-13}$ m^{2}s^{-1}. Every site within the CPM cells secreted the chemoattractant, which was degraded by the ECM. On every Monte–Carlo step the PDE evolved for about 30 s simulated time to make the cells move at approximately natural velocities. For these settings the pattern developed at a rate corresponding to experiments [25]. The Savill and Hogeweg [36] algorithm (See Eq.(30) in Chapter II.1) simulated the preferential extension of filopodia in the direction of chemoattractant gradients [11], which drives chemotaxis. A chemotactic strength $\mu = 500$ allowed for sufficient chemotactic migration. In the initial simulations the cells did not adhere to one another without chemotaxis ($J_{cc} = 2J_{cM}$).

Fig.3a and simulation MovII.3.3a show that chemotactic aggregation without cell adhesion was insufficient for growth of vascular networks. Starting from a random configuration, the endothelial cells organized into a number of round cellular clusters. Intuitively we can understand this patterning as follows: initially higher cell densities will create local "bumps" of chemoattractant which isotropically attract the surrounding cells. For reasons explained below, in this simulation the length constraint (Eq.(6) Chapter II.4) keeps cell shapes round, but the results hold for unconstrained cells. Indeed, this result resembles the famous Keller–Segel

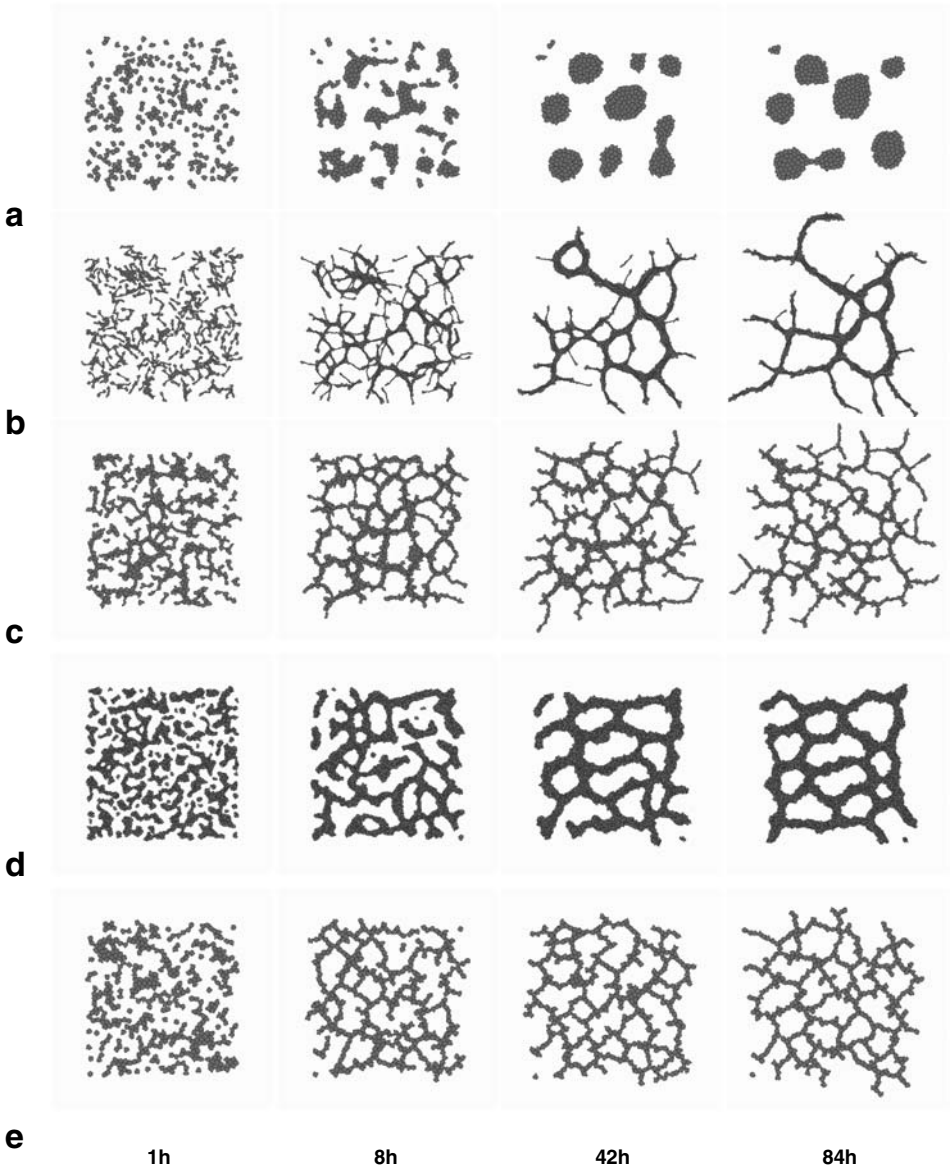

FIGURE 3. Hypothetical mechanisms of *de novo* vascular development. (a) Rounded cells aggregate into a vascular network. (b) Autonomously elongating virtual cells organize into a vascular network with coarsening dynamics corresponding to *in vitro* observations. (c) Short, steep gradients cause the cells–with unconstrained shaped–to elongate and organize into vascular networks. (d) Strong adhesivity also causes the cells to elongate. (e) Contact–inhibition of motility drives a cell–shape–independent mechanism of vasculogenesis. Reprinted from [26], with permission from IOP Publishing Ltd.

equations of chemotactic aggregation [18]. Apparently, chemoattractant secretion and chemotaxis alone are insufficient for vascular patterning.

Merks, Glazier and coworkers then went on and asked which additional endothelial phenomenology might be required for vasculogenesis, and identified four possible mechanisms. These mechanisms fall into two broad categories: those which cell shape change drives, and those which contact–inhibition of chemotaxis drives. The two categories seem to produce different patterning instability mechanisms. The contact inhibition mechanism also produces a patterning instability reminiscent of sprouting angiogenesis.

3.1.1. Cell Shape Changes. Endothelial cells dramatically change shape during angiogenesis and vasculogenesis. Are these shape changes coincidental, or are they important to the ECs' self–organization into vascular networks?

Merks *et al.* [25] explored this question by introducing a length constraint (Eq.(6) Chapter II.4) to mimic cell elongation due to internal, cytoskeleton remodeling (see Chapter II.1). Fig.3b and simulation MovII.3.3b show the aggregation of virtual ECs elongated to approximately 50 lattice sites ($100\mu m$). Elongated ECs rapidly organize into a fine–grained network with vascular cords enclosing lacunae. With time the pattern remodels: small lacunae collapse and large lacunae grow larger. Interestingly, the authors found that the dynamics of this process closely parallels pattern remodelling in endothelial–cell cultures [25].

Alternative mechanisms can also explain the organization of endothelial cells into network patterns. Fig.3c and simulation MovII.3.3c show a simulation where the chemoattractant diffuses more slowly than in the previous simulation, resulting in short, steep gradients. The gradients "trap" the virtual ECs, which elongate as a result. These passively elongated cells also organize into networks. Strong intercellular adhesion can also result in cell elongation necessary for vascular network formation, as in Fig.3d and simulation MovII.3.3d [27]. Merks *et al.* [25] found that these two mechanisms depend on the cells' passively elongated shape: when they forced the cells to be round (using the length constraint to keep the longest axis equal to the mean diameter) the cells organized into round, disconnected clusters similar to those in Fig.3. Also, because these cell behaviours cannot reproduce the coarsening behaviour as observed in cell culture experiments, passive cell elongation mechanisms (Fig.3c–d) probably do not correctly capture the biological mechanism, while active cell elongation (Fig.3b) seems a more likely candidate mechanism.

Elongated cells do not random walk like round cells. Instead they move more easily along their long axis than along their short axis [25]. Consequently, elongated cells migrating along a curved chemotactic gradient must reorient before moving again at full speed. This orientational variation in motility gives elongated cells' motion a longer persistence length than for rounded cells, and might explain why previous work [10, 38] needed cell inertia for vascular patterning. Persistence of motion and alignment of endothelial cells results in elongated cell clusters which may interconnect and form a percolating vascular network.

3.1.2. Contact–Inhibition of Motility. In addition to the mechanism described above, Merks *et al.* [28] identified a second class of mechanisms independent of cell shape. Blood vessel growth requires the cell–adhesion molecule VE–cadherin [12], which clusters at endothelial cell interfaces and modulates vascular–endothelial growth–factor–A's (*VEGF–A*) effect on ECs; VEGF–A is a potent growth–factor, which stimulates blood vessel sprouting. In the presence of VE–cadherin binding, VEGF–A inhibits EC motility and proliferation. In the absence of VE–cadherin binding, VEGF–A activates pathways related to actin polymerization and the cell cycle, triggering cell motility and proliferation in sub–confluent monolayers [20, 7]. Thus, Merks *et al.* [28] hypothesized that VE–cadherin binding at cell–cell interfaces represses the formation of chemotactic surface projections (filopodia), while they form normally at unbound parts of the cell surface.

Preventing chemotaxis at cell–cell interfaces modelled such contact–inhibition of motility. The authors modified Eq.(30) from Chapter II.1, setting $\mu = 0$ at cell–cell interfaces and $\mu = 500$ at cell–substrate interfaces (see Eq.(31) in Chapter II.1, where $\mu(\sigma_{\text{substrate}}) = 0$ and $\mu(\sigma_{\text{cell}}) = 500$). This mechanism drives vascular patterning even when a length constraint keeps the cells round (Fig.3e and simulation MovII.3.3e). Although this contact–inhibition poorly reproduced the pattern coarsening in HUVEC cultures, it suggested explanations for other experimental observations. Mice genetically modified to lack VE–cadherin proteins have severe vascular defects in the yolk sac [12], forming disconnected vascular islands instead of networks. The model by Merks *et al.* [28] reproduces this observation; simulations where chemotaxis is no longer inhibited at cell–cell interfaces (as in Fig.3a) also form vascular islands. Also the pattern in this model is dynamically maintained: new small lacunae disappear, while larger lacunae subdivide through sprouting); this phenomenon resembles experimental observations *in vivo* [35].

3.1.3. Angiogenesis. Interestingly, the "sprouting" observed in the vascular networks a contact–inhibition mechanism produces, also occurs in cell aggregates with a mechanism reminiscent of sprouting angiogenesis. Angiogenesis is the biological mechanism by which new blood vessel sprout from existing vessels. In Fig.4 and simulations MovII.3.4a and MovII.3.4b, we initiate our simulation with a mass of endothelial cells, keeping all other parameters the same. After an initial "roughening," the blob's surface digitates into a structure reminiscent of a vascular network (Fig.4), the first structure to develop both in *de novo* and in sprouting blood vessel growth [34]. Thus these simulations suggest that sprouting and *de novo* blood vessel growth might be two manifestations of a single process at the level of ECs.

The authors explain the instability mechanism as follows. At equillibrium, the chemoattractant has a Gaussian–like profile, which levels off towards the cluster's center. Thus, without contact–inhibition of chemotaxis all cells, also those in the cluster's interior, try to move towards the center, compressing interior cells (Fig.4) that resist displacement. Contact–inhibition of chemotaxis leaves the interior cells insensitive to the chemoattractant, which are easily pushed aside by ingressing

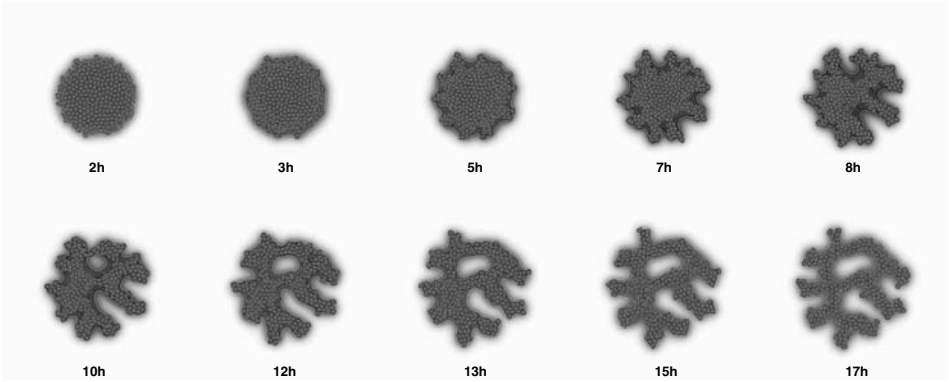

FIGURE 4. Sprouting instability in a simulation initiated with a clump of virtual endothelial cells experiencing contact inhibition. Reprinted from [26], with permission from IOP Publishing Ltd.

surface cells. Hence we may consider the cluster as a contracting shell undergoing a buckling–type instability.

4. Conclusions

In this section we have discussed the use of the Cellular Potts model in a range of biomedically relevant problems. Section 1 showed how the CPM in combination with sets of differential equations describing the cells' responses to extracellular signals, provides insight into robust patterning mechanisms in growing human tissues. Section 2 on tumour invasion demonstrated applications that made use of the CPM's straightforward representation of cell adhesion and cell migration. By screening a large range of parameters, these authors provided useful insights into the balance between haptotactic invasion, extracellular matrix degration and cell–cell adhesion; the outcome of this balance determines if a tumour will become malign or stay benign. Section 3 on vasculogenesis shows the use of the Cellular Potts model in "reverse engineering" a minimal set of experimentally confirmed cell behaviours that reproduces a biological mechanism. In so doing, we can compare a range of scenarios and compare their outcomes with experimental observations.

References

[1] J. C. Adams and F. M. Watt. Fibronectin inhibits the terminal differentiation of human keratinocytes. *Nature*, 340:307–309, 1989.

[2] J. C. Adams and F. M. Watt. Changes in keratinocyte adhesion during terminal differentiation - reduction in fibronectin binding precedes α-5-β-1-integrin loss from the cell-surface. *Cell*, 63:425–435, 1990.

[3] D. Ambrosi, A. Gamba, and G. Serini. Cell directional persistence and chemotaxis in vascular morphogenesis. *B. Math. Biol.*, 66:1851–1873, 2004.

[4] A. R. A. Anderson and M. A. J. Chaplain. Continuous and discrete mathematical models of tumor-induced angiogenesis. *B. Math. Biol.*, 60:857–899, 1998.

[5] Y. Barrandon and H. Green. Cell size as a determinant of the clone forming ability of human keratinocytes. *PNAS*, 82:5390–5394, 1985.

[6] Y. Barrandon and H. Green. Three clonal types of keratinocytes with different capacities for multiplication. *PNAS*, 84:2302–2306, 1987.

[7] E. Dejana. Endothelial cell-cell junctions: Happy together. *Nat. Rev. Mol. Cell Bio.*, 5:261–270, 2004.

[8] R. Dover and C. S. Potten. Cell cycle kinetics of cultured human epidermal keratinocytes. *J. Invest. Dermatol.*, 80:423–429, 1983.

[9] J. F. Dye, L. Lawrence, C. Linge, L. Leach, J. A. Firth, and P. Clark. Distinct patterns of microvascular endothelial cell morphology are determined by extracellular matrix composition. *Endothelium*, 11:151–167, 2004.

[10] A. Gamba, D. Ambrosi, A. Coniglio, A. De Candia, S. Di Talia, E. Giraudo, G. Serini, L. Preziosi, and F. Bussolino. Percolation morphogenesis and burgers dynamics in blood vessels formation. *Phys. Rev. Lett.*, 90:118101, 2003.

[11] H. Gerhardt, M. Golding, M. Fruttiger, C. Ruhrberg, A. Lundkvist, A. Abramsson, M. Jeltsch, C. Mitchell, K. Alitalo, D. Shima, and C. Betsholtz. VEGF guides angiogenic sprouting utilizing endothelial tip cell filopodia. *J. Cell Biol.*, 161:1163–1177, 2003.

[12] S. Gory-Fauré, M.-H Prandini, H. Pointu, V. Roullot, I. Pignot-Paintrand, M. Vernet, and P. Huber. Role of vascular endothelial-cadherin in vascular morphogenesis. *Development*, 126:2093–2102, 1999.

[13] G. Helmlinger, M. Endo, N. Ferrara, L. Hlatky, and R. K. Jain. Growth factors - formation of endothelial cell networks. *Nature*, 405:139–141, 2000.

[14] N. A. Hotchin, A. Gandarillas, and F. M. Watt. Regulation of cell-surface β-1 integrin levels during keratinocyte terminal differentiation. *J. Cell Biol.*, 128:1209–1219, 1995.

[15] U. B. Jensen, S. Lowell, and F. M. Watt. The spatial relationship between stem cells and their progeny in the basal layer of human epidermis: a new view based on whole–mount labelling and lineage analysis. *Development*, 126:2409–2418, 1999.

[16] Y. Jiang, J. A. Pjesivac-Grbovic, C. Cantrell, and J.P. Freyer. A multiscale model for avascular tumour growth. *Biophys. J.*, 89:3884–3894, 2005.

[17] P. H. Jones, S. Harper, and F. M. Watt. Stem cell patterning and fate in human epidermis. *Cell*, 80:83–93, 1995.

[18] E. F. Keller and L. A. Segel. Initiation of slime mold aggregation viewed as an instability. *J. Theor. Biol.*, 26:399–415, 1970.

[19] M. A. Knewitz and J. C. M. Mombach. Computer simulation of the influence of cellular adhesion on the morphology of the interface between tissues of proliferating and quiescent cells. *Comp. Biol. Med.*, 36:59–69, 2006.

[20] L. Lamalice, F. Houle, G. Jourdan, and J. Huot. Phosphorylation of tyrosine 1214 on VEGFR2 is required for VEGF-induced activation of Cdc42 upstream of SAPK2/p38. *Oncogene*, 23:434–445, 2004.

[21] S. Lowell, P. Jones, I. Le Roux, J. Dunne, and F. M. Watt. Stimulation of human epidermal differentiation by Delta-Notch signalling at the boundaries of stem-cell clusters. *Curr. biol.*, 10:491–500, 2000.

[22] S. Lowell and F. M. Watt. Delta regulates keratinocyte spreading and motility independently of differentiation. *Mech. Dev.*, 107:133–140, 2001.

[23] D. Manoussaki, S. R. Lubkin, R. B. Vernon, and J. D. Murray. A mechanical model for the formation of vascular networks in vitro. *Acta Biotheor.*, 44:271–282, 1996.

[24] S. R. McDougall, A. R. A. Anderson, M. A. J. Chaplain, and J. A. Sherratt. Mathematical modelling of flow through vascular networks: implications for tumour-induced angiogenesis and chemotherapy strategies. *B. Math. Biol.*, 64:673–702, 2002.

[25] R. M. H. Merks, S. V. Brodsky, M. S. Goligorksy, S. A. Newman, and J. A. Glazier. Cell elongation is key to in silico replication of in vitro vasculogenesis and subsequent remodeling. *Dev. Biol.*, 289(1):44–54, 2006.

[26] R. M. H. Merks and J. A. Glazier. Dynamic mechanisms of blood vessel growth. *Nonlinearity*, 19:C1–C10, 2006.

[27] R. M. H. Merks, S. A. Newman, and J. A. Glazier. Cell-oriented modeling of *in vitro* capillary development. In Peter M.A. Sloot, Bastien Chopard, and Alfons G. Hoekstra, editors, *Cellular Automata. 6th international conference on Cellular Automata for Research and Industry*, volume 3305 of *Lect. Notes Comput. Sc.*, pages 425–434, Berlin, 2004. Spinger Verlag.

[28] R. M. H. Merks, Erica D. Perryn, and James A. Glazier. Contact-inhibited chemotactic motility: Role in de novo and sprouting blood vessel growth. arXiv:q-bio.TO/0505033, 2005.

[29] T. M. Moore, G. H. Brough, P. Babal, J. J. Kelly, M. Li, and T. Stevens. Store-operated calcium entry promotes shape change in pulmonary endothelial cells expressing Trp1. *Am. J. Physiol.*, 275:L574–L582, 1998.

[30] J. D. Murray, D. Manoussaki, S. R. Lubkin, and R. B. Vernon. A mechanical theory of in vitro vascular network formation. In C. D. Little, V. Mironov, and E. Helene Sage, editors, *Vascular morphogenesis: in vivo, in vitro, in mente*, pages 173–188. Birkhauser, Boston, MA, 1998.

[31] P. Namy, J. Ohayon, and P. Tracqui. Critical conditions for pattern formation and in vitro tubulogenesis driven by cellular traction fields. *J. Theor. Biol.*, 227:103–120, 2004.

[32] A. Rangarajan, C. Talora, R. Okuyama, M. Nicolas, C. Mammucari, H. Oh, J. C. Aster, S. Krishna, D. Metzger, P. Chambon, L. Miele, M. Aguet, F. Radtke, and G. P. Dotto. Notch signalling is a direct determinant of keratinocyte growth arrest and entry into differentiation. *EMBO J.*, 20:3427–3436, 2001.

[33] J. P. Rieu, A. Upadhyaya, J. A. Glazier, N. B. Ouchi, and Y. Sawada. Diffusion and deformations of single hydra cells in cellular aggregates. *Biophys. J.*, 79:1903–1914, 2000.

[34] W. Riseau. Mechanisms of angiogenesis. *Nature*, 386:671–674, 1997.

[35] P. A. Rupp, A. Czirók, and C. D. Little. $\alpha v\beta 3$ integrin-dependent endothelial cell dynamics in vivo. *Development*, 131:2887–2897, 2004.

[36] N. J. Savill and P. Hogeweg. Modelling morphogenesis: from single cells to crawling slugs. *J. Theor. Biol.*, 184:229–235, 1997.

[37] N. J. Savill and J. A. Sherratt. Control of epidermal stem cell clusters by Notch-mediated lateral induction. *Dev. Biol.*, 258:141–153, 2003.

[38] G. Serini, D. Ambrosi, E. Giraudo, A. Gamba, L. Preziosi, and F. Bussolino. Modeling the early stages of vascular network assembly. *EMBO J.*, 22:1771–1779, 2003.

[39] E. L. Stott, N. F. Britton, J. A. Glazier, and M. Zajac. Stochastic simulation of benign avascular tumour growth using the Potts model. *Math. Comp. Model.*, 30:183–198, 1999.

[40] S. Turner and J. A. Sherratt. Intercellular adhesion and cancer invasion: A discrete simulation using the extended Potts model. *J. theor. Biol.*, 216:85–100, 2002.

[41] S. Turner, J. A. Sherratt, and D. Cameron. Tamoxifen treatment failure in cancer and the nonlinear dynamics of TGFβ. *J. Theor. Biol.*, 229:101–111, 2004.

[42] G. M. Walker, J. Sai, A. Richmond, M. Stremler, C. Y. Chung, and J. P. Wikswo. Effects of flow and diffusion on chemotaxis studies in a microfabricated gradient generator. *Lab Chip*, 5:611–618, 2005.

Nicholas J. Savill
Centre for Infectious Disease, University of Edinburgh, Ashworth Laboratories
Kings Buildings, West Mains Road, Edinburgh, EH9 3JF, Scotland
e-mail: `nick.savill@ed.ac.uk`

Roeland M. H. Merks
Department of Plant Systems Biology,
VIB Technologiepark 927, B-9052 Ghent, Belgium, and
Department of Molecular Genetics, Ghent University, Ghent, Belgium
e-mail: `roeland.merks@psb.ugent.be` or `post@roelandmerks.nl`

Single-Cell-Based Models in Biology and Medicine
ed. by A.R.A. Anderson, M.A.J. Chaplain, K.A. Rejniak
Mathematics and Biosciences in Interaction, 151–167

II. 4 The Glazier–Graner–Hogeweg Model: Extensions, Future Directions, and Opportunities for Further Study

Ariel Balter, Roeland M. H. Merks, Nikodem J. Popławski, Maciej Swat and James A. Glazier

Abstract. One of the reasons for the enormous success of the Glazier–Graner–HogewegGlazier–Graner–Hogeweg Model (*GGH*) model is that it is a framework for model building rather than a specific biological model. Thus new ideas constantly emerge for ways to extend it to describe new biological (and non-biological) phenomena. The GGH model automatically integrates extensions with the whole body of prior GGH work, a flexibility which makes it unusually simple and rewarding to work with. In this chapter we discuss some possible future directions to extend GGH modeling. We discuss *off-lattice* extensions to the GGH model, which can treat fluids and solids, new classes of model objects, approaches to increasing computational efficiency, parallelization, and new model-development platforms that will accelerate our ability to generate successful models. We also discuss a non-GGH, but GGH-inspired, model of plant development by Merks and collaborators, which uses the Hamiltonian and Monte-Carlo approaches of the GGH but solves them using Finite Element (*FE*) methods.

1. Off-Lattice Extensions to the GGH Model

While the use of a fixed lattice makes GGH computations very simple compared to FE methods, we have seen that this simplicity comes with certain costs (see chapter II.1, section 6). The inclusion of the *g*eneralized cell as an independent entity in the GGH allows the definition of *i*nternal cell states tied to the cell rather than the lattice. These internal cell states allows us to specify interactions that are calculated either partially or entirely *off-lattice*, *i.e.* they are not tied to the grid structure of the cell lattice or any external field lattices (as in section 1.2.2). The advantage of this addition is that it may overcome potential negative effects of lattice discretization without abandoning the speed and simplicity of a lattice-based formalism. The main costs of moving off lattice are increased memory usage and slower computation.

The original CPM included simple off-lattice concepts such as cell volumes and surface areas, but these quantities still had a granularity of one lattice site. An example of a strictly off-lattice quantity is a cell's *center of mass*:

$$c\vec{m}(\sigma) = v^{-1}(\sigma) \sum_{\vec{i}\ni\sigma'(\vec{i})=\sigma} \vec{i}, \tag{1}$$

where $v(\sigma)$ is the volume of cell σ and $\vec{i}$ is a lattice site vector. We can form new off-lattice entities from existing ones. For example, by tracking a cell's center of mass from one time step to the next, we can estimate its *velocity*:

$$v\vec{e}l(\sigma,t) = \frac{c\vec{m}(\sigma,t) - c\vec{m}(\sigma,t-\Delta t)}{\Delta t}. \tag{2}$$

Many of the current and imminent extensions of the GGH model employ off-lattice extensions. We will discuss several such extensions: implementation of inertia, viscous fluid flow and advective diffusion, cell shape and polarity control and rigid body motion. This use of off-lattice extensions to the GGH is completely different from a switch to entirely *lattice-free methods*, which omit the underlying lattice entirely in favor of FE-implementations of a GGH-like Hamiltonians. We will show one such implementation to illustrate this fundamental difference.

1.1. Persistent Cell Movement—Inertial Constraints

Normal motion in the GGH model is Aristotelian. Velocity is proportional to applied force, with no inertia. While this dynamics is often appropriate in a biological context, we also encounter situations in which motion is inertial, *e.g.*, in fluid flow or the motion of large objects, or persistent, *e.g.*, in cell migration (because cells take time to reorganize their internal machinery to change their direction of motion) [24]. Somewhat surprisingly, we can model both inertia and cytoskeletal persistence time by adding to our Hamiltonian an *inertial term* of form:

$$\mathcal{H}_{\text{inertia}}(\Delta t) = \sum_{\sigma} \lambda_{\text{inertia}}(\sigma) ||v\vec{e}l(\sigma,t) - v\vec{e}l(\sigma,t-\Delta t)||^2, \tag{3}$$

where $v\vec{e}l(\sigma,t)$ is the instantaneous center-of-mass velocity of cell σ and λ_{inertia} controls the persistence time. Typically, Δt is one or more MCS. If $\lambda_{\text{inertia}} = 0$, objects undergo uncorrelated Brownian motion. If λ_{inertia} is large, motion is ballistic. We are only beginning to explore the possibilities that an inertial term presents in GGH modeling and its relation to more traditional Newtonian formulations of inertia. It is worth noting that cell orientation (chapter II.2, section 7.2) and cell elongation [18] induce persistent cell motion.

1.2. Fluid Dynamics

Surprisingly, given that the GGH model does not have a concept of a solid object, it also lacks two features key to real fluids, viscous dissipation due to shear and advection of chemical fields (which are normally tied to an auxiliary lattice in GGH simulations – see chapter II.1, section 7.3). Off-lattice extensions allow us to recover both of these important behaviors.

1.2.1. Viscous flow. We can introduce viscosity in a fluid using a *relative velocity constraint* between generalized cells. For an incompressible fluid, we add to the Hamiltonian a viscous term [5]:

$$\mathcal{H}_{\text{visc}} = \lambda_{\text{visc}} \sum_{(\sigma,\sigma') \text{ neighbors}} S(\sigma,\sigma') \frac{(vel_x(\sigma) - vel_x(\sigma'))^2}{||\vec{cm}(\sigma) - \vec{cm}(\sigma')||^2}$$
$$\times \sqrt{\frac{(cm_y(\sigma) - cm_y(\sigma'))^2 + (cm_z(\sigma) - cm_z(\sigma'))^2}{||\vec{cm}(\sigma) - \vec{cm}(\sigma')||^2}}$$
$$+ \text{ cyclic permutation of } (x, y, z), \tag{4}$$

where $||\,||$ is the Euclidean norm, subscripts indicate directional components, and $S(\sigma,\sigma')$ is the common contact area between cells σ and σ'. The parameter λ_{visc} corresponds to the Navier–Stokes viscosity η. The GGH model, with $\mathcal{H}_{\text{visc}}$ added to the Hamiltonian, successfully reproduces Poiseuille flow and, with the advection diffusion of section 1.2.2, it reproduces Taylor–Aris dispersion [5]. No one has yet tried to combine inertial, Eq.(3) and viscous terms to solve the full Navier–Stokes equations using the GGH method. Such a fluid solver would probably be inefficient, especially at high Reynolds numbers, but it would be extremely convenient, and would allow modeling of situations like blood flow and biofilm growth in a flowing fluid, where inertia and transport are crucial. This method may also work for complex fluids, *e.g.*, in blood rheology.

1.2.2. Advective diffusion. One problem with recording the concentration of chemicals in external lattices is that they do not respond to flow occurring in the cell lattice. Moving biological cells or fluid particles should carry with them, or *advect* chemical fields. In the GGH model, chemicals remain fixed to the external lattice. Dan *et al.* implemented advection by allowing diffusion directly between generalized cells, fluid particles, or subcells, which carry all diffusing chemicals [5], abandoning external lattices and lattice diffusion solvers. Diffusion uses the forward-Euler method (chapter II.1, section 7.3.2), but between neighboring cells rather than lattice sites. If we like, we can weight by the inverse distance between centers of mass of neighboring cells, or by contact areas between neighboring cells. As with normal lattice diffusion (see chapter II.1, section 7.3.2), we can include spatially-varying diffusion constants, secretion and decay rates and reaction terms. One disadvantage of this method is that it coarsens our description of chemical fields so that we only resolve concentrations at the scale of individual cells.

1.3. Cell Polarity

Cells are often highly asymmetric, with their cytoskeleton primarily determining and maintaining the asymmetry. Cells in epithelial sheets have distinct apical, lateral and basal surfaces, and migrating cells have a leading and trailing surface. The basal–apical or trailing-surface–leading-surface vector usually defines a primary cell orientation, or *polarity*, but additional orientations may also be important. *E.g.*, in-plane polarization (via the planar polarity path) helps epithelial cells to form long-range patterns in response to external signals. In addition, cells

like neurons can have extremely complex structures. Since the cells of the basic GGH model are isotropic, representing even the simplest aspects of cell polarity and shape requires extensions. The off-lattice extensions needed to give structure to cells also permit the creation of movable elastic solids and visco-elastic materials with well-defined behaviors, both classes of material lacking in the basic GGH model.

1.3.1. Cell orientation. To track cell polarity, we can assign each cell an *orientation vector* as an internal state. Making all cell properties, *e.g.*, chemotaxis and adhesion, depend on this orientation is then straightforward. However, determining how the orientation vector should evolve is not obvious. Cell elongation (see section 1.3.2) creates polarized cells in which the orientation passively follows the cell geometry.

The simplest way to describe highly complex cell shapes and variations in properties within the cell is to use compartmental cells (section 1.3.3). Different compartments can respond to external stimuli (contact with certain cell types, presence of external fields, *etc.*) differently, causing them to orient in their surroundings. However, compartmentalization is computationally expensive. The optimal strategy will depend on the phenomena being modeled, and all methodologies require further study. One current off-lattice method associates an orientation vector with each cell (chapter II.2, section 7.2).

1.3.2. Inertia-tensor cell-shape constraints. Zajac used a constraint on the eigenvalues of cells' 2nd moment tensor, or *inertia tensor*, to control cell shape in a model of convergent extension [28]. Later, Merks used it to control cell elongation in a vasculogenesis model [20]. Define $I(\sigma)$, the inertia tensor of cell σ:

$$I_{\alpha\beta} = \sum_{\vec{i}\ni\sigma'(\vec{i})=\sigma} \left(i_\alpha i_\beta \delta(\alpha,\beta) - \frac{1}{v_\mathrm{t}(\sigma)} \sum_{\vec{j}\ni\sigma'(\vec{j})=\sigma} i_\alpha j_\beta \right), \tag{5}$$

where α and β denote directional indices.

The inertia tensor translates any object into an equivalent ellipsoid. Let $I_1 > I_2\,[> I_3]$ be the eigenvalues of I. If cells are roughly ellipsoidal, the eigenvalues of the inertia tensor give the ratios of the lengths of their principal axes. Scaling these ratios by the volume of the cell gives us the lengths. We can now constrain cells to maintain a given length or shape. For instance, in 2D, we could impose a length constraint [20]:

$$\mathcal{H}_\mathrm{l} = \sum_\sigma \lambda_\mathrm{l} \left(l(\sigma) - L_\mathrm{t}(\sigma) \right)^2, \tag{6}$$

where $l(\sigma)$ is the length along the long axis of the cell σ and $L_\mathrm{t}(\sigma)$ the target length. Alternatively, we could constrain the aspect ratio, $r = I_1/I_2$, where I_1 and I_2 are the principle axes:

$$\mathcal{H}_\mathrm{r} = \sum_\sigma \lambda_\mathrm{r} \left(r(\sigma) - R_\mathrm{t}(\sigma) \right)^2, \tag{7}$$

where R_t is the target ratio.

To prevent cells from splitting because of the shape constraint, Merks *et al.* introduced an approximate *local connectivity constraint* in 2D that penalizes cells

which become multiply-connected during an index-copy attempt [20]. To check whether an index copy into site $\vec{i}$ changes local connectivity, they counted how many neighbors $\vec{j}_n$ of site $\vec{i}$ have the same index as $\vec{i}$, while the next lattice site clockwise around $\vec{i}$ has an index different from that of $\vec{i}$. If the quantity:

$$\sum_n \delta(\sigma(\vec{i}),\sigma(\vec{j}_n))(2-\delta(\sigma(\vec{i}),\sigma(\vec{j}_{n+1}))-\delta(\sigma(\vec{i}),\sigma(\vec{j}_{n-1}))) > 2 \tag{8}$$

(with the sum running in cyclic order), and the local neighborhood contains more than two non-medium cells, changing the index at the site destroys the local connectivity. They then made cell fragmentation energetically costly by assigning a large energy penalty to updates that change local connectivity. No similar local rule has been developed in three dimensions (*3D*). Such an algorithm would be extremely useful. Inertia-tensor description of cell elongation can also be used to measure elastic strain and control mitotic rate in tumor growth (chapter II.2, section 4.2).

1.3.3. Compartmental cells. For his *myxobacteria* simulations, Andreas Deutsch modeled elongated bacteria that are able to bend, but not too much [1, 27]. He subdivided individual bacteria into strings of subcellular domains, where $m(\sigma)$ is the number of subcells in cell σ. He then defined contact energies between subdomains within a cell to give the cell a particular geometry. *E.g.*, high contact energy between the front and rear subcells prevents a bacterium from forming a loop.

To control side-to-side undulations, Deutsch introduced a *bending energy* from polymer physics. The elastic bending energy of a rod is proportional to its mean-squared curvature. In Deutsch's simulations, every three subcells define a local curvature. If we define $c\vec{m}(\sigma,\mu)$ to be the center of mass of the μ^{th} subdomain of cell σ, then the *local radius of curvature* is:

$$\begin{aligned} R_{\text{curve}}(\sigma,\mu) = {} & ||c\vec{m}(\sigma,\mu+1)-c\vec{m}(\sigma,\mu-1)|| \times [||c\vec{m}(\sigma,\mu+1)-c\vec{m}(\sigma,\mu)||^2 \\ & +||c\vec{m}(\sigma,\mu)-c\vec{m}(\sigma,\mu-1)||^2 - ||c\vec{m}(\sigma,\mu+1)-c\vec{m}(\sigma,\mu-1)||^2]^{-1}. \end{aligned} \tag{9}$$

Since the *mean curvature* $\kappa = \frac{1}{R_{\text{curve}}}$, and for a rod, $\mathcal{H}_{\text{bend}} = \int \lambda_{\text{bend}}(l)\kappa^2 dl$, where λ_{bend} is the *bending modulus* of the rod, the equivalent *bending energy* in the GGH model is:

$$\mathcal{H}_{\text{bend}} = \sum_\sigma \sum_{\mu=1}^{m(\sigma)-2} \lambda_{\text{bend}}(\sigma,\mu) R^{-2}_{\text{curve}}(\sigma,\mu). \tag{10}$$

Thus, the term resists bending of the bacterium.

Another approach to limiting bending is to constrain the angles between the centers of mass of the subcells:

$$\mathcal{H}_{\text{angle}} = \sum_\sigma \sum_{\mu=2}^{m(\sigma)-1} \lambda_{\text{angle}}(\sigma,\mu)(\Theta(\sigma,\mu,\mu-1)-\Theta_{\text{t}}(\sigma,\mu,\mu-1))^2, \tag{11}$$

where $\Theta(\sigma,\mu,\mu-1)$ is the angle between $c\vec{m}(\sigma,\mu)$ and $c\vec{m}(\sigma,\mu-1)$. This constraint places rotational springs at the joints between the lines connecting the subcells' centers of mass. Deutsch maintained the overall length of the cell by treating the

lines connecting the centers of mass as springs with an equilibrium length $L_{\mathrm{t}}(\sigma,\mu)$ and a spring constant $\lambda_{\mathrm{compression}}$:

$$\mathcal{H}_{\mathrm{compression}} = \sum_{\sigma} \sum_{\mu=1}^{\mu(\sigma)-1} \lambda_{\mathrm{compression}}(\sigma,\mu)(||c\vec{m}(\sigma,\mu) - c\vec{m}(\sigma,\mu-1)|| - L_{\mathrm{t}}(\sigma,\mu))^2. \quad (12)$$

1.4. Elastic Solids

All cell-based materials in the classical GGH model are intrinsically visco-elastic. The model has no elastic solids. We can implement elastic and plastic solids using a simple algorithm similar to that in Eq.(12). Take any object σ and divide it into $m(\sigma)$ subcells μ, where each subcell contacts at least two other subcells of σ and the triangulation defined by the connections between the centers of mass $(c\vec{m}(\sigma,\mu))$ of neighboring subcells is topologically rigid. Then:

$$\mathcal{H}_{\mathrm{elastic}} = \sum_{\sigma} \sum_{\mu,\nu=1\ (\mu,\nu\ \mathrm{neighbors})}^{m(\sigma)} \lambda_{\mathrm{rigid}}(\sigma,\mu,\nu)(||c\vec{m}(\sigma,\mu) - c\vec{m}(\sigma,\nu)|| - L_{\mathrm{t}}(\sigma,\mu,\nu))^2, \quad (13)$$

where $L_{\mathrm{t}}(\sigma,\mu,\nu)$ is the target length of the link between subcells μ and ν inside cell σ, and λ_{rigid} is the *Young's modulus* of the material, which defines the total stress energy of σ. If we define neighborhood by distance between centers of mass rather than adjacency, then the resulting cell is visco-elasto-plastic. For instance, we could include only contacting subcells, or all subcells within a cutoff distance. Once two subcells separate further than the cutoff, they no longer interact elastically, allowing slow, plastic creep.

1.5. A Lattice-Free, Finite Element, GGH-Inspired Model of Plant Development

To illustrate the difference between the off-lattice extensions of the GGH, which we have been discussing, and lattice-free methods, we present a FE model developed by Merks and collaborators, which uses a GGH-inspired Hamiltonian but makes all of its computations using a FE mesh.

Most developmental phenomena simulated with the GGH model are examples of *plastic* morphogenesis. Since the constituent cells swarm, mix, sort, or aggregate, the resulting tissues behave as living "clays" in which biological form and pattern arise primarily through cell motility. In plants and some animal tissues (*e*.g., in *Drosophila* epithelia, see [8]) the relative positions of the cells are effectively fixed, and only cell division changes tissue shape. Plant cells cannot migrate and, with very few exceptions, do not slide past each other. Consequently, plant morphogenesis depends on patterned cell division and cell expansion, instead of cell migration and tissue folding. This mode of development is often called *symplastic growth* [6, 23].

Although GGH modeling of symplastic development is possible, it requires computationally-expensive topology constraints or finely-tuned adhesion energies to suppress cell motility and surface fluctuations, precisely the phenomena that make the GGH model suitable for simulating animal development. Instead, Merks

and collaborators developed a FE, lattice-free, GGH-inspired model that explicitly excludes plastic cell movement.

As we discussed in chapter II.1, section 2.1, the energy-minimization philosophy of the GGH model does not require lattice-based Monte-Carlo solution methods. Instead, we use two-dimensional (*2D*) lattice-free, polygonal finite elements to represent cell walls in a tissue [21, 25]. However, we retain a Monte-Carlo-based energy minimization dynamics that allows straightforward modeling of cell behaviors, including expansion, division, and active shape change. We allow cell walls to move according to rules derived from the classic equations for cell expansion [16]:

1. The intracellular turgor pressure exerts a uniform force on cell walls, attempting to enlarge cells.
2. The elastic cell walls counteract the turgor pressures.
3. Walls expand irreversibly if stretched over a threshold, via *cell-wall yielding*.

As in GGH-models, we define a target area A_t at which the cell's turgor pressure balances the ambient pressure, and a target length L_t for each wall element. We denote the *actual* cell area, a, and wall-element length, l. We can then describe the balance between turgor pressure and cell wall resistance in terms of a *generalized energy* or *Hamiltonian*:

$$\mathcal{H} = \sum_i (a(i) - A_\mathrm{t}(i))^2 + \sum_j (l(j) - L_\mathrm{t}(j))^2, \tag{14}$$

where indices i and j sum over all cells and polygon edges, respectively. We can add additional terms to the Hamiltonian, *e.g.*, body forces like gravity, or cell-length constraints.

The simulation uses a Metropolis-like dynamics (chapter II.1, section 2.3.2). We iteratively choose a random node, and attempt to move it in a random direction $\vec{x}_\mathrm{new} = \vec{x}_x + \xi\vec{r}$, where $\vec{r} = \{\rho, \theta\}$ is a random vector chosen uniformly within the unit circle (*i.e.* $\rho \in [0, 1]$ and $\theta \in [0, 2\pi)$) and ξ is the step size. To model cell wall yielding, we introduce new nodes whenever a polygon edge's length exceeds a threshold value. Since we assume shape relaxation is fast compared to biological changes, we make biologically motivated changes, like turgor pressure increases, cell divisions or active cell shape changes, only after turgor pressures, cell expansion and any resulting cell displacements have equilibrated.

We are currently using this method to model leaf morphogenesis, which involves a dynamic interplay between leaf venation, cell expansion and cell division. Fig.1 shows a sample simulation, in which a set of ordinary differential equations (*ODE*s) in each cell implements Meinhardt's four-species reaction-diffusion model as a prototype for leaf venation [17]. See also a simulation MovII.4.1 from the accompanying DVD. Cell expansion, which we model as a gradual increase in cells target areas (Chapter II.1, section 7.2.1), is fastest where concentrations of a diffusing growth repressor are lowest, near the developing vasculature which drains it, while the vasculature itself expands four times more slowly than the surrounding tissue. Cells divide along their shortest axis when they reach twice their original

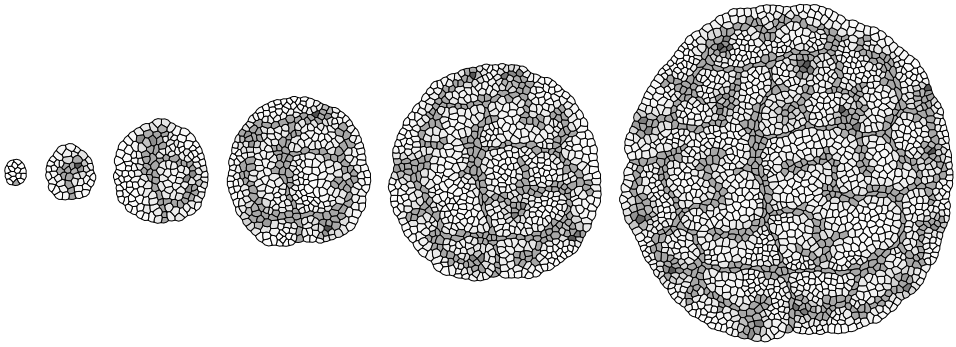

FIGURE 1. Relation between leaf growth and venation patterning in a symplastic growth model based on [17]. Dark grey cells are vascular. Light grey cells are normal leaf cells, with the degree of shading indicating the local concentration of the activator which regulates cell growth. See also a simulation MovII.4.1.

size (Chapter II.1, section 7.2.2). We are currently developing more realistic models of leaf venation patterning, which include several molecules known to regulate leaf venation, including the phytohormone auxin and its transporter protein PIN1. Eventually, the set of ODEs in each cell will describe the production, decay, regulation, cellular localization and transport of the molecules regulating leaf venation patterning.

2. Modeling Extracellular Matrix

Current GGH simulations either represent Extracellular Matrix (*ECM*) as a special cell, often the default cell index on lattice sites not occupied by any other cell, producing an ECM which behaves as an infinitely compressible, inviscid fluid, or as a non-diffusing chemical field which is non-deformable. These approximations may be adequate in many cases. However, in many morphogenetic processes (such as bone formation) ECM properties are crucial and require more realistic representation.

Although ECM tends to receive less attention than cells (which seem to do all the work during morphogenesis), it is a complex, varied and highly structured material, which includes networks of insoluble protein *fibrils* and numerous soluble components. *Collagens* and *elastins* are usually the two primary classes of structural proteins contributing to the fibrils. Soluble polymers, primarily long carbohydrate chains which bind water, link to these proteins. Rigid ECMs are crucial for maintaining tissue shape, and form the structural portion of most connective tissues and bones. ECM structure is heterogeneous, with important patterns at length-scales from tens of angstroms to millimeters, making it extremely difficult to model. Its fiber structure gives ECM highly anisotropic mechanical properties,

including visco-elasto-plasticity, and often provides crucial directional cues for cell migration.

ECM also mediates signaling between cells. ECM often binds cytokines and growth factors, acting as a chemical reservoir and greatly reducing the effective diffusion constant of diffusible signaling molecules. Ligands in the ECM also interact with specific cell-surface receptors (*integrins*) and cells can sense variations in ECM rigidity and fiber orientation. The ECM records the history of cell migration and differentiation during morphogenesis in its fibril pattern, which then guides further morphogenesis. Differences in ECM architecture account for much of the difference between normal and scar tissue. Appropriate synthetic ECM can induce tissue regrowth in adults, while metastasis occurs when tumor cells lose their binding to ECM.

Existing GGH methods can describe some ECM properties. For instance, we can model ECM binding of cytokines by lowering the diffusion constant of these chemicals in regions of ECM. However, many ECM properties, *e.g.*, visco-elasto-plasticity (see section 1.4) and fibril orientation (see section 2), call for a new *vector-field* class of object.[1]

Describing fiber orientation in terms of a vector field is complex because, at the typical scale of a GGH lattice, each lattice site will contain fibers of almost every possible orientation, requiring an impossibly complex description. A practical description of ECM requires careful optimization of the trade-offs among the number of allowed fiber orientations and fiber types per site and the angular resolution of those orientations. Options could range from a simple fiber with arbitrary orientation at each site, to a dozen fibers, each with variable concentration but only eight allowed orientations each at each site. The passage of cells can then change the fiber structure, which the field represents. We can model the effect of fiber orientation on morphogenesis by including terms in the Hamiltonian that couple ECM vector fields to cell chemotaxis, haptotaxis (chapter II.1, section 7.3), or cell polarization (section 1.3).

3. Improving Computational Efficiency Using Alternative Evolution Algorithms

Because it is extremely simple to implement, the modified-Metropolis algorithm has been a central part of GGH modeling. However, the modified-Metropolis algorithm rejects most index-copy attempts, making the algorithm inefficient and its stochasticity makes parallelization awkward. We also need to improve our diffusion

[1] Vector fields could provide an alternative method to implement fluid flow. Instead of using the fluid-particle method we described in section 1.2.1, we could define a flow field in the ECM and use a sophisticated Navier–Stokes-equation solver to update the fluid flow. Cell motion would impart vector boundary conditions and the simulation would become an immersed-boundary calculation.

solvers, since many current simulations spend only 10% of their time on GGH solutions and 90% solving the diffusion equation. Fortunately, diffusion algorithms, even Euler diffusion, are synchronous, and hence parallelize easily.

3.1. Rejection-Free Dynamics

Of the non-Metropolis Monte-Carlo algorithms, *rejection-free* algorithms such as the *N-fold way* and *kinetic Monte-Carlo* are particularly attractive [2, 9, 7, 15]. Rather than considering a trial index copy at each step, which we may or may not accept, these methods choose among allowed lattice updates at each step. Thus, while they spend much more time computing possible updates, they save the time normal Metropolis spends on rejected updates. The computational gain depends on the average number of possible updates, the fraction of possible updates that need to be recalculated after each update, and the average acceptance rate. If the product of these three numbers is less than one, rejection-free algorithms are faster. In some non-GGH cases, the gains can be dramatic (rejection-free code can be thousands, or even millions of times faster). Rejection-free methods can also facilitate parallel computing (section 4.2).

When we know the transition probabilities for a continuous-time Markov process, we can construct a discrete-time process or *embedded Markov chain* as well as a distribution of transition times. Consider the continuous-time Markov process with transition rates $w(j \to i) = \lim \underset{\Delta t \to 0}{\longrightarrow} p(i, t + \Delta t | j, t)$,

$$\frac{dp\,(i,t)}{dt} = \sum_j w\,(j \to i) p(j,t). \tag{15}$$

We can use Eq.(15) to calculate the probability for the transition $j \to i$ *given* that *some* transition has occurred:

$$f\,(j \to i) = \frac{w(j \to i)}{\sum\limits_{k \neq j} w(j \to k)}. \tag{16}$$

Eq.(16) is the jump probability for the discrete-time *master equation*:

$$p\,(i, n+1) = \sum_j f(j \to i) p(j,n), \tag{17}$$

where the index n measures how many transitions have occurred rather than the amount of time that has passed. Since the stochastic process underlying the master equation is memoryless, the waiting time to leave state j is exponentially distributed, with a rate parameter:

$$\lambda_j = \sum_{k \neq j} f\,(j \to k). \tag{18}$$

If the transition rates between states are proportional to $\exp[-\Delta\mathcal{H}/T]$ (Boltzmann weighting), where $\Delta\mathcal{H}$ is the difference in the states' energies, we can use the following rejection-free Monte-Carlo algorithm:

1. Determine all allowable lattice updates from the current lattice configuration.
2. Calculate the energy changes between them.

3. Calculate the time parameter for each of these transitions, λ_k.
4. Choose a random time parameter, λ_{random}, between 0 and $\max\{\lambda_k\}$.
5. Find the transition n for which $|\lambda_k - \lambda_{random}|$ is the smallest, and update the lattice using this transition.
6. Increment the time by a random time interval chosen with probability: $p(t)dt = \lambda_n \exp[-\lambda_n t]dt$.
7. Go to 1.

We may be able to bypass step 6 and simply increment the time by $1/\lambda_n$. Determining whether this approach works on average would be a nice research project. Because most of the allowed updates and their energy changes will *not* change after a given update, the complete set of possible updates needs to be evaluated only once at the beginning of a simulation, with much faster local updates thereafter. The longer the effective interaction range in the model, the larger the number of recalculations necessary after each step and the less efficient the algorithm. Thus, the gains of using rejection-free method are greatest for a simple, nearest-neighbor Ising model, while rejection-free algorithms are much worse than Metropolis for infinite-range interactions.

3.2. The Random-Walker Algorithm

A simple approach is to reduce but not eliminate the rejection rate. The *random-walker* algorithm keeps track of boundary lattice sites and selects only these as target sites in the modified-Metropolis algorithm, eliminating the automatic rejection of non-boundary sites in the normal algorithm [3]. For large cells and short interaction ranges, speed gains are substantial. For small cells or subcells, the increase in memory required outweighs the speed gains.

4. Parallelization for Large Simulations

Current practical single-processor GGH simulations can handle about 10^5cells. However, a full model of the morphogenesis of a complete organ or an entire embryo requires the simulation of 10^6–10^8cells. We also constantly demand more lattice detail and complex cell behaviors in our simulations. This need for speed suggests using distributed computing, which is widely available.

Parallel implementations of the GGH are an active area of research. The main difficulty in GGH parallelization is that the effective energies are non-local and updating is stochastic. For example, when a given cell crosses between nodes, any modification to it requires parameters passing between nodes or computations will use stale parameters.[2] Because in most current distributed computers (unlike in an IBM SP-1 or SP-2), processing is fast and interprocessor communications slow, a naive parallelization will cause the processes to spend almost all their time waiting rather than calculating.

[2]Studying the effect of stale parameter on GGH simulations would be a very valuable research project.

4.1. Checkerboard Algorithm

The standard approach to parallelizing Ising-type models is to divide the lattice into equivalent subgrids (with some overlap) one per processor. Each processor subdivides its subgrid into a checkerboard of sublattices [22], defined so that an update in one sublattice affects only the nearest-neighbor sublattices. We then define a set of non-interacting sublattices, *e.g.*, every 9^{th} square in 2D or every 27^{th} in 3D. If each processor then visits the same sublattice set and makes one update in each, the updates are guaranteed to be independent. The processors can then determine updates affecting neighboring processors, accumulate them and pass them synchronously, change the sublattice set and repeat. For examples of these methods see [4]. Gains from parallelization increase with the size of the subgrid per processor (which reduces the message-passing overhead) and decrease with the interaction range (which increases the message-passing overhead). To date, no one has implemented a fully-optimized checkerboard version of the GGH model.

4.2. Parallel Rejection-Free Algorithms

Rejection-free methods can use basic checkerboard parallelization, in which all processors perform equivalent computations, or can use an asymmetrical master–slave configuration, in which all processors can see the same lattice or in which the lattice is partitioned into subgrids. The master node (or nodes) determines all allowable updates, and delegates calculating the rates to slave nodes, which pass the rates back to the master node for steps 4 through 7 in the algorithm in section 3.1. Again, checkerboarding greatly improves the efficiency of the calculations. As far as we know, these methods have never been implemented in the GGH context.

5. Model Sharing Support

Because of the great simplicity of the GGH model's core algorithms (the GGH Hamiltonian and the modified Metropolis algorithm), a basic program that runs the GGH model takes less than one hundred lines of Fortran or C++ code. A result of this simplicity is that most of the major users of the GGH model wrote their own proprietary software without separating the individual model they were implementing from their GGH modeling framework. Current GGH simulations increasingly focus on complex cell behaviors, requiring detailed descriptions of the cell-cycle, transcription, and regulatory, metabolic and signaling networks. As the GGH model has accreted new capabilities, these proprietary versions have become more complex, with multiple, incompatible versions even within groups, making the replication of published results substantially more difficult and the adoption of new GGH extensions considerably slower [10, 11, 12, 26, 14]. Our efficiency would be much greater if our GGH implementations could either incorporate new methodologies in a simple way, or could communicate with programs that implement them, saving us from having to reinvent each-others' work and allowing

us to seamlessly combine the efforts of different researchers. As other, non-GGH agent-based cell-level models emerge, we would like to compare their results to those of the GGH model for validation purposes. In addition, increasing numbers of computationally-non-sophisticated scientists wish to develop GGH models. For these potential users, hard-coding complex initial conditions and interactions represents an insuperable barrier.

5.1. GGH Packages

Several groups have recently released open-source, extensible GGH modeling packages which allow less-sophisticated users to build simulations of a wide range of morphogenic phenomena. Wide adoption of a small number of these choices will enormously facilitate model development and sharing. We will briefly discuss the *Tissue Simulation Toolkit* [19], a modeling *library* which requires hard-coding of user modifications, and *CompuCell3D* [13], a modeling *environment*, which allows users to write models using high-level abstractions. Both allow users to reproduce published results and share new algorithms relatively painlessly, opening the field of GGH modeling to a much broader audience.

5.1.1. CompuCell3D. The CompuCell3D modeling environment (currently released under the SimTk license[3]) was developed collaboratively by groups at the University of Notre Dame[4] and the Biocomplexity Institute at Indiana University, Bloomington.[5] It supports the full GGH model, with unlimited numbers of chemical fields and complex diffusion equations. Instead of writing Fortran or C++ code, CompuCell3D users specify models using an XML-based markup language and run simulations from a flexible graphical *player*. CompuCell3D offers high-level Python scripting abilities that allow users full control of system-level variables and permit complex, conditional and time-dependent behavior specification without the need for hard-coding. CompuCell3D is under active development. Its development team welcomes participation by current and potential users in all aspects of its development. See also three simulations: MovII.4.2, MovII.4.3 and MovII.4.4 from the accompanying DVD.

5.1.2. Tissue Simulation Toolkit. Merks' open-source GGH library, the Tissue Simulation Toolkit (*TST*),[6] provides modules for simple 2D GGH simulations, with sample programs (available on the accompanying DVD) that allow users to reproduce published simulations. The TST includes a full range of GGH features and chemical fields. Visualization tools allow users to display the cell lattice by cell-type and chemical fields using color ramps and contour lines. The TST runs either interactively or in the background, making the package especially suitable for running large-scale parameter sweeps on computing clusters.

---

[3] https://simtk.org/home/compucell3d/.
[4] http://www.nd.edu/∼lcls/compucell/.
[5] http://biocomplexity.indiana.edu/.
[6] http://sourceforge.net/projects/tst.

5.2. Model Sharing

As other agent-based, cell-level models emerge, comparing results from different models will require a markup language that specifies cell-level models and cell behaviors in a generic way, independent of the simulation engine and modeling methodology. For example, to describe chemotaxis, the markup language might specify that epithelial cells of type C chemotax up TGF-β gradients with a sigmoidal response curve with saturation parameter α_1 and strength λ_1, and chemotax away from FGF-8 with a linear response with strength λ_2. Individual simulation packages would then implement this behavior in their own ways (perhaps, with some simplifications if they lacked specific features). CompuCell3D is already moving in this direction with its XML-based model specification. Furthermore, the XML-based markup language BioLogo (which is part of CompuCell3D) allows generic specification, coding and compiling of reaction-diffusion mechanisms. The Systems Biology Markup Language (*SBML*)[7] Level 3 is another markup language, which currently plans features for spatial, compartmentalized models.

Even more valuable than model sharing through markup languages would be model interoperability via *sockets* that allow communication between programs. Sockets would allow GGH implementations (such as the TST or CompuCell3D) to either incorporate their own engines to implement behaviors or communicate with other programs that do. Using sockets, a generic markup language could specify biological models in enough detail to allow sharing across model scales, connecting GGH-model implementations to microscopic models like BioSpice[8] and Systems Biology Workbench (*SBW*),[9] and to macroscopic models like Physiome.[10] The developers of CompuCell3D are currently working with the developers of SBW to implement sockets between their packages, allowing SBW to simulate the internal chemical pathways of the cell and CompuCell3D to simulate cells and intra-cellular behaviors. With a fully-defined markup language and set of sockets, a researcher building a CompuCell3D simulation would be able to use another researcher's existing model for internal cell behaviors, without recoding or reimplementation.

6. Conclusions

This chapter has presented some current areas of GGH model development and presented a view of its future, implicitly assuming that GGH modeling has a future. Fig.6 shows the number of papers that discuss or use GGH-related models. We would like to see an exponential rise rather than a peak followed by a leveling-off or a drop. The citation rate through 2005 increases roughly exponentially, albeit with a slow doubling time of five years, confirming a steady increase in interest in GGH models. As its power and flexibility increase through new methods, packages and

[7] http://sbml.org.
[8] http://biospice.org.
[9] http://sbw.sourceforge.net/.
[10] http://www.physiome.org/.

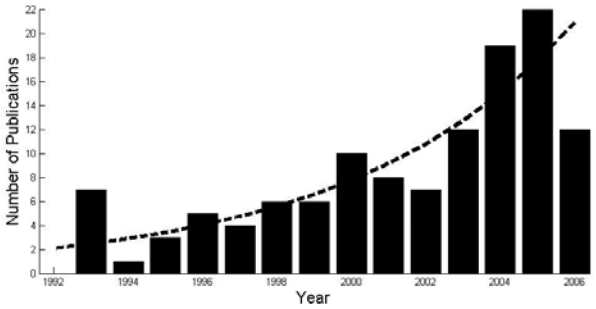

FIGURE 2. Number of publications using or citing GGH-related models by year (source: Web of Science, PubMed, ArXiv, *etc.*).

model sharing, we expect the GGH approach to become a standard method for cell-to-tissue level *in silico* biology, first replicating, then guiding *in vitro* experiments, and eventually leading to new experimental discoveries.

Acknowledgments

The leaf simulation project is a collaboration between R. M. H. Merks and G. T. S. Beemster, Y. Van de Peer and D. Inzé of the Department of Plant Systems Biology, VIB and Ghent University, Ghent, Belgium. R. M. H. Merks is supported by Marie Curie Intra-European Fellowship 2005-025084. A. Balter, N. J. Popławski, M. Swat and J. A. Glazier gratefully acknowledge support from the National Institutes of Health, National Institute of General Medical Sciences, grant 1R01 GM076692-01, an IBM Innovation Institute award, NASA Glenn Research Center, grant NAG 2-1619, the National Science Foundation, Division of Integrative Biology, grant IBN-0083653, and the Office of the Vice President for Research, the College of Arts and Sciences, the Pervasive Technologies Laboratories, the AVIDD and ODIN computer clusters and the Biocomplexity Institute at Indiana University.

References

[1] U. Börner, A. Deutsch, H. Reichenbach, and M. Bär. Rippling patterns in aggregates of myxobacteria arise from cell–cell collisions. *Phys. Rev. Lett.*, 89:078101, 2002.

[2] A. B. Bortz, M. H. Kalos, and J. L. Lebowitz. A new algorithm for Monte Carlo simulation of Ising spin systems. *J. Comp. Phys.*, 17:10, 1975.

[3] F. P. Cercato, J. C. M. Mombach, and G. G. H. Cavalheiro. High performance simulations of the Cellular Potts model. In *20th International Symposium on High-Performance Computing in an Advanced Collaborative Environment*, page 28, 2006.

[4] N. Chen, J. A. Glazier, and M. S. Alber. A parallel implementation of the Cellular Potts model for simulation of cell-based morphogenesis. *Lect. Notes Comput. Sci.*, 4173:58, 2006.

[5] D. Dan, C. Mueller, K. Chen, and J. A. Glazier. Solving the advection–diffusion equations in biological contexts using the Cellular Potts model. *Phys. Rev. E*, 72: 041909, 2005.

[6] R. O. Erickson. Symplastic growth and symplasmic transport. *Plant Physiol.*, 82: 1153, 1986.

[7] K. A. Fichthorn and W. H. Weinberg. Theoretical foundations of dynamical Monte Carlo simulations. *J. Chem. Phys.*, 95:1090, 1991.

[8] M. C. Gibson, A. B. Patel, R. Nagpal, and N. Perrimon. The emergence of geometric order in proliferating metazoan epithelia. *Nature*, 442:1038, 2006.

[9] D. T. Gillespie. A general method for numerically simulating the stochastic time evolution for coupled chemical reactions. *J. Comp. Phys.*, 22:403, 1976.

[10] P. Hogeweg. Evolving mechanisms of morphogenesis: on the interplay between differential adhesion and cell differentiation. *J. Theor. Biol.*, 203:317, 2000.

[11] P. Hogeweg. Computing an organism: on the interface between informatic and dynamic processes. *Biosystems*, 64:97, 2002.

[12] P. Hogeweg and N. Takeuchi. Multilevel selection in models of prebiotic evolution: compartments and spatial self-organization. *Orig. Life Evol. Biosph.*, 33:375, 2003.

[13] J. A. Izaguirre, R. Chaturvedi, C. Huang, T. Cickovski, J. Coffland, G. L. Thomas, G. Forgacs, M. S. Alber, H. G. E. Hentschel, S. A. Newman, and J. A. Glazier. Compucell, a multi-model framework for simulation of morphogenesis. *Bioinformatics*, 20: 1129, 2004.

[14] Y. Jiang, J. Pjesivac-Grbovic, C. Cantrell, and J. P. Freyer. A multiscale model for avascular tumor growth. *Biophys. J.*, 89:3884, 2005.

[15] K.-C. Lee. Rejection-free Monte Carlo technique. *J. Phys. A*, 28:4835, 1995.

[16] J. A. Lockhart. An analysis of irreversible plant elongation. *J. Theor. Biol.*, 8:264, 1965.

[17] H. Meinhardt. Morphogenesis of lines and nets. *Differentiation*, 6:117, 1976.

[18] R. M. H. Merks and J. A. Glazier. Dynamic mechanisms of blood vessel growth. *Nonlinearity*, 19, 2006.

[19] R. M. H. Merks and J. A. Glazier. A cell-centered approach to developmental biology. *Physica A*, 352:113, 2005.

[20] R. M. H. Merks, S. V. Brodsky, M. S. Goligorksy, S. A. Newman, and J. A. Glazier. Cell elongation is key to *in silico* replication of *in vitro* vasculogenesis and subsequent remodeling. *Dev. Biol.*, 289:44, 2006.

[21] T. Nagai and H. Honda. A dynamic cell model for the formation of epithelial tissues. *Philos. Mag.*, 81:699, 2001.

[22] M. E. J. Newman and G. T. Barkema. *Monte Carlo methods in statistical physics.* Oxford University Press, Oxford, 3rd edition, 1999.

[23] J. H. Priestley. Studies in the physiology of cambial activity. II. The concept of sliding growth. *New Physiol.*, 29:96, 1930.

[24] W.-J. Rappel, A. Nicol, A. Sarkissian, H. Levine, and W. F. Loomis. Self-organized vortex state in two-dimensional *Dictyostelium* dynamics. *Phys. Rev. Lett.*, 83:1247, 1999.

[25] T. Rudge and J. Haseloff. A computational model of cellular morphogenesis in plants. *Lect. Notes Comput. Sci.*, 3630:78, 2005.

[26] N. J. Savill and J. A. Sherratt. Control of epidermal stem cell clusters by Notch-mediated lateral induction. *Dev. Biol.*, 258:141, 2003.

[27] J. Starruß, T. Bley, and A. Deutsch. A new mechanism for swarming pattern formation of *Myxococcus xanthus*. Preprint, 2007.

[28] M. Zajac, G. L. Jones, and J. A. Glazier. Model of convergent extension in animal morphogenesis. *Phys. Rev. Lett.*, 85:2022, 2000.

Ariel Balter
Biocomplexity Institute and Department of Physics, Indiana University,
Swain Hall West 117, 727 East Third Street, Bloomington, Indiana 47405-7105, USA
e-mail: `abalter@indiana.edu`

Roeland M. H. Merks
Department of Plant Systems Biology,
VIB Technologiepark 927, B-9052 Ghent, Belgium, and
Department of Molecular Genetics, Ghent University, Ghent, Belgium
e-mail: `roeland.merks@psb.ugent.be` or `post@roelandmerks.nl`

Nikodem J. Popławski
Biocomplexity Institute and Department of Physics, Indiana University,
Swain Hall West 117, 727 East Third Street, Bloomington, Indiana 47405-7105, USA
e-mail: `nipoplaw@indiana.edu`

Maciej Swat
Biocomplexity Institute and Department of Physics, Indiana University,
Swain Hall West 117, 727 East Third Street, Bloomington, Indiana 47405-7105, USA
e-mail: `mswat@indiana.edu`

James A. Glazier
Biocomplexity Institute and Department of Physics, Indiana University,
Swain Hall West 159, 727 East Third Street, Bloomington, Indiana 47405-7105, USA
e-mail: `glazier@indiana.edu`

Single-Cell-Based Models in Biology and Medicine
ed. by A.R.A. Anderson, M.A.J. Chaplain, K.A. Rejniak
Mathematics and Biosciences in Interaction, 169

III. Off-lattice Cell Models

General Introduction

As is stated in the chapter by T. Newman: *One of the more challenging biological characteristics to build into a cell model is cell shape, and, along with this, cell response to local mechanical forces.*

In this Chapter entitled Off-lattice Cell Models mathematical models of single cells are presented whereby each cell is modeled as a discrete entity with well-defined individual cellular characteristics such as intracellular reaction kinetics and biomechanical properties. In this way, cell shape can be explicitly modeled and how a cell responds to local mechanical forces and interacts with neighbouring cells can be investigated. As computational power increases, this modeling approach offers a powerful tool to give insight into many biological and pathological cellular processes.

The chapter from D. Drasdo, Center-based Single-cell Models: An Approach to Multi-cellular Organization Based on a Conceptual Analogy to Colloidal Particles, presents a model framework for multi-cellular simulations where cells are treated in an analogous manner to colloidal particles. More precisely, each cell is approximated as a homogeneous, isotropic, viscoelastic entity, capable of migrating, growing, dividing and changing direction. Each cell is parameterized by biomechanical, cell-kinetic and cell-biological parameters, all of which can, in principle, be determined experimentally.

The chapter from J. Dallon, Models with Lattice-free Center-based Cells Interacting with Continuum Environment Variables, describes a discrete-continuum hybrid method where cells are modeled as discrete objects free to move in space, the forces which act on the cells are applied to their center of mass, and the cells interact with another variable (e.g. a soluble, diffusing chemical or extracellular matrix) represented as a continuum variable.

In the final chapter from T. Newman, Modeling Multicellular Structures Using the Subcellular Element Model, a new method for simulating grid-free multicellular structures is presented, in which the three-dimensional shape of each cell is dynamically adaptive to its local environment. This is achieved by constructing each cell from subcellular elements. This approach allows for key cellular processes such as cell growth and cell division to be modeled which explicitly incorporate cell shape.

Single-Cell-Based Models in Biology and Medicine
ed. by A.R.A. Anderson, M.A.J. Chaplain, K.A. Rejniak
Mathematics and Biosciences in Interaction, 171–196

III.1 Center-based Single-cell Models: An Approach to Multi-cellular Organization Based on a Conceptual Analogy to Colloidal Particles

Dirk Drasdo

To Zoubida and Marvin

Abstract. In this chapter we present a model framework for multi-cellular simulations which is built on conceptual analogies to colloidal particles. Cells are approximated as homogeneous isotropic elastic sticky objects, capable of migrating, growing, dividing and changing orientation. A cell is parameterized by biomechanical, cell-kinetic and cell-biological parameters. Each model parameter can in principle be determined experimentally. We show some simulation results for in-vitro systems and discuss the effect of model variants on simulated multi-cellular growth phenomena. The aim of this chapter is to provide an introduction and overview of the algorithms, technical concepts and the framework necessary to perform equivalent computational simulations with different model variants.

1. Introduction

Many experimental observations and their analysis by mathematical models indicate that many aspects of cell behavior, in particular in a culture medium, may well be approximated if one assumes that cells behave as colloidal particles. Isolated cells in suspension and in the absence of stimuli such as morphogens perform a random movement [1, 2]. This movement can perfectly be approximated by the same Fokker-Planck, or Langevin equation that is used to model the dynamics of colloidal particles. As a response on a chemoattractant cells perform a directed movement (e.g., [3, 4]). The collective moment of cells can be shown to follow Keller-Segel-type equations if one assumes that the movement of each individual cell follows a Langevin-equation of motion consisting of a random contribution and a term triggered by chemotaxis [5]. The adhesion forces of S180 cells have recently been shown to be well fitted by the Johnson-Kendall-Roberts-model (JKR) as long as no rupture of the cytoskeleton occurs [6]. The JKR-model describes the forces between homogeneous isotropic elastic adhesive spheres ([7] and refs.

therein). Based on the interpretation of cells as physical particles Beysens et. al. [8] derived a fluctuation-dissipation-like relation for cells, in analogy to Brownian particles. However, cells are not Brownian particles. For example, on a solid surface they perform an active movement rather than being passively pushed by random collisions with particles of a liquid suspension. So already for those observations that indicate a formal analogy between cells and colloids, the interpretation of the model parameters cannot be the same in both systems. Cells can also grow and divide in a way that colloidal particles cannot, and, more importantly, they can control and modify their properties, shape and their state of action by a complex intracellular machinery, which also colloidal particles cannot do. Moreover, cells may be committed to a strict genetic program which precisely determines the change of their parameters. Such a strict genetic program is found for example in early animal development.

However, many observations in unstructured cell populations and even in some intermediate phases in development can be explained by models that rely basically on the colloidal particle concept with only modest extensions i.e. they do not need complex differentiation or regulation processes. Here we present the basic framework and a number of model variations that underly models of multi-cellular phenomena in experimental *in-vitro* settings and selected *in-vivo* observations. We have used the different model variants to model aspects of monolayer cultures (e.g. [9, 10, 11, 12, 13, 14, 15, 16]), multi-cellular spheroids [17, 14, 16], epithelium such as intestinal crypts [18, 19] and systems in early development [20, 21, 16].

The chapter is organized as follows. Next we introduce a set of basic model assumptions and a number of variants designed to model the growth of monolayer populations in-vitro. We directly introduce some model variants. As the next step we turn the model assumptions into a computer algorithm and after this into a mathematical framework. Subsequently we present selected simulation results and finally close the article by a discussion. The discussion refers briefly to other methods described in this book, but this article focuses almost solely on center-based off-lattice models since other methods are explained in the other chapters of this book. The article is largely based on refs. [14, 13, 16] where further results may be found.

2. The model framework

2.1. Biological background

We demonstrate the modeling framework for cells growing in tissue cultures on a flat substrate. The cultures are used to study multi-cellular systems under well-defined conditions. In monolayer cultures cells usually grow on a flat surface covered by proteins, growth factors etc. [22, 23, 24, 25]. After cells have been seeded in culture they attach to the surface and subsequently migrate, grow and divide. Normal cells stop dividing at confluence that is, once they cover the floor of the culture dish. This is called contact inhibition of growth [26]. Different from normal

cells many malignant cells do not stop dividing at confluence. Moreover, often they do not need anchorage to the substrate in order to divide as normal cells do. And some malignant cell lines such as WiDr-cells, a colon carcinoma cell line, lack anchorage dependent cell death (anoikis) which for normal cells ensures that cells grow and divide only in their normal physiological environment.

We first briefly enumerate the set of basic model assumptions. Then we present an algorithmic and mathematical description of the model. The major model features and assumptions are:

I **Cell shape:**

(i) Motivated by the observation that isolated cells in cultures or suspensions often adopt a spherical shape [27] we assume each model cell to be spherical directly after cell division and to deform into a dumb-bell during mitosis. Within the cell cycle the cell volume doubles (Fig.1a).

(ii) As an alternative model we separated the growth and the deformation phase (Fig.1b, see for example [9, 16]). In this algorithm, the cell grows at spherical shape until it has doubled its volume and then deforms into a dumb-bell at constant cell volume.

(iii) As a slight modification of the division algorithm (ii) we studied an algorithm where the cells are considered to be separated immediately if the length of the dumb-bell axis in (Fig.1b) becomes $|\underline{a}_i| > 0$ [13]. This algorithm leads to unrealistic overlaps of the daughter cells which, however, disappear quickly since they only affect the deformation phase in algorithm (ii), and not the growth phase. The advantage of this algorithm is that cells are always intrinsically spherical which simplifies the mathematical treatment of the cell-cell interactions.

The deformation and growth steps in all three algorithms occur in very small steps $\delta a \ll l$ where l is the diameter of a cell immediately after its division. In our monolayer simulations we considered the typical size of rat C6 astrocyte

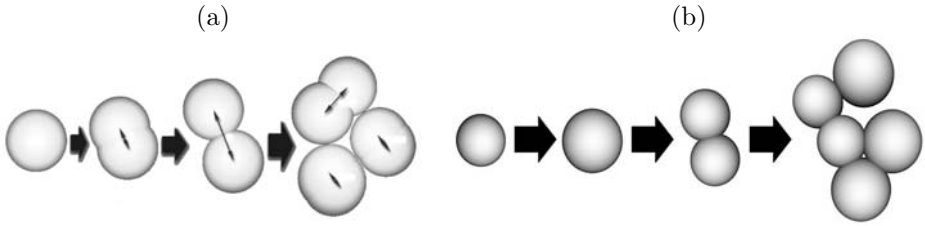

FIGURE 1. Illustration of the cell division algorithms. (a) During cell division, a cell deforms from a perfect sphere into a dumb-bell in small steps $\delta a \ll l$. l=2R is the cell diameter of a cell immediately after division, R the radius of each sphere of the dumb-bell. (b) A cell maintains its spherical shape during growth and deforms into a dumb-bell at constant mass after it has doubled its initial volume [16]. Both, growth and deformation are done in small steps $\ll l$.

glioma cells which are $l \approx 10\mu m$ (Bru, priv. communication and [28]). We further define $R = l/2$ as the radius of a cell directly after division. Step sizes and the frequency of the growth steps are chosen in such a way, that the resulting migration and growth process correctly reproduces prescribed experimental values. An explanation of this procedure can be found below [14, 16]. In early development, the mass of the cells does not double in the cell cycle so daughter cells are smaller than the mother cell. This leads to a small modification of the upper algorithms as described in Refs. [20, 29, 16] which we do not explain here where we focus on eukaryote cells at later developmental stages.

II **Cell-cell interaction:**
Cells in contact can form adhesive bonds. With decreasing distance between cell centers (e.g., upon compression) the contact area between them increases and with it, the number of adhesive bonds, resulting in an increasing attractive interaction. On the other hand, if cells in isolation are spherical, an increasing contact area is accompanied by an increasing deformation which results in a repulsive interaction. Furthermore cells under physiological conditions have only a moderate compressibility. We have used different models of the cell-cell (and cell-substrate) interaction (mathematical details are given below):
(i) The Johnson-Kendall-Roberts (JKR) model for isotropic homogeneous adhesive spheres where cells once they get into contact immediately form a strong adhesive contact and show a hysteresis behavior if they are pulled apart (Fig.2) [14, 16].
(ii) The Hertz-model for isotropic homogeneous spheres extended by a term that takes into account cell adhesion [13, 15]. This model does not show a hysteresis behavior.
(iii) Harmonic-like interaction energies where the form of the interaction energy assumes a cuboidal shape of the cells [9, 20, 17].

III **Cell migration:**

(a) *Isolated cells:* In the absence of chemotactic signals, isolated cells in suspension or culture medium have been observed to perform a random walk-like movement [1, 2] that we characterize by the cell diffusion constant D. More motile cells are assumed to have a larger D (we used $D \approx 10^{-11} cm^2/s$).

(b) *Cell aggregates:* While in mechanical contact with other cells, proliferating cells exert a pressure on their neighbors. The neighboring cells try to escape this pressure by moving actively against the friction caused by the other neighboring cells and extracellular material (e.g. extracellular matrix) by migration [30]. We assume that the migration can be characterized by an effective friction constant as for true friction. (In some situations the movement may be purely passive by pushing; in these cases the effective friction constants represent true friction.)

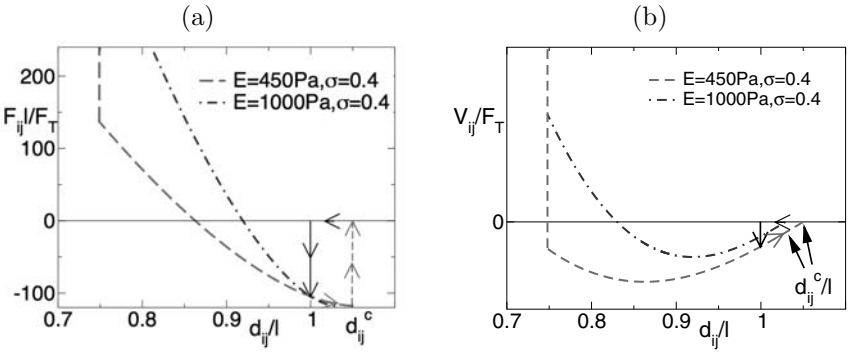

FIGURE 2. (a) Force F_{ij} and (b) interaction energy V_{ij} vs. distance d_{ij} (all in scaled units) for the JKR-model [14]. Here we assumed $R_i = R_j = R = l/2$. F_T is a reference energy and explained in the text. Typically we have chosen $F_T = 10^{-16}J$ (a value between those suggested in refs. [8] and [1], compare [14]). All quantities on the axes are referred to reference scales. Hence the quantities on the axes are dimensionless. When two cells approach each other (full black curve), they do not interact as long as $d_{ij} > l$. At $d_{ij} = l$ they spontaneously form a contact area driven by the cell-cell adhesion. Their preferred distance is at $d_{ij} \equiv d_{ij}^{(0)} \approx 0.85l$ for $E = 400Pa$, where the force on the cells is $F_{ij} = 0$. At this distance the deformation energy balances the adhesion energy. For $d_{ij} < d_{ij}^{(0)}$, the force is repulsive, for $d_{ij} > d_{ij}^{(0)}$, it is attractive. When the cells are pulled apart (dashed arrows) they deform and stick until a distance $d_{ij} \equiv d_{ij}^c > l$ at which their contact ruptures. This is a typical hysteresis behavior. Fig.(b) is the corresponding energy picture. The full (black) curve describes the energy when two cells approach each other, the dashed (color) curves describe cells that are pulled apart. Note, that for larger E, the repulsion for a given d_{ij} becomes larger since cells are harder to deform and compress. In most simulations we assumed a hard core-repulsion at a small cell-cell distance $d_{ij} = d_{HC}$ denoted by the vertical line. In (a) and (b) $d_{HC} = 0.75$.

We simulate a friction-dominated stochastic dynamics driven by physical interactions either by the standard Metropolis algorithm [31, 9] or stochastic partial differential equations of the Langevin type [13, 15, 16].

(i) As shown below the Metropolis method assumes that cells move in order to minimize the energy of the multi-cellular configuration. An energy minimization concept has already been proved useful to explain the sorting of embryonic cells by differential adhesion [32, 33].

(ii) Langevin-type of equations represent equations of motion for each cell where cells migrate under the influence of forces with an intrinsic random component (noise). They have been used to model the chemotactic movement of myxobacteria [5] or growing monolayers [13, 16].

IV **Control of cell division and cell death:**

We assume an average intrinsic cell cycle time to be influenced at the level

of individual cells by nutrients, regulatory factors and mechanical stress. By "intrinsic" cell cycle time we mean the cycle time of a cell in isolation. We denote τ as the average intrinsic cell cycle time of an isolated cell not affected by physical interactions with neighboring cells. In our model, a cell within a multicellular aggregate can grow only if it is not deformed (or compressed) greatly (i.e., if the central displacement of the surface of cell i at the contact point to its neighbor cell j does not become smaller than a critical "deformation threshold" of $(1-\zeta)l_i/2$ (in most simulations, we have chosen $\zeta = 0.75$) such that $d_{ij} > \zeta(l_i + l_j)/2$. i.e. we assume that cell growth can be controlled by the cell's degree of deformation (or compression) which may be sensed by the cell cytoskeleton [34]. This models a biomechanical form of contact inhibition of growth. Consequently the observed cell cycle time of deformed cells is typically larger than the intrinsic cycle time. Note that a large ζ means that a small deformation is needed to cause a growth stop hence a large ζ is equivalent to a large sensitivity towards contact inhibition of growth. We studied three cases.

(i) In ref. [14] we assumed that a cell subject to a critical deformation continues to grow as far as the deformation again falls below the critical threshold, independently of how long the critical deformation has lasted.

(ii) A cell that was subject to a critical deformation for a certain period of time τ^{th} does not re-enter the cell cycle again.

(iii) If a critical deformation has lasted for a certain period of time τ^{th} the cell instantaneously undergoes apoptosis (programmed cell death). A discussion of these cases can be found in ref. [14]. Here we focus on case (i).

V **Lysis of dead cells:**
We model idealized situations with very fast or very slow lysis of dead cells by (i) removing or (ii) not removing dead cells.

VI **Initial conditions:**
We started our simulation with a single cell. Since the initial cell population size $N(t = 0)$ in the experiments is not known, we shifted the curve along the time-axis until a good agreement between simulation results and experimental observations was obtained. The intersection of our computer simulation with the N-axis at $t = 0$ then permits to estimate $N(t = 0)$.

Below we discuss the computational aspects and mathematical concepts underlying the model assumptions in more detail.

2.2. Interaction energy: Compression, Deformation and Adhesion

For the interaction energy we have used the JKR-, Hertz- and a harmonic potential-energy-like model. For the biological situations we considered, they were found to yield qualitatively equivalent results. However, they may show quantitative differences depending on the biological situation considered. The final determination of the model that should be used has to be determined experimentally and will usually depend on the cell type and substrate considered.

JRK-model: This model describes the interaction between two isotropic homogeneous, strongly adhesive spheres [7, 14, 16]. "Strong" means that as soon as two cells come into contact at distance $d_{ij} = R_i + R_j$ (while they had no contact at $d_{ij} > R_i + R_j$) they immediately form a contact area of finite size by active deformation of the cell bodies (Fig.2). Here, d_{ij} denotes the distance between the nearest spheres of the neighboring dumb-bells i and j (a spherical cell is a dumb-bell with axis length $a = 0$). When two cells are pulled apart, however, they still have contact at distance $R_i + R_j < d_{ij} \leq d_{ij}^c$ (Fig.2) hence they show a hysteresis behavior. The force $F_{ij} \equiv |\underline{F}_{ij}(d_{ij})|$ in the JKR-model has to be calculated numerically from the implicit equation:

$$\delta = \frac{a^2}{\tilde{R}} - \left[16\pi\hat{\gamma}a/(3\tilde{E}_{ij})\right]^{1/2}, \tag{1}$$

where

$$a^3 = \frac{2\tilde{R}}{\tilde{E}_{ij}}\left[F_{ij} + 3\pi\hat{\gamma}\tilde{R} + \left[6\pi\hat{\gamma}\tilde{R}F_{ij} + (3\pi\hat{\gamma}\tilde{R})^2)\right]^{1/2}\right], \tag{2}$$

$\tilde{R}^{-1} = \frac{1}{R_i} + \frac{1}{R_j}$, and $d_{ij} = R_i + R_j - \delta$ (i.e., $\delta = \delta_i + \delta_j$ is the sum of the deformation along the axis between the centers of the closest spheres of the dumb-bells of cell i and cell j), and

$$\tilde{E}_{ij}^{-1} = \frac{3}{4}\left(\frac{1-\sigma_i^2}{E_i} + \frac{1-\sigma_j^2}{E_j}\right), \tag{3}$$

E_i, E_j are the elastic moduli, σ_i, σ_j the Poisson ratios of the cells i, j. This takes into account that a homogeneous, isotropic elastic body is completely characterized by two independent material constants, for example the Young modulus E and the Poisson ratio σ. We have chosen $E = 450Pa$ ([35, 36]) and $\sigma = 0.4$ [37, 38]). The latter characterizes the compressibility of the body. The Young modulus is a measure for the elasticity of the cell; a large Young modulus corresponds to a large stiffness (i.e. the cell is difficult to deform). $\hat{\gamma} \approx \varrho_m W_s$, where $\varrho_m \approx 10^{15} m^{-2}$ [39], [40] is the density of surface adhesion molecules in the contact zone and $W_s = 15 - 25k_BT$ is the binding energy of a single bond. Eq.(2) has to be solved implicitly to give $a(F_{ij})$. The value of a is plugged into Eq.(1) to give $\delta(a)$ and, by $d_{ij} = R_i + R_j - \delta$, $d_{ij}(a)$. Plotting F_{ij} vs. d_{ij} yields $F_{ij}(d_{ij})$, which cannot be given explicitly but can easily be fitted by a polynomial (we used a polynomial of degree three). The corresponding interaction energy is shown in Fig.2b. The full line at $d_{ij}/l \geq 1$ in Fig.2 describes two cells that approach each other. The dashed curve in Fig.2(b) has been obtained from the dashed curve in Fig.2(a) by $V_{ij}^c = V^c(d_{ij}) = -\int_\infty^{d_{ij}} (\underline{F}_{ij}\frac{r_j - r_i}{d_{ij}}) d(d_{ij})$ for $d_{ij} > \zeta(R_i + R_j)$. When two cells approach each other, $V_{ij} = 0$ if $d_{ij}/l \geq 0$, $V_{ij} = V_{ij}^c$ if $\zeta(R_i + R_j) < d_{ij}/l < 1$, and ∞ otherwise. This construction insures, that $F_{ij} = -|\underline{\nabla} V_{ij}|$. Note that only the energy difference enters the MC-simulation. At $d_{ij} = \zeta l$ with $\zeta \approx 0.75$ we assume a hard core repulsion. This takes into account that cells are almost incompressible with a Poisson ratio $\sigma \approx 0.4 - 0.5$ [38]. A smaller distance would require a significant cell compression. To calculate the interaction of a cell i with the substrate, the substrate s is treated as a cell with infinite radius $R_s \to \infty$.

Hertz model: As in the JRK-model in the Hertz model (see [41], [42]) we approximate each cell as a homogeneous spheroidal elastic body [13, 15]. Different from the JKR-model the Hertz model does not show a hysteresis behavior and both the interaction energy and interaction forces can be given by analytical expressions. In this case the potential interaction energy may be represented as a superposition of a repulsive and an attractive contribution:

$$V_{ij} = V_{ij}^{attr} + V_{ij}^{rep}, \tag{4}$$

where the repulsive contribution is given by the elastic energy which for two spherical elastic bodies in the case of small deformations is

$$V_{ij}^{rep} = (R_i + R_j - d_{ij})^{5/2} \frac{1}{5\tilde{E}_{ij}} \sqrt{\frac{R_i R_j}{R_i + R_j}}, \tag{5}$$

and $\tilde{E}_{ij}^{-1}$ is defined in Eq.(3) above. If the Young moduli and Poisson ratios of both spheres (cells) are equal, $E_i{=}E_j{\equiv}E^C$ and $\sigma_i{=}\sigma_j{\equiv}\sigma^C$, and consequently $\tilde{E}_{ij} = \frac{3}{2}(1-\sigma^C)/E^C$, hence $V^{rep} \propto E^C$ as for the harmonic-like repulsion energy (see below). The total energy is given by Eq.(4). The contact area of two interacting, spherical cells i, j with radii R_i and R_j in $d = 3$ dimensions is $A_{ij} \approx \pi R_i R_j \left(1 - \frac{d_{ij}}{R_i + R_j}\right)$. Note, that this approach takes into account the spheroidal cell shape. Due to the spheroidal shape the size of the contact area increases with decreasing distance and V_{ij}^{rep} is not quadratic in the cell-cell distance, as for cuboidal cells (see below). The attractive energy contribution due to cell-cell adhesion may be approximated by

$$V_{ij}^{attr} = -n_{mol} \frac{A_{ij}}{A_c} W_s = -\varrho W_s A_{ij} \tag{6}$$

where A_{ij} is the contact area of cells i, j, A_c is the surface area of the (larger) cell, n_{mol} the total number of adhesion molecules at the cell surface, W_s the adhesive energy of a single bond.

Harmonic-like potential energy: A simple model for the short range cell-cell interaction due to cell-cell adhesion and elastic deformations is to approximate two adhesively interacting cells by cuboidal objects with a non-deformable core, reversibly linked by linear springs [9, 20]:

$$V_{ij} = \begin{cases} \epsilon \left(\frac{2\tilde{d}_{ij}(t)}{\delta} + \sqrt{\frac{V_{ij}^{attr}}{\epsilon}} \right)^2 - V_{ij}^{attr}, & if \quad -\delta \le \tilde{d}_{ij}(t) \le 0, \\ \infty & if \quad \tilde{d}_{ij} < -\delta, \\ 0 & \text{otherwise}, \end{cases} \tag{7}$$

with $\tilde{d}_{ij} = d_{ij} - (R_i + R_j)$ where d_{ij} denotes the distance between the nearest spheres of the neighboring dumb-bells i, j (here, $R_i = R_j = R$). $V_{ij}^{attr} < 0$ is the adhesion energy (see Eq.(6)). δ approximately determines the range over which a cell can be stretched or compressed in a certain direction. The hard-core repulsion at $\tilde{d}_{ij} < 0$ takes into account that cells cannot be arbitrarily compressed or deformed and hence insures that a cell cannot occupy a region in space which

is already occupied by another cell (exclude volume effect). $\epsilon > 0$ measures the resistance against deformations, and can be related to the Young modulus by

$$\hat{\epsilon} \approx \hat{E}^C \frac{\hat{\delta}^2}{8}, \tag{8}$$

with $\hat{\epsilon} = \epsilon / F_T$ and $\hat{E}^C = E^C l^3 / F_T$, where E^C is the Young modulus of a cell in a multicellular aggregate. $\hat{\delta} = \delta / l$. The "8" in the denominator is for cuboidal cells—for spherical or cylindrical cells the factor is slightly different. In refs. [20, 18, 17] we used a further simplified model energy by setting $V_{ij}^{attr} = \epsilon$.

2.3. Mathematical concepts for cell movement and growth

In order to convert the above assumptions into a mathematical description within an individual-based approach, different model approaches may be chosen. One method is a direct numerical integration of the equations of motion for each individual cell. Since the cell movement comprises stochastic contributions this leads to stochastic differential equations for the state variables (e.g. position, velocity, orientation, ...) of each cell [13, 16]. Instead of tracking the trajectory of each cell, one may look at the multivariate probability distribution which includes all state variables of the cell. The equation for the time development of the multivariate probability distribution models the change of the cell configuration. Possible approaches are a master equation or a Fokker-Planck equation.

We have used a Langevin and a master equation-motivated approach. Below we introduce two algorithmic schemes that correspond to a master equation approach. In this subsection we mainly give a qualitative description of the algorithms and then present the most important mathematical relations.

2.3.1. Cell dynamics I: master equation approach.

Qualitative description. We assume cells can either migrate, grow, change their orientation, divide, or die. Each of these "moves" changes a given configuration of cells. The order in which the moves are performed depends on the choice of the update algorithm. So far we have mainly used three computational schemes:
Scheme I [9, 20]:

1. Generate an initial configuration of cells (in most simulations of in-vitro-systems we started with a single cell)
2. Choose cells from the configuration randomly for either a migration, orientation change, growth or division, or death trial according to a probability which reflects the relative time scales of migration, orientation changes, growth and division, or cell death (the time scales are specified below). Each trial is assessed based on the probability of the configurations between and after a move trial in order to decide whether the trial is accepted or rejected. In the latter case the cell is reset to its previous state. For the assessment we use the Metropolis algorithm [31, 9]. According to the Metropolis algorithm a

cell translation or orientation change takes place with a rate

$$\Pi^{(j)} \propto min\{1, exp[-(\sum_{i<j}(V_{ij}(t+\Delta t) - V_{ij}(t))/F_T]\}/T^{(j)}, \quad (9)$$

where t is time, Δt a time step, and F_T is a reference energy analogous to the thermal energy k_BT in fluids or gases (T: temperature, k_B:Boltzmann const.) [8]. $T^{(j)}$ defines the typical time between two successive Monte-Carlo-trials and depends on whether cell migration (j=1), growth (j=2), rotation (j=3), division (j=4) or death (j=5) is considered. The index j is used below to characterize the transition rates.

3. Increase t by $\Delta t/N$ where Δt has initially be determined as the time period between two successive Monte-Carlo trials for a single isolated cell. N is the population size.
4. Continue with step (2) until a certain stop criterion is fulfilled.

Scheme II [17]:

1. Generate an initial configuration of cells (in most simulations of in-vitro-systems we started with a single cell).
2. Generate a list that contains all cells at a given point of time t.
3. Choose cells from the list in random order for either a migration, orientation change, growth or division, or death trial according to a probability which reflects the relative time scales of migration, orientation changes, growth and division, or cell death (the time scales are specified below). Then remove the cell from the list. Continue this procedure until the list is empty. Each trial is again assessed based on the Metropolis algorithm as in Scheme I.
4. Increase t by Δt.
5. Continue with step (2) until a certain stop criterion is fulfilled.

Scheme III [14, 16]:

1. Generate an initial configuration of cells (in most simulations we start with a single cell).
2. Generate lists that contains all cells at a given point of time t, one for migration, one for orientation changes, one for growth and division, and one for cell death.
3. Set $t = t_0$.
4. Repeat the following steps (5)–(7) until a certain stop criterion (maximum time; maximum population size) is fulfilled.
5. Calculate the (expected) periods of time between two migration trials (of the same cell), Δt_m, orientation change trials (of the same cell), Δt_o, growth and division trials Δt_g (of the same cell), and cell death trials Δt_d (of the same cell) according to the relative time scales of migration, orientation changes, growth and division, and cell death. Then, the points of times at which list k is processed, are given by $t_k^{(q)} = t_0 + q\Delta t_k$ with $q = 0, 1, 2, ...$ for $k \in \{m, o, g, d\}$.
6. Sort the times $t_k^{(q)}$ $\forall q, k$ in chronological order and select the list k according to the chronological order for processing.

7. Processing: Suppose that list k has been chosen. Set $t{=}t_k^{(q)}$. Choose cells from the list k in random order and perform the respective move trial k. Then remove the cell from the list. Continue this procedure until the list is empty. Each trial is assessed based on the Metropolis algorithm as in Schemes I and II.

The last algorithm III ensures, that the time intervals between each type of move trials (migration, growth, orientation change, growth, division, and death) is fixed, while in the former, only the average time interval between each type of move trials are fixed. Hence, although the average number of moves of each type is the same in all three algorithms, the variation in the time period between two moves of the the same cell in scheme I, or of the same type of move trial for the same cell in scheme II (e.g. two migration trials) are not the same. However, we found the results were largely robust against this modification of the update rules.

Note that the analogy with respect to the effective temperature k_BT between fluids and gases on one hand and F_T for cells on the other hand has to be taken with caution. F_T here is not a consequence of collisions between cells and fluid particles but reflects the ability of a cell to actively explore its environment in a random movement [1, 2]. So cells may actively control the parameter F_T. Moreover, the choice of the Metropolis algorithm which ensures detailed balance in the master equation is inspired by the observations in fluids and gases where the probability distribution of a system in equilibrium with fixed particle number coupled to a heat bath follows a canonical distribution [43]. For cells this cannot be expected. However, the results should be qualitatively the same if one assumes that the cell translations and rotations attempt to drive the system into an equilibrium state. This corresponds to the Le Chatelier principle which again cannot be assumed to be true *a priori* for cells. Cells sometimes can differentiate and in this way encounter external influences (e.g. epithelia under mechanical stress often thicken and do not become thinner). The use of the Monte-Carlo simulation method is motivated by the assumption that after each growth step all cells move to relax the configuration at least into a local equilibrium [9]. Within the simulations this has the consequence that the cell population relaxes stress and slightly expands if cell division is repressed (shown in [14]).

In order to speed up the simulations, the space is sub-divided into cubes of edge length $2l + 2d^c + \Delta$ with $\Delta \ll 1$ so that only neighboring cubes have to be checked for possible interaction partners. An efficient way to store cells within the cubes is by an array of pointers, one pointer per cube, where each pointer points to a linked list of those cells that are contained in the respective cube. The pointer on cells that cross the border between two neighboring cubes is moved from the old to the new list. In this way simulations with up to about $10^4 - 4 \times 10^5$ cells within 1-4 weeks computation time (depending on the choice of the parameters) are feasible.

Mathematical concepts: The master equation approach has been extensively studied for physical and chemical systems (e.g. [44, 43]) and even in traffic [45] and

ecology [46]. In physics it is very often used to study systems close to, or in, equilibrium. Moreover, concepts from chemical systems have been used to model cell growth and random movement by a single-particle master equation which represent a mean-field approach (e.g. [3, 10]) or a population (or chemical) master equation which considers collectively all cells (e.g. [47, 15]). The latter approach is suited as a starting point to derive a coarse-grained cell-density description of large scales by quantum-field theoretic methods which if stochastic cell density fluctuations are neglected lead for small cell densities to a Fisher-Kolmogorov-Petrovskii-Piskounov (FKPP)-equation, a partial differential equation for the local cell density (e.g. [47, 15]), or, if the stochasticity is taken into account to lowest order, to a stochastic FKPP-equation (e.g. [15]). However, a closer look shows that a classical population master equation does not permit the inclusion of some of the physical interactions properly which is why some important aspects of the expansion dynamics of cell clusters are not correctly captured in the limiting FKPP-equation, too [48].

The previously introduced Monte Carlo schemes I–III describe agent-based models and cannot be formulated in terms of chemical equations from which a population master equation may be derived in a straightforward manner. Nevertheless for the first Monte Carlo scheme an analogy to the situation that underlies a (compartmental) chemical master equation can be drawn that helps to set up a master equation for this scheme. Consider the example where each spatial compartment is so small that only two cells fit into it and where division is possible only within the same compartment (alternatively one may think of compartments where only one cell fits and where cell division is possible only into a neighbor compartment). In these cases a division within a compartment can occur only if one cell is already present in that compartment (and in the latter case if at least one neighbor compartment is not occupied). The division term in the corresponding population master equation is then $\sum_i \lambda(N_i - 1)p(N_i - 1, \hat{N}; t)$. The sum is formed over all cell divisions that may lead to a reference state $N = (N_1, N_2, ..., N_M)$ where N_i denotes the number of cells in compartment i and $(N_i', \hat{N})$ differs from state N by N_i' only. $\lambda = 1/\tau f(N_i)$ is the division rate which depends on the crowding effect denoted by $f(N_i)$ (a typical approach is $f(N_i) = (1 - N_i/N^{max})$ where N^{max} is the maximum number of cells which fit into a compartment, (see [15]). In the case where only two cells fit into a compartment and cell division is possible only within a compartment, then the transition rate $r_i = \lambda(N_i - 1)$ is non-zero only if $N_i = 2$ hence $r_i = \lambda = f(N_i)/\tau$.

We here consider a similar approach for cells with migration, growth and division (we omit cell death here, which, however, is easy to include). A cell i is characterized by its position $\underline{r}_i$, its axis length $|\underline{a}_i|$ (for formal reasons we write $\underline{a}_i$), and its orientation $\underline{\Omega}_i$. Be $\underline{y}_i = (\underline{r}_i, \underline{a}_i, \underline{\Omega}_i)$ a vector that characterizes the state of cell i. Be further $(\underline{Y}; N) = (\underline{y}_1, \underline{y}_2, \underline{y}_3, ..., \underline{y}_i, ..., \underline{y}_N)$ a (multi-)vector that denotes the state of a system of N cells. Be further $(\underline{x}_j', \hat{\underline{Y}_j}; N) = (\underline{y}_1, \underline{y}_2, ..., \underline{y}_{j-1}, \underline{y}_j', \underline{y}_{j+1}, ..., \underline{y}_N)$ be a (multi-)vector for which component x_j of cell j has the value $\underline{x}_j'$ with $\underline{x}_j' \in \{\underline{r}_j', \underline{a}_j', \underline{\Omega}_j'\}$ i.e. component $\underline{x}_j$ of $\underline{y}_j$ deviates from its value in $(\underline{Y}, N)$. For example, if $(\underline{r}_j', \hat{\underline{Y}_j}; N)$ denotes a state, in which the position vector of cell j is $\underline{r}_j'$,

and all other component vectors are as in $(\underline{Y};N)$. Analogously, $(\underline{y}'_j, \underline{\hat{Y}}_j;N)$ denotes a state where each of the components of cell j deviate from its state in $(\underline{Y};N)$. Be $w(\underline{Y},t;N)$ the probability density to find N cells in a configuration $\underline{Y} = \underline{y}_1, \underline{y}_2, ..., \underline{y}_N$, i.e., the probability density to find at time t N cells with one cell being at position $\underline{r}_1$, having orientation $\underline{\Omega}_1$, axis length a_1, another cell being at position $\underline{r}_2$, having orientation $\underline{\Omega}_2$, axis length a_2, etc. Then the master equation can be written

$$\begin{aligned}
&\frac{\partial w(\underline{Y},t;N)}{\partial t} = \\
&\sum_{k=1}^{N}\int_{\Gamma_1}\Pi^{(1)}(\underline{r}'_k \to \underline{r}_k)w(\underline{r}'_k,\underline{\hat{Y}}_k,t;N) - \Pi^{(1)}(\underline{r}_k \to \underline{r}'_k)w(\underline{Y},t;N)d\underline{r}'_k \\
&+\sum_{k=1}^{N}\int_{\Gamma_2}\Pi^{(2)}(\underline{\Omega}'_k \to \underline{\Omega}_k)w(\underline{\Omega}'_k,\underline{\hat{Y}}_k,t;N) - \Pi^{(2)}(\underline{\Omega}_k \to \underline{\Omega}'_k)w(\underline{Y},t;N)d\underline{\Omega}'_k \\
&+\sum_{k=1}^{N}\int_{\Gamma_3}\Pi^{(3)}(a'_k \to a_k)w(a'_k,\underline{\hat{Y}},t;N) - \Pi^{(3)}(a_k \to a'_k)w(\underline{Y},t;N)da'_k \\
&+\sum_{k=1}^{N-1}\int_{\Gamma_4}\Pi^{(4)}((N-1) \to N;\underline{y}'_k \to (\underline{y}_k,\underline{y}_N))w(\underline{y}'_k,\underline{\hat{Y}},t;N-1)dy'_k \\
&-\sum_{k=1}^{N}\int_{\Gamma_4}\Pi^{(4)}(N \to (N+1);\underline{y}_k \to (\underline{y}'_k,\underline{y}_{N+1}))w(\underline{Y},t;N)d\underline{y}'_k, \qquad (10)
\end{aligned}$$

where $\Gamma_1, ..., \Gamma_4$ denote the integration regions which are given by the possible values of step sizes for migration, orientation changes and growth, respectively. The first line of Eq.(10) describes moves, the second orientation changes, the third growth, and the last two lines describe cell division. The master equation shown permits only one cell division within one unit of time so is closest to scheme I. In case of synchronous or multiple cell divisions N can change by many cells, at most by N cell if all cells divide within one period of time. This complicates the master equation significantly.

Note that the position and orientation of the daughter cells depend on that of the mother cells. For example, if $(N-1) \to N$ by division of cell k, then $\underline{y}'_k = (\underline{r}'_k - Re_{\underline{\Omega}_k}, a_k = 0, \Omega_k)$, $\underline{y}'_N = (\underline{r}'_k + Re_{\underline{\Omega}_k}, a_k = 0, \Omega_k)$ i.e. the daughter cells are spherical. Cell division is only possible for those cells which have an axis length of $a = 2R$ (see below). The transition rates are

$$\Pi^{(1)}(\underline{r}'_k \to \underline{r}_k) = \frac{1}{T^{(1)}}e^{-\Delta V((\underline{r}_k,a_k,\underline{\Omega}_k)\to(\underline{r}'_k,a_k,\underline{\Omega}_k))/F_T}, \qquad (11)$$

for cell movement and

$$\Pi^{(2)}(\underline{\Omega}_k \to \underline{\Omega}'_k) = \frac{1}{T^{(2)}}e^{-\Delta V((\underline{r}_k,a_k,\underline{\Omega}_k)\to(\underline{r}_k,a_k,\underline{\Omega}'_k))/F_T}, \qquad (12)$$

for cell rotation. Here $\underline{r}_k$ denote the position of the cell k. For the step sizes $\Delta\underline{r} = \underline{r} - \underline{r}' = |\Delta\underline{r}|\underline{e}_{\Delta\underline{r}}$, $|\Delta\underline{r}| \in [0, \xi_m^{max})$ with $\xi_m^{max} \ll l$, and the unit vector $\underline{e}_{\Delta\underline{r}}$ is chosen due to an isotropic distribution (see section 3 for a description of how the step sizes are linked to the physical parameters). For the selection of the rotation

angles we choose the method by Barker and Watts (see [49]). This allows one to store the orientation of a cell as a vector. $T^{(1)}$ is the characteristic time between two "migration" events. The time for orientation changes $T^{(2)}$ will in general be different from $T^{(1)}$, but as long as $\mathbf{O}(T^{(1)}) \approx \mathbf{O}(T^{(2)})$, these differences leave the kinetics and the morphology almost unaffected [9].
For cell growth,

$$\Pi^{(3)}(a_k' \to a_k) = \frac{1}{T^{(3)}} e^{-\Delta V^{(3)}((\underline{r},a_k,\underline{\Omega})\to(\underline{r},a_k',\underline{\Omega}))/F_T}. \tag{13}$$

The growth step size $\Delta a_k = a_k' - a_k$ is uniformly distributed in $\Delta a_k \in [0, \xi_g^{max})$, with the condition that $\Delta a_k \leq 2R_k - a_k$ (see section 3 for a description of how the step sizes are linked to the physical parameters). In most cases we assumed that $V^{(3)}$ is a hard core repulsive potential energy where $V^{(3)}{=}\infty$, if the cell would be deformed stronger than the deformation threshold $(1-\zeta)l_i/2$, and $V^{(3)}{=}0$ otherwise.

If $a' = 2R$, the cell divides (last contribution to the master Eq.10) and a is reset to $a = 0$ for both daughter cells. The daughter cells of a cell k then have the positions $\underline{r}_k = \underline{r}_k - Re_{\underline{\Omega}_k}$ and $\underline{r}_N = \underline{r}_k + Re_{\underline{\Omega}_k}$, where $\underline{r}_k$ denotes the position of cell k immediately before the cell division.

$$\Pi^{(4)} = \frac{1}{T^{(3)}} \delta_{(\underline{r}_k, \underline{r}_k' - Re'_{\underline{\Omega}_k})} \delta_{(\underline{r}_N, \underline{r}_k' + Re'_{\underline{\Omega}_k})} \delta_{(a_k,0)} \delta_{(a_N',0)}. \tag{14}$$

Here, $\delta_{(x,x')}{=}1$ if $x{=}x'$ and zero otherwise. i.e., once a cell has passed through the mitotic phase (i.e. has axis length 2R) it divides into two daughter cells k, N both with axis length zero, one placed at position $\underline{r}_k{=}\underline{r}_k' - Re'_{\underline{\Omega}_k}$, the other at position $\underline{r}_N{=}\underline{r}_k' + Re'_{\underline{\Omega}_k}$ on a time scale $T^{(3)}$, the same time scale as the growth process.

2.3.2. Equations of motion for the cells. The idea is to set up an equation of motion for each individual cell. This equation of motion is generally stochastic. However, if the deterministic terms are much larger than the stochastic term, then the stochastic term can be dropped [18].

Migration: The movement of cells can be summarized in the following Langevin equation of motion for cell i, if hydrodynamic interactions between the cells due to the solvent(culture medium) are neglected when compared with direct interactions [16]:

$$\underbrace{\left(\gamma + \underline{\underline{\Gamma}}_{is}^{f}\right)\underline{v}^i}_{(1)} + \underbrace{\sum_{j\ nn\ i} \underline{\underline{\Gamma}}_{ij}^{f}\left(\underline{v}^i - \underline{v}^j\right)}_{(2)} = \underbrace{\sum_{j=0}^{N} \underline{F}^{ij}}_{(3)} + \underbrace{\underline{\eta}^i(t)}_{(4)}. \tag{15}$$

Here $\underline{v}^i = d\underline{x}^i/dt$ is the velocity, $\underline{x}^i$ the position of the center of cell i, γ denotes an effective friction coefficient that determines the speed of an isolated cell subject to an external force. Term (1) denotes cell-substrate friction, (2) cell-cell friction, (3) adhesive and repulsive forces between cells and cells and the substrate ($\underline{F}^{i0}$, where the substrate is approximated by a cell with index "0" and radius $R = \infty$), (4) denotes the random components of the cell movement. We have used the division algorithms (ii)

(illustrated in Fig.1B) for which we found that each proliferating cell spends most of its time in the spherical growth phase (and not in the dumb-bell-deformation phase) [16], and algorithm (iii) where cells remain spherically all the time [13]. For this reason we neglected rotations of dumb-bells by a torque. For spherical cells, $\underline{\underline{\Gamma}}^f_{iy} = \gamma_\parallel^{(iy)} \underline{n}_{iy}\underline{n}_{iy} + \gamma_\perp^{(iy)} \left(\underline{\underline{E}} - \underline{n}_{iy}\underline{n}_{iy}\right)$. Here $y = j$ denotes cell-cell, and $y = s$ cell-substrate interactions. $\underline{n}_{iy} = \frac{\underline{x}_y - \underline{x}_i}{|\underline{x}_y - \underline{x}_i|}$. $\underline{n}_{iy}\underline{n}_{iy}$ here denotes the dyadic product i.e. is a 3×3-matrix. $\gamma_\parallel^{(iy)}$ and $\gamma_\perp^{(iy)}$ are the parallel and perpendicular friction constants, respectively (for example, $\left(\underline{\underline{E}} - \underline{n}_{is}\underline{n}_{is}\right) \underline{v}$ is the projection of $\underline{v}$ onto a plane perpendicular to $\underline{n}_{is}$, so if $\underline{v} \perp \underline{n}_{is}$, then the friction is solely given by $\gamma_\perp^{(is)}$). To calculate $\underline{x}_i - \underline{x}_y$ if $y = s$ denotes a flat substrate, approximate the flat substrate by a sphere and consider the limit where the radius of the sphere diverges.

In (radially) expanding monolayers the velocity of neighboring cells is very similar due to the circular monolayer shape so that the friction between cells may be neglected and hence the sum on the lhs of Eq.(15) be dropped. The autocorrelation function of the noise is then $\langle \eta_m^i(t)\eta_n^j(t')\rangle = A_{ij}\delta_{ij}\delta_{mn}\delta(t-t')$. If the cell-cell friction is neglected in the autocorrelation function of the noise and if $\gamma_\perp^{(is)} = \gamma_\parallel^{(is)}$, then $A_{ii} = 2(\gamma + \gamma_\perp^{(is)})F_T$. If the cell-cell friction term is not neglected and if $\gamma_\perp^{iy} = \gamma_\parallel^{iy}$ for both, cell-cell and cell-substrate-friction (i.e., $y = j, s$), then $A_{ii} \approx 2(\gamma + \gamma_\perp^{(is)} + \sum_{j\ nn\ of\ i} \gamma_\perp^{(ij)})F_T$ if $\underline{v}_j \approx 0$ [13, 50], otherwise the autocorrelation functions for the noise for different cells do not decouple. Note that $\gamma_\parallel^{iy}$ and $\gamma_\perp^{iy}$ include the information about the contact area. By the Stokes friction one can relate the friction constants with the radius of the contact area and the viscosity of the medium. In colloidal particle physics, the diffusion constant and the friction coefficient are related by the Einstein relation $D = k_B T/\gamma$, a special case of the fluctuation-dissipation theorem. Beysens et al. [8] proposed an equivalent relation for cells which for cells in liquid suspension (so that $\gamma_\perp^{(is)} = \gamma_\parallel^{(is)} = 0$), and if cell-cell friction (term (2) in Eq.(15)) is small and can be neglected, is

$$D = F_T/\gamma, \tag{16}$$

where F_T is the previously introduced temperature equivalent in cellular systems. Thereby, F_T can be calculated from the friction coefficient and the diffusion constant. The fluctuation-dissipation theorem can analogously be formulated if the friction is characterized by matrices [51]. This has been used to determine the amplitude of the autocorrelation functions A for the special cases considered above. This relation links the Metropolis-method which is based on energy changes of the multi-cellular configuration to the Langevin description.

In order to move (migrate or crawl) the cells must exert forces on a substrate or a 3D extracellular matrix. The reaction of the matrix is not modeled. We rather assume that the substrate and the matrix are stiff enough so that their architecture is mainly unaffected by the cell migration. Moreover, friction coefficients are effective quantities and should be understood as parameters that reflect the response

of a cell to an external force rather than true friction. Correspondingly one may assume that the effective friction coefficients depend on the number of cell adhesion receptors and thereby link the effective friction coefficients to the cell-cell and cell-substrate adhesion forces in that both the effective friction coefficients and the adhesion forces may be proportional to the number of receptors [52]. Only if the migration is not active but really by pushing, then the coefficients reflect true friction. Such a pushing movement has been assumed in [52] for tumor spheroids and may, for example, be present in the hepatocyte walls of liver lobules (George Michalpopulus, priv. communication).

The miggration equation neglects memory effects and anisotropies [15]. A memory effect usually results in a memory kernel i.e. the velocity becomes dependent on values at previous times. This can be expressed by replacing $\underline{\underline{f}}\underline{v}_i \rightarrow \int_{-\infty}^{\infty} \underline{\underline{f}}(t-t')\underline{v}_i(t')dt'$, where $\underline{\underline{f}}$ represents the friction matrix $\{\underline{\underline{\Gamma}}^f_{is}, \underline{\underline{\Gamma}}^f_{ij}, \gamma\underline{\underline{E}}\}$ (the latter is the unit matrix) and $\underline{\underline{f}}(t-t')$ represents a memory kernel (a matrix) that will generally differ for cell-cell and cell-substrate friction. In the case where no memory effects are present $\underline{\underline{f}}(t-t') = \delta(t-t')\underline{\underline{f}}$ so that $\int_{-\infty}^{\infty} \underline{\underline{f}}(t-t')\underline{v}_i(t')dt' = \underline{\underline{f}}\underline{v}_i$. Sometimes persistence effects where cells tend to maintain a chosen direction are modeled as inertia terms $\propto M_i d\underline{v}_i/dt$ which should be interpreted rather as an effective inertia term in which M_i is not interpreted as the cell mass (which would be so in the case of true inertia). The more proper description is by a memory term. True inertia effects in cell movement can be neglected since the Reynolds numbers are small [53].

In the case of either an anisotropic potential energy, which may occur, for example, for polar cells, or for non-spherical objects, such as dumb-bells, the inclusion of rotations may be essential. Then, a moving cell that collides with another cell may not only affect the position the other cell but may also cause this cell to change orientation by exerting a torque [15]. Usually, however, migration of cells is active rather than passive and an orientation change of a cell rather is a shape change that approximately has the same effect as if the cell would have rotated [54].

If memory effects are neglected, standard schemes for the numerical solution of stochastic ordinary differential equations such as the Euler or Heun method maybe used [55]. The limiting step usually is the solution of large matrices that occur since the $3N$ coupled differential equations (for N cells) are solved synchronously. With increasing system size N we find that the Metropolis algorithm is increasingly faster than the numerical solution of the Langevin equations (Hoehme, Drasdo, unpublished).

We use the cell diameter l as a reference length scale, the intrinsic cell cycle time τ as a reference time scale and F_T as a reference energy scale. As in the MC-simulation, growth is modeled by a deformation of the cell into a dumb- bell by small stochastic increments $\ll l$ (Fig.1).

2.4. Cell growth: explicit cell volume control

In most of our simulations we assume that cells stop growing if the distance of a cell to at least one neighbor becomes smaller than a certain threshold. We found that whether we assume that the deformation or compression must last for a longer period of time [14], or whether we make the decision of the cell to either stop in the restriction point, a cell cycle check point at the end of the first cell cycle sub-phase (G_1), or to re-enter the proliferating phase dependent on the state of deformation or compression at the restriction point, does not affect the qualitative multi-cellular growth kinetics (Drasdo and Hoehme, unpubl.). However, in this case one must set $d_{HC} < \zeta l$ so the condition for stopping growth becomes $d_{ij} < \zeta l$. If cells, once they have passed the restriction point, grow and divide with probability one, then the length distribution of the cell cycle time is a Γ-distribution for all proliferating cells that is, independent of whether cells in the population are contact-inhibited or not. On the other hand, if growth can be repressed at any time in the cell cycle, the precise shape of the (still) Γ-(like-)distribution depends on the fraction and location of contact-inhibited cells [14].

Consider the former case (growth stop only in the restriction point). Then for growth algorithm I(i) the dumb-bell axis $a(t)$ changes according to

$$a(t+\Delta t) \;=\; \begin{cases} a(t) + \int_t^{t+\Delta t} \xi(t')dt', & \text{if} \quad a(t+\Delta t) < 2R, \\ 2R & \text{else.} \end{cases} \tag{17}$$

Here, $\xi(t')$ is a random number uniformly distributed in the interval $[0, 2v_a)$ with mean value $\langle \xi(t') \rangle = v_a$ (such that $a(t) \leq 2R$). The above models do not distinguish between isotropic and anisotropic compression that is, between a cell that is circumvented by other cells and a cell that is at the border of a cell cluster. One way to do this is to define a pressure on cell i by $P_i = \sum_{jnni} \frac{|\underline{F}_{ij}|\underline{n}_{ij}}{A_{ij}}$ with $\underline{n}_{ij} = (\underline{r}_j - \underline{r}_i)/|\underline{r}_j - \underline{r}_i|$ and re-press division if P_i overcomes a threshold value [52]. Another way is to explicitly introduce a dynamical equation for the cell volume that permits direct monitoring of the degree of compression of a cell [12, 13]. Assuming that the cells are intrinsically spherical, the volume is $V \propto R^3$.

A simple effective way to include the effect of surrounding cells on the volume of an interior cell is to change the radius of a cell depending on its compressibility on the one hand and the forces exerted on the cell by its neighboring cells on the other hand. An approximative description may be given by [13]:

$$\underbrace{\left(b + B_{cs}^f\right) u^i}_{(1)} + \underbrace{\sum_{j\ nn\ i} B_{cc}^f \left(u^i - u^j\right)}_{(2)} = \underbrace{\sum_{j=1}^{N} F^{ij}}_{(3)} + \underbrace{\tilde{\eta}^i(t)}_{(4)}. \tag{18}$$

Note the analogy to equation (15). Here, $u_i = dR_i/dt$, B_{cs}^f, B_{cc}^f and b are scalar friction coefficients with the substrate, the neighbor cell, and inner friction, respectively. A reasonable choice is $B_{cs}^f = \gamma_{\parallel}^{cs}$, $B_{cc}^f = \gamma_{\parallel}^{cc}$, where b is the cell-internal friction. F^{ij} is a generalized force and may be defined by $F^{ij} = -dV_{ij}/dR_i$. Stochastic radius fluctuations maybe neglected [13]. As shown in ref. [13], this effective

description yields a reasonable qualitative description of the growth process which includes cell volume control.

3. Link between the model and experimental parameters

Here we denote how the cycle time and the diffusion constant are linked to the step sizes in the Metropolis algorithm-approach. The model parameters, not specified so far (the step sizes for migration, growth and the number of migration and rotation trials between two successive growth trials), are linked to literature parameters in the following way:

(1.) *time interval*:

$$\tau = \frac{n_g l \Delta t}{\delta a_{max}/2} = \frac{n_g l \Delta t}{\delta a_{max}/2} \Rightarrow \Delta \hat{t} \equiv \frac{\Delta t}{\tau} = \frac{\delta \hat{a}_{max}}{2 n_g}. \tag{19}$$

(2.) *Diffusion constant*:

$$\hat{D} = \frac{\langle (\delta \hat{\underline{r}})^2 \rangle}{2d\Delta \hat{t}} = \frac{(k \hat{\xi}^2_{max})}{(2d\Delta \hat{t})} \tag{20}$$

Here, $\hat{D}{=}D\tau/l^2$ is the dimensionless diffusion constant, $k{=}2/5$ in $d{=}3$, and $k{=}1/2$ in $d{=}2$. $l{=}2R$.

The parameters have been determined as follows.

(i) The diffusion constant D, the cell diameter l and the cycle time τ have been chosen to be typically $D \approx 1.3 \times 10^{-11} cm^2/s$ and $\tau \approx 19h$ (Bru, priv. commun.).

(ii) Eq.(19) is inserted into Eq.(20).

(iii) The parameters $\delta \hat{a}_{max} \ll 1$ (≈ 0.02) and $n_g \gg 1$ are chosen, which, together with D, determine $\hat{\xi}^2_{max}$. $\hat{\xi}_{max}(\delta a_{max}, n_g, \hat{D})$ was chosen sufficiently small ($\ll 1$) in order to obtain a linear velocity-force relationship (i.e., increasing the applied force by a certain factor increases the migration velocity by the same factor). In case of purely active movement, the speed of the intracellular re-organization processes is expected to limit the migration velocity which we assume is not the case for the migration velocities considered here. Notice also, that the choice of $\delta \hat{a}_{max}$ and n_g, together with τ also determines $\Delta \hat{t}$, which denotes the period of time between two successive move trials.

4. Results

4.1. Basic growth scenarios in monolayer cultures

We here focus on monolayer cultures to illustrate our simulation model. First we consider the example of a mono-clone growing on a flat substrate. We use the model described by the assumptions I(i), II(i), III(i), IV(i), V(ii), VI. We use the Metropolis-method III(i) according to scheme III and assume that cell-cell and cell-substrate adhesioncell!adhesion are of comparable size [16]. The simulation result is shown in Fig.3. Note, that the cells can freely proliferate until a cell population size of $N \approx 1000$ is reached. Accordingly, N grows exponentially fast until this population size (Fig.4(a)). For sufficiently large population sizes

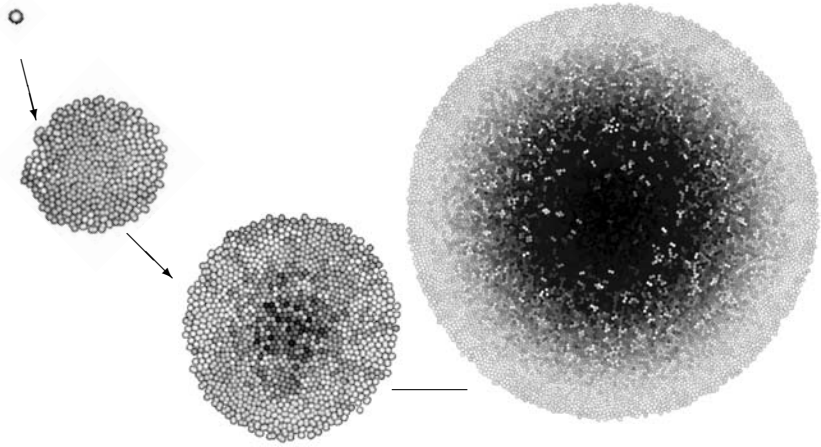

FIGURE 3. Typical monolayer growth scenario. Shown are snapshots at $N = 1$, 250, 1000, 12500 cells, respectively. The lighter the cells the shorter is their cell cycle time. Until $N \approx 1000$ cells all cells can proliferate. For larger population sizes, however, the cell proliferation is increasingly limited on a boundary layer of finite size. Accordingly, until about 1000 cells the population grows exponentially fast while for larger populations sizes where proliferation is limited to a proliferating rim, the monolayer diameter is found to grow linearly (see Fig.4). Color picture at the end of the book.

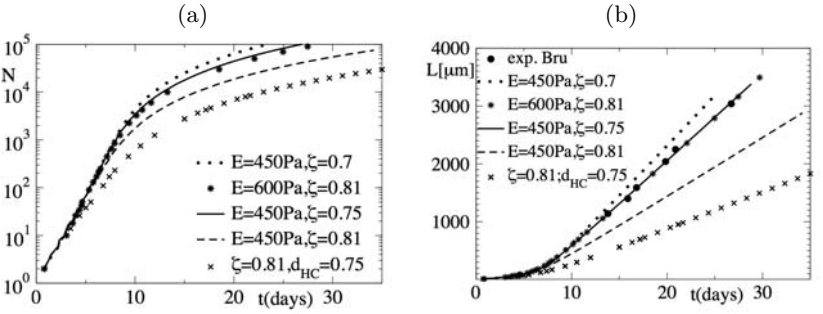

FIGURE 4. Growth kinetics for monolayer. (a) Population size N vs. time t, (b) diameter L vs. t. The filled circles denote experimental results by Bru [56]. The simulations that fit the experimental data show a proliferation pattern as that shown in Fig.3. We have varied the growth threshold ζ, the Young modulus E and the relation between growth threshold ζ and hard core radius, d_{HC}. The lowest curve have $E = 450Pa$, $\zeta l = 0.81 > d_{HC} = 0.75$ while in all other curves, $\zeta = d_{HC} l$.

the growth curve crosses over into a sub-exponential growth regime. In the sub-exponential growth regime, the monolayer diameter L grows linearly (Fig.4(b)). As shown in the figure, the simulation results agree quantitatively with published data

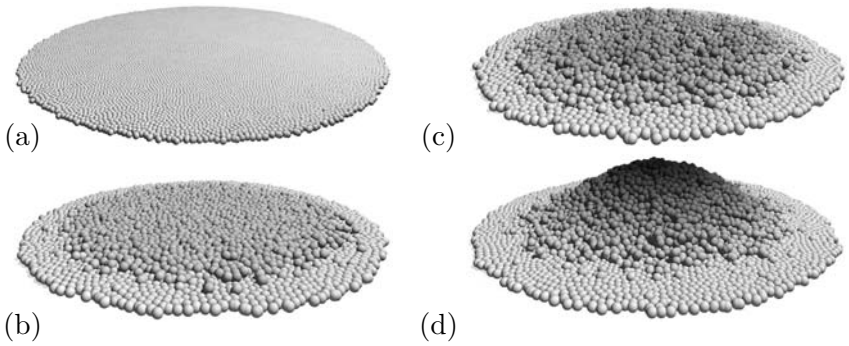

FIGURE 5. Simulated knockout of growth control mechanisms [16]. The color indicates the distance from the substrate. (a) A perfect monolayer forms if contact inhibition of growth, anchorage-dependent growth control and anchorage-dependent apoptosis all function normally. (b) In the absence of contact inhibition of growth some cells are pushed out of the basal layer but do not divide and are eliminated by anoikis. (c) Even if in addition anchorage-dependent growth is switched off still a quasi-monolayer is formed due to anoikis. (d) Only if also anoikis is switched off, a multi-layered cell aggregate forms. A piling up as in (d) can be observed for example in WiDr-cell lines. See also simulations MovIII.1.1 and MovIII.1.2 from the accompanying DVD. (Color picture at the end of the book.)

on growing C6 rat astrocyte glioma cells [56]. For monolayers, we found $N \propto L^2$ over the whole range [14, 16]. If the threshold for contact inhibition ζ is increased so that contact inhibition occurs a smaller deformations then the exponential phase becomes shorter and the growth velocity of the diameter in the regime where L grows linearly decreases. An increase of Young modulus E has the opposite effect since the force necessary to cause the same deformation increases with increasing stiffness E. If the hard-core repulsion which reflects the limited compressibility sets in at larger deformations than the contact inhibition of growth, that is, if $d_{HC} < \zeta l$, then the growth becomes slower. The reason for this behavior is that a re-entrance into the cell cycle according to assumption IV(i) is unlikely in the case of $d_{HC} < \zeta l$ while if $d_{HC} = \zeta l$, random fluctuations of the cell configuration can result in further growth.

Normal and some transformed cell lines such as C6 astrocyte glioma and HCT 116 cells form almost perfect monolayers. However, some cell lines such as WiDr cells, a colon cancer cell line, piles up at a certain population size. To study which mechanism may lead to a piling up we successively knock out growth control mechanisms that have been found to limit uncontrolled growth in populations of normal cells. Besides contact inhibition of growth these are anchorage-dependent proliferation where normal cells grow and divide only if they have substrate contact, and anchorage dependent apoptosis (anoikis) where cells die about 4–6 hours after they lose substrate contact. In Fig.5 we show a scenario where these three growth control mechanisms have successively been knocked out [16].

FIGURE 6. Comparison of the simulation result on growing cell populations on a flat substrate in the absence of contact inhibition of growth, anchorage-dependent growth control and anoikis (case (d) in Fig.5) between the JKR model (Fig.5) and the Hertz model [16]. Red: Hertz model, blue: JKR-model, violet: overlap. The hysteresis behavior causes the cells to detach slower in the JKR than in the Herz model even though all material parameters where the same. Compare the colour figure at the end of the book.

4.2. Model variants

We have studied the robustness of the simulated phenomena by a number of model variations. We discuss some examples here and further examples can be found in refs. [13, 16]. For simulations of expanding perfect monolayers we found almost no difference for the different forms of cell-cell interaction potential energies if the same material parameters were chosen. However, in the piling-up-simulations, the hysteresis effect of the JKR-model delays the detachment of cells from the substrate compared to the Hertz model although the simulations for the perfect monolayers did not show any differences (Fig.6, [16]). On the other hand, the qualitative growth scenarios are the same for both interaction types. Also if in addition to the change of the interaction energy from JKR into Hertz model the cell volume is explicitly controlled using Eq.(18), the same qualitative growth scenario is found.

Whether the Metropolis algorithm may be used for simulations of the multicellular dynamics or Langevin equations of motion should be used for the simulation of the multi-cellular dynamics is an open question. In Fig.7 we show an example of model simulations with both models (scheme III of the Metropolis algorithm vs. Eq.(15)) where the same parameter set for both simulation methods have been used. The differences between the simulations with both methods are very small and within the range of a change of cell division algorithm I(i) to I(ii) (Fig.7, [16]). For the data set chosen, the difference is very small and can probably be reduced further if the step sizes in the Metropolis-algorithm are reduced.

5. Discussion

In this chapter we have given an introduction to and overview of the basic model versions of center-based models to individual cells in some algorithmic and mathematical detail. The term "center-based" may be used to denote that the interaction is mainly defined between the neighboring centers of adjacent cells. To illustrate a basic model and alternative model variants we considered the example of cell populations growing on a flat substrate. We have shown that the framework of colloidal particles is largely suited to model multi-cellular growth phenomena by

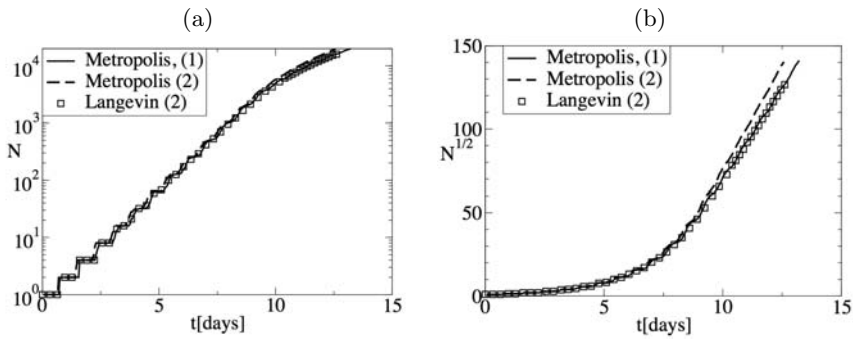

FIGURE 7. Comparison between a Langevin-equations-based simulation and a Monte Carlo simulation using the Metropolis algorithm and scheme III for one parameter set [16]. Shown is the population size $N(t)$ in (a) a lin-log-plot of N vs. t and (b) a plot of $N^{1/2}$ vs. t. (1) denotes the cell division algorithm of Fig.1(a), (2) the cell division algorithm in Fig.1(b). The simulations start with one cell. The stair cases in (a) reflect the initial synchronization which is lost with increasing number of cell divisions. Note that $N \propto L^2$ so $N^{1/2} \propto L$.

only moderate model extensions. We here focused on the cell kinetics, proliferation pattern and morphology of the cell populations in case of perfect one-cell-thick monolayers and in the case of a piling up occurring as a consequence of knockouts that affect the growth control mechanisms. The model show a very good agreement with published data. By a change of model parameters predictions are obtained that can be tested experimentally and thus permit the validation of the model. We have shown, for example, that a reduction in the sensitivity to contact inhibition of growth leads to a longer exponential growth phase and subsequently to a larger (constant) monolayer diameter growth velocity.

We have illustrated that the results do not depend on whether the Metropolis algorithm (for which we have shown the corresponding master equation) or a Langevin dynamic is used. So in other words, whether the time development of the probability distribution for the whole multi-cellular configuration is considered (the multi-particle master equation) or the trajectory of each individual cell is investigated using a Langevin equation of motion, did almost make no difference for the parameter set chosen [16].

We have used the models to analyze multicellular processes in multi-cellular spheroids [17, 14, 16], intestinal crypts [18, 19] and developmental biology [20, 21, 16]. In multi-cellular spheroids, glucose and oxygen penetrate into the tumor and this is different from monolayers since not all cells have contact to the growth medium. The glucose diffusion and consumption can be simulated by a reaction-diffusion equation [14, 52, 16]. Intestinal crypts form one-cell-thick pockets in the intestinal wall which are responsible for the fast cell-turnover of the intestine [57]. Blastula formation and gastrulation belong to the earliest stages

in animal development and denote the process from the zygote (single cell) to a hollow sphere (blastula) which invaginates (inward budding) to become a gastrula [58]. In some species the blastula and the gastrula are one-cell thick. In order to maintain one-cell-thick structures the effect of a stabilizing membrane layer (hyaline layer in the case of blastula formation) and the polarity of the cells have to be taken into account. This can be done either by explicitly considering bending and shear energy contributions in addition to the isotropic interaction energy contribution in this article or by consideration of anisotropic interaction potential energies [20, 21, 18, 16, 19].

For very large population sizes it is often sufficient to consider further abstractions of the models considered here, namely, cellular automaton (CA) models in which a single cell is identified with a node on a lattice. Such CA models are rule-based and do not represent a direct physical description of a model but the computation time is significantly shorter which is why they may facilitate a systematic parameter sensitivity analysis of growing monolayers or tumors or forming ensemble averages over many realization of a pattern formation process which is usually not possible for off-lattice models [48]. Often, the rules can well be chosen from a careful analysis of the biological system as explained by the chapters of Anderson and Deutsch in this book, or the rules and parameters of the cellular automaton model can be linked to the parameters of the off-lattice model [15]. The cellular automaton model sometimes provides an easier starting point to set up continuum equations for cell densities which are particularly suited for exploring the pattern formation and growth processes of even larger multicellular systems of billions of cells which is usually not accessible for single-cell-based models.

Still, the models considered here may fail to give a correct description of the multi-cellular dynamics if cells deform largely during the pattern formation or growth processes. In this case the cell shape may further be parameterized (see contributions by Dallon and Palsson in this book) or the cell may be represented by sub-elements either on the lattice (see contributions by Glazier and Hogeweg in this book) or in lattice-free space (see contribution by Newman in this book).

Acknowledgment

I thank Stefan Hoehme for his help in the preparation of Figs. 3, 5, 6 and acknowledge support by the DFG-grant BIZ 6-1/1 and BMBF-grant Hepato-Sys project 0313081.

References

[1] M. Schienbein, K. Franke, and H. Gruler: *Random walk and directed movement: comparison between inert particles and self-organized molecular machines*, Phys. Rev. E **49**, 5462 (1994).

[2] J. Mombach and J. Glazier: *Single cell motion in aggregates of embryonic cells*, Phys. Rev. Lett. **76**, 3032 (1996).

[3] H. Othmer and A. Stevens: *Aggregation, blowup and collapse: The abc's of generalized taxis in reinforced random walks*, SIAM J. Appl. Math. **57**, 1044 (1997).

[4] E. Palsson and H. Othmer: *A model for individual and collective cell movement in dictyostelium discoideum*, Proc. Natl. Acad. Sci. USA **12**, 10448 (2000).

[5] A. Stevens: *The derivation of chemotaxis equations as limit dynamics of moderately interacting stochastic many-particle systems*, SIAM J. APPL. MATH. **61**, 183 (2000).

[6] Y.-S. C. et. al.: *Johnson-kendall-roberts theory applied to living cells*, Phys. Rev. Lett. **280**, 312 (1999).

[7] R. Carpick, D. F. Ogletree, and M. Salmeron: *A gerneral equation for fitting contact area and friction vs load measurements*, J. Colloid and Interface Sci **211**, 395 (1999).

[8] D. Beysens, G. Forgacs, and J. Glazier: *Cell sorting is analogous to phase ordering in fluids*, Proc. Natl. Acad. Sci. USA **97**, 9467 (2000).

[9] D. Drasdo, R. Kree, and J. McCaskill: *Monte-carlo approach to tissue-cell populations*, Phys. Rev. E **52**, 6635 (1995).

[10] D. Drasdo: *Different growth regimes found in a monte-carlo model of growing tissue cell populations*, in *Self organization of complex structures: From individual to collective dynamics*, edited by F. Schweitzer (Gordon and Breach, 1996), pp. 281–291.

[11] D. Drasdo: *A monte carlo approach to growing solid non-vascular tumors*, in *Networks in Biology and Physics*, edited by G. Forgacs (Springer, Berlin Heidelberg New York, 1998), pp. 171–185.

[12] J. Galle, M. Loeffler, and D. Drasdo: *On the temporal-spatial organization of epithelial cell populations in-vitro.*, in *Mathematical Modelling & Computing in Biology and Medicine*, edited by V. Capasso (Marcel Dekker Inc, 2003), pp. 375 – 385.

[13] J. Galle, M. Loeffler, and D. Drasdo: *Modelling the effect of deregulated proliferation and apoptosis on the growth dynamics of epithelial cell populations in vitro*, Biophys. J. **88**, 62 (2005).

[14] D. Drasdo and S. Hoehme: *A single-cell based model to tumor growth in-vitro: monolayers and spheroids*, Physical Biology **2**, 133 (2005).

[15] D. Drasdo: *Coarse graining in simulated cell populations*, Adv. Complex Syst. **8**, 319 (2005).

[16] D. Drasdo, S. Hoehme, and M. Block: *On the role of physics in the growth and pattern formation of multi-cellular systems: What can we learn from individual-based systems?*, J. Stat Phys. (in press).

[17] D. Drasdo and S. Höhme: *Individual-based approaches to birth and death in avascular tumors*, Math. and Comp. Modelling **37**, 1163 (2003).

[18] D. Drasdo and M. Löffler: *Individual-based models on growth and folding in one-layered tissues: Intestinal crypts and blastulation*, Nonl. Anal. **47**, 245 (2001).

[19] J. Galle, G. Aust, G. Schaller, T. Beyer, and D. Drasdo: *Single-cell based mathematical models to the spatio-temporal pattern formation in multi-cellular systems*, Cytometry 69A, 704–710 (2006)

[20] D. Drasdo and G. Forgacs: *Modelling the interplay of generic and genetic mechanisms in cleavage, blastulation and gastrulation*, Dev. Dyn. **219**, 182 (2000).

[21] D. Drasdo: *Buckling instabilities in one-layered growing tissues*, Phys. Rev. Lett. **84**, 4244 (2000).

[22] H. Eagle: *Nutriention needs of mammalian cells in tissue culture*, Science **122**, 43 (1955).

[23] R. Ham: *Clonal growth of mammalian cells in a chemically defined, synthetic medium*, Proc. Natl. Acad. Sci. **53**, 288 (1965).

[24] I. Hayashi and G. Sato: *Replacement of serum by hormones permits growth of cells in defined medium*, Nature **239**, 132 (1976).

[25] G. Sato, A. Pardee, and D. Sirbasku: *Growth of Cells in Hormonally Defined Media* (Cold Spring Harbour Laboratory, 1982).

[26] B. Alberts, A. Johnson, J. Lewis, M. Raff, K. Roberts, and P. Walter: *The Cell* (Garland Science Publ., New York, 2002).

[27] D. Drubin and W. Nelson: *Origins of cell polarity*, Cell **84**, 335 (1996).

[28] DSMZ: *German collection of microorganism and cell cultures*, http://www.dsmz.de/

[29] G. Forgacs and S. Newmann: *Biological Physics of the Developing Embryo* (Cambridge University Press, Cambridge, 2005).

[30] P. Rosen and D. Misfeldt: *Cell density determines epithelial migration in culture*, Proc. Natl. Acad. Sci. **77**, 4760 (1980).

[31] N. Metropolis, A. Rosenbluth, M. Rosenbluth, A. Teller, and E. Teller: *Equation of state calculations by fast computing machines*, J. Chem. Phys. **21**, 1087 (1953).

[32] M. Seinberg: *Reconstruction of tissues by dissociated cells*, Science **141**, 401 (1963).

[33] M. Pfeiffer: *Birds flock together*, Nature **395**, 324 (1998).

[34] S. Huang and D. Ingber: *The structural and mechanical complexity of cell-growth control*, Nature Cell Biol. **1**, E131 (1999).

[35] L. Davidson, M. Koehl, R. Keller, and G. Oster: *How do sea urchins invaginate? Using bio-mechanics to distinguish between mechanisms of primary invagination*, Development **121**, 2005 (1995).

[36] M.Lekka, P.Laidler, D.Gil, J.Lekki, Z.Stachura, and A.Z.Hrynkiewicz: *Elasticity of normal and cancerous human bladder cells studied by scanning force microscopy*, European Biophysics Journal **28**, 312 (1999).

[37] R. Mahaffy, C. Shih, F. McKintosh, and J. Kaes: *Scanning probe-based frequency-dependent microrheology of polymer gels and biological cells*, Phys. Rev. Lett. **85**, 880 (2000).

[38] J. Alcaraz, L. Buscemi, M. Grabulosa, X. Trepat, B. Fabry, R. Farre, and D. Navajas.: *Microrheology of human lung epithelial cells measured by atomic force microscopy*, Biophys. J. **84**, 2071 (2003).

[39] S. Chesla, P. Selvaraj, and C. Zhu: *Measuring two-dimensional receptor-ligand binding kinetics by micropipette*, Biophys. J **75**, 1553 (1998).

[40] J. Piper, R. Swerlick, and C. Zhu: *Determining force dependence of two-dimensional receptor-ligand binding affinity by centrifugation*, Biophys. J. **74**, 492 (1998).

[41] D. Landau: *Theory of elasticity* (Pergamon, 1975).

[42] H. Hertz: *über die berührung fester elastischer körper (on the contact of elastic solids).*, J. Reine Angewandte Math. **92**, 156 (1882).

[43] D. Landau and K. Binder: *A Guide to Monte Carlo Simulations in Statistical Physics* (Cambridge University Press, 2000).

[44] Gardiner: *Handbook of Stochastic medthods* (Springer, New York, 1990).

[45] D. Helbing: *Traffic and related self-driven many particle systems*, Rev. Mod. Phys. **73**, 1067 (2001).

[46] F. Schweitzer: *Brownian agents and active particles* (Springer, Berlin, Heidelberg, 2003).

[47] D. Elderfield: *Field theories for kinetic growth models*, J. Phys. A: Math. Gen. **18**, L773 (1985).

[48] M. Block, E. Schoell, and D. Drasdo: *Classifying the expansion kinetics and critical surface dynamics of growing cell populations*, Cond. mat. **physics/0610146** (2006).

[49] M. Allen and D. Tildersley: *Computer Simulation of Liquids* (Oxford Science Publ., Oxford, 1987).

[50] J. Dhont: *An Introduction to Dynamics of Colloids* (Elsevier, Amsterdam, 1996).

[51] H. Oettinger: *Stochastic Processes in Polymeric Fluids* (Springer, Berlin Heidelberg, 1993).

[52] G. Schaller and M. Meyer-Hermann: *Multicellular tumor spheroid in an off-lattice voronoi-delaunay cell model*, Phys. Rev. E. **71**, 051910 (2005).

[53] G. Odell, G. Oster, P. Alberch, and B.Burnside: *The mechanical basis of morphogenesis*, Dev. Biol **85**, 446 (1981).

[54] I. Bischofs and U. Schwarz: *Cell organization in soft media due to active mechanosensing*, Proc. Natl. Acad. Sci. (USA) **100**, 9274 (2003).

[55] J. Honerkamp: *Stochastic Dynamic Systems* (Wiley, 1993).

[56] A. Bru, J. Pastor, I. Fernaud, I. Bru, S. Melle, and C. Berenguer: *Super-rough dynamics of tumor growth*, Phys. Rev. Lett. **81**, 4008 (1998).

[57] C. Potten and M. Loeffler: *Stem cells: attributes, cycles, spirals, pitfalls and uncertainties. lessons for and from the crypt*, Development **110**, 1001 (1990).

[58] S. Gilbert: *Develoment* (Sinauer Associates Inc., New York, 1997).

Dirk Drasdo
French National Institute for Research in Computer Science and Control (INRIA),
Rocquencourt, B.P. 105, 78153 Le Chesnay Cedex, France [1]
and
Mathematics Institute and Center for Systems Biology,
University of Warwick, Coventry CV4 7AL, UK
and
Interdisciplinary Centre for Bioinformatics, University of Leipzig,
Härtelstr. 14-16, D-04107 Leipzig, Germany
e-mail: dirk.drasdo@inria.fr

[1] permanent address

Single-Cell-Based Models in Biology and Medicine
ed. by A.R.A. Anderson, M.A.J. Chaplain, K.A. Rejniak
Mathematics and Biosciences in Interaction, 197–219

III.2 Models with Lattice-free Center-based Cells Interacting with Continuum Environment Variables

John C. Dallon

Abstract. In this chapter we describe a discrete continuum hybrid method applied to two biological systems. The cells are modeled as discrete objects which are free to move in space (lattice-free), the forces which act on the cells are applied to their center of mass (center-based), and the cells interact with something represented as a continuum variable. Dictyostelium discoideum is the first system modeled by the method. The cells move and communicate with each other through a diffusible chemical. In the second system, scar tissue formation, the cells interact with the extracellular matrix which is represented as a continuous vector field.

1. Introduction

Since the time of Newton, continuum mathematical models have been used to describe the behavior of what we believe to be fundamentally discrete physical systems. As a result, much time and effort has been spent in justifying these continuum formulations with methods from statistical mechanics by using the fundamental properties, including the discreteness of the system, to derive the models. In an ironic twist due to the advent of computers, these continuum models of discrete systems are frequently approximated by discrete models which can be solved numerically. As computers have become more powerful, there has been renewed interest in models maintaining a discrete formulation from the outset.

In this chapter we describe a discrete and continuum hybrid method applied to biological systems. The method is ideal for understanding macroscopic behavior of discrete systems interacting with continuum systems or a system with a much smaller space scale. For example, the applications given here are cells interacting with a diffusible chemical and cells interacting with non diffusing proteins which form an extracellular matrix. In both cases the discrete system of cells has a much larger space scale, on the order of microns, than the systems with which they interact, the diffusible chemical and the non diffusible proteins. The first of these applications models the early aggregation of the cellular slime mold *Dictyostelium*

discoideum (Dd) [7] and the second models the process of collagen production and alignment during wound healing [9]. For a discussion focused on the numerical scheme and implementation and less on the applications see [6].

When deciding how to model a system one must determine what modeling framework to use. A fundamental issue is whether to use a discrete representation, a continuous representation or some mixture of the two. This is resolved by examining the strengths and weaknesses of the different representations in the context of why the model is being developed. Continuum models are more commonly used and, perhaps as a consequence, the mathematical techniques to analyze them are readily available. Thus if the goal of the model is to understand stability, bifurcations or other general qualitative features of the system, a continuum approach will yield more insight. If on the other hand, a more quantitative model is desired with specific questions relating to local interaction, such as how the interactions of individual cells influence the system, a discrete approach may be more appropriate. Of course there are many other questions to consider. Is there a natural discrete structure to the system? Is the phenomenon being modeled a macroscopic or microscopic one? Are the interactions causing the phenomenon local or global? Are the densities such that a continuum is realistic? How is the model going to be understood analytically – through simulations or in some other way? An example of the importance of modeling approach is provided by Durrett and Levin [12] who compare four different modeling approaches for the same biological system: a spatially homogeneous model, a reaction diffusion formulation, and two models with discrete spatial structures. They find that in some circumstances the models give different results, indicating the importance of how the model is formulated.

In this book, several types of cellular models are discussed. Some have variables that are defined on a fixed lattice, an array of discrete fixed sites connected to each other so that they have well defined neighbors, or as discrete particles which are allowed to move freely in the domain. In this section and chapter, the cells are not constrained to move on a lattice and thus are called lattice-free models. Although the discrete system representing the cells does not use a lattice, in this chapter the smaller space scaled system which interacts with the cells will be represented for numerical purposes on a lattice. Of course alternate implementations of the models could solve the systems in different manners. A useful analogy can be made with two different views frequently used in fluid dynamics: Eulerian, fixed spatial coordinates, and Lagrangian, coordinates which move with the fluid. Although in that context these views are applied to continuum models, here we apply them to discrete modeling methods.

The first viewpoint, Eulerian, gives rise to most of the discrete modeling, in which a fixed lattice is defined. These lattice based models include the process mentioned above of numerically solving continuum models by discretizing the domain and solving the equations based on finite differences. Here the discrete structure is imposed for numerical reasons and is not motivated by the physical system, which was originally modeled with a continuum method. In essence, these discrete computational schemes model mathematical equations and only indirectly

represent the physical system. This contrasts with another group of models where an underlying discrete physical structure motivates the lattice based modeling approach. These models, while discrete in space, use continuous time variables. Typically they give rise to a large number of coupled ordinary differential equations and are commonly used in solid state physics where the crystalline structure of the material defines a natural physical lattice. The discrete nature of the models along with nonlinear interactions can give rise to solutions which are not possible in their continuum counterparts [31].

The second viewpoint which can be taken in discrete modeling is a Lagrangian view of tracing particles which are unconstrained in the domain. In these models, usually numerical treatments of continuum models, if a grid is defined, it is defined by particle positions which change as the particles move. This gives a major disadvantage if the particles' motion with respect to its neighbors is great. The mesh deforms and particles which started as nearest neighbors are no longer close. If near neighbor interactions are important the solutions will become numerically unstable. To correct this, remeshing is employed or, more typically, hybrid numerical methods of the Lagrangian and Eulerian views are used. In the hybrid numerical method particle-in-cell, the moving or Lagrangian particles define only nodes and not a mesh, eliminating the problem. Originally the particles in this method carried mass and as they moved from one grid cell to another they transferred mass, momentum, and energy to different parts of the Eulerian grid. It was on the fixed grid which defined the computational cells where the average values of velocity, pressure, energy and other quantities were calculated. The method has evolved into a group of particle-mesh methods commonly used in physics and chemistry to solve models of plasmas, fluid flow, and combustion problems [29, 15, 20]. In these methods there is both a fixed (Eulerian) grid and moving (Lagrangian) particles. The field quantities are typically solved on the fixed grid and the particle properties remain with the particles. In plasma flow, this means the charges are located with the particles and the electric field is solved on the fixed grid. For combustion models, the convection current is solved on the fixed grid and the reacting particles are solved using the moving particles. For the models discussed in this chapter, we adapt this technique and apply it to a modeling method which mixes continuum and discrete variables. We numerically solve the continuum variables on a fixed grid using finite differences and allow the discrete variables to be unconstrained in the domain.

One other method which uses the Lagrangian views and is very similar to both the particle-in-cell method and our models is the immersed boundary method [22] developed for a model of the heart. This numerical method uses an Eulerian approach for the fluid flow of blood and a Lagrangian approach for the fibers which model the heart tissue.

Finally, in this chapter all the interactions acting on a cell act on the cell's center of mass. In other words, for most of the interactions in this chapter the cell can be thought of as a point mass. Thus the models fall into the category of lattice-free center-based cell models.

2. Mathematical model

The applications we discuss in this chapter are modeled using the following general framework. Let $\mathbf{u}$ represent the continuum variable which is defined over the entire spatial domain. The discrete variables $\mathbf{v}^i$ are not defined on the spatial domain and represent properties of the cells, with the superscript i denoting a particular cell. For example, $\mathbf{v}^i$ could have two components representing the location of the cell and thus its range would be a subset of the spatial domain for $\mathbf{u}$. The manner in which these variables interact with each other is determined by the system being modeled. In wound healing the system consists of coupled ordinary differential equations, while for Dd the system is made up of coupled ordinary differential equations and a partial differential equation. In general, the interactions can be represented:

$$\mathcal{L}_1(\mathbf{u}) = \mathbf{F}(\mathbf{u}) + \sum_{i=1}^{N} w(\mathbf{x}, \mathbf{v}^i)\mathbf{F}_i(\mathbf{u}, \mathbf{v}^i) \tag{1}$$

$$\mathcal{L}_2(\mathbf{v}^i) = \mathbf{G}_i(\mathbf{u}, \mathbf{v}^i), \tag{2}$$

where $\mathbf{x}$ is the spatial variable (i.e., in $\Re^2$). We have in mind that $\mathcal{L}_i$ are linear differential operators such as differentiation with respect to time. The $\mathbf{F}_i$'s describe how the cells modify the continuum variables and the weights w determine if the cell influence is local or not.

The numerical algorithm used to solve the system is similar to the particle-in-cell method mentioned earlier. For Eq.1 the domain is discretized and values for $\mathbf{u}$ are solved on a fixed or Eulerian grid. Eq.2 is solved by treating $\mathbf{v}^i$ as Lagrangian particles which are unconstrained in their movement. Immediately the key issue is apparent – how can the variables interact when one, $\mathbf{u}$, is constrained to a lattice and the other, $\mathbf{v}^i$, is not. The solution is to interpolate the information from the cell locations to the lattice and to discretize the function w in a manner appropriate for the lattice or Eulerian grid.

For Dd the influence is modeled as a Dirac delta function making it a point source or sink. In wound healing, the weight is a localized pyramid-like function. Choosing two very different types of interpolant for similarly sized cells is due primarily to how the cells modify their environment and also to the domain size being considered. In Dd the cells modify their surroundings by degrading or outputting a diffusible substance. In wound healing, the fibroblast and extracellular matrix interactions we consider are not diffusible. In addition, the size scale of interest for wound healing is at least one order of magnitude smaller than that in Dd.

2.1. Exchanging Information between cells and grid

By letting $\bar{\mathbf{u}}$ be the discrete version of $\mathbf{u}$ and writing the difference operator approximating $\mathcal{L}_1$ as $\bar{\mathbf{L}}_1$ and $\mathbf{F}$ as $\bar{\mathbf{F}}$, Eq.1 and Eq.2 become:

$$\bar{\mathbf{L}}_1(\bar{\mathbf{u}}) = \bar{\mathbf{F}}(\bar{\mathbf{u}}) + \sum_{i=1}^{N} \left[\bar{w}(\mathbf{x}, \mathbf{v}^i)\mathbf{F}_i(\mathbf{I}(\bar{\mathbf{u}}, \mathbf{x}^i), \mathbf{v}^i)\right] \tag{3}$$

$$\mathbf{L}_2(\mathbf{v}^i) = \mathbf{G}_i(\mathbf{I}(\bar{\mathbf{u}}, \mathbf{x}^i), \mathbf{v}^i), \tag{4}$$

where $\mathbf{I}$ interpolates $\bar{\mathbf{u}}$ to the location of the cell, $\mathbf{x}^i = (x^i, y^i)$ and $\bar{w}$ is a discretized approximation to w, which determines how the cell information is transfered to the lattice. The interpolator and form of $\bar{w}$ which are chosen will depend on the system being modeled.

In some particle-mesh simulations in physics, $\bar{w}$ is chosen such that $\bar{w} = \mathbf{I}(\mathbf{w})$. For problems with charged particles, it can be shown that in order to conserve momentum the interpolation from the mesh to the particles must be the same as the interpolation from the particles to the mesh. This ensures that a particle does not exert any force on itself [17]. In the immersed boundary method, the transfer of information between the grids is also done in a symmetric manner. The interpolant developed by Peskin & McQueen [22] for the immersed boundary method approximates the Dirac function and was developed to satisfy certain properties determined by the physical system being modeled – blood flow in the heart. The authors defined a smoothed δ-function in three dimensions as:

$$\delta_h(\mathbf{x}) = h^{-3}\phi\left(\frac{x_1}{h}\right)\phi\left(\frac{x_2}{h}\right)\phi\left(\frac{x_3}{h}\right)$$

where $\mathbf{x} = (x_1, x_2, x_3)$. The function ϕ is uniquely defined by five properties of the interpolant including small support, conservation of momentum and angular momentum, and ensuring that the force exerted by one boundary point on another is no greater than the force on itself.

3. Applications

In this chapter we will discuss two biological applications which we model with this method. The first is the widely studied system of Dd. The life cycle of Dd exhibits key features in developmental biology, including chemotaxis or the ability to move in response to a chemical stimulus. During its life cycle, the individual amoebae feeds on bacteria and multiplies by cell division. Under adverse conditions the individual amoeba aggregate together to form a slug. It is the early aggregation of these cells which we have modeled using the method described above. In the second system, dermal wound healing and scar formation, amoeboidal cells called fibroblasts migrate into the wound region and create new dermal tissue to heal the wound. In both systems, there are two space scales which are vastly different. In Dd the cells are around 10 microns in diameter and they communicate via a chemical gradient. The chemical is a discrete system and its space scale is nanometers. Further, we are interested in patterns which form on the scale of millimeters. Thus we model the cells as discrete objects and the chemical as a continuum. In the second system of wound healing, the cells range from 20 to 100 microns in length and the tissue which they repair is made up of fibrous proteins which have diameters on the scale of nanometers. Again, we model the cells as discrete objects and the tissue as a continuum.

3.1. Dd

The cellular slime mold *Dictyostelium discoideum* live as individual amoebae when food is abundant. When food becomes scarce and the amoebae starve they undergo

several developmental changes. Two of these changes, which occur between six and eight hours after starvation, are obtaining a chemotactic sensitivity to the chemical cyclic adenosine 3',5'-monophosphate, or cAMP, and becoming relay competent. The first means they move up chemical gradients of cAMP. The second, relay competence, means that a cell can relay a signal of cAMP. In other words, if a cell is stimulated with cAMP it will produce and output its own burst of cAMP, thus relaying the signal. So if relay competent cells are spread on a substrate, they can form an excitable medium which is capable of supporting traveling waves of cAMP. If in addition the cells are chemotactically sensitive, they will reorganize themselves. Thus, due to the presence of cells which periodically emit signals of cAMP called pacemakers, the other cells aggregate towards the pacemaker and form a multicellular organism.

3.1.1. Model of early aggregation. In this biological setting where cell motion is key to the development of the organism, we first formulate a model of the early aggregation phase. We represent the chemical concentration of cAMP as the continuous variable $u(\mathbf{x}, t)$, a scalar which depends on space and time. The individual amoebae are treated as discrete entities and the variables $\mathbf{v}^i$ have ten components, two give the cell location, one gives movement information, and the other seven represent internal chemicals which depict the state of the cell. Typical aggregation territories have from 10,000 to 120,000 cells in the region. Thus a continuous representation of cell density would be feasible [23], but with the discrete depiction the properties of the cells are more easily modeled and altered giving the method more flexibility. This is an important feature since a major goal of the work is to understand how cell properties alter the overall density patterns. In addition, the discrete representation of the cells allows the model to easily capture the detailed streaming behavior of the system (see Fig.1) and the rough profile of the global cAMP wave which is the result of the relay response of each individual cell (see Fig.2). The chemotactic ability of the cells is simulated using various motion rules such as: if the time derivative of cAMP exceeds a threshold the cells move, they move at a fixed speed, for a fixed time, and in the direction of the gradient of cAMP. The relay competence is modeled with ordinary differential equations which represent the various internal chemical complexes which are involved in the signal transduction pathway for cAMP relay in a model developed by Tang and Othmer [30]. The external concentration is determined by a parabolic partial differential equation. Thus we have individual cells which modify the continuum variable, which in turn modifies the behavior of the cells. The specific form of Eq.1 for the Dd model is given by

$$\begin{aligned} \frac{\partial u(\mathbf{x})}{\partial \tau} &= D\nabla^2 u(\mathbf{x}) - \gamma_9 \frac{u(\mathbf{x})}{u(\mathbf{x}) + \gamma_8} \\ &\quad + \sum_{i=1}^{N} \frac{V_c}{V_o} \delta(\mathbf{x} - \mathbf{x}^i) \left(sr(v_7^i) - \gamma_7 \frac{u(\mathbf{x})}{u(\mathbf{x}) + \gamma_6} \right) \end{aligned} \tag{5}$$

where u is the cAMP concentration, ∇^2 is the Laplace operator in two dimensions, sr is a non decreasing function, D, γ_6, γ_7, γ_8, γ_9, V_c, and V_o are positive parameters.

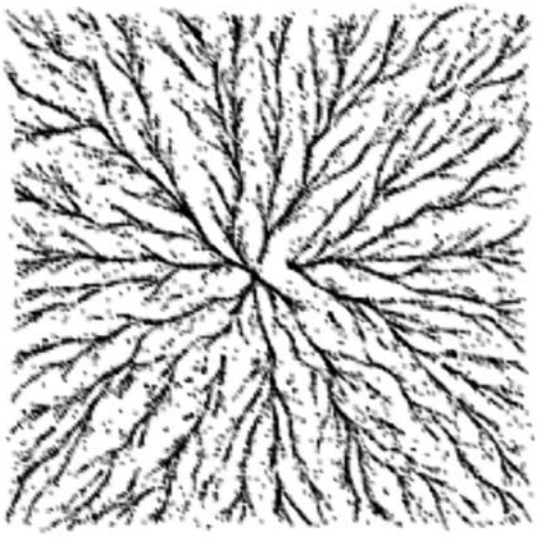

FIGURE 1. Aggregation patterns for a typical simulation of the Dd model. The discrete nature of the cells allows the model to easily simulate the intricate branching patterns seen during aggregation.

Eq.2 takes the following form:

$$
\begin{aligned}
v_1^i &= \frac{\alpha_0 u(\mathbf{x}^i) + (\beta_5 - \alpha_0 u(\mathbf{x}^i))v_6^i}{\alpha_1 + \alpha_0 w_5(\mathbf{x}^i) + \beta_4 v_5^i} \\
v_2^i &= \frac{\alpha_2\alpha_3 c_1 v_1^i (1 - v_4^i)}{1 + \alpha_4 + \alpha_2\alpha_3 c_1 v_1^i - \alpha_4 v_4^i} \\
v_3^i &= \frac{\beta_0 w_5(\mathbf{x}^i)}{\beta_1 + \beta_0 w_5(\mathbf{x}^i)} \\
\frac{dv_4^i}{d\tau} &= \alpha_4 v_2^i - v_4^i - \alpha_4 v_2^i v_4^i \\
\frac{dv_5^i}{d\tau} &= \beta_2\beta_3 c_2 v_3^i - \beta_5 v_5^i + \beta_6 c_3 v_6^i - c_3\beta_4 v_1^i v_5^i - \beta_2\beta_3 c_2 v_3^i (v_5^i + c_3 v_6^i) \\
\frac{dv_6^i}{d\tau} &= -(\beta_5 + \beta_6) v_6^i + \beta_4 v_1^i v_5^i \\
\frac{dv_7^i}{d\tau} &= \gamma_1\gamma_2 v_4^i + \Gamma_5(1 - \Gamma_7 v_4^i) - \gamma_4 \frac{v_7^i}{v_7^i + \gamma_3} - sr(v_7^i).
\end{aligned}
\tag{6}
$$

The α_i's, β_i's, γ_i's, Γ_i's and c_i's are constant positive parameters and are defined in Dallon & Othmer [7].

The algorithm we have developed to solve these equations can be summarized as follows. Given the initial cell states and the cell distribution, which may be uniform or random, in a square domain, with a particular initial distribution of extracellular cAMP, we perform the following steps:

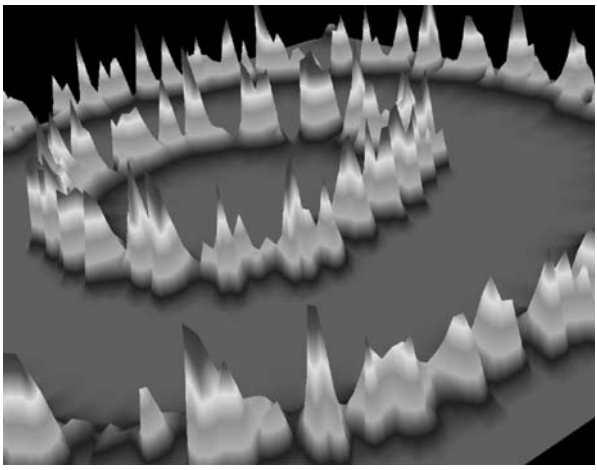

FIGURE 2. Here the concentration of cAMP is plotted. The rough profile is due to the high and low amoeba density regions. The discrete cell representation enhances this feature of the system.

(i) Solve the extracellular Eq.5 on a regular grid, using an Alternating-Direction Implicit (ADI) method for the partial differential equation, lagging the secretion term.
(ii) Interpolate cAMP from the grid to the cell positions (using I) and update the intracellular variables (6) by an implicit scheme.
(iii) Update cell movement. If a cell is not moving, should it begin to move? If so, compute the direction and start movement. If it is moving, should it continue and should it change direction?
(iv) Transfer the secreted cAMP to the grid (using $\bar{w}$) and repeat the cycle.

The interpolation from the Eulerian grid to the cell locations is a tensor product interpolant with quartic Lagrangian interpolation in each direction [24] defined by:

$$I(u, \mathbf{x}^i) = \sum_{n=-2}^{2} \left(\sum_{m=-2}^{2} \bar{u}_{j-m,k-n} \ell_{j-m}(x^i) \right) \ell_{k-n}(y^i) \tag{7}$$

where

$$\ell_j(x) = \frac{(x - x_{j-2})(x - x_{j-1})(x - x_{j+1})(x - x_{j+2})}{(x_j - x_{j-2})(x_j - x_{j-1})(x_j - x_{j+1})(x_j - x_{j+2})}. \tag{8}$$

In Eq.7, $\bar{u}_{j,k}$ is the value of u at the grid point (x_j, y_k) which is the closest grid point to $\mathbf{x}^i = (x^i, y^i)$, thus j and k depend on $\mathbf{x}^i$. The error introduced by I is $O(h_x^5) + O(h_y^5)$ where $O(x) \propto x$ and h_x and h_y are the mesh sizes in the x and y directions respectively.

The Dirac distribution is the weight for the influence of the cells or the function w. So in this application, the support of the weight function is smaller than the mesh size (regardless of the mesh). The amoebae influence the concentration

of cAMP by acting as point sources or sinks. We choose the discretized version of w or $\bar{w}$ to have properties consistent with the physical phenomena being modeled – point sources of a diffusing chemical. Thus $\bar{w}$ has the following three features:

(i) $\bar{w}(\mathbf{x}, \mathbf{x}^i) = \dfrac{1}{h_x h_y}$.
(ii) $\sum_{support} \bar{w} h_x h_y = 1$ (we define $\bar{w}$ to be zero where it is not positive).
(iii) $\bar{w}$ should decrease from (x^i, y^i) at the same rate in the x and y directions.

By restricting $\bar{w}$ to be a tensor product, continuous, bivariate, piecewise linear polynomial, the three conditions above uniquely define the function. The second condition ensures that the amount of chemical produced (or degraded) by the cell is conserved. The other two ensure that only the four nearest grid points are in the support of $\bar{w}$ and the maximum value of $\bar{w}$ is attained at the cell location. The third property also implies that the cAMP diffuses at the same rate in both directions. If the amoeba is located exactly at a grid point, $\bar{w}$ acts as the Dirac distribution.

The function $\bar{w}$ is defined as:

$$\bar{w}(\mathbf{x}, \mathbf{x}^i) = a_x a_y \tag{9}$$

where

$$a_x = \max\left(\frac{h_x - |x^i - x|}{h_x^2}, 0\right) \tag{10}$$

$$a_y = \max\left(\frac{h_y - |y^i - y|}{h_y^2}, 0\right). \tag{11}$$

Geometrically we think of the function as being equal to the complementary area of the point it is centered at (see Fig.3). The particle-mesh method cloud-in-cell uses the same type of function when exchanging information from the particles to the cells [17].

This discretized version of the Dirac distribution, depending on the grid size, the time step, and the diffusion coefficient, has the effect of more rapidly or more slowly diffusing the contribution of the amoebae to the grid. Consider an initial point source in the plane that satisfies the heat equation with the same diffusion coefficient used in our model and the largest time step used in our numerical simulations, approximately ninety percent of the diffusing substance is contained in the circle centered at the source with diameter equal to the mesh size. This shows that our discretization of the Dirac distribution initially speeds up the diffusion of cAMP until it reaches the grid. The error introduced by $\bar{w}$ can be either considered as temporal, spatial or both in the numerical algorithm.

This model is able to successfully reproduce key features, help explain, and give new ideas about certain aspects of the system. The two variables we are most interested in are the extracellular cAMP and the cell density. The cell density is the biologically visible variable which forms the patterns of interest. In Fig.4 we show the cell density after 150 minutes of simulation. The cells have formed

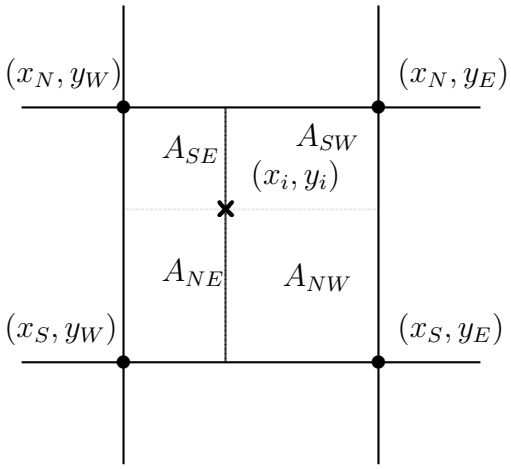

FIGURE 3. The complementary areas are shown for each of the four surrounding grid points. The location of the cell is marked by $\times$ and the grid points are marked by $\bullet$. A_{SW} is the complementary area for the grid point (x_S, y_W).

streams and are aggregating into the two circular cores. This is caused by two spiral waves of cAMP which cells are producing due to their excitability.

The model reproduces features of the system which are observed experimentally. There are two types of aggregation observed: one where cells stream into a pacemaking region and the other where cells spiral in and rotate around a circular core [7]. The model captures both types of aggregation. It is also the first model we know of where spiral waves in Dd are generated without imposing initial conditions designed to specifically initiate spiral waves. The model also reproduces aggregation patterns of various mutants including the streamer F mutant. The streamer F mutant is observed to move about five times longer than wild type cells and form large, long streams and have larger aggregation territories [26]. By altering the movement rules and allowing the cells to move 5 times longer than normal cells the model reproduced the features of the streamer F mutant's aggregation patterns. Finally the model reproduces experiments where caffeine is added to the system. In these experiments, the size of the core about which the cells rotate is affected [27]. Caffeine lowers the excitability of the cAMP system. In the signal transduction model which we use, lowering the value of γ_2, a parameter indicating the activity of aenylyl cyclase, lowers the excitability of the system [7]. The cores generated by the model had sizes which compared favorably with the experimentation (see Fig.5).

The cAMP waves are also of interest and help explain the features of the cellular aggregation. Typically the cAMP waves are generated at pacemaking cells and expand outward as one would expect in an excitable media. They can be very

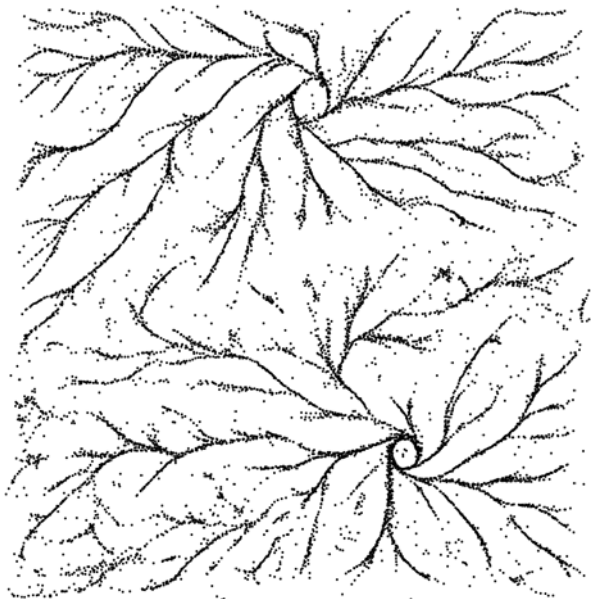

FIGURE 4. Density plot for a simulation at time 150 minutes. Initially 10089 cells where randomly placed on the domain. Two spiral waves form and cause the cell to aggregate and form two circular cores. The parameters are such that approximately 0.1% of the cells are pacemakers and they are randomly located. These computations use a 101 by 101 grid.

rough depending on the underlying cell density (see Fig.2). The waves considered on the space scale of an individual cell are created by bursts of cAMP produced by an excited cell. When considered on a larger space scale, the waves can form expanding circles or spirals which can cause the cells to globally aggregate to a center. A typical simulation starts out with a roughly uniform density of cells. The oscillatory cells initiate a cAMP wave which propagates outward into the excitable media formed by the cells. The cells then start to move and organize themselves according to the cAMP wave. As they move and aggregate they change the excitability of the system by changing the cell density. Thus the low density regions eventually do not propagate cAMP waves. Due to the rough nature of the cAMP waves, we experimented with various motion rules to determine how the cells successfully aggregate without getting misdirected. We examined what happened when the cells reorient themselves to the cAMP gradient every 20 seconds compared to reorienting every 100 seconds. It is experimentally observed that the cells in natural aggregations move for about 100 seconds [26], but can when properly stimulated reorient within 20 seconds [14]. As Fig.6 shows, the 20 second reorientation rule does not give realistic density patterns. Yet if an additional rule, designed to mimic the ability of cells to maintain a leading edge by having the

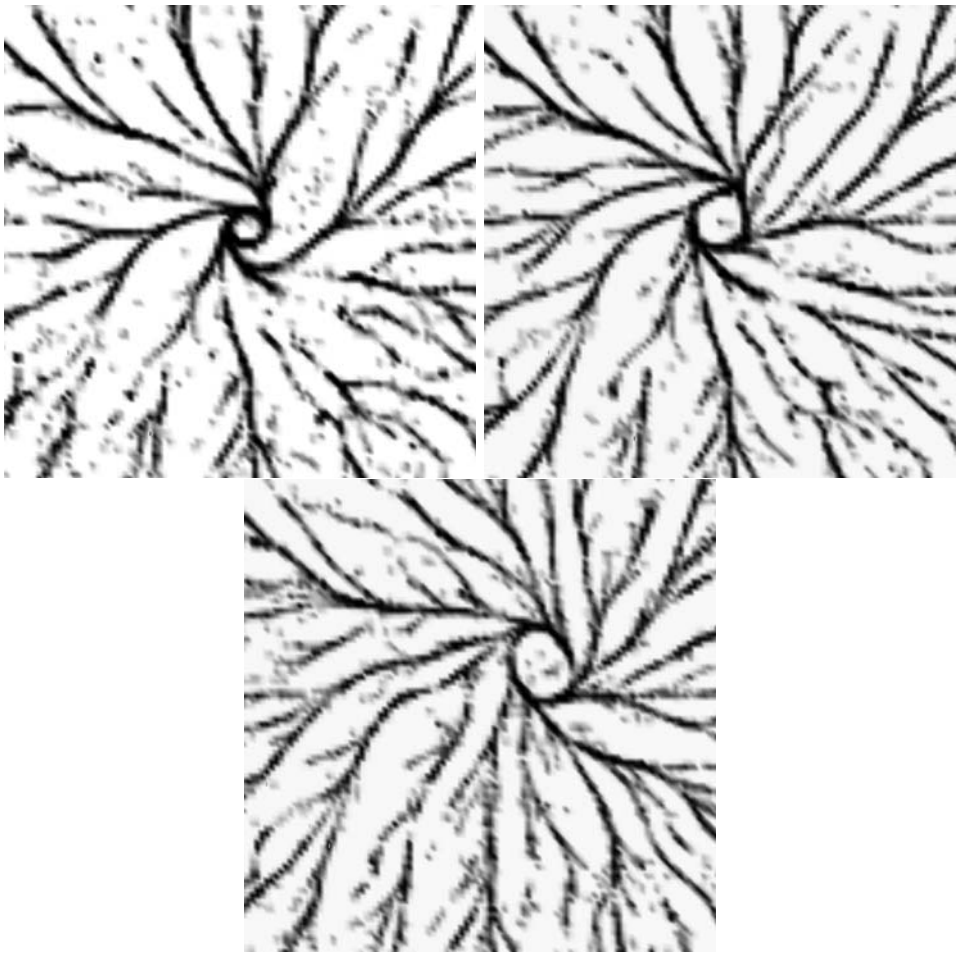

FIGURE 5. Aggregation patterns under changes in the excitability. In (a) $\gamma_2 = 0.17$, in (b) $\gamma_2 = 0.155$, and in (c) $\gamma_2 = 0.14$. The pattern is shown at 150 minutes, cell densities greater than 1.5 are shown in black, and cells move according to the u_2 rules. A spiral wave was initiated in a 1 cm square domain by elevating cAMP in a strip extending from the center to one side, and imposing a refractory region behind it. The central square of side 0.5 cm is shown.

cells consider their current direction when choosing a new direction is added, the 20 second rule gives more realistic density patterns.

Overall our modeling work was validated by its ability to reproduce observed aggregation patterns and experiments. By manipulating the cell properties we learned more about strategies the cell can use to successfully aggregate in the inherently rough and noisy chemical environment which directs its motion [7].

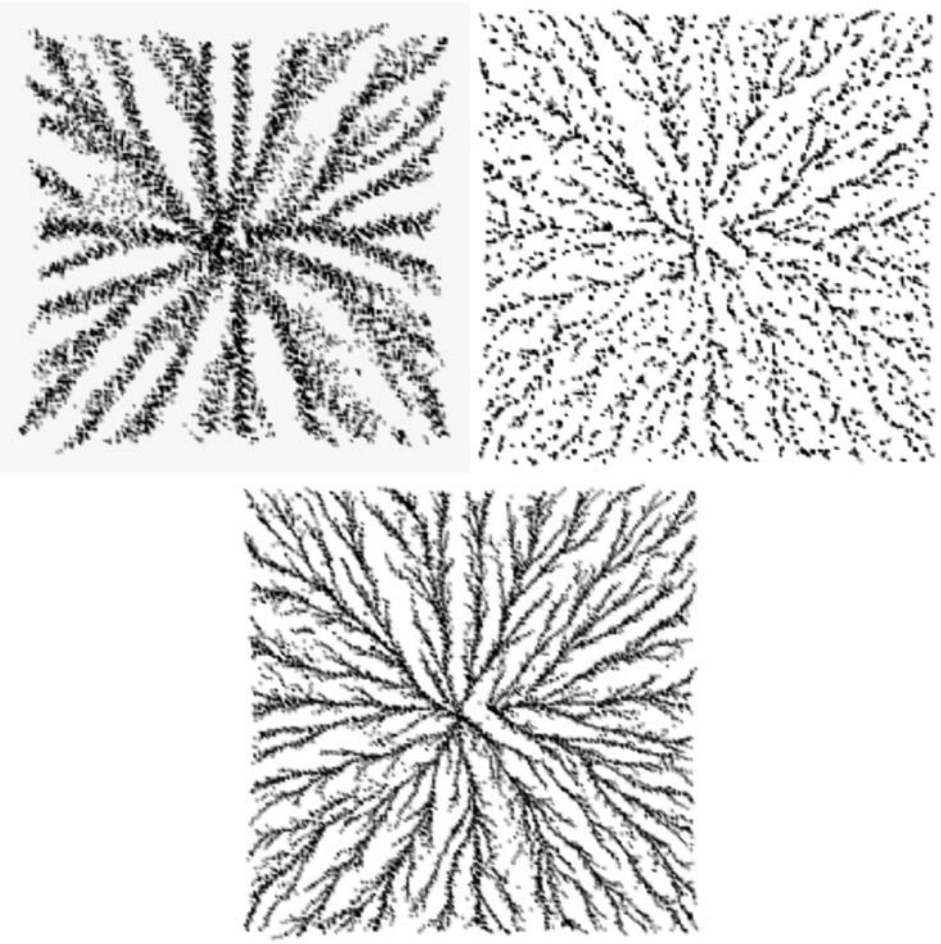

FIGURE 6. Aggregation patterns for simulated cells. The aggregation patterns shown are: in (a) for the wild-type cells with a movement duration of 100 seconds, in (b) for cells with movement duration 20 seconds and in (c) for cells which move 20 seconds and maintain a leading edge. The final time is 95 minutes, and cell densities greater than or equal to 1 are shown in red. (A cell density of 1 represents approximately 800,000 cells/cm^2.) Cells in the center are oscillatory with γ_2 ranging between 0.4 and 0.17.

3.1.2. Model of Dd breakup. In subsequent work we wanted to examine the effect of altering cell adhesion on the aggregation patterns [10]. This was motivated by the observation that countin factor (CF), a protein complex which regulates stream breakup [1, 25] (see Fig.7) also regulates cell-cell adhesion [28, 25]. In the normal life cycle of *Dictyostelium discoideum* the cells will aggregate into a slug which then, at some point, forms a fruiting body. The fruiting body is made up of a stalk

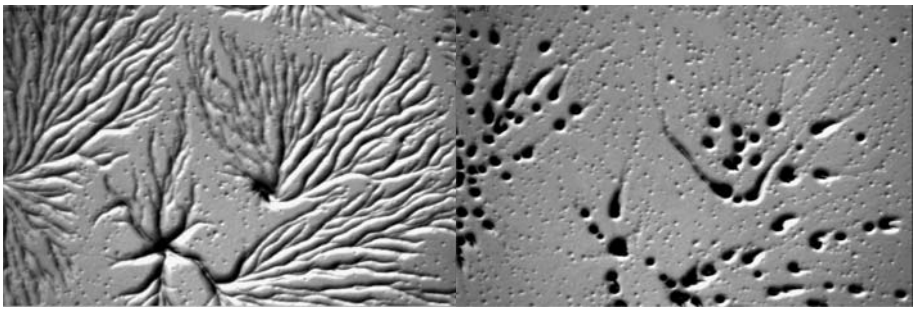

(a) (b)

FIGURE 7. Actual photos of aggregation from Richard Gomer's lab at Rice University (with permission). In (a) the large aggregation territories are about to breakup and form smaller aggregation centers (compare with Fig.8). In (b) the cells have aggregated to several smaller centers (compare with Fig.9b).

and spores. If the fruiting body is too large the stalk cannot support the spores and it will topple over. If the fruiting body is too small the spores are not elevated sufficiently to be effectively dispersed. Thus size regulation of the slug and hence fruiting body are critical. A mutant which lacks CF forms large aggregations and slugs. When CF is added to wild type cells they form very small aggregates.

In order to investigate the effect of cell adhesion on aggregation size, it is necessary to modify the model for Dd. We now consider the cells as spherical objects and we consider the forces acting on them. Thus cells respond as before to their external cAMP signal, but they now also respond to forces acting on them. In this modeling effort we will incorporate elements of viscoelastic models (discussed in other chapters) with the lattice-free center-based cell models. The cells' motion is determined by solving force equations involving adhesion, drag, and the force they exert based on the cAMP signal to which they are responding. The cAMP signal is determined as previously explained using the Tang and Othmer signal transduction pathway and by a diffusion equation. In this model when a cell responds to the cAMP stimuli, it may output cAMP and exert force in response to the stimuli in an attempt to move. By outputting cAMP and moving, the cell will change the external stimuli. In order to deal with cell-cell adhesion we incorporated force equations and a viscoelastic cell body which has a fixed spherical shape and volume. Therefore we used a simplied version of the cell-cell interaction model introduced in Palsson and Othmer [21] and modified in Dallon and Othmer [8].

This model considers forces due to three types of cell interactions: cell adhesion, active cell motion and interactions due to the physical presence of other cells (or the substrate) including their viscoelastic nature which is modeled with a Kelvin body. We also include reactive forces which are the equal and opposite forces from Newton's third law. Because cell motion is determined by force equations, including adhesional forces to investigate the effects of countin factor is possible

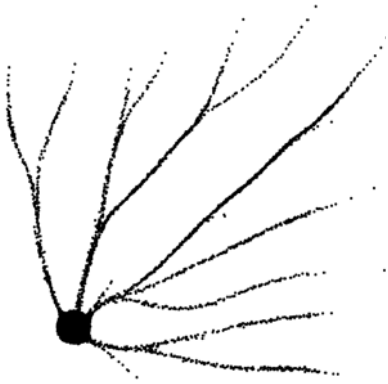

FIGURE 8. All of the simulations with the model to test the effects of CF start from this initial condition which is obtained by running the simulations, starting with a random distribution of cells on the surface, with no adhesion and no random motion for 300 minutes.

with this model framework. The forces causing cell motion are all assumed to act on the center of mass of the cell (a lattice free center-based cell model). Although we constrain the cells to be spherical in shape, they maintain their viscoelastic nature in the sense that when two cells collide, the forces they experience are determined by the viscoelastic nature of the cells. This simplification is motivated by computational constraints and the belief that allowing the cells to take on an ellipsoidal shape will not alter the results of our investigation.

All the simulations for this investigation start with the cell density shown in Fig.8 where the cells have already formed a stream. We modeled the known effects of countin factor, modulating adhesion, motility and external PDE[10]. A mechanism using these three components would work in the following manner. Aggregation starts, and as part of the natural process the extracellular PDE starts to increase. If there is a high density of cells, the associated high density of CF causes more random motion and less adhesion. The combination of very high levels of PDE and the effect of CF on adhesion and motility leads to the breakup of the streams. Once the streams break up, the natural process of cells becoming pacemakers starts (since they are no longer being stimulated by waves of cAMP), and the new aggregation centers restart the aggregation of the small broken streams. Without the increase in the extracellular PDE, the random motion and low adhesion are not sufficient to stop the original aggregation. And without the ability of cells to become pacemakers, the stream fragments will not aggregate anew. The simulations suggest that this mechanism: changes in adhesion, random motion, and external PDE is unlikely to be the primary cause for the breakup of the streams. Despite many attempts, we could not find reasonable parameters which gave simulation results similar to biological experiments (see Fig.9). Although we

a b

FIGURE 9. Density patterns for simulations studying the effects of CF showing the two proposed mechanisms. In a) the density of a typical aggregation pattern where the adhesion, motility, and external PDE are varied. In b) a typical simulation is shown where the alternate mechanism of altering the frequency of cell orientation is used. See also simulations MovIII.2.9a and MovIII.2.9b.

can not rule out this type of mechanism, our simulations suggest something else is happening.

The simulations suggest that a mechanism that alters the frequency of cell orientation would be robust and could explain the experiments. In this mechanism, aggregation begins but when local cell density is great enough, the cells are allowed to follow the cAMP gradient more closely. As was shown in Dallon and Othmer [7], if the cells follow the cAMP gradient too closely they will aggregate towards local regions of high density and not necessarily to the global site of aggregation due to the rough nature of the cAMP concentration. The effects of CF on adhesion and motility reinforce the breakup but they would not be the dominant cause (see Fig.9). In this scenario, the breakup and reaggregation are partially due to the same cause – the cells moving toward a higher density region in the stream. Our simulations thus predict that the cells may be able to reorient more frequently when CF is present, and that this is the dominant and more robust factor in stream breakup.

By applying this method to Dd, we have been able to learn different mechanisms which the cells could employ to successfully aggregate and more about what would be required to disrupt the process in order to regulate the size of the resulting fruiting bodies. Overall, this modeling method had provided insight into

the mechanisms used in Dd that cause the early aggregation of the cells. We now turn to another application of the method.

3.2. Wound healing

In dermal wound healing, after the skin is injured, several interacting events are initiated including inflammation, tissue formation, angiogenesis, tissue contraction and tissue remodeling [3]. Crucial to all of these events is the interaction of the cells with the extracellular matrix (ECM), in a the dermis a collagen based fibrous matrix. After the blood clot has formed during the inflammatory response, white blood cells invade the wound region by migrating through the extracellular matrix. Fibroblasts subsequently migrate into the region and begin to replace the blood clot with collagen. They biochemically alter the extracellular matrix by degrading fibrin and producing collagen [19]. While new tissue is being generated, endothelial cells migrate into the region forming a new vasculature in the process known as angiogenesis [4]. The optimal outcome is a healed wound with new tissue identical to that surrounding the wound, but this is typically not the case. The new tissue is usually characterized by a new architecture that differs from the original and is frequently less functional than the original tissue. This remodelled tissue is known as a scar.

The characteristics of scars are a result of altered structure and composition in the dermis. Scars typically have fewer blood vessels supplying the denser connective tissue which is less elastic. The most significant difference between normal tissue and scar tissue seems to be the orientation of the fibrous matrix. In rodents, normal tissue has a reticular collagen pattern, whereas the collagen in scar tissue forms large parallel bundles at approximately right angles to the basement membrane [32]. Human scar tissue is similar, with greater collagen density, larger fibers, and more alignment than normal tissue, although the alignment is parallel to the skin [13]. Further structural differences between scars and normal tissue include a different ratio of collagen types and a lack of hair follicles and sweat glands. In the work discussed here we focus on the fiber alignment in scar tissue.

The model uses the same basic framework discussed previously in this chapter. The cells are discrete objects which interact with the ECM which has a much smaller spatial scale. We assume a few well known interactions which are briefly summarized. First, fibroblast movement is directed by the orientation of the matrix, a phenomenon known as “contact guidance” [16, 18, 2]. Second, the extracellular matrix affects the speed of the fibroblasts. It is known that the matrix composition influences the motility of fibroblasts, which migrate more easily on fibronectin gels than on collagen gels [33]. Third, the composition of the extracellular matrix alters the production of different proteins by the fibroblasts [5, 34]. Fourth, the extracellular matrix in the wound region contains a plethora of growth factors and cytokines which alter fibroblast behavior. And finally, fibroblasts organize the thin collagen fibrils into the fibrous structure seen in the dermis [13].

In the model for wound healing, Eq.1 is

$$\begin{aligned} \frac{d\angle \mathbf{c}}{dt} &= \kappa \|\mathbf{f}\| \sin(\angle \mathbf{f} - \angle \mathbf{c}) \\ \frac{d\|\mathbf{c}\|}{dt} &= (p_c - d_c\|\mathbf{c}\|) \sum_{i=1}^{N} w(\mathbf{x}, \mathbf{f}^i) \\ \frac{d\|\mathbf{b}\|}{dt} &= -d_f \|\mathbf{b}\| \sum_{i=1}^{N} w(\mathbf{x}, \mathbf{f}^i) \end{aligned} \tag{12}$$

where

$$\mathbf{f}(\mathbf{x}, t) = \sum_{i=0}^{N} w(\mathbf{x}, \mathbf{f}^i(t)) \frac{\mathbf{f}^i(t)'}{\|\mathbf{f}^i(t)'\|}. \tag{13}$$

Here $\mathbf{c}$ represent the collagen fibers, $\mathbf{b}$ represents the fibrin fibers (the blood clot) and these two vectors taken together form $\mathbf{u}$ (in Eq.1), whereas $\mathbf{f}^i$ represents the path of the fibroblasts and thus forms part of $\mathbf{v}^i$ (in Eq.2). The parameters κ, p_c, d_c and d_f are positive constants, the prime denotes differentiation with respect to time and $\angle \mathbf{c}$ denotes the angle of the vector $\mathbf{c}$. Eq.2 is given by

$$\begin{aligned} \mathbf{f}^i(t)' &= s\left(\|\mathbf{c}(\mathbf{f}^i(t))\|, \|\mathbf{b}(\mathbf{f}^i(t))\|\right) \frac{\mathbf{w}^i(t)}{\|\mathbf{w}^i(t)\|} \\ \mathbf{w}^i(t) &= (1-\alpha)\mathbf{c}(\mathbf{f}^i(t)) + \alpha \mathbf{b}(\mathbf{f}^i(t)), \end{aligned} \tag{14}$$

where α is a positive constant and the function s is the speed of the cells which depends on the density of the fibrin and collagen at the cells location. The numerical algorithm used to solve these equations is as follows:

(i) Interpolate (using $\mathbf{I}$) the magnitude of the collagen and fibrin as well as the direction of the collagen to the fibroblast locations.
(ii) Distribute the infuence of the fibroblasts to the extracellular matrix using w (Eq.13).
(iii) Determine the fibroblasts direction (Eq.14) using an explicit Euler method.
(iv) Solve the direction and magnitude of the collagen and the magnitude of the fibrin (Eq.12) on a fixed grid using an explicit Euler method.
(v) Move the fibroblasts to their new locations.

In the wound healing example, we take $\bar{w}(\mathbf{x}, \mathbf{x}^i)$ to be w defined on the lattice. Recall that the Lagrangian particles are fibroblasts. They modify the extracellular matrix primarily through processes localized at the cell surface. For the most realistic model, the support of w should coincide with the shape of the fibroblasts. The next approximation would be to have an elongated support in the direction of the fibroblasts' motion. For simplicity we take the support to be a square region with sides of length 20 microns. We choose a piecewise linear function whose maximum is at the cell location defined by

$$w(\mathbf{x}, \mathbf{x}^i) = a_x a_y \tag{15}$$

where

$$a_x = \max\left(1 - \frac{|x^i - x|}{L}, 0\right) \tag{16}$$

$$a_y = \max\left(1 - \frac{|y^i - y|}{L}, 0\right). \tag{17}$$

Here L is a parameter that determines the support of w and is taken to be 10 microns. A graph of w is shown in Fig.10. This function differ from the $\bar{w}$ used in the Dd example. In Dd the function approximated the Dirac distribution and so its support depended on the grid size. In this example it does not.

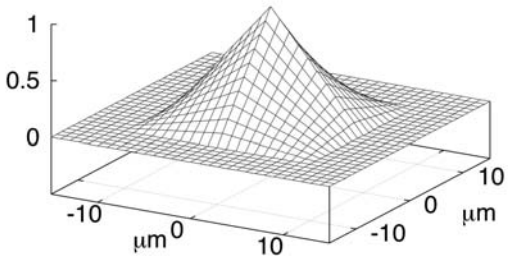

FIGURE 10. Graph of w for the wound healing model.

Fig.11 shows typical results from the model of how fibroblasts can remodel the collagen matrix. Fig.11(a) shows an example of a random initial orientation for either the collagen or the fibrin fibrous networks. In 11(b) a simulation is shown where there is no fibrin, thus the cells simply remodel and give more structure to the collagen matrix. After 100 hours the fibroblasts have considerably altered the original collagen configuration. The degree to which they smooth the vector field depends on several factors.

By choosing the modeling framework to have discrete cells it is easy to manipulate the properties of the cells and run hypothetical experiments taking into account the known effects of various cytokines. In order to explain the observed effects of transforming growth factor-β (TGFβ), we used this model and considered the specific effects of TGFβ on the fibroblasts [11]. The results of the investigation showed that by assuming certain types of interactions with TGFβ and the fibroblasts the overall effect on scarring of TGFβ could be explained (see Fig.12).

4. Conclusions

The modeling technique described in this chapter for lattice-free center-based cells interacting with continuum environment variables has many applications and advantages. Any system biological or not where there are discrete objects which

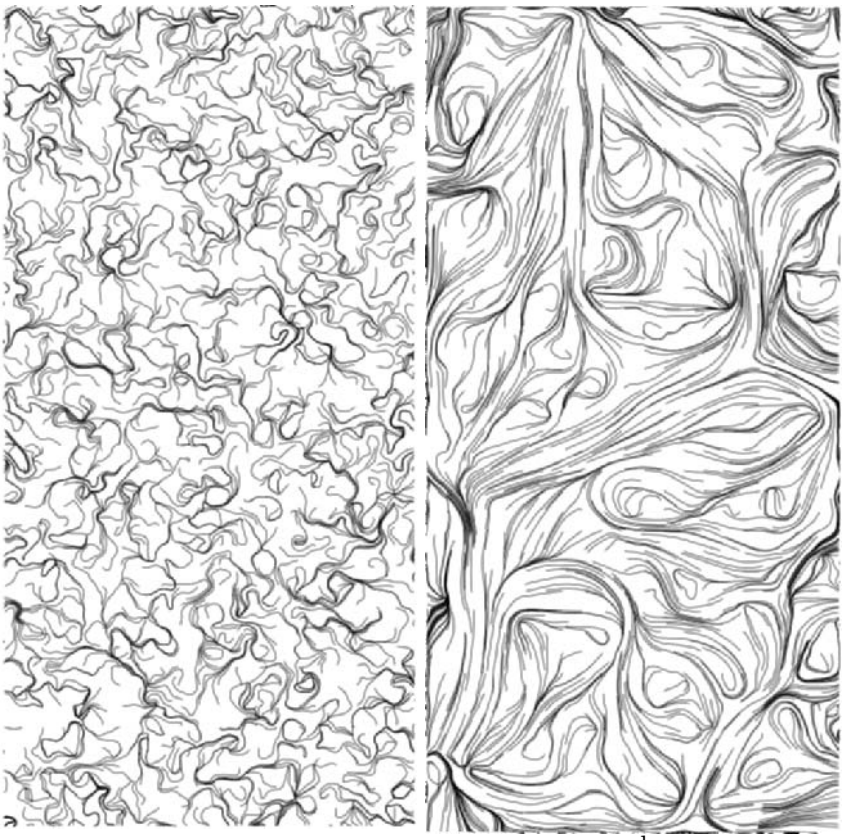

FIGURE 11. The collagen orientations for typical simulations. In (a) the initial random collagen orientation is shown and in (b) the collagen orientation is shown after 100 hours of remodeling by the fibroblasts on a domain of 0.5 mm by 1.0 mm. The alignment is shown by drawing lines whose tangent corresponds to the collagen vector field (the streamlines).

interact via some other variable with a much smaller space scale could use this technique. This includes planets interacting via a gravitational field, cells interacting via chemical signals, or animals interacting due to vegetation density. The advantages include a more realistic formulation of the discrete entities over a continuous distribution and a formulation which allows observable individual interactions to be more readily incorporated into the model. This makes it easier to simulate complex systems and determine the effects of specific types of interactions on the overall behavior of the system.

The disadvantages of the method are the computational difficulties if the density of the discrete objects is large and the models are typically less amenable

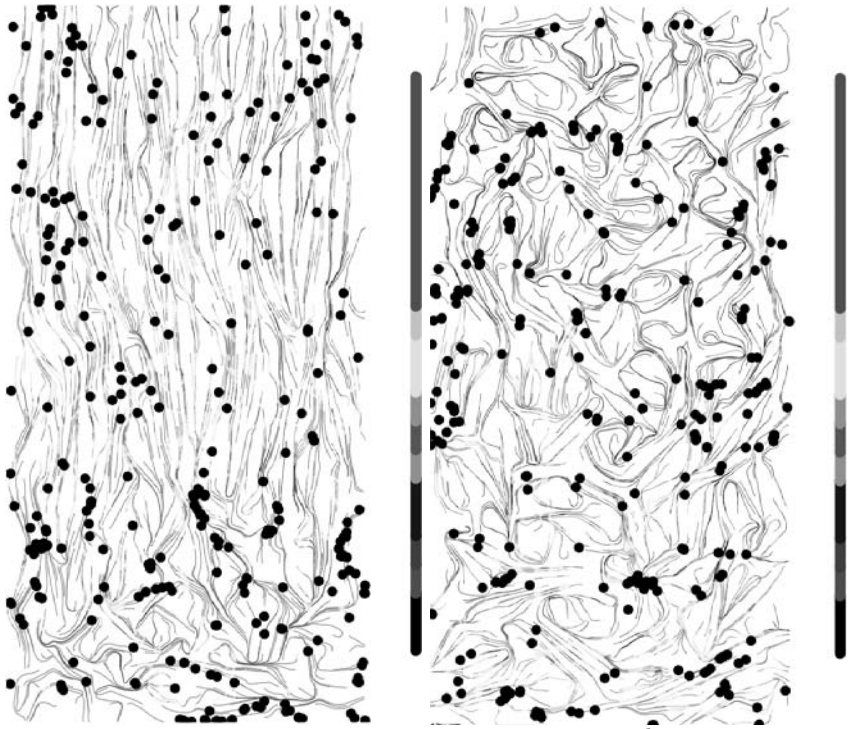

FIGURE 12. The collagen orientations for typical wound healing simulations designed to explore the effects of TGFβ. In (a) the alignment and density of the collagen fibers is shown for a typical wound healing scenario. In b) the results of a simulation designed replicate the removal of TGFβ_1 and TGFβ_2 (two isoforms of TGFβ) is shown. The results are 240 hours or about 12 after wounding. The color indicates the density of the collagen with red being high and blue low. The top would be the top of the skin and the sides would be the normal tissue surrounding the wound which is 0.5 mm by 1.0 mm. The alignment is shown by drawing lines whose tangent corresponds to the collagen vector field (the streamlines). The black circles represent the location of about one fourth of the fibroblasts in the wound region.

to mathematical analysis. Despite these disadvantages, this modeling technique is another powerful tool to help understand the complex biological systems in the world around us.

References

[1] D. A. Brock, F. Buczynski, T. P. Spann, S. A. Wood, J. Cardelli, and R. H. Gomer. A Dictyostelium mutant with defective aggregate size determination. *Development*, 122:2569–2578, 1996.

[2] P. Clark, P. Connolly, A. S. G. Curtis, and C. C. W. Wilkinson. Topographical control of cell behaviour. ii. multiple grooved substrata. *Dev.*, 108:635–644, 1990.

[3] R. A. F. Clark. Wound repair. *Curr. Opin. Cell Biol.*, 1:1000–1008, 1989.

[4] R. A. F. Clark. Wound repair overview and general considerations. In R. A. F. Clark, editor, *The Molecular and Cellular Biology of Wound Repair*, pages 3–50. Plenum Press, 2 edition, 1996.

[5] R. A. F. Clark, L. D. Nielsen, M. P. Welch, and J. M. McPherson. Collagen matrices attenuate the collagen-synthetic response of cultured fibroblasts to TGF-β. *J. Cell Sci.*, 108:1251–1261, 1995.

[6] J. C. Dallon. Numerical aspects of discrete and continuum hybrid models in cell biology. *Applied Numerical Mathematics*, 32:137–159, 2000.

[7] J. C. Dallon and H. G. Othmer. A discrete cell model with adaptive signalling for aggregation of *Dictyostelium discoideum*. *Phil. Trans. Roy. Soc. London: Series B*, 352(1357):391–417, 1997.

[8] J. C. Dallon and H. G. Othmer. How cellular movement determines the collective force generated by the *Dictyostelium discoideum* slug. *J. Theor. Biol.*, 231:203–222, 2004.

[9] J. C. Dallon, J. A. Sherratt, P. K. Maini, and M. W. J. Ferguson. Biological implications of a discrete mathematical model for collagen deposition and alignment in dermal wound repair. *IMA J. Math. Appl. Med. Biol.*, 17:379–393, 2000.

[10] J. C. Dallon, W. Jang, and R. H. Gomer. Mathematically modeling the effects of counting factor (cf) in dictyostelium discoideum. *Math. Med. Biol.*, 23:45.

[11] J. C. Dallon, J. A. Sherratt, and P. K. Maini. Modeling the effects of transforming growth factor-β on extracellular matrix alignment in dermal wound repair. *Wound Repair and Regeneration*, 9(4):278–286, 2001.

[12] R. Durrett and S. Levin. The importance of being discrete (and spatial). *Theor. Popul. Biol.*, 46:363–394, 1994.

[13] H. P. Ehrlich and T. M. Krummel. Regulation of wound healing from a connective tissue perspective. *Wound Repair Regen*, 4:203–210, April-June 1996.

[14] R. Futrelle, J. Traut, and W. G. McKee. Cell behavior in *Dictyostelium discoideum*: preaggregation response to localized cyclic AMP pulses. *J. Cell. Biol.*, 92:807–821, 1982.

[15] M. R. Gibbons and D. W. Hewett. Characterization of the darwin direct implicit particle-in-cell mehod and resulting guidelines for operation. *J. Comp. Phys.*, 130(1):54–66, 1997.

[16] S. Guido and R. T. Tranquillo. A methodology for the systematic and quantitative study of cell contact guidance in oriented collagen gels. *J. Cell Sci.*, 105:317–331, 1993.

[17] R. W. Hockney and J. W. Eastwood. *Computer Simulations Using Particles*. Institute of Physics Publishing, 1988.

[18] P. Hsieh and L. B. Chen. Behavior of cells seeded on isolated fibronectin matrices. *J. Cell Biol.*, 96:1208–1217, 1983.

[19] R. W. Jennings and T. K. Hunt. Overview of postnatal wound healing. In N. S. Adzick and M. T. Longaker, editors, *Fetal Wound Healing*, pages 25–52. Elsevier Science Publishing Company, 1992.

[20] P. J. O'Rourke and J. U. Brackbill. On particle-grid interpolation and calculating chemistry in particle-in-cell methods. *J. Comp. Phys.*, 109:37–52, 1993.

[21] E. Palsson and H. G. Othmer. A model for individual and collective cell movement in dictyostelium discoideum. *Proc. Nat. Acad. Sci. USA*, 97:10448–10453, 2000.

[22] C. S. Peskin and D. M. McQueen. Fluid dynamics of the heart and its valves. In H. G. Othmer, F. R. Adler, M. A. Lewis, and J. C. Dallon, editors, *Case Studies in mathematical Modeling Ecology, Physiology, and Cell Biology*. Prentice Hall, 1997.

[23] T. Höfer, J. A. Sherratt, and P. K. Maini. *Dictyostelium discoideum*: cellular self-organization in an excitable biological medium. *Proc. R. Soc. Lond. B*, 259(1356):249–257, March 1995.

[24] A. Ralston and P. Rabinowitz. *A First Course in Numerical Analysis*. McGraw Hill Book Company, New York, 1978.

[25] C. Roisin-Bouffay, W. Jang, D. R. Caprette and R. H. Gomer. A precise group size in Dictyostelium is generated by a cell-counting factor modulating cell-cell adhesion. *Molecular Cell*, 6:953–959, October 2000.

[26] F. M. Ross and P. C. Newell. Streamers: Chemotactic mutants of *Dictyostelium discoideum* with altered cyclic gmp metabolism. *J. Gen. Microbiol.*, 127:339–350, 1981.

[27] F. Siegert and C. J. Weijer. Digital image processing of optical density wave propagation in *Dictyostelium discoideum* and analysis of the effects of caffeine and ammonia. *J. Cell Sci.*, 93:325–335, 1989.

[28] C-H. Siu and R. K. Kamboj. Cell-cell adhesion and morphogenesis in *Dictyostelium discoideum*. *Developmental Genetics*, 11:277–387, 1990.

[29] D. Skulsky, S. J. Zhou, and H. L. Schreyer. Application of a particle-in-cell method to solid mechanics. *Comp. Phys. Commun*, 87(1–2):236–252, 1995.

[30] Y. Tang and H. G. Othmer. A G-protein-based model of adaptation in *Dictyostelium discoideum*. *Math. Biosci.*, 120(1):25–76, March 1994.

[31] M. Toda. *Theory of nonlinear lattices*, volume 20 of *Springer series in solid-state sciences*. Springer, 2 edition, 1989.

[32] D. J. Whitby and M. W. J. Ferguson. The extracellular matrix of lip wounds in fetal, neonatal and adult mice. *Dev.*, 112:651–668, 1991.

[33] B. Wojciak-Stothard, M. Denyer, M. Mishra, and R. A. Brown. Adhesion orientation, and movement of cells cultured on ultrathin fibronectin fibers. *In Vitro Cell. Devel. Biol.*, 33(2):110–117, 1997.

[34] J. Xu and R. A. F. Clark. Extracellular matrix alters PDGF regulation of fibroblast integrins. *J. Cell Biol.*, 132:239–249, 1996.

John C. Dallon
Department of Mathematics, Brigham Young University
312 TMCB, Provo, UT 84602-6539, U.S.A.
e-mail: `dallon@math.byu.edu`

Single-Cell-Based Models in Biology and Medicine
ed. by A.R.A. Anderson, M.A.J. Chaplain, K.A. Rejniak
Mathematics and Biosciences in Interaction, 221–239

III.3 Modeling Multicellular Structures Using the Subcellular Element Model

Timothy J. Newman

Abstract. This chapter describes a new method for simulating grid-free multicellular structures, in which the three-dimensional shape of each cell is dynamically adaptive to its local environment. This is achieved by constructing each cell from "subcellular elements." I describe in detail the underlying mathematical equation of motion for the elements, and the additional algorithms which allow for cell growth and cell division. The model is illustrated with the simple example of a growing three dimensional cluster of cells.

1. Introduction

As cell modeling progresses, it will become increasingly important to embed biological plausibility and functionality into the foundations of the algorithms and modeling frameworks. As is shown by the chapters in this book, there is no unique way of achieving this. Various modeling strategies can accomplish similar goals, and, likewise, different modeling strategies will be needed to achieve diverse biological modeling goals. The type of model one builds will depend on whether, for the biological problem at hand, one requires a sensitive description of cell biomechanics and viscoelasticity, or whether biochemical processes, such as signalling and metabolism are more important. Also crucial, from a pragmatic standpoint, is the scale of the biological problem. If one is modeling a tumor with 10^6 cells, then, given the limitations of computational power, each cell can be imbued with only primitive properties. Alternatively, if one is modeling a small cluster of cells (for example, a very early embryo, or a specific cell-cell interaction) then it is possible to imbue each cell with a sophisticated range of functionality, appropriate to the nature of the biological problem at hand.

One of the more challenging biological characteristics to build into a cell model is cell shape, and, along with this, cell response to local mechanical forces. A number of the chapters in this book address this problem, to varying degrees; for example, the Potts model approach of Glazier and coworkers [1], the ellipsoidal cell approach of Palsson and Othmer [2], the model by Drasdo *et al* [3] in which the "dumbbell" shape of cell division is accounted for, and the recent work,

based on the immersed boundary approach, of Rejniak [4]. In this chapter I will describe another approach, the Subcellular Element Model, which was introduced recently [5].

Cells are typically not spherical [6]. Unicellular yeast cells are approximately spherical (when not budding), but this simplicity vanishes at the next higher level of biological complexity, in both fungi (e.g. filamentous hyphal cells) and unicellular animal cells (e.g. motile amoeba, such as *Dictyostelium*). In multicellular organisms, especially animals, there is a wide range of tissue types, and in each, one finds various cell types, with "shape phenotypes" adapted to their role in that tissue. In adipose (fat) tissue, adipocytes do have an approximately spherical shape, but are in close conjunction with irregularly shaped fibroblasts. In tissues such as epithelia, muscle, and neuronal tissue, one finds a whole host of complicated cell shapes (columnar, filamentous, and branching, respectively).

It is important to remember that although I have used the loose phrase "shape phenotype," in reality cell shape is generally dynamic and adaptive, responding to both internal signals and to the local environment. Cell shape change affects the gross properties of the tissue in which cells are embedded. A striking example of this is the process of convergence and extension [7] which has been observed in a number of early embryonic processes, particularly in *Xenopus*. Cells are observed to become highly polarized in shape – loosely speaking, changing from spherical to cigar-shaped – and, in so doing, create anisotropic elastic forces in the region of tissue in which they are embedded. These forces result in large-scale morphogenic changes in the embryo.

As soon as one considers cell shape change, one is compelled to address the closely related issue of the biomechanical properties of the cell [8, 9]. In a closely packed tissue, such as an epithelium, cell shape change will create local forces which will then provoke cell shape change in neighboring cells. Those secondary shape changes create new forces, and so it goes on through the non-linear feedback between the balance of intercelluar forces among cells and the cells' three-dimensional shapes.

Thus, if one is modeling a multicellular system in which biomechanics is believed to play an important role, it is important to consider using a model which can accommodate adaptive cell shape change. With this motivation, over the past year or so, my group has constructed and developed the Subcellular Element Model (SEM). The SEM has turned out to be a flexible framework in which other biological processes can be fairly easily accommodated. I will complete this Introduction by describing the motivation of the SEM in more detail, after which I will get down to brass tacks and describe the mathematical and algorithmic details underlying the model.

There follows a list of desirable properties that formed the basis of the SEM:

- emergent cell-shape dynamics
- seamless multiscalability
- simple underlying mechanics

- computationally optimizable
- fully three-dimensional
- flexible accommodation of cell biology

I discuss these bulleted points in sequence below.

The first requirement arises from consideration of cell shape, as discussed at length above. The first generalization from purely spherical cells is ellipsoidal cells. One then has three principal axes to vary for a given cell, deforming its shape to either prolate (cigars) or oblate (pancakes). Palsson and Othmer [2] constructed an elegant model of this type to describe collective motion of *Dictyostelium* cells. When one views cells either crawling through ECM, or nestled beside each other in an epithelial sheet, one sees that their shape can be highly non-ellipsoidal – with, respectively, multiple protrusions, or quasi-hexagonal symmetry for tight packing. It is difficult to parameterize more general cell shapes beyond the ellipsoidal approximation. This difficulty led me to the idea that one should abandon parameterizing shape altogether, and allow shape to emerge from the model dynamics. In other words, the cell shape should be adaptive. This simple idea lead very quickly to the idea of constructing a cell from a "cloud" of N subcellular entities (which I call "elements"). These elements (belonging to a single cell) would be labeled so that together they define that cell. Through their relative positions, in response to internal and external forces, they define in a non-trivial way the shape of the cell. Because of the viscoelastic interactions between elements, it is appropriate to regard each element as a coarse-grained region of cell cytoskeleton. This analogy has been given a more quantitative validity recently, as I discuss in the conclusions.

The number N of elements per cell can be varied from a very large value (say, 10^5) to unity (in which limit the SEM becomes equivalent to a model of spherical cells, i.e. the single element becomes identical to the cell it represents). Assuming that our computational resources allow us to track no more than, say, 1 million elements for a substantial number of iterations, then by using the SEM we can simulate a range of multicellular systems in roughly the same CPU time frame: systems of a few cells, each described in fine detail by 100,000 elements, to one thousand cells each described by one thousand elements, all the way up to one million cells, each described as a sphere. We term this property "seamless multiscalability." The SEM allows simulation of a broad range of scales within the same modelling framework, thereby eliminating the uncertainties of some multiscale modeling in which qualitatively different algorithms are patched together to span scales. It is even possible to model cells with differing numbers of elements within the same system, if more detail is needed to describe a subclass of cells at a particular stage of the simulation. Such a multi-scale element approach is analogous to a multigrid approach for solving multi-scale differential equations.

The SEM is phenomenological, and, as such, the underlying dynamics of the elements are described by simple biomechanical forces. Even with 1 million elements per cell, each element still represents a relatively large intracellular region

of linear dimension 0.1 microns. This is on the borderline of a scale in which specific protein-complex structures need to be modeled in realistic detail. Across all the scales I have discussed, the elements should be regarded as smeared out regions of cytoskeleton (or cytoplasm), and hence their interactions can only be described in an averaged, or simplified, fashion.

Grids can be expensive to implement, in terms of computer memory, in three dimensions; and under some circumstances they can lead to dynamical artifacts [10]. As such the SEM is implemented completely off-lattice, with relative element positions encoded with sectors and linked lists [11]. Assuming local interactions, this leads to $O(N)$ algorithms in both two and three dimensions.

An attractive feature that presents itself when one considers the SEM is that one is free to assign different attributes to the elements constituting a single cell. For example, this allows one to model a cell with a fairly rigid interior and a fluctuating cortex – mimicking to some degree the real features of the cell cytoskeleton. As we shall see, additional cell biological processes such as cell growth and division are also naturally accommodated into the SEM.

2. Mathematical Model

The SEM is formulated in the framework of stochastic processes, in particular Langevin equations [12]. The fundamental stochastic variables are the position vectors of the elements. I adopt the convention that Roman letters $i, j, ...$ represent labels of individual cells, while Greek letters $\alpha, \beta, ...$ represent elements. To denote element α belonging to cell i, I write α_i. The position vector of this element is written $\mathbf{y}_{\alpha_i}$. For clarity, I use $\mathbf{y}$ to denote positions of elements, and $\mathbf{x}$ either with an index to denote positions of cells, or with no index to denote a position vector of an arbitrary point in three-dimensional space.

The dynamics of the elements is assumed to be overdamped. Thus, inertial terms in the equation of motion for the elements are discarded. For the simplest case in which movement of elements is due to random noise and biomechanical interactions we have:

$$\dot{\mathbf{y}}_{\alpha_i} = \eta_{\alpha_i} - \nabla_{\alpha_i} \sum_{\beta_i \neq \alpha_i} V_{\text{intra}}(|\mathbf{y}_{\alpha_i} - \mathbf{y}_{\beta_i}|) - \nabla_{\alpha_i} \sum_{j \neq i} \sum_{\beta_j} V_{\text{inter}}(|\mathbf{y}_{\alpha_i} - \mathbf{y}_{\beta_j}|) \ . \qquad (1)$$

On the right-hand-side, the noise term η_{α_i} is a Gaussian distributed random variate with zero mean and correlator

$$\langle \eta^m_{\alpha_i}(t) \eta^n_{\beta_j}(t') \rangle = 2D\delta_{i,j}\delta_{\alpha_i,\beta_j}\delta^{mn}\delta(t-t') \ , \qquad (2)$$

where m and n are vector component labels in the three-dimensional space. This last equation simply indicates that the random forces are uncorrelated in all possible variables: between cells, between elements within a cell, between spatial dimensions, and between any two different instants of time.

It is crucial in the SEM that there are two distinct sets of potentials: intracellular potentials, which are stronger, and bind elements belonging to the same cell into a contiguous configuration; and intercellular potentials, which are weaker,

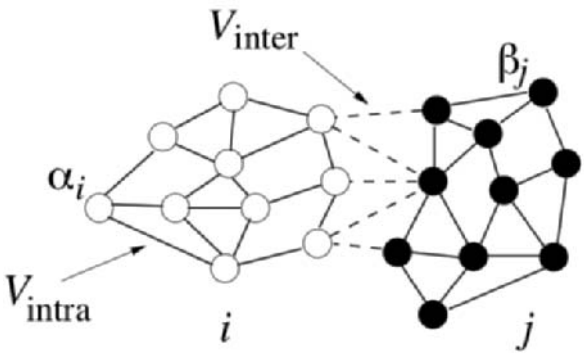

FIGURE 1. A schematic figure showing two cells constructed from elements, with intracellular potentials binding elements of a given cell to each other, and intercellular potentials weakly binding adjacent elements from neighboring cells. We illustrate this in two dimensions for the sake of clarity.

and provide cell-cell adhesion (if and when appropriate) by binding together surface elements between neighboring cells. A schematic figure illustrating these two types of element-element interactions is shown in Fig.1. It is possible to add extra interactions in the fundamental element equation, in particular, "viscous" terms proportional to the relative velocities of elements. Such terms allow one greater freedom in tuning the viscoelastic properties of the cell.

The potentials are phenomenological in nature. By this, I mean that they are not derived from some more microscopic process, such as the dynamics of actin polymerization and cross-linking, or the formation and destruction of intercellular junctions. Instead, I make the simplest assumption that the potentials are repulsive at short distances (modeling volume exclusion of neighboring regions of cytoskeleton) and weakly attractive over slightly longer scales (modeling the adhesive forces between these regions). Beyond a moderate scale, the potential is essentially zero. I do not believe the precise form of the potentials is of critical importance, at least for a semi-quantitative understanding of cell mechanics. In (quasi-) equilibrium, the elements will be close to the local mechanical equilibria of the potentials of their neighboring elements, and so will be interacting via harmonic potentials. Anharmonicity of the potentials is important for i) making the potentials local, and ii) allowing elements to smoothly release each other under larger forces, such as during cell division or cell migration. We typically use a short-range potential constructed from two Gaussian functions, as defined in Eqn.(3) and illustrated in Fig.2.

$$V(r) = V_0 \exp(-r^2/\xi_1^2) - U_0 \exp(-r^2/\xi_2^2) \ . \tag{3}$$

This ends the purely mathematical definitions of the SEM. In the rest of this chapter I will examine some simple applications of the SEM, and use these

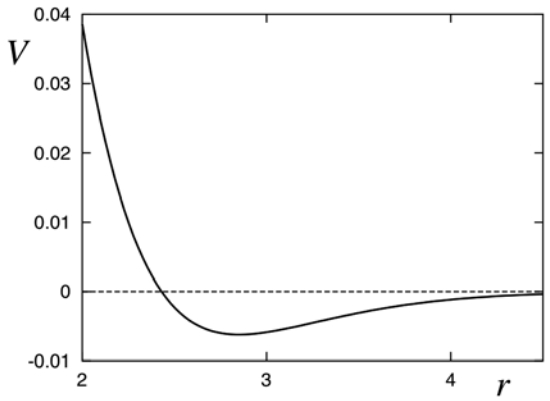

FIGURE 2. A typical example of the intra-cellular potential, based on Eqn.(3). All length scales are in microns. The parameters are V_0=1.1, U_0=0.1, ξ_1=1.21, ξ_2=1.90. These parameters are appropriate for a cell of mean radius 10 μm comprised of 256 elements, in which case, the equilibrium distance between elements will be approximately 2.85 μm, as confirmed in this figure.

to describe the algorithmic instantiation of other biological processes not directly related to biomechanics. I start with a discussion of modeling the equilibrium of single cell, and then describe how cell growth and cell division processes can be modeled. These processes are then combined to model the growth of a relatively large cell cluster of ∼1000 cells.

3. Applications

3.1. Equilibration of a Single Cell

Let us start by examining a single cell. In the absence of other cells Eqn (1) becomes:

$$\dot{\mathbf{y}}_{\alpha_i} = \eta_{\alpha_i} - \nabla_{\alpha_i} \sum_{\beta_i \neq \alpha_i} V_{\text{intra}}(|\mathbf{y}_{\alpha_i} - \mathbf{y}_{\beta_i}|) \ . \tag{4}$$

It is clear, without explicit numerical iteration of this equation, that the equilibrium shape of this cluster of elements will be approximately spherical. The overdamped dynamics will slowly push the system into a deep metastable state – the particular state depending on the initial configuration. Over very large time scales, the noise will buffet the system between low-lying metastable states, and the internal energy of the element configuration will slowly converge towards the "ground-state." This is not particularly interesting from a biological viewpoint, as one is essentially simulating a fluid-like droplet, which will round up, in the absence of external forces, to minimize its surface energy. Before adding more biological processes, I will present simulations of this simplest problem to confirm that our intuition is on the mark.

I use the phenomenological potential Eqn. (3) with the parameters $V_0 = 1.1$ and $U_0 = 0.1$, and take the number of elements $N = 256$. In order to set the length scales of the potential, I need to set the radius of the elements. Clearly, the element radius will be proportional to the cell radius, but the proportionality constant will depend on the number of elements, and their geometrical packing. I will present a simple argument for this relationship and confirm it to good numerical precision.

Given the mean radius of the cell, r_c (which will be of the order of 10 microns), I estimate the radius of an element, r_e, by assuming close-packed elements in three dimensions. Then, on equating the volume of the cell to the volume of N elements, we have

$$\frac{4}{3}\pi r_c^3 = \frac{N}{p_3} \times \frac{4}{3}\pi r_e^3 \ , \tag{5}$$

where p_3 is the occupied volume of close-packed spheres in three dimensions. As derived by Gauss, it has the value $p_3 = \pi/3\sqrt{2} \simeq 0.741$. Eqn. (5) is not exact as, first, I cannot guarantee that the elements in our cell will be close-packed, and second, this equation ignores inescapable deviations from close-packing in the surface layer. However, it is a reasonable way to estimate r_e and becomes increasingly accurate as the number of elements N increases. Rearranging (5) we then have

$$r_e = \left(\frac{p_3}{N}\right)^{1/3} r_c \ . \tag{6}$$

The equilibrium distance between two elements will be $r_{\rm eq} = 2r_e$. To give an idea of scale, for $r_c = 10\mu m$ and $N = 256$, we have $r_e \simeq 1.4\mu m$, and an inter-element distance of $r_{\rm eq} = 2r_e \simeq 2.8\mu m$. Now we have r_{eq} we can set the length scales ξ_1 and ξ_2, with the additional constraint that the potential has some given minute value at $r \sim 2r_{\rm eq}$ (the numerical limit of the range of the potential).

To verify this form for the element radius, I present some numerical simulations of a cell composed of 256 elements. Elements are given the radius calculated above. The initial configuration is created by randomly placing the elements in a sphere of radius 10 μm, making sure that no two elements are separated by a distance less than the element radius. This latter condition is required to avoid initially violent element movements, due to the strong excluded volume interaction in the equation of motion. The noise strength D is set to zero for simplicity. Thus, the elements move under purely relaxational dynamics. In Fig.3 (right panel) I show the configuration of elements after 100,000 iterations (with a time step of $dt = 0.1$). It is difficult to get a sense of the three-dimensional element configuration from a static two-dimensional image such as this. Using software to rotate the configuration, one sees that the elements are very evenly spaced. We use ray-tracing software (POVRAY) to render the element configuration, thus producing a three-dimensional isosurface of the cell. A cut-away version of this is shown in Fig.3 (left panel). This image gives a sense of the smoothness of the cell shape.

I can quantify the equilibrium configuration of the cell by measuring two quantities: the "internal energy" of the cell, E, and the cell's mean squared radius

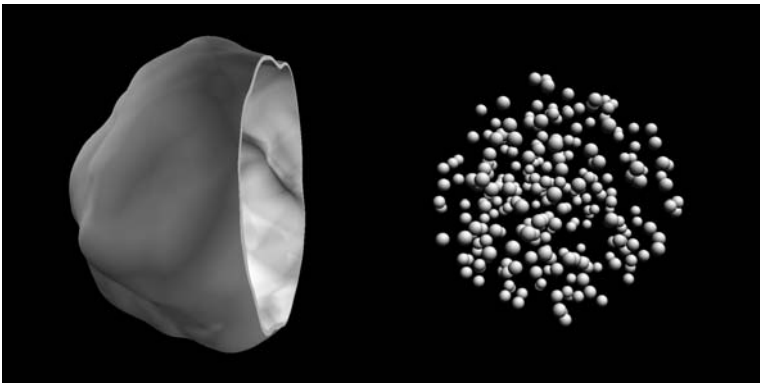

FIGURE 3. A typical equilibrium configuration of a cell composed of $N = 256$ elements. The left panel show a cut-away view of the cell isosurface after rendering with ray-tracing software. The right panel shows a perspective view of the individual elements.

R^2. These quantities are defined via:

$$E = \sum_{\alpha=1}^{N-1} \sum_{\beta=\alpha+1}^{N} V_{\text{intra}}(|\mathbf{r}_\alpha - \mathbf{r}_\beta|) \ , \tag{7}$$

and

$$R^2 = \frac{1}{N} \sum_{\alpha=1}^{N} (\mathbf{r}_\alpha - \mathbf{r}_0)^2 \ , \tag{8}$$

where $\mathbf{r}_0$ is the center of mass of the cell. I must make absolutely clear that the use of the term "internal energy" is not of biological significance, but is merely a convenient theoretical quantity with which to gauge the accuracy of our computational procedures. In cell biology, when one thinks of energy, one usually considers cell metabolism and ATP production – here, we are simply tracking stored elastic energy in a coarse-grained model of the cell cytoskeleton. Typical late-time evolution of the internal energy and the mean squared radius is shown in Fig.4a and 4b respectively. Note in Fig.4a that the internal energy decreases monotonically, as is required, since, with no noise, there is no energy input into the cell. The plateaux in the data indicate long-lived saddle points in phase space, from which the cell gradually escapes as neighboring elements slide past each other.

I will make a quantitative analysis of the equilibrium energy in the next subsection. It is a simpler matter to analyze the mean squared radius. If we take the limit of infinitely many elements, then the cell, in equilibrium, can be considered as a sphere of uniform density. One can then calculate R^2 directly:

$$R^2 = \frac{\int_0^{r_c} dr \ r^2 \ r^2}{\int_0^{r_c} dr \ r^2} = \frac{3}{5} r_c^2 \ . \tag{9}$$

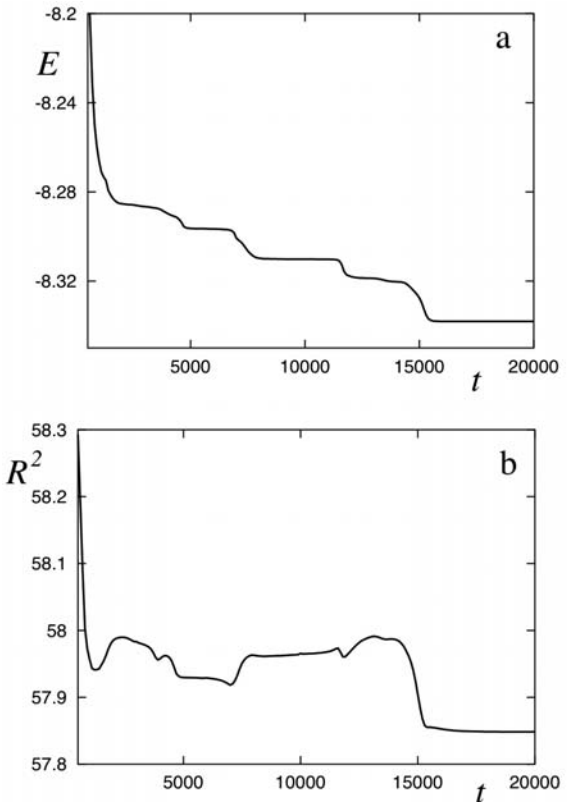

FIGURE 4. Typical time series for the internal energy E (panel a) and mean square radius R^2 (panel b). These data result from equilibration of a cell consisting of N=256 elements, with a time step of dt=0.1, and zero noise (D=0). Throughout the temporal range shown, the cell is close to equilibrium. The various features result from small scale rearrangements of elements moving under deterministic relaxational dynamics.

Thus, for the chosen value of $r_c = 10\mu m$ one would expect the numerical value of R^2 to be close to $60\mu m^2$. I computed the equilibrium value of R^2 from 10 independent realizations (i.e. different random initial conditions), and calculated the mean and standard deviation. The results are shown in Table 1 for cells composed of $N = 128$ elements and $N = 256$ elements. The agreement is very good, indicating that i) the estimate of the element radius, as given in Eqn.(6) is accurate, and ii) the equilibrated cell is approximately spherical, and composed of a spatial distribution of elements that is uniform to a good degree of accuracy.

Adding small levels of noise (i.e. setting $D > 0$) has a relatively modest effect on the equilibration process. Large noise levels are to be avoided as they overwhelm the internal mechanics and destroy the coherence of the cell.

N	R^2	error
128	58.6	$\pm$ 0.7
256	58.0	$\pm$ 0.3

TABLE 1. Measured values of mean square radius (sample average and error) for cells composed of N=128 and N=256 elements. The theoretical estimate for large N is R^2=60μm^2.

3.2. Surface Effects of Cell Equilibration

It is worthwhile to examine the numerical effect of the looser packing of elements on the surface [13]. We estimate this by calculating the energy of the equilibrium cell configuration taking into account surface effects, and comparing with simulation.

We first need to find the fraction of elements in the surface layer. The volume of the cell is the sum of two contributions: the inner core of elements, which are close packed in three dimensions, and the outer half layer of surface elements which are close packed in (quasi) two dimensions. (We only count the outer half layer, as the inner hemispheres of the surface elements are close-packed in three dimensions with the subsurface elements.) From this construction, and letting N_s indicate the number of surface elements, one obtains the following two equations:

$$\frac{4}{3}\pi r_c^3 = \frac{4}{3}\pi r_e^3 \, \frac{(N-N_s)}{p_3} + \frac{2}{3}\pi r_e^3 \frac{N_s}{p_2} \tag{10}$$

and

$$4\pi r_c^2 r_e = \frac{2}{3}\pi r_e^3 \frac{N_s}{p_2} \; . \tag{11}$$

The packing fraction $p_2 = \pi/3\sqrt{3}$ is the fraction of space occupied by close-packed spheres in a plane. By eliminating the ratio r_e/r_c from these two equations, we derive a self-consistent expression for the fraction of surface elements. Defining $\sigma = N_s/N$ we have

$$\sigma N^{1/3} = \frac{6p_2}{p_3^{2/3}} \left[1 - \frac{p_3 \sigma}{2} \left(\frac{2}{p_3} - \frac{1}{p_2} \right) \right]^{2/3} \; . \tag{12}$$

By equating σ to unity, we can estimate the critical number of elements N_c below which all elements are essentially surface elements. We find $N_c = 54p_2 \sim 32$. For large N we can solve Eqn.(12) perturbatively, to find

$$\sigma \sim \frac{6p_2}{p_3^{2/3}} N^{-1/3}(1 - aN^{-1/3}) \; , \tag{13}$$

where

$$a = \frac{4p_2}{p_3^{2/3}} \left(1 - \frac{p_3}{2p_2} \right) \; . \tag{14}$$

Numerically, the leading term yields $N_s \sim 4.4 \; N^{2/3}$. From this, one finds the sobering fact, that even with $N = 256$ elements, the fraction of surface elements is roughly 70%. Now, in the minimal energy configuration, each element-element interaction will contribute a gain of $-\Delta V$ to the energy. Core elements, if close-packed, will have 12 neighbors, while surface elements, if close-packed, will have 9

neighbors. The minimum energy will then be

$$E_{\rm bulk/surf} \simeq -\frac{\Delta V}{2} N[9\sigma + 12(1-\sigma)] \ . \tag{15}$$

I have recorded the equilibrium internal energy of cells (i.e. the element-element binding energies) for $N = 128$ and $N = 256$, collecting data from 10 realizations in each case. Table 2 gives the results, along with the comparison to the naive estimate (neglecting surface effects, i.e. setting $\sigma = 0$), and the estimate given in Eqn.(15). In all cases, $\Delta V \simeq 0.0063$. The agreement is good, and shows the importance of the surface energies for moderately large values of N. The situation is actually more complicated, as there are small contributions from elements which are next nearest neighbors – due to the exponential tail of the interaction potential. I have found that these interactions lead to artifacts in cells composed of large numbers (thousands) of elements, unless the energy scale of the interaction is appropriately scaled with N.

N	$E_{\rm av}$	error	$E_{\rm bulk}$	$E_{\rm bulk/surf}$
128	3.90	$\pm$ 0.02	4.84	4.02
256	8.36	$\pm$ 0.03	9.68	8.29

TABLE 2. Measured values of internal energy (average and error) compared with theoretical estimates considering bulk interactions only, $E_{\rm bulk}$, and bulk/surface interactions, $E_{\rm bulk/surf}$; for cells composed of N=128 and N=256 elements.

I should stress that in this discussion of energetics I have not given units to the energy scale. This is because the energy scale has yet to be calibrated with real cells. One approach would be to consider coarse-graining individual actin filaments (whose energetics are quantitatively available from experiment) to a small patch of cytoskeleton (i.e. an element), and calculate the increase in element-element interaction energy as a function of coarse-graining scale. This is work in progress.

3.3. Cell Growth and Cell Division

I now turn to a discussion of two essential cellular processes: cell growth and cell division.

Cell growth is characterized by an increase in the volume of the cell. The rate at which this process occurs will depend on the availability of nutrients, the space available for growth, and the presence or not of cell regulatory processes, such as contact inhibition. I assume here that nutrients are not limiting, and do not consider contact inhibition, although these effects can be straightforwardly modeled if necessary. The algorithm for growth is as follows. At each time step we allow a subset of elements in the cell to attempt a replication process with some small probability. For a given element α at a position $\mathbf{r}_\alpha$ we randomly select a point $\mathbf{r}_{\alpha'}$ a distance r_e from element α. If this point is sufficiently far from neighboring elements (meaning that $|\mathbf{r}_{\alpha'} - \mathbf{r}_\beta| > d_{min}$) then a new element is placed at the point.

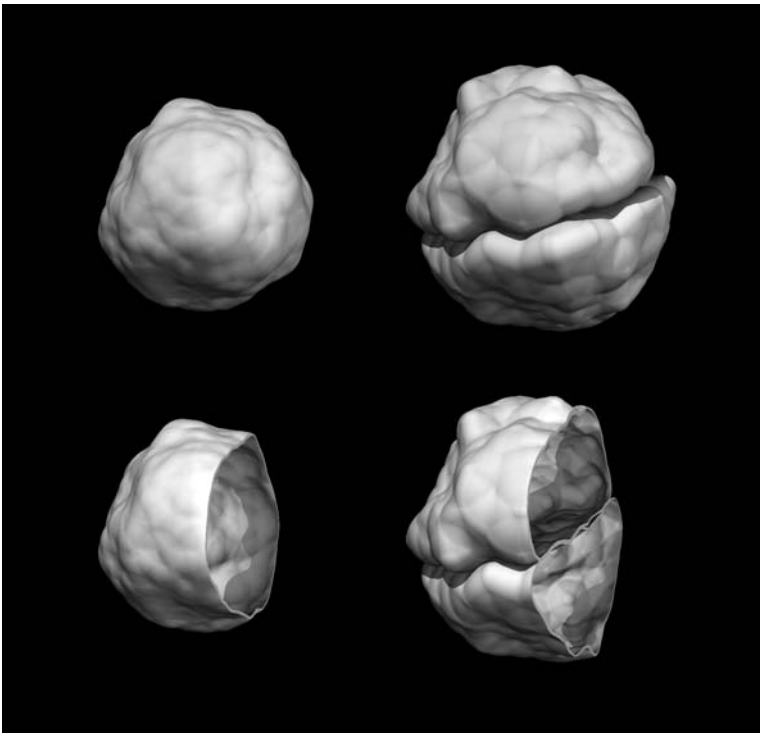

FIGURE 5. Two different views of cell division. The parent cell (left panels) has approximately 120 elements just before division into two daughter cells (right panels).

Several iterations of the internal element biomechanics will locally equilibrate the new element into the structure. I mentioned that only elements from a particular subset are allowed to replicate. This subset is generally chosen to consist of those elements which are in the core region of the cell. Surface elements clearly have more free space around them, and allowing them to replicate can cause cells to grow in a filamentous or invasive manner. This is not appropriate for cell growth in most tissue types, but would be relevant for more advanced cell types, such as neurons, or for modeling growth of filamentous fungal cells.

Cell division is relevant to most tissue types, but is especially important for developmental processes, wound healing, and tumor growth. When discussing cell division in the context of development it is important to distinguish early cleavage divisions (by which the zygote divides into a large number of individual cells, but does not change in size) and later stage cell divisions involving cell separation (cytokinesis) and an increase in the overall size of the embryo. We focus here on the latter, although cleavage divisions can also be implemented in the SEM in a relatively straightforward manner.

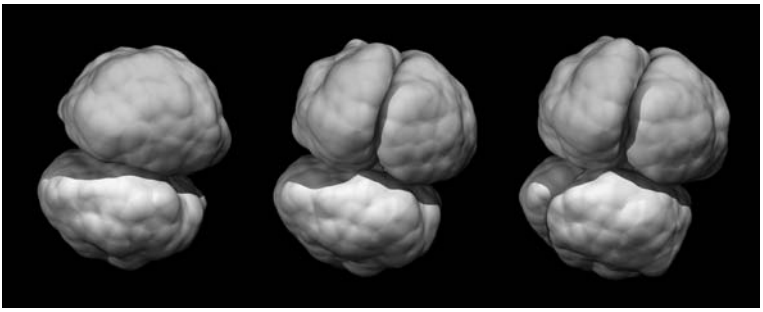

FIGURE 6. A sequence of views a few hundred iterations apart. The daughter cells from Fig.5 have grown to full size (left panel) and divide, one after another, producing three (middle panel), and then four (right panel) new daughter cells. The division planes are chosen according to the algorithm described in the main text.

Cell division is implemented to mimic cytokinesis, without attempting detailed modeling of processes involving cellular structures such as centrioles and the spindle. Once the cell has reached an appropriate size, the algorithm instructs the cell to divide. The first step is to select an axis (parallel to the spindle axis of mitosis), perpendicular to which will be the division plane. The simplest procedure is to choose a randomly oriented axis passing through the center of mass of the cell. This is not recommended though, as it will produce perverse cell divisions for parent cells which deviate from a spherical shape. Better is to choose the axis approximately parallel to the "long axis" of the cell. A rigorous method for finding this axis is to calculate the inertia tensor of the cell, and diagonalize this to find the principal axes. The longest principal axis will be the required axis. I actually use a simpler method. Once a cell is marked for division we search for the two elements in the cell whose mutual separation is greatest. [This is an $O(N_i^2)$ operation for a cell composed of N_i elements, but cell division is a rare process compared to the much smaller timescale of local biomechanics, and so there is no practical overhead in using this method.] The vector joining these two points, $\mathbf{n}$, is then chosen to be the axis which defines the division plane. To divide the cell roughly evenly about this plane, I take each element in turn and construct the dot product $(\mathbf{r}_{\alpha_i} - \mathbf{r}_i) \cdot \mathbf{n}$, where $\mathbf{r}_i$ is the position vector of the center of mass of the parent cell i. If the dot product is positive (negative) the element is defined to be in daughter cell i' (i''). Elements are relabeled accordingly, and the local biomechanics equilibrates the two new cells. If the intercellular adhesion is fairly strong, the two new cells will tend to remain closely bound. If the intercellular adhesion is weak, the cells will remain closely associated for a substantial time before "rounding up." This process would need to be augmented by additional repulsive interactions to simulate more rapid cytokinesis and cell separation in certain tissue types. Two snapshots are

given in Fig.5 showing a parent cell just before division (left panel) and the two new daughter cells a short time afterwards (right panel).

In Fig.6 I show the next two divisions, taking two cells to four. The division axes chosen by the algorithm are seen to be biologically plausible, with four evenly sized and evenly shaped cells resulting from two divisions. These figures are generated from an algorithm of cell growth and division. It would be straightforward to start with a large cell modeling a zygote, and to perform cleavage divisions following this algorithm. In this case, one could produce a virtual blastula, and compare the distribution of cell sizes and growth trajectory with experimental samples.

3.4. Multicellularity

In this final subsection I present images of a growing multicellular cluster. I begin with a single cell, which grows and divides, and the daughter cells, likewise, grow and divide, and this process continues. There is no further algorithmic control of the process. There is simply growth, division (as described above), and the continual churning of local biomechanics, following Eqn.(1).

In Fig.7 and Fig.8 are shown two visualizations of a large cluster of roughly one thousand cells. The daughter cells have 64 elements, and a cell is instructed to divide once it has more than 128 elements. The simulation, by this time, is tracking the position vectors, cell labels, and interactions of $\sim 100,000$ elements, comprising ~ 1000 cells.

In Fig.9–11 are shown similar images, but this time the cells are composed of four times as many elements, i.e. the daughter cells have 256 elements, and a cell divides once it has more than 512 elements. The cluster in this case has of order 100 cells. Each of these simulations required approximately one day of computer time on a single 2GHz workstation. High resolution versions of these figures are available on the book DVD, along with some color images showing the elements embedded in the cross-sectional views. We have also included two movies showing the growth of the cell clusters. More movies (showing a range of cell behaviors) are available on the group website [14].

Particularly striking, at least to the author, are the emergent cellular arrangements, visible in the cut-away images. Although this application of a growing multicellular spheroid is of limited interest biologically, it provides, I believe, proof of principle, and gives a good indication of the type of three-dimensional structures which can be produced on a relatively short time-scale by the SEM. We are in the process of converting our code to multi-processor form, so that we can make use of parallel computing on a cluster. The SEM is ideally suited to parallelization, as the interactions between elements are short-ranged.

4. Conclusions

In this chapter I have attempted to give an introduction to the SEM, concentrating on the local biomechanics, and the processes of cell growth and cell division. I have illustrated the power of the method by combining these processes to grow a

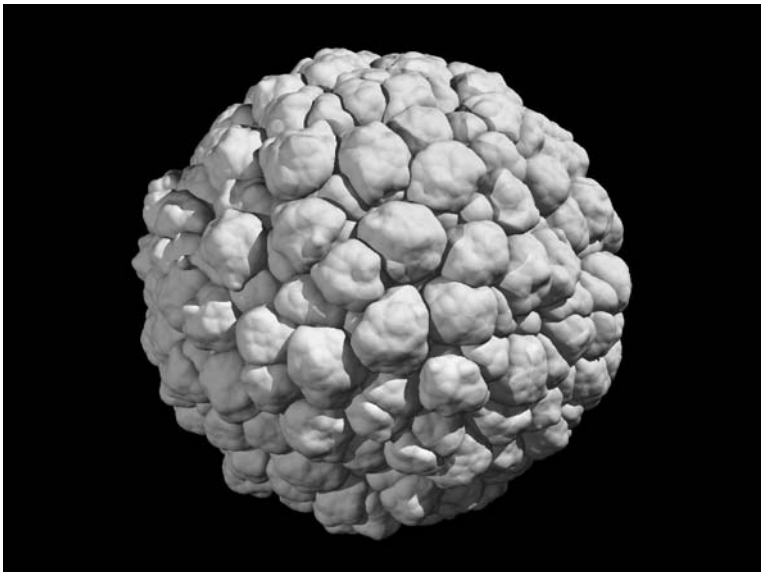

FIGURE 7. A large cluster of more than 1000 cells. Each cell is composed of approximately 100 elements. The cluster started as a single cell, and grew from repeated cell growth and cell division.

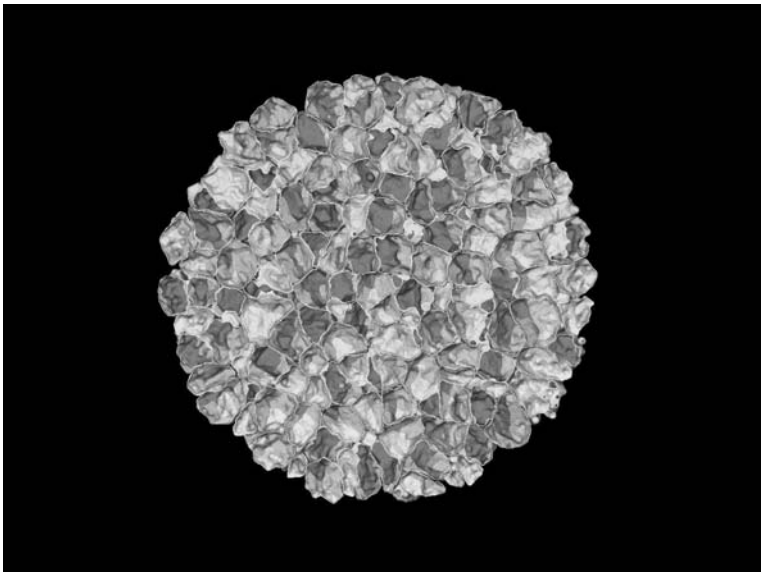

FIGURE 8. A cross-sectional view of the cluster shown in Fig.7. This visualization gives a view of the distribution of cell shapes inside the cluster.

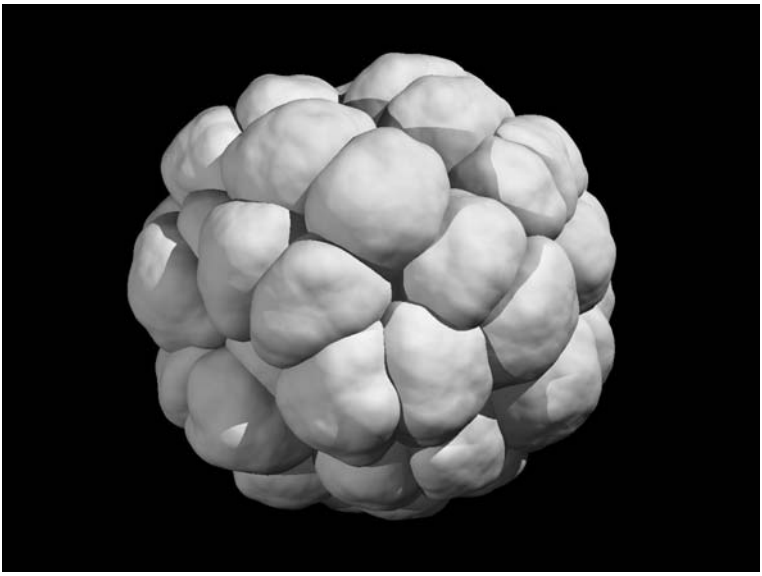

FIGURE 9. A smaller cluster of roughly 100 cells, but with each cell composed of several hundred elements. The cells are therefore smoother, and their shape less dependent on the placement of individual elements. See also a simulation MovIII.3.9 from the accompanying DVD.

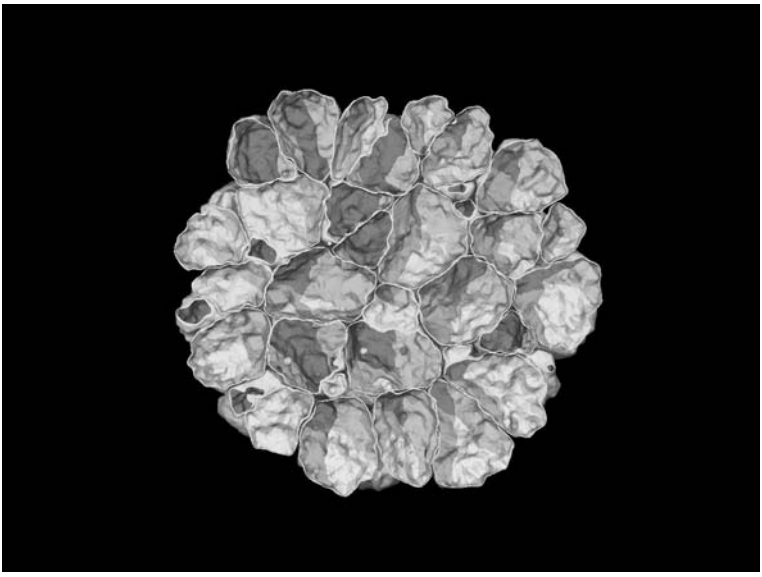

FIGURE 10. A cross-sectional view of the cell cluster shown in Fig.9.

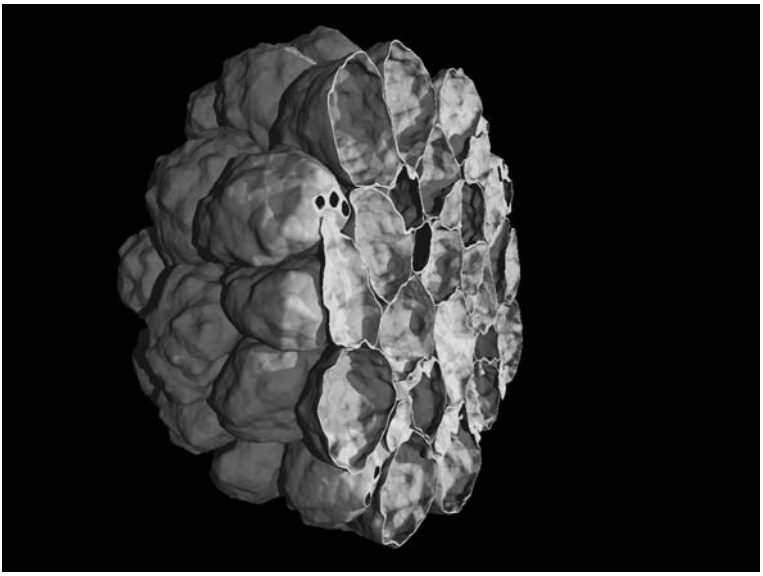

FIGURE 11. A third visualization of the cell cluster previously shown in Fig.9 and Fig.10, now showing both the three-dimensional structure, and a sense of the internal cross-sectional shapes of individual cells.

relatively large three-dimensional cluster of cells, in which each cell is composed of $\sim$ 100 elements. As the figures illustrate, the emergent dynamics from this algorithm yields strikingly realistic cellular shapes and multicellular structures. The simple system simulated here, in the absence of additional cell signaling, might be regarded as a crude model of a small avascular tumor, but we have formulated it here more in the spirit of a theoretical illustration. Our group is applying the SEM to specific multicellular structures, in particular the epiblast of the early chick embryo.

On a different tack, in recent months work in our group has focused on taking the SEM beyond the level of a qualitative algorithm for three dimensional cellular structures. We have used the SEM to perform *in silico* micro-rheology measurements of the viscoelastic properties of the cell cytoskeleton [13]. In particular we measure the frequency- dependent storage and loss moduli, and compare these quantitative results to the numerous experimental measurements on actin gels. We have found that the SEM can reproduce some of the experimental results over several decades of frequency, which indicates that the simple phenomenological dynamics of the SEM may be sufficient to capture the low to intermediate frequency response of cytoskeletal networks. This is an important advance, as it brings large-scale multicellular modeling (in the guise of the SEM) into direct contact with biophysical and bioengineering measurements of intracellular mechanics, thus lending credence to the coarse-grained phenomenological approach.

A feature of the SEM that allows for accommodation of additional biological detail is the ability to specify particular properties to each element. Restricting our attention to the intra-cellular potentials, by ascribing different binding strengths to elements, one can simulate a cell with internally varying viscoelastic properties. In principle one can utilize heterogeneous subcellular elements to describe more of the intracellular structure. At the limit of single processor computational power (for a few days of processing), one can simulate $\sim 10^6$ elements for one hundred thousand iterations. In such a simulation, each element has a physical dimension of about 100 nm. Bearing in mind that the diameter of a microtubule is about 25 nm, and that the diameter of a microvesicle is about 100 nm, one sees that a lot of intra-cellular dynamics could be encoded in the SEM in this case. Such a simulation would need careful preparation, since, with many types of elements, one would need to define a large matrix of the different types of interactions.

In conclusion, I believe that the SEM has the potential to become a powerful modeling platform for multicellular systems, particularly for cases in which plausible three-dimensional cell shape and biomechanics are required. The SEM is flexible enough to accommodate additional diverse biological processes, such as intracellular chemical kinetics, intercellular signaling, and cell differentiation. Our group is focusing applications of the SEM on early developmental processes, although its potential scope is far wider. Our programs are written in Fortran 90 modules, and will be available on our website [14] for academic use in the near future.

Acknowledgment

I would like to thank my current and former students Ralph DeSimone, Ramon Grima, Sebastian Sandersius, Erick Smith, and Jens Weismüller, for their crucial contributions to the development and visualization of the SEM. In particular I would like to thank Jens Weismüller for his care in producing the beautiful SEM visualizations in this chapter. This work has been partially supported by the National Science Foundation and National Institutes of Health, under grants IOB-0450680 and DMS/NIGMS-0342388.

References

[1] J. A. Glazier and F. Graner, *Simulation of the Differential Adhesion Driven Rearrangement of Biological Cells* Phys. Rev. E **47** (1993), 2128–2154.

[2] E. Palsson and H. G. Othmer, *A Model for Individual and Collective Cell Movement in Dictyostelium discoideum* Proc. Natl. Acad. Sci. (USA) **97** (2000), 10448–10453.

[3] D. Drasdo, R. Kree, and J. S. McCaskill, *Monte Carlo Approach to Tissue-Cell Populations* Phys. Rev. E **52** (1995), 6635–6657.

[4] K. A. Rejniak, *A Single Cell Approach in Modeling the Dynamics of Tumor Microregions* Math. Biosci. Eng. **2** (2005), 643–655.

[5] T. J. Newman, *Modeling Multicellular Systems Using Subcellular Elements* Math. Biosci. Eng. **2** (2005), 611–622.

[6] B. Alberts *et al*, *Molecular Biology of the Cell* 4th Edition, Garland, New York 2002.

[7] R. E. Keller and M. Danilchik, *Regional Expression, Pattern and Timing of Convergence and Extension During Gastrulation of Xenopus laevis* Development **103**, 193–209.

[8] L. A. Davidson, M. A. R. Koehl, R. Keller, and G. F. Oster, *How Do Sea Urchins Invaginate – Using Biomechanics to Distinguish Between Mechanisms of Primary Invagination* Development **121** (1995), 2005–2018.

[9] M. E. Gracheva and H. G. Othmer, *A Continuum Model of Motility in Amoeboid Cells* Bull. Math. Biol. **66** (2004), 167–193.

[10] R. Grima, *Ph.D. Thesis* Arizona State University (2005).

[11] D. C. Rapaport, *The Art of Molecular Dynamics Simulation* Cambridge University Press 2004.

[12] N. G. van Kampen, *Stochastic Processes in Physics and Chemistry* North Holland, Amsterdam 1992.

[13] S. Sandersius and T. J. Newman, in preparation.

[14] Group website: http://phy.asu.edu/biodyn

Timothy J. Newman
Department of Physics, Arizona State University
P.O. Box 871504, Tempe, AZ 85287, USA
e-mail: `timothy.newman@asu.edu`

Single-Cell-Based Models in Biology and Medicine
ed. by A.R.A. Anderson, M.A.J. Chaplain, K.A. Rejniak
Mathematics and Biosciences in Interaction, 241

IV. Viscoelastic Cell Models

General Introduction

As is stated in the chapter by E. Palsson: *cell elasticity is important—sometimes cells need to have the ability to use other cells as stepping stones to move upwards, such as when Dictyostelium pre-spore cells crawl up the stalk cells to form a fruiting body. The force responsible for the upwards motion must be transmitted down to the ground and this can only be achieved if the cells have a solid elastic component.*.

In this chapter entitled Viscoelastic Cell Models, mathematical models are presented in which each cell contains some elastic and some viscous components that allow for cell deformation simultaneously preserving cell volume. This approach allows for an explicit use of adhesive and cohesive links between cells to model cell adhesion and repulsion, and for the modelling of various forces acting on individual cells during their collective behaviour.

In chapter by A. Fogelson, two approaches in modelling platelet aggregation during blood clotting are discussed. The microscopic scale allows for the inclusion of a detailed mechanism of platelet biding and unbinding, platelet response to stimuli sensed from the surrounding fluid and chemistry on the platelet's surfaces. The macroscopic scale model treats the same cell interactions in a continuum manner and can be used to describe events in large diameter blood vessels.

The Chapter by E. Palsson, A 3-D Deformable Ellipsoidal Cell Model with Cell Adhesion and Signalling, uses *Dictyostelium discoideum* as a model system to discuss different cell-cell interactions and signalling, including cell sorting, cell aggregation and slug movement, cAMP signalling from pacemaker cells and the formation of 3-dimensional mounds.

In the chapter by K. Rejniak, Modelling the Development of Complex Tissues using Individual Viscoelastic Cells, an immersed boundary model of a fully deformable elastic cell is presented together with several cellular processes, such as cell growth, division, apoptotic death, epithelial polarisation and directional cell movement. Furthermore, applications to model tissue folding, multicellular growth and the formation of epithelia are also discussed.

Single-Cell-Based Models in Biology and Medicine
ed. by A.R.A. Anderson, M.A.J. Chaplain, K.A. Rejniak
Mathematics and Biosciences in Interaction, 243–269

IV.1 Cell-based Models of Blood Clotting

Aaron L. Fogelson

Abstract. The formation of platelet aggregates during blood clotting is modeled on two scales. The microscopic scale models track individual platelets, their mechanical interactions with one another and the surrounding fluid, their detection of and response to chemical activators, and the formation of cohesive and adhesive 'links' between platelets and between platelets and the vascular wall. These models allow inclusion of detailed mechanisms of binding-unbinding, platelet stimulus-response, and chemistry on the platelets' surfaces. The macroscopic scale models treat the same interactions in terms of concentrations of platelets and distributions of cohesive and adhesive links, and can be used to study platelet aggregation in vessels of clinical interest including the coronary and cerebral arteries.

1. Introduction

In this chapter we discuss modeling of thrombosis (intravascular blood clotting). Intravascular clots (thrombi) are initiated by damage to the endothelial cell lining of a blood vessel and involve the formation on the damaged surface of clumps of cells intermixed with a fibrous protein gel. This happens in the face of continued blood flow past the injury, and the interplay between the development of the clot and the local fluid dynamics is one of our principal concerns. Under some conditions, the clot grows to completely occlude the vessel. In other situations, it grows to a maximum size and then portions of it break away and the clot's size may settle into a rough steady state. We wish to be able to capture both kinds of behavior in our models, and to understand why they occur.

Clot formation involves two intertwined processes both of which are initiated by damage to the vessel lining. One process is platelet aggregation and begins when circulating blood platelets adhere to the damaged wall. Other platelets can be activated by chemicals released by these first platelets and then bind to the already wall-adherent platelets; this results in the buildup of a platelet aggregate or thrombus. The other process is coagulation which we view as itself comprised of

This work was funded, in part, by grants from the National Science Foundation: DMS-9805518, DMS-0139926, and DMS-0540779.

two distinct subprocesses. The first of these involves a network of tightly-regulated enzymatic reactions that begins with reactions on the damaged vessel wall and continues with important reactions on the surfaces of activated platelets. The end product of this reaction network is the enzyme thrombin which (i) activates additional platelets and (ii) creates monomeric fibrin which polymerizes into the fibrous protein gel component of the clot. This polymerization process is the second subprocess of coagulation. Both platelet aggregation and the two parts of coagulation occur in the presence of moving blood, and are strongly affected by the fluid dynamics in ways that we would like to understand. Just one indication of the effect of different flow regimes is that clots that form in the veins, where blood flow is relatively slow, are comprised mainly of fibrin gel (and trapped red blood cells), while clots that form under the rapid flow conditions in arteries are comprised largely of platelets. Ultimately, we would like to understand why there is this fundamental difference in venous and arterial clotting.

This chapter is mostly concerned with models of platelet aggregation but we are developing these models with the future inclusion of coagulation in mind. Thus, for example, we make provision for the later inclusion of coagulation chemistry on surfaces of model activated platelets. Two classes of platelet aggregation model are described in this chapter. One involves the behavior of a collection of individual platelets interacting with the suspending fluid, the vessel wall, and platelet activating chemicals. We refer to these as our microscale platelet models, and note that they are appropriate for small diameter arterioles and venules (approximately 50 microns in diameter), as well as, perhaps, for detailed studies of the aggregation process in small portions of a larger clot. The other, macroscale type of model, tracks the dynamics of the same sorts of interactions but on a larger scale appropriate for larger vessels. These continuum models involve the spatial-temporal evolution of a platelet thrombus using density functions to describe the distribution of the relevant platelets and other species. For the microscale modeling a major tool is the Immersed Boundary (IB) method. For the macroscale models, the classical immersed boundary method motivates our modeling approach.

Because it is important to understand the fundamentals of the IB method in order to understand how we model platelet aggregation events in both scale models, we begin the body of this chapter with a brief introduction to the IB method. Then we describe aspects of platelet biology important in our modeling efforts. After that we describe the microscale aggregation models based on the immersed boundary method. Finally, we discuss how these ideas are extended to much larger spatial scales in our macroscale models.

2. Immersed Boundary Method

The fundamental problem for which the IB method has been developed concerns the interactions of a viscous incompressible fluid with one or more moving and/or deformable elastic objects in contact with that fluid. The motion of the fluid influences the motion of the elastic objects and *vice versa*, and so the IB method

involves coupled equations of motion for both types of material (fluid and elastic) and solves for both motions simultaneously. To introduce the IB method we focus on a simple model problem in which a single fluid-filled closed elastic membrane is immersed in a viscous fluid (see Fig.1). For simplicity we describe a two-dimensional model problem, but emphasize that the IB method has been used extensively for three-dimensional studies in a number of application areas. We also assume that the fluid inside and outside the membrane has the same density

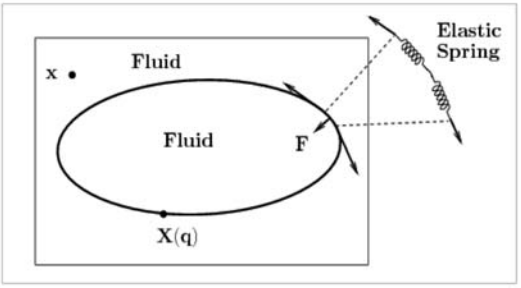

FIGURE 1. Model Problem: Massless elastic membrane immersed in fluid. Here, $\mathbf{x}$ is a point in the fluid, $\mathbf{X}(q)$ is a material point on the immersed elastic membrane, and $\mathbf{F}$ is the force generated at a point in the membrane because the membrane is stretched.

and viscosity (although this is not essential). The physics of the model problem is that the elastic membrane is under tension and exerts force on the adjacent fluid. These forces may cause the fluid to move and, in that case, points on the membrane move along with the fluid. In the IB method, the fluid is described in Eulerian terms through a velocity field $\mathbf{u}(\mathbf{x},t)$ and pressure field $p(\mathbf{x},t)$ defined at every point $\mathbf{x}$ in the physical domain Ω. The elastic membrane is described in Lagrangian terms. Let the elastic membrane be parameterized by q, and denote by $\mathbf{X}(q,t)$ the spatial coordinates at time t of the membrane point labeled by q. The IB equations are coupled equations of motion for the fluid variables $\mathbf{u}(\mathbf{x},t)$ and $p(\mathbf{x},t)$ and the membrane configuration $\mathbf{X}(q,t)$. The basic IB equations are:

$$\rho(\mathbf{u}_t + \mathbf{u}\cdot\nabla\mathbf{u}) = -\nabla p + \mu\Delta\mathbf{u} + \mathbf{f}, \qquad \nabla\cdot\mathbf{u} = 0, \tag{1}$$

$$\mathbf{F}(q,t) \;=\; \mathbf{F}(\mathbf{X}(q,t), \mathbf{X}_q(q,t)) \tag{2}$$

$$\mathbf{f}(\mathbf{x},t) \;=\; \int \mathbf{F}(q,t)\;\delta(\mathbf{x}-\mathbf{X}(q,t))\;dq, \tag{3}$$

$$\frac{\partial\mathbf{X}}{\partial t}(q,t) = \int_\Omega \mathbf{u}(\mathbf{x},t)\;\delta(\mathbf{x}-\mathbf{X}(q,t))d\mathbf{x}. \tag{4}$$

Eqs.(1) are the Navier Stokes equations which describe the dynamics of a viscous incompressible fluid, of constant density ρ and constant viscosity μ, driven by a force density $\mathbf{f}$ which here arises because of the elastic deformation of the immersed membrane. Eq.(2) specifies the elastic force (per unit q) at each point of the immersed boundary object. The functional dependence of this

force on the state of the boundary is specified appropriately to the material being modeled. An example is given below. Eq.(3) defines the fluid force density $\mathbf{f}(\mathbf{x}, t)$ in terms of the immersed boundary elastic force density $\mathbf{F}$. By integrating both sides of this equation over an arbitrary region of the fluid, we see that the total fluid force on this region equals the total elastic force along the portions of the immersed boundary, if any, that pass through this region. So the fluid force density is concentrated along the immersed boundary curve. Eq.(4) specifies that the velocity of each immersed boundary point equals the fluid velocity at the same location. This is a formulation of the no-slip boundary condition for viscous flows. The key idea in this formulation that makes the IB approach so useful in modeling biofluid problems is that as far as the fluid is concerned, the immersed objects are seen only through the force field $\mathbf{f}$. Even if the objects move or deform substantially, there is no change in the geometry of the fluid region; fluid is everywhere and only the distribution of forces exerted on the fluid by the elastic objects changes. In the model problem and the platelet applications discussed in this chapter, we assume that the IB objects are neutrally buoyant; the IB membrane itself carries no mass, its mass is attributed to the fluid in which it sits.

To illustrate the specification of the IB force function, we consider the case of the forces generated within a stretched fiber. Let the points on the fiber be denoted by $\mathbf{X}(q)$, assume that the only force the fiber can sustain is tension along the fiber direction $\boldsymbol{\tau}(q)$, and let $T\left(\|\frac{\partial \mathbf{X}}{\partial q}\|\right)$ give the dependence of the tension on the local stretch of the fiber. Consider a segment of the fiber, as shown in Fig.2, and let $\boldsymbol{\mathcal{F}}$ denote the force that this segment of fiber exerts on the surrounding fluid. Because the fiber segment is massless, we have the balance of forces,

$$0 = -\boldsymbol{\mathcal{F}} + (T\boldsymbol{\tau})|_{q=q_2} - (T\boldsymbol{\tau})|_{q=q_1} = -\boldsymbol{\mathcal{F}} + \int_{q_1}^{q_2} \frac{\partial}{\partial q}(T\boldsymbol{\tau})dq. \tag{5}$$

Hence, $\mathbf{F} = \frac{\partial}{\partial q}(T\boldsymbol{\tau})$ gives the force density (per unit q) in the fiber, and the force exerted on the fluid by this fiber segment is given by the integral of $\mathbf{F}$ over the segment. Specifying the function T, *e.g.*, $T = S(\|\frac{\partial \mathbf{X}}{\partial q}\| - r)$ for positive constants S and r, determines the fiber's elastic properties.

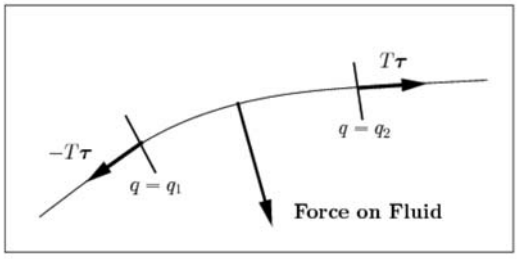

FIGURE 2. Force on segment of elastic fiber.

In actual IB calculations, the Navier Stokes equations are approximated at points of a Cartesian grid placed over the domain Ω. A second grid of Lagrangian points is used to discretize each elastic object, and the $\delta-$functions in Eqs.(2)–(4) are approximated by smooth but very localized functions. This implies that the fluid force density is nonzero only for fluid grid points close to the immersed boundary and that the velocity of each immersed boundary point is computed as an average of the fluid velocity at grid points near that IB point. Much more information about the IB method can be found in Peskin's review article [25] and the references cited therein.

3. Platelet Biology

Platelets are anuclear blood cells that have a discoid shape when circulating with the blood in their usual dormant or unactivated state. They have a diameter of about 2 μm and a number density of about 250,000-300,000/μl. They are much smaller and less numerous than the red blood cells that make up about 45% of the blood's volume, and so individual platelets have a negligible effect on the flow of the blood. In their unactivated state, platelets do not adhere to one another nor to the intact endothelial cell lining of blood vessels. Disruption of the endothelial layer exposes to the blood collagen and adsorbed von Willebrand factor (vWF) molecules in the subendothelial matrix. Platelets adhere to both molecules via specific platelet surface receptors. In addition to slowing or stopping platelet motion over the subendothelium, this binding triggers intracellular signaling pathways that lead to platelet activation.

Platelet activation is multifaceted: (i) The platelet's cytoskeleton is reorganized and the platelet balls up into a spherical shape and extends a number of appendages called pseudopodia. The platelet becomes sufficiently flexible that over time it can spread out over the surface to which it is adhered. (ii) The platelet surface membrane changes in important ways: Integrin ($\alpha_{IIb}\beta_3$) receptors are activated and become capable of binding dimeric fibrinogen molecules and multimeric vWF molecules from the blood plasma. By binding to receptors on two platelets, these molecules serve as links between the platelets. The platelet membrane also undergoes processes, e.g., flipping negatively-charged phosphatidylserine molecules from the cytoplasmic to exterior face, that makes it able to support important reactions of the coagulation process. (iii) The activated platelet secretes chemicals into the surrounding blood plasma. Probably the most important of these are ADP released from cytoplasmic storage granules and the coagulation enzyme thrombin, activated by the prothrombinase enzyme complex that can form on the surface of activated platelets. A platelet has specific surface receptors for ADP and thrombin and binding of these molecules to an unactivated platelet can trigger the activation process in that platelet. These chemicals provide a second pathway to platelet activation that does not require direct contact of the platelet with the injured vessel wall, and allows the activation process to be propagated away from the wall.

Exposure of the subendothelium also brings the passing blood into contact with Tissue Factor molecules embedded in the matrix and initiates the coagulation process. The first coagulation enzymes are produced on the subendothelial matrix and released into the plasma. If they make their way through the fluid to the surface of an activated platelet, they can participate in the formation of enzyme complexes on the platelet surface that continue and accelerate the pathway to thrombin production. Thrombin released from the platelet surface feeds back on the enzyme network to accelerate its own production, activates additional platelets (as mentioned above), and converts soluble fibrinogen molecules in the plasma into insoluble fibrin monomers. Once formed, the fibrin monomers spontaneously bind together into thin strands, these strands join side to side into thicker fibers, and a branching network of fibrin fibers grows between and around the platelets in a wall-bound platelet aggregate. Ends of the fibrin strands may be anchored to the surfaces of the platelets by binding of fibrin to integrin ($\alpha_{IIb}\beta_3$) receptors. The coagulation process, in particular, the interactions of coagulation biochemistry with flow and platelet events, is a fascinating subject, but it is not the focus of this chapter. If interested, see [13, 17, 20].

The red blood cells, which make up almost half of the blood's volume, have significant effects on the motion and distribution of platelets in blood flowing in a tube. For one, platelets exhibit much larger transverse excursions (across the tube) than under similar flow conditions in plasma alone. This motion is often described as an enhanced diffusivity (above Brownian motion), and experimental studies suggest that the degree of enhancement depends on the flow shear rate. A second effect is that the concentration of platelets is higher (by up to eight fold) a few microns from the tube wall than at other distances from the wall. This effect is seen only for shear rates above 200 sec^{-1} at which red blood cells deform, and, in experiments, is a function of the volume fraction occupied by red blood cells. The rheological processes that lead to these observed effects are not understood; a rough picture is that tumbling and colliding of red blood cells generates local flow disturbances that lead to these behaviors. Whatever their cause, the enhanced random motion and the enhanced near-wall concentrations are likely important in determining the rate at which platelets contact the vessel wall and the rate at which wall-bound aggregates grow.

4. Microscale Platelet Aggregation Models

Our microscale platelet aggregation models [6, 7, 8, 28] track the motion and behavior of a collection of individual platelets as they interact with the suspending fluid, one another, and the vessel walls. These models also track fluid concentrations of platelet activating species such as ADP, cell-cell and cell-surface forces, fluid motion, and the local fluid forces on the growing thrombus. In the models, nonactivated platelets are activated by contact with reactive sites on the injured wall, or through exposure to a sufficiently high concentration of activator in the

fluid. Activation enables a platelet to cohere with other activated platelets, and to secrete additional activator. The platelets and the secreted chemical move by advection with the fluid and diffusion relative to it. Each platelet and each vessel wall is represented as an IB object, *i*.e., as a collection of elastically linked Lagrangian points that each move at the local fluid velocity. New elastic links are created dynamically to model the adhesion of a platelet to the injured wall or the cohesion of activated platelets to one another. The multiple links, which in the models can form between a pair of activated platelets or between a platelet and the injured wall, collectively represent the ensemble of molecular bridges binding real platelets to one another or to the damaged vessel. The links exert forces on the surrounding fluid to resist motions which would otherwise separate the linked entities. Through the forces generated by the platelet-platelet and platelet-wall links, aggregate growth can profoundly influence the flow, even to the extent that vessel closure can occur. Links may break if subject to sufficiently high stress by the fluid motion. As we discuss below, the models consist of stochastic and partial differential equations and auxiliary 'change of state' conditions. Model variables are fully coupled: the fluid carries the activator and platelets, while the interplatelet forces, potentiated by chemically-induced activation of the platelets, determine the local flow.

There are two major aspects of platelet behavior that the models attempt to capture. One is the mechanical interactions among the platelets, fluid, and vessel walls. The other is the platelet's detection and response to stimuli that can induce its activation. The IB approach is key to our modeling of the mechanical interactions. It also provides the scaffolding on which the platelet stimulus-response behaviors are modeled. We turn next to our use of the IB method in modeling the mechanical features of platelet aggregation.

4.1. Mechanical interactions

Our representation of discrete platelets as IB objects has evolved over the years: Initially, we treated platelets as point particles whose effective volume within the fluid was determined by the support of the approximate δ-function and whose effective interaction distance with other platelets was determined by the range of an interplatelet repulsive force that was intended to prevent platelets from overlapping one another [8]. Currently, we model platelets as closed curves of interconnected IB points in 2D and closed surfaces of interconnected IB points in 3D (see Fig.3). Their area or volume is determined by the region enclosed by the curve or surface, respectively, and is preserved because of the incompressibility of the fluid. There is no need for an explicit repulsive force, as the IB formulation automatically detects contact between the platelets and prevents one platelet from penetrating into the space occupied by another. This is an important advantage of the IB method over many other particle-tracking methods.

We describe the microscale model in its two-dimensional version for simplicity, and we describe the IB components of the model in discretized form, because

that is how they are actually implemented and for some of these components, *e.g.*, cohesive link formation, this is the natural way to describe them.

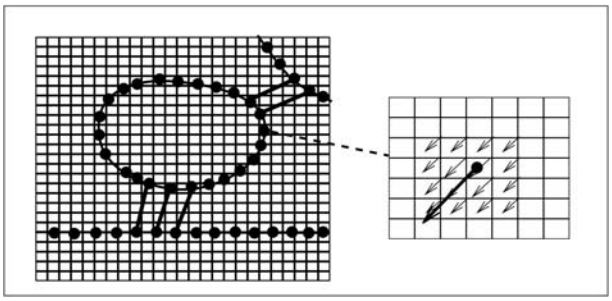

FIGURE 3. Left: Schematic of discrete Cartesian grid for fluid and Lagrangian grids for platelets and vessel wall. Right: IB force is transmitted to a 4-by-4 portion of the grid.

In our microscale platelet aggregation calculations, the Navier Stokes equations are discretized using finite difference methods on a simple uniform Cartesian grid. Hence, the fluid velocity, pressure, and force density are defined only at nodes $\mathbf{x}_g$ of this grid. Each platelet is represented by a ring of elastically-linked Lagrangian IB points as shown schematically in Fig.3. Let $\mathbf{X}_{p,i}$ denote the i^{th}point of the ring that represents the p^{th}platelet. We track the locations of these IB points for each platelet as time evolves. Between each pair of consecutive points $\mathbf{X}_{p,i}, \mathbf{X}_{p,i+1}$ on the platelet we assume there is a spring that generates forces on each of these points to try to maintain the separation between them at a prescribed value. (Arithmetic in the subscript i is modulo the number of IB points in each platelet ring.) In addition, to give the platelet some rigidity, we assume that for each triplet of consecutive points $\mathbf{X}_{p,i-1}, \mathbf{X}_{p,i}, \mathbf{X}_{p,i+1}$, there is a 'hinge spring' that generates forces that try to maintain the angle formed by the vectors $\mathbf{X}_{p,i} - \mathbf{X}_{p,i-1}$ and $\mathbf{X}_{p,i+1} - \mathbf{X}_{p,i}$ at a prescribed value. (An alternative way to give the platelet rigidity, used in our 3D modeling, is to include an additional IB point initially at the platelet's center of mass and to add spring forces that try to maintain the distance between this point and each IB point on the platelet surface at a prescribed value.) The (linear) spring force on platelet point $\mathbf{X}_{p,i}$ due to connections with its neighbors in the ring is:

$$S(\|\mathbf{X}_{p,i} - \mathbf{X}_{p,i+1}\| - r)\frac{\mathbf{X}_{p,i+1} - \mathbf{X}_{p,i}}{\|\mathbf{X}_{p,i+1} - \mathbf{X}_{p,i}\|} + S(\|\mathbf{X}_{p,i} - \mathbf{X}_{p,i-1}\| - r)\frac{\mathbf{X}_{p,i-1} - \mathbf{X}_{p,i}}{\|\mathbf{X}_{p,i-1} - \mathbf{X}_{p,i}\|}. \quad (6)$$

Suitable rearrangement of this expression shows that it is a discretization of the tension force expression $(\partial(T\boldsymbol{\tau})/\partial q)\, dq$ discussed earlier in the case of a Hookean tension rule with stiffness S and rest length r. The expression for the hinge-spring force is more complex (see [6].)

The walls of the blood vessel are also modeled as chains of elastically-linked IB points. In addition to the spring forces and hinge forces between neighboring wall points, each IB point $\mathbf{X}_{w,i}$ on the wall is connected by a spring to a corresponding

'tether point' $\mathbf{X}_{w,i}^{\text{tether}}$. For stationary vessel walls, the location of each tether point is held fixed in time. To model vasoconstriction or other vascular motions that can accompany vessel injury, the motion of the tether points would be a prescribed function of time or other model variables.

When a cohesive link connects IB points on two different platelets, there is an additional force on each of these points. Suppose link l connects point $i_1(l)$ on platelet $p_1(l)$ to point $i_2(l)$ on platelet $p_2(l)$. Then, a force increment

$$S^{\text{coh}}(\|\mathbf{X}_{p_2(l),i_2(l)} - \mathbf{X}_{p_1(l),i_1(l)}\| - r^{\text{coh}}) \frac{\mathbf{X}_{p_2(l),i_2(l)} - \mathbf{X}_{p_1(l),i_1(l)}}{\|\mathbf{X}_{p_2(l),i_2(l)} - \mathbf{X}_{p_1(l),i_1(l)}\|} \tag{7}$$

is applied at point $\mathbf{X}_{p_1(l),i_1(l)}$ and the negative of this force increment is applied at point $\mathbf{X}_{p_2(l),i_2(l)}$. Here, S^{coh} and r^{coh} are the stiffness and rest length of cohesive links. A similar expression is used to calculate the forces generated by an adhesive link joining an IB point on a platelet to an IB point on a vessel wall. (Of course nonlinear spring forces can be used for the intraplatelet springs and cohesive/adhesive links if desired.)

The mechanical state of the model system at any time is described by the fluid velocity and the locations of all of the IB points, as well the configuration of elastic links which join IB points to one another and the properties of these links. Here we summarize how the fluid velocity and IB point locations are advanced during one timestep of a simulation. Below we describe how other aspects of the model system (activator chemical distribution, platelet activation status, configuration of cohesive and adhesive links) are updated.

There are four steps to updating the velocity and IB point locations. First, the resultant $\mathbf{F}_q$ of all of the IB force contributions that act on the q^{th}IB point are calculated for each q. Next, these forces are distributed to the Eulerian grid used for the fluid dynamics equations using a discrete version of Eq.(3):

$$\mathbf{f}(\mathbf{x}_g) = \sum_q \mathbf{F}_q \delta_h(\mathbf{x}_g - \mathbf{X}_q) dq. \tag{8}$$

Here, $\mathbf{x}_g$ and $\mathbf{X}_q$ are the coordinates of grid point g and IB point q, respectively, $\mathbf{F}_q$ is the IB force (per unit q) on this point, dq is the increment in parameter q between consecutive discrete IB points, and δ_h is a discrete approximation to a two-dimensional δ-function. With the fluid force density $\mathbf{f}_g$ now known at each grid point, the fluid velocity is updated taking one step with a discrete Navier-Stokes solver. We use a projection-method type of Navier-Stokes solver [16]. Denoting the new velocity field by $\mathbf{u}_g^{\text{new}}$, the fourth step of the update process is described by a discrete analog of Eq.(4)

$$\mathbf{X}_q^{\text{new}} = \mathbf{X}_q + dt\mathbf{U}_q = \mathbf{X}_q + dt \sum_g \mathbf{u}_g^{\text{new}} \delta_h(\mathbf{x}_g - \mathbf{X}_q) h^2, \tag{9}$$

where h is the fluid grid spacing and δ_h is the same approximate δ-function as used in Eq.(8). (Below we discuss an additional term in the update equation for $\mathbf{X}_q$ that may be used to model the effect of red blood cells on platelet motion.)

The function δ_h is chosen to be a tensor product of one-dimensional approximate δ-functions,

$$\delta_h(\mathbf{x}) \equiv \frac{1}{h^2}\phi\left(\frac{x}{h}\right)\phi\left(\frac{y}{h}\right) \tag{10}$$

where $\mathbf{x} = (x, y)$. A common choice for the function $\phi(r)$ is

$$\phi(r) = \begin{cases} \frac{1}{4}\left(1 + \cos\left(\frac{\pi r}{2}\right)\right), & -2 \le r \le 2 \\ 0, & \text{otherwise.} \end{cases} \tag{11}$$

which ensures that the entire IB force is transmitted to the grid, that the force density on the grid is a continuous function of the IB point locations, and that the communication between grid and IB points is very localized. In fact, the IB force $\mathbf{F}_q$ is spread to a 4-by-4 region of the grid surrounding IB point $\mathbf{X}_q$, and the velocity of this IB point is interpolated from the velocity values at the same grid points (see Fig.3).

4.2. Red-blood-cell-induced platelet motion

As noted in Section 3, tumbling and colliding red blood cells impart to the platelets a 'random' motion that is often modeled as diffusion. There are a number of ways of incorporating this phenomenon into the microscale models without explicitly treating the red blood cells in detail. The simplest approach is to add a random step to each platelet's motion during each time step. This is accomplished by specifying that the motion of platelet IB points satisfy the equation,

$$d\mathbf{X}_{p,i}(t) = \mathbf{u}(\mathbf{X}_{p,i}(t), t)dt + d\mathbf{B}_p \tag{12}$$

where $d\mathbf{B}_p = (2Ddt)^{1/2}\mathbf{R}$ with $\mathbf{R}$ a Gaussian random variable with mean 0 and variance 1, and $\mathbf{u}(\mathbf{X}_{p,i}(t),\, t)$ is the interpolated velocity given in Eq.(9). The diffusion coefficient D may be allowed to depend on the local shear rate. The random step is taken only by individual platelets, not by aggregated ones, because the effect of the red blood cells should be less for platelets bound together in an aggregate.

An alternative way to incorporate the effect of the red blood cells is, for each platelet p, to add a random force $\mathbf{F}_p^{\text{random}}$ to the IB force at each point on platelet p before its IB forces are transmitted to the surrounding fluid. The random force thus contributes to the local force density on the fluid. In this case the platelet motion is by advection in the resulting velocity field, without the additional random step ($d\mathbf{B}_p$). In this approach, the platelets and the surrounding fluid are both affected by the random forces and there is no relative motion between the platelets and the fluid. We are currently experimenting with this approach, choosing a random force vector for each platelet and distributing this force evenly among the IB points of the platelet. The magnitude of the random force has to be tuned (possibly through numerical experiments) to give the desired platelet motion.

4.3. Activator transport and secretion

When a platelet becomes activated, it begins to secrete activator chemical (*e*.g., ADP or thrombin) into the fluid, and so the platelet serves as a (moving) source of activator. Once the chemical has been released into the fluid, we assume it moves

by advection with the fluid and diffusion relative to the fluid. We also allow for the possibility that the activator is degraded in the fluid. The equation describing the evolution of the activator concentration $c(\mathbf{x}, t)$ is therefore

$$c_t + \mathbf{u} \cdot \nabla c = D_c \Delta c + s(\mathbf{x}, t) - Kc \tag{13}$$

where D_c is the activator diffusion coefficient, K is its degradation rate, and $s(\mathbf{x}, t)$ is the source of chemical due to secretion by platelets. The source function is defined by the sum,

$$s(\mathbf{x}, t) = \sum_k H(\mathbf{x}, \mathbf{X}_{k,1}(t), \mathbf{X}_{k,2}(t), ...) G(t - t_k). \tag{14}$$

Here, k ranges over the indices of activated platelets in the domain, t_k is the time of activation of platelet k, G describes the (prescribed) timecourse of activator secretion following platelet activation, and H describes the spatial distribution of the source due to platelet k. For example, in a variant of the model in which the activator diffuses both within the platelets and in the surrounding fluid, the secreted activator can be distributed uniformly within the region bounded by the IB curve that represents the platelet. The secreted chemical then gradually diffuses across the platelet boundary into the fluid.

In reality, the activator chemical should move only in the portions of the domain occupied by fluid, not in those occupied by platelets. That is, activator should be able to diffuse up to but not across platelet walls. The same is true with regard to the vessel walls. For straight vessel walls, it is simple to impose the no flux condition on the activator chemical within the context of a finite-difference approximation to Eq.(13). For irregular vessel walls and for moving platelets, it is more difficult. One approach that we have used for irregular vessel walls is to use the Immersed Interface method (IIM) which is a method for modifying the finite difference stencils near a boundary to impose boundary or jump conditions [12, 21, 22]. This works well for stationary irregular boundaries, but since there is significant overhead in determining the modified stencils, it is less well suited to moving boundaries. There are two other approaches which we are currently investigating for the moving platelet boundaries. One involves introducing a variable diffusion coefficient into the activator transport equation Eq.(13), that is, replacing the term $D_c \Delta c$ with $\nabla \cdot (D_c(\mathbf{x}, t) \nabla c)$ where D_c is essentially constant in the fluid outside of the platelets and drops to zero inside the current platelet boundaries. The second is to define a potential field Φ with respect to the current platelet boundaries and to update the chemical concentration by taking a step of a discretized version of the modified transport equation

$$c_t + \mathbf{u} \cdot \nabla c = -\nabla \cdot (-D_c \nabla c - c \nabla \Phi) + s(\mathbf{x}, t) - Kc \tag{15}$$

Since the additional term describes a flux of chemical down gradients in Φ, we can design Φ to be a barrier to chemical crossing the platelet boundary from the fluid. In fact, Φ can be defined by using the discrete δ-function δ_h to spread to the computational grid an appropriate scalar function defined at the IB points which make up each platelet's boundary. In tests, both the variable diffusion coefficient and the potential barrier approaches show promise.

4.4. Modeling activation, adhesion, and cohesion

As our treatment of mechanical interactions using the IB method evolves, so is our handling of other aspects of platelet behavior including activation, adhesion, and cohesion. Recall that activation of a platelet can be stimulated by a platelet's interaction with specific molecules exposed on damaged vascular wall or its interaction with activator chemical in the blood plasma. Recall also that platelet binding to the injured wall or to another platelet is accomplished by the formation of molecular bonds involving specific molecular species on the respective surfaces and in the blood plasma. Until recently, our modeling of these events has been relatively simplistic, and while this has allowed us to make qualitative comparisons between simulation results and real aggregation, it precludes meaningful quantitative comparisons. New biological information allows us to begin to make more sophisticated models and to begin to make quantitative comparisons between simulated and real aggregation events. It is a strength of our computational approaches that they facilitate incorporation into the models of various levels of detail about platelet responses to stimuli and about platelet adhesion and cohesion properties.

In the past we have made the following assumptions about platelet *adhesion* to the damaged wall: (i) Whenever a platelet comes within a prescribed distance of the injury, it immediately adheres. (ii) Adhesion is accomplished by formation of an elastic link between an IB point on the platelet and a nearby IB point on the vessel wall. (iii) Additional links form quickly as long as there are pairs of unbound IB points on the platelet and vessel wall that are sufficiently close to one another. (iv) Each link behaves like a Hookean spring with a stiffness coefficient that is constant in time. (v) Link formation is irreversible except that a link breaks if subject to a sufficiently large force. Although, we think of each link as representing a collection of molecular bonds, treating its stiffness as constant is tantamount to assuming that all of these bonds form simultaneously. Similar assumptions have governed our modeling of *cohesion* between activated platelets.

We have modeled *activation* itself as an immediate response to a platelet's contact with the injured wall or its exposure to a sufficiently high concentration of activator, and we have assumed that activation (i) instantaneously allows the platelet to cohere to other (nearby) activated platelets and (ii) instantaneously causes activator release into the surrounding fluid. As with adhesion, whenever an unactivated platelet comes within a prescribed distance of the injury, it is activated. To respond to the chemical activator, unactivated platelets must sense the level of activator in their vicinity. Currently, for each unactivated platelet, we interpolate the activator concentration from the grid to each of its IB points. If the average of these interpolated concentrations is above a prescribed threshold level, the platelet becomes activated.

For each platelet we track its activation status with a simple activation flag with values true and false. We track each cohesion and adhesion link by maintaining lists from which we can extract, for any link l, the indices of the IB objects (platelets or walls) and of the IB points within those objects joined by link l, as

well as the resting length and stiffness of that link. From this information we can access the coordinates of the points joined by the link and can calculate the force generated by the link, see Eq.(7). This force (with appropriate sign) is added to the IB force at each of the two IB points joined by the link. When a new link forms, the relevant information is added to these lists; when an existing link breaks, the corresponding information is removed.

A real platelet's surface is studded with large numbers of molecules that perform different (but in some cases overlapping) roles in the platelet's detection and response to vascular injury. These include approximately 25,000 GPIb receptors that can bind to vWF molecules adsorbed onto the exposed subendothelial matrix, large numbers of receptors (GP-VI and $\alpha_2\beta_1$) that bind to subendothelial collagen, about 50,000 $\alpha_{IIb}\beta_3$ receptors that are involved both in platelet-platelet and platelet-wall binding, and at least two different types of receptors for each of the activators ADP and thrombin. In principle we can represent all of these receptors and their associated reactions in the model. To see how, suppose that we partition the surface of each model platelet into small patches around each of its IB points, and to each IB point assign a proportionate number of each type of receptor on the platelet surface. As simulation events unfold, ligands bind to and unbind from some of these receptors, and we could track these events by associating with each IB point a vector whose components are the number densities of bound and unbound receptors of each type at that IB point. Using appropriate kinetic equations, we could follow the formation/breaking of new bonds, the activation of receptors, and the overall stimulus for activation to which the platelet is exposed. It is not clear that such detail is necessary to understand platelet events, and in any case, most of the current information about the behavior of platelet receptors is qualitative, and does not provide a basis for such detailed kinetic calculations.

We are investigating models whose complexity falls between those of our past models of adhesion, cohesion, and activation, and of the detailed models just described. These models incorporate the important recent observation that platelet adhesion binding involves 'fast' and 'slow' bonds. More specifically, platelet adhesion to an injured vascular wall is now believed to involve two steps: Rapid binding of numerous platelet GPIb receptors to vWF molecules adsorbed on the subendothelium substantially slows the platelet's travel over that surface. These bonds cannot arrest the platelet's motion because they dissociate quickly, but by slowing the platelets, they allow bonds to form between platelet receptors ($\alpha_2\beta_1$ and GP-VI) and subendothelial collagen, and this activates $\alpha_{IIb}\beta_3$ receptors and allows them to form bonds with adsorbed vWF and fibrinogen which firmly attach the platelet to the wall. Cohesion between platelets also involves $\alpha_{IIb}\beta_3$ receptors which must be activated prior to binding, and there is some evidence that the fast/slow process is important in cohesion as well, at least for rapid flow conditions.

In the adhesion models we are developing, an elastic link between IB points on the platelet and subendothelium is regarded as a composite 'bond' representing all of the fast and slow molecular bonds between the two IB points. As in past models, link formation occurs when two IB points come sufficiently close to one another,

but instead of a link being created instantly with constant mechanical properties, we follow the dynamics of fast and slow bonds and relate the mechanical properties of the link at each instant to the number and type of each bond present then. Let $n^{\mathrm{F}}(t)$ and $n^{\mathrm{S}}(t)$ denote the number density of fast and slow bonds, respectively, between a particular pair of linked IB points. The magnitude of the force that the link exerts on the platelet is $S\,da\left(n^{\mathrm{F}}(t)+n^{\mathrm{S}}(t)\right)(l(t)-l_0)$, where $l(t)$ is the distance between the two IB points joined by the link, l_0 is its resting length, S is the stiffness of an individual bond, and da is the area of the surface patch associated with the IB point. As with any IB force, this link force is transmitted to the fluid grid near the corresponding linked IB points.

The evolution of $n^{\mathrm{F}}(t)$ and $n^{\mathrm{S}}(t)$ is assumed to be governed by equations of the form:

$$\frac{dn^{\mathrm{F}}}{dt} = k_+^{\mathrm{F}}(n_{\max}^{\mathrm{F}} - n^{\mathrm{F}}) - k_-^{\mathrm{F}}\left(\frac{f}{n^{\mathrm{F}}+n^{\mathrm{S}}}\right)n^{\mathrm{F}} \tag{16}$$

and

$$\frac{dn^{\mathrm{S}}}{dt} = k_+^{\mathrm{S}}(\mathcal{A}\; n_{\max}^{\mathrm{S}} - n^{\mathrm{S}}) - k_-^{\mathrm{S}}\left(\frac{f}{n^{\mathrm{F}}+n^{\mathrm{S}}}\right)n^{\mathrm{S}}. \tag{17}$$

Here, $\mathcal{A}$ (between 0 and 1) indicates the platelet's activation state with respect to slow receptor availability, and f is the force on the link, that results from flow-mediated stretching and which we assume is distributed equally to all the $n^{\mathrm{F}}(t)+n^{\mathrm{S}}(t)$ bonds that make up this link. We assume that the bond dissociation rates k_-^{F} and k_-^{S} grow with the force on the bond as is typical for molecular bonds. Since platelets can be activated in a number of ways, a model platelet may already be activated ($\mathcal{A}=1$), but we focus here on adhesion without prior activation. Then we can describe $\mathcal{A}$ by the equation

$$\frac{d\mathcal{A}}{dt} = k(n^{\mathrm{F}})(1-\mathcal{A}) \tag{18}$$

reflecting an assumption that the platelet becomes activated at a rate that depends on how many fast bonds exist. In simulations, at the time a platelet comes sufficiently close to the wall to adhere, a link is created; n^{F}, n^{S}, and $\mathcal{A}$ are set to 0, and we begin to solve the three ODEs. Initially $\mathcal{A}=0$ so only fast bonds can form. As they form, $k(n^{\mathrm{F}})$ increases from its initial value of 0, the platelet's activation level $\mathcal{A}$ increases, slow receptors are activated, and slow bonds can form and perhaps anchor the platelet firmly to the subendothelium.

Cohesion between IB points on two activated platelets is modeled somewhat differently from platelet-wall adhesion because a cohesive bond involves a plasma protein (usually fibrinogen) that forms a bridge between an $\alpha_{IIb}\beta_3$ receptor on each of the two platelets. When a platelet becomes activated, its $\alpha_{IIb}\beta_3$ receptors begin to bind to fibrinogen molecules. For two platelets to cohere, a fibrinogen molecule attached to one platelet's receptor must bind to an empty receptor on the other platelet; two receptors, each bound to a distinct fibrinogen molecule, cannot form a bond with one another. Let $r_{p,i}$ be the number density of $\alpha_{IIb}\beta_3$ receptors associated with the i^{th}IB point on the p^{th}(activated) platelet, and let $b_{p,i}$ be the number density of such receptors that are bound to a fibrinogen molecule.

Then $b_{p,i} = 0$ at the time the platelet is first activated, and subsequently evolves according to the equation

$$\frac{db_{p,i}}{dt} = k_{\text{on}}(r_{p,i} - b_{p,i}) - k_{\text{off}} b_{p,i}.$$

The on-rate k_{on} incorporates the plasma fibrinogen concentration, which, because of fibrinogen's abundance, can be assumed to be constant. Now suppose that unlinked IB points on two activated platelets (points (p, i) and (q, j) say) come near enough to one another to form a link. Let $n(t)$ be the number density of cohesive bonds between these two IB points. Then $n(t)$ will grow at a rate proportional to the quantity $b_{p,i}(r_{q,j} - b_{q,j}) + b_{q,j}(r_{p,i} - b_{p,i})$ which measures the chance that a receptor bound to fibrinogen on one platelet comes into contact with an empty receptor on the other platelet. (This implies that the strongest binding occurs between a recently activated platelet with few attached fibrinogen molecules and an earlier activated platelet with many attached fibrinogen molecules [15].) The bond number density $n(t)$ will decrease at a rate that depends on the force experienced by the link. As with adhesive links, the force generated by this link will be proportional to the number of bonds that exist and to the amount the link is stretched.

A platelet's interaction with activator chemical in the plasma can be handled using similar ideas. Suppose the number of receptors associated with IB point (p, i) is denoted $r_{p,i}$ and that the number of these receptors occupied by an activator molecule is $b_{p,i}$. Then $b_{p,i}$ evolves according to the equation

$$\frac{db_{p,i}}{dt} = k_{\text{on}} c(\mathbf{X}_{p,i})(r_{p,i} - b_{p,i}) - k_{\text{off}} b_{p,i} \tag{19}$$

where $c(\mathbf{X}_{p,i})$ is the concentration of activator at location $\mathbf{X}_{p,i}$ interpolated from nearby grid points, and k_{on} and k_{off} are binding constants. The activation state $\mathcal{A}$ of the platelet can then be made to increase at a rate that depends on the number of occupied receptors on the platelet. (Note that the activator concentrations at the grid points from which $c(\mathbf{X}_{p,i})$ is interpolated have to be adjusted to account for the interactions of activator and receptor embodied in Eq.(19)).

When we incorporate the coagulation enzyme network into our platelet aggregation models, we expect to use a similar approach to model coagulation reactions on the surfaces of activated platelets. At each platelet IB point, we will track the number densities of multiple coagulation species. For each species that moves between plasma and platelet surface by binding to and unbinding from surface receptors, an equation like Eq.(19) will be used. For each surface-bound species that is formed by interaction of two other surface-bound species, an ODE relating their surface densities will be used. Movement of receptors and other species along the platelet's surface can also be included by defining an appropriate diffusive or other flux of these species between adjacent IB points on the platelet.

4.5. Microscale simulation results

Fig.4 shows snapshots of microscale aggregation simulations using the two-dimensional model, and Fig.5 shows a snapshot from a three-dimensional simulation [28].

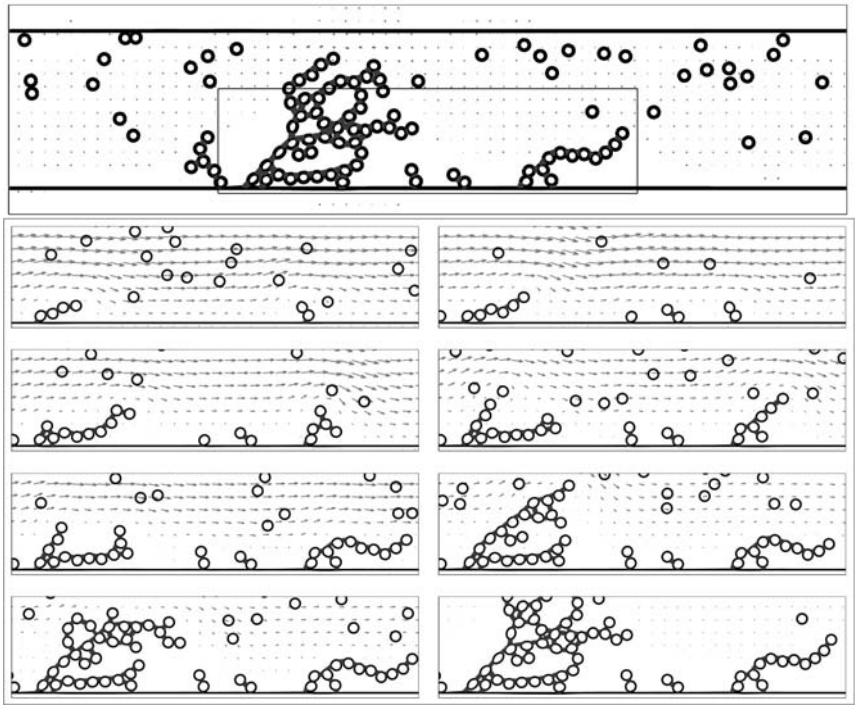

FIGURE 4. Top frame shows full domain at end of 2D microscale simulation. Remaining frames show development of aggregates in inset region; as time advances move left to right and top to bottom.

5. Continuum Models of Platelet Thrombosis

Our continuum models of platelet aggregation are intended to describe events in large diameter blood vessels such as the coronary arteries in which it is infeasible to track all platelets and all adhesive and cohesive links individually. These models are based on the same interactions as the microscale models but follow the evolution of density functions that describe the distribution of nonactivated and activated platelets and of cohesive and adhesive links.

As indicated in Fig.6, two spatial scales arise in this problem. One, the macroscale, is the scale of the vessel (1-2 millimeters) which also is the scale of clots that grow to substantially or completely occlude the vessel. The other, the microscale, is that of platelets (1-2 microns). As a consequence two *sets* of spatial variables appear in the models. The vector $\mathbf{x}$ refers to the macroscale and the statement $\|\mathbf{x}\| = O(1)$ signifies distances on the order of a millimeter. The vector $\mathbf{y}$ refers to the microscale and $\|\mathbf{y}\| = O(1)$ means distances on the order of a micron. The ratio of the platelet scale to the vessel scale is denoted by $\epsilon \ll 1$, and the model's equations are actually the leading order terms in expansions in ϵ.

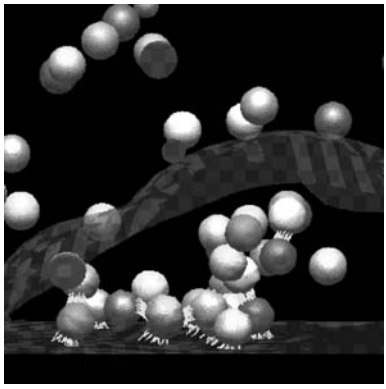

FIGURE 5. Close up of a small aggregate that formed during a 3D microscale simulation. Each 'ball' is actually an IB representation of a platelet using a triangulated surface mesh of 362 elastically connected points. (The colors of the platelets are not meaningful.) Line segments show cohesive and adhesive links. Below the red isosurface the activator concentration is sufficiently high to activate platelets. See [28] for more information.

5.1. Fluid-phase multiscale model

We begin with a description of the models in the absence of vessel walls, so that all interactions are between fluid-phase species. (Below we show how interactions with the vessel walls are added to the models.) The unknowns in the models are the fluid velocity $\mathbf{u}(\mathbf{x},t)$ and pressure $p(\mathbf{x},t)$, the concentrations of nonactivated and activated platelets, $\phi_n(\mathbf{x},t)$ and $\phi_a(\mathbf{x},t)$ respectively, the concentration of activator chemical $c(\mathbf{x},t)$, and a function $E(\mathbf{x},\mathbf{y},t)$ that describes the distribution of interplatelet cohesive links. We refer to this function as the 'elastic link function'. E is defined so that $E(\mathbf{x},\mathbf{y},t)d\mathbf{x}d\mathbf{y}$ is the number of elastic links which connect activated platelets at location $\mathbf{x}$ to activated platelets a short distance away at $\mathbf{x}+\epsilon\mathbf{y}$; hence, E has dimensions of number of links per volume per volume. From

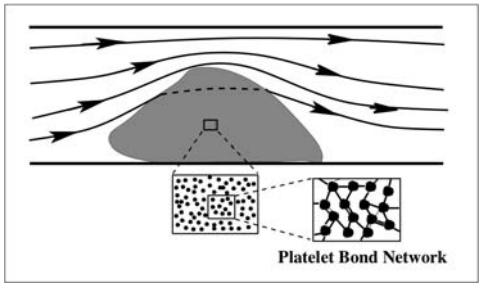

FIGURE 6. The continuum models involve two spatial scales; the vessel scale is on the order of millimeters, and the platelet-platelet cohesion scale is on the order of microns.

the distribution of elastic links at any time t, we can calculate the stresses that the links exert on the fluid.

The equations for the solution-phase model fall into three groups. The first group consists of the Navier-Stokes equations for the fluid motion.

$$\rho(\mathbf{u}_t + \mathbf{u}\cdot\nabla\mathbf{u}) \;=\; -\nabla p + \mu\Delta\mathbf{u} + \nabla\cdot\underline{\underline{\sigma}}^{\mathrm{P}}, \qquad \nabla\cdot\mathbf{u} = 0 \tag{20}$$

These equations contain a forcing term $\nabla\cdot\underline{\underline{\sigma}}^{\mathrm{P}}$ which involves the 'cohesive stress tensor' $\underline{\underline{\sigma}}^{\mathrm{P}}$ that is generated by the interplatelet elastic links as we describe below.

The second group of equations governs the transport of platelets and activator chemical:

$$(\phi_n)_t + \mathbf{u}\cdot\nabla\phi_n \;=\; D_n\Delta\phi_n \;-\; R(c)\,\phi_n \tag{21}$$

$$(\phi_a)_t + \mathbf{u}\cdot\nabla\phi_a \;=\; R(c)\,\phi_n \tag{22}$$

$$c_t + \mathbf{u}\cdot\nabla c \;=\; D_c\Delta c \;+\; A\,R(c)\,\phi_n - K\,c \tag{23}$$

Eq.(21) embodies the assumptions that nonactivated platelets move by advection and diffusion, and that they disappear, through activation, at a rate that depends on the local concentration of activator chemical. The diffusive term in this equation is intended to model the effect of red blood cells on platelet motion. According to Eq.(22), activated platelets move by advection and appear due to activation of nonactivated platelets. No diffusive term appears here, because, as in the microscale models, we assume that the effect of red blood cells on aggregating platelets is small. Eq.(23) indicates that activator chemical moves by advection and diffusion, and that it is produced at each location at a rate proportional to the rate of platelet activation there.

The third group of equations pertains to the interplatelet links. The equation

$$E_t \;+\; \mathbf{u}\cdot\nabla_x E \;+\; (\mathbf{y}\cdot\nabla\mathbf{u})\cdot\nabla_y E \;=\; \alpha(\|\mathbf{y}\|)\,\phi_a^2 - \beta(\|\mathbf{y}\|)\,E \tag{24}$$

describes the evolution of the elastic link function by advection in $\mathbf{x}$ at velocity $\mathbf{u}$, advection in $\mathbf{y}$ at velocity $\mathbf{y}\cdot\nabla\mathbf{u}$, formation of new links at rate $\alpha(\|\mathbf{y}\|)\,\phi_a^2$, and breaking of existing links at rate $\beta(\|\mathbf{y}\|)\,E$. The unusual advection term $(\mathbf{y}\cdot\nabla\mathbf{u})\cdot\nabla_y E$ arises because of the slight difference in velocity at the two ends of a link. The link formation and breaking rate functions, $\alpha(\|\mathbf{y}\|)$ and $\beta(\|\mathbf{y}\|)$ are assumed to depend on the distance $\|\mathbf{y}\|$ between the linked platelets. Link formation occurs at a rate proportional to ϕ_a^2 because each link joins two activated platelets, and is isotropic (in $\mathbf{y}$) because α depends only on the length of $\mathbf{y}$. In a shear flow, the advection term $(\mathbf{y}\cdot\nabla\mathbf{u})\cdot\nabla_y E$ has the important effect of progressively stretching the links and aligning them with the flow. The equation

$$\underline{\underline{\sigma}}^{\mathrm{P}}(\mathbf{x},t) = \int_{\mathbf{y}} E(\mathbf{x},\mathbf{y},t)\,\left\{\frac{1}{2}S(\|\mathbf{y}\|)\mathbf{y}\mathbf{y}^T\right\}\,d\mathbf{y} \tag{25}$$

shows how the cohesive stress tensor is determined from the distribution of elastic links. In Eq.(25), $S(\|\mathbf{y}\|)$ denotes the stiffness of a single link of length $\|\mathbf{y}\|$. The formula for $\underline{\underline{\sigma}}^{\mathrm{P}}$ can be derived by summing up the individual contributions to the stress at $\mathbf{x}$ of each link which joins a platelet at $\mathbf{x}$ to a platelet elsewhere.

The model, although formulated completely in terms of Eulerian variables, is similar to the IB method in a very important way. As platelet aggregates grow in

the model, the fluid is affected solely through the forcing term $\nabla \cdot \underline{\underline{\sigma}}^{\mathrm{p}}$ in Eq.(20); there is no change in geometry as a result of aggregate growth.

It is useful to introduce an additional variable $z^{\mathrm{p}}(\mathbf{x},t) = \int_{\mathbf{y}} E(\mathbf{x},\mathbf{y},t)d\mathbf{y}$ which measures the concentration of elastic links emanating from activated platelets at $\mathbf{x}$. Since the presence of an aggregate is manifest only through the stresses from these links, we regard z^{p} as a useful indicator of the extent of aggregation at point $\mathbf{x}$, and refer to z^{p} as the 'aggregation intensity'. For now, z^{p} is just a diagnostic variable that allows us to monitor where aggregation has occured, but later it will enter into an approximate form of the model.

5.2. Model reductions

Through the function $E(\mathbf{x},\mathbf{y},t)$, the model just presented describes both microscale and macroscale events. E impacts the rest of the model only through the stress tensor $\underline{\underline{\sigma}}^{\mathrm{p}}$, and this stress tensor and all other model variables depend only on the macroscale spatial variables $\mathbf{x}$. This prompts the question of whether an evolution equation for $\underline{\underline{\sigma}}^{\mathrm{p}}$, which involves only the macroscale variable $\mathbf{x}$, can be derived. Toward this end, multiply Eq.(24) by $\left\{\frac{1}{2}S(\|\mathbf{y}\|)\mathbf{y}\mathbf{y}^T\right\}$ and integrate over the microscale variable $\mathbf{y}$ to obtain:

$$\begin{aligned}\underline{\underline{\sigma}}^{\mathrm{p}}{}_t + \mathbf{u}\cdot\nabla\underline{\underline{\sigma}}^{\mathrm{p}} &= \underline{\underline{\sigma}}^{\mathrm{p}}\underline{\underline{\nabla\mathbf{u}}} + (\underline{\underline{\sigma}}^{\mathrm{p}}\underline{\underline{\nabla\mathbf{u}}})^T + \alpha_2\,\phi_a^2\,\underline{\underline{I}} - \int \beta(\|\mathbf{y}\|)\,E\left\{\frac{1}{2}\,S(\|\mathbf{y}\|)\mathbf{y}\mathbf{y}^T\right\}d\mathbf{y} \\ &+ \int (\mathbf{y}^T\,\underline{\underline{\nabla\mathbf{u}}}\,\mathbf{y})\left\{\frac{1}{2}\,S'(\|\mathbf{y}\|)/\|\mathbf{y}\|\right\}E\,\mathbf{y}\mathbf{y}^T\,d\mathbf{y} \qquad (26)\end{aligned}$$

where $\alpha_2 = \int_{\mathbf{y}}\left\{\frac{1}{2}\alpha(\|\mathbf{y}\|)S(\|\mathbf{y}\|)\|\mathbf{y}\|^2\right\}d\mathbf{y}$ is a constant that reflects the rate of stress-production due to new link formation. The first five terms in Eq.(26) involve only the macroscale variable $\mathbf{x}$. The last two terms are problematic in general; they cannot be expressed in terms of the existing model variables that depend only on the macroscale variable $\mathbf{x}$.

If we impose two restrictions on the model, namely, that the links behave as linear springs so $S(\|\mathbf{y}\|) = S_0$ and $S'(\|\mathbf{y}\|) = 0$, and that links break at a constant rate independent of how stretched they are so $\beta(\|\mathbf{y}\|) = \beta_0$, then the two problematic terms vanish, and we have an *exact* evolution equation for $\underline{\underline{\sigma}}^{\mathrm{p}}$.

$$\underline{\underline{\sigma}}^{\mathrm{p}}{}_t + \mathbf{u}\cdot\nabla\underline{\underline{\sigma}}^{\mathrm{p}} = \underline{\underline{\sigma}}^{\mathrm{p}}\underline{\underline{\nabla\mathbf{u}}} + (\underline{\underline{\sigma}}^{\mathrm{p}}\underline{\underline{\nabla\mathbf{u}}})^T + \alpha_2\,\phi_a^2\,\underline{\underline{I}} - \beta_0\underline{\underline{\sigma}}^{\mathrm{p}}. \qquad (27)$$

Under the same restrictions, the aggregation intensity z^{p} satisfies the evolution equation:

$$z^{\mathrm{p}}{}_t + \mathbf{u}\cdot\nabla z^{\mathrm{p}} = \alpha_0\,\phi_a^2 - \beta_0\,z^{\mathrm{p}} \qquad (28)$$

where $\alpha_0 = \int_{\mathbf{y}}\alpha(\|\mathbf{y}\|)d\mathbf{y}$. The set of equations Eqs.(20)–(23) and Eq.(27) form a closed system of equations that govern the behavior of the model under the restrictions that $S = S_0$ and $\beta = \beta_0$ are constant. We refer to these equations as the 'special' form of the model. We studied its properties [9, 10], and among other things, saw that it can demonstrate a phase transition that we interpret as platelet aggregation. Consider a period box in which initially $\phi_n = 1$ and $\phi_a = 0$ for all $\mathbf{x}$. Suppose that a background force is applied to the fluid to drive a periodic stagnation-point flow as shown in Fig.7a, and that at $t = 0$ a sufficiently high

concentration of activator is added in a region centered at the stagnation point. Early on, activation occurs, links form, and this early aggregate is stretched by the elongational flow along the x-direction. As time progresses, further activation and net link formation occur and the link distribution becomes more and more aligned with the flow and therefore able to generate forces to resist further elongation. By the end of the simulation, the core of the aggregate has solidified and the flow within it has dropped essentially to zero.

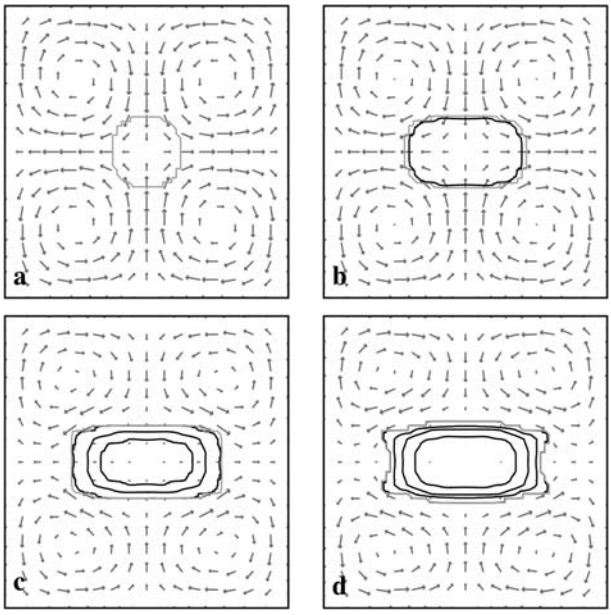

FIGURE 7. (a-d) Snapshots at increasing times of the velocity field, an outer contour that encloses the region in which c is sufficiently high to induce platelet activation, and inner contours which show levels of the aggregation intensity z^{P} (highest near the aggregate's center).

The special form of the model is limited by the restrictions imposed in its derivation. In particular, the requirement that links break at a rate that is independent of stretch leads to nonphysical behaviors and makes it impossible to cause an aggregate to break up by subjecting it to force. Since real clots do break up (embolize), presumably because of the stresses the flowing blood applies to them, this is an unacceptable limitation. The full multiscale version of the model does allow the link breaking rate to depend on stretch, but using it means having to contend with the substantial computational expense of dealing with two sets of spatial variables. Referring to Eq.(26), recall that the reason we cannot in general get a macroscale equation for $\underline{\underline{\sigma}}^{\mathrm{P}}$ is that $\beta(\|\mathbf{y}\|)$ cannot be brought outside of the integral in the next to last term in this equation. (We are content for now with the restriction that the stiffness $S(\|\mathbf{y}\|)$ be constant, so the final term in Eq.(26) vanishes.) If β were not a function of $\|\mathbf{y}\|$ itself, but of some macroscale quantity

that reasonably represents $\|\mathbf{y}\|$, then β could be brought outside of the integral and this term would reduce to $\beta\underline{\underline{\sigma}}^{\mathrm{p}}$. Consider the macroscale quantity $\mathrm{Tr}(\underline{\underline{\sigma}}^{\mathrm{p}})/z^{\mathrm{p}}$, where $\mathrm{Tr}(\underline{\underline{\sigma}}^{\mathrm{p}})$ denotes the trace of the tensor $\underline{\underline{\sigma}}^{\mathrm{p}}$. Recalling the definitions of $\underline{\underline{\sigma}}^{\mathrm{p}}$ and z^{p} we see that

$$\frac{\mathrm{Tr}(\underline{\underline{\sigma}}^{\mathrm{p}})}{z^{\mathrm{p}}} = \frac{S_0}{2}\left\{\frac{\int E(\mathbf{x},\mathbf{y},t)\,\|\mathbf{y}\|^2\,d\mathbf{y}}{\int E(\mathbf{x},\mathbf{y},t)d\mathbf{y}}\right\} = \frac{S_0}{2}\left\langle\, \|\mathbf{y}\|^2 \,\right\rangle(\mathbf{x},t), \tag{29}$$

that is, $\mathrm{Tr}(\underline{\underline{\sigma}}^{\mathrm{p}})/z^{\mathrm{p}}$ is a constant multiple of the mean-squared length of links emanating from platelets at $\mathbf{x}$. It therefore serves as a reasonable surrogate for the actual link length, and so we make the approximation that β is a function of this macroscale quantity rather than of $\|\mathbf{y}\|$. With this closure approximation, the equation for $\underline{\underline{\sigma}}^{\mathrm{p}}$ is

$$\underline{\underline{\sigma}}^{\mathrm{p}}{}_t + \mathbf{u}\cdot\nabla\underline{\underline{\sigma}}^{\mathrm{p}} \;=\; \underline{\underline{\sigma}}^{\mathrm{p}}\underline{\underline{\nabla\mathbf{u}}} + (\underline{\underline{\sigma}}^{\mathrm{p}}\underline{\underline{\nabla\mathbf{u}}})^T \;+\; \alpha_2\,\phi_a^2\,\underline{\underline{I}} - \beta\left(\,\mathrm{Tr}(\underline{\underline{\sigma}}^{\mathrm{p}})/z^{\mathrm{p}}\,\right)\underline{\underline{\sigma}}^{\mathrm{p}}. \tag{30}$$

Since the variable z^{p} is important in determining the local link breaking rate, it is now an actual component of the model (not just a diagnostic variable), and we follow its evolution using the equation:

$$z^{\mathrm{p}}{}_t + \mathbf{u}\cdot\nabla z^{\mathrm{p}} \;=\; \alpha_0\,\phi_a^2 - \beta\left(\,\mathrm{Tr}(\underline{\underline{\sigma}}^{\mathrm{p}})/z^{\mathrm{p}}\,\right) z^{\mathrm{p}}. \tag{31}$$

We refer to the version of the model consisting of Eqs.(20-23,30,31) as the 'approximate closure model'.

Asymptotic and numerical analyses of the approximate closure and full multiscale models under simple shear flow show, given a breaking rate function in the multiscale model, how to choose the function $\beta\left(\mathrm{Tr}(\underline{\underline{\sigma}}^{\mathrm{p}})/z^{\mathrm{p}}\right)$ so that the two models' behavior matches very closely for all shear rates [14]. In Fig.8 we show a different comparison between the two models. The experiment shown is an extension of that depicted in Fig.7. Events begin as in the earlier experiment, but after a specified time has elapsed, further activation is shut off, and extra forces are applied (at the locations indicated by the bars in Fig.8) to accelerate the fluid and increase the stress on the aggregate in an attempt to break it into two pieces. We see that the approximate closure model does a good job of capturing the behavior of the full multiscale model in this complex situation, and we note that the closure model calculations took about 1% of the computational time of the multiscale calculation. In corresponding calculations with a constant link breaking rate, it proved impossible to break the aggregate; the central portion of the aggregate did neck off to an extent but did not break. Calculations with the full multiscale model and constant breaking rate showed that the explanation was the existence of a relatively few nonphysically long links that generated most of the force resisting rupture.

5.3. Vessel walls in the continuum model

To model intravascular events, the vessel wall must be modeled and the nature of platelet interactions with it must be defined. We use an IB approach to build the actual structure of the wall; that is, we use strings of IB points connected elastically to one another and to prescribed tether point locations (see section

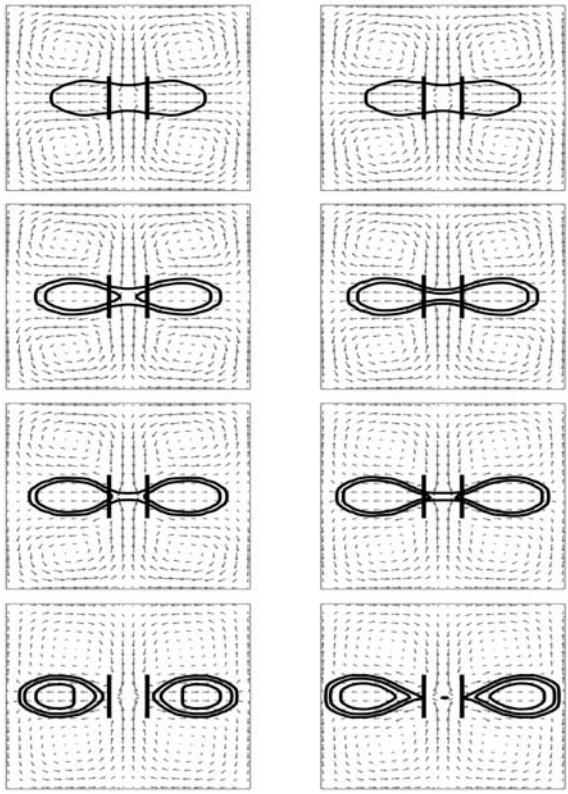

FIGURE 8. Succession of snapshots of the velocity field and aggregation intensity contours for calculations with (left) the full multiscale model Eqs.(20-24) and (right) the approximate closure model Eqs.(20-23,30,31). Bars in each picture denote locations of applied pulling force. Full multiscale model computations were done as described in [27].

4.1) to construct an approximately stationary vessel wall with the geometry of the vessel we wish to simulate. To define the injured portion of the wall, we introduce a density function $w(\mathbf{x}, t)$ of reactive wall sites. The function w is defined everywhere in the domain, but it is nonzero only in a thin layer of space along the portion of the wall deemed injured. Platelets interact with these sites in two ways; they can be activated and they can form adhesive links where $w > 0$. It is straightforward to incorporate these interactions into the model. To add the possibility of platelet activation by contact with the reactive wall sites, an additional term is added to each of the transport equations Eqs.(21)-(23) as illustrated here for the equation for ϕ_n:

$$(\phi_n)_t + \mathbf{u} \cdot \nabla \phi_n \;=\; D_n \Delta \phi_n - R(c)\phi_n \;-\; \tilde{R}(w)\phi_n \tag{32}$$

The new term $\tilde{R}(w)\phi_n$ represents activation of platelets at a per platelet rate $\tilde{R}(w)$ that is positive only where $w > 0$. To add adhesive platelet-wall links to the

full multiscale model, we would introduce an adhesive link function E^w analogous to the cohesive link function E. Here, we skip to the analogue of the closure approximation for $\underline{\underline{\sigma}}^{\mathrm{p}}$ and z^{p} and introduce the following equations for an adhesive link stress tensor $\underline{\underline{\sigma}}^{\mathrm{w}}$ and adhesive link intensity z^{w}:

$$\underline{\underline{\sigma}}^{\mathrm{w}}{}_t + \mathbf{u}\cdot\nabla\underline{\underline{\sigma}}^{\mathrm{w}} = \underline{\underline{\sigma}}^{\mathrm{w}}\underline{\underline{\nabla\mathbf{u}}} + (\underline{\underline{\sigma}}^{\mathrm{w}}\underline{\underline{\nabla\mathbf{u}}})^T + \alpha_2^w\,\phi_a\,w\,\underline{\underline{I}} - \beta^w\left(\mathrm{Tr}(\underline{\underline{\sigma}}^{\mathrm{w}})/z^{\mathrm{w}}\right)\underline{\underline{\sigma}}^{\mathrm{w}} \tag{33}$$

$$z^{\mathrm{w}}{}_t + \mathbf{u}\cdot\nabla z^{\mathrm{w}} = \alpha_0^w\,w\phi_a - \beta^w\left(\mathrm{Tr}(\underline{\underline{\sigma}}^{\mathrm{w}})/z^{\mathrm{w}}\right) z^{\mathrm{w}}. \tag{34}$$

The divergence of this stress tensor is added to the forces driving the fluid motion on the right hand side of the Navier-Stokes equations (20). The adhesive link breaking rate β^w is assumed to be a function of the macroscale quantity $\mathrm{Tr}(\underline{\underline{\sigma}}^{\mathrm{w}})/z^{\mathrm{w}}$. Eq.(33) is very similar to the equation for $\underline{\underline{\sigma}}^{\mathrm{p}}$; one difference is that the rate of formation of adhesive links depends on the product $w\,\phi_a$ since these links join reactive wall sites and platelets. The constants α_2^w and α_0^w are analogues of the constants α_2 and α_0 in Eqs.(30-31).

One application of this extended model is to investigate thrombosis in a stenotic (constricted) vessel following the rupture of an atherosclerotic plaque and the consequent exposure of strongly thrombogenic stimuli. Atherosclerotic plaques can develop slowly over many years and, in themselves, may cause little problem. However they are mechanically fragile and can rupture and trigger thrombosis that, in a matter of minutes, can lead to occlusion of the vessel in which the plaque resides, or can lead to the dispersal of clot fragments into the blood that end up blocking smaller vessels downstream.

Simulations in a 50% stenosis (see [11]) show that, under some conditions, the thrombus grows to occlude the vessel. In Fig.9, we show two simulations, identical except for the location of the rupture within the stenosis. With a rupture at the downstream end, where the flow through the stenosis is decelerating and the shear stresses are relatively low, a solid thrombus grows slowly out into the sheltered recirculation zone downstream of the plaque. With a rupture of identical size, but at the upstream end of the stenosis, where the flow is accelerating and the shear stresses are relatively high, the evolution of the thrombus is very different. As it begins to grow, the initial thrombus is subject to high stresses which cause a high rate of cohesive link breaking. The thrombus never becomes fully solid; it behaves more as a weakly-elastic very viscous fluid. Pieces of it fragment and are carried downstream. The thrombus remains small, and eventually is broken apart (not shown) by continued shear stress. Meanwhile, the fast flow carries activating chemical through the stenosis and into the recirculating zone where a larger thrombus develops. The center of this thrombus becomes quite solid, but the thrombus is not anchored to the injured portion of the vessel wall and cannot adhere to the healthy portions of the vessel wall, so it too is eventually washed downstream. The two simulations, identical in set up except for the location of the injury relative to the flow, give a striking illustration of the importance of fluid dynamics in the clotting process.

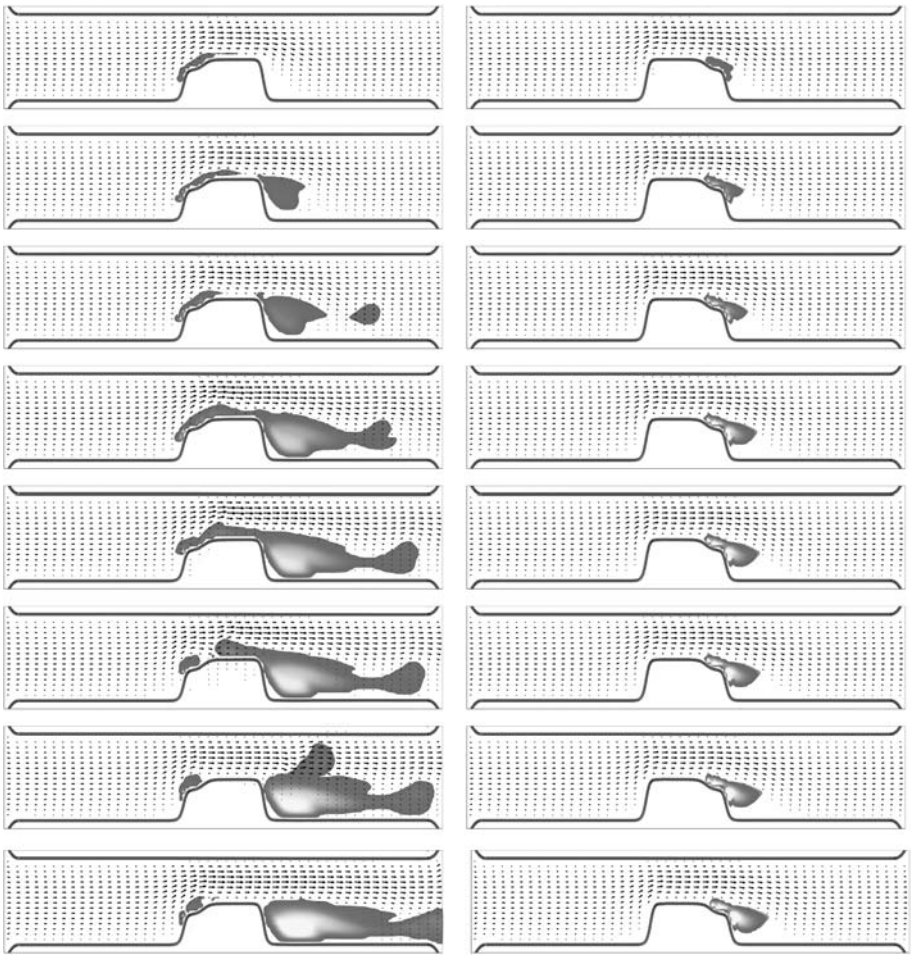

FIGURE 9. Snapshots at corresponding times from two simulations of thrombosis following rupture of 50% stenosis. Flow conditions and kinetic parameters are the same for both simulations; only the location of the rupture differs. Left: Rupture at upstream end of stenosis where flow is accelerating and shear stress is high. Right: Rupture at downstream end of stenosis where flow is slowing and shear stress is relatively low. Each plot shows velocity field and the aggregation intensity $z^{\mathrm{p}}+z^{\mathrm{w}}$ (red: low, yellow: high).

6. Conclusions

We have presented both semidiscrete microscale and continuum macroscale models of platelet aggregation during blood clotting. The microscale models represent each platelet as a separate entity using Peskin's Immersed Boundary method. The continuum models are motivated by the IB idea of representing biological tissue

as a composite incompressible fluid-elastic material, so that changes in geometry or phase are manifest solely through changes in mechanical forces within the material. Both types of models are able to capture salient behaviors in the platelet aggregation process including the influence of aggregate growth on the flow, shear-stress-related limitations of aggregate growth, and the possibility of complete vessel occlusion.

The IB method used for the microscale models is well suited for studying the mechanics of cells, either individual cells or groups of interacting cells. It has been used for detailed calculations of red blood cell [5] and leukocyte deformation [19] in three dimensions. In both of these studies, a very fine Lagrangian mesh was used in order to accurately capture the mechanical behavior of a single cell and both used strain-energy models as constitutive laws for the cell's mechanics. Recently, a two-dimensional study of aggregation of two red-blood cells made use of the IB method, a similar strain-energy model, and stochastic cell-cell binding and unbinding dynamics [1] patterned after Hammer's 'Brownian adhesion dynamics' [18]. The mechanical effects of the bonds are similar to those of the elastic links in our microscale models. Other applications of the IB method to individual cells or groups of cells include studies of adherent bacteria in biofilms [4], deformation of amoeba [2], trophoblast development [26], and on a subcellular scale, internal mechanics of axonemes [3]. Each of these projects involved dynamic formation and breaking of IB links to model molecular binding and unbinding. As sketched in this chapter, surface chemistry more generally can be treated using the Lagrangian nodes of the IB mesh on the cell's surface as the sites on which to also do the chemical calculations.

The IB method may seem complex, but its implementation is relatively straightforward, since it uses a fixed Eulerian grid, compared to other computational methods for treating deforming objects interacting with a fluid. One significant limitation in computing with the IB method is in having to use very small timesteps to maintain stability when doing explicit time-stepping. Recently, new insights have been developed into what is needed in an implicit discretization in order to achieve unconditional stability in IB calculations [23, 24]. This may well lead to the development of efficient implicit IB methods that will lessen the current timestep restrictions.

We believe that the macroscale continuum models can be the basis of models of biological gels and their mechanics. We are working to extend it to model fibrin formation during blood clotting, and to look at the behavior of the mucus gel lining of the digestive system. It may be also useful in modeling cytoskeletal network dynamics, and in modeling other biological gels, *e.g.,* respiratory or cervical mucus, where, as in the examples just cited, the viscoelastic properties of the gel are dynamic properties modified by other components in the system.

Acknowledgments Much of the continuum modeling work was done in collaboration with Robert D. Guy. Other portions of this work were done in collaboration with Nien-Tzu Wang and Haoyu Yu.

References

[1] P. Bagchi, P. C. Johnson, and A. S. Popel, *Computational fluid dynamic simulation of aggregation of deformable cells in a shear flow*, J Biomech Eng, 127 (2005), pp. 1070–80.

[2] D. C. Bottino and L. J. Fauci, *A computational model of ameboid deformation and locomotion*, Eur. Biophys. J., 27 (1998), pp. 532–539.

[3] R. H. Dillon and L. J. Fauci, *An integrative model of internal axoneme mechanics and external fluid dynamics in ciliary beating*, J. Theor. Biol, 207 (2000), pp. 415–430.

[4] R. H. Dillon, L. J. Fauci, A. L. Fogelson, and D. P. Gaver, *Modeling biofilm processes using the immersed boundary method*, J. Comput. Phys., 129 (1996), pp. 57–73.

[5] C. D. Eggleton and A. S. Popel, *Large deformation of red blood cells ghosts in a simple shear flow*, Physics of Fluids, 10 (1998), pp. 1834–1845.

[6] L. J. Fauci and A. L. Fogelson, *Truncated Newton methods and the modelling of complex immersed elastic structures*, Comm. Pure Appl. Math., 46 (1993), pp. 787–818.

[7] A. Fogelson, A. Kuharsky, and H. Yu, *Computational modeling of blood clotting: Coagulation and three-dimensional platelet aggregation*, in Polymer and Cell Dynamics: Multicsale Modeling and Numerical Simulations, Birkhaeuser-Verlag, Basel, 2003.

[8] A. L. Fogelson, *A mathematical model and numerical method for studying platelet adhesion and aggregation during blood clotting*, J. Comput. Phys., 56 (1984), pp. 111–134.

[9] A. L. Fogelson, *Continuum models of platelet aggregation: Formulation and mechanical properties*, SIAM JAM, 52 (1992), pp. 1089–1110.

[10] A. L. Fogelson, *Continuum models of platelet aggregation: Mechanical properties and chemically-induced phase transitions*, Contemp. Math., 141 (1993), pp. 279–294.

[11] A. L. Fogelson and R. D. Guy, *Platelet-wall interactions in continuum models of platelet aggregation: Formulation and numerical solution*, Mathematical Biology and Medicine, 21 (2004), pp. 293–334.

[12] A. L. Fogelson and J. P. Keener, *Immersed interface methods for Neumann and related problems in two and three dimensions*, SIAM J. Sci. Comput., 22 (2000), pp. 1630–1654.

[13] A. L. Fogelson and N. Tania, *Coagulation under flow: The influence of flow-mediated transport on the initiation and inhibition of coagulation*, Pathophysiology of Haemostasis and Thrombosis, 34 (2005), pp. 91–108.

[14] R. D. Guy, *Asymptotic analysis of PTT type closures for network models with variable junction concentrations*, J. Non-Newtonian Fluid Mech., 123 (2004), pp. 223–235.

[15] R. D. Guy and A. L. Fogelson, *Probabilistic modeling of platelet aggregation: Effects of activation time and receptor occupancy*, Journal of Theoretical Biology, 219 (2002), pp. 33–53.

[16] R. D. Guy and A. L. Fogelson, *Stability of approximate projection methods on cell-centered grids*, Journal of Computational Physics, 203 (2005), pp. 517–538.

[17] R. D. Guy, A. L. Fogelson, and J. P. Keener, *Modeling fibrin gel formation in a shear flow*, Mathematical Medicine and Biology, 24 (2007). pp. 111–130.

[18] D. A. Hammer and S. M. Apte, *Simulation of cell rolling and adhesion on surfaces in shear flow: general results and analysis of selectin-mediated neutrophil adhesion*, Biophysical Journal, 63 (1992), pp. 35–57.

[19] S. Jadhav, C. D. Eggleton, and K. Konstantopoulos, *A 3-d computational model predicts that cell deformation affects selectin-mediated leukocyte rolling*, Biophysical Journal, 88 (2005), pp. 96–104.

[20] A. L. Kuharsky and A. L. Fogelson, *Surface-mediated control of blood coagulation: The role of binding site densities and platelet deposition*, Biophysical Journal, 80 (2001), pp. 1050–1074.

[21] R. J. LeVeque and Z. Li, *The immersed interface method for elliptic equations with discontinuous coefficients and singular sources*, SIAM J. Numer. Anal., 31 (1994), pp. 1019–1044.

[22] Z. Li and K. Ito, *The Immersed Interface Method: Numerical Solutions of PDEs Involving Interfaces and Irregular Domains*, SIAM, Philadelphia, PA, 2006.

[23] Y. Mori and C. S. Peskin, *Implicit second order immersed boundary methods with boundary mass*. submitted for publication, 2006.

[24] E. Newren, A. Fogelson, R. Guy, and R. Kirby, *Unconditionally stable discretizations of the immersed boundary equations*, Journal of Computational Physics, 222 (2007), pp. 702–719

[25] C. S. Peskin, *The immersed boundary method*, Acta Numerica, 11 (2002), pp. 479–517.

[26] K. A. Rejniak, H. J. Kliman, and L. J. Fauci, *A computational model of the mechanics and growth of the villous trophoblast bilayer*, Bull Math Biol, 66 (2004), pp. 199–232.

[27] N. T. Wang and A. L. Fogelson, *Computational methods for continuum models of platelet aggregation*, J. Comput. Phys., 151 (1999), pp. 649–675.

[28] H. Yu, *Three Dimensional Computational Modeling and Simulation of Platelet Aggregation on Parallel Computers*, PhD thesis, University of Utah, 2000.

Aaron L. Fogelson
Departments of Mathematics and Bioengineering, University of Utah
155 South 1400 East, 233 JWB, Salt Lake City, Utah 84112
e-mail: `fogelson@math.utah.edu`

Single-Cell-Based Models in Biology and Medicine
ed. by A.R.A. Anderson, M.A.J. Chaplain, K.A. Rejniak
Mathematics and Biosciences in Interaction, 271–299

IV.2 A 3-D Deformable Ellipsoidal Cell Model with Cell Adhesion and Signaling

Eirikur Palsson

Abstract. In this chapter a three-dimensional model of ellipsoidal cells is presented and used to study how cell-cell signaling, cell adhesion, chemotaxis and differentiation all work together in a coordinated fashion to give rise to the developed organism. The *Dictyostelium discoideum* is used as a model system, since it is simple, yet has all the basic cell-cell interactions. Another goal of introducing this model is to achieve visualization of cell movements and signal propagation in 3-D space.

1. Introduction

The purpose of this book is to present different types of modeling approaches for modeling cells and cell-cell interactions and the various chapters present different modeling approaches used on very diverse systems, ranging from models of: tumor invasion (A. Anderson), pattern formation (D. Drasdo) to blood clotting (A. Fogelsson). From the models and systems discussed in each chapter we see many of the benefits of mathematical modeling in biology and how different approaches to modeling cell movements can give us answers to different questions relevant to the biological system. In general, mathematical modeling of biological cells provides us with a basic framework that helps us understand complex systems. It does this by predicting the behavior of many "units" based on the rules of behavior for a single "unit". Usually when designing the model one must make a number of assumptions and simplify things, and these simplifications can reveal the most important processes underlying the observed behavior, and can also put constraints of what kind of interactions are possible. This is demonstrated in the model that I present here. For example, I am assuming that the cells are deformable ellipsoids. This is not exactly correct so I try to work around this problem as I explain in the model description. Still this is a simplification and thus does not exactly represent real cells, but as will be demonstrated later in this chapter the model still gives many insights into the biological system and can explain many cell-cell interaction phenomena.

This work was completed with the support of NSERC grant number RGPIN249789.

An important use of a model, which is often ignored, is to use it to predict new phenomena and to understand the subtleties of the biological system, by putting them into the right context. For instance explaining why, from biological and evolutionary reasons, a system may have certain features. A good model is more than just an animation of the biological system.

There are a number of systems where cell movements driven by either chemotaxis, cell adhesion or both, play a vital part throughout the lifespan of organisms: Single cell organisms often find food or avoid repellents by chemotaxis, the coordinated movement of cells driven by chemotaxis and cell adhesion can lead to the segregation of different cell types and formation of specific structures and patterns that occur during gastrulation, in wound healing [1, 2], cancer cell invasion into tissues [3], the development of *Dictyostelium discoideum* [4] and limb bud regeneration [5]. The collective cell motion in these multicellular systems is usually different from the motion of isolated individual cells. The combined effect of cell-cell interactions and production and propagation of chemotactic signals, sometimes in the form of chemical waves, is often very complex. Therefore, it is not always obvious what underlying mechanism is responsible for the observed patterns and movements. The need to develop a model to study these phenomena comes from the fact that a large number of "individual units" are involved, and that makes understanding the complex interactions without a model very difficult. For example in chemical waves these units are molecules, whereas in cell movements the natural unit is a single cell. Often to make things more complex, wave propagation and signaling are directly involved in coordinating cell movements, which in turn affects the wave propagation.

Wave propagation is common in a number of biological systems. For example waves of excitability in the heart [6, 7], calcium waves in a fertilized frog egg [8], waves of insect outbreak [9] wave spread of diseases such as rabies and the plague and cAMP waves in Dictyostelium discoideum. The dynamics in many of these systems can be classified as that of excitable media, and a general understanding of excitable media gives insight into wave propagation in all these systems. Systems that are excitable can under certain conditions exhibit spiral wave propagation rather than planar traveling waves. A spiral wave is self generating whereas a planar or circular wave needs to be re-initiated. Spiral waves have been observed in: Dictyostelium [10], in cardiac tissues [6] and in Larch budmoth outbreak in the alps [9].

In this article I present a 3-dimensional cell-based model that I developed with the aim of exploring these mechanisms. The main goal of the model was to achieve visualization of cell movements and signal propagation, in 3-D, and give an understanding of how simple cell-cell interactions, signaling and adhesion lead to the observed complex cell movements in different biological systems.

There were several reasons why I chose to develop an individual compressible ellipsoidal cell based model. **First**, I believe that cell individuality plays a significant role in the biological systems I am interested in. Cells are not just a fluid element—cell size, shape and stiffness have a significant effect on cell motility in

multicellular systems. **Second**, cell elasticity is important—sometimes cells need to have the ability to use other cells as stepping stones to move upwards, such as when Dictyostelium pre-spore cells crawl up the stalk cells to form a fruiting body. The force responsible for the upwards motion must be transmitted down to the ground and this can only be achieved if the cells have a solid elastic component. For fluid type models the roundabout way of simulating this motion has often been to give the "cells" some propulsive jet engine so they don't need any cells to support their upward force. This violates the force balance. **Third**, when cells are modeled as individual units it is much easier to give them specific properties that directly correspond to properties of the real cells. For instance the visco-elastic properties of the cells can be measured experimentally and directly incorporated into the properties of the computational cells. **Fourth**, every cell has a signaling system consisting of receptors and intracellular components, so during cell-cell signaling, the cell detects the signaling molecule and responds in some fashion, often by production and secretion of more signaling molecules. Therefore it is important to have the signaling system move with the cells. Not all cells are the same—the activity of their signaling system may differ, sometimes in a continuous fashion. When these cells are mixed together it is preferable to model each cell's response appropriately and not lump them all together with some average response. This can not be modeled properly if the signal response is calculated on some grid outside the cells. One would need to keep track of a large number of populations (one for each degree of signaling differences) that differed in their signaling response. **Fifth**, the systems I am using the model for can be simulated with 100,000 or fewer cells so it is computationally feasible to model each cell individually, this would not always be the case if the systems had millions of cells in which case continuum models are preferable.

I wanted to study how cell-cell signaling, cell adhesion, chemotaxis and cell differentiation all work together in a coordinated fashion to give rise to the developed organism. I use *Dictyostelium discoideum* (*Dd* hereafter) as a model system, since it is simple, yet has all the basic cell-cell interactions that I want to explore. Another simplification is that in *Dd* cell division is separated from the developmental process that occurs later.

The cellular slime mold, *Dd*, has an interesting life cycle, Fig.1. It begins with free ranging amoebae that feed on bacteria and multiply by cell division [4, 11]. When the food source has been depleted a few of the starving cells begin emitting a single cyclic Adenosine-3',5'-Monophosphate (cAMP) pulse that is relayed from cell to cell, spreading outward as a circular wave. At the same time, cells move chemotactically towards the cAMP source. Early during starvation, the system is called weakly excitable, because new circles emerge only to die out. As time goes on the excitability increases, circular waves begin to propagate and they occasionally interact with new pulses, breaking up and forming spirals [12].

These cAMP wave patterns can form in a field of randomly distributed cells because of the properties of the cAMP signaling system: If external cAMP levels rise above a certain threshold, cAMP binds to its receptor, stimulating internal

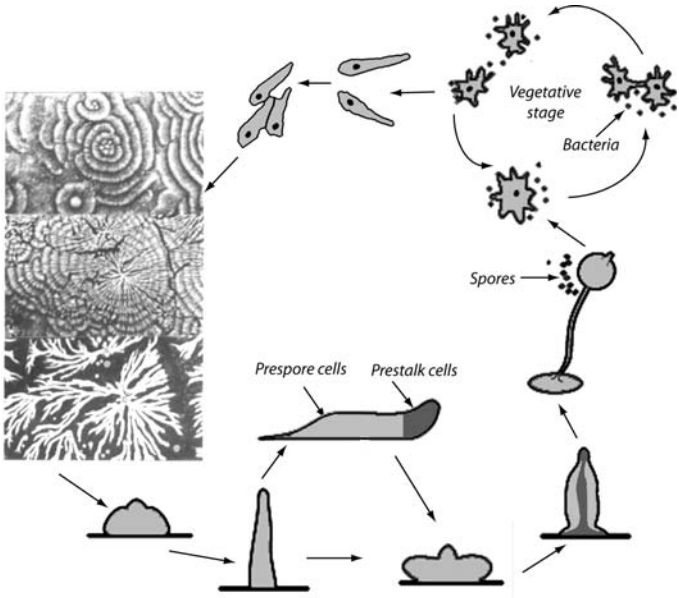

FIGURE 1. The lifecycle of *Dictyostelium discoideum.*

cAMP production. Most of the cAMP is secreted, and external levels rise, which in turn stimulates increased production by binding to more receptors, creating a positive feedback loop. The system soon becomes adapted and cAMP production halts. External cAMP levels then drop because of diffusion and the activity of a cAMP-degrading enzyme phosphodiesterase (PDE) [13], and cells slowly begin to become sensitive to cAMP once again. This production and relay of cAMP pulses by the excitable cells, coupled with chemotactic movement towards the cAMP signaling center (a pacemaker region or the center of a spiral), facilitates the organization of large territories [10]. In early aggregation the cells move autonomously, but later they form connected streams that flow towards the aggregation centers. The migration of cells towards the signaling center leads to the formation of a mound of cells that rises upward and eventually topples over to form a cigar-shaped mass called the slug [4], containing up to 10^5 cells. It is thought that cAMP waves are responsible for organizing the transformation of the mound into a slug, the migration of the slug over the substratum, and its culmination into a fruiting body [14]. One of the questions I am looking at, is how the observed cAMP wave patterns, spiral and targets, are generated and how these waves in combination with chemotaxis, cell adhesion and cell stiffness, orchestrate the movement of cells observed during *Dd* development. Many of the questions explored here have many things in common with other biological systems and therefore a similar methodological approach can be used on them.

2. Mathematical model

I developed this model as a postdoc at the university of Utah in 1998 [15, 16]. The model has undergone a number of changes and improvements since then, mostly in the handling of the signaling system itself. But the basic features, deformable autonomous ellipsoidal cells, conservation of all the forces, movement in a viscous environment, drag between cells, re-orientation of the cells either randomly or towards a chemical signal and signal detection have remained the same. In the early model, even though the cells and their movements were in 3-D the handling of the signal propagation was only really 2-D. Now the model is truly 3-D and I am using better methods for communication between the cells and the extracellular grid, where the diffusion of the signal occurs. The details of the models will be described in this section.

The building blocks of the model are individual cells. To make it feasible to model cell motion in systems comprising thousands of cells, I made the simplification that all cells are ellipsoids, restricting the admissible deformations to those that only change the relative lengths of the 3 semi-axes while conserving the cell volume. In addition these computational cells have characteristics and responses that correspond to properties observed in real cells. These characteristics include the stiffness of the cell, cell adhesion, locomotive force generation and response to environmental cues. The response of a cell depends on its internal parameter state, and on the information it receives from its external environment, which includes neighbor cells, the extracellular matrix, and chemical signals. The internal parameter state of the cell changes with time and is found by solving a set of differential equations that describe the response of the signaling system to external and internal signals. These equations in turn depend on a number of parameters such as the number of receptors, activity of phosphodiesterase, etc. The parameters are unique for each cell, so one cell cell may have some number of receptors while its neighbour cell has a different number. The cells are then moved and deformed according to the equations of motion and deformation, based on all the forces acting on them, including adhesive and chemotactic forces from other cells.

Before designing the model one must know the typical properties of real cells, so here I summarize the important aspects. Cells have many features in common; they can deform, they can exert forces onto other cells and they respond to chemical or mechanical cues, but the exact response differs. In suspension a cell is spherical, when resting on a surface it can be slightly flattened, and when it moves it elongates in the direction of movement [17]. When subjected to a force, a cell initially resists deformation, an elastic response, but under sustained force the actin network in the cytoskeleton can break and re-form producing a viscous response [18, 19]. The stiffness of a cell can vary by up to 2 orders of magnitudes—a fibroblast has stiffness 0.6 mdyne/μm whereas a red blood cell has a stiffness of 10^{-3} mdyne/μm,[20]. The adhesion differs for different type of cells [21], and the locomotive force a cell applies also varies more than a order of

magnitude [22, 23, 24, 25, 26]. In the model these values can be changed for each cell individually thus making the model very flexible, and applicable to a large number of different multicellular systems.

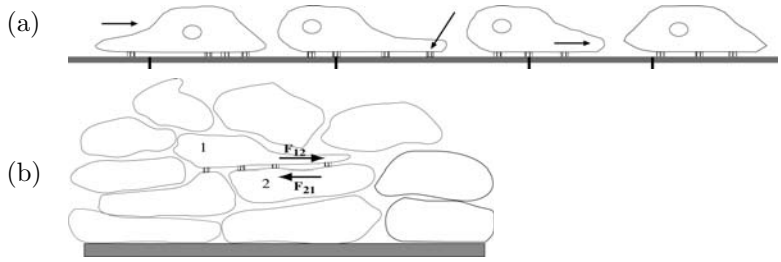

FIGURE 2. (a) The crawling of a cell on a surface by pseudopod extension. (b) The forces between cells in a multicellular aggregate.

Before a *Dd* amoeboid cell moves, either randomly or in response to a chemotactic signal, it sends out pseudopods. One of the pseudopods eventually dominates and attaches strongly to the surroundings or to a neighbor cell [27, 28]. This determines the direction of motion, as the cell realigns its axis towards the pseudopod and the rest of the cell body is 'pulled' towards the attached pseudopod. Once the direction is established the cell becomes polarized and is more likely to continue moving in that direction. The realignment is not achieved by rotation, but by disassembly and reassembly of several proteins [29, 30]. The establishment of a new pseudopod and realignment of the axis is not instantaneous [31, 32], but once established it can move in the new direction for up to several minutes. For *Dictyostelium* new pseudopods form about once every 3 min [30]. The formation of a new pseudopod is most probable in the direction that the cell was moving, or towards a new chemical gradient. The extensions of pseudopods and the retraction of the rest of the cell body requires active force generation, and the force necessary for retraction is applied at the site of pseudopod attachment (Fig.2a). When a cell is moving on a surface, the pseudopod will attach onto the surface and the applied force is transmitted directly to the surface. However, when the cell is inside a multicellular aggregate the pseudopod attachment is to another cell (Fig.2b). It is important to realize that when a cell attaches its pseudopod to another cell, and pulls itself forward, the other cell experiences an equal force in the opposite direction, and if that cell is not firmly attached to the ground it is pulled backwards; for a good discussion see [33]. Also, cells can only pull towards an attachment, they can't push off. Therefore a complete model of cell movements must balance all the forces.

As mentioned in the introduction there have been several different approaches used to model the collective motion of cells in multicellular systems, and many of them are presented in this book. Here a detailed description of this model is given. The basic units in the model, as mentioned above, are individual ellipsoidal cells,

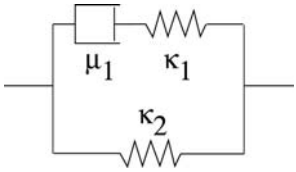

FIGURE 3. The combination of springs and viscous elements that I use to model the viscoelastic properties of the ellipsoid axes. Here μ_1 is the viscous constant and κ_1 and κ_2 are the spring constants for Hookean springs.

each of which is characterized by its location and orientation, its state of stress, its internal dynamics and the forces it exerts in response to the local environment. Knowing this for each cell, the movement of all cells, and hence of an aggregate of cells can be calculated.

The physical location and orientation of a cell is given by its center of mass coordinates and by the orientation and length of the principal ellipsoidal axes, which are denoted by the vectors $\mathbf{a}, \mathbf{b}$ and $\mathbf{c}$. I incorporate the viscoelastic properties of single cells into the model as follows: Cells are assumed to be deformable ellipsoids with axes of length a, b and c. Each axis contains a linear spring in parallel with a spring and a viscous element in series (Fig.3), following Skalak *et al.* [34, 18], κ_1, κ_2 are the spring constants and μ_1 is the viscosity of the element. This allows the cell to respond elastically to a brief force application and then deform in a viscous manner under prolonged force, and then finally relax slowly back to a spherical shape, when the force is removed. The cytosol, or fluid inside the cell is mostly water and is for all practical purposes incompressible (bulk modulus is $2 \times 10^9 Nm^{-2}$), so the cell must conserve volume almost instantaneously. Thus elongation and compression of the three axes are not independent; when one of the axis is compressed the other axes must be stretched (volume conservation) so a counteracting force is generated, this is the basis for the modifying force, F_{mod} given below. This gives us Eq.(1)–(2) for the deformation of the i-axis of a cell for a given force on that axis ($\mathbf{F}_i$).

$$\frac{dr_i}{dt} = \frac{\kappa_1(F_i - F_{mod})}{\mu_1(\kappa_1+\kappa_2)} + \frac{\frac{dF_i}{dt}}{(\kappa_1+\kappa_2)} - r_i \frac{\kappa_1\kappa_2}{\mu_1(\kappa_1+\kappa_2)}\,, \tag{1}$$

$$r_a r_b r_c = r_{a0} r_{b0} r_{c0} = V_{ellipse}/(\frac{4}{3}\pi)\,. \tag{2}$$

Here r_i stands for the length of either the a, b or c axis in units of 10 μm, and F_{mod} is a modifying force that is calculated from the volume constraint, by solving (1) and (2) simultaneously (solution of a 3rd order polynomial for F_{mod}).

Orientation

In vivo, the first step in cell movement is to establish a dominant pseudopod and realign its anterior-posterior axis in that direction (polarization). As discussed in the introduction the selection of the dominant pseudopod is a stochastic process, strongly biased towards the gradient of a chemotactic signal, $\nabla\gamma$, and/or the direction of the cell's previous orientation. These observations are incorporated

into the model: The cell has a specific delay period, *nrdt*, where it does not choose a new direction. After that in each successive timestep there is a given probability, moveprob, of choosing a new direction. When it does the cell determines if the gradient of the chemotactic signal is above a given threshold, if so, the new direction, r_{new}, is picked from a random Gaussian distribution of directions centered around the direction of the gradient, otherwise, the new direction is picked randomly with a bias towards the previous direction Eq.(3). I usually used a 2 minute time interval for *nrdt* to correspond with the time of pseudopod formation in Dd. The cell then realigns its anterior-posterior axis towards the new direction, according to the equations below. For simplicity, I define the a-axis of the ellipsoid to be the anterior-posterior axis of the cell. After the cell has chosen a new direction andx while the signal remains above threshold, the cell becomes polarized and does not easily change its orientation.

$$r_i^{new} = \begin{cases} \nabla\gamma_i(1-2\exp(-10\eta(v_i^{ran})^2)) & \text{if } \gamma_{max} > \gamma_{thresh}, \\ \vec{a}(1-2\exp(-3\eta(v_i^{ran})^2))) & \text{if } \gamma_{max} \le \gamma_{thresh}, \end{cases} \tag{3}$$

$$\frac{d\vec{a}}{dt} = \beta(1-u)(r_{\vec{new}} - \vec{a}), \tag{4}$$

$$\vec{a} = \frac{\vec{a}}{\|\vec{a}\|}, \tag{5}$$

$$\frac{du}{dt} = \begin{cases} k_2(\frac{\gamma_{max}}{\gamma_{thresh}} - 1)(1-u) & \text{if } \gamma_{max} > \gamma_{thresh}, \\ -k_3 u & \text{if } \gamma_{max} \le \gamma_{thresh}. \end{cases} \tag{6}$$

Here γ_{max} is the cell's local cAMP concentration, and γ_{thresh} is a predetermined threshold concentration. $\vec{v_{ran}}$ is a normalized vector with randomly chosen coordinates. The parameter u takes into account the polarization of the cell. When u is 1 the cell does not change direction. β reflects the rate of orientation, k_2 and k_3 are respectively, the rates of the polarization and de-polarization of the cell and η gives the weight of the stochastic part. Typical values were $\beta = 108/min$, $k_2 = 0.288/min$, $k_3 = 1.2/min$ and $\eta = 30$. Once the new $\vec{a}$ is found the Gram-Schmidt process is used to find the new $\vec{b}$ and $\vec{c}$, using the old $\vec{b}$ and $\vec{c}$ as the previous orthonormal basis. $\vec{a}$, $\vec{b}$ and $\vec{c}$ are unit vectors of the ellipsoid axis, the length of the axis is given by *ra, rb, rc* and the new lengths *ra', rb' and rc'* are found by finding where the new vectors $\vec{a}$, $\vec{b}$ and $\vec{c}$ would have cut the surface of the old ellipsoid and then the volume is readjusted. This process makes the change in direction less abrupt and simulates the realignment of the filaments and other matrix proteins. Eq.(4) describes the time it takes to reestablish a new direction for the cell.

Forces

The forces acting on a cell are of three types, active, passive and viscous drag forces. The active forces come from the locomotive forces that cells apply or are exposed to from other cells. The passive forces arise from adhesive and elastic interactions between cells, and the viscous drag forces come from the viscous drag from the surrounding fluid and the drag associated with sliding past neighbor cells.

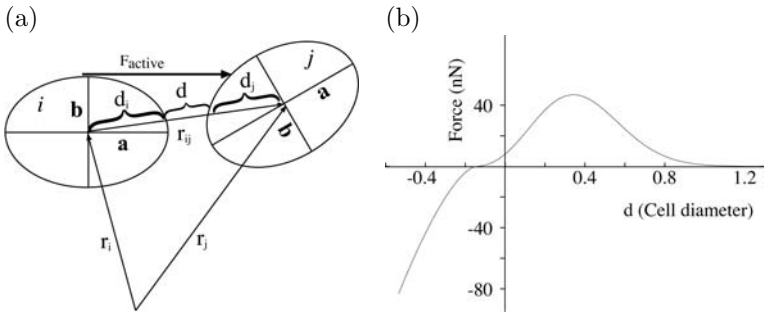

FIGURE 4. (a) Shows how d, the distance between the surfaces of the two ellipsoid cells, is determined. In (b) we see how the passive force, F_{pass}, between two cells depends on the distance d. F_{active} is the tactic force that the cell i applies onto cell j.

The active force is generated when a cell sends out a pseudopod in the direction of movement, attaches it and applies a force onto either another cell or the surface, and, in effect, pulls up the main body towards the pseudopod [35]. The direction of the pseudopod can be either random or in response to a chemotactic signal. Since the pseudopod is very narrow, and the volume is less than 10% of total cell volume [36], I assume that the force required to extend the pseudopod is negligible compared to the force required to move the whole cell, and that in effect the pseudopod is a rigid extension with no volume, that the cell can use to attach and apply force onto the surroundings. When cell i actively tries to move in the model, it is assumed that it attaches a "pseudopod" to the substrate, if close enough, or to that neighbor cell j in front of it which has the smallest angle between the vector $\mathbf{r}_{ij}$, which connects the cell centers of i and j, and the direction of movement (Fig.4a). The active force is always directed along the cell's anterior-posterior axis which, as mentioned before, is the a-axis of the ellipsoid.

When the attachment is to the substrate on which it is moving, the active locomotive force is applied directly to the substrate, and the force on the moving cell is the reaction force that pulls the cell forward. However, when the pseudopod attaches to a neighbor cell, the active force pulls the neighbor cell toward the first cell, and the opposing reaction force pulls the first cell forward. Thus, the active force enters into the equation of motion for the second cell and the reaction force enters into the equation of motion for the first cell. These internal forces will cancel and produce no net force on the whole system unless some of the active force can be transmitted to the substrate through a network of connected cells, one or more of which is in contact with the substrate. The magnitude of force generated for movement depends on several factors. What type of cell it is, the average local chemical concentration and whether the cell is moving randomly or towards a chemical (cAMP) gradient.

Parameter	Typical range in model	Experimental justification
Active force, $\mathbf{F}^{act}$	$2 - 10 \times 10^{-3}$ dyne	$3 - 8 \times 10^{-3}$ dyne Leukocytes [22] Cells in Dd slug [25]
Cell stiffness, κ	$0.3 - 1.0 \times 10^{-3}$ dyne/μm	$10^{-3} - 0.6 \times 10^{-3}$ dyne/μm [20] red blood cells - fibroblasts
Normalized viscosity μ_s	$8 - 20 \times 10^{-3}$ dyne s/μm	Estimated from active force and 20 μm/min cell velocity [37]
Cell adhesion, α	$0 - 10 \times 10^{-3}$ dyne	Estimated from surface tension measurements

TABLE 1. Table of parameters.

When the cAMP concentration exceeds a threshold the cell applies a chemotactic force in the direction of the cAMP gradient. If the cAMP concentration is below the threshold, the cell will instead apply a force in a randomly chosen direction. When the cell moves randomly it does not migrate as much as when it is moving in response to a chemotactic signal. I model this observation by making the random force smaller than the chemotactic force. The active random force was set to be about 20% of the chemotactic force. A similar effect can be achieved by letting the duration of the random force be shorter, or by reducing the frequency of pseudopod formation when cAMP is below threshold. Table 1 gives typical measured values for the force. In our standard simulation I set the active chemotactic force to be constant at $\sim 5 \times 10^{-3}$ dyne (1 dyne = 10 μN) whenever the chemical concentration exceeds a threshold.

The passive forces acting on a cell come from adhesive and elastic interactions with neighboring cells and are based on qualitative assumptions about the force, similar to the work by Evans [38, 39] and also [40]. The magnitude of the adhesion force between two cells depends on their proximity, since this determines the membrane area that the two cell have in common, and thus how many adhesion molecules can bind. There is also a repelling force that arises from a cell's resistance to deformation and it counteracts the adhesive force when cells get too close, Fig.4b. Estimates of the magnitude of the adhesion force and repulsive force between cells are given in [41, 42, 43, 44]. The passive force is always parallel to the $\mathbf{r}_{ij}$ direction ($\mathbf{r}_{ij}$ is the vector connecting the centers of the two cells, Fig.4a).

Electron micrographs of multicellular tissues, for example of a Dd slug [45], show that there is little free space between cells: they deform so as to fill up most available space and as a result have a larger contact area than if they were restricted to ellipsoidal shapes, as in the model. To compensate for this, the distance, d, between the surfaces of two ellipsoidal cells, shown in Fig.4a, does not represent the actual distance between two adhering cell membranes but instead provides an estimate of how much surface area the cells have in common. For instance the equilibrium state where the adhesive and repelling force balance, $F = 0$, occurs for $d = min_{dist}$ which is slightly less than zero. This can be seen in Fig.4b which shows how the passive force varies with the the distance d between the surfaces of the two ellipsoidal cells. This compensates for our constraint that the cells are

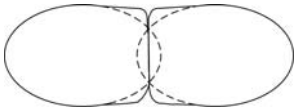

FIGURE 5. Two overlapping ellipsoids are used to represent close contact between neighboring cells. Here d would be negative. The dotted lines indicate the ellipsoid shape.

ellipsoids, since cells do not overlap each other in real life but instead deform into the vacant space (see Fig.5). We choose the equilibrium value of min_{dist} to be such that the volume of a cube of these cells, stacked in the cubic closest packing, would be close to the sum of the individual cell volumes, giving $min_{dist} \approx -0.1_{cell}$. The exact form of how the adhesion force varies with d does not seem to be all that important, but for numerical purposes it is preferable that the derivative of the force is small at the point where the force changes signs. The range of the adhesion force, i.e. the distance, d, where the adhesion becomes zero, does however, play an important role. I used the following relation for the force between two cells.

$$F = \begin{cases} F_{comp}\chi(-x)^{\frac{3}{2}} & x < 0 \\ -\alpha\chi\{(x+x_0)\exp(-\lambda(x+x_0)^2) - v_0\exp(-\lambda x^2)\} & x \geq 0 \end{cases} \tag{7}$$

$$\chi = \frac{r_{cell}}{2}\left(\frac{1}{d_i}+\frac{1}{d_j}\right),\ x = \left(\frac{d}{r_{cell}} - b\right),\ x_0 = (2\lambda)^{-1/2},\ b = min_{dist}, \tag{8}$$

$$\mathbf{F} = F\frac{\vec{r_{ij}}}{\|\vec{r_{ij}}\|}. \tag{9}$$

Here, α is the adhesion strength, F_{comp} is the strength of the repelling force, x_0 and v_0 are matching constants to make $F(x=0)=0$ and the right derivative $F'(x=0)=0$. In Fig.4b the exponent is $\lambda = 7$. When the ellipsoids are deformed, their respective orientation, whether their longest axes are for instance parallel or perpendicular, changes the common surface area between the two cells and thus their adhesion strength. I try to take this into account by the value of $\chi = \frac{rcell}{2}(\frac{1}{d_i} + \frac{1}{d_j})$, which is a correction to the force, here d_i and d_j is the distance to the surface for ellipsoid i and j respectively. When the ellipsoids are side by side d_i and d_j are small and the force is larger.

The two types of forces I have listed above, the active and the passive, are "static" forces *i.e.* they do not depend on the cells relative velocities. The magnitude and direction of the static force for cell i, $\mathbf{F}_i^{\mathbf{stat}}$, is then found by summing all the above forces acting on the cell:

$$\mathbf{F}_i^{\mathbf{stat}} = \mathbf{F}_{i(j/s)}^{act} + \sum_{j\in\mathcal{N}(i)} \mathbf{F}_{ij}^{pass} - \sum_{j\in\mathcal{N}(i)} \mathbf{F}_{ji}^{act}. \tag{10}$$

Here $\mathbf{F}_{i(j/s)}^{act}$ is the reactive force from the active force cell i applies to cell j or to the surface. $\mathbf{F}_{ij}^{pass}$ are the adhesive, elastic and repulsive forces, from neighbor cells on cell i and $\mathbf{F}_{ji}^{act}$ are the active forces that the neighbor cells may apply to cell i, $\mathcal{N}(i)$ denotes all the neighbors of i.

The third type of force, the viscous drag force $\mathbf{F^D}$, depends on the relative velocity of the cells. One contribution comes from the viscosity of the surrounding fluid (usually water) and viscosity due to cell-surface interactions and is proportional to the speed of the cell relative to the laboratory frame. For a cell moving alone, this is the only contribution to the drag force. However, when the cell is moving in a multicellular system there is another contribution to the drag force that comes from the viscosity between cells. This force is directly proportional to the cells relative velocity and their common surface area. Included in this cell-cell viscosity, is the time-dependent force associated with the breaking up of cell-cell adhesion bond. Thus, in a multicellular system, $\mathbf{F^D}$ is a composite force and depends on both the speed of the cell relative to the laboratory frame and on the relative velocity of the cell in question with its neighbor cells.

$$\mathbf{F^D}_i = \mu_s \frac{A_{is}}{A}\mathbf{v}_i + \mu_c \sum_{j\in\mathcal{N}(i)} \frac{A_{ij}}{A}(\mathbf{v}_i - \mathbf{v}_j), \tag{11}$$

$$= \mu_s \frac{A_{is}}{A}\mathbf{v}_i + \mu_c A_i^T \mathbf{v}_i - \mu_c \sum_{j\in\mathcal{N}(i)} \frac{A_{ij}}{A}\mathbf{v}_j, \tag{12}$$

$$A_i^T = \sum_{j\in\mathcal{N}(i)} \frac{A_{ij}}{A}. \tag{13}$$

Here A_{ij} is the estimated common surface area between cell i and cell j and A_{is} is the surface area of cell i that is in contact with the external fluid or surface and is not shared with any other cell. $\mathcal{N}(i)$ denotes all the neighbors of i, and A is the surface area of a spherical cell of the given volume ($4\pi R^2$). μ_s and μ_c are viscosity coefficients, μ_s was estimated from the measured velocity of a single crawling amoebae and the force that it generates when it moves. There is no good estimate for μ_c, the viscosity, per unit surface, between two cells, in the model I set it to be $3\mu_s$. Since the Reynolds number, $\Re$, of a moving cell, 10 μm long and moving at a speed of 10 μm/min in water is very low, $\Re \approx 10^{-6}$ I can ignore the effect of inertia in the equation of motion. This in effect means that $\mathbf{F^{stat}}$ is balanced by the drag force, $\mathbf{F^D}$. Equating $\mathbf{F^{stat}}$ and $\mathbf{F^D}$ from Eq.(12) gives us the equation of motion (15).

$$\mathbf{F^{stat}} = \mathbf{v}_i(\mu_s \frac{A_{is}}{A} + \mu_c A_i^T) - \mu_c \sum_{j\in\mathcal{N}(i)} \frac{A_{ij}}{A}\mathbf{v}_j, \tag{14}$$

$$\frac{d\mathbf{x_i}}{dt} = \frac{\mathbf{F^{stat}} + \mu_c \sum_{j\in\mathcal{N}(i)} \frac{A_{ij}}{A}\mathbf{v_j}}{\mu_s \frac{A_{is}}{A} + \mu_c A_i^T}. \tag{15}$$

The time-stepping algorithm works as follows. To find the new position $\mathbf{x}_i$ at time $(t + \Delta t)$ I use Eq.(15), using the velocities at time t sweeping through the array of cells and then I update the new velocities. Before each new timestep, the cell order that is used in the sweep through is randomized. This randomization of the order has been shown to avoid spurious results in cell automata models [46].

I modified a model of the cAMP signal transduction and relay system that had been used previously to study spiral wave formation during *Dd* aggregation [47, 48] to describe the evolution of the local cAMP concentrations. The model was extended to 3-dimensions and now the reaction-diffusion equations that govern the detection and production of cAMP is solved within each cell. The extracellular cAMP concentration is stored on a regular 3-D grid and the diffusion and degradation of extracellular cAMP is calculated on this grid. The cells move within this grid but are not restricted to grid cubes, and therefore cAMP is interpolated from the grid to each cell. This is done by assigning the weight of grid cube to be proportional to the the fraction of the cell volume inside that grid. Therefore the local external cAMP concentration at cell p, $[cAMP]_{cell-p}$, is found as follows:

$$[cAMP]_{cell-p} = \sum_{i=l-1}^{i=l+1} \sum_{j=m-1}^{j=m+1} \sum_{k=n-1}^{k=n+1} \frac{V_{cell-p}^{ijk}}{V_{cell-p}} [cAMP]_{ijk}$$

Here V_{cell-p}^{ijk} is the fraction of volume of cell p inside grid cube (i, j, k) and V_{cell-p} is the total volume of cell p. $[cAMP]_{ijk}$ is the cAMP concentration in grid cube (i, j, k). l, m and n are respectively, the grid indexes corresponding to the x, y and z location of cell p. The production of cAMP by each cell is based on the dynamics of its internal signaling system in response to the $[cAMP]_{cell-p}$. The secreted cAMP is then distributed back to the grid to give the cAMP distribution for the next step.

$$[cAMP]_{ijk}^{new} = [cAMP]_{ijk}^{old} + \sum_{p \in \mathcal{N}(p)} \frac{V_{cell-p}^{ijk}}{V_{cell-p}} cAMP_{cell-p}^{secreted}$$

$\mathcal{N}(p)$ stands for all the the cells that overlap grid cube (i,j,k).

A previous version of the model used a different model for the signaling system [15]. The 2-D results where qualitatively similar regardless of which model of the cAMP signaling system we used. To determine the chemical gradient at each cell I assume that a cell can sense a chemical gradient across its body. The cell compares the chemical concentration in all the grids adjacent to the grid cube that the cell belongs to. In three dimensions this amounts to 26 grid cubes around the cell, and from that information the chemical gradient, $\nabla\gamma$, for a cell, is determined.

Step 1. : For each cell:

a) Determine if the cAMP concentration in the cell's vicinity is above threshold, if so find the direction of the local cAMP gradient and orient the cell in that direction.

b) Locate all cells that are within a minimum distance from each cell, these are the neighbor cells.

c) Find all the forces that act on the cell, $\mathbf{F^{stat}}$ from each of the neighbor cells found in b. These are the passive and active forces, deform the axes of the ellipsoid, and move the cell according to the equation of motion (15).

Step 2. : Update the cAMP concentration.

Step 3. : Repeat 1 and 2 for every time step.

Parameter Values In the model, the parameter values were chosen to lie within the experimentally observed ranges (see Table 1). Since these parameters are based on experimental measurements, changes made in the model parameters reflect a specific biological mechanism or property. Therefore, the model allows us to explore the effect these mechanisms have on the slug movement and how sensitive the system is to variations in the parameters.

The code The program for the model is written in C, where the cell is defined as a structure with a number of properties. The equations of motion and deformation were solved using an explicit forward Euler scheme, an implicit method would be preferable since then a larger timestep could be used. However, then the computational time would go up as n^2 rather than linearly, when increasing the number of cells.

Visualization The visualization of the results were done using a code that I wrote in the openGL programming language. The program reads the output file and produces images of the cells and cAMP concentrations at each timestep.

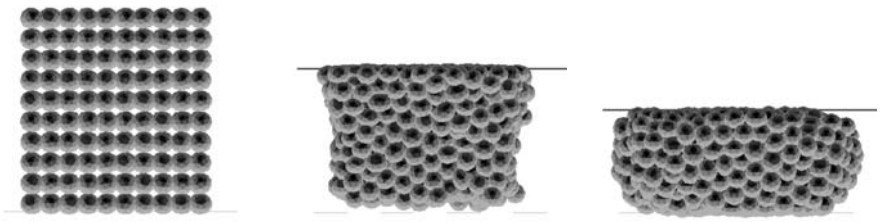

FIGURE 6. The changes in the aggregate when it is compressed between 2 parallel plates. The distance between the plates is H=5.0 and the adhesion strength is α=25. The time for each frame is, 0, 50 and 400 min from left to right. After about 300 minutes the aggregate has rounded up and reached the equilibrium state.

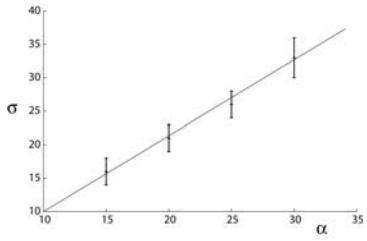

FIGURE 7. This plot shows how the calculated surface tension σ varies adhesion strength, α. H is constant.

3. Applications

First the model was used to simulate the behavior of a multicellular aggregate in the absence of chemotaxis. In these simulations we compressed cells between 2 parallel plates, and determined the force exerted on the plates. Fig.6 shows a time sequence of one of these simulations. Initially the force is large but as the cell mass re-arranges the force required to hold the plates at a fixed distance decreases until the aggregate reaches equilibrium shape (a smooth rounded surface), at which point the force stabilizes. This behavior is characteristic of a viscoelastic fluid—the initial force comes from the elastic response of the cells, and the fluid like behavior of the aggregate comes from the movement of cells past each other. The final equilibrium force is due to the surface tension of the aggregate, which is proportional to cell adhesion strength.

The surface tension can then be calculated from the geometric shape of the aggregate and the applied force on the plate using Eq.(16) from [49], where R_1, R_2 and R_3 are as shown in the diagram in Table 2.

$$\sigma = \frac{F}{\pi R_3^2}\left(\frac{1}{R_1} + \frac{1}{R_2}\right)^{-1} \tag{16}$$

Table 2 shows the calculated σ from simulations using different plate separation, H, and adhesion, α. From the table one can see that with fixed α=25 we got approximately the same value for σ for different H even though the force differed. This is in agreement with theory; the surface tension of a cell aggregate only depends on the cell-cell adhesion strength [50], and it should not depend on the separation between the plates. On the other hand when H is fixed and α is varied, σ increases linearly with the adhesion strength, this is seen more clearly in Fig.7.

α	H	Surface Tension (dyne/cm)	Plate Force (nN)
15	5.0	16 ± 2	292 ± 8
20	5.0	21 ± 2	350 ± 10
25	5.0	26 ± 2	440 ± 15
30	5.0	33 ± 3	550 ± 50
25	4.5	23 ± 2	575 ± 30
25	5.0	26 ± 2	440 ± 15
25	5.5	26 ± 2	340 ± 20

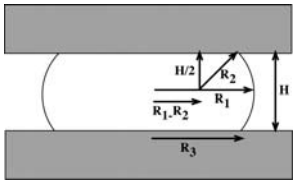

TABLE 2. The table shows the calculated surface tension, σ, for a number of simulations. H is the separation between the two plates and α is a non-dimensional parameter for the adhesion. The figure to the right shows how the R_1, R_2, R_3 and H are found.

These results showed that the simulated multicellular aggregate has the properties of a viscoelastic fluid and the surface tension lies within the range of previous

measurements of embryonic tissue by Steinberg and coworkers [51, 52, 44], using the same configuration.

The sorting of cells due to differences in adhesion was first suggested by Steinberg [53] and is referred to as the Differential Adhesion Hypothesis (DAH). The DAH states that two cells types with different adhesion strengths, or equivalently differences in energy of adhesion, sort out in such a fashion that the cells with stronger adhesion sort together in the center completely enveloped by the cells with weaker adhesion. The reasoning for this was based on thermodynamic considerations which state that in thermodynamic equilibrium the potential energy is minimized. Steinberg's group verified the DAH by mixing together cells, that had different adhesion strength, allowing the system to reach equilibrium, and showing that invariably the cells with stronger adhesion sorted to the center [51].

I used the model to simulate sorting of two cell types in an aggregate with no chemotaxis. Here the force arises from differences in adhesive forces between the two cell types and from the random force. The results of these simulations are shown in Fig.9. The sorting parameter, s, is found by dividing the number of neighbor cells of the same type with the *total* number of neighbor cells. When one cell type is completely enveloped by the other cell type, I use the term complete sorting. For an infinite number of cells, s=1 at complete sorting, however, when the number of cells is small, s can be significantly less than 1 at complete sorting, since a large fraction of the cells are on the boundary between the two cell populations. For example for 400 and 1350 cells, complete sorting occurs at $s \simeq 0.69$ and $s \simeq 0.77$, respectively.

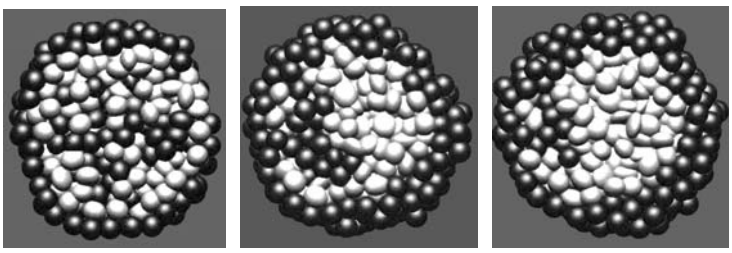

FIGURE 8. These figures show a cross section through the middle of the aggregate at three different time points: 5 min, 60 min and 150 min. Notice how the lighter cells, which are more adhesive, sort in the middle and push the darker less adhesive cells to the outside. See also a simulation MovIV.2.8.

Fig.8 shows typical cell sorting simulations. Here the lighter cells are 2 times more adhesive than the darker cells. As can be seen, the lighter cells move into the center of the aggregate, and at the same time they push the darker and less adhesive cells out to the surface.

Fig.9a shows the sorting for different adhesion strengths. When the adhesion is low, α=20, the cells do not sort well, since the adhesion force is not always sufficient to pull cells past each other; cells get stuck in their local minima and

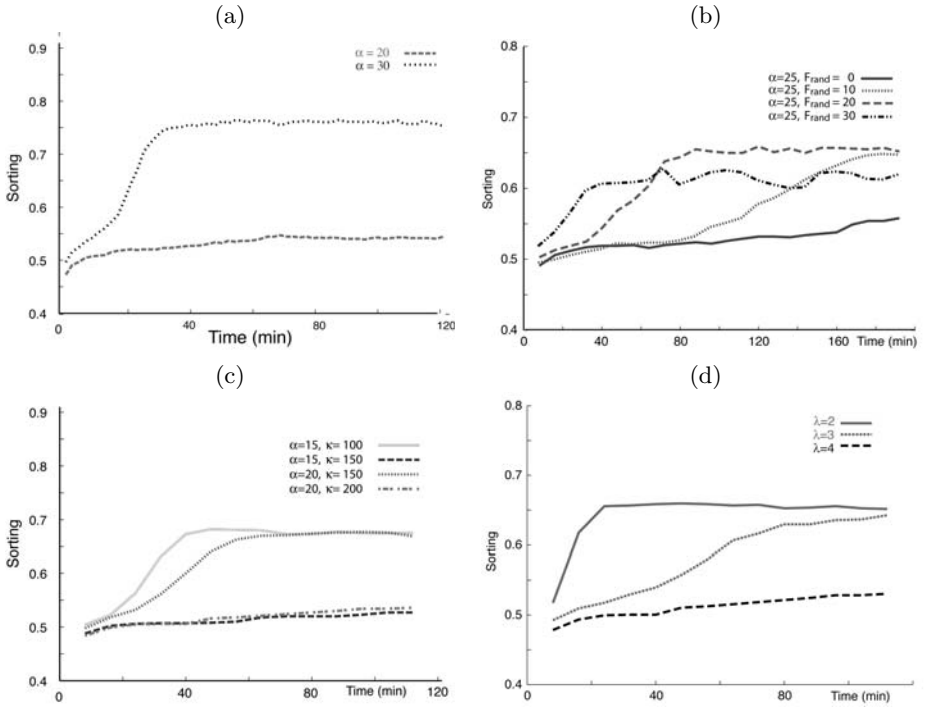

FIGURE 9. (a) The sorting for 2 types of cells with a total of 400 cells with different adhesion constant. The Maximum sorting occurs at 0.69. The cells with the lower adhesion do not sort. In all graphs the adhesion energy for cell 1 and 2 are $E_{2-2} = 0.5 \times E_{1-1}$ and $E_{1-2} = 0.75 \times E_{1-1}$. E_{1-1} is the adhesion energy between two cells of type 1. Spring constant, κ=200nN, F_{rand} = 20nN. (b) The sorting for 2 types of cells with a total of 400 cells with different random force F_{rand}. (c) Changes in the spring constant, κ, affect cell sorting. Low κ means easily deformable cells. Notice how cells sort easily when the κ=100 is low and α=15 but the sorting is severely hampered when κ=150. Increasing the adhesion to α=20 counteracts the effect of increasing the compression constant. F_{rand} = 15nN. (d) The sorting for 2 types of cells with a total of 400 cells. Here, κ=200, α=20. When λ is large the exponential falls of rapidly so the adhesion is short range, small λ gives long range adhesion.

can not escape. However, at higher adhesion, α=30, there is a sharp change where complete sorting is achieved very rapidly, in about 20 min. Increasing the random motion but keeping adhesion constant, increases the rate of sorting, Fig.9b. The time it takes to completely sort depends strongly on the magnitude of the random force. Complete sorting takes 25 min, 40 min, and 100 min when the Random force is 30nN, 20nN and 10nN, respectively. Note that the sorting is more complete when the random force is low, this is because when the random movements are large the

cells move in and out of the minimum energy state, rather than remain fully sorted. Changing the stiffness of the cells affects the sorting quite dramatically, Fig.9c. When the cells are easily deformable, low spring constant, κ=100, complete sorting occurs rapidly, since cells can easily move past each other. As the cells become stiffer, κ=150, the cells do not sort unless either the adhesion strength and/or random cell movement is increased. The initial configuration, whether it is random or a regular 3D checkerboard pattern has very little effect on the time of sorting, the sorting occurs just slightly faster when the initial configuration is random. The range of the adhesion force between two cells was changed by modifying the exponent λ in the adhesion force Eq.(7), Fig.9d. As one could predict, increasing the range of the adhesion force, increased the rate of sorting and lowered the adhesion necessary for complete sorting. A simulation with 1350 cells gives similar results but the difference between Random force = 0 and Random force = 20nN was now much more significant and the sorting took much longer time, 90 min. This is due to the fact that when the number of cells goes up, the effect of the surface is diminished and cells are more likely to be trapped in local minima where they need random movement to escape.

Takeuchi *et al* [54] dissociated a *Dictyostelium* slug and remixed the cells, thus randomizing the distribution of pre-spore cells and pre-stalk cells. The cell aggregate was then allowed to reassemble. They showed that after 2 hrs the pre-stalk cells sorted to the center of the aggregate and where completely enveloped by the pre-stalk cells. But after 8 hrs the pre-stalk and pre-spore cells occupied each hemisphere. I used the model to show that this type of sorting is possible based on differential adhesion alone Fig.10, if I assume the following: To begin with the energy of the adhesive bonds between 2 cells was as follows

$$E_{st-st} > E_{st-sp} > E_{sp-sp}$$

where the subscripts *st* and *sp* refer to pre-stalk and pre-spore cells respectively. After 60 min I slowly increase E_{sp-sp} until $E_{st-st} > E_{sp-sp} > E_{st-sp}$ and continue the evolution of the system. The biological explanation for this change in

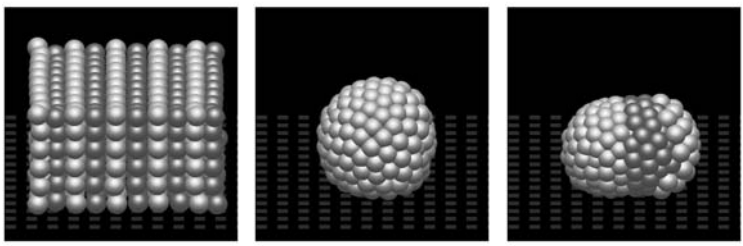

FIGURE 10. These figures show the initial state, the sorting after 60 min and the final state when mixing Dd pre-spore and pre-stalk cells. See also a simulation MovIV.2.10 from the accompanying DVD.

adhesion could be that the pre-spore cells begin to express adhesion molecules that are cell specific and do not bind or bind weakly to the pre stalk cells. As we can see from the figure these conditions reproduce the experimental observations of Takeuchi, however when we have a large number of cells the reverse sorting becomes quite slow and takes much longer than 8 hrs so I believe that even though this change in adhesion could account for this behavior, it is not the only mechanism, rather it is helping some kind of chemotactic sorting.

The close agreement between the results of computational experiments and laboratory findings suggests that the model can reproduce the essential properties of multicellular systems, and therefore can be used to investigate other aspects of cell movement in multicellular aggregates. In the remainder of this chapter I apply the model to chemotactic aggregation and slug movement in *Dd*.

Simulations of aggregation and slug movement in *Dictyostelium discoideum.* I began by studying aggregation and mound formation in *Dd*. In these simulations a few cells (darker) in the center are more excitable, effectively making them pacemakers. These pacemaker cells, periodically initiate outwards propagating circular cAMP waves, that trigger relay of the cAMP signal and chemotaxis in the remainder of the aggregation territory. A spiral generating rotating cAMP waves would also work as a signaling center [48]. However, since pacemakers are easier to initiate and both types have been observed [37, 55], I chose to use pacemakers.

Fig.11 shows the time series of a simulation of the aggregation of 40000 cells. The animation of the computational results shows both the evolution of streams during aggregation and how the mound forms when the pacemaker cells are lifted up by the inward motion of the other cells. The mound formation is clearly seen in Fig.14. When looking at the movies of the cAMP wave during the mound stage (not shown here), one can see that the signal is initiated at the top of the mound. It then travels down the center and at the same time begins to spread towards the outside of the mound. So first there is a narrow column of cells excited and then the outside and bottom cells become excited.

Fig.12 shows how the initial circular waves initiated from the pacemaker cells, can sometimes break up and form spirals. These spirals are self sustaining, the tip rotates around a core and re-initiates the wave continuously. The spirals do not need pacemaker cells for survival. The result is formation of many smaller aggregation territories as can be clearly seen in the last frame of Fig.12. This is a common phenomenon in *Dd* aggregation.

Dictyostelium cells have both a membrane bound phosphodiesterase (PDE_m) and a secreted phosphodiesterase (PDE_s). Both of these PDEs degrade cAMP and have a strong effect on the excitability of the system. If the activity of PDE is too high, cAMP is degraded rapidly and no cAMP waves can propagate. If PDE activity is low, all the cells become pacemakers. At even lower activity levels the system gets saturated with cAMP and no waves can propagate. I explored the differences that membrane bound vs. secreted PDE has on the aggregation. Fig.13 shows the results from two simulations where the ratio between PDE_m

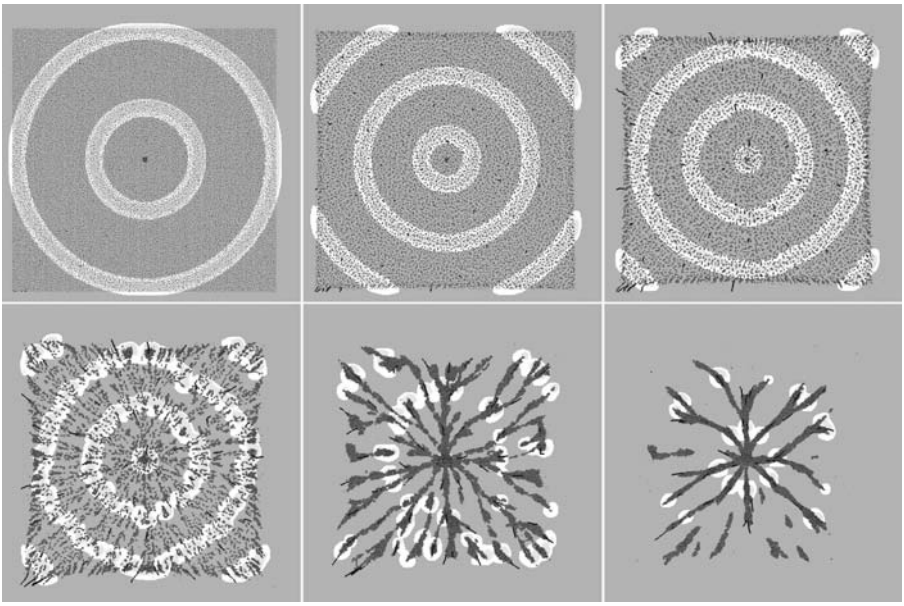

FIGURE 11. Aggregation of Dictyostelium cells in response to cAMP signaling from pacemaker cells that are located in the center (slightly darker cells) Here the time for each frame is 25, 125, 250, 500, 1000 and 1800 minutes respectively. The bright bands correspond to high cAMP concentrations. The time for aggregation is longer than observed since here the computational cells move at a speed 5 times less than experimental cells. The total number of cells is 40000. The field of each figure is 4mm x 4mm. See also a simulation MovIV.2.11 from the accompanying DVD.

and PDE_s was changed. In the upper half the PDE_m/PDE_s ratio is high (≈ 8) and aggregation proceeds normally. In the lower half the PDE_m/PDE_s ratio is much lower (≈ 1), and aggregation is interrupted later on when the cell density has increased. This happens because at higher densities many other cells become pacemakers and begin to signal and initiate new territories. An explanation for this is that as the density increases the excitability increases since the production of cAMP is proportional to number of cells, but the activity of PDE_s per unit volume remains the same, so many new cells become pacemakers. This increase in excitability is reduced when the PDE_m/PDE_s ratio is high because, as the cell density increases, the activity of PDE_m per unit volume increases as well since the PDE_m is associated with the cells. Therefore new pacemaker cells are not formed and the aggregation is not disrupted.

I also studied cell movement and cell sorting in a 2-D slug to simulate recent experiments by Bonner [56], who has created an essentially 2D slug experimentally by forcing slugs to move between a glass plate and a layer of mineral oil, Fig.15. His results show that many of the characteristic patterns of movement that are

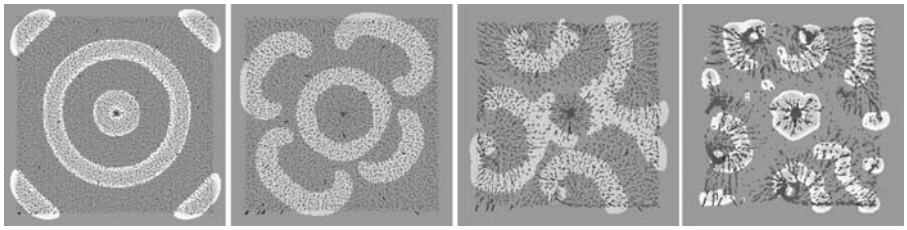

FIGURE 12. Aggregation of Dictyostelium cells in response to cAMP signaling from pacemaker cells that are located in the center (slightly darker cells). We can clearly see the formation of several spirals that end up forming new aggregation territories. Here the time of for each frame is 60, 110, 250 and 375 minutes respectively. The bright bands correspond to high cAMP concentrations. The total number of cells is 10000. The field of each figure is 2mm x 2mm. See also simulations MovIV.2.12a and MovIV.2.12b.

observed in 3D aggregates, such as rotary cell motion, also occur in 2D. To simulate this I constrained the cells between 2 parallel plates separated by 1.5 cell diameters, thus effectively forcing the slug to be about only one cell layer thick.

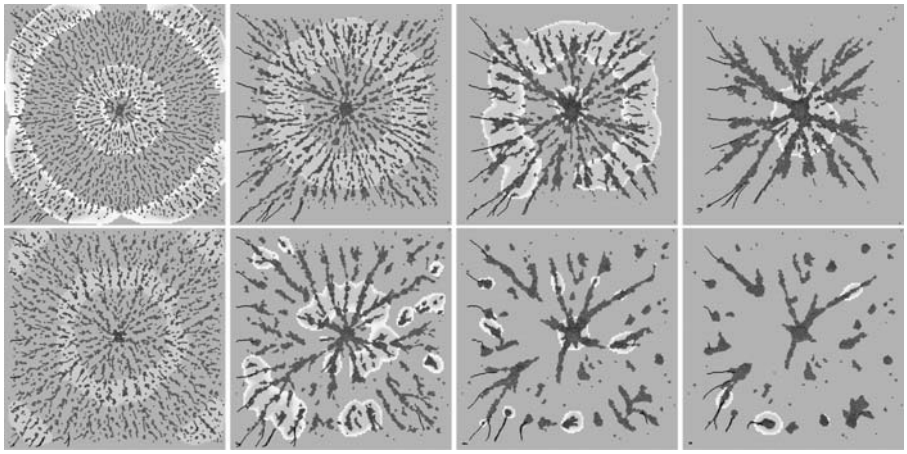

FIGURE 13. Aggregation of Dictyostelium cells for low and high PDE_m/PDE_s ratios. cAMP signaling from pacemaker cells that are located in the center (slightly darker cells). In the upper half the PDE_m/PDE_s ratio is high ($\approx$8) same as in Fig.11 and Fig.12, so aggregation proceeds normally. In the lower half the PDE_m/PDE_s ratio is much lower ($\approx$1), and aggregation is interrupted later on when the density has increased, because now many new signaling centers form. The time for each frame is 100, 200, 300 and 400 minutes respectively. The bright bands correspond to high cAMP concentrations. The total number of cells is 4900. The field of each figure is 1.4mm x 1.4mm.

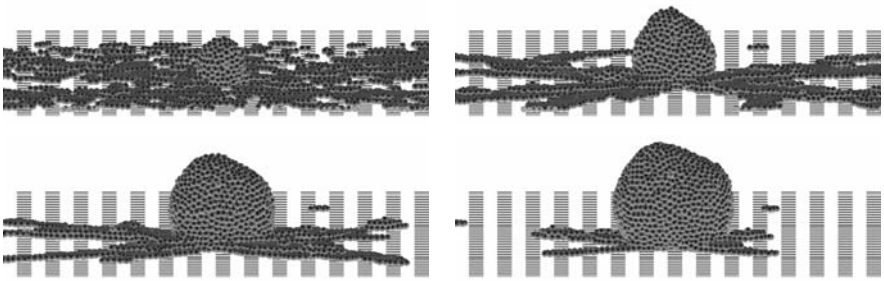

FIGURE 14. A side view of the aggregation field. The formation of the mound as the outer cells move towards the center, is demonstrated. Frames are at times 400, 800, 1600 and 3200 min respectively. See also simulations MovIV.2.14a and MovIV.2.14b from the accompanying DVD.

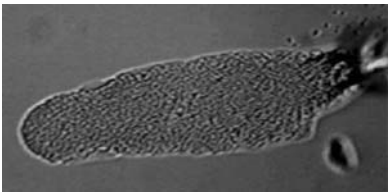

FIGURE 15. A 2-D Dd slug with $\simeq$ 2000 cells moving between the boundary of oil and a glass plate. The slug is about 500 μ long. Courtesy of John Bonner

The cell interactions with the plates were the same above and below, which differs from the experimental conditions. However, the results show that this difference is apparently not very significant.

Initially the cells where arranged in a regular square between the two plates and a few pacemaker cells (darker cells), where placed on the midline at the right edge. As before, these cells initiate cAMP waves that are relayed throughout the slug, which begins to elongate and move forward. In the movie of this simulation one can clearly see the cells move forward in response to the cAMP wave emanating from the pacemakers, and this forward motion then pushes the pacemaker cells forwards, giving rise to a net forward movement for the slug.

In the simulation shown in Fig.16 I grafted another group of pacemaker cells onto one side of the slug after 50 minutes of migration. These new pacemakers begin to send out cAMP signals and thus compete with the pacemakers at the anterior end. Eventually the signals from the grafted pacemaker dominate the signals from the anterior pacemaker in a region surrounding the grafted pacemakers, with the result that the slug splits up into two smaller slugs, each one controlled by its own pacemaker. Such splitting is common in grafting experiments using 3D slugs, but recently it has also been observed in 2D slugs [56].

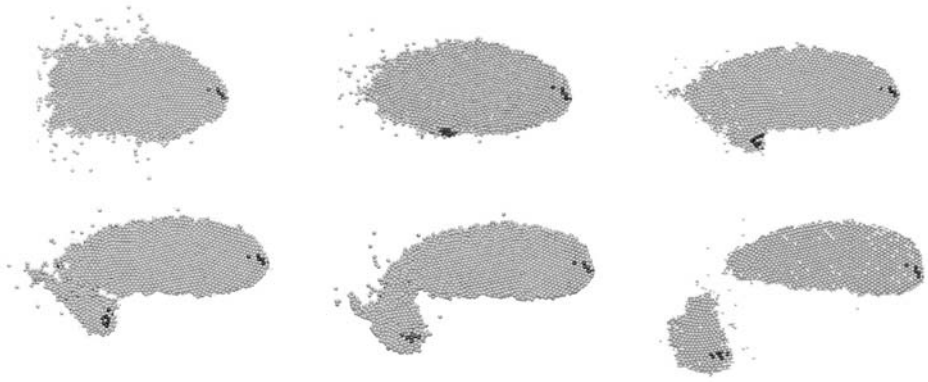

FIGURE 16. The movement of a *Dictyostelium* slug with 2500 cells in response to a few pacemaker cells at the front (darker cells). The frames are taken after 40, 60, 80, 100, 120 and 150 min. respectively. At time = 50 minutes I initiated another pacemaker at the side of the slug. Notice how the new pacemaker takes away cells.

To explore sorting of pre-stalk and pre-spore cells during the *Dd* slug stage I did simulations of a 2D slug comprised of those two cell types, where the active force is 60% larger for the pre-stalk cells. Initially these cell types were uniformly distributed in the slug. I discovered that even though the more powerful cells have a tendency to move toward the front, most of them had not sorted to the front by the end of four hours. In early aggregation the result is quite different, because the more powerful cells move about 60% faster, and quickly move ahead of the wild type cells. In these simulations the adhesive forces were identical for both cell types, and this suggests that when the cells interact strongly, as they do in the slug, simply exerting more force is not always enough to produce rapid sorting. Making the cells more deformable improves the sorting, but not dramatically. A possible mechanism that might speed up the cell sorting would be if a column of more active cells was moving towards the front. In this case, the less active cells wouldn't be as much in the way. I decided to explore this possibility. When cells adhere more strongly to cells of the same type, i.e. cell specific cell adhesion, the different cell populations tend to group together inside the aggregate. It has been shown that in a disaggregated Dd slug pre-spore and pre-stalk cells preferentially adhere to themselves [57, 58]. Based on this knowledge I set out to study if the sorting out of pre-spore and pre-stalk cells was enhanced when the cells have cell specific adhesion. Fig.17 shows a time series of the cell sorting in a slug. The chemotactic force for the grey cells (pre-stalk) is 60% larger than the lighter cells (pre-spore). When there is no differential cell adhesion, Fig.17 top row, only a few pre-stalk cells make it to the front of the slug, in the given time. This is because despite the fact that the pre-stalk cells have a larger chemotactic force they do not manage to move past the less active pre-spore cells, instead the pre-spore cells

get pushed forward as the pre-stalk cells attempt to squeeze by. In Fig.17 bottom row, the pre-spore and pre-stalk cells preferentially adhere to themselves, and here the pre-stalk cells also rapidly sort to the front. Notice that now the pre-stalk cells form small groups that move as a unit to the front of the slug which differs slightly from the cell movement in the middle row. This grouping of the pre-stalk cells helps them move past the pre-spore cells, since now the collective chemotactic force of the group is sufficient to allow them to move past the pre-spore cells. This is possible because the total chemotactic force of the group is proportional to the number of cells in the group, whereas the force required to deform and move past the cells ahead is proportional to the cross section of the group. Therefore the easiest way for stronger cells to move up to the front is in a narrow stream up the center, since here the cells do not need to deform much and the force required to move past the slower cells comes mostly from the drag from sliding past them. This could explain why streams of cells moving are often observed moving up the center of the slug [33].

FIGURE 17. These snapshots show the sorting of pre-stalk, grey cells, and pre-spore, light cells, in a *Dictyostelium* slug for different cell adhesion. The black cells at the front are pacemakers, periodically emitting cAMP. The grey cells comprise 20% of the slug and have a chemotactic force that is 60% larger than the lighter cells. The light bands indicate high cAMP concentration. The lower images are transections through the middle of the slug. In **a)** the lighter and darker cells have the same adhesion, notice no significant sorting of grey cells occurs. In **b)** the grey cells are more adhesive than the light cells. The adhesion energy $E_{light,light} = 1.0, E_{light,gray} = 1.3, E_{gray,gray} = 1.6$. We can see that sorting of pre-stalk cells to the front is facilitated when the adhesion between pre-spore and pre-stalk cells differs. In both a) and b) the snapshots are taken at 250, 750, 1250 and 1750 minutes respectively. See also simulations MovIV.2.17a–MovIV.2.17d from the accompanying DVD.

4. Conclusions

The objective of this chapter was to demonstrate how models provide an invaluable tool for exploring how cells in multicellular systems interact, and in particular the benefits of an individual based compressible ellipsoidal cell model. These cell movements arise from the behavior of individual cells in response to the chemical and mechanical environment they experience. Because of the complex cell-cell interactions, the collective motion is often quite different from the motion of isolated individuals, as evidenced by tissue movements during embryogenesis [5] or in the slug stage of *Dictyostelium*. I introduced a model that simulated the movement of cells in multicellular systems in 3-D, and enabled us to visualize both the cell movements and the wave propagation.

It was shown that the simulations of multicellular aggregates behave as viscoelastic fluids, in agreement with experimental results from embryonic tissues. The cell aggregate still retains cell individuality, however, as demonstrated in the cell sorting simulations. This was shown for both chemotactic and adhesion driven cell sorting, since the stiffness, cell-cell adhesion strength and random movement of the cells significantly affected the rate and completeness of cell sorting. Since the cells have a given size, we were able to study the effects cell size and cell deformability have on cell sorting and motility, something not easily done with fluid based models. Experiments that could be done to to test these results include mixing together cells that express very few adhesion molecules and measuring the time it takes for the cells to sort, and compare the results with findings from cells expressing a higher number of adhesion molecules. Since many cells become stiffer as they age the effect of cell stiffness can be tested by performing the cell sorting experiments with cells of different age.

Dd was used as a model system to explore the cell sorting and movement along with cAMP wave propagation in early aggregation and during the slug stage. A number of simulations highlighted different phenomena in cell-cell communications and interactions. I also made predictions and compared some of the results to experimental findings. A comparison of the simulations with experimental observation will help determine the most important factors controlling the movement of cells. Many of these simulations were relatively simple to do with the model, whereas it would be quite difficult, although still feasible, to perform those same experiments in vivo. Therefore we can use the model to explore a number of different scenarios, and when interesting results are found such as the effect of membrane vs. secreted PDE, the next step is to set up an experiment, in vivo, to check the predictions of the model. This is yet another example of the benefits of mathematical modeling in biology.

The simulations showed that the observed collective, coordinated motion of cells in Dd, from the aggregation to the slug stage, follows directly from the behavior of individual cells in response to cAMP—no additional assumptions nor mechanisms are necessary to reproduce the motion of a slug. However, this does

not mean that these are the only mechanisms operating, but only that these mechanisms are sufficient. It is known that slug movement is not quite that simple, but this can be a good start. One can see from the aggregation simulations how the stream formation comes out naturally, all that is needed is to couple the cAMP secretion with the cells. Essentially this coupling causes the cAMP secretion to be higher where the cell density is higher, and since the cells aggregate in the direction of the cAMP gradient, the cells chemotact towards higher density regions further increasing the density. When the active locomotive force that the cells apply is increased the cell speed increases as well, and this affects the overall pattern and cell movements. When cell speed is high (active locomotive force is large) cells tend to move straight towards the center rather than join into streams so streams do not really develop.

As mentioned in the introduction, when cells inside a multicellular system actively try to move they can only do so by pulling on or pushing off neighbor cells. All the forces are carefully balanced in the model, so I can use it to study the difference between movement where cells get traction from the boundary vs. movement where they get only traction from other cells.

A new discovery that came from the simulations, which should be explored experimentally, is the possible importance of the ratio of membrane bound phosphodiesterase (PDE_m) to secreted phosphodiesterase (PDE_s). This effect has not been studied before by either modelers or experimentalists. I demonstrated that PDE_m is important to make the system less sensitive to the cell density changes that occur during aggregation. When the ratio of membrane bound to external PDE becomes to low, spontaneous oscillating centers form at new locations when the cell density increases during aggregation. This disrupts the aggregation and triggers the formation of many aggregation centers with smaller territories that might have an evolutionary disadvantage. A future use of the model will be to get a more detailed understanding of the interaction between the membrane bound and secreted PDE. *Dd* could use other mechanism to compensate for increased cell density, such as up- or down- regulation of genes and proteins. It is know that a number of genes are turned on or off during *Dd* development [59], but yet again this just suggest that many processes are at work to make the cell motion during development robust, controlling (PDE_m) to (PDE_s) ratios is just one of them.

Another interesting discovery and understanding comes from the cell sorting simulations in the slug where the pre-stalk cells have a 60% larger chemotactic force than the pre-spore cells. The simulations demonstrated how important *cell specific adhesion* is to facilitate the sorting of the pre-stalk cell to the front of the slug. From these results I suggest that chemotaxis alone is not sufficient to achieve the observed sorting in *Dd* in a timely manner, but when combined with cell specific adhesion the pre-stalk cells sort to the front of the slug and distinct pre-spore, pre-stalk boundaries form, as observed in the *Dd* slug.

These observations explain one of the reasons why the pre-stalk and pre-spore cells exhibit cell specific adhesion [60]: it may be necessary in order to achieve proper separation of the two cell types in the mound and the slug stage of *Dd*. I will

continuing to use the model to study the cell movement and sorting of pre-spore and pre-stalk cells in the late mound and slug stage of Dictyostelium and include cell differentiation. I also want explore in more detail the 3-dimensional shape of the cAMP wave. In *Dd* the movement of cells has been observed using confocal microscopy but so far the spatial distribution and profiles of the chemotactic signals can't be measured inside the slug. So here the model can help us by showing what kind of signal profiles can give rise to the observed cell movements [61, 62]. Being able to visualize the movement and trajectories of individual cells can help us gain understanding and insight of how cell movement and sorting transpires and the effect external or internal factors have. This application of the model can be both useful in basic research as well as for teaching purposes.

References

[1] Alberts, B, Bray, D, Lewis, J, Raff, M, Roberts, K, & Watson, J. D. (1994) *Molecular Biology of The Cell.* (Garland, New York and London). 1994.

[2] Elul, T, Koehl, M. A. R, & Keller, R. (1997) *Developmental Biology* **191**, 243–258.

[3] Takeichi, M. (1993) *Curr. Opin. Cell Biol.* **5**, 806–811.

[4] Bonner, J. T. (1967) *The cellular slime molds. Second edition.* (Princeton Univ. Press, Princeton, NJ).

[5] Gilbert, S. F. (1997) *Developmental Biology.* (Sinauer Associates, Inc., Sunderland Massachusetts), Fifth edition.

[6] Davidenko, J. M, Pertsov, A. V, Salomonsz, R, Baxter, W, & Jalife, J. (1992) *Nature* **355**, 349–351.

[7] Jalife, J & Antzelevitch, C. (1979) *Science* **206**, 695–697.

[8] Jaffe, L. F. (1995) *Ciba Found Symposium* **188**, 4–12.

[9] Ludwig, D, Jones, D. D, & Holling, C. S. (1978) *Journal Animal Ecology* **47**, 315–332.

[10] Alcantara, F & Monk, M. (1974) *J. Gen. Microbiol.* **85**, 321–334. J. Gen. Microbiol.

[11] Konijn, T. M, van de Meene, J. G. C, Bonner, J. T, & Barkley, D. S. (1967) *Proc. Natl. Acad. Sci. USA* **58**, 1152–1154. Proc. Natl. Acad. Sci. USA.

[12] Palsson, E, Lee, K. J, Goldstein, R. E, Franke, J, Kessin, R. H, & Cox, E. C. (1997) *Proc. Natl. Acad. Sci. USA* **94**, 13719–13723.

[13] Wu, L, Franke, J, Blanton, R. L, Podgorski, G. J, & Kessin, R. H. (1995) *Dev. Biol.* **167**, 1–8.

[14] Siegert, F & Weijer, C. J. (1992) *Proc. Natl. Acad. Sci. USA* **89**, 6433–6437.

[15] Palsson, E & Othmer, H. (2000) *Proc. Natl. Acad. Sci. USA* **97**, 10448–10453.

[16] Palsson, E. (2001) *Future Generation Computer Systems* **17**, 835–852.

[17] Swanson, J & Taylor, D. L. (1982) *Cell* **28**, 225–232.

[18] Chien, S, Schmid-Schonbein, G. W, Sung, K. L. P, Schmaizer, E. A, & Skalak, R. (1984) in *Basic Science and Clinical Aspects.* pp. 3–18.

[19] Evans, E. A. (1985) *Biophys J. Biophysical Society* **48**, 175–183.

[20] Bray, D. (1992) *Cell Movements.* (Garland Publishing, Inc, New York and London).

[21] Richardson, P. D & Steiner, M. (1994) *Principles of Cell Adhesion.* (CRC Press., London). 1994.

[22] Usami, S, Wung, S, Skierczynski, B, Skalak, R, & Chien, S. (1992) *Biophysics J.* **63**, 1663–1666.

[23] Oliver, T, Jacobson, K, & Dembo, M. (1988) *Methods in Enzymology* **298**, 623.

[24] Lee, J, leonard, M, Oliver, T, Ishihara, A, & Jacobson, K. (1994) *Journal of Cell Biology.* **127**, 1957–1964.

[25] Inouye, K & Takeuchi, I. (1980) *Journal of Cell Science* **41**, 53–64.

[26] Guilford, W. H, Lantz, R. C, & Gore, R. W. (1995) *American Journal of Physiology.* **268**, 1308–1312.

[27] Wessels, D, Vawter-Hugart, H, Murray, J, & Soll, D. R. (1994) *Cell Motility and the Cytoskeleton* **27**, 1–12.

[28] Wessels, D, Voss, E, Bergen, N. V, Burns, R, Stites, J, & Soll, D. R. (1998) *Cell Motility and the Cytoskeleton* **41**, 225–246.

[29] Varnum-Finney, B, Edwards, K. B, Voss, E, & Soll, D. R. (1987) *Cell Motility and the Cytoskeleton* **8**, 7–17.

[30] Varnum-Finney, B. J, Voss, E, & Soll, D. R. (1987) *Cell Motility and Cytoskeleton* **8**, 18–26.

[31] Wessels, D, Vawter-Hugart, H, Murray, J, & Soll, D. R. (1994) *Cell Motility and the Cytoskeleton* **27**, 1–12.

[32] Wessels, D, Voss, E, Bergen, N. V, Burns, R, Stites, J, & Soll, D. R. (1998) *Cell Motility and the Cytoskeleton* **41**, 225–246.

[33] Odell, G. M & Bonner, J. (1986) *Phil. Trans.R. Soc. Lond.* **312**, 487–525.

[34] Skalak, R, Chien, S, & Schmid-Schonbein, G. W. (1984) in *Basic Science and Clinical Aspects.* pp. 3–18. 1984.

[35] Taylor, D. L, Heiple, J, Wang, Y. L, Luna, E. J, Tanasugarn, L, Brier, J, Swanson, J, Fechheimer, M, Amato, P, Rockwel, M, & Daley, G. (1982) *CSH Symp. Quant. Biol.* **46**, 101–111.

[36] Wessels, D, Titus, M, & Soll, D. R. (1996) *Cell Motility and the Cytoskeleton* **33**, 64–79.

[37] Alcantara, F & Monk, M. (1974) *JGM, Journal of General Microbiology* **85**, 321–334.

[38] Evans, E. A. (1985) *Biophysical Journal* **48**, 175–183.

[39] Evans, E. A. (1985) *Biophysical Journal* **48**, 185–192.

[40] Zhu, C, Williams, T. E, Delobel, J, Xia, D, & Offerman, M. K. (1994) in *Cell mechanics and Cellular engineering.*, eds. Van, C. M & et al. (Springer, New York), pp. 160–180. 1994.

[41] Philips, H. M & Steinberg, M. S. (1978) *Journal of Cell Science* **30**, 1–20.

[42] Philips, H. M, Steinberg, M. S, & Lipton, B. H. (1977) *Developmental Biology* **59**, 124–134.

[43] Bell, G. I. (1978) *Science* **200**, 618–627.

[44] Forgacs, G, Foty, R. A, Shafrir, Y, & Steinberg, M. S. (1998) *Biophysical Journal* **74**, 2227–2234.

[45] Fuchs, M, Jones, M. K, & Williams, K. L. (1993) *J. Cell Sci.* **105**, 243–253.

[46] Schonfisch, B & Roos, A. d. (1999) *Biosystems* **51**, 123–143.

[47] Martiel, J. L & Goldbeter, A. (1987) *Biophys. J.* **52**, 807–828.

[48] Palsson, E & Cox, E. C. (1996) *Proc. Natl. Acad. Sci. USA* **93**, 1151–1155.

[49] Ramsey, A. F, Gabor, F, Cathie, M. P, & Malcolm, S. S. (1994) *Physical Review Letters* **72**, 2298–2301.

[50] Rowlinson, J. S & Widom, B. (1989) *Molecular theory of capillarity.* (Clarendon Press., Oxford). 1989.

[51] Foty, R. A, Pfleger, C. M, Forgacs, G, & Steinberg, M. S. (1996) *Development* **122**, 1611–1620.

[52] Davis, G. S, Phillips, H. M, & Steinberg, M. S. (1997) *Developmental Biology* **192**, 630–644.

[53] Steinberg, M. S. (1975) *J. Theor. Biol.* **55**, 431–443.

[54] Takeuchi, I, Kakutani, T, & Tasaka, M. (1988) *Dev. Genet.* **9**, 607–614. Dev. Genet.

[55] Gross, J. D, Peacey, M. J, & Trevan, D. J. (1976) *Journal of Cell Science* **22**, 645–656.

[56] Bonner, J. T. (1998) *Proc. Natl. Acad. Sci. USA*. **95**, 9355–9359.

[57] Tasaka, M & Takeuchi, I. (1979) *Journal of Embryology and Experimental Morphology* **49**, 89–102.

[58] Takeuchi, I, Kakutani, T, & Tasaka, M. (1988) *Developmental Genetics* **9**, 607–614.

[59] Iranfar, N, Fuller, D, & Loomis, W. F. (2003) *Eukaryotic Cell* **2**, 664–670.

[60] Lam, T. Y, Pickering, G, Geltosky, J, & Siu, C. H. (1981) *Differentiation* **20**, 22–28.

[61] Siegert, F & Weijer, C. J. (1991) *Physica D* **49**, 224–232.

[62] Rietdorf, J, Siegert, F, & Weijer, C. J. (1996) *Developmental Biology* **177**, 427–438.

Eirikur Palsson
Department of Biology, Simon Fraser University
8888 University Dr, Burnaby, BC V5A 1S6, Canada
e-mail: `epalsson@sfu.ca`

Single-Cell-Based Models in Biology and Medicine
ed. by A.R.A. Anderson, M.A.J. Chaplain, K.A. Rejniak
Mathematics and Biosciences in Interaction, 301–323

IV.3 Modelling the Development of Complex Tissues Using Individual Viscoelastic Cells

Katarzyna A. Rejniak

Abstract. This chapter describes a biomechanical model of individual deformable viscoelastic cells that can be arranged into tissues of various topologies. The model is based on an immersed boundary method with distributed sources and couples a continuous description of a viscous incompressible cytoplasm with the dynamics of separate elastic cells. Several key cellular processes, such as cell growth, division, apoptosis and polarisation, are also defined within this framework. This approach enables one to focus on the biomechanical properties of individual cells and on communication between cells and their microenvironment, and to investigate how individual cells cooperate and contribute to the overall structure and function of a particular tissue. Three applications of this model are presented: the folding of a trophoblast bilayer, clonal tumoural growth and self-arrangement into a hollow acinus, the hollow multicellular sphere. Further extensions of this model are also discussed.

1. Introduction

Interactions between individual cells and between cells and their local environment play a very important role in the development of normal tissues and in maintaining the tissue structural and functional integrity. On the other hand, some alterations in cell collaborative behaviour may lead to tissue deformations and to the initiation of growth of a tumour. The exchange of various mechanical and biochemical signals between neighbouring cells starts at an early stage of human development when a single fertilised cell upon consecutive divisions and cell differentiations gives rise to all the distinct and highly specialised tissues and organs of the body. In an adult human body *cell turnover* (a process in which dying cells are replaced by newly born cells) is present in every tissue. However, a cell lifespan ranges from three days for skin cells, and four months for red blood cells, to several years for bone cells. Investigations of collaborative or competitive interactions between individual cells help to understand mechanisms that are crucial for normal or abnormal tissue growth. With continuously improving experimental techniques that allow for staining and visualization of various inter- and intracellular cell components, more information is available about the signalling pathways and cell response to various

environmental cues. However, every biological experiment depends on multiple factors that are hard to control and test in isolation. Therefore, mathematical models can provide a way for a systematic investigation of how specific biochemical or biomechanical factors influence the development of the whole tissue. In order to investigate how individual cells cooperate and contribute to the overall structure and function of a particular tissue, such computational models are needed that allow for:

- individually defined cells of deformable shapes,
- time- and space-dependent individually regulated cell processes,
- cell-to-cell interactions defined on the level of cell receptors.

I propose in this chapter a biomechanical model of a eukaryotic cell defined as a viscoelastic body, with its cell shape defined by a mesh of elastic springs and cell mass provided by a viscous incompressible fluid. Each cell in this model is an individual entity containing several subcellular elements, such as the elastic plasma membrane enclosing the cell cytoplasm and the cell nucleus. All points on the cell membrane play an additional role of cell molecular complexes, such as adherens junctions providing connection and communication between neighbouring cells, or the contractile ring enabling the physical division of the cell into two daughters. All cell processes, such as cell growth, division, death, or polarisation, are regulated independently for each individual cell, but separate cells can interact with other cells and with the environment via a set of discrete cell membrane receptors located on the cell boundary. The cells can be arranged into geometrically different tissues and then used to study tissue deformations, development or turnover by focusing on the processes of individual cells and on communication between cells and their microenvironment.

The mathematical framework underlying this model captures interactions between immersed elastic bodies of cells and the viscous incompressible fluid representing the cytoplasm inside the cells and the extracellular matrix outside the tissue. The immersed boundary method has been introduced by Peskin [1, 2] for the study of flow patterns around heart valves and then successfully applied in modelling different phenomena concerning fluid-structure interactions (for a review and a list of references up to 2002 see [3]). This mathematical framework has also been used to address certain problems in collective cellular behaviour. Individual micro-organisms modelled as single points in gravitational and chemotactic fields were used to investigate a collective behaviour of large microbial colonies [4]. Individual cells represented as small circles (in 2-dimensional models) or small spheres (in 3-dimensional models) were used to model biofilm processes and chemotactic motility of bacterial colonies of moderate sizes [5, 6, 7], collective sperm motility [8, 9, 10], and platelet aggregation and coagulation during blood clotting ([8, 11, 12], see also chapter IV.1). Single deformable cells have been used to model ameboid locomotion [13, 14] and leukocyte adhesion and rolling [15, 16]. The first immersed boundary model of tissue growth was proposed by Dillon and

Othmer in [17]. They investigated the spatio-temporal patterns of different morphogens arising during the development of a vertebrate limb. In their model the whole limb tissue was treated as a viscous incompressible fluid that grows by acquiring the necessary fluid from the extracellular matrix surrounding the limb. This transport of fluid across the tissue boundary was achieved by introducing distributed sources inside the limb bud to account for the total increase of its volume due to the collective cell proliferation, and distributed sinks outside the tissue to ensure conservation of mass in the whole computational system. Individual cells were traced as fluid markers to recover their trajectories and spatio-temporal interactions with morphogens during the tissue growth. This particular application of the immersed boundary method has inspired me to propose a model of individual growing cells that can deform and be arranged in tissues of different topologies and then used to investigate how interactions between separate cells influence the behaviour of a whole tissue. This model was introduced in [18, 19] to simulate the formation of abnormal tissue folding in the human trophoblast bilayer. The model has evolved since then by acquiring more biologically faithful details and by including algorithms of several different cell life processes. It has been used to simulate the growth of avascular tumours in different topologies of the surrounding tissues [20], the emergence of tumour microregions due to cell competition for nutrients [21], the formation of micro-architectural patterns in ductal carcinomas in situ due to the gradual dedifferentiation of ductal epithelial cells [22], the development of normal and mutated epithelial lobules and ducts [23, 24].

In this chapter I will show how the immersed boundary framework can be used to model the structure of a eukaryotic cell and several cell processes, including cell growth, division, death, and polarisation. I will present three particular applications of this model that address different aspects of tissue morphology—the formation of tissue folds in the placental trophoblast bilayer, multicellular clonal growth due to cell competition for nutrients sensed from the extracellular space and the development of stable acinar structures composed of one layer of polarised epithelial cells surrounding the hollow lumen. This chapter will end with a discussion on possible model extensions, including the chemotactic and haptotactic motility and the three-dimensional implementations of certain cellular processes and their morphological deformations.

2. Mathematical model

In general, the immersed boundary method couples the mechanics of immersed elastic bodies (here: cells) with the dynamics of a viscous incompressible fluid (here: the cytoplasm and the extracellular matrix). The fluid flow is influenced by sources and sinks used to model transport of the fluid across the cell membranes, as well as forces generated by the deforming elastic cell boundaries, while at the same time all elastic structures move at the local fluid velocity. The strength of the immersed boundary method (and of this model) is that it can handle the complicated and

time dependent geometries of individual elastic cells which can be arranged into tissues of different topologies, and that it does so while using a fixed regular lattice for the fluid computation. It is relatively easy to introduce different intracellular components in the form of networks of linear elastic or stiff springs, and distinct locations of fluid sources and sinks that may depend on the tissue homeostatic properties and on biological questions that the model is addressing. In general, each cell in this model contains its own elastic plasma membrane enclosing the fluid cytoplasm and a point nucleus. All boundary points play an additional role of membrane receptors that are used to communicate with other cells and with the cell microenvironment. Moreover, the adhesive links between separate cells are used to model interactions between neighbouring cells. The details about the cell structure and several cell processes are presented in the next few sections.

2.1. Mathematical formulation

The mathematical formulation of the model uses a two-dimensional domain Ω with fixed Cartesian coordinates $\mathbf{x} = (x_1, x_2)$. The elastic membranes of all cells form a collection Γ of closed curves defined in the curvilinear coordinates $\mathbf{X}_i(l,t)$, where l is a position along the boundary of the i^{th} cell. The fluid inside and outside the cells is modelled as a homogeneous continuum with the same constant density ρ and viscosity μ. The sources and sinks used to model the transport of fluid across the cell membranes are placed in the fluid domain along the cell boundaries. The boundary forces can be divided into two groups—intracellular forces, that arise from elasticity of the cell plasma membrane and cell contraction during its division into two daughter cells; and intercellular forces, that form the interactions between distinct cells, or between the cells and other elements of the tissue, such as the basement membranes.

The fluid motion is governed by the Navier-Stokes equations:

$$\rho\left(\frac{\partial \mathbf{u}(\mathbf{x},t)}{\partial t} + (\mathbf{u}(\mathbf{x},t)\cdot\nabla)\mathbf{u}(\mathbf{x},t)\right) = -\nabla p(\mathbf{x},t) + \mu\Delta\mathbf{u}(\mathbf{x},t) + \frac{\mu}{3\rho}\nabla s(\mathbf{x},t) + \mathbf{f}(\mathbf{x},t), \quad (1)$$

where ρ is the fluid density, p is the fluid pressure, μ is the fluid viscosity, s is the local fluid expansion due to the sources and sinks of fluid distributed in the fluid domain, and $\mathbf{f}$ is the external force density. The source-sink distribution and the external forces are taken around each cell separately and then collectively applied to the fluid, that is $s(\mathbf{x},t) = \sum_i s_i(\mathbf{x},t)$ and $\mathbf{f}(\mathbf{x},t) = \sum_i \mathbf{f}_i(\mathbf{x},t)$.

The continuity equation with a source term describes the law of mass balance, where the source distribution s is identically equal to zero on the whole fluid domain except at the isolated point sources and sinks that are used to model cell processes, such as cell growth or death:

$$\rho\nabla\cdot\mathbf{u}(\mathbf{x},t) = s(\mathbf{x},t). \quad (2)$$

Conservation of mass must be preserved globally in the fluid domain Ω at each time t; that is, $\int_\Omega s(\mathbf{x},t)\,d\mathbf{x} = \rho\int_\Omega \nabla\cdot\mathbf{u}(\mathbf{x},t)\,d\mathbf{x} = 0$.

The source-sink distribution defined for the i^{th} cell is composed of point sources $\mathbf{Y}^+_{i,k}$ and point sinks $\mathbf{Y}^-_{i,m}$ located around the cell boundary and then

transmitted to the surrounding fluid using the two-dimensional Dirac delta function, $\delta(\mathbf{x}) = \delta(x_1) \cdot \delta(x_2)$:

$$s_i(\mathbf{x},t) = \sum_{k\in\Xi_i^+} S_+(\mathbf{Y}_{i,k}^+,t)\ \delta(\mathbf{x}-\mathbf{Y}_{i,k}^+)\ +\ \sum_{m\in\Xi_i^-} S_-(\mathbf{Y}_{i,m}^-,t)\ \delta(\mathbf{x}-\mathbf{Y}_{i,m}^-). \tag{3}$$

The boundary forces $\mathbf{F}_i(l,t)$ in the i^{th} cell $\mathbf{X}_i(l,t)$ represent a sum of various forces arising from the internal cell structure $\mathbf{F}_{cell(i)}$ and from the interactions with other cells $\mathbf{F}_{inter(i)}$. They are then transmitted to the surrounding fluid using the two-dimensional Dirac delta function δ:

$$\begin{aligned} \mathbf{f}_i(\mathbf{x},t) &= \int_{\Gamma_i} \mathbf{F}_i(l,t)\ \delta(\mathbf{x}-\mathbf{X}_i(l,t))\ dl, \\ \mathbf{F}_i(l,t) &= \mathbf{F}_{cell(i)}(l,t) + \mathbf{F}_{inter(i)}(l,t). \end{aligned} \tag{4}$$

The no-slip condition of a viscous fluid implies that the material points on cell boundaries are carried along with the fluid:

$$\frac{\partial \mathbf{X}_i(l,t)}{\partial t} = \mathbf{u}(\mathbf{X}_i(l,t),t) = \int_\Omega \mathbf{u}(\mathbf{x},t)\ \delta(\mathbf{x}-\mathbf{X}_i(l,t))\ d\mathbf{x}. \tag{5}$$

2.2. Model implementation

In order to numerically implement the model described above, the fluid domain Ω is discretised using a uniform square grid with a constant mesh width h. Similarly, each cell membrane is represented by Lagrangian points $\mathbf{X}_{i,l}$ with boundary points separation of $\Delta l \approx h/2$. The computation proceeds in time steps of duration Δt. For convenience we use the superscript notation, that is $\mathbf{u}^n(\mathbf{x}) = \mathbf{u}(\mathbf{x}, n\Delta t)$. At the end of time step n the fluid velocity field $\mathbf{u}^n$ and the configuration of the boundary points $\mathbf{X}_{i,l}^n$ are known. These values are updated at the next time step in the following way:

1. Calculate the total force density $\mathbf{F}^n$ from the configuration of cell boundaries; spread these values to the neighbouring grid points to determine the forces $\mathbf{f}^n$ acting on the fluid (compare Fig.1a):

$$\begin{aligned} \mathbf{f}^n(\mathbf{x}) &= \sum_i \left(\sum_l \mathbf{F}_i^n(l,t)\ \ \delta_h(\mathbf{x}-\mathbf{X}_{i,l})\ \Delta l \right), \\ \mathbf{F}_i^n(l,t) &= \mathbf{F}_{cell(i)}^n(l,t) + \mathbf{F}_{inter(i)}^n(l,t). \end{aligned} \tag{6}$$

2. Determine the source-sink distribution S^n at points $\mathbf{Y}_k^+$ and $\mathbf{Y}_m^-$ located along the boundaries of all expanding or shrinking cells; spread these values to the neighbouring grid points to find the local expansion rate s^n of the fluid (compare Fig.1b):

$$s^n(\mathbf{x}) = \sum_i \left(\sum_{k\in\Xi_i^+} S_+^n(\mathbf{Y}_{i,k}^+,t)\ \delta_h(\mathbf{x}-\mathbf{Y}_{i,k}^+)\ +\ \sum_{m\in\Xi_i^-} S_-^n(\mathbf{Y}_{i,m}^-,t)\ \delta_h(\mathbf{x}-\mathbf{Y}_{i,m}^-) \right). \tag{7}$$

3. Solve the Navier–Stokes equations for the fluid velocity field $\mathbf{u}^{n+1}$ by using the fast Fourier transform algorithm with periodic boundary conditions imposed on the fluid domain. The equations are discretised using the first order finite difference scheme with the spatial difference operators: forward D^+, backward D^-, centred D^0 and upwind $D^{\pm}$; $r = 1, 2$ denotes the first and second vector field components, respectively:

$$\begin{cases} \rho\left(\frac{u_r^{n+1}-u_r^n}{\Delta t} + \sum_{s=1}^{2} u_s^n D_s^{\pm} u_r^n\right) = -D_r^0 p^{n+1} + \mu \sum_{s=1}^{2} D_s^+ D_s^- u_r^{n+1} + \frac{1}{3}\frac{\mu}{\rho} D_r^0 s^n + f_r^n, \\ \rho \sum_{s=1}^{2} D_s^0 u_s^{n+1} = s^n. \end{cases} \tag{8}$$

4. Interpolate the fluid velocity field $\mathbf{u}^{n+1}$ to each immersed boundary point (compare Fig.1a) and compute their new positions $\mathbf{X}_{i,l}^{n+1}$ by moving them at the local fluid velocity using a forward Euler scheme:

$$\begin{aligned} \mathbf{u}^{n+1}(\mathbf{X}_{i,l}^n) &= \sum_{k,j} \mathbf{u}^{n+1}(\mathbf{x}_{k,j})\ \delta_h(\mathbf{x}_{k,j} - \mathbf{X}_{i,l}^n)\ h^2, \\ \mathbf{X}_{i,l}^{n+1} &= \mathbf{X}_{i,l}^n + \Delta t \cdot \mathbf{u}^{n+1}(\mathbf{X}_{i,l}^n). \end{aligned} \tag{9}$$

Interactions between the fluid grid and the material points are implemented using the discrete approximation $\delta_h(\mathbf{x}) = \delta_h(x_1)\cdot\delta_h(x_2)$ to the Dirac delta function. I follow [2] and use a bell-shaped symmetrical continuous function of bounded support, where

$$\delta_h(r) = \begin{cases} \frac{1}{4h}\left(1 + cos(\frac{\pi r}{2h})\right) & \text{if} \quad |r| < 2h, \\ 0 & \text{if} \quad |r| \geq 2h. \end{cases} \tag{10}$$

Fig.1 shows a schematic of fluid-structure interactions in the immersed boundary method. For the discrete delta function defined in the text, a local neighbourhood corresponding to one boundary point consists of 16 points in the fluid grid. Fig.1a shows a region that is used for spreading of the boundary force to the fluid

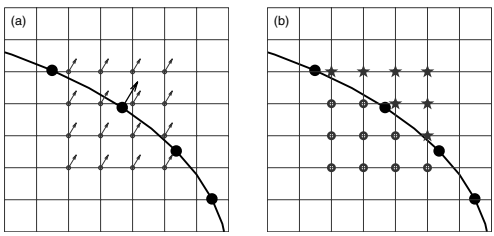

FIGURE 1. Schematic diagrams of fluid-structure interactions in the immersed boundary method. (a) a local neighbourhood for spreading the boundary force to the fluid grid, and for interpolating the boundary velocity from the neighbouring fluid velocity field; (b) a local neighbourhood—outside (*) or inside (o) the cell boundary (black curve)—for determining a source-sink distribution at the fluid grid.

grid, and for calculating the boundary velocity by interpolation from the fluid velocity field. Fig.1b shows the same 16-point diagram neighbourhood used for determining tha source-sink distribution on the fluid grid. Points located outside the cell boundary are denoted by stars (*), points located inside the cell are indicated by circles (o). The cell boundary is shown as a thick black line.

More details about the numerical implementation of this algorithm and the numerical solution of the Navier-Stokes equations can be found in [18] and [19].

2.3. Single cell growth—an illustrative example

A simple example illustrating how fluid sources and boundary forces can influence the growth of a single cell is presented in Fig.2. Each row shows a different stage of cell expansion. For illustrative purposes, the internal cell structure is defined by several off-diagonal Hookean springs (thin lines across the cell in Fig.2a) and cell mass is increased through a single cell source placed in the cell centre (stars in Fig.2a), whereas the balancing sinks are located at four corners of the computational domain (not shown). This single point source produces a radially symmetric flow during the whole simulation, but the final fluid velocity field is also influenced by the actions (stretching or contracting) of the internal springs. Since the springs resting lengths are slightly larger than the cell diagonal, the off-diagonal forces tend to stretch the cell until all springs reach their resting lengths and then tend to prevent all internal springs from further stretching. The top row of Fig.2 shows cell expansion in the first phase of its growth when the internal springs have not

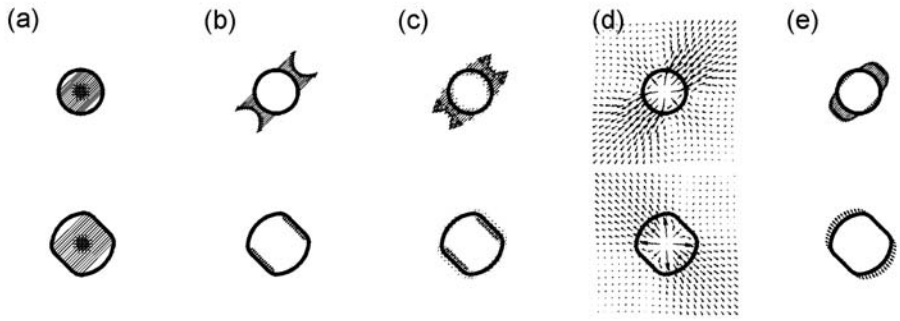

FIGURE 2. Interplay between the off-diagonal forces and a central point source in the growing cell (a). Top row: due to the stretching of the off-diagonal forces (b) that are transmitted to the fluid grid (c), the resulting fluid flow is directed along the force field (d) and the cell growth is off-diagonal (e); Bottom row: the off-diagonal forces are in the resting state (b) and prevent the off-diagonal expansion (c), thus, the fluid flow produced by the active fluid source can only move across the unforced boundaries of the cell (d) and the cell grows along its diagonal (e). See also a simulation MovIV.3.2 from the accompanying DVD.

yet reached their resting lengths. The boundary forces arising as a result of stretching the internal springs, Fig.2b, are spread to the fluid grid, Fig.2c (compare also Eq.(6) and Fig.1a). The radially symmetric fluid flow produced by a single point source is dominated by the stretching forces, Fig.2d, that in turn results in the off-diagonal cell growth, Fig.2e, since the cell boundary points move at the local fluid velocity. Pictures in the bottom row of Fig.2 show boundary forces, fluid force field, fluid velocity field and boundary velocity, respectively, in the second phase of cell growth, when the inner off-diagonal forces have already reached their resting lengths. In this case the boundary forces act to prevent cell deformation along the inner connections (Fig.2b–c), and the only direction for cell expansion due to the still active fluid point source is along the diagonal (Fig.2d–e). This example shows how both the boundary forces defining the cell structure and the point sources defining the cell processes can be used together to achieve differences in cell morphology.

2.4. Building the tissue

Every tissue in this model is built from individual cells that can interact with one another through elastic adhesive-repulsive forces and can exchange information with other cells and with their local microenvironment via a set of discrete cell membrane receptors located on the cell boundaries. Every cell consists of its own elastic plasma membrane modelled as a network of linear springs, and the fluid cytoplasm providing the cell mass. Fig.3 shows a small cluster of eukaryotic cells with boundary points (dots) connected by adjacent springs defining the cell shape (thin lines). Separate cells are linked through linear adherent connections (thick lines). A small part of the cell local microenvironment that is used to sense signals from the extracellular matrix is shown a grey region around the cell boundary. Two linear contractile connections defining the contractile ring in the dividing cells are represented by arrows. This approach allows for certain cell deformability

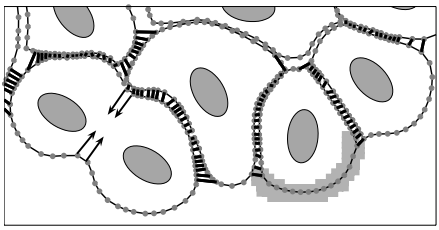

FIGURE 3. A small cluster of eukaryotic cells. The boundary points (dots) are connected by short linear springs (thin lines) enclosing the cell cytoplasm modelled as a viscous incompressible Newtonian fluid; cell nuclei (ellipses) are located inside the cells; the contractile ring in a dividing cell is shown as arrows; separate cells are connected by the adherent links (thick lines); a small portion of the cell local microenvironment is shown as a grey area.

and plasticity and enables the arrangement of separate cells into tissues of various geometries. Mathematical formulation of all cell components is presented below.

Cell structure: A simplified approach is taken here by assuming that the cell elasticity is provided by a mesh of elastic springs forming the cell boundary and that the cell's interior has no additional structure other than that provided by the fluid viscosity. A configuration Γ_i of the membrane of the i^{th} cell is represented by a discrete collection of points $\{\mathbf{X}_{i,l}(t)\}$ that form a closed curve. Here, l is a position along the cell boundary. These points are connected by short linear springs defining the response of the membrane to stretching. The adjacent links $\mathbf{F}_{adj(i)}$ determine the cell geometry and its area (thin lines connecting the boundary points in Fig.3) and satisfy Hooke's law with a constant resting length $\mathcal{L}_{adj}$ and a constant spring stiffness $\mathcal{F}_{adj}$. Thus the adjacent force $\mathbf{F}_{adj(i)}$ defined at a point $\mathbf{X}_{i,l}(t)$ and exerted by an adjacent boundary point $\mathbf{X}_{i,l+1}(t)$ has the following form:

$$\mathbf{F}_{adj(i)}(l,t) \;=\; \mathcal{F}_{adj}\;\frac{\|\mathbf{X}_{i,l+1}(t)-\mathbf{X}_{i,l}(t)\|-\mathcal{L}_{adj}}{\|\mathbf{X}_{i,l+1}(t)-\mathbf{X}_{i,l}(t)\|}\;\;(\mathbf{X}_{i,l+1}(t)-\mathbf{X}_{i,l}(t))\,. \tag{11}$$

Note that the cell boundary forms a closed curve, so the $l{+}1^{st}$ boundary point is taken modulo the total number of boundary points. Both constants $\mathcal{L}_{adj}$, $\mathcal{F}_{adj}$ are positive.

Cell microenvironment: Every cell can sense mechanical and chemical signals from its immediate neighbourhood, called *the cell microenvironment* (grey area in Fig.3). If $\mathbf{X}$ denotes a point on the cell boundary, then its microenvironment $\Theta^{\varepsilon}_{\mathbf{X}}$ is defined as a set of points lying within a distance ε, called *the radius of the microenvironment*,

$$\Theta^{\varepsilon}_{\mathbf{X}} = \{\mathbf{x} : \|\mathbf{x}-\mathbf{X}\| < \varepsilon\}\,. \tag{12}$$

Similarly, if $\Gamma = \{\mathbf{X}_k\}$ denotes the cell boundary (a collection of membrane receptors), then the cell microenvironment $\Theta^{\varepsilon}_{\Gamma}$ is defined as an ε-neighbourhood corresponding to the local area around the cell plasma membrane, that is,

$$\Theta^{\varepsilon}_{\Gamma} = \bigcup_{\mathbf{X}_k\in\Gamma} \{\mathbf{x} : \|\mathbf{x}-\mathbf{X}_k\| < \varepsilon\}\,. \tag{13}$$

Cell-to-cell adhesion: All cells can adhere directly to one another by forming specialised cell-to-cell junctions. In this model all points located on the cell boundary serve as potential sites of cell-to-cell adhesion (thick lines between separate cells in Fig.3) and their formation depends only on the distance between neighbouring cells. Adherens junctions are defined between any two distinct cells i^{th} and j^{th} provided that their boundary points $\mathbf{X}_{i,l}(t)$ and $\mathbf{X}_{j,k}(t)$ are within their local microenvironments of radius $\mathcal{L}^{max}_{adh}$, and they take the form of a short linear contractile-repulsive spring $\mathbf{F}_{adh(i,j)}$:

$$\mathbf{F}_{adh(i,j)}(l,t) \;=\; \mathcal{F}_{adh}\;\frac{\|\mathbf{X}_{j,k}(t)-\mathbf{X}_{i,l}(t)\|-\mathcal{L}_{adh}}{\|\mathbf{X}_{j,k}(t)-\mathbf{X}_{i,l}(t)\|}\;(\mathbf{X}_{j,k}(t)-\mathbf{X}_{j,l}(t))\,, \tag{14}$$

provided that $\|\mathbf{X}_{j,k}(t)-\mathbf{X}_{i,l}(t)\| \le \mathcal{L}^{max}_{adh}$ and is zero otherwise. Here, $\mathcal{F}_{adh}$ is a positive spring stiffness and $\mathcal{L}_{adh} < \mathcal{L}^{max}_{adh}$ is the spring resting length.

Additional tissue elements: It is relatively easy to add new structures in this model, such as some cell organelles; some parts of the cell cytoskeleton: actin bundles or microtubules; the basement membranes that separate cells from the extracellular matrix and provide mechanical support to the cells; extracellular fibers of collagen or laminin; stromal cells of different kinds: fibroblasts, macrophages, lymphocytes. All of them can be incorporated into the model as additional immersed bodies and their elastic or stiff properties can be achieved by appropriately chosen values of spring stiffness. Adding these new structures to the whole system is computationally inexpensive, since the immersed boundary method makes use of the fixed fluid grid, and no fluid grid rearrangement is needed when new immersed bodies are introduced. In particular, the basement membranes are usually modelled as stiff and immobile bodies. To keep them intact, each point $\mathbf{Z}_l(t)$ on basement membrane is connected to its initial location $\mathbf{Z'}_l(t)$ by a linear tethered spring $\mathbf{F}_{th}$ with a constant spring stiffness $\mathcal{F}_{th}$:

$$\mathbf{F}_{th}(l,t) \; = \mathcal{F}_{th} \; \left(\mathbf{Z}_l(t) - \mathbf{Z'}_l(t)\right). \tag{15}$$

2.5. Defining cellular processes

Several cellular processes, such as cell growth, division, apoptotic death or epithelial polarisation, are modelled with the immersed boundary framework. Some of them—cell growth or death—require the fluid to be transported across the cell boundary; other—cell division or epithelial polarisation—require introduction of additional forces that model cell deformability or cell-to-cell interactions. All processes are defined for a single cell, and all individual cells follow identically defined cell processes. However, since cells interact with one another, the initiation and progression of some cellular processes may be a result of the cells' collaborative or competitive behaviour. Fig.4 shows a small cluster containing cells of different

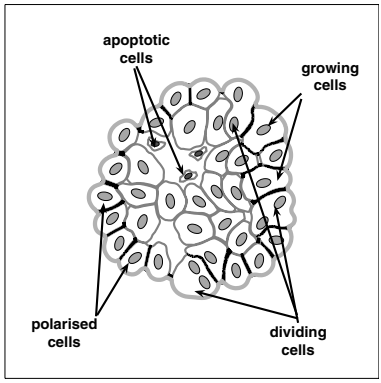

FIGURE 4. Morphological alterations in phenotypically different cells—enlargement of growing cells, formation of the contractile furrow between a pair of daughter nuclei in the dividing cells, shrinkage of the area in apoptotic cells, and development of distinct membrane domains in polarised cells.

phenotypes arising from several cell processes: characteristically enlarged growing cells, dividing cells containing two daughter nuclei and the contractile furrow, dying cells with characteristically diminished areas and irregular shapes, and polarised cells of cuboidal shapes and well developed connections with their neighbours. The mathematical formulation of all these processes is presented below.

Fluid transport through the cell membrane: All living cells maintain their internal homeostasis by instantly exchanging various ions and water molecules through the pores and channels located on the cell plasma membrane. Transport of the fluid across the membrane Γ_i of the i^{th} cell is modelled here in a simplified way by placing point sources and sinks of fluid in the cell local microenvironment $\Theta^{\varepsilon}_{\Gamma_i}$, on both sides of the cell boundary. In this way the same amount of fluid is created on one side of the cell boundary as it is lost on the other. When the cell acquires the fluid from the extracellular matrix, a finite set Ξ_i^+ of point sources $\mathbf{Y}_{i,k}^+$ is located inside the cell and a finite set Ξ_i^- of balancing point sinks $\mathbf{Y}_{i,m}^-$ is placed outside the cell, both within the local cell microenvironment $\Theta^{\varepsilon}_{\Gamma_i}$ (grey region in Fig.3). The fluid flux for each water channel is assumed to be identical and the overall fluid recruitment depends on the number of active channels. Therefore, we fix the strength of each fluid source $S_+(\mathbf{Y}_{i,k}^+, t)$ to be a step function that takes a constant positive value $\mathcal{S}_+^0$ over the time of cell process.

$$S_+(\mathbf{Y}_{i,k}^+, t) = \begin{cases} \mathcal{S}_+^0, & \text{during the cell process,} \\ 0, & \text{otherwise.} \end{cases} \tag{16}$$

The strength of each balancing fluid sink $S_-(\mathbf{Y}_{i,m}^-, t)$ is determined for each host cell separately to balance the total source distribution in that cell.

$$\sum_{k\in\Xi_i^+} S_+(\mathbf{Y}_{i,k}^+, t) \; + \; \sum_{m\in\Xi_i^-} S_-(\mathbf{Y}_{i,m}^-, t) = 0. \tag{17}$$

If K_i point sources are located inside the i^{th} cell and M_i point sinks are located outside the cell boundary, then the strength of each fluid sink is again a step function taking the same constant value $\mathcal{S}_-^0 = \sum_{k=1}^{K_i} S_+(\mathbf{Y}_{i,k}^+, t)/M_i$ during the time of cell process:

$$S_-(\mathbf{Y}_{i,m}^-, t) = \begin{cases} \mathcal{S}_-^0, & \text{during the time of cell process,} \\ 0, & \text{otherwise.} \end{cases} \tag{18}$$

To release the fluid from the cell to the extracellular space the sinks of fluid are placed inside the cell local microenvironment along its membrane, and the balancing fluid sources are located outside the cell local microenvironment along the same part of the cell membrane (grey area in Fig.3).

Cell growth: An increase of the fluid volume inside a growing cell is achieved by introducing couples of fluid source-sinks around the cell membrane that model the transport of fluid from the extracellular matrix into the cell. Fluid sources are located inside the host cell and fluid sinks are placed outside the cell boundary. This creates a flow that pushes on a boundary of the growing cell and increases its area. Those sources and sinks are deactivated when

the cell area is doubled. The corresponding outgrowth of the cell membrane is modelled by introducing additional boundary points. Fig.4 shows a few characteristically enlarged growing cells. Compare also the simulation movies.

Cell division: After the area of a growing cell is doubled the axis of cell division is selected and the contractile ring is formed by contractile forces acting on the opposite sides of the cell boundary. This results in the formation of a contractile furrow that causes division of the cell into two daughter cells of approximately equal areas, each with its own point nucleus. Fig.4 shows three cells having two daughter nuclei each, that are in the process of splitting. The contractile forces $\mathbf{F}_{div(i)}$ in the dividing i^{th} cell are defined between two opposite boundary points $\mathbf{X}_{i,l}(t)$ and $\mathbf{X}_{i,k}(t)$. They act on the cell boundaries until the opposite points reach a distance $\mathcal{L}_{div}^{min}$, and then the dividing cell is split into two daughter cells. Each contractile force satisfies Hooke's law with the constant resting length $\mathcal{L}_{div}$ and constant spring stiffness $\mathcal{F}_{div}$,

$$\mathbf{F}_{div(i)}(l,t) \;=\; \mathcal{F}_{div}\;\frac{\|\mathbf{X}_{i,k}(t)-\mathbf{X}_{i,l}(t)\|-\mathcal{L}_{div}}{\|\mathbf{X}_{i,k}(t)-\mathbf{X}_{i,l}(t)\|}\,(\mathbf{X}_{i,k}(t)-\mathbf{X}_{i,l}(t))\,, \tag{19}$$

provided that $\|\mathbf{X}_{i,l}(t)-\mathbf{X}_{i,k}(t)\| \geq \mathcal{L}_{div}^{min}$ and is zero otherwise. All constants $\mathcal{L}_{div} \leq \mathcal{L}_{div}^{min}$ and $\mathcal{F}_{div}$ are positive. The orientation of cell division may depend on the cell shape and its location within the tissue. In general, two new nuclei are located along the cell's longest axis and the contractile ring is placed between them orthogonally to the cell's longest axis in such a way to split the cell into two approximately equal parts. Different orientations of cell divisions may be observed in cells that have acquired some special properties. For example, a cell in the epithelial layer may divide along its apical-basal axis (compare cell division in the trophoblast bilayer in section 3.1 and in an outer layer of the acinus in section 3.3).

Cell apoptosis: An apoptotic cell undergoes characteristic changes in its morphology, including detachment from the neighbouring cells, shrinkage of the cell volume, collapse of the cytoskeleton and alternations in the cell surface resulting in a bubbling appearance [25]. This process is modelled by a gradual shrinkage of the cell area due to release of the fluid to the outside environment. This is achieved first by disassembling all cell adherens junctions and by placing the sink-source couples along the membrane of the whole cell with sinks located inside the cell and the balancing sources outside. The resulting fluid flow causes the cell boundary to collapse and the cell area is gradually reduced. Fig.4 shows three apoptotic cells with characteristically diminished areas—two of them are indicated by arrows.

Cell epithelial polarisation: A mature epithelial cell acquires three different types of membrane domain: an unbounded apical side facing free space inside the epithelium (lumen), a bounded side in direct contact with the extracellular matrix (a basal side), and two sides adhering to membranes of other cells (lateral sides), [26]. During the formation of an epithelial layer the cells must distinguish between these different domains in order to undergo the process of cell epithelial polarisation. This process can be modelled by inspecting the

local microenvironments of all cell boundary receptors to recognise if they are either in contact with the extracellular matrix that constitutes the basal membrane domain, or in contact with other cells that constitutes the lateral membrane domains, or free form any cell-to-cell contacts that constitutes an apical domain. Fig.4 shows several polarised cells of cubical shapes, with basal domains facing the external medium (thick grey lines), tight connections between neighbouring cells (thick black lines), and apical domains facing either the hollow lumen or other inner cells that have not yet started dying by apoptosis.

3. Applications

The previously described model of viscoelastic cells allows for the arrangement of individual cells into tissues of various topologies that can consequently be used to investigate how biomechanical properties of individual cells and communication between cells and their microenvironment influence the development and maintenance of the whole tissue. In this section three applications of the model of viscoelastic cells are presented. Each of them addresses a different morphological aspect of the developing tissues, such as the formation of tissue folds in the placental trophoblast bilayer (section 3.1), multicellular clonal growth due to competition for nutrients sensed from the extracellular space (section 3.2), and cell self-organisation into a stable acinar structure composed of one layer of polarised epithelial cells surrounding the hollow lumen (section 3.3). The corresponding simulations are included in the companion DVD.

3.1. Trophoblast tissue folding

The model of viscoelastic cells was first used to simulate the growth of a placental trophoblast bilayer during the second trimester of pregnancy and to investigate the formation of abnormal tissue folding, [18, 19]. The trophoblast tissue in the human placenta plays the role of a very selective and protective barrier between the blood stream of the foetus and that of the mother and is responsible for the proper exchange of nutrients and waste products between these two organisms. The structure of the trophoblast tissue during the second trimester of pregnancy consists of two distinct continuous layers—the inner cytotrophoblast (CT) is composed of tightly packed individual cells that are capable of growth and cellular division; the outer syncytiotrophoblast (ST) constitutes a syncytium, i.e. it is made from large masses of the cytoplasm with numerous nuclei that are, however, not capable of proliferation, and the ST layer can grow only through cell fusion from the CT layer. However, the ST layer continuously covers the CT layer, but its width may vary throughout the tissue. An example of an *in vivo* trophoblast bilayer is shown in Fig.5a.

A mathematical model of the trophoblast bilayer consists of one layer of identical, initially rectangular, cells representing the CT cells and a layer of multinucleated cytoplasm representing the syncytium, Fig.5b. The ST layer is treated

as a large single cell and similarly to all CT cells, it is modelled as an elastic immersed body in the way described in section 2.4. However, in addition to adjacent springs that define the boundaries of ST and all CT cells, a network of vertical springs is introduced in each layer to prevent all growing CT cells and the surrounding ST layer from large vertical deformations, Fig.5c. The stiffness of these internal springs is different in each layer—smaller for the ST layer, since its width may vary significantly throughout the tissue, and larger for CT cells, because they shapes are less flexible.

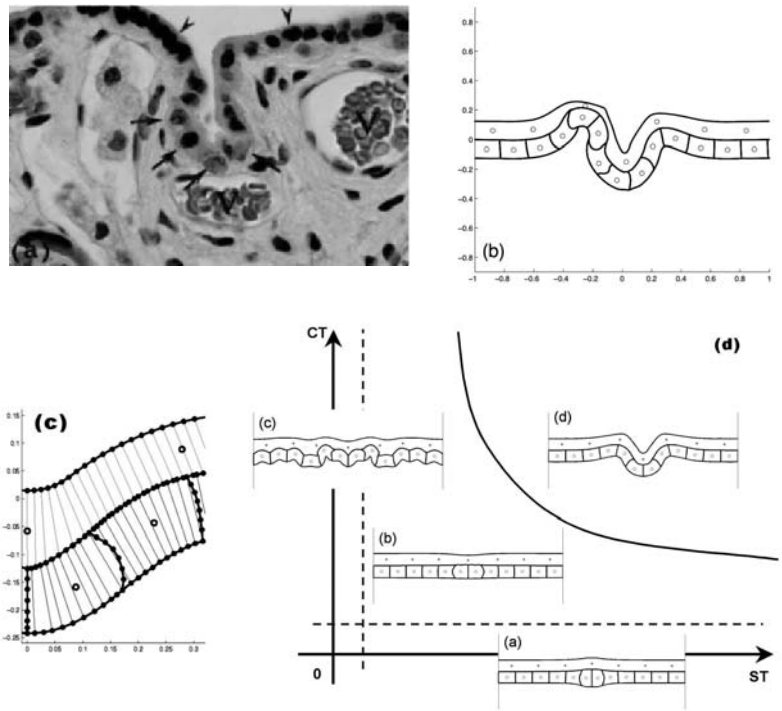

FIGURE 5. Model of the trophoblast bilayer. (a) An *in vivo* trophoblast invagination showing cytotrophoblast cells (arrows), syncytial layer (arrow heads) and a vessel containing fetal erythrocytes (V). (b) Corresponding computer simulated trophoblast invagination. (c) Structure of the CT cells and ST layer in the mathematical model. (d) Diagram showing different configurations of a trophoblast bilayer upon the proliferation of one CT cell—in each case the viscoelastic properties of cytotrophoblasts (CT) and of the syncytium (ST) are different. Figures (a) and (b) reprinted from [19], with permission from Elsevier. See also simulations MovIV.3.5a and MovIV.3.5b from the accompanying DVD.

This model is able to reproduce several different topologies of trophoblast tissues. One example is shown in Fig.5a and represents a deep inward tissue bending, called an invagination. It consists of several CT cells grouped near the base of tissue fold that are covered by a thin continuous layer of syncytium. The similar effect in an accompanying computer simulation, Fig.5b, has been obtained by multiple proliferation of CT cells occupying the same small area of the tissue (see a simulation movie). Other patterns of normal and abnormal development of the trophoblast bilayer are discussed in detail in [19].

The same model was also used to investigate, how changes in the stiffness of the CT cells and ST layer influence the overall tissue geometry in a very simple case when a single cell located in the middle of the CT layer has grown and divided in such a way to keep continuity of the CT layer. The results, graphically summarised in Fig. 5d, show that there are four different regimes of tissue deformation depending on the relative stiffness of each layer of the placental trophoblast. If the growing CT cells are too flexible they acquire significantly different shapes than the other CT cells (a). Moderate stiffness of both layers leads to a regular flat tissue without any visible bending (b). If CT cells remain stiff, but the surrounding ST layer become flexible the proliferating CT cells can squeeze into one irregular layer (c). However, by increasing stiffness of both layers, even a single cell division leads to a significant tissue folding (d). Compare a simulation movie showing all four cases. Therefore, the abnormal invaginations of the trophoblast bilayer may be a result of tumour-like over-proliferation of the CT cells, or increased condensation of differentiated masses of the cytoplasm, or a combination of both factors.

3.2. Multicellular clonal growth

The model of viscoelastic cells has been extended in [21] to include concentrations of external factors γ that control cellular processes and was used to investigate the emergence of tumour microregions containing inhomogeneous subpopulations of cells and steep gradients of oxygen. In this example the kinetics of γ is defined on the fluid grid $\mathbf{x} = (x_1, x_2)$, and includes a constant source of value γ_0 continuously applied at the domain boundaries, uniform diffusion of γ in the whole computational domain (with the diffusion coefficient $\mathcal{D}_\gamma$), and its degradation within the cell local microenvironment Θ_Γ that is defined using the Michealis-Menten formulation (with a maximum velocity $\mathcal{V}_\gamma$ and the Michaelis constant κ_γ). It is also assumed that initially the whole computational domain Ω is filled uniformly with an optimal concentration γ_0. Therefore, the rate of change of γ in the whole domain is defined by the reaction-diffusion equation with the following boundary and initial conditions (here χ is a set characteristic function):

$$\frac{\partial \gamma(\mathbf{x},t)}{\partial t} = \mathcal{D}_\gamma \, \Delta\gamma(\mathbf{x},t) - \mathcal{V}_\gamma \, \frac{\gamma(\mathbf{x},t)}{\kappa_\gamma + \gamma(\mathbf{x},t)} \cdot \chi(\Theta_\Gamma), \tag{20}$$

$$\gamma(\mathbf{x},t_0) = \gamma_0 \quad \text{for} \quad \mathbf{x} \in \Omega,$$

$$\gamma(\mathbf{x},t) = \gamma_0 \quad \text{for} \quad \mathbf{x} \in \partial\Omega \quad \text{and} \quad t \geq t_0.$$

In this model, the growth and survival of each cell depend on the concentration of γ in the cell vicinity. Therefore, the fluid source defined in Eq.(16) to model the growth of i^{th} cell depends here on the concentration of γ at the material points of

cell nuclei $\mathbf{Z}_i(t)$, i.e. $S_+ = S_+(\gamma(\mathbf{Z}_i, t), t)$, and the value of γ at the material point $\mathbf{Z}_i(t)$ is equal to its local concentration around that point:

$$\gamma(\mathbf{Z}_i, t) = \int_\Omega \gamma(\mathbf{x}, t)\ \delta(\mathbf{x} - \mathbf{Z}_i(t))\ d\mathbf{x}. \tag{21}$$

Two sets of snapshots from a representative simulation of a growing tumour cluster are shown in Fig.6 (for colour figures see the end of the book and the DVD). This simulation starts with a cluster of seven cells placed at the centre of the domain that has been filled with a uniform concentration of γ_0. Initially, all cells sense high concentrations of γ, and continuously proliferate which leads to the formation of a small round aggregate of growing cells, (top row of Fig.6). However, degradation of γ by tumour cells results in the formation of its gradient (right column in Fig.6) that causes cells starvation and their necrotic death in the areas of γ depletion. This in turn leads to the emergence of three distinct cell subpopulations (middle column in Fig.6): a centrally located necrotic core (blue cells), an outer rim of proliferating cells (red), and a zone of quiescent cells (grey) in between them. Therefore, the fate of each cell depends entirely on the evolution of γ in the cell microenvironment, and the evolution of γ depends on the location of boundaries of all tumour cells. Further tumour growth leads to a

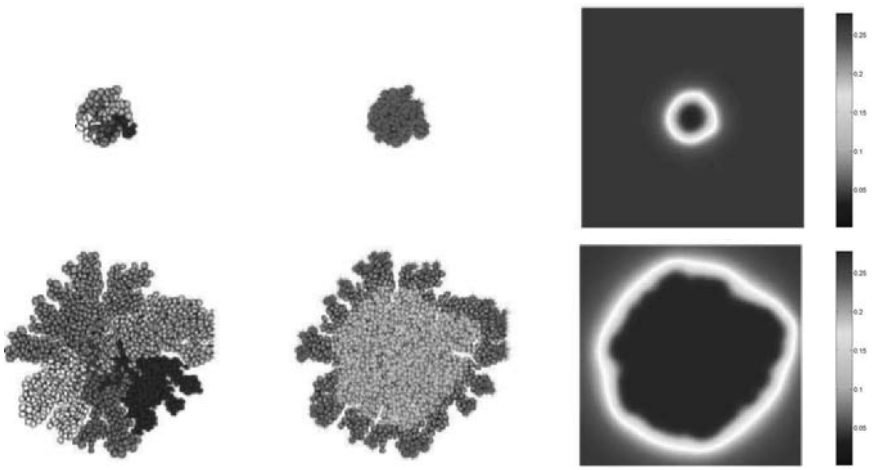

FIGURE 6. Clonal growth of tumour cells due to cell competition for nutrients. Left: colour-coded clones of cells arising from common predecessors. Middle: three different cell subpopulations: an inner core of necrotic cells (blue), an outer rim of proliferating cells (red) and a zone of quiescent cells between them (grey). Right: concentration profile of oxygen. Top row: round and regular tumour cluster at an early stage of tumour growth. Bottom row: fingering of tumour mass due to competition for nutrients between individual tumour cells. See also a colour version at the end of the book, and a simulation MovIV.3.6 from the accompanying DVD.

strong competition for γ and to the formation of finger-like structures growing towards the areas of higher concentrations of oxygen (bottom row in Fig.6). The left column in Fig.6 shows seven colour-coded clones of cells arising from common predecessors.

More details about this particular model can be found in [21]. Examples showing tumour growth in different environments are presented in [20] and [22].

3.3. Formation of hollow epithelial acini

The epithelial acini are experimental culture structures that resemble the architecture of normal breast lobules and enable *in vitro* investigations of genotypic and molecular abnormalities associated with epithelial cancers, [27, 28]. The well developed epithelial acini are composed of one layer of tightly packed epithelial cells surrounding the hollow lumen. The model of viscoelastic cells has been recently used to simulate self-arrangement of individual eukaryotic cells into a stable hollow acinar structure. This simulation approach allows one to gain more information about the consecutive stages of acini development and to provide an insight into the transformations of eukaryotic cells that are necessary for their successful arrangement into an epithelium, [23, 24].

In this model a single eukaryotic cell (Fig.7a) undergoes several consecutive divisions and gives rise to a small cluster of randomly oriented cells containing two different populations: the *inner* cells entirely surrounded by other cells; and the

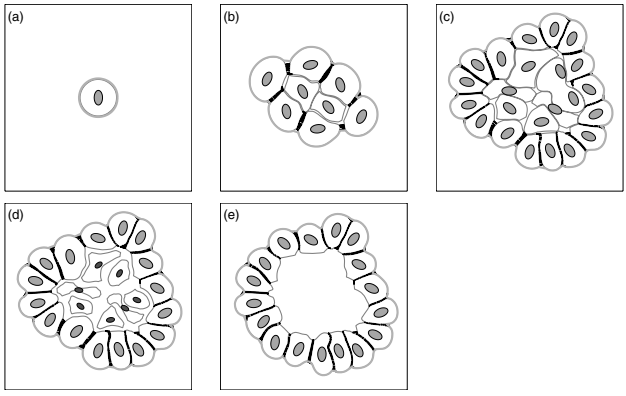

FIGURE 7. Development of a hollow acinar structure. Starting with a single eukaryotic cell (a), a small cluster of randomly oriented cells is produced (b), upon cell-to-cell interactions all cells in the outer layer develop an apical-basal epithelial polarisation (c), that triggers the inner cells to start apoptotic death (d), that in turn leads to a hollow acinar structure (e). See also a colour version at the end of the book and a simulation movie MovIV.3.7 from the accompanying DVD, where intercellular elements are stained as follows: cell nuclei (blue), apoptotic cells (red), cell membranes (green), cell basal domains (red), cell-to-cell tight junctions (yellow).

outer cells partially facing the external medium (Fig.7b). Further cell proliferation leads to the expansion of the whole cluster and induces close interactions between neighbouring outer cells that results in the development of tight adherent junctions between them. This is followed by further differentiation of outer cells and results in their apical-basal orientation and self-arrangement into one layer of polarised epithelial cells of regular cubical shapes (Fig.7c). The inner cells are then triggered by polarised cells to enter the process of cell apoptotic death, that in turn results in the creation of the inner lumen (Fig.7d). Consequently, proliferation of polarised cells is suppressed and the final structure stabilises in the form of a hollow epithelial acinus (Fig.7e).

Note that the initial stage of acinar development is very similar to the initial growth of a multicellular cluster of tumour cells presented in section 3.2. However, in the case of tumour growth, individual cells compete for nutrients that leads finally to their expansion and results in tissue fingering. The formation of acinar structure demands immense cell-to-cell interactions and close collaboration between outer cells in forming tight adhesive connections that results in self-arrangement into one epithelial layer. Moreover, the processes of cell proliferation, polarisation and apoptosis need to be well co-ordinated in order to maintain the hollow acinar structure in a stable manner. Otherwise, the cell overgrowth may lead to intraductal carcinomas. Preliminary results of our research show that there is a wide spectrum of biomechanical parameters relating different cell processes (such as cell proliferation and epithelial polarisation; or cell proliferation and apoptosis) that allow for the development of normal acinar structure, and that the degenerate cases corresponding to mutant acini require significant alternations in the typical pathway of acinar growth observed in biological experiments.

4. Conclusions and model extensions

A two-dimensional computational model of a single deformable viscoelastic cell has been presented here and applied in three different scenarios. It has been shown that individual viscoelastic cells can be arranged into tissues of various topologies—such as the trophoblast bilayer, a freely growing cluster of tumour cells showing a finger-like morphology, or a cluster of cells that self-organise into a stable acinar structure composed of one layer of epithelial polarised cells surrounding the hollow lumen. This allows for a biologically realistic representation of the whole tissue composed of individual cells inhomogeneous in their shape, function and behaviour, but acting together as one complex organism. Several cellular processes, such as cell growth, division, apoptotic and necrotic death, epithelial polarisation and cell-to-cell adhesion have also been incorporated into this biomechanical model. This approach allows one to focus on the properties of individual cells and communication between cells and their microenvironment and to investigate how the collaborative or competitive behaviour of individual cells influence the development and maintenance of the whole tissue.

Three applications presented in this chapter show that the model can be applied in a variety of developmental problems, including growth and formation of different multicellular tissues and organisms, in various geometrical configurations and incorporating several cellular processes. Many problems in embryonic development can be addressed with this model, including asymmetric cell division, emerging cell patterns and cell sorting. The model of trophoblast folding is geometrically similar to crypts of intestines and can be adjusted to investigate cell renewal, differentiation and migration along the crypts as well as certain diseases of cryptal epithelium. Another possible extension of this approach is to model a stratified epithelium in the skin that will involve different types of cell, with different geometry and distinct physicochemical properties and functions. The cell turnover and renewal by stem cells as well as wound healing may also be a subject of further application of this model. Two specific model extensions are now discussed briefly: a directional cell migration and a 3-dimensional implementation of cell proliferation, apoptotis and epithelial polarisation.

4.1. Directional cell migration

It was shown in section 3.2 that cells can inspect their local microenvironment and sense concentrations of external factors in their vicinity. Here I will show how this information can be used to model cell migration in response to such extracellular stimuli. This approach can be used to model cell chemotaxis (movement towards the highest concentration of diffusive factors) or haptotaxis (movement up a gradient of cellular adhesion sites or substrate-bound chemoattractants). All eukaryotic cells are capable of "directional sensing", i.e. they can determine the direction and the relative steepness of the gradient of an external stimulus in its local microenvironment. The receptors responsible for directional sensing are distributed uniformly around the cell perimeter, however, when the cell is exposed to the stimulus for a longer time, it may become less sensitive at the sites of lower concentration of the chemoattractant, [29].

Cell directional movement in response to gradients of chemoattractants distributed in the extracellular matrix can be modelled by introducing additional linear drag motility forces defined at all points on the cell boundary that play the role of chemotactic receptors. If $\mathbf{X}_k$ denotes a cell membrane receptor and $\mathbf{x}_*$ is a point in that receptor local microenvironment $\Theta_{\mathbf{X}_k}$, at which the concentration of stimulus $\gamma(\mathbf{x}_*, t)$ is the highest, then the drag motility force $\mathbf{F}_{mov}(\mathbf{X}_k)$ exerted on $\mathbf{X}_k$ by $\mathbf{x}_*$ has the following form:

$$\mathbf{F}_{mov}(\mathbf{X}_k) \;=\; \mathcal{F}_{mov}(\gamma(\mathbf{X}_k, t)) \;\; \|\mathbf{X}_k - \mathbf{x}_*\| \;\; \frac{\nabla\gamma(\mathbf{x}_*, t)}{\|\nabla\gamma(\mathbf{x}_*, t)\|} \tag{22}$$

where $\mathbf{x}_*$ is such that $\gamma(\mathbf{x}_*) = \max\{\gamma(\mathbf{x}) : \mathbf{x} \in \Theta_{\mathbf{X}_k}\}$, and the spring stiffness $\mathcal{F}_{mov}$ may depend on the stimulus concentration sensed by the receptor to allow for the situation when the cell membrane receptor does not respond if the concentration of γ falls below a certain threshold.

Fig.8 shows a haptotactic gradient of some stimulus and a single cell migrating through the extracellular space due to the drag motility forces defined at its

boundary (compare also the colour version and the simulation movie). The highest concentration of the stimulus is in three circular regions at the top of the domain, the gradient decreases toward the bottom and its irregular shape has been obtain by locating three linear traps inside the domain. Fig.8a shows a small region around the moving cell with drag motility forces defined along the whole cell perimeter and pointing up the local gradient sensed by each cell receptor separately. As a result, all cell boundary points are moved separately that gives the effect of cell crawling. Fig.8b shows a trace of a cell migrating through the extracellular space starting from the bottom of the domain toward the highest concentration of the stimulus at the top of the domain. The cell contour is shown in equally spaced time intervals that allows for a comparison of changes in cell shape and in cell speed along its path. The initially circular cell changes its shape due to the individual response of each cell receptor to the local gradient of the stimulus. Note that the cell acquires an elliptical shape closer to the source of the stimulus, since the boundary points at the cell front move faster here that these located at the rear. Notice also, that the cell moves with different speeds when approaching and passing the oblique trap due to differences in the steepness of the chemoattractant gradient sensed by the cell.

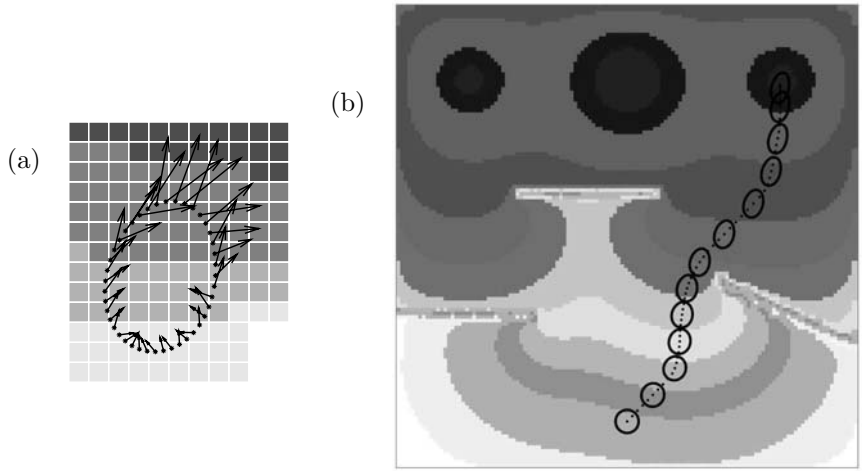

FIGURE 8. Cell chemotactic/haptotactic motility. (a) Drag motility forces defined on the cell boundary and directed toward the increased concentration of chemo/hapto-attractant. (b) Trace of a single cell migrating up the gradient of chemo/hapto-attractanct distributed in the extracellular matrix. See also to a colour version at the end of the book and a simulation movie MovIV.3.8 from the accompanying DVD.

4.2. 3D model extension

The model of a viscoelastic cell and cellular processes can be extended to three-dimensional space in a straightforward way. All equations defining the immersed boundary method, Eq.(1)–(5), can be carried over to 3-dimensional (3D) space without changes. Numerical implementation requires a 3D version of the discrete Dirac delta function that is, however, analogous to the function in Eq.(10). A more complex network of elastic springs may be needed to define the cell structure, but all additional boundary points and forces can be incorporated into the 3D model analogously as presented here. The algorithms defining cell processes can also be carried into 3D space with only small changes. Three examples presented in Fig.9a–c show 3-dimensional cells undergoing three different processes that can be modelled as follows. Cell apoptotic death, as presented in Fig.9a, has been achieved by placing several fluid sinks inside the normal cell and the balancing fluid sources outside the cell, that results in a decrease of cell volume and in a collapse of cell boundaries. The star-like shape of the apoptotic cell is a consequence of placing the fluid sinks symmetrically inside the dying cell, however, differently chosen locations of the inner sinks will result in a more irregular cell shape. Cell growth is achieved similarly as in the 2D case, that is by defining couples of fluid sources and sinks located inside and outside the cell, respectively, to increase the amount of fluid inside the cell and expand its volume. The contractile ring may be introduced as a collection of contractile springs forming a closed curve running around the cell perimeter that contracts splitting the cell into two parts, Fig.9b. Individual cells can be arranged into an epithelial layer as shown in Fig.9c. Here, an epithelial configuration was computed for a square of 3 by 3 cells, but one of them was deleted from the picture to show flat areas of cell-to-cell adhesion defined between boundary points of separate epithelial cells.

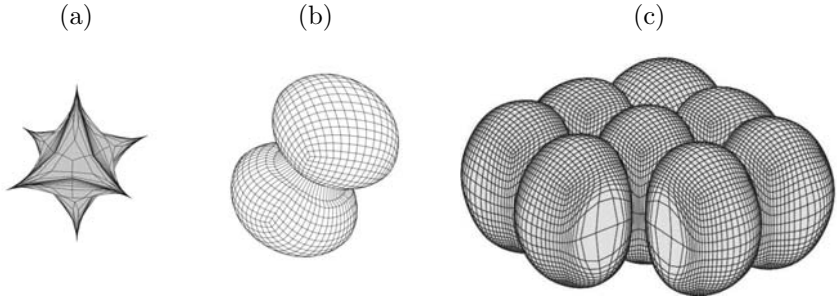

FIGURE 9. A schematic representation of three-dimensional cells undergoing three different cell processes: (a) shrinkage of cell volume and collapse of cell shape during the process of cell apoptotic death; (b) expansion of the cell volume and formation of the contractile ring splitting the cell into two daughters during the process of cell proliferation; (c) development of flat lateral sides between neighbouring polarised cells within an epithelial layer.

Acknowledgement

The work on the computational model of the formation of abnormal folding of the placental trophoblast was conducted in collaboration with Lisa Fauci and Harvey Kliman, and was supported by grant DMS-9805492. The work on the computational model of clonal tumour growth was supported by the Mathematical Biosciences Institute under agreement no. 0112050 with the U.S. National Science Foundation. The work on the computational model of the development of epithelial acini was conducted in collaboration with Sandy Anderson and Vito Quaranta's laboratory group and was supported by the U.S. National Cancer Institute Integrative Cancer Biology Program (U54 CA 113007). I also would like to thank Mark Chaplain, Robert Dillon, Avner Friedman and Howard Levine for helpful discussions.

References

[1] C. S. Peskin, Flow patterns around heart valves: A numerical method, *J. Comput. Phys.*, **10** 252–271 (1972).

[2] C. S. Peskin, Numerical analysis of blood flow in the heart, *J. Comput. Phys.*, **25** 220–252 (1977).

[3] C. S. Peskin, The immersed boundary method, *Acta Numerica*, **11** 479–517 (2002).

[4] M. M. Hopkins and L. J. Fauci, A computational model of the collective fluid dynamics of motile micro-organisms, *J. Fluid Mech.*, **455** 148–174 (2002).

[5] R. Dillon, L. J. Fauci and A. Gaver III, A microscale model of bacterial swimming, chemotaxis and substrate transport, *J. theor. Biol.*, **177** 325–340 (1995).

[6] R. Dillon, L. J. Fauci, A. Fogelson and A. Gaver III, Modeling biofilm processes using the immersed boundary method, *J. Comp. Phys.*, **129** 57–73 (1996).

[7] R. Dillon and L. J. Fauci, A Microscale model of bacterial and biofilm dynamics in porous media, *Biotechnology and Bioengineering*, **68** 536–547 (2000).

[8] L. J. Fauci and A.L. Fogelson, Truncated Newton methods and the modeling of complex immersed elastic structures, *Comm. Pure and Appl. Math*, **46** 787–818 (1993).

[9] L. J. Fauci and A. McDonald, Sperm motility in the presence of boundaries, *Bulletin of Mathematical Biology*, **57** 679–699 (1995).

[10] R. H. Dillon, L. J. Fauci and Ch. Omoto, Mathematical modeling of axoneme mechanics and fluid dynamics in ciliary and sperm motility, *Dynamics of Continuous, Discrete and Impulsive Systems, Series A*, **10** 745–757 (2003).

[11] A. L. Fogelson, A mathematical model and numerical method for studying platelet adhesion and aggregation during blood clotting, *J. Comput. Phys.*, **56** 111–134 (1984).

[12] A. L. Fogelson, A. Kuharsky and H. Yu, Computational modeling of blood clotting: coagulation and three-dimensional platelet aggregation, in *Polymer and Cell Dynamics: Multiscale Modeling and Numerical Simulations*, Birkhäuser-Verlag, Basel (2003)

[13] D. C. Bottino and L. J. Fauci, A computational model of ameboid deformation and locomotion, *Eur Biophys J.*, **27** 532–539 (1998).

[14] D. C. Bottino, Modeling viscoelastic networks and cell deformation in the context of the immersed boundary method, *J. Comp. Phys.*, **147** 86–113 (1998).

[15] N. A. N'Dri, W. Shyy and R. Tran-Son-Tay, Computational modeling of cell adhesion and movement using a continuum-kinetics approach, *Biophys. J.*, **85** 2273–2286 (2003).

[16] S. Jadhav, Ch. D. Eggleton and K. Konstantopoulos, A 3-D computational modeling predicts that cell deformation affects selectin-mediated leukocyte rolling, *Biophys. J.*, **88** 96–104 (2005).

[17] R. Dillon and H. G. Othmer, A mathematical model for outgrowth and spatial pattering of the vertebrate limb bud, *J. Theor. Biol.*, **197** 295–330 (1999).

[18] K. A. Rejniak, A computational model of the mechanics of growth of a trophoblast tissue, PhD thesis, Tulane University, (2002).

[19] K. A. Rejniak, H. J. Kliman and L. J. Fauci, A computational model of the mechanics of growth of the villous trophoblast bilayer, *Bull. Math. Biol.*, **66** 199–232 (2004).

[20] K. A. Rejniak, An immersed boundary framework for modelling the growth of individual cells: an application to the early tumour development, *Journal of Theoretical Biology*, in print, DOI: 10.1016/j. jtbi. 2007.02.019

[21] K. A. Rejniak, A single-cell approach in modeling the dynamics of tumor microregions, *Mathematical Biosciences and Engineering*, **2** 643–655 (2005).

[22] K. A. Rejniak and R. H. Dillon, A single cell based model of the ductal tumour microarchitecture, *Computational and Mathematical Methods in Medicine*, in print, DOI: 10.1080/17486700701303143

[23] K. A.Rejniak and A. R. A. Anderson, A computational study of the development of epithelial acini. I: Sufficient conditions for the formation of a hollow structure, *Bulletin of Mathematical Biology*, *submitted*.

[24] K. A. Rejniak and A. R. A. Anderson, A computational study of the development of epithelial acini. II: Necessary conditions for structure and lumen stanility, *Bulletin of Mathematical Biology*, *submitted*.

[25] M. J. Ardens and A. H. Wyllie, Apoptosis: Mechanisms and roles in pathology, *International Review of Experimental Pathology*, **32** 223–254 (1991).

[26] W. J. Nelson, Adaptation of core mechanisms to generate cell polarity, *Nature*, **422** 766–774 (2003).

[27] J. Debnath and J. S. Brugge Modelling glandular epithelial cancers in three-dimensional cultures, *Nature Reviews Cancer*, **5** 675–688 (2005)

[28] J. Debnath, K. R. Mills, N. L. Collins, M. J. Reginato, S. K. Muthuswamy and J. S. Brugge, The role of apoptosis in creating and maintaining luminal space within normal and oncogene-expressing mammary acini, *Cell* **111** 29–40 (2002).

[29] C. A. Parent and P. N. Devreotes, A cell's sense of direction, *Science* **284** 765–770 (1999).

Katarzyna A. Rejniak
Division of Mathematics, University of Dundee
Dundee DD1 4HN, Scotland, UK
e-mail: `rejniak@maths.dundee.ac.uk`

Addresses

Mark Alber
email: malber@nd.edu
Department of Mathematics
Center of Study of Biocomplexity
University of Notre Dame
Notre Dame, IN 46637
USA

Alexander R. A. Anderson
email: anderson@maths.dundee.ac.uk
Division of Mathematics
University of Dundee
Dundee DD1 4HN
Scotland, UK

Ariel Balter
email: abalter@indiana.edu
Biocomplexity Institute
and Department of Physics
Indiana University
Swain Hall West 117
727 East Third Street
Bloomington, Indiana 47405-7105
USA

Mark A.J. Chaplain
email: chaplain@maths.dundee.ac.uk
Division of Mathematics
University of Dundee
Dundee DD1 4HN
Scotland, UK

Nan Chen
email: nchen1@nd.edu
Department of Mathematics
Center of Study of Biocomplexity
University of Notre Dame
Notre Dame, IN 46637
USA

John C. Dallon
email: dallon@math.byu.edu
Department of Mathematics
Brigham Young University
312 TMCB
Provo, UT 84602-6539
USA

Andreas Deutsch
email: andreas.deutsch@tu-dresden.de
Center for Information Services
and High Performance Computing
Dresden University of Technology
Zellescher Weg 12
D-01062 Dresden
Germany

Dirk Drasdo
email: dirk.drasdo@inria.fr
French National Institute for Research
in Computer Science and Control
(INRIA)
Rocquencourt, B.P. 105
78153 Le Chesnay Cedex
France

Aaron L. Fogelson
email: fogelson@math.utah.edu
Departments of Mathematics and Bioengineering
University of Utah
155 South 1400 East, 233 JWB
Salt Lake City, Utah 84112
USA

James A. Glazier
email: glazier@indiana.edu
Biocomplexity Institute
and Department of Physics
Indiana University
Swain Hall West 159
727 East Third Street
Bloomington, Indiana 47405-7105
USA

Tilmann Glimm
email: glimmt@wwu.edu
Department of Mathematics
Western Washington University
Bellingham, Washington 98225
USA

Verônica A. Grieneisen
email: V.Grieneisen@uu.nl
Theoretical Biology and Bioinformatics
Utrecht University
Padualaan 8, 3584 CH Utrecht
Netherlands

Paulien Hogeweg
email: P.Hogeweg@uu.nl
Theoretical Biology and Bioinformatics
Utrecht University
Padualaan 8, 3584 CH Utrecht
Netherlands

Pavel Lushnikov
email: plushnik@math.unm.edu
Department of Mathematics and Statistics
University of New Mexico
Albuquerque, NM 87131
USA

Athanasius F. M. Marée
email: A.F.M.Maree@uu.nl
Theoretical Biology and Bioinformatics
Utrecht University
Padualaan 8, 3584 CH Utrecht
Netherlands

Roeland M. H. Merks
email: roeland.merks@psb.ugent.be
or post@roelandmerks.nl
Department of Plant Systems Biology
VIB Technologiepark 927
B-9052 Ghent,
Belgium
and Department of Molecular Genetics,
Ghent University,
Ghent, Belgium

Timothy J. Newman
email: timothy.newman@asu.edu
Department of Physics
Arizona State University
P.O. Box 871504
Tempe, AZ 85287
USA

Eirikur Palsson
email: epalsson@sfu.ca
Department of Biology
Simon Fraser University
8888 University Dr
Burnaby, BC V5A 1S6
Canada

Nikodem J. Popławski
email: nipoplaw@indiana.edu
Biocomplexity Institute
and Department of Physics
Indiana University
Swain Hall West 117
727 East Third Street
Bloomington, Indiana 47405-7105
USA

Katarzyna A. Rejniak
email: rejniak@maths.dundee.ac.uk
Division of Mathematics
University of Dundee
Dundee DD1 4HN
Scotland, UK

Nicholas J. Savill
email: nick.savill@ed.ac.uk
Centre for Infectious Disease
University of Edinburgh
Ashworth Laboratories
Kings Buildings, West Mains Road
Edinburgh, EH9 3JF
Scotland

Maciej Swat
email: mswat@indiana.edu
Biocomplexity Institute
and Department of Physics
Indiana University,
Swain Hall West 117
727 East Third Street
Bloomington, Indiana 47405-7105
USA

Index

Chapter I.1 A Hybrid Multiscale Model of Tumour Invasion: Evolution and the Microenvironment *Alexander R.A. Anderson*

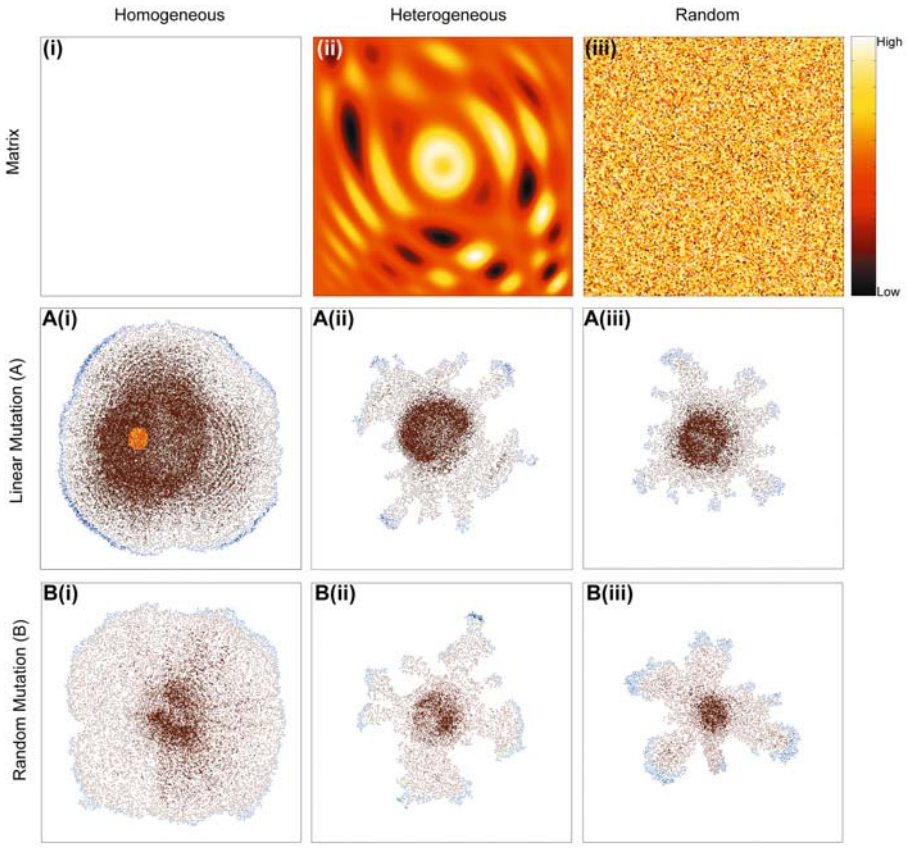

FIGURE 3. HDC tumour simulation results (see text for more details).

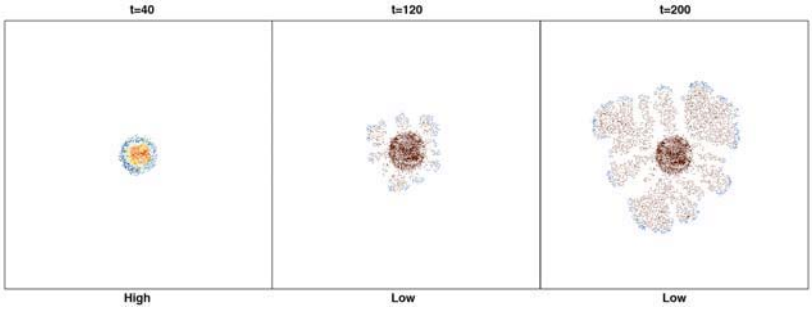

FIGURE 6. HDC tumour simulation results in a homogeneous MM (see text for more details).

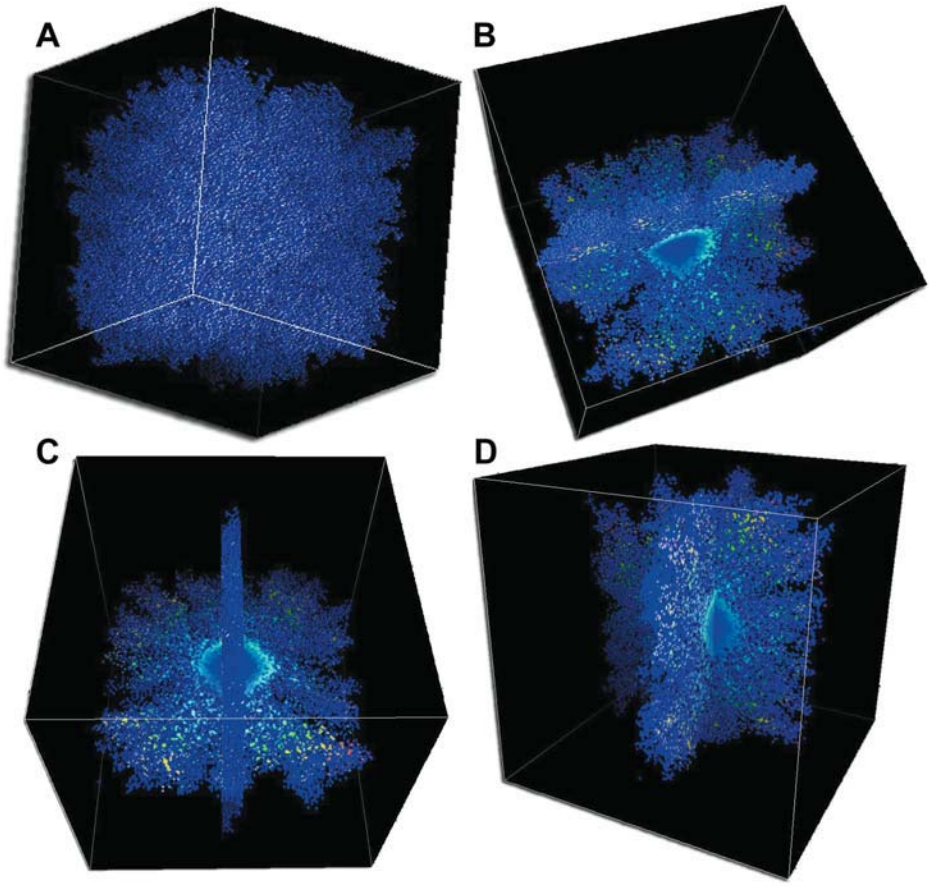

FIGURE 8. Three dimensional HDC tumour simulation results (see text for more details).

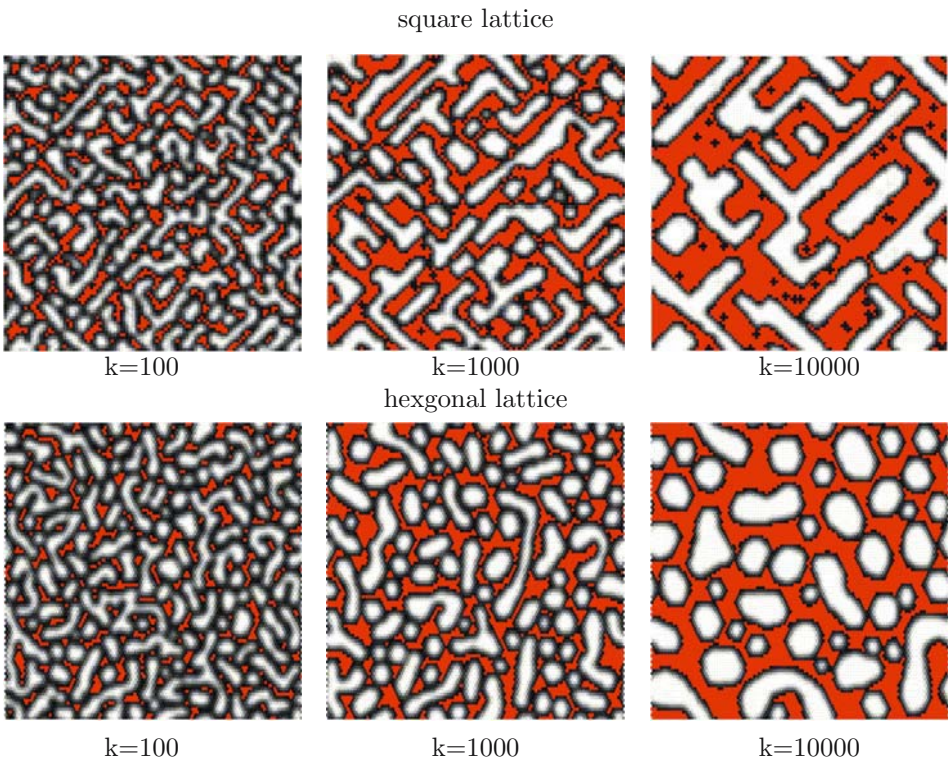

FIGURE 5. Adhesive pattern formation in the LGCA model on different lattices. Different gray levels represent cell densities (dark: low cell density), red marks empty nodes; parameters: parameters: $\alpha = 0.8$ ($> \alpha_c$), $= 0.4$, $\bar{\rho} = 0.4$, $L = 100$.

Chapter II.2 The Cellular Potts Model and Biophysical Properties of Cells, Tissues and Morphogenesis
Athanasius F.M. Marée, Verônica A. Grieneisen, Paulien Hogeweg

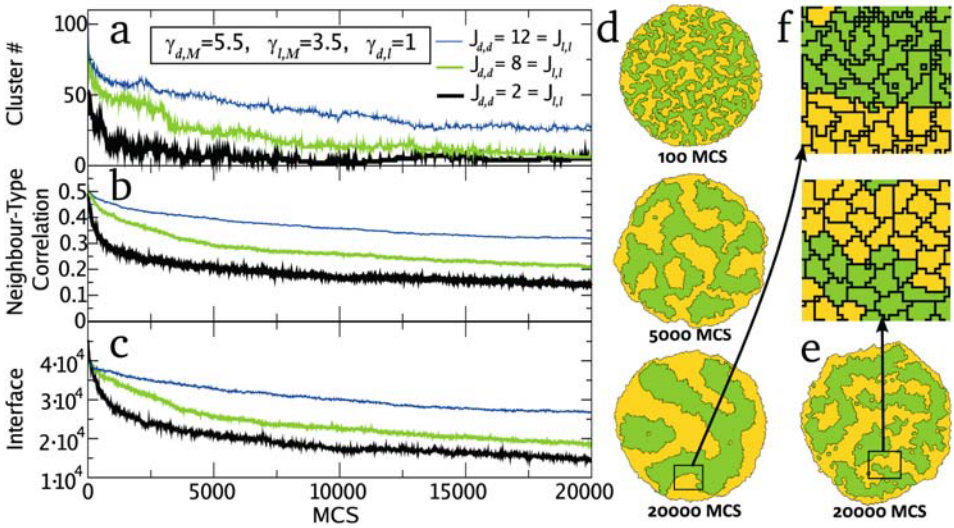

FIGURE 3. Cell sorting dynamics (see text for more details).

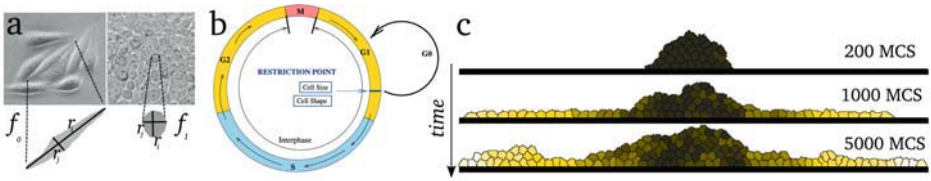

FIGURE 4. Cell deformation as cell regulation (see text for more details).

Chapter II.2 The Cellular Potts Model and Biophysical Properties of Cells, Tissues and Morphogenesis
Athanasius F.M. Marée, Verônica A. Grieneisen, Paulien Hogeweg

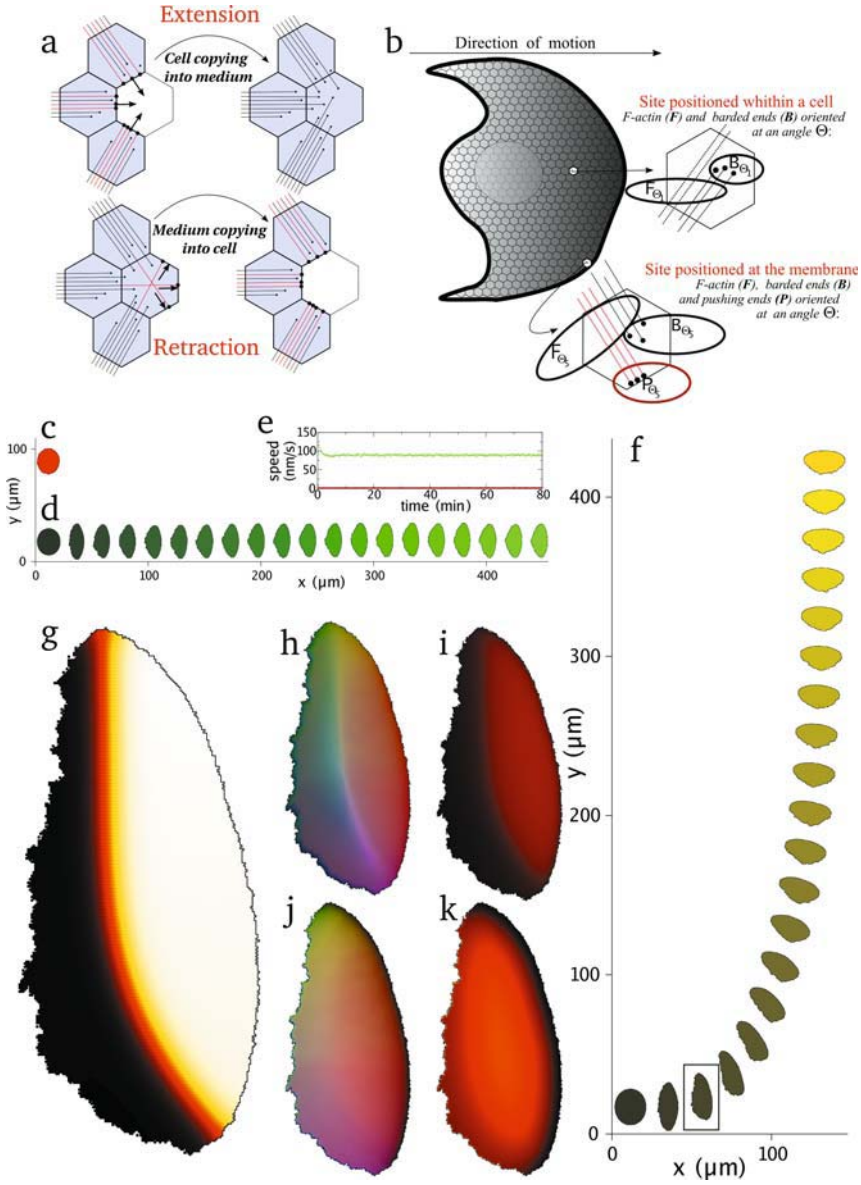

FIGURE 8. Cytoskeleton and the keratocyte (see text for more details).

Chapter II.2 The Cellular Potts Model and Biophysical Properties of Cells, Tissues and Morphogenesis
Athanasius F.M. Marée, Verônica A. Grieneisen, Paulien Hogeweg

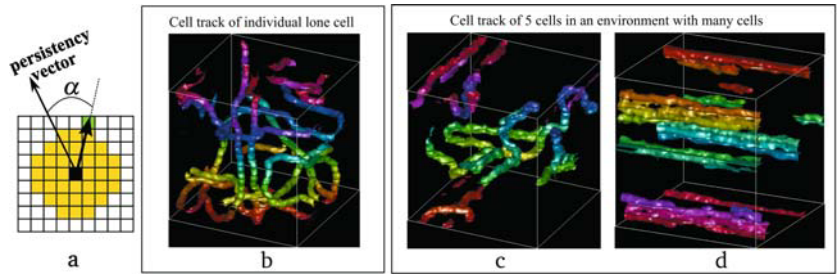

FIGURE 9. From persistency to coherence. (see text for more details).

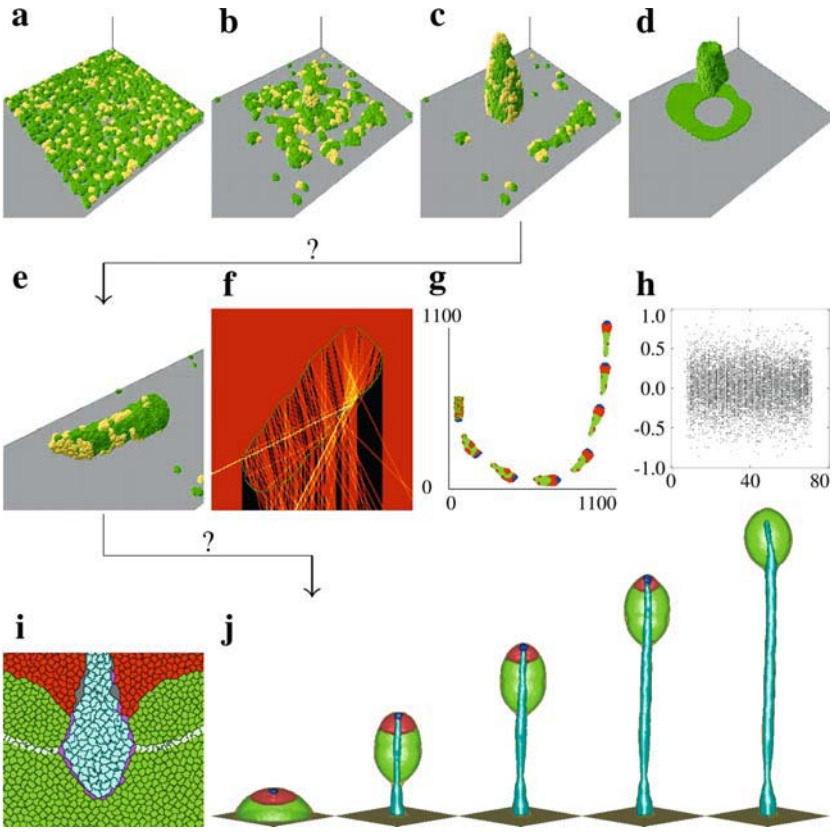

FIGURE 11. Modelling an organism (see text for more details).

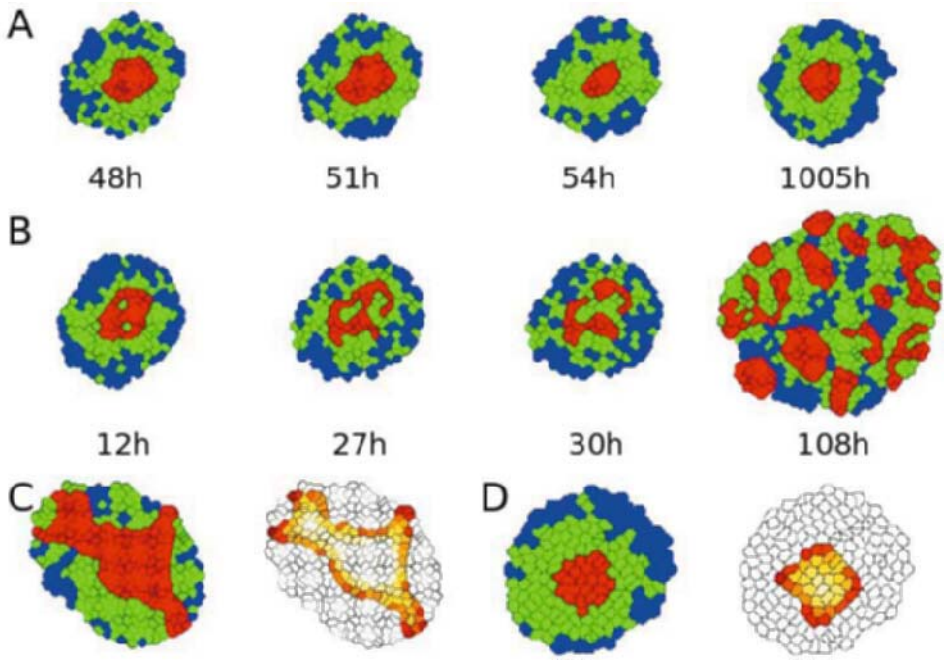

FIGURE 1. Stem cell clusters with different signalling and stability (see text for more details). Reprinted from [36], with permission from Elsevier.

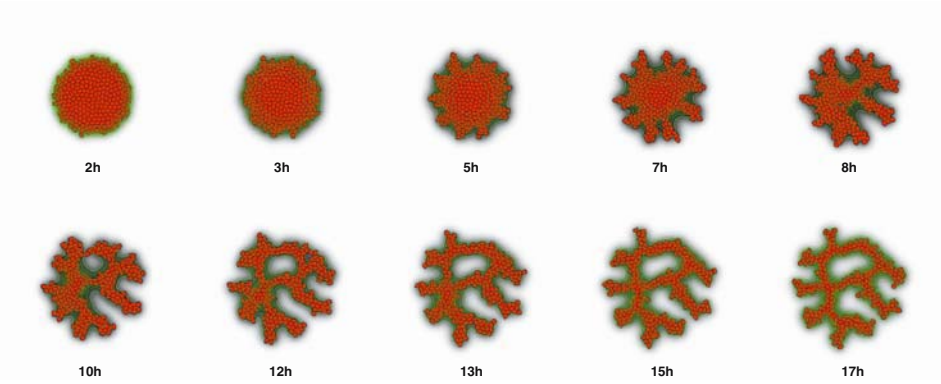

FIGURE 4. Sprouting instability (see text for more details). Reprinted from [25], with permission from IOP Publishing Ltd.

Chapter III.1 Center-based Single-cell Models: An Approach to Multi-cellular Organization Based on a Conceptual Analogy to Colloidal Particles, *Dirk Drasdo*

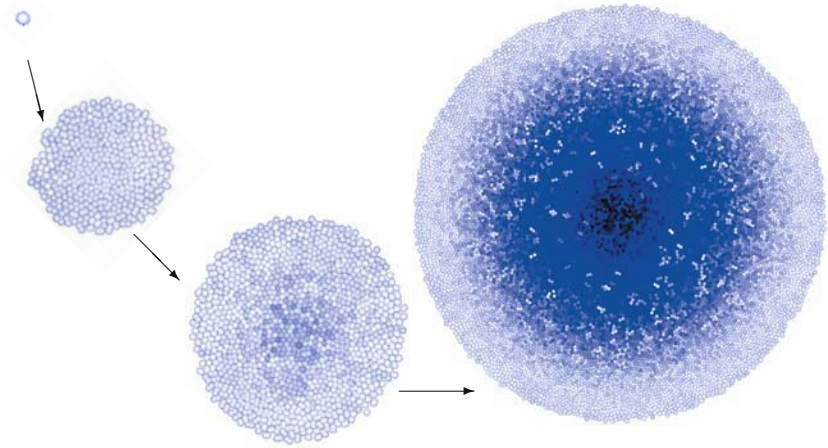

FIGURE 3. Typical monolayer growth scenario (see text for more details).

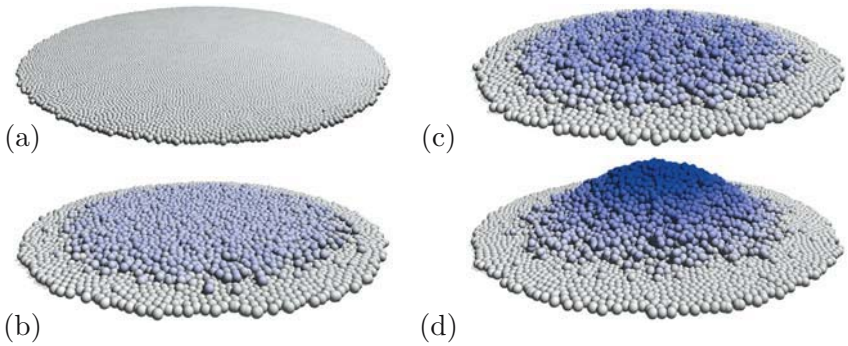

FIGURE 5. Simulated knockout of growth control mechanisms (see text for more details).

FIGURE 6. Comparison of the simulation result on growing cell populations on a flat substrate in the absence of contact inhibition of growth, anchorage-dependent growth control and anoikis (see text for more details).

Chapter III.2 Models with Lattice-free Center-based Cells Interacting with Continuum Environment Variables, *John C. Dallon*

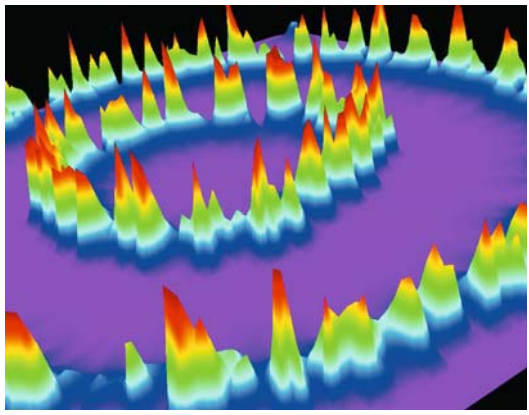

FIGURE 2. Concentration of cAMP (see text for more details).

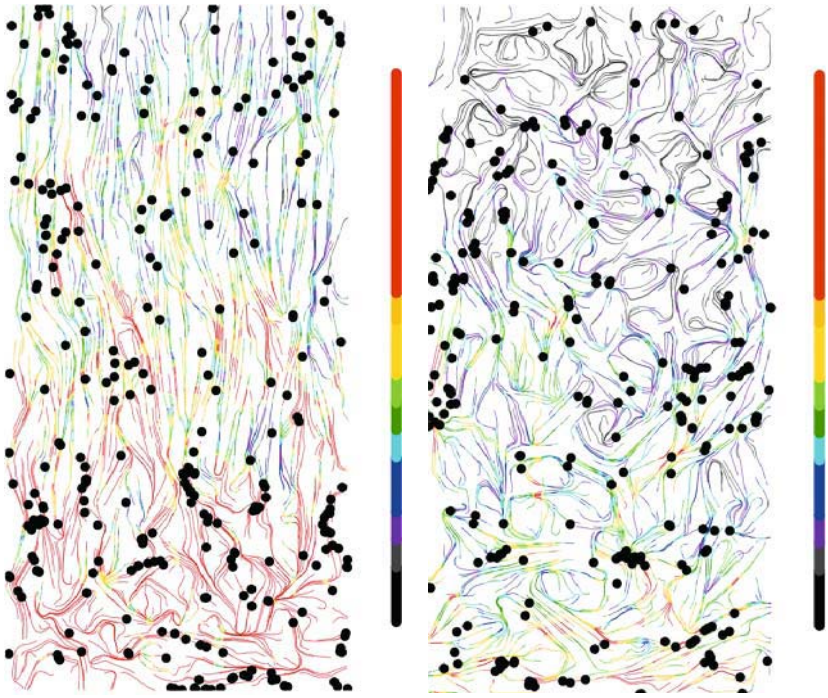

FIGURE 11. The collagen orientations for typical wound healing simulations (see text for more details).

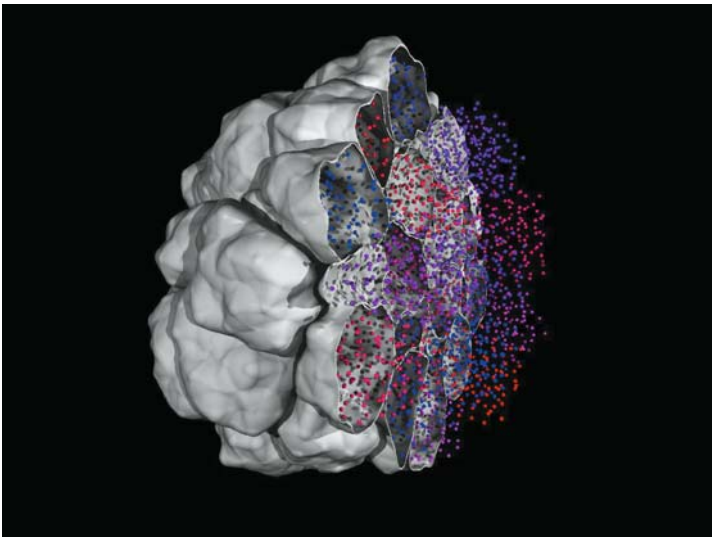

FIGURE 12. A cut-away view of the cell cluster. The actual elements of each of the cut cells are displayed, with different colored elements corresponding to different cells.

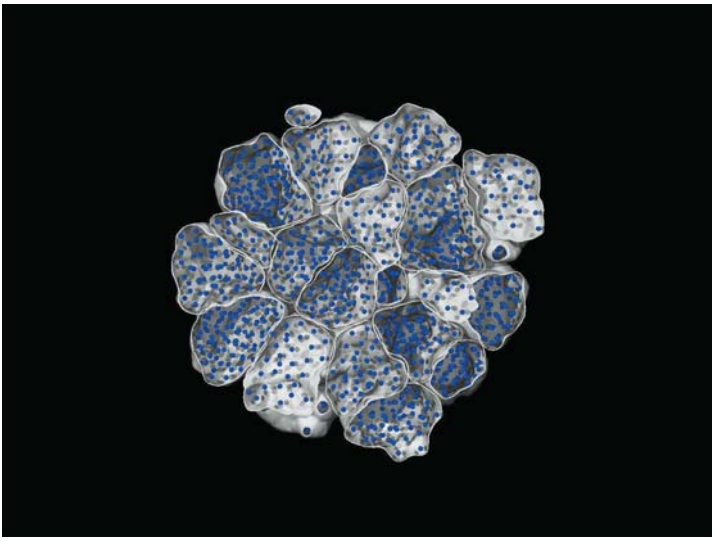

FIGURE 13. Head-on view of the bisected cluster, showing the elements embedded in their parent cells.

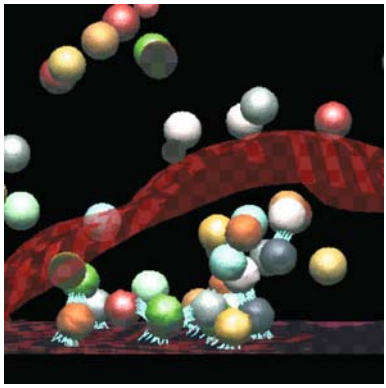

FIGURE 5. Close up of a small aggregate that formed during a 3D microscale simulation (see text for details).

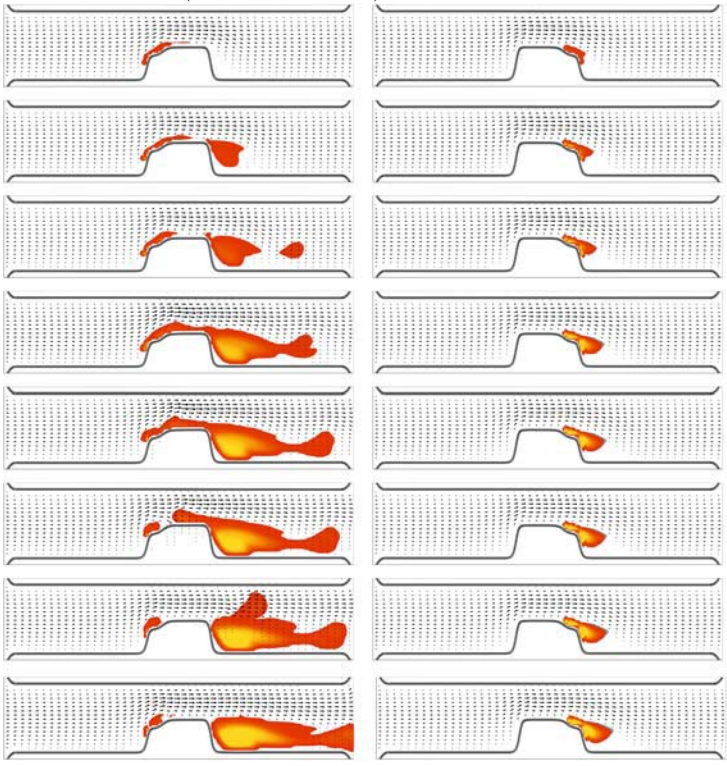

FIGURE 9. Snapshots at corresponding times from two simulations of thrombosis (see text for details).

Chapter IV.2 A 3-D Deformable Ellipsoidal Cell Model, with Cell Adhesion and Signalling *Eirikur Palsson*

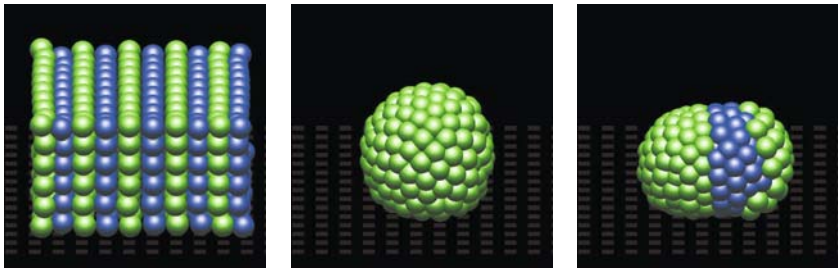

FIGURE 11. These figures show the initial state, the sorting after 60 min and the final state when mixing Dd pre-spore (green) and pre-stalk (blue) cells (see text for details).

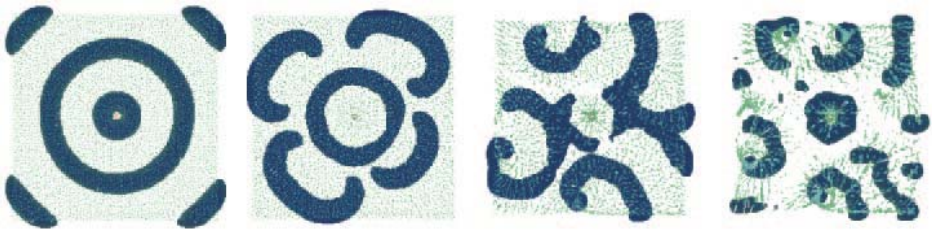

FIGURE 13. Aggregation of Dictyostelium cells in response to cAMP signaling from pacemaker cells that are located in the center (red cells), see text for more details.

a)

b)

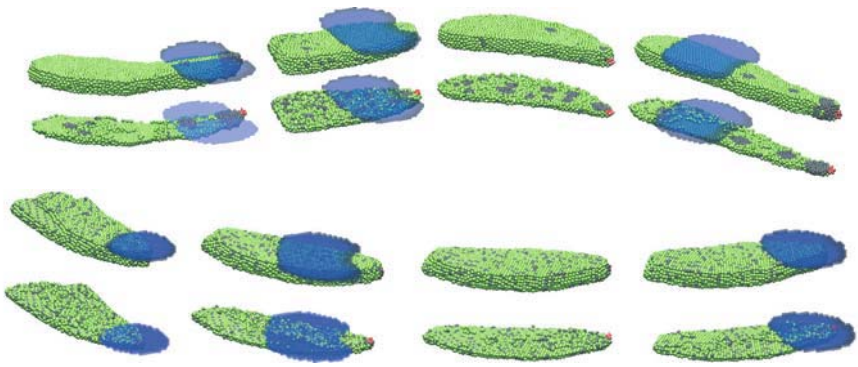

FIGURE 18. These snapshots show the sorting of pre-stalk, grey cells, and pre-spore, green cells, in a *Dictyostelium* slug for different cell adhesion (see text for more details).

Chapter IV.2 A 3-D Deformable Ellipsoidal Cell Model, with Cell Adhesion and Signalling *Eirikur Palsson*

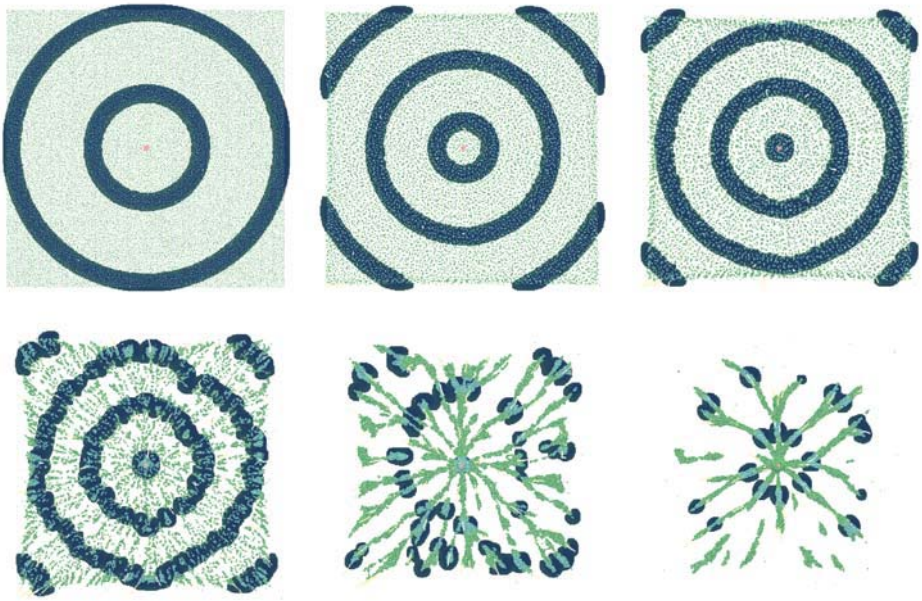

FIGURE 12. see text for more details.

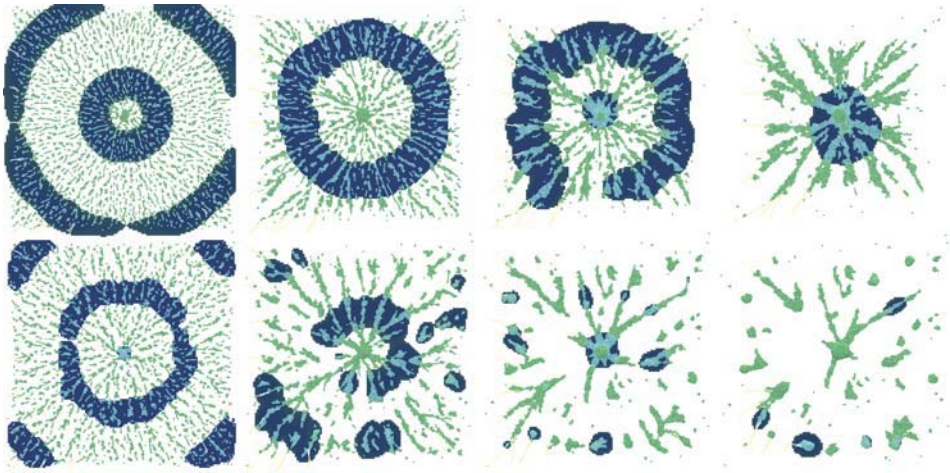

FIGURE 14. see text for more details.

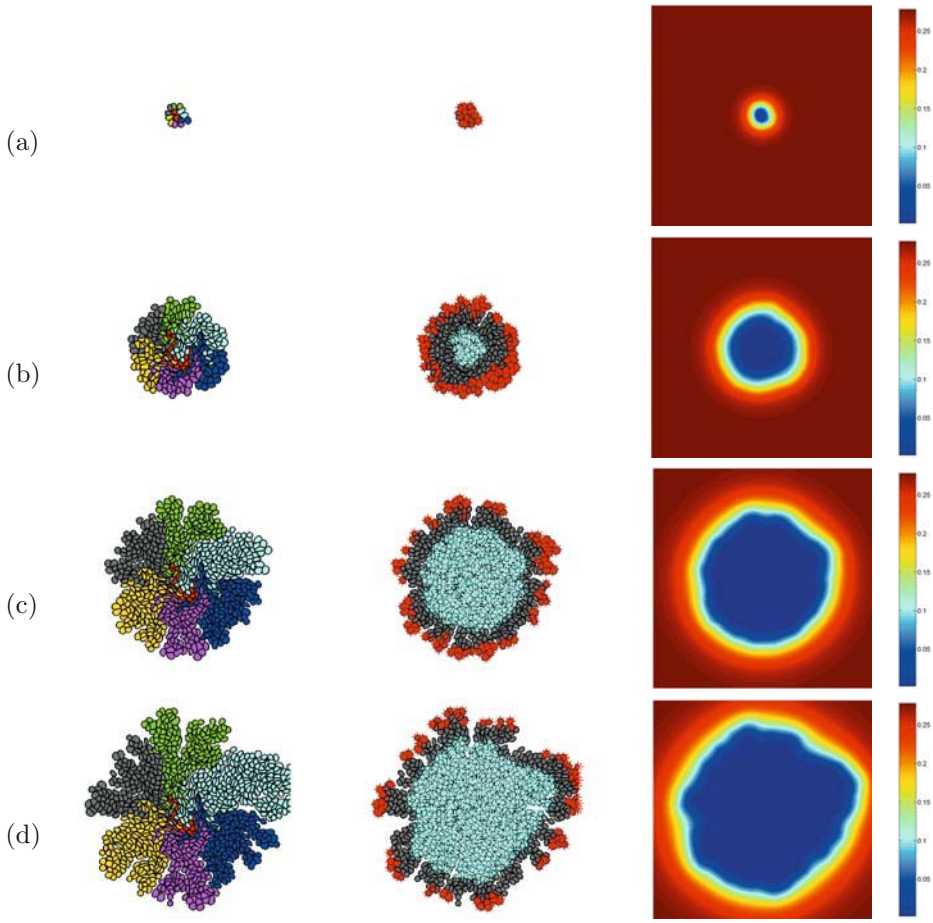

FIGURE 6. Clonal growth of tumour cells due to the competition for nutrients (see text for more details).

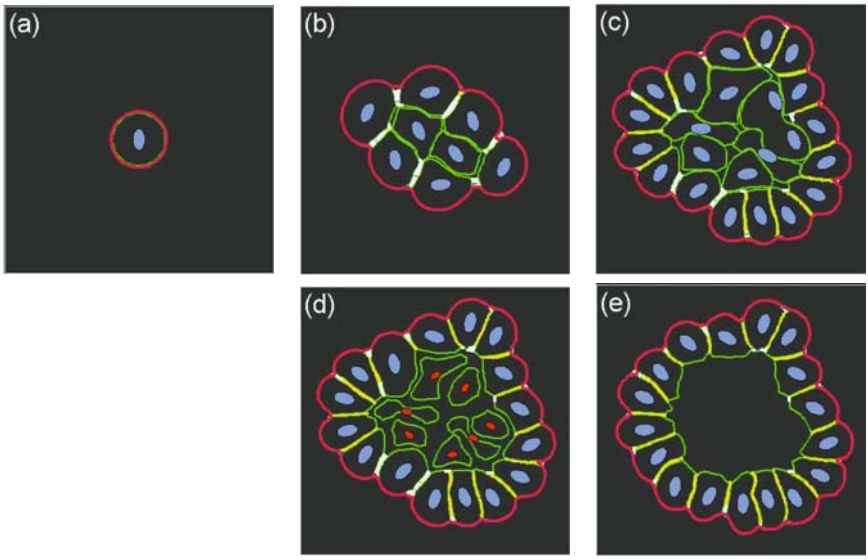

FIGURE 7. Development of a hollow epithelial acinus (see text for more details).

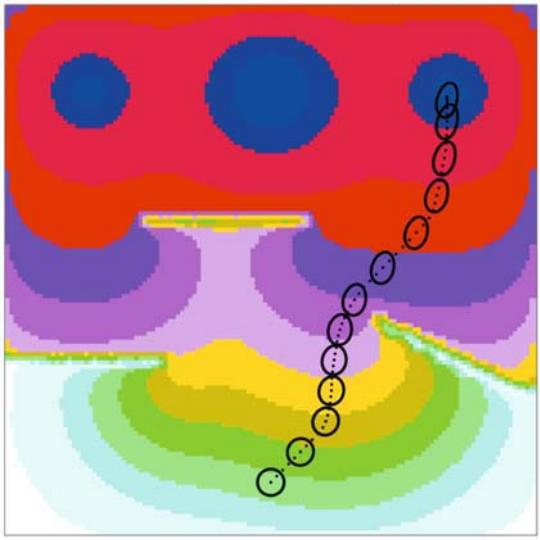

FIGURE 8. Cell chemotactic and/or haptotactic motility (see text for more details).